The Concentration of Lithium in Plagioclase Crystals of the Minoan Tephra, (Santorini, Greece)

Sandra Panienka

INAUGURAL - DISSERTATION

zur
Erlangung der Doktorwürde
der
Naturwissenschaftlich-Mathematischen
Gesamtfakultät
der
Ruprecht-Karls-Universität
Heidelberg

Vorgelegt von
Diplom-Mineralogin Sandra Panienka
aus: Marburg
Tag der mündlichen Prüfung: 27.01.2012

Thema

The Concentration of Lithium in Plagioclase Crystals of the Minoan Tephra, (Santorini, Greece)

Gutachter: Prof. Dr. Rainer Altherr
Dr. habil. Thomas Zack

Nothing happens in contradiction to nature, only in contradiction to what we know of it.

Special Agent Dana Scully, The X-Files

Contents

Kurzfassung

Im Rahmen dieser Arbeit wurden Gesteine aus den Ablagerungsprodukten der Minoischen Eruption, die im zweiten Jahrtausend vor Christus auf der ägäischen Vulkaninsel Santorin zu einem Kalderakollaps führte, analysiert. Es wurden insgesamt zehn Bimsproben aus den vier Minoischen Einheiten (A–D) – darunter eine kristallreiche Probe – und zehn mafische Schlackekomponenten untersucht. Der Schwerpunkt lag auf Lithiumkonzentrations- und Lithiumisotopenprofilen, die mit Hilfe eines Sekundärionenmassenspektrometers (SIMS) in minoischen Plagioklaskristallen gemessen wurden.

Innerhalb der Minoischen Einheit A war die Breite der Lithiumkonzentrationsverteilungen am größten, was sich durch besonders hohe und niedrige Lithiumgehalte in den unterschiedlichen Schlackekomponenten widerspiegelte. Die Verteilung von Lithium innerhalb der Bimse variiert kaum innerhalb der Minoischen Einheiten A–D.

Unter Gleichgewichtsbedingungen korreliert Lithium negativ mit dem Anorthit-Gehalt in den minoischen Plagioklasen. Dabei zeigen sich unterschiedliche Steigungen für Plagioklas mit $\overline{X}_{\mathrm{An}} < 0.60$ und $\overline{X}_{\mathrm{An}} > 0.60$. Die Lithiumkonzentration als Funktion des X_{An} lässt sich mit Hilfe zweier Modelle, die auf den Arbeiten von Blundy & Wood (1994) und Coogan (2011) basieren, modellieren und über einen *least squares fit* an die gemessenen Daten anpassen. Daraus ergibt sich ein $\ln K_{\mathrm{D}} > -2.5$ für Lithium in Plagioklasen mit einer schwacher Korrelation und ein $\ln K_{\mathrm{D}} \leq -5$ für Lithium in Plagioklasen mit starker Korrelation. Die Mischkristallreihe zwischen den Plagioklas-Endgliedern Albit und Anorthit ist nicht kontinuierlich, sondern durch Phasenübergänge und Mischungslücken charakterisiert. Die Unterschiede in den $\ln K_{\mathrm{D}}$ Werten können daher wahrscheinlich auf den $C\overline{1} \rightleftharpoons I\overline{1}$ Phasenübergang in Plagioklas zurückgeführt werden, der bei magmatischen Temperaturen ungefähr im Bereich von An_{55-60} verläuft. Minoische Plagioklase mit schwacher Korrelation befinden sich im $C\overline{1}$ Phasenfeld, während Plagioklase mit starker Korrelation im $I\overline{1}$ Phasenfeld liegen.

Neben der Lithium-Verteilung im Gleichgewicht zeigen minoische Plagioklase außerdem Lithium-Diffusion an den Kristallrändern. Lithium diffundiert (mit einigen Ausnahmen) auf einer Länge von $30 - 40\,\mu\mathrm{m}$ in den Plagioklas. Auf den ersten Mikrometern ist die Diffusion des Lithiums in den Kristall durch Diffusion aus dem Kristall heraus überprägt. $\delta^7\mathrm{Li}$ Isotopenprofile zeigen außerdem, dass die Diffusion

in den Plagioklas hinein von einer Phase ausging, die im Lithium stärker angereichert war, als dies durch Matrixglas oder Schmelzeinschlüsse widergespiegelt wird.

Die unterschiedlichen Diffusionsprofile wurden mit Hilfe eines Zweistufen-Modells in einem Programm für Diffusionsmodellierung rekonstruiert. Diffusion aus einer im Lithium angereicherten Phase heraus und in den Plagioklas und die Schmelze hinein konnte für Zeiträume von wenigen Sekunden bei magmatischen Temperaturen ($\sim 860\,^\circ$C) simuliert werden und fand wahrscheinlich in der Magmenkammer kurz vor der Eruption statt. Profile, die das Herausdiffundieren von Lithium an Plagioklasrändern zeigen, sind nach der Ablagerung bei $\sim 300\,^\circ$C entstanden. Bei $\sim 300\,^\circ$C sind die Lithium-Diffusionskoeffizienten in Glas und Plagioklas so verschieden, dass innerhalb von 40 Tagen das Glas homogenisiert werden kann, während im Plagioklas nur am äußersten Rand ($\sim 10\,\mu$m) Lithium aus dem Kristall heraus diffundiert.

Daraus folgt, dass Verteilungskoeffizienten, die für Lithium zwischen Plagioklas und Matrixglas berechnet werden, in diesem Fall falsch sind. Denn diese würden unter der (falschen) Annahme ermittelt, dass die Ränder der Plagioklase und das Glas in der Matrix die Lithiumkonzentrationen im Gleichgewicht kurz vor der Eruption bei magmatischen Temperaturen widerspiegeln. Das Lithium, das in der Schmelze kurz vor dem Ausbruch angereichert wurde, hatte allerdings genug Zeit, nach der Ablagerung wieder aus dem Glas heraus zu entgasen und die Li-Konzentration am Rand der Plagioklase war *nicht* im Gleichgewicht.

Abstract

For this thesis lithium concentration and δ^7Li profiles were analyzed by secondary ion mass spectrometry in plagioclase phenocrysts sampled from tephra of the Late Bronze Age Minoan eruption that took place at Santorini, Greece, in the second millenium B.C. In the four Minoan Units A–D lithium concentrations are most variable in Minoan A, which is due to the wide span of concentrations found in plagioclase of mafic Minoan scoria clasts that were erupted simultaneously. Lithium concentrations in plagioclase of the pumice samples were almost homogeneous throughout all units.

Under equilibrium conditions lithium shows a negative correlation with anorthite content in Minoan plagioclase. Based on this correlation, plagioclase crystals can be divided into two groups: (1) Plagioclase crystals with a weak correlation and $\overline{X}_{An} < 0.60$, and (2) Plagioclase crystals with a strong correlation and $\overline{X}_{An} > 0.60$. Two simple models based on Blundy & Wood (1994) and Coogan (2011) were applied and fit to the observed data by performing a least squares fit.

Fitting resulted in a $\ln K_D > -2.5$ for plagioclase with $\overline{X}_{An} < 0.60$ and a $\ln K_D \leq -5$ for plagioclase with $\overline{X}_{An} > 0.60$. This phenomenon may be associated with the $C\overline{1} \rightleftharpoons I\overline{1}$ transition line which divides the $C\overline{1}$ phase field from the $I\overline{1}$ phase field close to An$_{55-60}$ at magmatic temperatures. Plagioclase crystals with $\overline{X}_{An} < 0.60$ plot in the $C\overline{1}$ phase field while plagioclase crystals with $\overline{X}_{An} > 0.60$ plot in the $I\overline{1}$ phase field.

Disequilibrium of lithium in Minoan plagioclase phenocrysts is characterized by diffusion of lithium into the crystal on short diffusion lengths, mainly of $\sim 30 - 40\,\mu$m. Diffusion profiles are overprinted by a loss of lithium at the rim. δ^7Li profiles show that diffusion into the crystal was caused by a phase with higher lithium concentrations than recorded by melt inclusions or matrix glass. Recreation of analyzed lithium profiles by applying a two-step model based on numerical diffusion modeling yielded the following results: 1. Diffusion into the crystal took place at $\sim 860\,^\circ$C prior to the eruption at time scales of seconds and must have been caused by a lithium-rich vapor flux from deeper parts of the Minoan plumbing system. 2. Diffusive loss of lithium took ~ 40d at $\sim 300\,^\circ$C and must have happened after emplacement due to degassing of lithium from the pumice deposits.

These results have an important impact on lithium partition coefficients calculated under the assumption that the analyzed lithium concentrations in pumice ma-

trix glass reflect those in the melt prior to the eruption. Those partition coefficients are incorrect, because all the lithium concentrations analyzed in matrix glass represent those after degassing of lithium from the pumice deposits came to a hold at much lower temperatures, and because the lithium concentrations at the rim of the plagioclases do not represent an equilibrium.

1. Introduction

Kallisti—the most beautiful—was a name given to Santorini by the Phoenicians, a maritime trading culture that founded a site on the island around 1200 BC (alta-maresantorini.com, 2011).

Santorini is indeed of an extraordinary beauty rarely found amongst islands around the world. Its caldera is transected by the Aegean Sea allowing a breath-taking view at two small, relatively young islands located in its middle. The older islands represent caldera wall remnants and give a stunning insight into Santorini's volcanic history—a history shaped by multiple explosive eruptions (Druitt *et al.*, 1989, 1999).

The most significant eruption by far to have ever occurred on Santorini is the Late Bronze Age Minoan eruption that devastated the island about 1620 BC (Friedrich *et al.*, 2006). This eruption is thought to have buried a Minoan settlement located at Akrotiri under large amounts of white pumice, while heavy ashfall and a disastrous tsunami caused by the eruption are under debate for the demise of the Minoan civi-lization on the island of Crete (Marinatos, 1939; Antonopoulos, 1992; Lamoreaux, 1995; Callender, 1999; Pareschi & Boschi, 2006).

Santorini is currently considered to be the most active volcano in the Aegean region, and the Minoan eruption itself has been one of the most violent in the Mediterranean area (Stiros *et al.*, 2003). The last eruption occurred in AD 1950 on the post-caldera Kameni islands (Martin *et al.*, 2006). Santorini is a potentially dangerous volcano for the 13.400 people that inhabit the island today, which leads us to the importance of understanding magma chamber dynamics and forecasting volcanic eruptions.

Sparks (2003) wrote that volcanoes are complex dynamic systems that have the potential to behave highly unpredictable. Berlo *et al.* (2010) list a number of key parameters that may influence how and when eruptions take place. The magma ascent rate is such a parameter, which itself is influenced by the amount of dissolved gas within the magma and the interplay of degassing and crystallization.

Many volcanoes show regular periodic eruption patterns expressed by recurrence time intervals between their eruptions. There are volcanoes like Sangay in Ecuador that have been erupting almost daily, while others like Arenal in Costa Rica erupt on a 0.1 to 10-year timescale. Mount St. Helens or Mount Pinatubo even have as long as hundred to hundreds of years between eruptions (Davidson & De Silva,

1999). Recurrence time intervals for major explosive eruptions on Santorini are much larger—about 30 ka—while smaller eruptions on the Kameni islands occurred in intervals of 10 to several 100 years (Druitt *et al.*, 1999).

Sparks (2003) figured that these eruption patterns are usually constrained by physical laws, and that therefore it should be possible to approach these laws empirically and by modeling.

Many old text books on volcanism depict drawings of huge single magma chambers beneath volcanic edifices. These chambers are usually connected to the crater by a single conduit; sometimes a second conduit was drawn to illustrate a flank eruption. But in recent years petrological, textural, geochemical and geophysical methods have changed our knowledge on traditional magma chamber models. Nowadays geoscientists speak of complex volcanic plumbing systems (Zellmer & Annen, 2008; Blundy *et al.*, 2008; Kahl *et al.*, 2011), defined by multiple reservoirs which are connected by different pathways through which magmas migrate and mingle until they finally reach the surface.

For Santorini a rather simple magma chamber model was developed by Druitt *et al.* (1999), which is characterized by a mostly silicic magma body inside the chamber and occasional replenishment by mafic to intermediate magmas—especially prior to the eruption (Fig. 1.1).
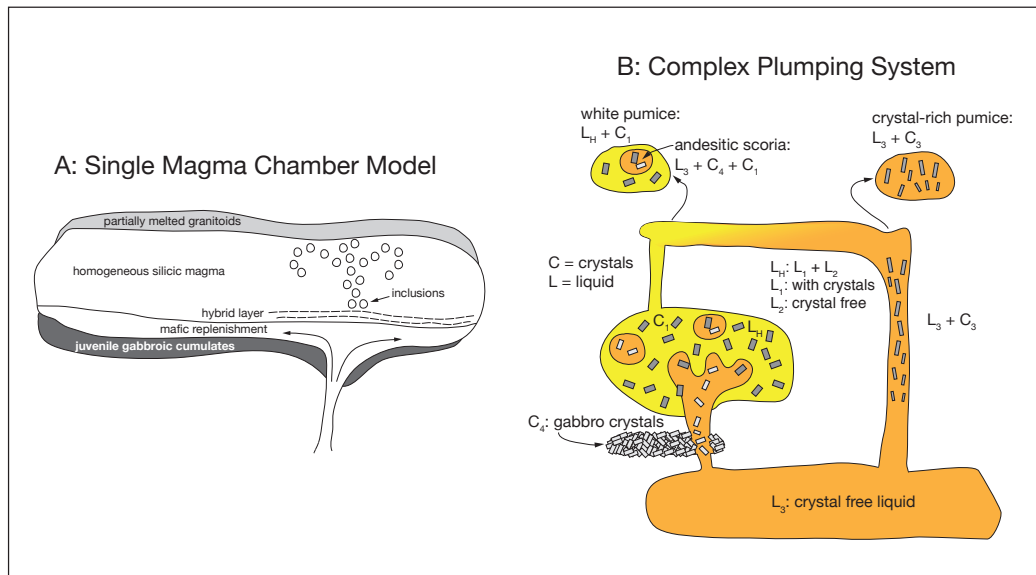

Fig. 1.1. Single magma chamber model *vs* complex plumbing system. Slightly modified sketches of the Minoan magma chamber after Druitt *et al.* (1999) (A) and Martin *et al.* (2010) (B).

Cottrell *et al.* (1999) suggested a two-stage model based on water and sulfur content of melt inclusions in plagioclase feldspars. They reconstructed that the main magma body must have been stored at $> 200\,\text{MPa}$, and later moved on to $\sim 50\,\text{MPa}$ before the eruption commenced.

The most detailed model for the Minoan eruption was developed by Martin *et al.* (2010). They used Sr isotopes to distinguish different populations of glass and plagioclase. The insight gained from their data revealed a rather complex plumbing system beneath Santorini. The white Minoan pumice must have been formed from two isotopically distinct liquids (Fig. 1.1). The andesitic scoria clasts that can be found within the white pumice are supposed to be derived from an initially crystal-free liquid that intruded and entrained gabbro before entering the main chamber, while the crystal-rich pumice is supposed to have formed from the same liquid as the andesitic scoria, but erupted from a separate vent without entraining the gabbro (see also Chapter 2).

1.1. Plagioclase Feldspar in Igneous Rocks

Plagioclase feldspar is the most abundant mineral in the continental crust and it is ubiquitous in igneous rocks, where it can be found from basalts to rhyolites—it basically crystallizes over the entire compositional and temperature range of igneous differentiation products (Ginibre *et al.*, 2002; Costa *et al.*, 2003; Bédard, 2006).

Plagioclase occurs as large $2 - 20\,\text{mm}$ phenocrysts in mafic to intermediate volcanic rocks (Davidson & Tepley III, 1997), where it is thought to crystallize due to decompression, degassing or by cooling (Ruprecht & Wörner, 2007).

Sluggish NaSi-CaAl diffusion rates (Grove *et al.*, 1984; Stamatelopoulou-Seymour *et al.*, 1990) in plagioclase preserve records of the chemical and physical evolution of magma chambers during its growth (Anderson, 1984; Pearce *et al.*, 1987; Blundy & Wood, 1991; Davidson & Tepley III, 1997) and help to identify processes, such as differentiation, replenishment, magma mixing, and crystal cycling (Price *et al.*, 2005; Smith *et al.*, 2009; Martin *et al.*, 2010).

The growth zones of plagioclase are characterized by changes in anorthite content (compositional zoning), textural discontinuities, inclusion zones, and reaction rims (Ginibre *et al.*, 2002). The compositional zoning of plagioclase spans a wider fraction of the solid solution series than any other mineral and it is therefore of particular interest in the interpretation of magma chamber processes (Costa *et al.*, 2003).

Textures in Plagioclase

A variety of different textures are observed in plagioclase phenocrysts and can be interpreted as being archives for different dynamical processes in magma chambers. The most common ones are briefly introduced below and in Fig. 1.2.

Normal zoning is defined by an anorthite-rich core that is surrounded by a rim of lower anorthite content (Fig. 1.2). This type of texture can develop from crystallization in a simple closed decompressing water saturated magmatic system (Smith *et al.*, 2009) due to degassing and cooling of magma, retention within convective cycling (Singer *et al.*, 1993), and during crystallization in the rim facies of a magma chamber in which rapid cooling and removal of water from the residual melt take place (Loomis & Welber, 1982).

Reverse zoning is the opposite of normal zoning (Fig. 1.2). It is usually attributed to magma mixing processes (Singer *et al.*, 1993; Blundy *et al.*, 2006) or heating due to exothermic crystallization (Blundy *et al.*, 2006).

Oscillatory zoning is another prominent texture which is defined by fine concentric euhedral zones of contrasting anorthite content. It can be related to convective processes in a magma chamber (Homma, 1932; Singer *et al.*, 1995; Kuritani, 1998; Tepley III *et al.*, 1999; Costa & Singer, 2002), fluctuations in anorthite content due to slow kinetics during crystal growth (Bottinga *et al.*, 1966), latent heat release during crystal growth (Blundy *et al.*, 2006), increase in overpressure as a result of crystallization and fluctuations in X_{H_2O} during crystallization or due to decompression driven crystallization during ascent (Humphreys *et al.*, 2006; Smith *et al.*, 2009).

Other common textures in plagioclase are variably and sometimes inconsistently described as sieved, dusty, spongy, honeycomb, patchy, resorbed or corroded (e.g. Luhr & Carmichael, 1980; Tsuchiyama, 1985; Stamatelopoulou-Seymour *et al.*, 1990; Singer *et al.*, 1993; Wallace & Carmichael, 1994; Singer *et al.*, 1995; Davidson & Tepley III, 1997; Nakamura & Shimakita, 1997; Kuritani, 1998; Coombs *et al.*, 2000; Luhr, 2000; Kuscu & Floyd, 2001; Chertkoff & Gardner, 2004; Stewart & Pearce, 2004; Blundy *et al.*, 2006; Humphreys *et al.*, 2006; Reubi & Blundy, 2008; Smith *et al.*, 2009; Crabtree & Lange, 2011).

Resorption phenomena leading to patchy cores or irregular oscillatory zoning bands in plagioclase are thought to develop from degassing (Stamatelopoulou-Seymour *et al.*, 1990), raised temperature T (Tepley III *et al.*, 1999), turbulent magma movement or convection in the magma chamber (Loomis & Welber, 1982; Singer *et al.*, 1995).

Crabtree & Lange (2011) suggest that patchy textures are induced by crystallization from degassing, while Humphreys *et al.* (2006) discuss H_2O-undersaturated
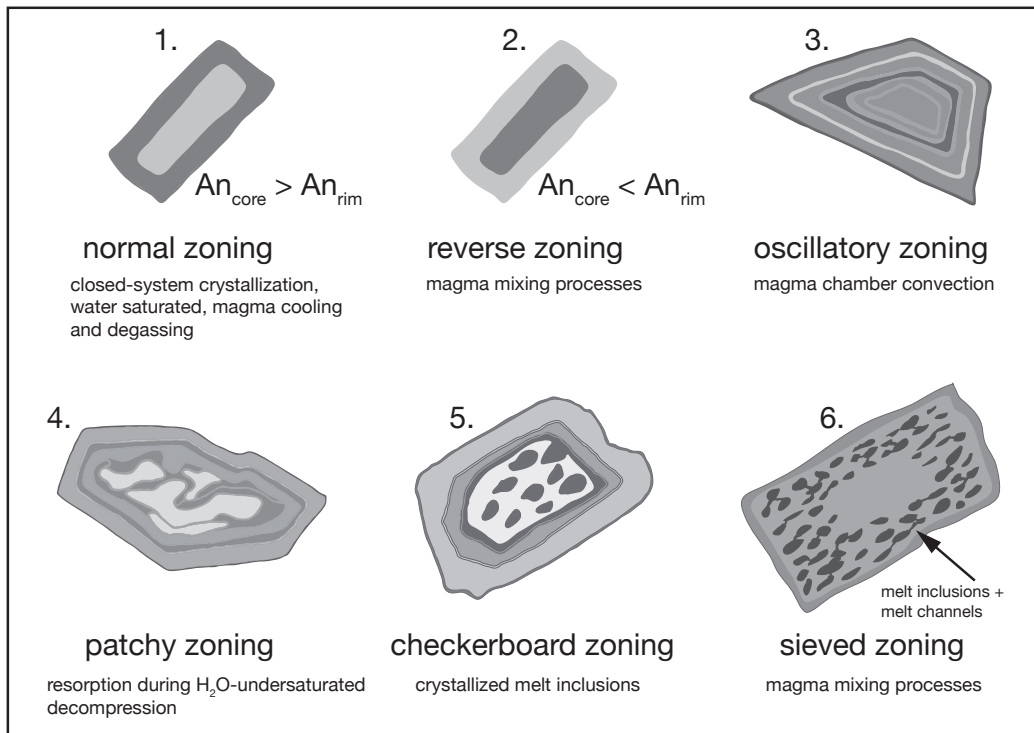
Fig. 1.2. Sketches of plagioclase textures commonly found in igneous rocks. Theories for the development of these kinds of textures are introduced in the text. Coloration is based on plagioclase appearance in back-scattered electron (BSE) images (Scanning Electron Microscopy). Light grey shades represent areas with higher mean atomic number (higher X_{An}) while darker grey shades represent areas with a lower mean atomic number (lower X_{An}).

decompression as a possible explanation for this type of texture. Kuritani (1998) believe that patchy zoning develops due to the transition of plagioclase between the magma chamber body and a low temperature H_2O-rich mushy boundary layer along the chamber's wall.

Checkerboard or spongy patterns in plagioclase may be derived from crystallizing melt inclusions (Blundy *et al.*, 2006). Commonly, areas of low anorthite content are found in a core of higher anorthite content; sometimes single melt inclusions are still visible in these checkerboard zones. Davidson & Tepley III (1997) assume that plagioclase crystals immerse from dacitic into mafic magma which leads to the development of spongy textures.

Sieved textures are characterized by multiple tiny melt inclusions interconnected by thin melt channels. These are either concentrated in a single anorthite zone or between two zones. A common explanation for sieve textures is magma mix-

ing (Tsuchiyama, 1985; Sparks & Marshall, 1986; Eichelberger, 1978; Davidson & Tepley III, 1997; Tepley III *et al.*, 1999; Coombs *et al.*, 2000; Kuscu & Floyd, 2001; Humphreys *et al.*, 2006). Changes in *T* and/or *P* and/or *X* (composition) leading to growth and/or dissolution are discussed for this type of texture (Stamatelopoulou-Seymour *et al.*, 1990; Nelson & Montana, 1992; Singer *et al.*, 1993; Coombs *et al.*, 2000; Stewart & Pearce, 2004).

1.2. Trace Elements in Plagioclase

As it is not possible to distinguish important factors such as changes in *P*, *T*, melt composition and H_2O content from textures alone, these need to be combined with minor- and trace-element analyses for further interpretations (Ginibre *et al.*, 2002).

Trace element zoning is therefore of great importance in our understanding of the chemical and physical evolution of magma chamber processes recorded by plagioclase phenocrysts. They also play an important role in deciphering those processes that lead to a certain kind of texture (Smith *et al.*, 2009). Blundy & Wood (2003) mention that low concentrations and chemical diversity make trace elements especially attractive for analyses because they are passive, have negligible influence in the outcome of particular processes and different elements will behave differently in a certain situation.

Plagioclase feldspar incorporates many trace elements making it especially valuable for the study of melt evolution through fractionation, partial melting or mixing (Bindeman *et al.*, 1998, and references therein).

In this study the light elements Li, Be and B as well as Mg, Sr and Ba were analyzed in plagioclase.

The light elements Li, Be and B and their isotopes are very sensitive tracers for geochemical fractionation especially during subduction-related processes due to their ability to fractionate differently between mineral/melt, mineral/fluid and fluid/melt systems. Li, Be and B behave incompatibly in partial melting processes in the Earth's upper mantle, with $D_B \leq D_{Be} < D_{Li}$. The experimentally determined fluid/mineral partition coefficients by Brenan *et al.* (1998a) are in the following order: $D_B < D_{Li} << D_{Be}$.

Distribution coefficients between mantle minerals and melts are $D_{Li} \approx 0.1 - 0.2$ (Ryan & Langmuir, 1987; Blundy *et al.*, 1998; Brenan *et al.*, 1998a; Blundy & Dalton, 2000), $D_{Be} \approx 0.02 - 0.04$ (Tatsumi & Isoyama, 1988; Ryan & Langmuir, 1988; Brenan *et al.*, 1998a) and $D_B \approx 0.01 - 0.03$ (Ryan & Langmuir, 1993; Chaussidon & Jambon, 1994; Brenan *et al.*, 1998a). Be can behave compatible when plagioclase or cordierite are present during partial melting in the Earth's crust (Evensen

& London, 2002, 2003). Li and B are extremely mobile elements which may fractionate into the fluid phase under mineral/fluid or melt/fluid equilibrium conditions. Be is hardly soluble in fluids, but it can build complexes for transport in F- and/or Cl-rich fluids (Webster *et al.*, 1987; Domanik *et al.*, 1993; Brenan *et al.*, 1998a). The solubility of Be increases at higher pressures ($< 0.6 - 1.0\,\mathrm{GPa}$) (Kessel *et al.*, 2005).

Diffusion profiles of the lithophile trace elements Mg, Sr and Ba are of special interest, as they can be used to calculate residence times of plagioclase phenocrysts in magma chambers (Zellmer *et al.*, 2003; Costa *et al.*, 2003) and therefore contribute to volcanic hazard issues and their mitigation.

In the following paragraphs Li, Be, B, Mg, Sr and Ba are briefly introduced as significant trace elements that were analyzed by SIMS (Secondary Ion Mass Spectrometry) for this thesis.

Lithium – Li is a monovalent ion of lithophile character. It can be found in 4-, (4+2)-, 6- or 8-fold coordination by oxygen in terrestrial systems (Wenger & Armbruster, 1991; Olsher *et al.*, 1991). Li's ionic radius is $76\,\mathrm{pm}$ for six-fold coordination. Its size is very similar to eight-fold coordinated Mg ($72\,\mathrm{pm}$) and Fe^{2+} ($78\,\mathrm{pm}$). In Mg-Fe-rich mineral phases Li can therefore easily substitute for these elements (Chen, 1999).

Lithium isotopes Li has two stable isotopes, ^{6}Li and ^{7}Li, with a natural distribution of 7.5 % and 92.5 %. The two isotopes have a relative mass difference of 16 % leading to significant variations in the ^{6}Li/^{7}Li ratio. There is an equilibrium fractionation between crystal and melt that is only be seen at temperatures below 600°C (Tomascak *et al.*, 1999; Teng *et al.*, 2006b). Diffusion on the other hand mostly works at high temperatures (Teng *et al.*, 2006b) where the heavier ^{7}Li will prefer the site with the smaller coordination and will therefore fractionate into the fluid in a rock/fluid system (Tomascak, 2004). In general, ^{6}Li will diffuse faster than ^{7}Li (Richter *et al.*, 2003; Parkinson *et al.*, 2007), a behavior which can be used to estimate time scales of magmatic processes (e.g. Sonntag, 2007).

Beryllium – Be is divalent and has exclusively four-fold coordination in minerals (Hawthorne & Huminicki, 2002). Be^{2+}'s ionic radius is $27\,\mathrm{pm}$ for four-fold coordination and is similar to the radius of Si^{4+} (Shannon, 1976). Due to a difference in charge, substitution between both elements is limited. Be rather substitutes for tetrahedral Al^{3+} ($39\,\mathrm{pm}$) or B^{3+} ($11\,\mathrm{pm}$).

Boron – B   is exclusively trivalent and in minerals, melts and fluids it is trigonally or tetrahedrally coordinated (Hawthorne & Huminicki, 2002). B forms covalent bonds with oxygen in the form of $B(OH)_3$, $B(OH)_4^-$. The ionic radius in tetrahedrally coordinated B is 11 pm, but 1 pm in trigonally coordinated B. It substitutes for C in calcite, aragonite and diamond. In silicate minerals B^{3+} can substitute for Si^{4+} on the tetrahedral position. This can lead to a slight distortion of TO_4-units and it makes a charge balance necessary (Hawthorne & Huminicki, 2002).

Boron isotopes   Boron has two stable isotopes, ^{10}B and ^{11}B, with a natural isotope distribution of 19.9 % and 80.1 %. The isotopic fractionation behavior can be used for evaluating geochemical processes. For example, B isotopes can be used to prove the involvement of subduction related materials in fluids, serpentinites and island-arc basalts (Ishikawa & Nakamura, 1994; Bebout *et al.*, 1999).

There are large differences in the fractionation behavior due to the tetrahedrally and trigonally coordination of B to oxygen in minerals, melts and fluids. ^{11}B usually goes into the material with higher bond strength (Chacko *et al.*, 2001), which is stronger in trigonal coordination and therefore ^{11}B will preferentially be incorporated in these kind of sites. This leads to a relative accumulation of ^{10}B at tetrahedrally coordinated sites (Palmer & Swihart, 2002).

Magnesium – Mg   Magnesium is a lithophile element that is divalent under natural conditions and is usually in 6-fold coordination as a major constituent in many rock-forming minerals. In this coordination state its ionic radius is 72 pm. It is highly compatible during mantle melting and remains compatible during crystallization of magmas due to olivine or clinopyroxene being liquidus phases.

Magnesium is mostly concentrated in the Earth's mantle but is also abundant in the oceanic and the lower continental crust. In highly evolved igneous systems it is a minor and trace element (Mittlefehldt, 1999). Based on its distribution coefficient, Mg is of particular interest as a trace element for estimating residence times in plagioclase feldspars as it diffuses two orders of magnitude faster than Sr (Cherniak & Watson, 1994; Giletti & Casserly, 1994; Costa *et al.*, 2003).

Strontium – Sr   Sr is a lithophile element that mostly substitutes for Ca^{2+} in plagioclase and calcite or for K^+ in alkali feldspars. Therefore its distribution is controlled by the presence of feldspars. Its mineral-melt distribution coefficient for feldspar minerals is greater than unity. It is enriched in the crust relative to the Earth's mantle where its overall abundance is $\sim 260\,\mu g/g$. In mantle systems it is incompatible and therefore enriched in melts (Simmons, 1999).

8

Barium – Ba Barium is a lithophile element of divalent character that mainly substitutes for K^+ in igneous and metamorphic rocks. It can also substitute for Pb^{2+}, Sr^{2+} and Ca^{2+}. Potassium feldspar and micas are the most important carriers of Ba in the silicate mineral group. Its average concentration in the Earth's crust is $\sim 500\,\mu g/g$ and $\sim 728\,\mu g/g$ in intrusive igneous rocks where its content increases with increasing SiO_2 (Ryan, 1999).

1.3. Background and Aim of the Study

This study investigates trace elements of volcanic phenocrysts, their melt inclusions and matrix glass taken from rhyodacitic pumice and scoria clasts deposited during the violent Late Bronze Age Minoan eruption on Santorini Volcano with an emphasis on lithium in plagioclase.

Plagioclase, clinopyroxene, orthopyroxene, olivine, melt inclusions in phenocrysts and matrix glass were analyzed by EPMA (Electron Probe Microanalysis) and SIMS (Secondary Ion Mass Spectrometry) between 2007 and 2011. Based on analytical results the main emphasis was put on trace element profiles in plagioclase and the investigation of matrix glass, glass attached to phenocrysts (glass selvages) and melt inclusions in phenocrysts, where especially lithium, next to Be, B, Mg, Sr and Ba, was analyzed. This thesis contributes to several SIMS projects based on the investigation of the light elements lithium, beryllium and boron in subduction zone settings that were started by the research group Petrology and Geochemistry (Institute of Earth Sciences, University of Heidelberg) in 2000. For further information on publications, please see the research group's publication website (http://www.rzuser.uni-heidelberg.de/~hb6/index_en.html).

Cabato (2006) was one of the first to deal with the *in situ* analysis of light elements in volcanic phenocrysts from the Aegean volcanic arc, and one of the questions that couldn't be answered satisfactorily was the one of a possible dependence of the Li partition coefficient between melt and plagioclase on anorthite content.

Bindeman *et al.* (1998) for example showed, that Li is moderately incompatible in plagioclase, but his experiments yielded no systematic variations in plagioclase-melt partition coefficients with varying temperature or anorthite content, so he assumed that the Li partition coefficient between plagioclase and melt is almost independent from plagioclase composition.

Sonntag (2007) however presented high resolution Ca-Li profiles in plagioclase analyzed by SIMS clearly showing that Li in plagioclase is correlated with anorthite content, and suggested that the partition coefficient might increase from high to low anorthite contents. This is also supported by experiments performed by Coogan

(2011). Sonntag (2007) also suggested that Li might be a tracer for magma chamber processes but due to its high mobility (experiments by Giletti & Shanahan (1997) demonstrated that Li diffusion is rapid in plagioclase) its usage in interpreting magmatic processes is restricted. Therefore lithium is not useful for the determination of plagioclase residence times in magma chambers, but it may be useful for the determination of short time processes during explosive volcanic eruptions like degassing or cooling rates in the upper oceanic crust (Sonntag, 2007; Coogan, 2011, and references therein).

In the framework of studies carried out by our research group, Helbling-Marschall (2011) performed light element analyses on volcanic rocks from Lesbos Island (Aegean volcanic arc) and developed a model based on high temperature devitrification with which she was able to show the degassing of a Li-rich H_2O vapor phase after the deposition of ignimbrite.

The aim of this study is to shed further light on the partition behavior of lithium between plagioclase and melt and its behavior prior, during and after the Minoan eruption.
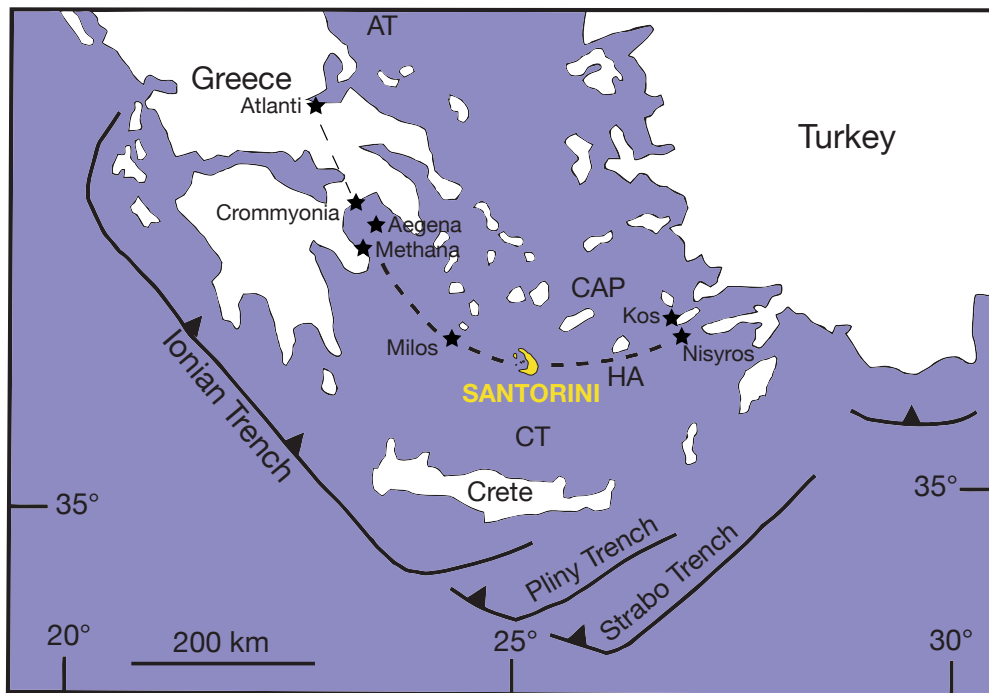
2. Geological Setting of Santorini

Fig. 2.1. Sketch of the Hellenic Arc modified after Druitt *et al.* (1999) and Jackson (1994). **AT**: Anatolian Trough, **CAP**: Central Aseismic Plateau, **HA:** Hellenic Arc, **CT:** Cretan Trough. Santorini (marked in yellow) is located at the southern end of the Hellenic Arc. Santorini is not to scale.

Santorini is an active Quartenary volcanic field located at the southern end of the Hellenic Arc about 120 km north of Crete (Bond & Sparks, 1976; Pfeiffer, 2001) in the Aegean Sea (Fig. 2.1) . Santorini's geologic setting is defined by very complex and subduction-related tectonics with a long geological history (Jackson, 1994; Druitt *et al.*, 1999). This chapter can only provide a very brief overview based on the works mentioned above. For further reading on the entire geologic history of Santorini, the work of Druitt *et al.* (1999) and references therein is highly recommended.

2.1. The Aegean Sea and the Hellenic Arc

The Aegean Sea belongs to the Alpine-Himalayan mountain belt, and is situated on a small, relatively fast moving continental microplate which contains parts of mainland Greece, Crete, Rhodes and western Turkey (McKenzie, 1970; Jackson, 1994).

The thickness of the Aegean crust varies between $20 - 32$ km. It consists of Variscan basement overlain by metamorphic and sedimentary rocks of Permian to Tertiary age. The prevolcanic basement can be grouped into two tectonic units (Dürr *et al.*, 1978; Robertson & Dixon, 1984; Dürr, 1986; Altherr & Siebel, 2002), of which the lower unit underwent significant deformation and metamorphism during the Alpine Orogeny: a Paleocene-Eocene high-pressure and a Miocene low- to medium-pressure regime (Altherr *et al.*, 1979, 1982; Wijbrans & McDougall, 1988; Bröcker *et al.*, 1993; Okay & Kelley, 1994). The upper unit consists of Upper Jurassic ophiolite segments, Paleogene molasse deposits, late Cretaceous high-temperature/low-pressure metamorphic rocks and I- and S-type granitoids (Altherr *et al.*, 1994; Altherr & Siebel, 2002; Bröcker & Franz, 1998).

The collision of the Aegean microplate with the Mediterranean sea floor created the Hellenic trench south of Crete (Fig. 2.1), where the eastern Mediterranean sea floor is being subducted beneath the Aegean Sea at a speed of $5 - 6$ cm/a (Druitt *et al.*, 1999). The Hellenic trench is extending over a length of 1000 km and can be divided into two parts: The western part, the Ionian trench, consists of three segments striking almost perpendicular to the subduction direction. The eastern part, the Pliny and Strabo trenches, represents a double system that is nearly parallel to subduction (Huchon *et al.*, 1982; Jackson, 1994).

The development of the subduction zone of the present trench system dates back ~ 200 Ma (Faccenna *et al.*, 2003; van Hinsbergen *et al.*, 2005, and references therein). Between $\sim 90 - 75$ Ma subduction-related volcanic arc activity commenced in southern Bulgaria (von Quadt *et al.*, 2005). A gap in arc magmatism and high-P metamorphism between $\sim 85 - 60$ Ma suggests that subduction came to a hold for about 20 Ma (Ring *et al.*, 2010). At $\sim 55 - 50$ Ma a rollback of the Hellenic slab lead to a southward migration of the magmatic arc by more than 100 km, and a southward shift of the subduction-related high-P metamorphism (Ricou *et al.*, 1998; Pe-Piper & Piper, 2002; Faccenna *et al.*, 2003; Marchev *et al.*, 2004; van Hinsbergen *et al.*, 2005; Ring *et al.*, 2010). Due to further retreat of the slab, the magmatic arc reached the Cyclades at ~ 17 Ma and its recent position at $\sim 3 - 4$ Ma (Fytikas *et al.*, 1984).

The present Aegean magmatic arc is well defined, ~ 500 km long and $\sim 20 - 40$ km wide (Druitt *et al.*, 1999). It has been interpreted as a double struc-

ture, with an inner and outer part, the latter being known as the so-called Hellenic Arc, which extends from the Isthmus of Corinth to the Bodrum peninsula of southwestern Turkey (Fytikas & Marinelli, 1976; Innocenti *et al.*, 1979; Fytikas *et al.*, 1984; Nicholls, 1971; Pichler & Pichler, 2007). Next to Santorini, it comprises the islands of Aegina, Poros, the Methana peninsula, Milos, Nisyros and Kos (Fig. 2.1).

Rocks within the inner arc are not directly related to the subduction based volcanism of the outer arc, and are therefore chemically different (Innocenti *et al.*, 1981). Basalts and rhyolites are dominating the eastern part of the Aegean arc, while rock types in its western parts range from mafic andesite to dacite with andesites and dacites predominating (Druitt *et al.*, 1999).

Main volcanic activity started $\sim 3\,$ka and reached its peak in the Quaternary with Santorini and Nisyros still being active today.

2.2. Santorini Volcanic Field

Santorini is a Quaternary volcano and part of the Hellenic arc. It consists of five islands: Thera, Therasia and Aspronisi are the remnants of an already dissected caldera structure which was enlarged during the third phase of the Minoan eruption about 3600 years ago. Palea Kameni and Nea Kameni lie within the center of the caldera and represent stages of effusive and constructive volcanism that commenced after the Minoan eruption (Druitt *et al.*, 1999).

Up until today, Santorini is the most important and most active volcano in the Aegean Sea (Stiros *et al.*, 2003). To scientists it became the center of attention due to the sudden demise of the Minoan culture in the Aegean which might have been caused by the Minoan eruption (Marinatos, 1939; Watkins *et al.*, 1978). It was probably the largest eruption that ever occurred on the island (Bond & Sparks, 1976; Heiken & McCoy, 1984; Sparks & Wilson, 1990), although Druitt *et al.* (1989) indicate that other eruptions may have been equally large.

There were several attempts to date the exact time frame at which the eruption occurred to find a link to the decline of the Minoan Civilization. The latest studies based on radiocarbon dating place the eruption to the later 17th century B.C. (Manning *et al.*, 2006) and $1627 - 1600$ B.C. (Friedrich *et al.*, 2006).

The Minoan eruption had worldwide effects (Friedrich *et al.*, 2006) and the volcanos eruptive history demonstrates that there is a potentially high risk for a massive, explosive eruption in the future of the island (Fytikas *et al.*, 1990a; Druitt *et al.*, 1999).
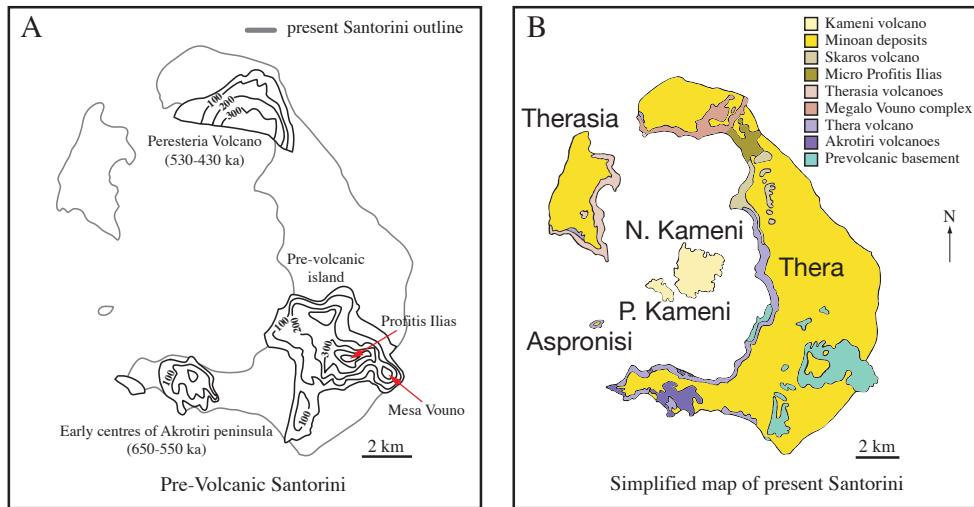
Fig. 2.2. A: Sketches of the pre-volcanic Santorini, the early centers of Akrotiri Peninsula and Peresteria Volcano modified after Druitt *et al.* (1999). **B:** A simplified geological map of present Santorini modified after Huijsmans & Barton (1989). N. Kameni and P. Kameni = Nea and Palea Kameni

The Pre-Volcanic Island   The extent of pre-volcanic Santorini is estimated to have been about $54 \, km^2$ (Heiken & McCoy, 1984). It mainly consisted of ridges located in the southwestern part of Santorini with a submarine ridge extending SSW from the island (Fig. 2.2). The highest ridges are still exposed and represented by Mount Profitis Ilias (564 m), Mesa Vouno (369 m), and Gavrilos Ridge (180 m). The lithologies exposed within the ridges consists of massive marbles, phyllites, metaconglomerates, and metatuffs; they represent lithologies common in rocks of southern Greece.

The major structural feature of the prevolcanic island is a thrust fault, with an average strike of N20°E, dipping 30°E that underlies Mesa Vouno. The fault plane begins at Perissa Beach, passes through the saddle between Mesa Vouno and Mount Profitis Ilias, and then intersects the sea at Kamari Beach on the north side of the mesa.

Volcanism on Santorini   began 650 ka ago with minor submarine eruptions; the earliest volcanic activity occurred on the Akrotiri Peninsula in southern Thera, where only remnants of the oldest volcanoes are preserved. Major explosive activity started around 360 ka. Twelve main eruptions and at least a hundred smaller ones are still preserved over large areas of Santorini, and given that minor eruptions are hardly ever being detected there might as well have been over a thousand

eruptions during stages of constructive volcanism on Santorini (Druitt *et al.*, 1999).

Mappings by Druitt *et al.* (1999) divide the main eruption products into six units: the early centers of Akrotiri Peninusla, Peristeria Volcano, the products of two 180 ka year cycles, and the Kameni islands (Fig. 2.3).

The nature of each 180 ka cycle is based on temporal variations in magma composition. A characteristic feature is the termination of each cycle with a caldera collapse after a major silicic eruption (Druitt *et al.*, 1999). In the history of Santorini these eruptions were the Lower Pumice 2 eruption at the end of the first cycle and the Minoan eruption at the end of the second cycle.

The twelve major explosive eruptions have average recurrence times of about 30 ka; each major explosive eruption commonly began with a Plinian fallout phase, followed by pyroclastic flows, generated by eleven of these eruptions. Approximately four eruptions terminated with a collapse of the caldera (Druitt & Francaviglia, 1992).

The Minoan eruption at the end of the second cycle is termed the most violent eruption that ever occurred on the island. Its ignimbrite outcrops can be found all over the Santorini island complex, while most of the ignimbrite and scoria-flow deposits from other climactic eruptions are buried on the flanks of the islands or under the sea (Fig. 2.3).

After large explosive eruptions that ended with a caldera collapse, usually growth of intracaldera volcanoes and accumulation of minor tephra sequences occurred (Druitt *et al.*, 1999). Minor pyroclastics and associated lavas are mostly basaltic to andesitic in nature. The development of the Skaros shield, which began around 61 ka, followed by the growth of the Therasia dome complex on its western flank, are examples for effusive intracaldera centers in the past of Santorini. The shield then collapsed approximately 50 ka after its inception (Druitt *et al.*, 1999, and references therein).

Today constructive volcanism within the caldera is represented by the Kameni islands, whose construction started approximately 3.6 ka ago. The last eruptive activity on Nea Kameni occurred in AD 1950 (Martin *et al.*, 2006).
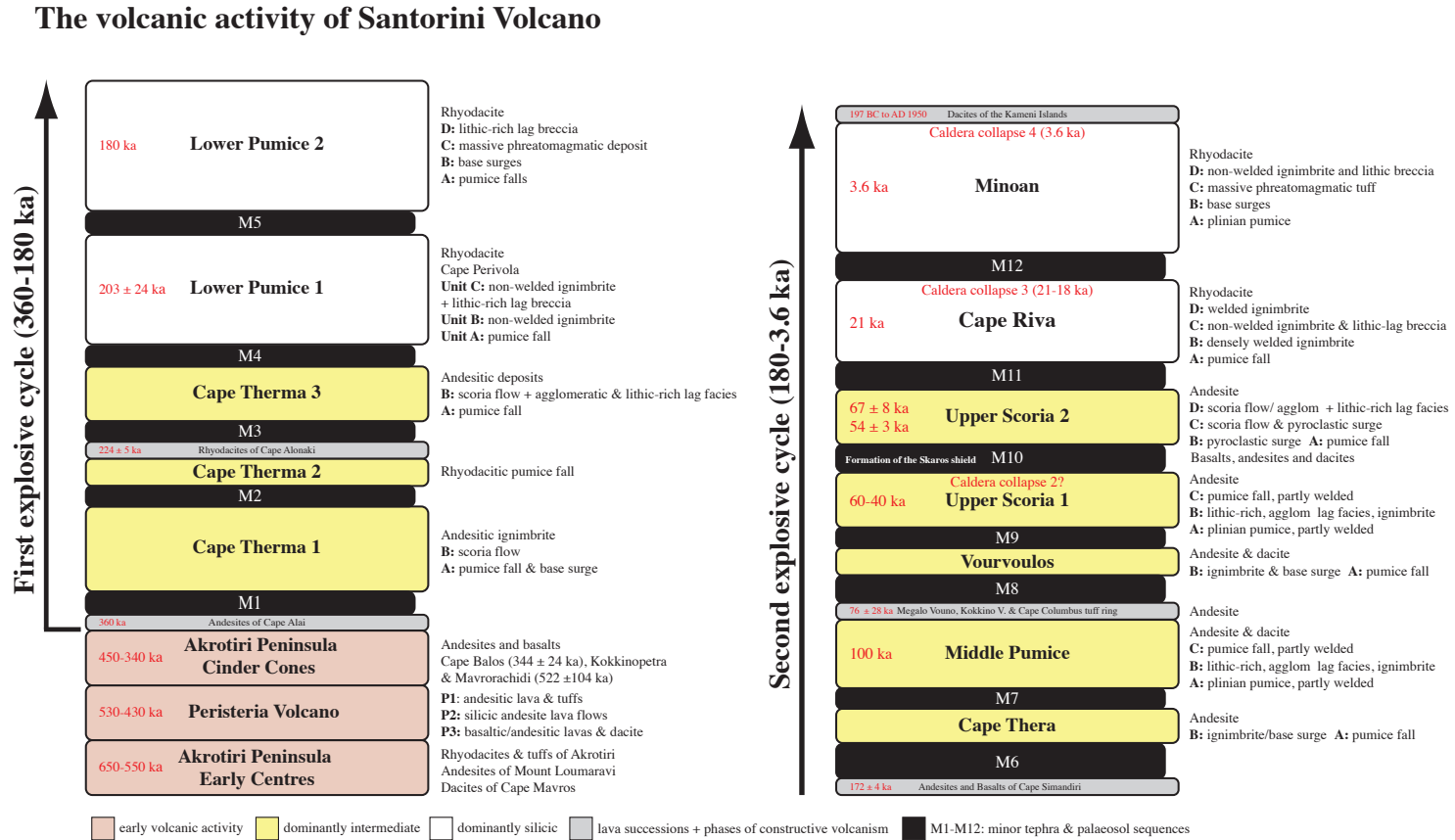
The volcanic activity of Santorini Volcano

Fig. 2.3. Volcanic activity on Santorini Volcano slightly modified after Druitt *et al.* (1999).

Regional Tectonics   The volcanism on Santorini has been strongly influenced by regional tectonics. The tectonical environment is defined by complex extensional and subduction-related processes (Druitt *et al.*, 1999). The Santorini area is mostly affected by an extensional stress regime, demonstrated by the thickness of the crust of ~ 30 km beneath the island. The crust is continental in nature (Makris, 1978). Crustal thickness varies from $20 - 32$ km, in the entire Aegean, while the crust's thickness beneath the rest of Greece and Turkey varies from $40 - 60$ km (Druitt *et al.*, 1999). It has been estimated that the crustal thickness of the Aegean has been halved by extension during the last 5 Ma (McKenzie, 1978). This extension has been concentrated in two grabens, the Anatolian and Cretan troughs. The Central Aseismic Plateau, which is a crustal block with low seismicity, is located between these two troughs (Druitt *et al.*, 1999).

Santorini itself is situated on the southern margin of the Central Aseismic Plateau and has developed on the northern flank of a NE–SW trending basement horst—the Santorini-Amorgos ridge (Papazachos & Panagiotopoulos, 1993). This ridge belongs to a series of alternating horsts and grabens north to the island. The fault that defines the northern margin of the Santorini-Amorgos ridge also passes through the Santorini caldera.

The Santorini basement massif of SE Thera is a subaerial expression of this ridge, while the northern half of the island lies in a graben which is the continuation of the Anydros Basin. Most of the effusive activity since 530 ka has occurred in this graben (Druitt *et al.*, 1999). This NE–SW fault-trend is reflected by several eruptive centers which are aligned along a NE–SW trending lineament termed the Kameni Line. It passes through the centre of the caldera, including the Kameni islands (Fig. 2.4). A second NE–W lineament is the Columbo Line, which is defined by the Megalo and Kokkino Vouno cinder cones and the Cape Columbos tuff ring.

The island was constructed against a pre-existing island of volcanic basement rocks. Its two massifs, Mount Profitis Ilias and Gavrillos Ridge, are exposed in the SE of Thera and mostly consist of low-grade metapelites (schists and phyllites) and crystalline limestones.

2.3. The Minoan Eruption

The Late Bronze Age Minoan eruption on Santorini volcano is considered the most violent volcanic event that occurred in the Mediterranean in the second millenium BC and one of the largest known explosive eruptions in post-glacial time (Watkins *et al.*, 1978; Hammer *et al.*, 1987). The eruption produced at least 28 km^3 of tephra from a shallow storage region heated by several intrusions of basalt (Cot-

trell *et al.*, 1999) and resulted in the formation of a caldera covering an area of $83\,\text{km}^2$ and having a depth of $\sim 600 - 800\,\text{m}$. The tephra-fall caused by the eruption was widespread in the Eastern Mediterranean and Turkey (Bond & Sparks, 1976; Watkins *et al.*, 1978; Heiken & McCoy, 1984; Sullivan, 1988).
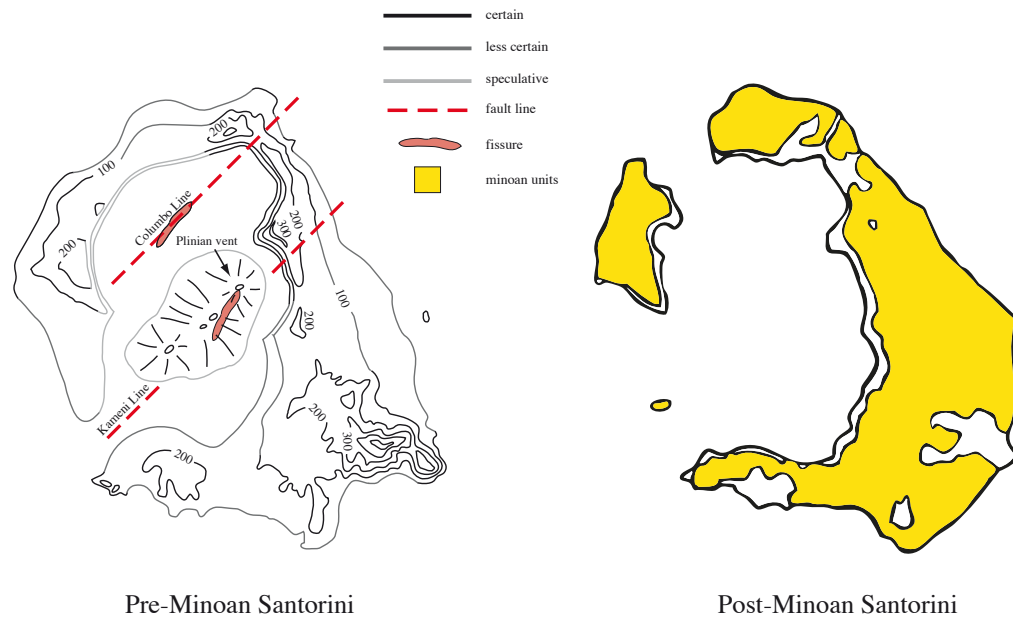

Pre-Minoan Santorini   Post-Minoan Santorini

Fig. 2.4. Left: A reconstruction of Bronze-Age Santorini before the Minoan eruption (modified after Druitt & Francaviglia (1992); Pfeiffer (2001). **Right:** Caldera shape and coverage of Minoan Santorini right after the eruption (modified after Druitt *et al.* (1999).

Pre-Minoan Santorini   The pre-minoan shape of Santorini volcano is often misinterpreted to be a single cone (Reck, 1936; Pichler & Pichler, 2007); in earlier works Pichler & Friedrich (1980) assumed that Santorini was an island composed of several large stratovolcanoes which they called Stronghyle.

Fouqué (1879) already described Santorini volcanic field as a large variety of volcanic landforms with diverse compositions rather than several stratovolcanoes.

Newer works based on structural framework and distribution, stratigraphy, and petrogenesis of pyroclastic deposits and lavas by Heiken & McCoy (1984) and Druitt & Francaviglia (1992) show that during the course of volcanic activity over the last 250 ka the volcanic complex was partially dissected by collapse more than

once and that the pre-minoan Santorini was a caldera flooded by the sea, in the middle of which was a volcanic island group similar to todays Kameni islands (Pyle, 1997) (Fig. 2.4).

Heiken & McCoy (1984) describe the pre-minoan Santorini as being composed of two overlapping calderas superimposed upon a complex volcanic field that developed along a NE trending line of vents. It consisted of three lava shields in the northern half of the island and a flooded depression surrounded by tuff deposits in the southern half.

Differences in eruption style during the Minoan eruption indicate mostly sub-aerial activity in the northern half of the volcanic field, producing lava flows, whereas eruptions in the southern half produced mostly phreatomagmatic tuffs (Heiken & McCoy, 1984).

The Minoan Eruption The eruption can be divided into four phases: (1) a plinian phase, (2) phreatomagmatic base surges, (3) a phreatomagmatic phase creating multiple facies and (4) non-welded ignimbrites; each reflecting a different vent geometry and eruption style (Heiken & McCoy, 1984; Pfeiffer, 2001). The eruption was preceeded by a short sequence of phreatic ashfall explosions, lasting only a few weeks (Heiken & McCoy, 1990). The number of eruptive phases can slightly vary depending on the interpretation of facies by different authors, e.g., Bond & Sparks (1976).

All eruption phases produced mostly glassy pyroclasts of rhyodacitic composition, with varying amounts of lithic fragments, the latter being divided into seven groups by Heiken & McCoy (1984): (1) aphanitic blocks of grey lavas, (2) hydrothermally altered, aphanitic black and grey lavas, (3) dark brown fine-grained tuffs, (4) green and white tuffs, grey dacite lavas, (5) red scoria, (6) welded tuffs, marble, phyllites, sandstones and schists, and (7) glassy, black porphyritic lavas. In the following paragraphs the four eruptive phases were linked to the Minoan Units A, B, C and D as described by Heiken & McCoy (1984) and Druitt *et al.* (1999).

The First Eruptive Phase – Deposit Minoan A The eruption started with a Plinian phase from subaerial vents on the easternmost of the lava shields near Nea Kameni (Heiken & McCoy, 1984; Druitt *et al.*, 1999) mostly producing a coarse tephra fall deposit (Watkins *et al.*, 1978) with a mass of $1.4\,\mathrm{km}^3$ that is compositionally zoned. Within several hours the eruption column must have reached a height of $\sim 36-38\,\mathrm{km}$. Pumice falling from the column was white in color sometimes with a pink or reddish hue (Bond & Sparks, 1976; Heiken & McCoy, 1984; Tait *et al.*, 1998). Due to westwinds the fallout was heterogeneously distributed

over the island reaching an average thickness of $\sim 6\,\text{m}$ (Druitt *et al.*, 1999).

Bond & Sparks (1976) give a lithics content of $4 - 15\,\%$ for this unit; Heiken & McCoy (1984) $1 - 2\,\%$ for the upper third of the deposit. Taddeucci & Wohletz (2001) divide the lithics of this unit into six different groups: (1) gray scoria, (2) red scoria, (3) gray lava, (4) red lava, (5) yellowish hydrothermally altered lava and (6) sedimentary and metamorphic rocks. The abundance of lithics increases upwards in Unit Minoan A (Druitt *et al.*, 1999).

The pumice ashes were drifted away further east and have been identified from seafloor sediments of the eastern Mediterranean and in western Turkey (Watkins *et al.*, 1978; Sullivan, 1988). Fine pumice ash and acid gases were accelerated into the higher parts of the stratosphere, were they were distributed by high winds around the northern hemisphere and detected in ice cores of Greenland (Pichler & Pichler, 2007).

The Second Eruptive Phase – Deposit Minoan B   The eruption vents on the easternmost of the lava shields grew toward the SW into the flooded depression (Heiken & McCoy, 1984) leading to access of seawater. Subsequent activity deposited large-scale base surge deposits, up to $12\,\text{m}$ thick with lithic contents of $1 - 2\,\%$ in the lowest third and $3 - 20\,\%$ in the middle of the deposit. In the upper third big lithic blocks of up to $\sim 50\,\text{cm}$ can be found (Heiken & McCoy, 1984).

This phase was dominated by heavy phreatomagmatic explosions which differed strongly from the eruptions of the first phase leading to fine grained pumice ashes with a shift to more whitish colors. The base surge deposits contain cross-layering features and unidirectional bedforms. Big lava blocks within the deposit demonstrate the force of impact caused by these explosions (Heiken & McCoy, 1984).

Thermal demagnetization temperatures yielded $150 - 250\,^{\circ}\text{C}$ for the base surge deposit (Druitt *et al.*, 1999).

The Third Eruptive Phase – Deposit Minoan C   The origin of deposits from the third phase is still on debate. Heiken & McCoy (1984) describe the phase as being phreatomagmatic in nature and producing $60\,\%$ of the volume of the Minoan Tuff with $5 - 40\,\%$ of lithic fragments.

The multi-emplacement facies consists of ballistic deposits on the caldera rim, base surge deposits in the southwestern parts of the caldera complex, mudflow deposits on the outer walls of Thera and Therasia, as well as slumping deposits on the steep slopes of Profitis Ilias (Heiken & McCoy, 1984).

The thickness of the deposit reaches up to $55\,\text{m}$ on the caldera rim and decreases away from the caldera with blocks of dacite and dacitic hyaloclastite of about $10\,\text{m}$

in diameter occurring within the deposits (Druitt *et al.*, 1999). Emplacement temperatures for this deposit were below 300 °C (Druitt *et al.*, 1999).

These deposits are also interpreted to be water-saturated mudflows (Bond & Sparks, 1976) and ashflows (Pichler & Friedrich, 1980).

With a thickness of about 55 m it is a massive deposit that reflects the most complicated phase of the entire eruption (Heiken & McCoy, 1984). Many authors agree that the third phase probably marks the onset of caldera collapse (Bond & Sparks, 1976; Pichler & Friedrich, 1980; Heiken & McCoy, 1984; Wilson & Houghton, 1990; Druitt & Francaviglia, 1992).

The Fourth Eruptive Phase – Deposit Minoan D   The eruption products form a deposit of up to 40 m in thickness (Druitt *et al.*, 1999) and can be separated into non-welded ignimbrite flow units, intraformational flood deposits and very fine grained co-ignimbrite tephra fall deposits (Watkins *et al.*, 1978). Small lithic clasts similar to those in Minoan Unit A can be found within this deposit. Emplacement temperatures for this deposit were $\sim 300 - 350$ °C (Druitt *et al.*, 1999).

This phase was dominated by the eruption of ignimbrites from vents on the eastern shield, which—at this stage—was not involved in the collapse (Heiken & McCoy, 1984). Caldera collapse continued after the eruption of the ignimbrites with sinking of the eastern half of the caldera.

The collapsing volume was about 19 km^3, overlapping the older caldera to form the present caldera complex.

B

Unit B: base surges

Minoan Units

D = 40m

C = 55m

B = 12m

A = 6m

D

Unit D: non-welded ignimbrites and lithic breccia

A

Unit A: plinian pumice
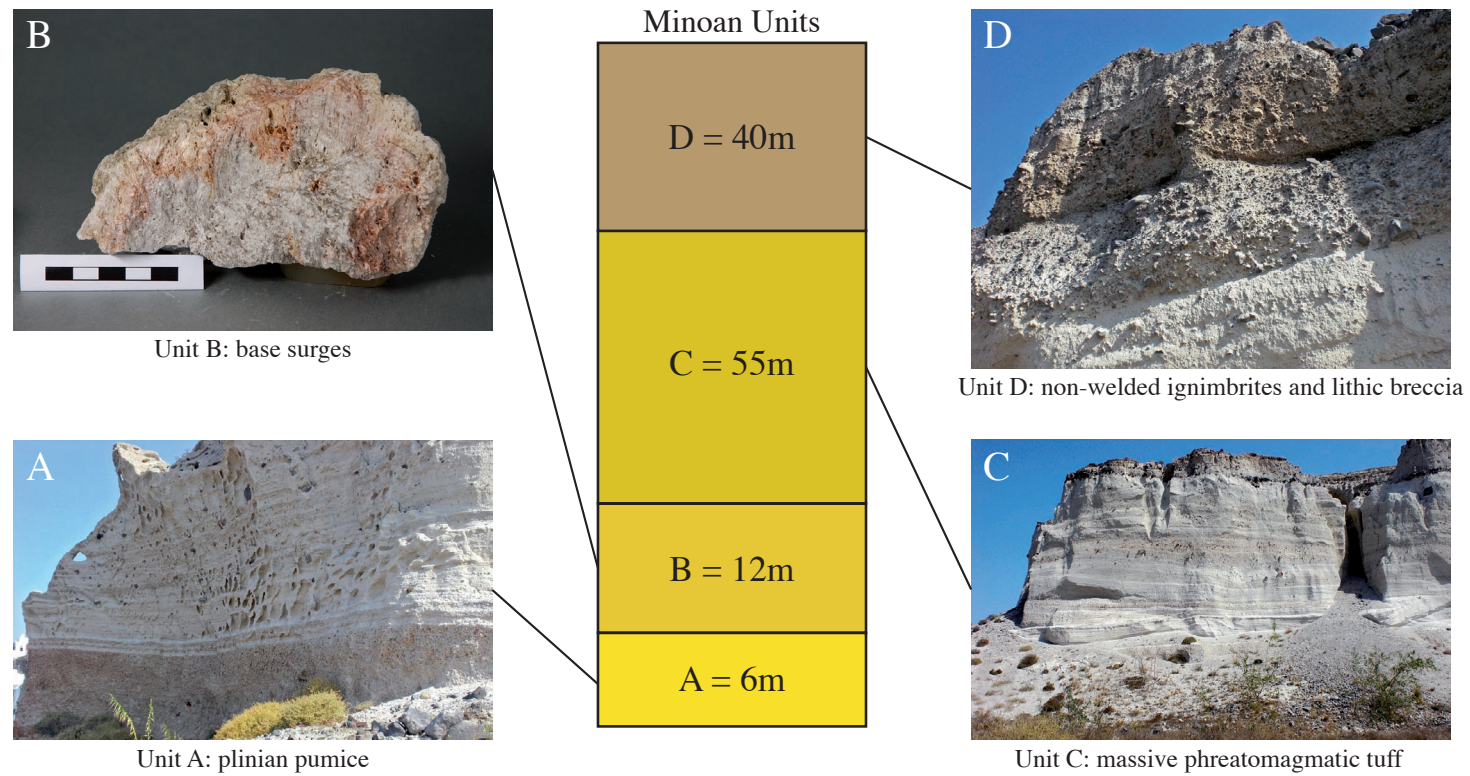
C

Unit C: massive phreatomagmatic tuff

Fig. 2.5. Maximum thickness of the four Minoan Units resembling the four phases of the Minoan eruption (not to scale). Minoan A and Minoan C: Locality SSW of Meghalochori, close to Agrios Ioanis; Minoan B: Sample taken at the southern end of the quarry south of Fira; Minoan D: Locality close to Karteradhos Beach; Pictures A, C and D were provided by Michael Hanel (Institute of Earth Sciences, University of Heidelberg).

3. Petrography

3.1. Introduction

Ten rhyodacitic pumice clasts sampled from Minoan Units A–D, ten mafic scoria clasts and a small mafic crystal clot from Minoan Unit A were investigated.

Pumice clasts were hand crushed with an agate mortar and pestle to avoid contamination; phenocrysts of plagioclase, clinopyroxene and orthopyroxene, as well as pieces of matrix glass were handpicked and embedded in epoxy. Polishing led to a flat surface of mineral grains which is important for further geochemical analysis with EPMA and SIMS. Ultrasonic cleaning of phenocrysts before embedding was avoided to preserve glass components attached to phenocrysts (glass selvages). Polished thin sections were prepared for detailed measurements of the Minoan scoria. Petrographic studies on rhyodacitic pumice samples were done with backscattered electron (BSE) imaging on a scanning electron microscope (Type LEO 440) at the Institute of Earth Sciences, University of Heidelberg. Thin sections of scoria clasts were studied with a polarized microscope (Type Leitz LaborLux 12 Pol-S) and the LEO 440 scanning electron microscope.

The first part of this chapter will introduce the reader to the sample locations on Thera and their approximate positions within the Minoan Units.

To do justice to the huge amount of textures investigated and characteristics occurring within the Minoan pumice and mafic scoria clasts, the most important and interesting characteristics of the samples will be presented in the following parts of this chapter. Abbreviations used for mineral phases within the text are based on the *List of Mineral Abbreviations* by Siivola & Schmid (2007).

Despite the fact that each Minoan Unit represents a change in eruption style, glass textures and phenocryst characteristics within the Minoan pumice are very similar throughout all units.

Mafic scoria clasts and crystal clots found within the Minoan pumice are a good example for multiple magma mingling events that must have taken place during the developing stages of the Minoan magma.
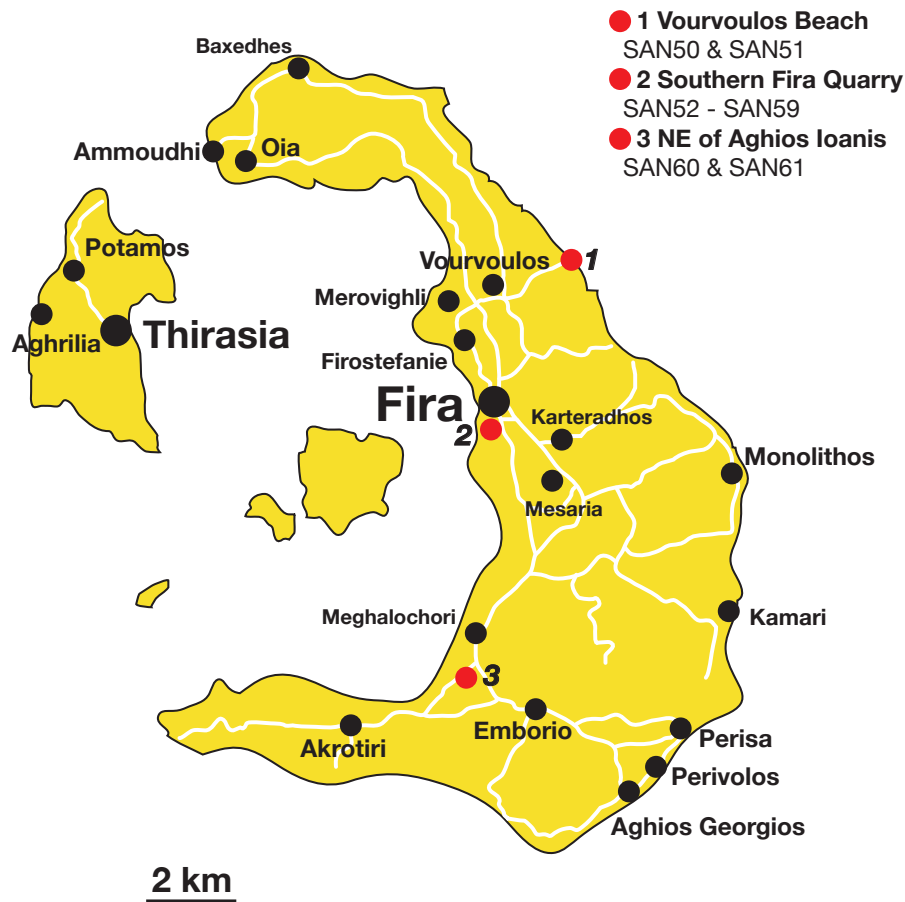
3.2. Sample Locations

Fig. 3.1. A simplified sketch of Santorini volcanic field modified after greeka.com (2011). Red dots mark locations where samples were taken. (1) Vourvoulos Beach: Samples SAN50 and SAN51; (2) Southern Fira Quarry: Samples SAN52 to SAN59; (3) NE of Aghios Ioanis: Samples SAN60 and SAN61.

Samples Investigated   Rock samples were taken from three different locations at Thera.

Sampling area 1 is located at Vourvoulos Beach at the northeastern shoreline of Thera; samples taken at this location are rhyodacitic pumices SAN50 and SAN51 from Minoan Unit D (ignimbrite deposit).

Sampling area 2 is located at the southern end of the quarry south of Fira. SAN52, SAN54, SAN55 and SAN57 are rhyodacitic pumices from Minoan Unit A (Plinian pumice fall deposit). Fig. 3.2 gives a detailed overview of positions from which the samples were taken within the four units.

Sample positions
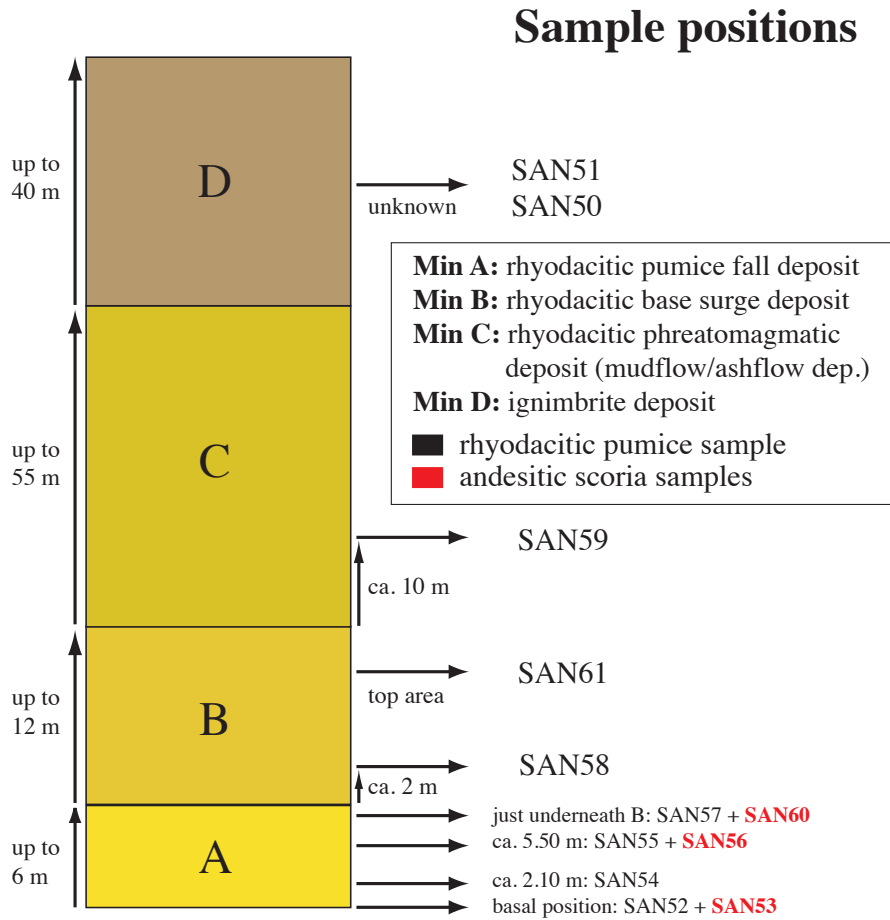
Fig. 3.2. A simplified illustration depicting the sampling locations within the Minoan units (not to scale!). Values for thickness refer to the maximum thickness of a deposit reported by Heiken & McCoy (1984) and Druitt *et al.* (1999). The thickness of a deposit is typically bigger at the rim of the caldera, i.e. proximal to the vent area, and tends to fade out towards the coast line, i.e. distal to the vent area. Unlike other deposits, the ignimbrite deposit (Minoan D) reaches a maximum thickness along the coastal plains (Heiken & McCoy, 1984).

Samples labeled as SAN53 (SAN53-1 to SAN53-7) and SAN56 comprise the andesitic scoria components which are characterized by slightly different stages of differentiation and undercooling with SAN53-2, SAN53-5 and SAN53-6 being

25

more silicic (Minoan Unit A).

Sampling area 3 is located south of Meghalochori, NE of Aghios Ioannis. Samples taken where a mafic scoria clast, SAN60, and a rhyodacitic pumice clast, SAN61 (Minoan Unit B).

3.3. Minoan Pumice Clasts

Table 3.1. Mineral Assemblages of Minoan Pumice Samples

Unit	Minoan A	Minoan A	Minoan A	Minoan A	Minoan B	Minoan B	Minoan C	Minoan D	Minoan D
Sample	SAN52	SAN54	SAN55	SAN57	SAN58	SAN61	SAN59	SAN50	SAN51
Phenocrysts ($> 300\,\mu$m)	pl opx cpx	pl opx	pl opx cpx	pl opx cpx	pl opx cpx	pl opx/cpx opx/cpx	pl opx cpx	pl opx cpx	pl opx cpx
Microcrysts ($< 300\,\mu$m)	pl opx	pl opx	pl opx	pl opx	pl opx	pl opx/cpx Ol	pl opx	pl opx	pl opx
Accessories	mag ilm ap	mag ilm ap	mag ilm ap	mag ilm ap	mag ilm ap	mag ilm ap	mag ilm ap	mag ilm ap	mag ilm ap
Groundmass	glass	glass	glass	glass	glass	glass pl px mag	glass	glass	glass

It should be noticed that sample SAN61 is a thin section comprising the transition from rhyodacitic pumice into the mafic scoria groundmass. Olivine microcrysts and groundmass crystals belong to the mafic scoria's mineral assemblage.

About 99 % of the magma erupted during the Minoan eruption is rhyodacitic in composition. The mafic scoria component that was erupted simultaneously has an overall abundance of about $\sim 1\,\%$ within the Minoan deposits. It increases in abundance towards the top of the Plinian deposit, Minoan A (Druitt *et al.*, 1999).

Rhyodacitic clasts sampled from all four units vary in size between $3 - 20$ cm. Their coloration is very similar throughout the deposit. Beige to yellow hues as well as grey to white pumice clasts are common in Minoan Unit A and D. In Minoan Unit B and C clasts are dominantly grey. A very prominent feature throughout pumice of all units is the occurrence of maroon reaction zones, which were caused by oxidation before cooling (Tait *et al.*, 1998).

The rhyodacite consists of highly pumiceous rhyolitic glass with vesicularities ranging from $\sim 73 - 81\,\%$ (Thomas *et al.*, 1994) and SiO_2 contents varying between $70 - 72$ wt% ($\sim 73.5 - 74$ wt%, Cottrell *et al.* (1999); $\sim 70.5 - 71.4$ wt%, Druitt *et al.* (1999)).

Bubble cavities within the glassy groundmass reach sizes up to 8 mm and are more often elongate than round. Some cavities are filled with plagioclase-orthopyroxene-magnetite crystal clots. These clots reach sizes up to 4 mm (SAN52Agg2 shown in Fig. 3.25 on page 63 is such a crystal clot).

Dark grey bands with a thickness up to 5 mm are common within Minoan pumice. These so-called schlieren textures are due to mingling with more mafic components. Furthermore, numerous andesite nodules with sizes $\leq 500\,\mu m$ and mafic scoria clasts reaching $\sim 20\,cm$ are indicators of one or several mingling events that took place during the developing stages of the Minoan magma.

Phenocrysts are usually euhedral to subhedral, and make up $\sim 3-20\,wt\%$ of the pumices (Druitt *et al.*, 1999); in order of abundance these are plagioclase + orthopyroxene + clinopyroxene + magnetite $\pm$ ilmenite. Small apatite inclusions are ubiquitous within all phenocrystic mineral phases. Bigger plagioclase phenocrysts are visible to the eye, but hardly reach sizes that exceed 2 mm. They are tabular, whitish or clear in appearance and are often intergrown with pyroxene; orthopyroxene and clinopyroxene grains on the other hand show numerous inclusions of small magnetites and to a lesser degree ilmenite. Brown, acicular orthopyroxene is common within Minoan samples. Clinopyroxene makes up a much smaller portion of handpicked specimens and is mostly acicular. Pyroxene crystals can reach sizes up to 2 mm, but most of them barely exceed 1 mm.

3.3.1. Matrix Glass Textures

BSE images reveal bubble sizes as large as $500\,\mu m$ and bigger (B_{he}, abbreviations are explained in Table 3.2). Common bubble shapes are represented by elongate (B_{se} and B_{he}) and smaller more rounded vesicles (B_{sr}).

Tubular bubble shapes make up the most prominent textures within Minoan pumice clasts (B_{ts}). They are most likely caused by shear stresses due to high vesiculation rates during expansion of the magma (Klug *et al.*, 2002). Coalescence phenomena are omnipresent and *pore apertures* belong to the most fascinating textures found within bubble wall remnants. The term was first used by Klug *et al.* (2002) and refers to small holes (B_{cap}) penetrating a bubble's wall (see image in the upper right corner of Fig. 3.3).

Small wrinkled melt films representing leftovers of former bubble walls (B_{csr}, B_{chr} and B_{cap}) make up another notable coalescence feature. Bubble walls have a thickness of only $\sim 1-2\,\mu m$, although melt shreds of $10-20\,\mu m$ can be found occasionally and are good for analysis by EPMA and SIMS. In contrast to all other samples investigated, SAN51 from Minoan Unit D is the only one lacking tubular bubble shapes. This sample has a variety of small round or elongate vesicles, often

Table 3.2. Bubble Textures in Pumice Clasts of Minoan Units A–D

Abbr.	Type	Texture	Size (μm)
B_{sr}	vesicle	small, round	< 40
B_{se}	vesicle	small, elongate	< 40
B_{csr}	bubble	coalesced, small, thin wall remnant	< 100
B_{chr}	bubble	coalesced, huge, thin wall remnants	> 100
B_{cap}	bubble	coalesced, pore apertures	
B_{he}	bubble	huge, elongate	> 400
B_{ts}	bubble	tubular, highly sheared	

Abbreviations for bubble textures were modified after Klug *et al.* (2002).

disrupted by large bubble cavities. Abbreviations for bubble textures were modified after Klug *et al.* (2002) (Table 3.2). Fig. 3.3 shows a nice example of a handpicked piece of pumice displaying many of the textures described above within a range of about a couple of $100\,\mu$m.
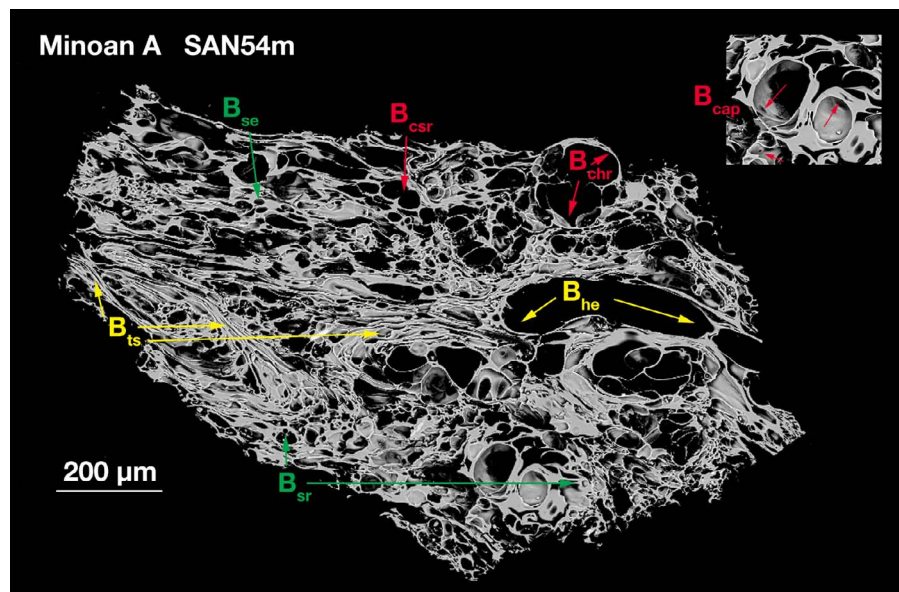
Fig. 3.3. Handpicked pumice from SAN54 (Minoan A). Many different bubble textures can be found in a range of $\sim 100 - 500\,\mu$m. Abbreviations are explained in the text and in Table 3.2.
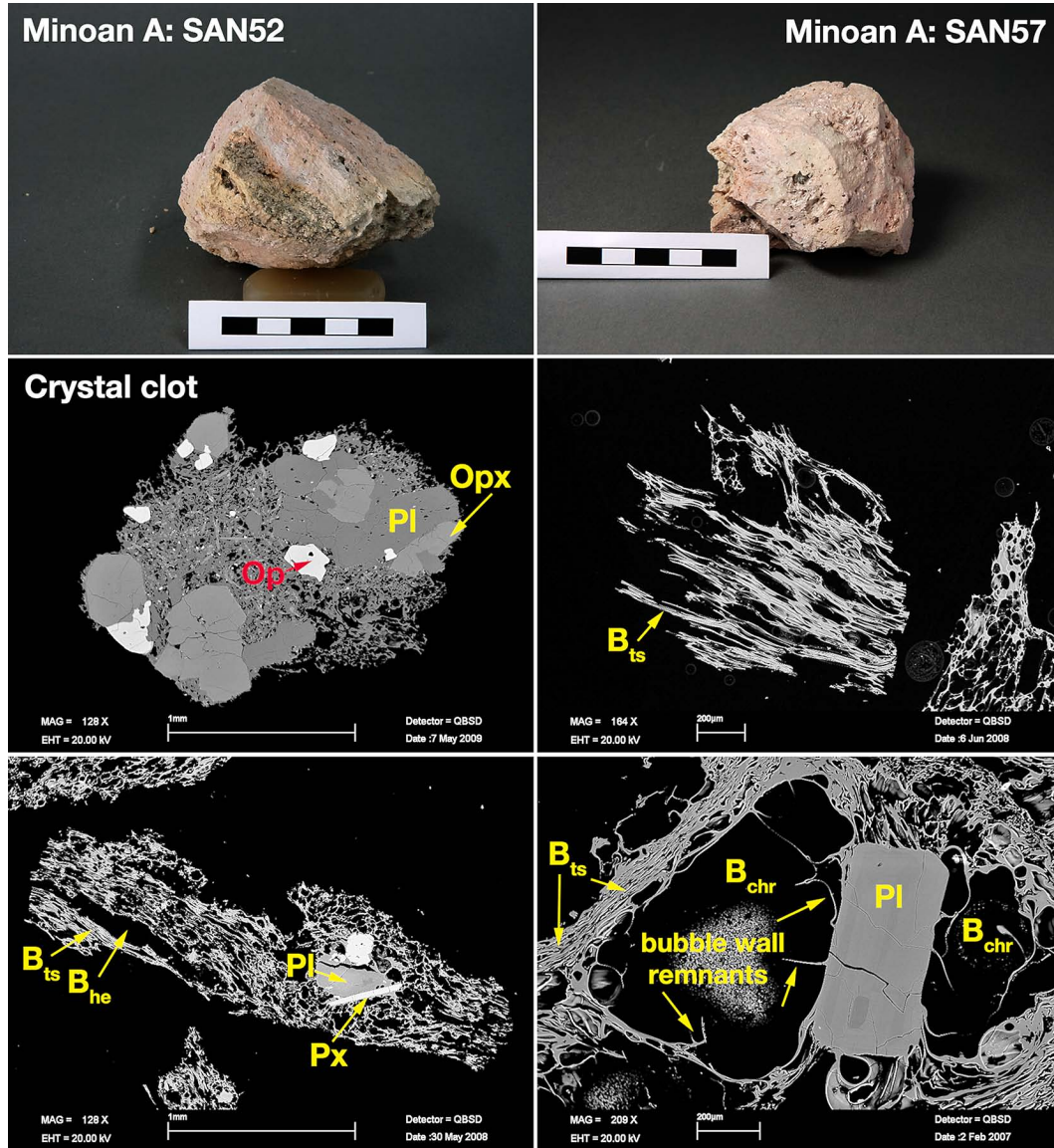
Fig. 3.4. Left column – Minoan A – SAN52: Maroon and yellow colored, oxidized pumice clast with grey schlieren. A handpicked crystal clot reveals a glomeroporphyritic texture with phenocrysts of pl + opx + op, and tiny needles of pl + px in a glassy matrix. Handpicked pieces of pumice are dominated by tubular features and highly elongate bubbles. **Right column – Minoan A – SAN57:** Oxidized pumice clast. Pumice textures show tubular shaped bubbles and huge bubble cavities with remnants of former vesicle walls. Scale bar: 5 cm.
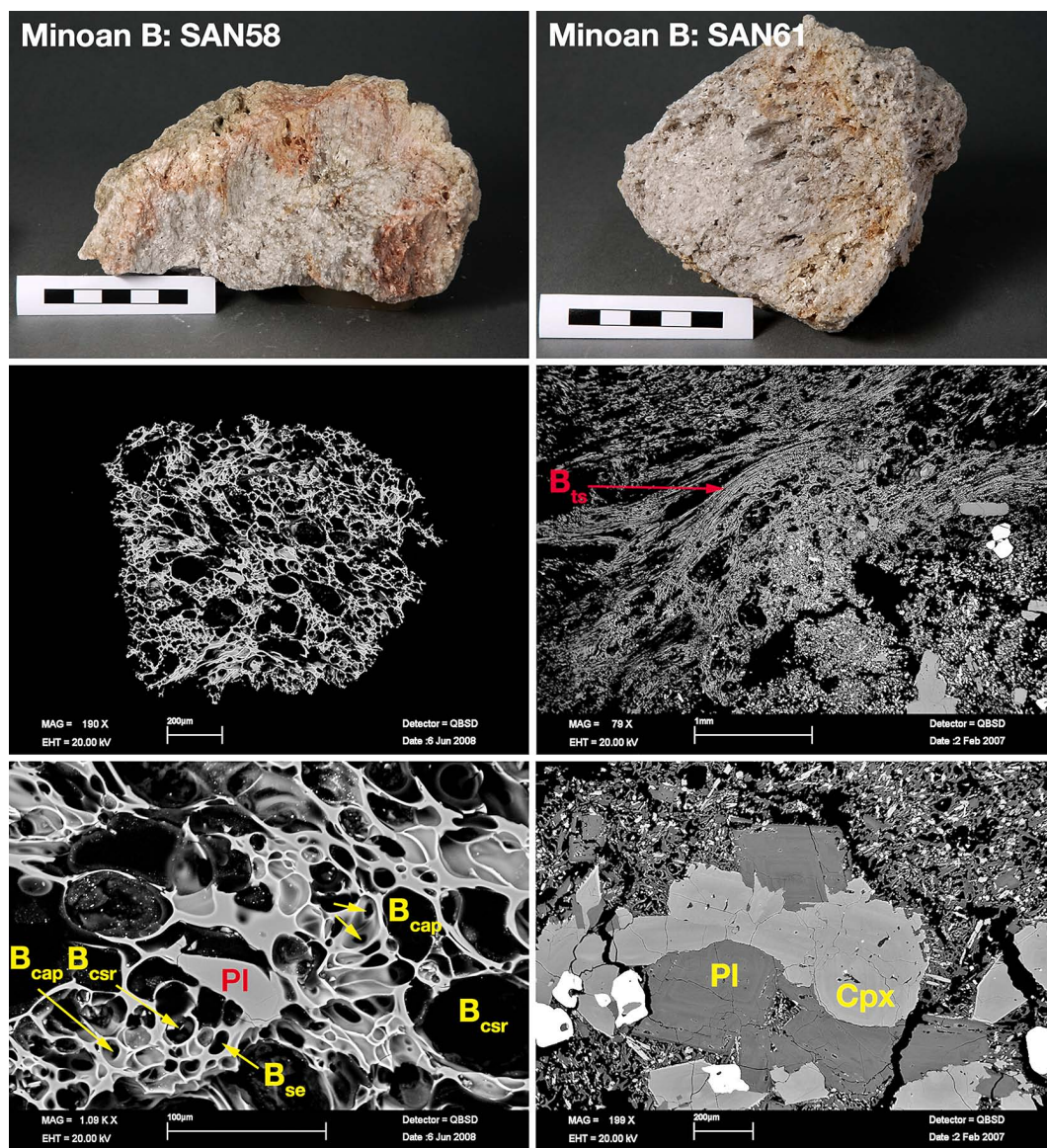
Fig. 3.5. Left column – Minoan B – SAN58: Grey pumice clast with maroon oxidation zone. Bubbles are round or slightly elongate; pore apertures are visible. **Right column – Minoan B – SAN61:** Grey pumice clast with a maroon oxidation horizon. The image below shows the contact between pumice in the upper left (tubular bubble shapes indicate deformation), and a mafic scoria clast with glomeroporphyritic texture. Phenocrysts of pl + cpx + op and microcrysts of pl + cpx + op are surrounded by a glassy matrix. Scale bar: 5 cm.
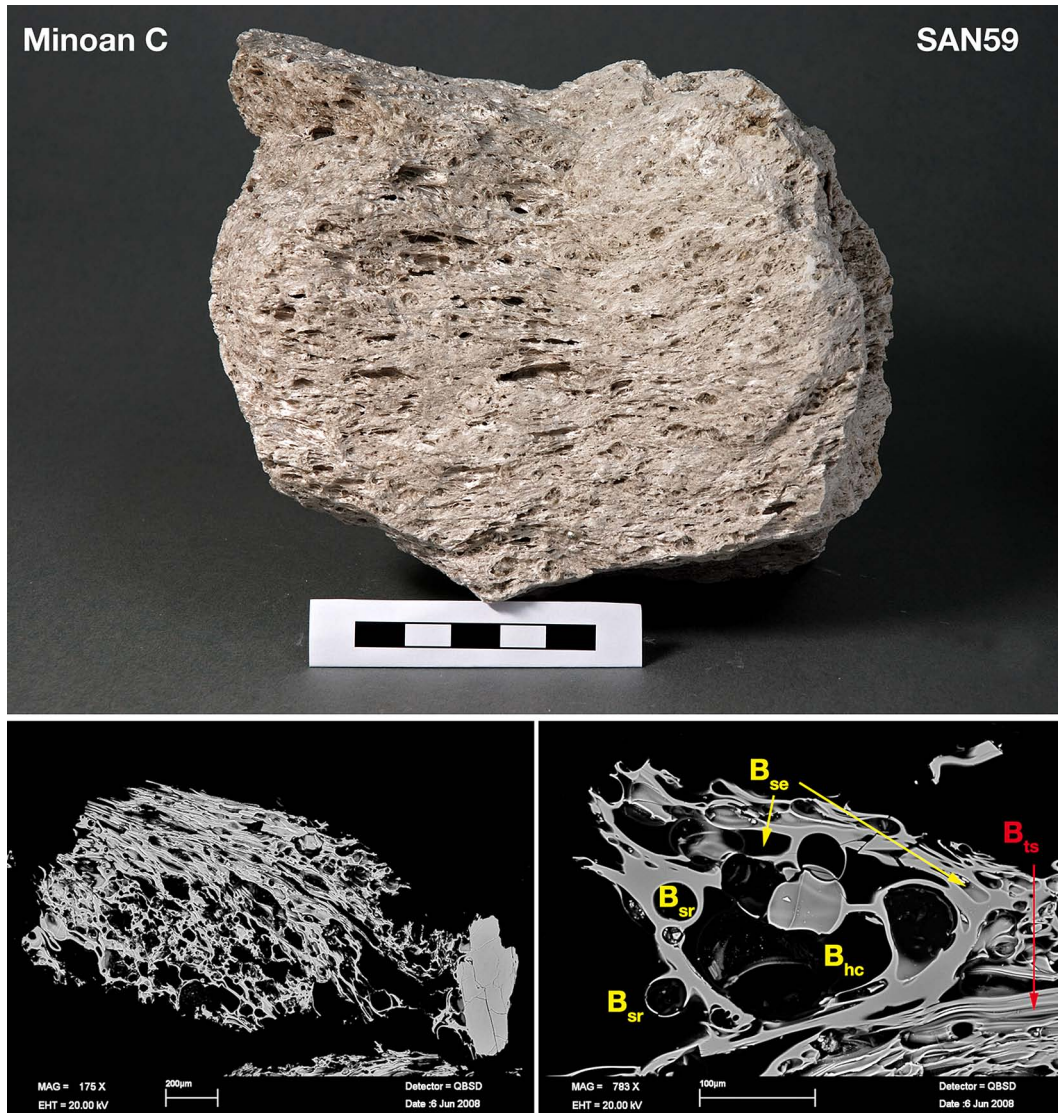
Fig. 3.6. This grey pumice clast from Minoan Unit C shows no signs of oxidation. Elongate bubble cavities are well visible. The BSE image shows tubular bubbles and huge coalesced vesicle cavities. However, round bubbles appear as well. Scale bar: 5 cm.
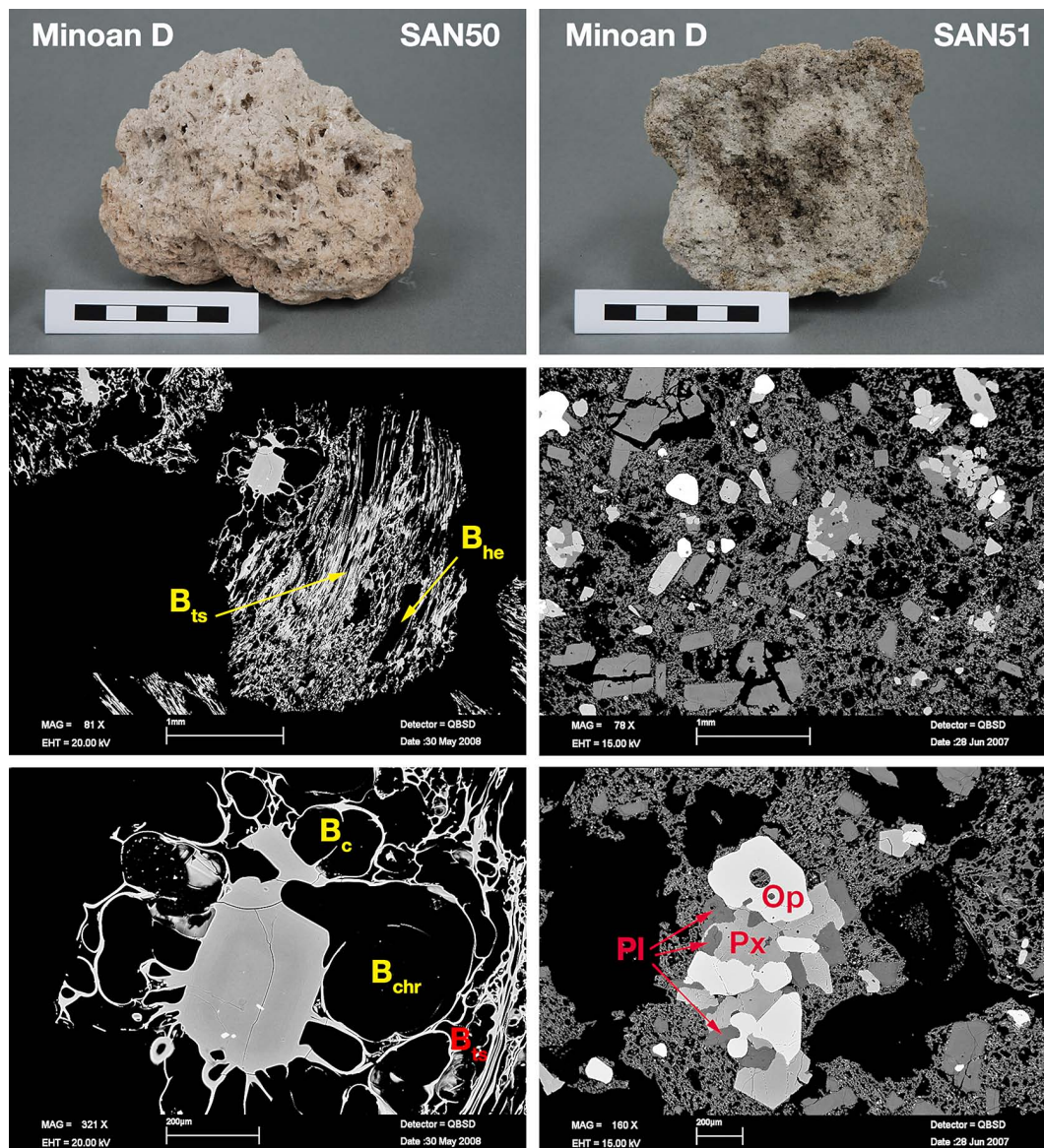
Fig. 3.7. Left column – Minoan D – SAN50: Grey Pumice clast with a reddish oxidation hue; BSE images show tubular and elongate bubble cavities as well as huge coalesced bubbles attached to pl. **Right column – Minoan D – SAN51:** Grey pumice clast with dark gray patches. This sample is characterized by a higher amount of phenocrysts (pl + px + op) in a glassy, glomeroporphyritic matrix with coalesced bubble cavities. There are no tubular bubbles visible. Scale bar: 5 cm.

3.3.2. Plagioclase – Pl

Phenocrystic plagioclase is the most abundant mineral phase within the Minoan tephra. Grains are subhedral to anhedral with tabular shapes, complex zoning, and contain abundant melt inclusions, as well as minor amounts of clinopyroxene + magnetite + apatite. Dissolution features are ubiquitous and defined by irregular rounded or wavy, anhedral zonation horizons often directly followed by a slight increase in anorthite content.

Despite the fact that crystal cores display a wide range of textures and compositions, the most dominant features are subhedral to anhedral resorbed *patchy cores* with a wide span of different anorthite contents. Table 3.3 groups a representative number of plagioclase phenocrysts based on their anorthite contents within crystal cores. These crystal cores can be interpreted as relics from earlier crystallization episodes or xenocrysts from magma mingling events. The patchy texture may develop due to resorption during H_2O-undersaturated decompression (Humphreys *et al.*, 2006). There are a couple of phenocrysts displaying a conspicuous checkerboard pattern. This pattern indicates that crystals underwent a large resorption event. This distinctive zonation type is associated with sieve-textures, which are usually characterized by a large amount of melt inclusions on a fine-scale basis leading to a spongy appearance.

Smith *et al.* (2009) assume that a large resorption event dissolved a huge portion of more sodic plagioclase and generated irregular crystal shapes that were subsequently filled with more calcic plagioclase or melt inclusions. It should be assumed that different stages of sieve-textures can be preserved within a plagioclase crystal. These stages should be distinguished in descriptions. This work will refer to plagioclase crystals with a huge amount of melt inclusions on a fine scale basis as sieve-textured (see Pl-9, scoria clast SAN53-7 on page 57). Plagioclase grains showing a checkerboard pattern of more calcic and more sodic patches or single melt inclusions will be characterized as relics of sieve-textures.

Oscillatory zoning is common towards the rim of most crystals; grains solely containing oscillatory zoning are rare (Fig. 3.11), and even those crystals display a variety of dissolution features in oscillatory zoning bands. X_{An} varies between $0.38 - 0.41$ at the rim; some grains from SAN51 show higher values of $X_{An} > 0.50$.

Table 3.3. Zoning Patterns in Plagioclase Phenocrysts of Minoan Units A–D

Sample	Mineral	Type of Zoning	X_{An} core	Texture Description
Unit A: SAN52A	Pl-5	patchy Ia	$0.7 - 0.8$	anhedral, resorbed core + broad, slightly resorbed zoning bands around core + narrow oscillatory zoning towards rim
Unit B: SAN58A	Pl-13	patchy Ia	$0.7 - 0.9$	anhedral, resorbed core + broad, slightly resorbed zoning bands around core + narrow oscillatory zoning towards rim
Unit B: SAN61-1A	Pl-17	patchy Ia	$0.7 - 0.85$	anhedral, resorbed core + broad, slightly resorbed zoning bands around core + narrow oscillatory zoning towards rim
Unit D: SAN50C	Pl-3	patchy Ia	$0.6 - 0.75$	anhedral, resorbed core + alternating broad and narrow subhedral oscillatory zoning
Unit B: SAN61-1A	Pl-1	patchy Ib	$0.7 - 0.85$	resorbed core, weak euhedral to subhedral zoning towards rim
Unit D: SAN51-1B	Pl-17	patchy Ib	$0.64 - 0.7$	resorbed core, weak anhedral zoning towards rim
Unit D: SAN50A	Pl-4	relictic sieve-texture IIa	$0.48 - 0.58$	core with relictic sieve-texture + subhedral, oscillatory zoning towards rim
Unit D: SAN50A	Pl-1	patchy + relictic sieve-texture IIb	$0.4 - 0.54$	strongly resorbed core + relictic sieve-texture, high-An zone + subhedral, oscillatory zoning towards rim
Unit B: SAN58A	Pl-15	patchy IIa	0.5	resorbed core + narrow anhedral to subhedral oscillatory zoning towards rim
Unit B: SAN61-2	Pl-6	patchy IIb	$0.5 - 0.6$	patchy core, weak subhedral, resorbed zonation bands towards rim
Unit C: SAN59C	Pl-3	patchy IIc	$0.45 - 0.65$	strongly resorbed core + oscillatory zoning towards rim
Unit D: SAN50A	Pl-6	patchy IId	$0.44 - 0.52$	patchy, strongly resorbed core, schlieren pattern
Unit A: SAN54A	Pl-4	patchy III	$0.44 - 0.46$	resorbed core, multiple zoning + resorption events
Unit A: SAN52A	Pl-3	patchy III	$0.45 - 0.48$	resorbed core, multiple zoning + resorption events
Unit D: SAN50C	Pl-4	patchy III	$0.45 - 0.5$	resorbed core, multiple zoning + resorption events
Unit A: SAN54A	Pl-6	patchy IVa	$0.35 - 0.4$	large, anhedral, resorbed core + subhedral, oscillatory zoning with resorption bands towards rim
Unit D: SAN50A	Pl-7	patchy IVb	$0.32 - 0.34$	large, anhedral, resorbed core + subhedral, oscillatory zoning with resorption bands towards rim
Unit C: SAN59C	Pl-2	patchy IVc	$0.36 - 0.42$	large, anhedral, resorbed core + subhedral, oscillatory zoning with resorption bands towards rim
Unit A: SAN57A	Pl-1	oscillatory	NA	core visible, multiple resorption events
Unit A: SAN54A	Pl-1	oscillatory	$0.32 - 0.37$	core visible, multiple resorption events
Unit B: SAN61-2	Pl-21	multiple Ia	$0.86 - 0.87$	no visible resorption bands, core visible
Unit D: SAN51-1A	Pl-3	multiple Ib	$0.79 - 0.82$	slightly resorbed bands, core visible
Unit A: SAN57A	Pl-9	multiple IIa	$0.50 - 0.55$	multiply zoned, core resorbed

The plagioclase phenocrysts are divided into four groups. The first three groups are defined by the X_{An} of the crystal's core. The last group was characterized by type of zoning. Detailed descriptions of features found within plagioclase phenocrysts are depicted in Fig. 3.8 to Fig. 3.11. NA = not analyzed.
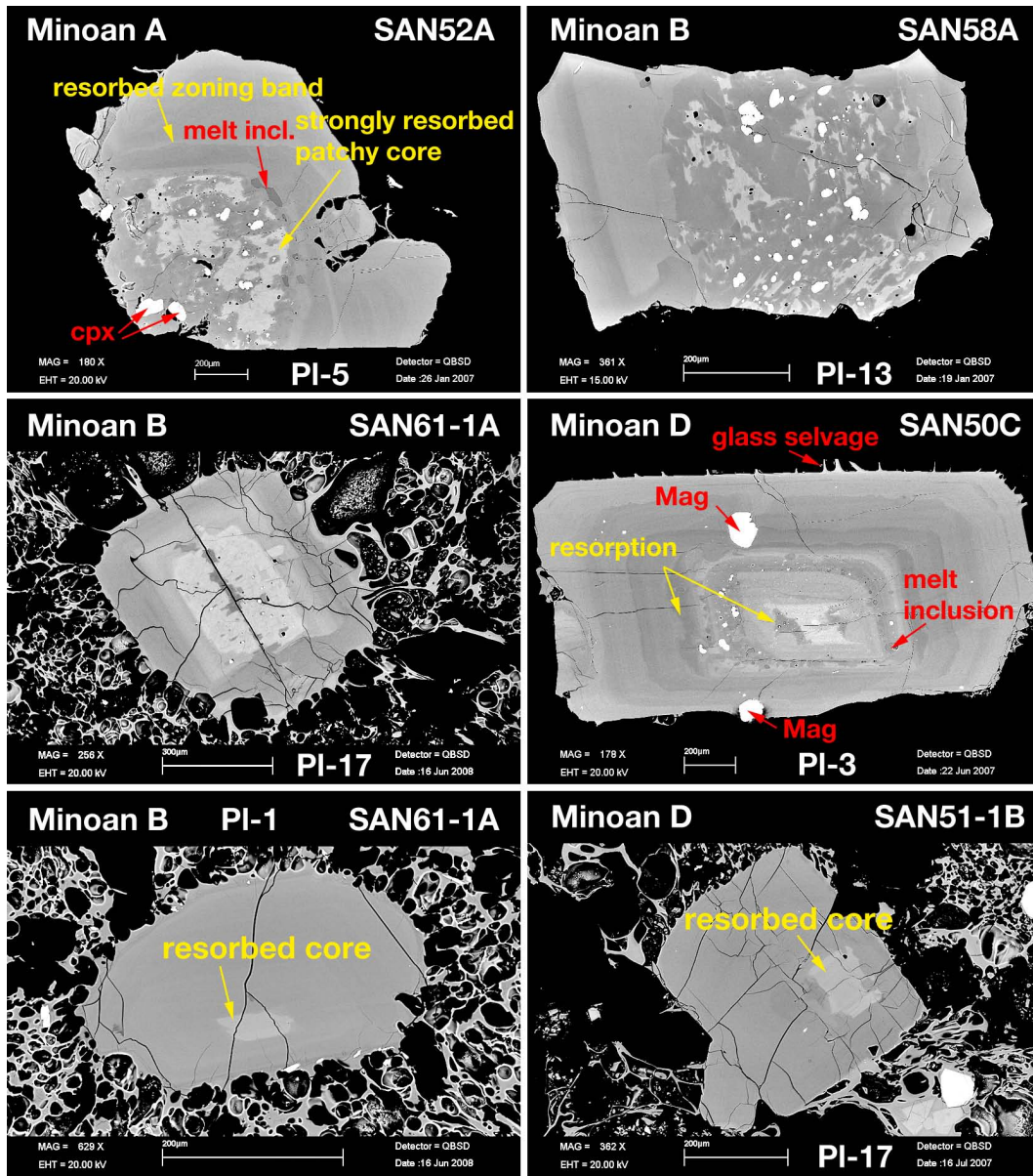
Fig. 3.8. Type I zonations: *Pl-5 (SAN52A)* has a strongly resorbed core. The low-An patches contain inclusions of cpx + mag. Melt inclusions occur within a zone around the resorbed core. Multiple resorption events lead to irregularities within the oscillatory zonation towards the crystal's rim. A strong late stage resorption event heavily affected the overall shape of the crystal. *Pl-17 (SAN61-1A)* and *Pl-3 (SAN50C)* have anhedral, resorbed cores. Zonation within *Pl-3* is oscillatory towards the rim with multiple resorption events; a melt inclusion rich low-An zone is well visible within the outer core region. The core region itself is filled with multiple tiny inclusions of an opaque phase. The low-An zone within the core contains several melt inclusions. *Pl-1 (SAN61-1A)* and *Pl-17 (SAN51-1B)* contain resorbed, anhedral cores; further zonation towards the rim is less developed.

35
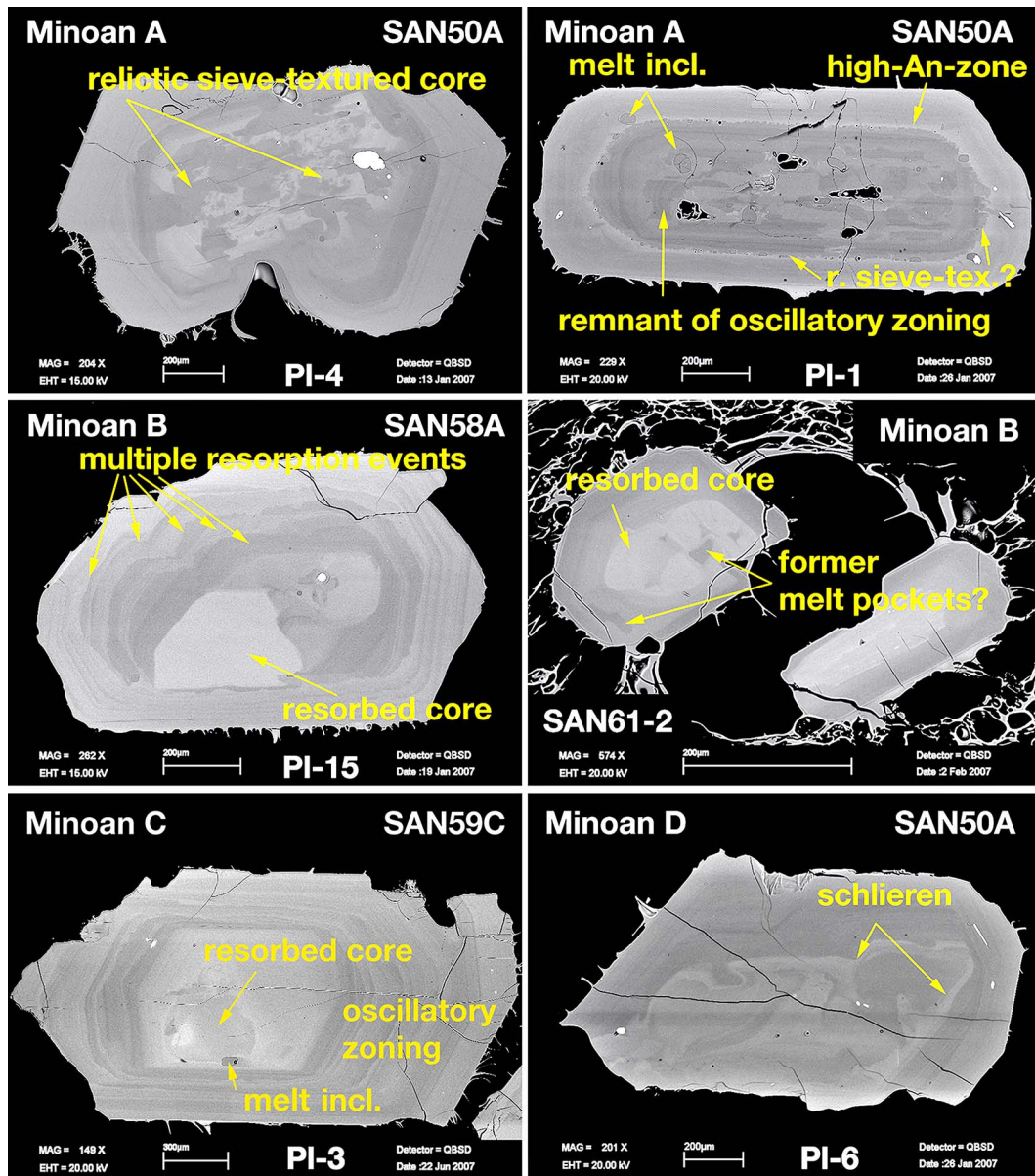
Fig. 3.9. Type II zonations: The checkerboard pattern within the core of *Pl-4 (SAN50A)* may have been caused by a strong resorption event. *Pl-1 (SAN50A)* has a very complex texture. The resorbed core shows remnants of an old oscillatory zoning. Melt inclusions are visible. The core is surrounded by a high-An zone enriched in small melt inclusions and tiny low-An patches reaching into the high-An zone. These patches might be relicts of melt within a sieved-textured rim zone. Oscillatory zoning is dominant towards the rim. *Pl-15 (SAN58A)*, *Pl-6 (SAN61-2)* and *Pl-3 (SAN59C)* show different stages of partially resorbed *patchy* cores with oscillatory zoning towards the rim. *Pl-6 (SAN50A)* has a strongly resorbed core with a schlieren-like pattern.
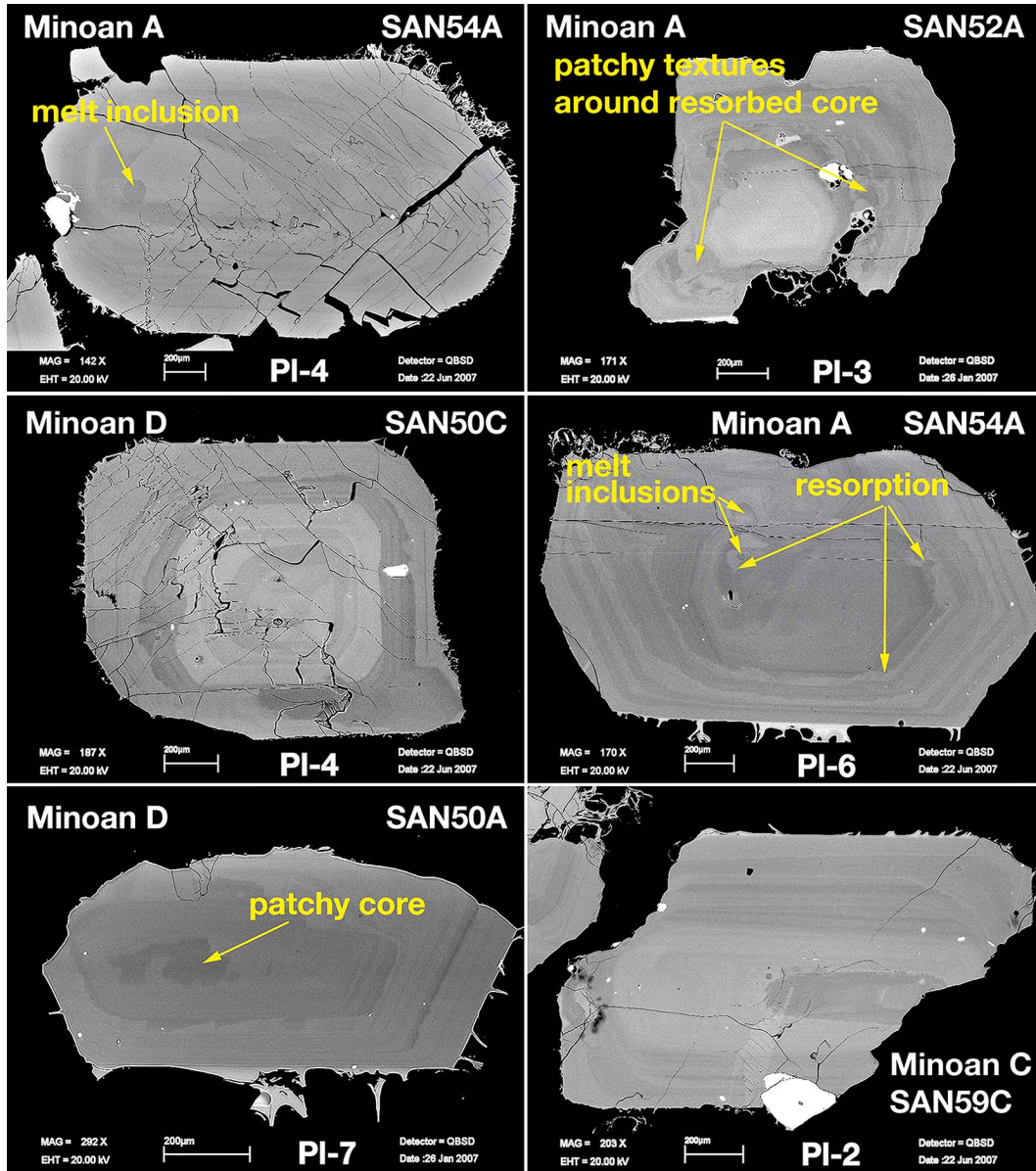
Fig. 3.10. The depicted crystals are subhedral to anhedral. **Type III zonations:** *Pl-4 (SAN54A), Pl-3 (SAN52A), Pl-4 (SAN50C)* show a well developed resorbed core. Oscillatory zoning towards the rim is disrupted by multiple resorption events. Both *Pl-4* crystals are heavily cracked, while *Pl-3 (SAN52-A)* has a strongly resorbed outer rim. **Patchy Type IV:** Resorbed low-An cores surrounded by oscillatory zoning patterns with small resorption events. These crystals are usually subhedral.
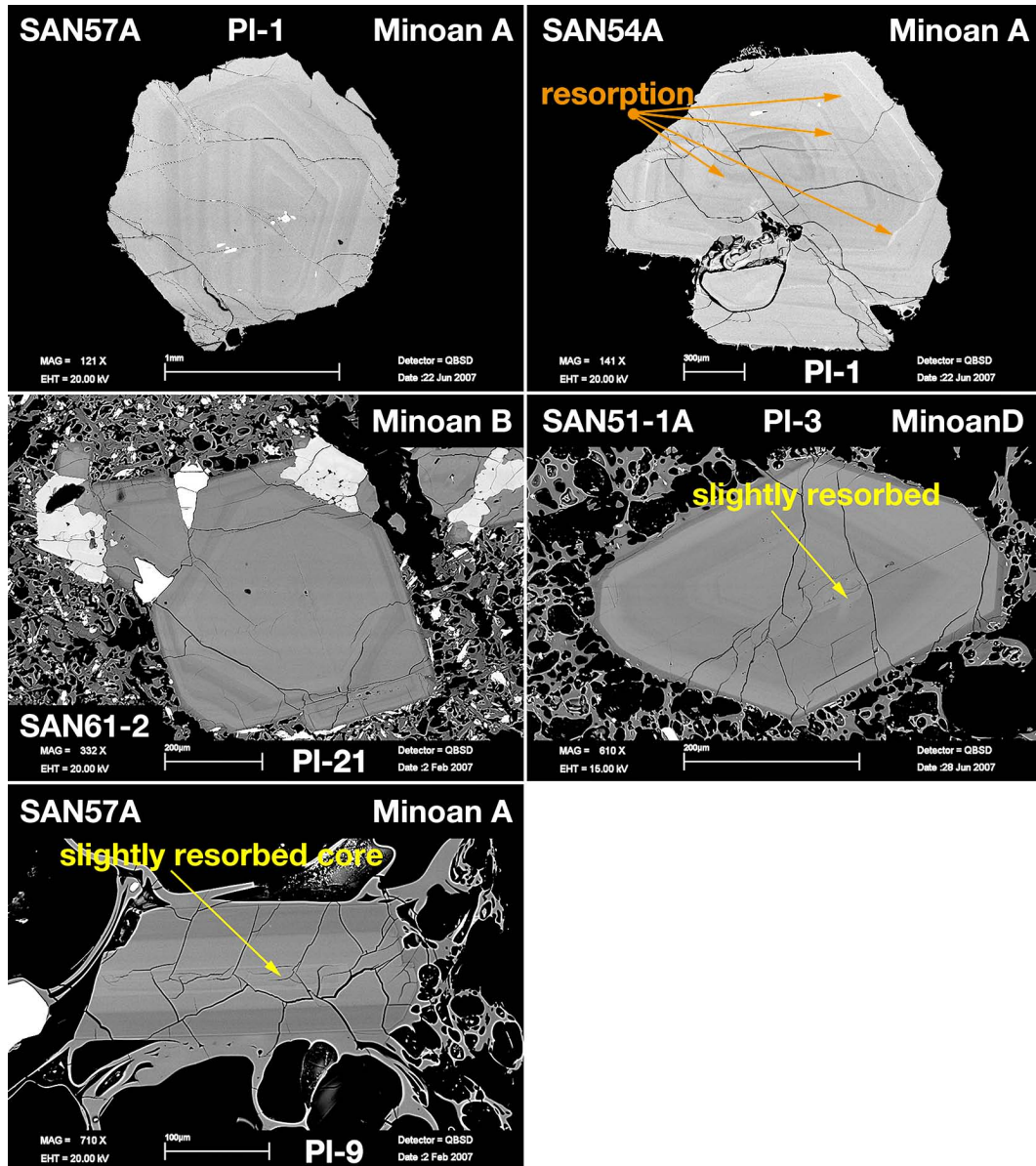
Fig. 3.11. Oscillatory zoning: *Pl-1 (SAN57A)* and *Pl-1 (SAN54A)* are subhedral, and show oscillatory zoning from core to rim. Oscillatory zoning is often disrupted by several resorption horizons. *Pl-1 (SAN54A)* contains at least two irregular, conspicuous high-An horizons. **Multiple zoning:** *Pl-21 (SAN61-2)* and *Pl-3 (SAN51-1A)* are almost euhedral with well developed crystal faces; zoning patterns are hardly affected by resorption. *Pl-9 (SAN57A)* has a well developed core and is subhedral. However the crystal's rim does not seem to be affected by resorption but has mostly broken edges. The crystal is heavily cracked, the core however has a smaller, more resorbed region.

3.3.3. Orthopyroxene – Opx

Orthopyroxene is the dominant Fe-Mg phenocryst next to clinopyroxene within Minoan pumice samples (Druitt *et al.*, 1989). Orthopyroxene phenocrysts are subhedral to anhedral, mostly unzoned or weakly zoned and relatively homogeneous ($X_{Mg} = 0.58 - 0.60$). There are several phenocrysts containing a more patchy zoning pattern. They are slightly enriched in MgO and can be separated into two groups with $X_{Mg} = 0.62 - 0.63$ and $X_{Mg} = 0.66 - 0.69$. A third population of orthopyroxene has $X_{Mg} = 0.7 - 0.73$. These grains can be found in SAN51 from Unit Minoan D—a crystal rich pumice. Orthopyroxenes with similar X_{Mg} values were found within a crystal aggregate sampled from Unit Minoan A (SAN52Agg).

Orthopyroxene grains contain abundant melt inclusions, Fe-Ti oxides and apatite. Tiny microlites of apatite and opaques can be found within melt inclusions. Table 3.4 and Fig. 3.12 introduce the most common textures found in orthopyroxene crystals.

3.3.4. Clinopyroxene – Cpx

Clinopyroxene crystals in Minoan pumice clasts are zoned; they have $X_{Mg} = 0.66 - 0.70$. A clinopyroxene grain in SAN52B has $X_{Mg} = 0.75$. Only clinopyroxene in sample SAN51-1A has a similar X_{Mg} value.

Clinopyroxene crystals usually contain abundant inclusions of plagioclase + opaques + apatite. Melt inclusions are less abundant in the grains investigated.

Table 3.4. Zoning Patterns in Opx and Cpx Phenocrysts of Minoan Units A–D

Sample	Mineral	Type of Zoning	$\overline{X}_{Mg}$	Texture Description
SAN55D	Opx-6	patchy Ia	0.66	many inclusions: melt + op + ap
SAN59D	Opx-7	patchy Ib	0.63	less inclusions: melt + op + ap
SAN54D	Opx-6	zoned	0.58	weak zonation close to rim + inclusions of melt + op + ap
SAN57D	Opx-4	zoned	0.59	weak zonation close to rim + inclusions of melt + op + ap
SAN51-1A	Opx-8	unzoned	0.70	many inclusions: melt + op (ap possible)
SAN61-2	Opx-18	resorbed core	0.71	resorbed Ca-rich core
SAN52B	Cpx-9	unzoned	0.75	inclusions of pl + op + ap (melt possible)
SAN51-1A	Cpx-2	weakly zoned	0.76	Ti-rich core, no inclusions
SAN57A	Cpx-12	weakly zoned	0.70	inclusions of pl + op + ap (melt possible)
SAN58D	Cpx-1	zoned	0.68	inclusions possible
SAN55D	Cpx-4	zoned	0.67	inclusions of pl + op + ap (melt possible)
SAN52D	Cpx-7	zoned	0.68	inclusions of pl + op + ap (melt possible)

Detailed descriptions of characteristics listed in this table can be found in the captions of Fig. 3.12 and Fig. 3.13.
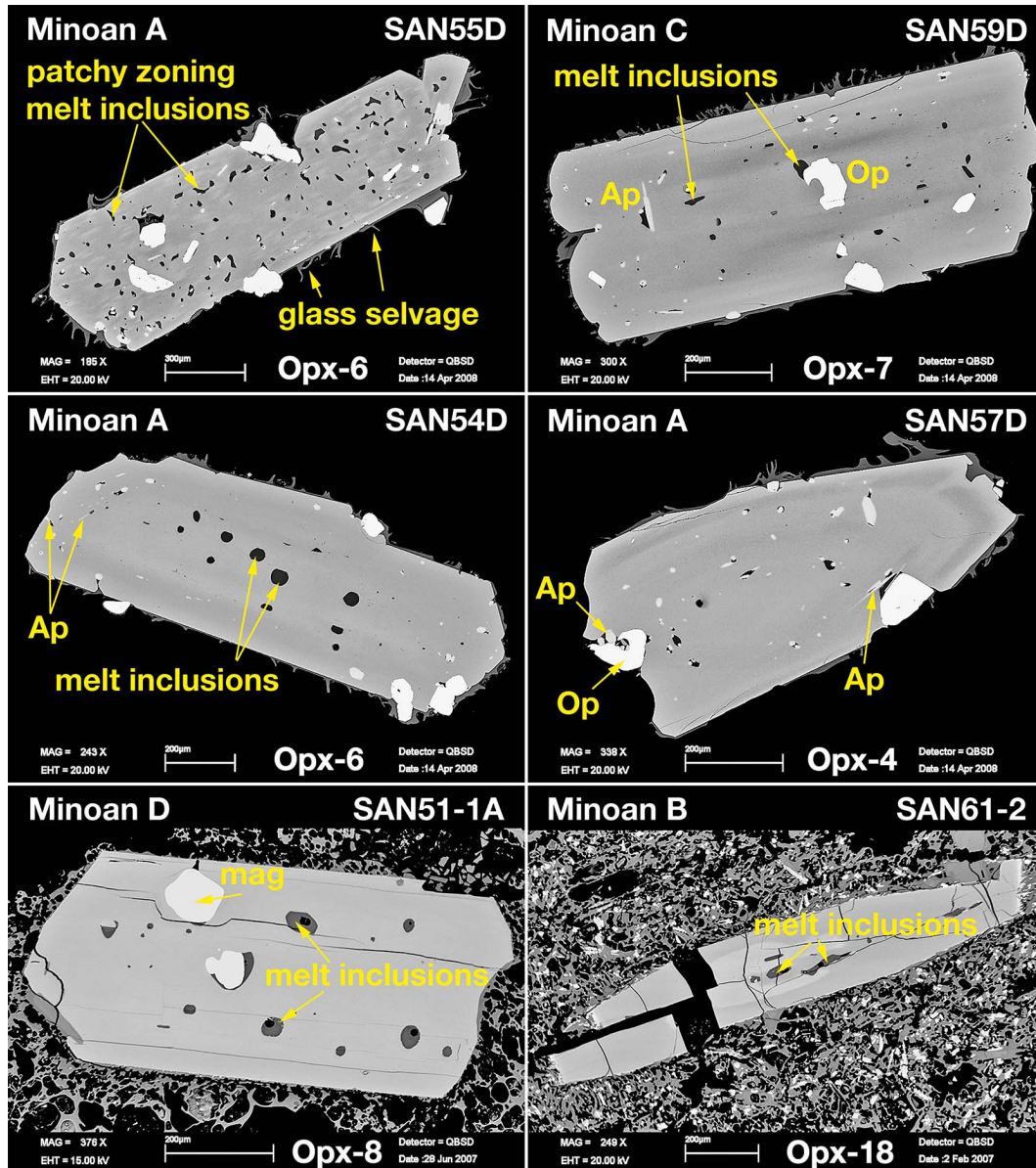
Fig. 3.12. Patchy Ia: *Opx-6 (SAN55D)* has a strong patchy texture, multiple dark melt inclusions are visible. Other inclusions include mag + ap ± ilm. **Patchy Ib:** *Opx-7 (SAN59D)* has a weak patchy zonation, inclusions are melt + mag + ap. **Zoned texture:** *Opx-6 (SAN54D)* and *Opx-4 (SAN57D)* are slightly zoned with inclusions of melt + mag + ap. **Unzoned texture:** *Opx-8 (SAN51-1A)* is rather unzoned, inclusions include melt + op. **Resorbed core:** *SAN61-2* is very different in shape and has a core with a pale hue which is enriched in Ca.
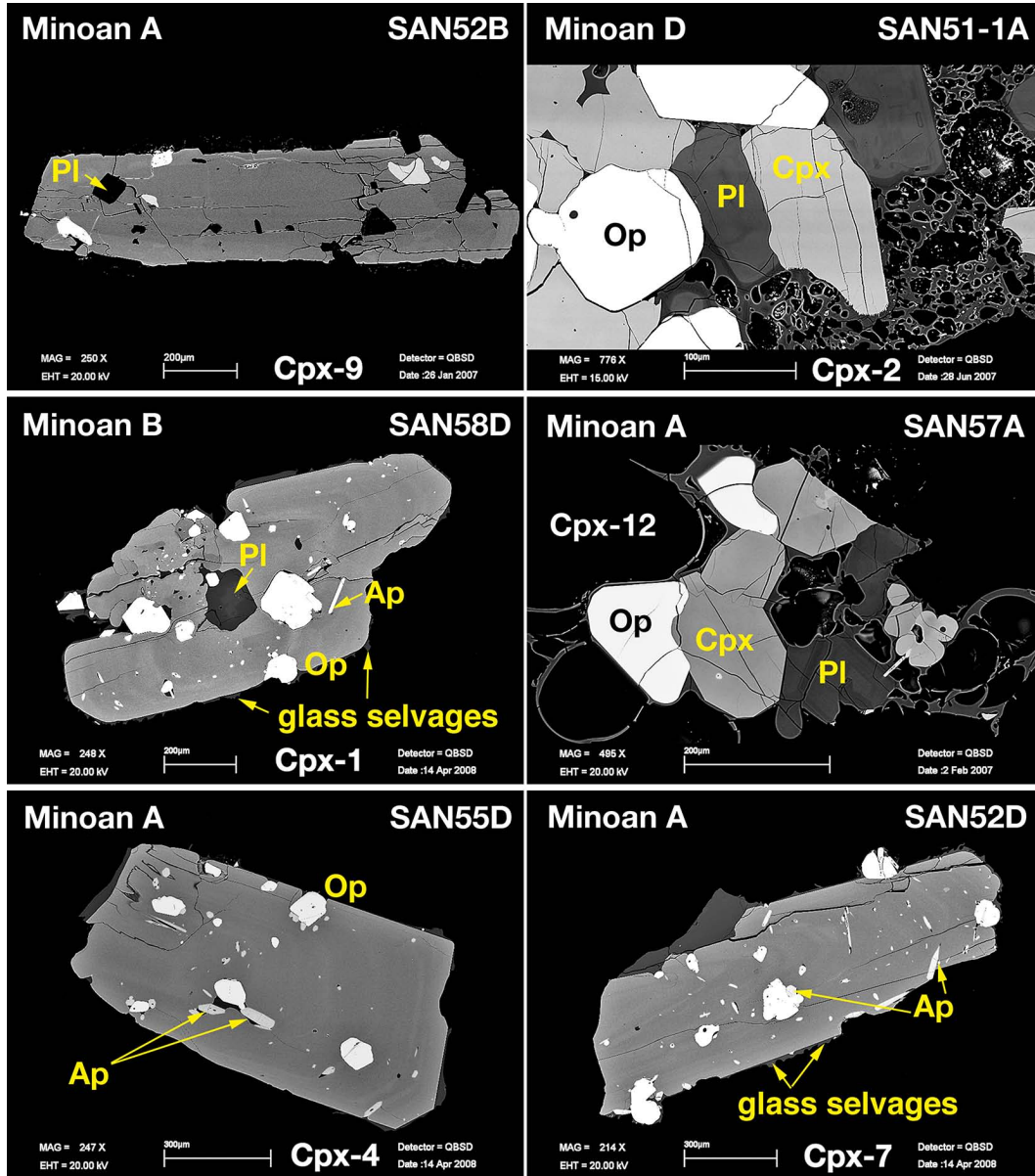
Fig. 3.13. Clinopyroxene textures: *Cpx-9 (SAN52B), Cpx-2 (SAN51-1A)* and *Cpx-12 (SAN57A)* are unzoned or weakly zoned subhedral to anhedral phenocrysts. The first two of them are characterized by much higher X_{Mg} values. *Cpx-1 (SAN58D), Cpx-4 (SAN55D)* and *Cpx-7 (SAN52D)* appear zoned in BSE images. Crystals contain abundant inclusions of mag + apatite $\pm$ ilm.

3.3.5. Olivine (ol) and Accessories

Although xenocrystic olivine is reported in the literature (Druitt *et al.*, 1999), it only occurred within the mafic scoria parts of SAN61-2. Opaques are abundant in all pumice samples, especially as inclusions in orthopyroxene and clinopyroxene; these include in order of abundance: magnetite + apatite $\pm$ ilmenite.
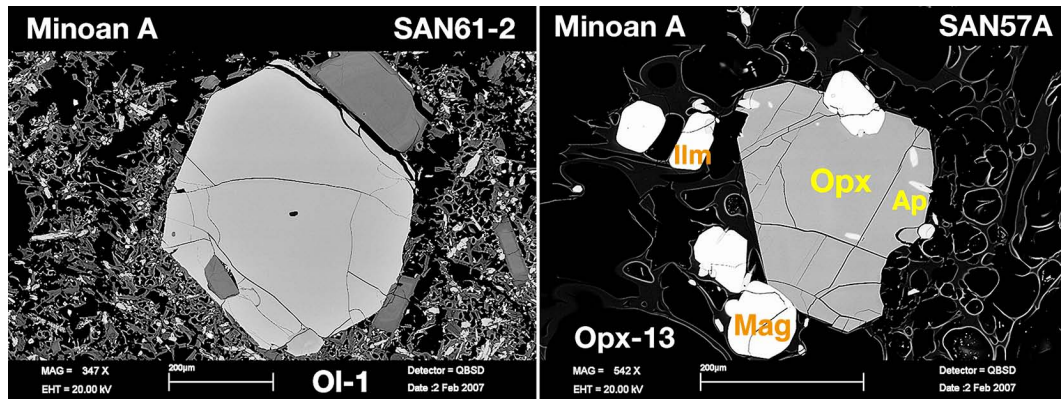
Fig. 3.14. Left – Ol-1: Subhedral olivine grain with a small plagioclase inclusion. **Right – Opx-13:** The matrix surrounding this orthopyroxene grain contains small crystals of magnetite and ilmenite.

3.4. Minoan Scoria Clasts

Unit Minoan A contains dark grey scoria clasts of mostly andesitic to basaltic composition, and pale grey scoria clasts that are slightly more differentiated (SAN53-2, SAN53-5 and SAN53-6). The clasts increase in abundance towards the top of the unit to 20 % but decrease in the overlying deposits. The overall abundance of erupted scoria components is estimated to be $1-2$ vol% of the entire Minoan deposit (Druitt *et al.*, 1999).

Clasts are mostly ellipsoidal or tabular with a surface texture similar to that of a cauliflower which earned them the name 'mafic cauliflowers'. Their sizes range from $\sim 1-26$ cm; vesicularities vary between $36-65$ % and increase with silica content. Clasts usually appear separately within the Minoan pumice.

Crystal content ranges from $\sim 10-40$ vol%. Phenocrysts of plagioclase + clinopyroxene + orthopyroxene + olivine + opaques are set either in a quite dense or vesicular, glassy groundmass of small elongate crystals mainly comprising plagioclase + pyroxene + opaques $\pm$ hornblende. The difference between the dense groundmass of the more silicic clasts and the glassy groundmass of the more mafic clasts indicates different degrees of undercooling.

Phenocrysts are euhedral to subhedral; shapes are acicular, hopper or branch-like and characteristic of rapid cooling. Grains occur individually or as glomerocrysts: plagioclase + clinopyroxene + olivine + orthopyroxene + magnetite. Hornblende is rarely found within the matrix of SAN53-2 and SAN56-1, although Cottrell *et al.* (1999) reported that hornblende can make up $30-40$ % of the groundmass of individual clasts.

Multiple smaller clasts contain pale specks of more silicic composition and xenocrystic crystals and therefore support extensive interaction with the Minoan magma. On the other hand, small glomerocrystic crystal clots of mafic material containing crystals of plagioclase + orthopyroxene + magnetite with or without a groundmass or single xenocrysts from the mafic scoria can be found within the rhyodacitic groundmass (Fig. 3.4 and Cottrell *et al.* (1999); Druitt *et al.* (1999)).

Table 3.5. Mineral Assemblages of Minoan Scoria Clasts from Minoan Unit A

Sample	SAN53-1	SAN53-2	SAN53-3	SAN53-4	SAN53-5	SAN53-6	SAN53-7	SAN56	SAN60	SAN52Agg
Phenocrysts	pl	pl	pl	pl	pl	pl	pl	pl	pl	pl
		cpx		cpx	cpx	cpx	cpx	cpx	cpx	
		opx	opx	ol		opx				opx
			ol	mag			ol	ol	ol	mag
								op	mag	
							qtz			
Matrix	pl	op	pl	pl	pl	op	pl	pl	pl	
	px	px	px	cpx	px		cpx	cpx	cpx	
	op		mag + ilm	mag	mag + ilm	mag + ilm	mag	op	mag	
		ap	ap		ap	ap		ap	ap	
	qtz	qtz			qtz	qtz				
		hbl						hbl		
			glass	glass			glass	glass	glass	glass
Inclusions	glass		glass	glass			glass	glass	glass	glass
		op	op	op	op	op	op	op	op	op
		ap	ap	ap	ap	ap	ap		ap	
			ab	pl			pl	pl	pl	
		px		px		px	cpx	px	px	

A list of mineral phases and inclusions in phenocrysts which were found in the ten scoria samples investigated (Minoan Unit A).

3.4.1. SAN53-1 – Minoan A – Base

Thin sections were prepared from a pale grey scoria clast of $\sim 4 \times 4\,$cm with a glomerophyritic to porphyritic texture. Plagioclase phenocrysts occur in a fine-grained matrix of subhedral to anhedral plagioclase + pyroxene + quartz + opaques (Fig. 3.15).

Plagioclase Plagioclase phenocrysts form a glomeroporphyritic to porphyritic texture and are euhedral to subhedral with tabular or prismatic grain shapes and sizes of $\leq 600\,\mu$m. Textures within grains vary highly. Patchy zoning, oscillatory zoning, sieve-textures and normal zoning can be found. Melt inclusions within sieve-textured plagioclase grains are partially altered to palagonite.
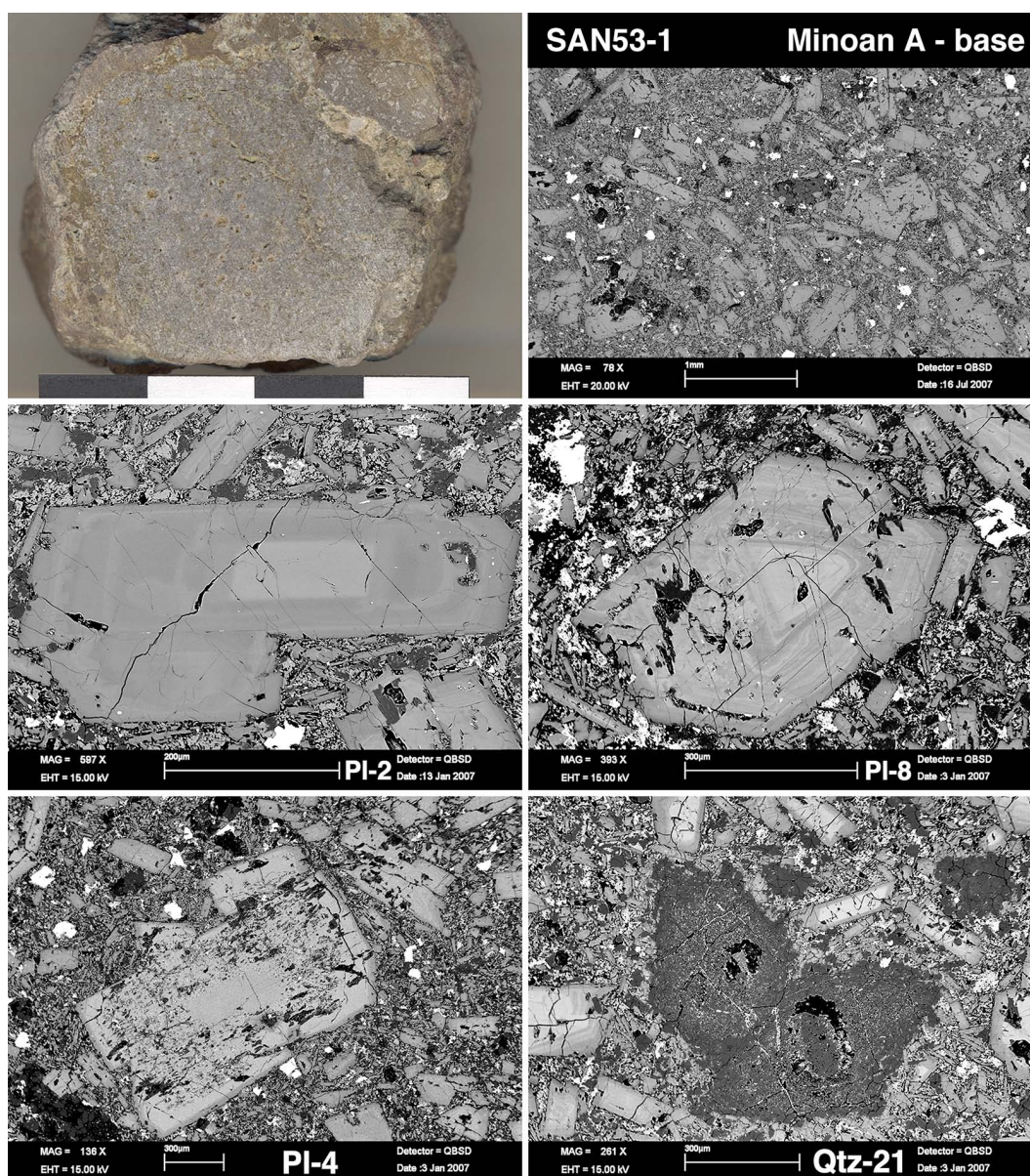
Fig. 3.15. SAN53-1: Pale grey scoria clast. The main phenocrystic phase is pl. *Pl-2* contains an An-rich core with resorbed broad oscillatory zoning bands. *Pl-8* also has an An-rich core with resorbed but more narrow oscillatory zoning bands. *Pl-4* is a sieve-textured crystal with inclusions of qtz and probably altered melt inclusions, i.e. palagonite. Qtz (*Qtz-21*) is an abundant phase within the sample's groundmass. Scale bar: 4 cm.
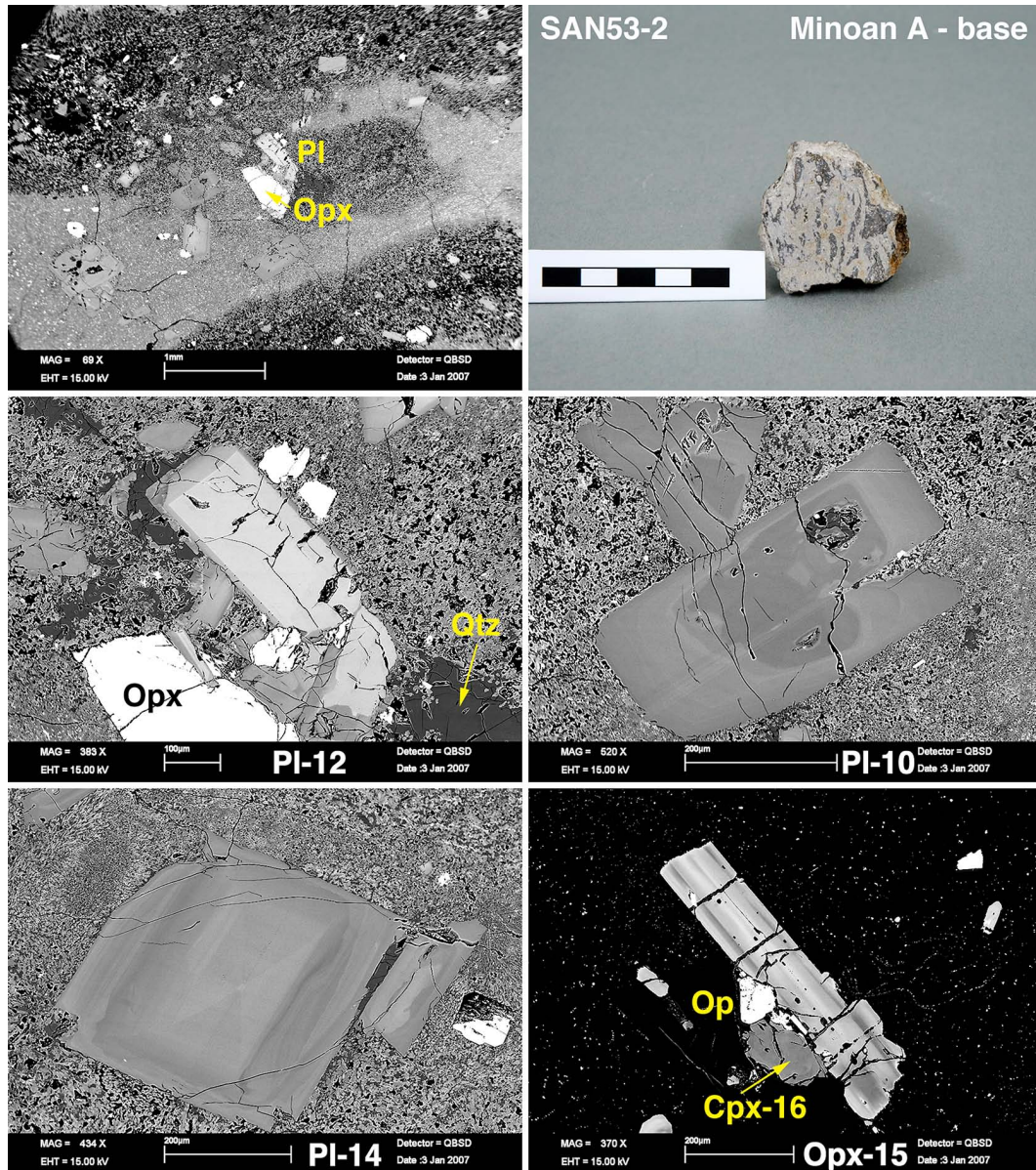
45

Fig. 3.16. SAN53-2: Pale grey scoria clast with dark grey schlieren displaying intensive mingling between two magmas. This sample contains pl + opx + cpx + qtz + op + hbl. *Pl-12* displays simple zoning with a sharp An-rich core, while *Pl-10* has a patchy An-low core. *Pl-15* shows sector zoning within the slightly lighter core, indicating a fast crystallization event. *Opx-15* is a needle shaped subhedral opx crystal next to a resorbed, anhedral cpx. Scale bar: 5 cm.

3.4.2. SAN53-2 – Minoan A – Base

SAN53-2 is a pale grey scoria clast with dark grey schlieren. The clast has a size of $\sim 4 \times 5\,\text{cm}$. The darker more mafic shreds and the more silicic pale grey patches seem to mesh with each other. The texture is glomerophyritic to porphyritic, and the groundmass appears to be quite dense. Phenocrysts include: plagioclase + orthopyroxene + clinopyroxene. Microcrysts within the matrix are mostly anhedral and include opaques + quartz + apatite + hornblende.

Plagioclase   Plagioclase phenocrysts form a glomeroporphyritic to porphyritic texture and are euhedral to subhedral with tabular or prismatic grain shapes, simple twinning, and sizes of $\leq 700\,\mu\text{m}$. A variety of textures can be found ranging from patchy zoning and oscillatory zoning to normal and reverse zoning patterns. A very important texture indicating a very fast growing event for some of the plagioclase crystals is the observed sector zoning within plagioclase cores.

Orthopyroxene   Most orthopyroxene grains are anhedral with strongly resorbed grain boundaries. They have sizes of $\leq 350\,\mu\text{m}$ and usually show slighty resorbed cores and rims. Opx-15 however is an almost idiomorph acicular grain with strong less resorbed zoning and inclusions of opaques and an unknown phase appearing quite dark in the BSE image. Opx-15 forms a glomeroporphyritic texture with plagioclase, clinopyroxene and opaques.

Clinopyroxene   Two types of clinopyroxene were identified. The first one is an anhedral clinopyroxene with an average X_{Mg} of 0.68. This crystal has a patchy texture and is heavily resorbed.

The second type of clinopyroxene has an average X_{Mg} of 0.70. This kind of crystal is subhedral with better developed grain boundaries and is intergrown with opaques and apatite. Zoning is visible within grains but disrupted by resorption patterns.
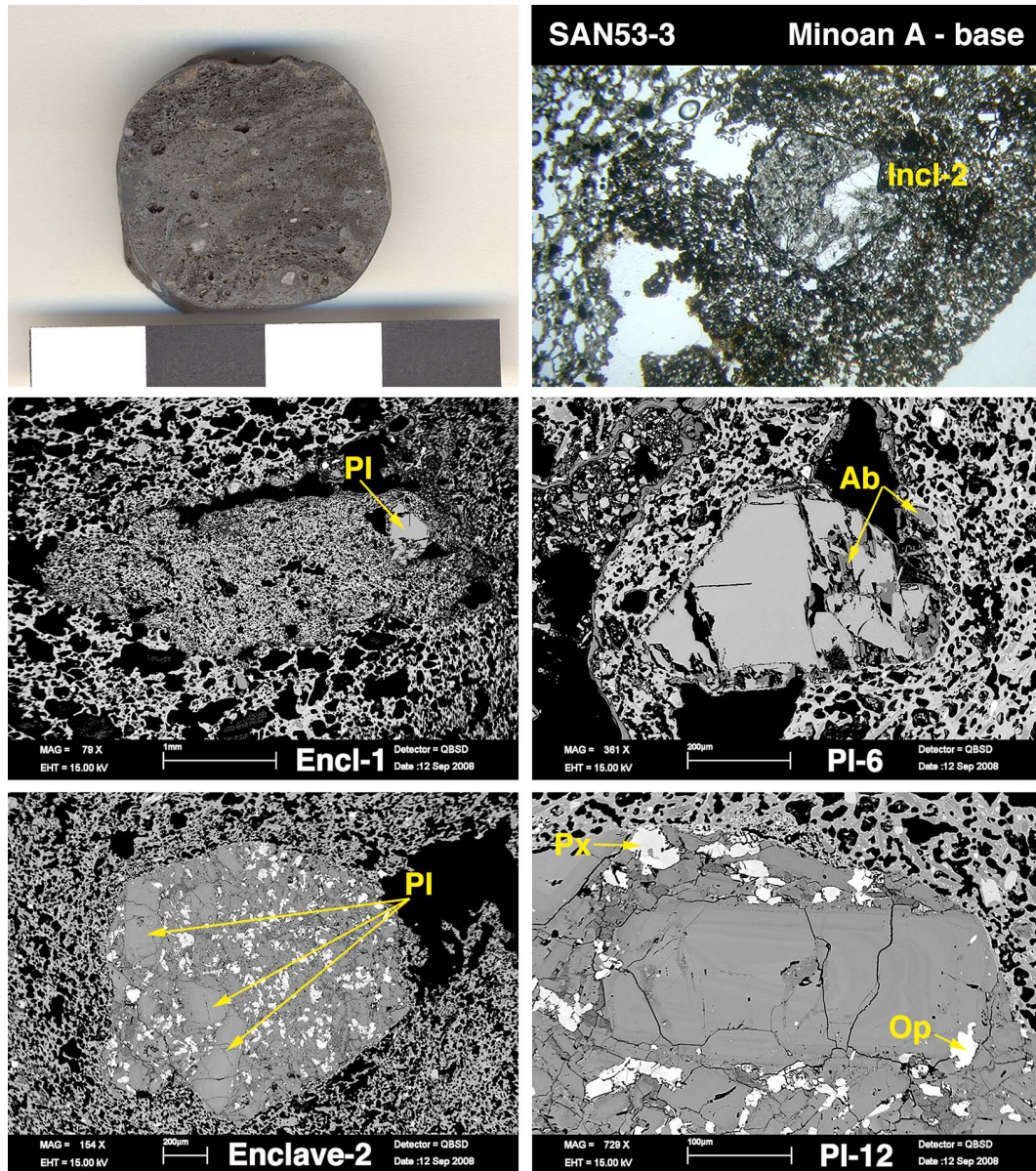
Fig. 3.17. SAN53-3A: This ochre and dark brown colored specimen has a very complex texture. Embedded in a vesicular, glassy matrix are darker groundmass patches, often containing enclaves of inherited material. *Enclave-1* is surrounded by a dark brown altered rim; the matrix itself is glassy with tiny needles of pl + px; one phenocryst—Pl-6—is visible. *Pl-6* has cracks often filled with ab. Tiny ab crystals also occur within the inclusions' matrix. *Pl-12* is embedded within *Enclave-2*. This enclave differs from *Enclave-1*. There is no glassy matrix but rather a dense groundmass of pl + px + op microcrysts with several pl phenocrysts. Scale bar: 4 cm.

3.4.3. SAN53-3 – Minoan A – Base

Sample SAN53-3 is a small scoria clast of $\sim 4 \times 5$ cm with ochre and dark brown colored schlieren. Compared to other scoria clasts this sample is relatively light weighted. BSE images reveal a glassy pumiceous matrix with microcrysts of plagioclase + pyroxene + opaques. Phenocrysts of plagioclase + orthopyroxene + olivine + opaques occur within the glassy glomeroporphyritic to porphyritic groundmass. Incorporated were various different kinds of enclaves (Table 3.6). Some of them are surrounded by a reaction rim that seems to represent altered glass (palagonite). These inherited enclaves are usually dark brown in thin section. Some contain a glassy matrix with microcrysts of plagioclase and pyroxene + phenocrystic plagioclase that appears to be heavily corroded and shows specks of a more albitic composition. Other enclaves have a matrix of pyroxene + plagioclase + opaques with phenocrystic, weakly zoned plagioclase. Pl-17 in Enclave-3 seems to be surrounded by bits and pieces of mineral debris (Fig. 3.18).

Plagioclase Phenocrysts vary in composition from $X_{An} = 0.92$ to $X_{An} = 0.49$. All grains are euhedral to subhedral and only slightly zoned. Grain size varies between $100 - 350$ μm. Grains within Enclaves-2 and 3 (Pl-17) are heavily cracked and seem partly corroded. Cracks might have been filled with inclusions that were lost during preparation. Inclusions occurring within plagioclase are melt + ap + ab.

Table 3.6. Types of Plagioclase Phenocrysts Discovered in Sample SAN53-3

Plagioclase	An (mole %)	Zoning	Type of Texture
Pl-1	$44 - 51$	weak oscillatory	no inclusion
Pl-3	$78 - 83$	weak patchy core	no inclusion
Pl-6	$85 - 92$	weak	Enclave-1
Pl-12	$44 - 72$	oscillatory	Enclave-2
Pl-17	NA	weak	Enclave-3
Pl-14	$47 - 53$	weak oscillatory	no inclusion

A brief overview of different types of plagioclase grains that occur as phenocrysts within the groundmass and within inherited enclaves of sample SAN53-3. NA = not analyzed.

Orthopyroxene Orthopyroxene grains are smaller than plagioclase phenocrysts and usually subhedral in shape; tabular or acicular grains are common. Inclusions within grains include melt + apatite + opaques.

Olivine Subhedral to anhedral normal zoned olivine grains with sizes ≤ 300 μm are found within SAN53-3.
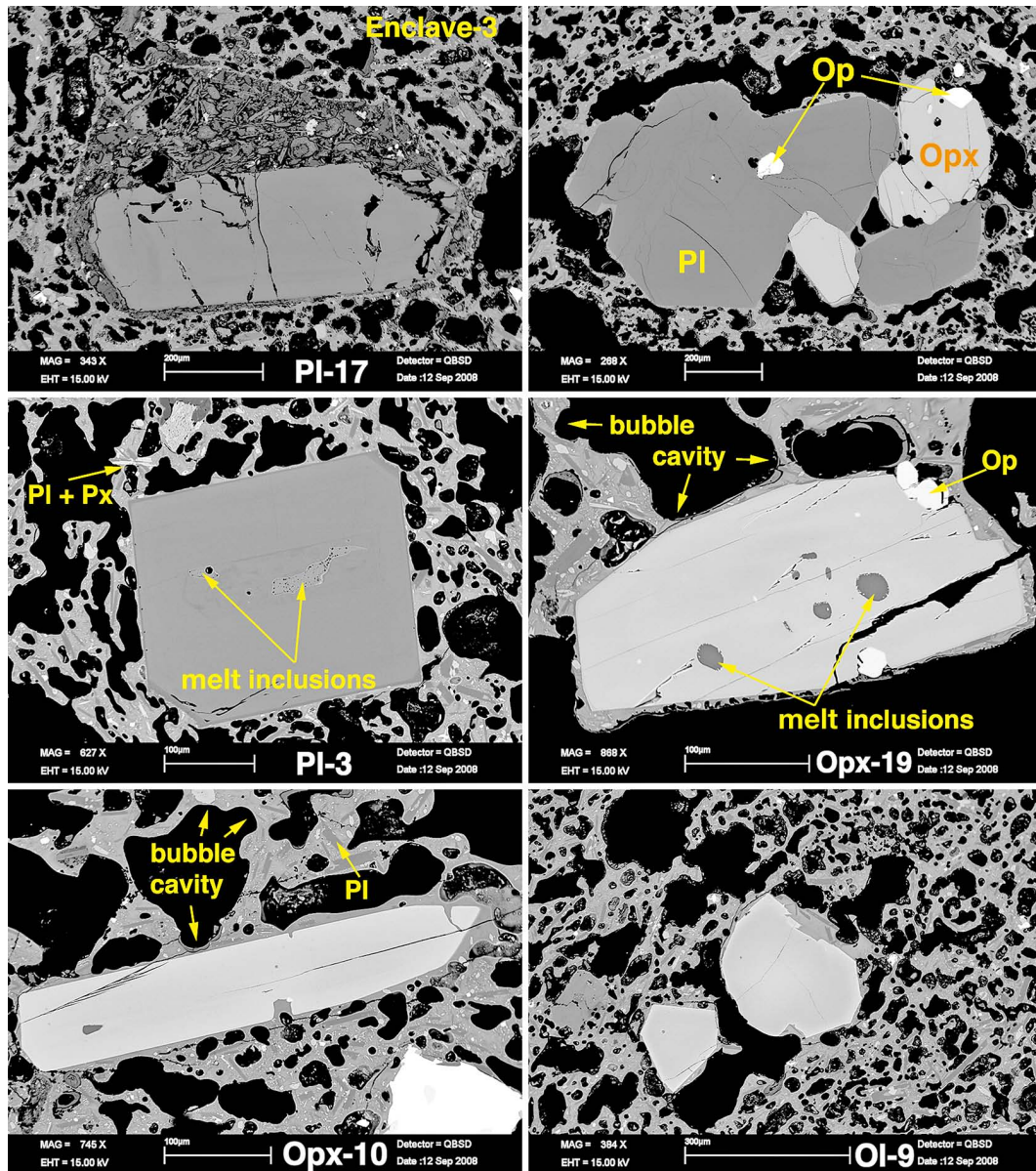
Fig. 3.18. SAN53-3B: *Pl-17* in *Enclave-3* contains several cracks and is embedded in a matrix with tiny pieces of anhedral or needle shaped crystal material. It is surrounded by a thin, glassy margin. Phenocrysts of the original sample are slightly zoned pl + opx. Pl + opx crystals are euhedral to subhedral and contain melt inclusions. Melt inclusions show tiny crystals. Op and Ol occur as well. The matrix shows irregular or elongate bubble cavities. Microlites within the matrix glass are tiny needles of pl + px. Contacts to px crystals are irregular while the rest of the crystal is fairly euhedral with melt attached to the outer rim.
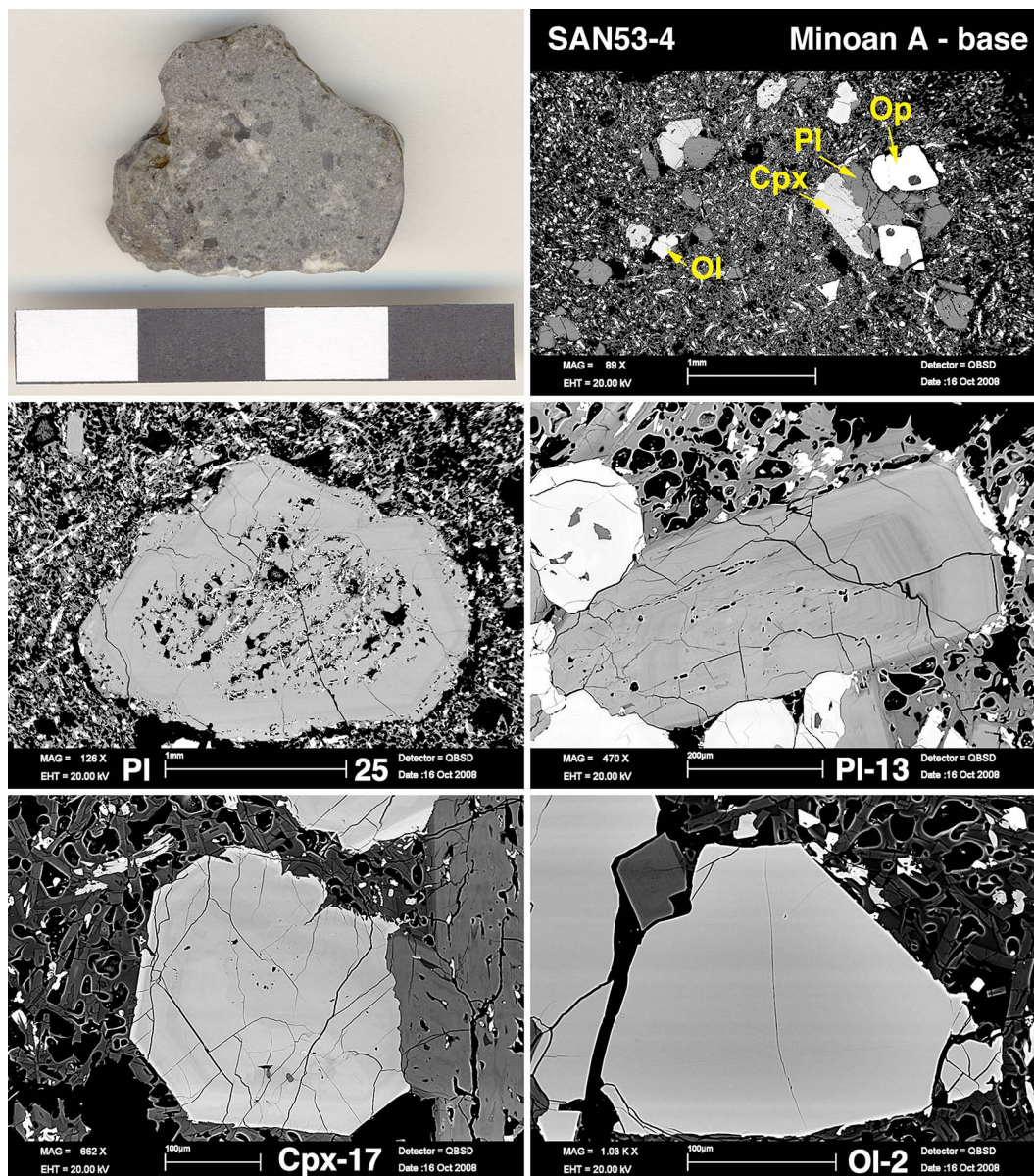
Fig. 3.19. SAN53-4: This specimen contains phenocrysts of pl + cpx + ol + mag in a glassy matrix with needles of pl + px and tiny opaques. *Pl-25* is anhedral with a spongy core. Former melt pockets are filled with tiny needles of px. *Pl-13* is elongate and oscillatory zoned. *Cpx-17* is subhedral and shows sector zoning. The lower parts of the crystal retained nice crystal faces, while the upper parts of the crystal are clearly resorbed. *Ol-2* is subhedral and normally zoned. Scale bar: 4 cm.

3.4.4. SAN53-4 – Minoan A – Base

SAN53-4 is a small grey scoria clast with a size of $\sim 1 \times 2$ cm. The groundmass is glassy with microcrysts of plagioclase + pyroxene + opaques. The clasts' texture is glomeroporphyritic with phenocrysts of plagioclase + clinopyroxene + olivine + magnetite.

Plagioclase   Plagioclase grains are bytownitic and reach sizes of $\sim 600\,\mu$m with a single sieve-textured grain reaching a size of about 2 mm. Grains appear to be subhedral with tabular shapes. They are often cracked, zoning is mostly oscillatory and not very pronounced, skeletal zones within plagioclase grains are probably remnants of sieve-textures, and melt pockets are replaced by inclusions of melt + pyroxene + opaques.

Clinopyroxene   Clinopyroxene grains reach sizes of $\leq 450\,\mu$m and are usually subhedral to anhedral. The latter especially when intergrown with plagioclase grains. Sector zoning is well visible and often disrupted by resorption. Grains contain multiple cracks. The most common inclusions are melt + opaques.

Olivine   Olivine grains are rarely $> 100\,\mu$m. They are subhedral to anhedral and normally zoned. Cracks are common. Inclusions include melt + plagioclase.

Magnetite   Single magnetite grains reach sizes of $\sim 400\,\mu$m. They are subhedral with inclusions of plagioclase and melt.
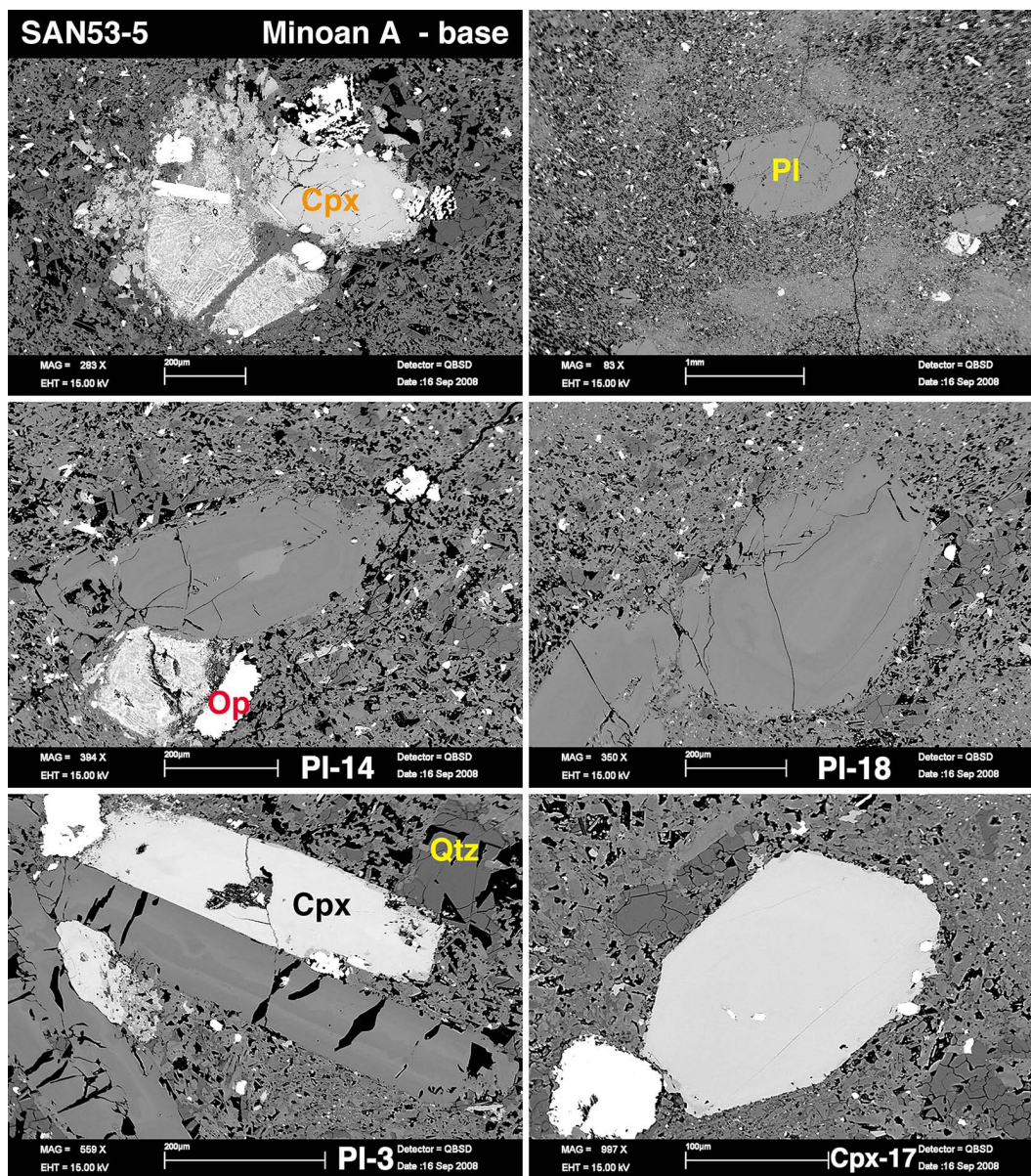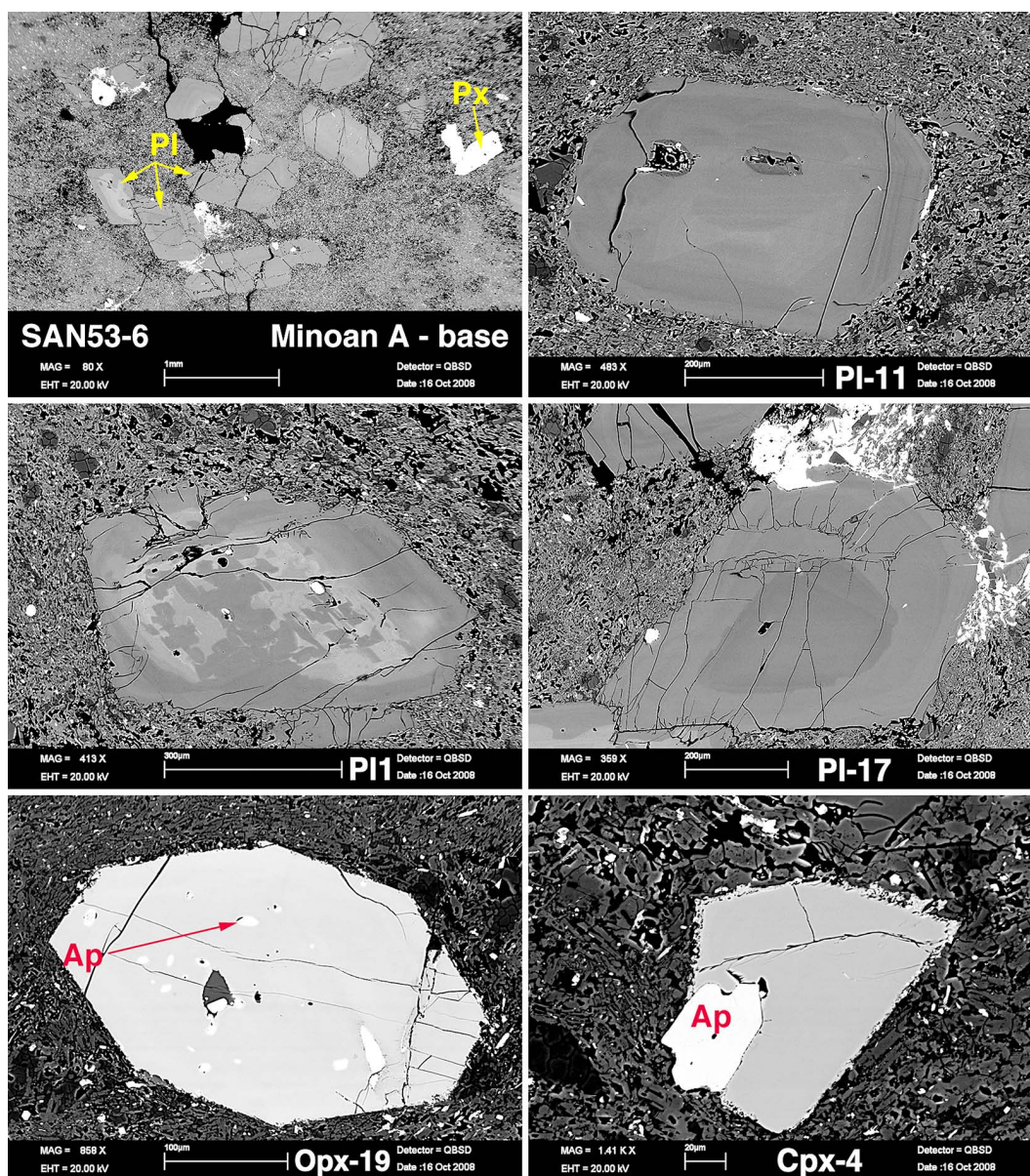
Fig. 3.20. SAN53-5: This sample contains phenocrysts of pl + cpx + op in a fine-grained matrix. Pl crystals are usually subhedral to anhedral while cpx crystals are euhedral to anhedral. *Pl-14* is an anhedral crystal with a high An-core surrounded by oscillatory zoning. *Pl-18* is anhedral with oscillatory zoning. Cpx crystals are usually heavily altered and often only 'skeletal' features are left.

3.4.5. SAN53-5 – Minoan A – Base

SAN53-5 is a small dark grey phenocryst with pale grey specks which are more silicic in composition. The texture is mostly glomeroporphyritic. The groundmass is fine-grained with microcrysts of plagioclase + pyroxene + quartz + magnetite + ilmenite. Opaques are often anhedral. Phenocrysts are mainly plagioclase + clinopyroxene.

Plagioclase Plagioclase is subhedral to anhedral, with acicular and tabular grain shapes. Grain size does not exceed $800\,\mu$m. Typical zonation types are oscillatory and patchy core textures. Grains are mostly andesitic with more An-rich cores of labradoritic composition.

Clinopyroxene Clinopyroxene crystals are subhedral to anhedral and often display a breakdown of clinopyroxene into a fine-grained light colored (BSE images) unknown mineral phase. Grains reach a size of $\leq 700\,\mu$m. Clinopyroxene crystals show no significant zoning.

Fig. 3.21. SAN53-6: This sample contains phenocrysts of pl + opx + cpx + op + ap in a fine-grained matrix. Pl phenocrysts are subhedral to anhedral and show various forms of zonation and resorption. *Pl-11* is a nice example for a sector zoned plagioclase. *Pl-1* is subhedral and has a patchy strongly resorbed core. *Pl-17* is reversely zoned with a low-An core. Opx is more common within this sample than cpx. Pyroxene crystals are usually euhedral to subhedral. Ap is a common inclusion in pyroxene grains.

55

3.4.6. SAN53-6 – Minoan A – Base

Sample SAN53-6 is a small grey scoria clast with specks and schlieren of more silicic composition. The sample's texture is porphyritic to glomerophyritic. The groundmass is fine-grained and appears to be quite dense. Phenocrysts are plagioclase + orthopyroxene + clinopyroxene. Opaques and apatite can be found as well, the latter often as an inclusion in orthopyroxene or intergrown with clinopyroxene.

Plagioclase Plagioclase grains are euhedral to subhedral and mostly have a tabular shape. Grains reach sizes of up to $600\,\mu m$. Resorption textures are common. Zoning types include patchy, oscillatory and sector zoning. Compositionally the grains fall in the field of andesine. An-rich cores are labradoritic in composition, darker cores lie on the low-An end of andesine.

Orthopyroxene + Clinopyroxene Orthopyroxene is the dominant pyroxene phase in this sample. Clinopyroxene can occur. Grain size does not exceed $500\,\mu m$. Grains are euhedral to subhedral, some of them more lath shaped while others appear to be more tabular. Most pyroxenes are weakly zoned. Intergrowth with inclusions of opaques and apatite is common.
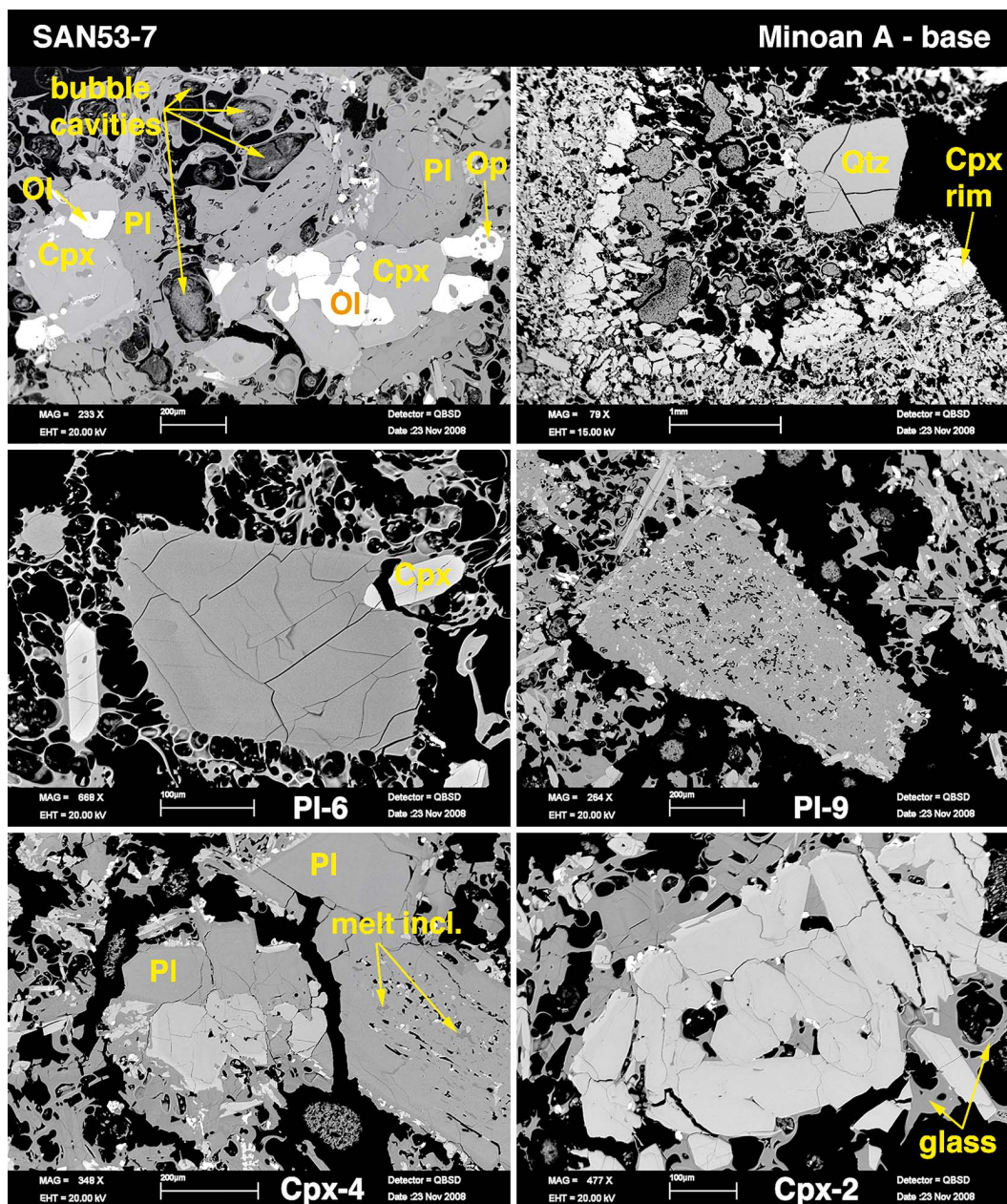
Fig. 3.22. SAN53-7: This sample has a very complex texture. Main phenocrystic phases are pl + cpx + ol + op in a highly glassy matrix with pronounced needle shaped px microcrysts and to a lesser degree pl. Bubble shapes are well developed, round or elongate with aperture pores and bubble wall remnants. A qtz crystal of almost 1 mm can be found within a glassy pocket surrounded by a rim of tiny cpx crystals (picture in the upper right corner). *Pl-6* is subhedral in shape and intergrown with a small cpx crystal. *Pl-9* is sieve-textured, with tiny melt veins, and fine needles of px. Cpx crystals can be intergrown with each other and/or pl to form glomeroporphyritic textures with irregular crystal faces.

3.4.7. SAN53-7 – Minoan A – Base

SAN53-7 is a small grey scoria clast with tiny specks of more silicic composition. The texture is porphyritic to glomeroporphyritic. The groundmass is glassy and vesicular with laths of clinopyroxene and plagioclase, tiny opaques are visible in BSE images. Phenocrysts are mainly plagioclase and clinopyroxene. A large quartz grain ($\sim 600\,\mu$m in diameter) is found in a glassy, vesicular matrix surrounded by clinopyroxene crystals.

Plagioclase   Plagioclase grains are subhedral and tabular to lath shaped and range in size from $100 - 1000\,\mu$m. They are often intergrown with clinopyroxene grains forming irregular boundaries. Common types of zoning include sieve-textured plagioclase grains with abundant inclusions of melt + clinopyroxene + opaques. Most grains are bytownitic in composition, although some grains with andesitic compositions are common.

Clinopyroxene   Clinopyroxene grains are subhedral, and lath-shaped. Grains reach sizes of up to $500\,\mu$m. Sector zoning and resorption features are common. Grains are often intergrown with plagioclase. Inclusions include melt + opaques.

Olivine   Rarely small subhedral and normally zoned olivine grains not exceeding sizes of $350\,\mu$m can be found.
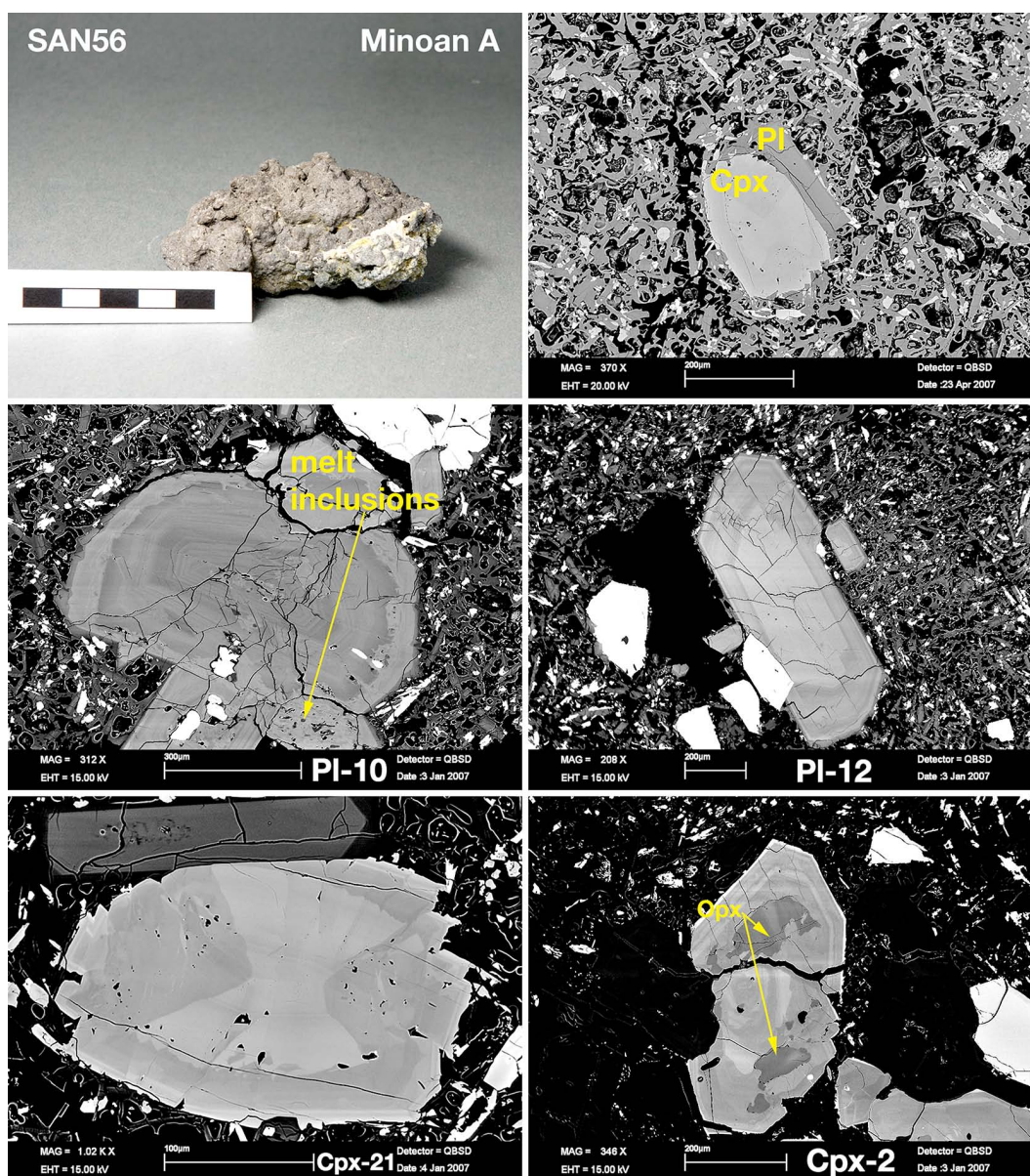
Fig. 3.23. SAN56: This specimen is a grey scoria clast with phenocrysts of pl + cpx + ol + op. The matrix is glomeroporphyritic to porphyritic and consists of tiny needles of pl + cpx as well as op + glass. Phenocrysts of pl + cpx are euhedral to subhedral, rims are often partly resorbed. Pl crystals show oscillatory zonation with inclusions of melt + op. Clinopyroxenes show sector zoning and resorption textures (*Cpx-21* and *Cpx-2*). Scale bar: 5 cm.

3.4.8. SAN56 – Minoan A

Scoria clasts of SAN56 were sampled from Minoan Unit A. Clasts vary in length between $2-8$ cm and in width between $2-5$ cm. They are dense with a cauliflower-like surface. Bubble cavities are visible and reach sizes of up to 0.5 cm in diameter; they are round or slightly elongate. Small phenocrysts are visible to the eye. The texture is glomeroporphyritic to porphyritic. Phenocrysts in this sample are plagioclase + clinopyroxene + olivine + opaques. The glassy matrix contains tiny needles of plagioclase + clinopyroxene, and specks of opaques.

Plagioclase Plagioclase phenocrysts vary in size between $200-900\,\mu$m. They are euhedral to subhedral. Rims are slightly resorbed and are usually less rich in anorthite with glassy matrix material still attached to the crystal. Oscillatory zoning is well developed. Partially resorbed cores and zones can be visible, but patchy features are less pronounced compared to plagioclase crystals in Minoan pumice. Some plagioclase crystals have sieve-textured cores filled with melt pockets and tiny pyroxene needles.

Clinopyroxene Clinopyroxene grains are euhedral to subhedral and show strong resorption textures. Crystal size varies between $100-650\,\mu$m. Clinopyroxene grains commonly display sector zonation. Zonation faces are often patchy. Common inclusions within clinopyroxene are plagioclase + melt and to a lesser degree magnetite.

Olivine Olivine crystals are usually subhedral and have sizes between $100-400\,\mu$m. Some show zoning with a darker Mg-rich core and an Fe-rich rim, others appear unzoned in BSE images. Inclusions of plagioclase + clinopyroxene + melt are common. Often tiny crystals can be found in melt inclusions.
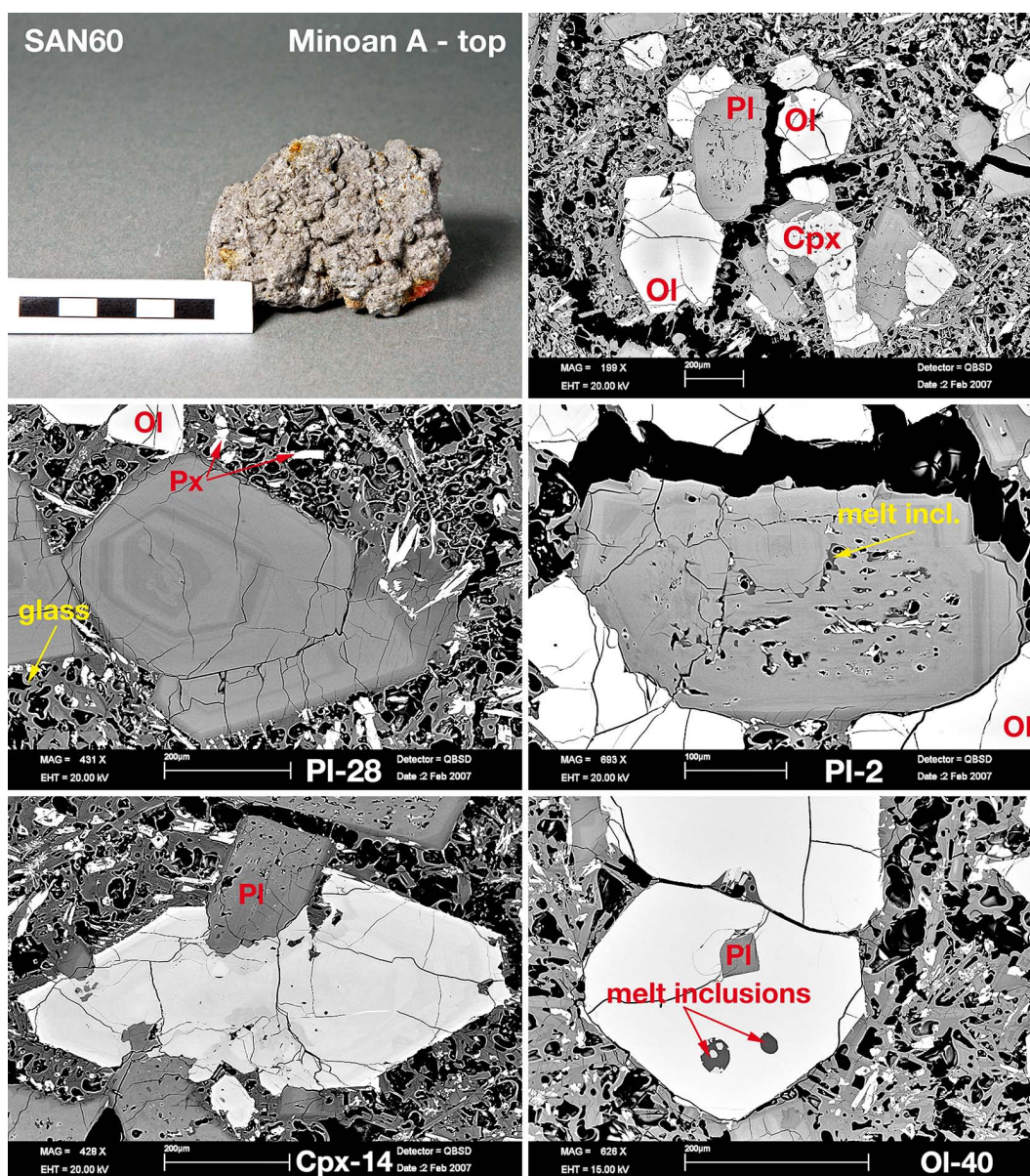
Fig. 3.24. SAN60: This sample is a grey scoria clast with phenocrysts of pl + cpx + ol. Groundmass microcrysts are pl + needles of cpx + glass. Phenocrysts of pl + cpx are euhedral to subhedral with partially resorbed rims. Pl crystals are zoned with resorption textures and inclusions of melt + px. Cpx crystals are sector zoned and resorbed. Ol grains are subhedral to anhedral with inclusions of pl + melt. Scale bar: 5 cm.

61

3.4.9. SAN60 – Minoan A – Top

Scoria clasts of SAN60 were sampled from the top of Minoan Unit A. Clasts reach sizes of $\sim 7\,\mathrm{cm}$. They are dense with cauliflower-like shapes. Bubble cavities are visible and up to $0.3\,\mathrm{cm}$ in diameter, usually round or slightly elongate. Small phenocrysts are visible to the eye. Phenocrysts within this sample are plagioclase + clinopyroxene + olivine + opaques. The matrix consists of tiny needles of plagioclase + clinopyroxene, and glass.

Plagioclase   Plagioclase phenocrysts hardly reach sizes of $1\,\mathrm{cm}$. Most grains reach sizes of $\sim 0.5\,\mathrm{cm}$ or less. They are subhedral, rims often show resorption features. Oscillatory zoning is developed to a lesser degree compared to pumice plagioclase. Partially resorbed cores can be visible, but patchy features are less pronounced compared to plagioclase crystals in Minoan pumice. Some Plagioclase crystals have cores with many tiny holes that are often filled with melt pockets and tiny pyroxene needles (sieve-textures).

Clinopyroxene   Clinopyroxene crystals are euhedral to anhedral and mostly reach sizes of less than $0.5\,\mathrm{cm}$ with some needle shaped crystals reaching sizes of $0.8\,\mathrm{cm}$. Clinopyroxene grains show sector zonation. Zonation faces are often patchy indicating a strong resorption event. When intergrown with plagioclase, clinopyroxene phenocrysts are heavily resorbed without any clear crystal faces visible. Plagioclase often occurs as an inclusion in clinopyroxene crystals. Melt inclusions are hardly found in clinopyroxenes.

Olivine   Olivine grains are normally zoned and usually subhedral and have sizes of about $0.5\,\mathrm{cm}$ and less. Inclusions of plagioclase + melt can be found.

3.4.10. SAN52Agg2 – Minoan A – Base – Crystal Clot
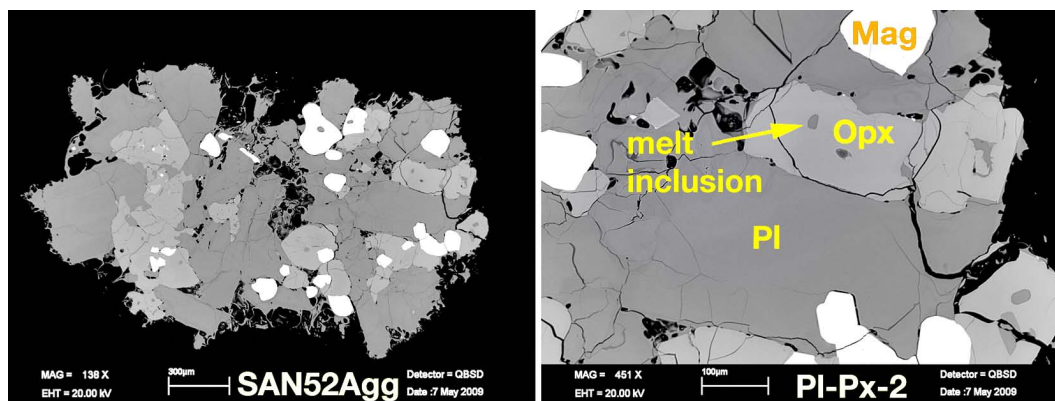
Fig. 3.25. SAN52Agg2: A crystal clot that was handpicked from a Minoan pumice clast (SAN52, Minoan Unit A). The clot consists of pl, opx and mag which form a glomeroporphyritic texture. Melt inclusions can be found in the crystals, especially opx. Glass selvages attached to crystals are found in abundance.

Crystal clots consisting of phenocrysts of plagioclase, orthopyroxene and magnetite in a glassy matrix and forming a glomeroporphyritic texture are abundant in Minoan pumice. They are interpreted as evidence for intensive mingling of the rhyodacitic host magma with more mafic magma (Cottrell *et al.*, 1999; Druitt *et al.*, 1999). Phenocrysts of crystal clots are usually subhedral to anhedral showing resorbed rims. Melt inclusions—especially in orthopyroxene—are common. Clots reach sizes up to 4 mm, and are often found in bubble cavities of the Minoan pumice. The crystal clot shown in Fig. 3.25 was handpicked from SAN52—a pumice clast sampled from the base of Minoan Unit A (Plinian pumice fall deposit).

4. Major, Minor and Trace Elements in Minoan Samples

4.1. Matrix Glass and Melt Inclusions
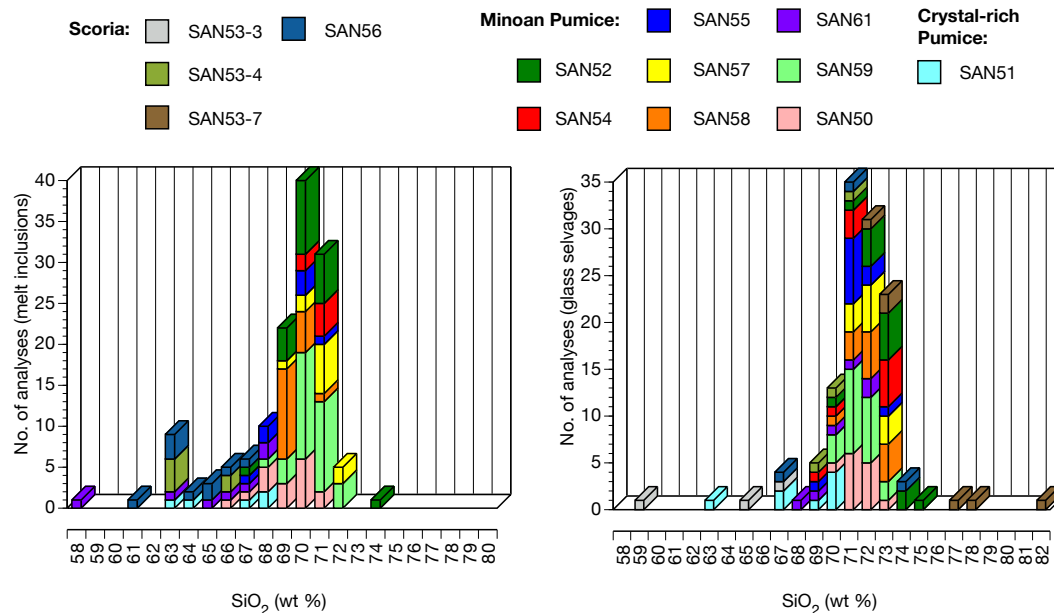
Fig. 4.1. Histograms of SiO_2 concentration (wt%) in melt inclusions of phenocrysts (left diagram) and matrix glass + glass selvages (right diagram) of Minoan pumice and scoria samples.

Melt inclusions in phenocrysts (plagioclase, orthopyroxene, clinopyroxene and olivine), matrix glass and glass selvages (selvage = glass attached to phenocrysts) were analyzed in samples of the Minoan pumice (Minoan Units A–D), the Crystal-rich pumice (SAN51, Minoan D), and four scoria clasts (Minoan A) with a glassy matrix (Table 4.1 and Table 4.2).

SiO_2 concentrations (wt%) in melt inclusions of phenocrysts as well as matrix glass and glass selvages of samples analyzed are depicted in Fig. 4.1. Most analyses of melt inclusions of the Minoan pumice range between $\sim 68 - 72$ wt% SiO_2. Melt

inclusions from SAN50 (Minoan D) cover a slightly wider range of $\sim 66 - 71\,\text{wt}\%$ SiO_2.

SiO$_2$ contents of the Crystal-rich pumice SAN51 (Minoan D) overlap with those of SAN50 and the scoria samples. SiO_2 contents of melt inclusions from Minoan scoria range between $\sim 61 - 67\,\text{wt}\%$. Melt inclusions of sample SAN61 from Minoan D overlap with those of the scoria clasts.

The SiO_2 contents of glass selvages range from $\sim 69 - 82\,\text{wt}\%$. Compared to melt inclusions, there is more overlap in SiO_2 concentrations between scoria, Crystal-rich pumice and the Minoan pumice due to mingling.
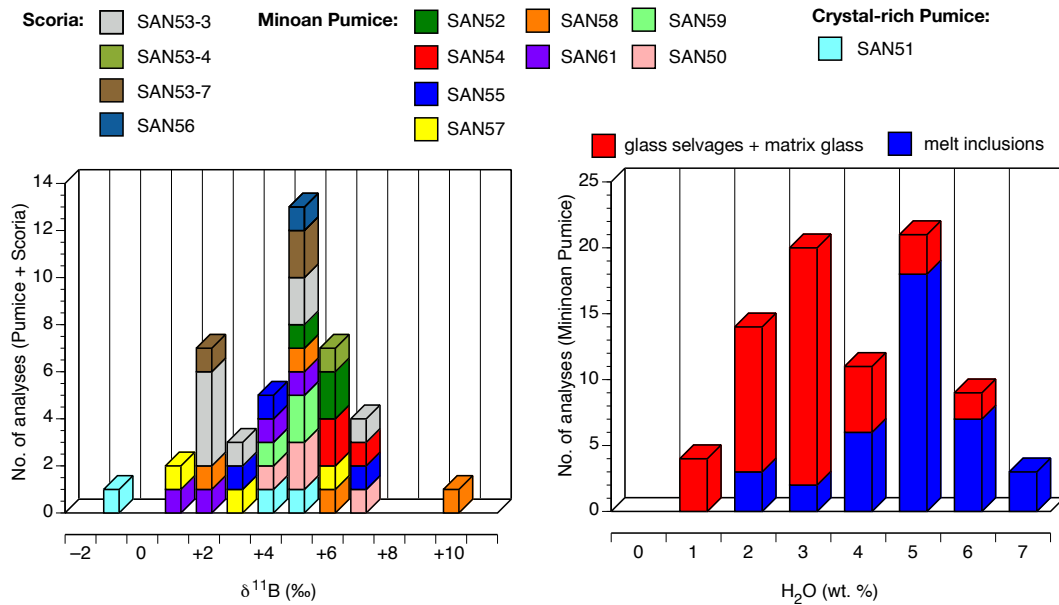
Fig. 4.2. Distribution of $\delta^{11}B$ (‰) in Minoan pumice and scoria samples (left diagram), and H$_2$O (wt %) distributions in melt inclusions and glass selvages of Minoan pumice phenocrysts (right diagram).

δ^{11}B and H$_2$O δ^{11}B (‰) values and H$_2$O (wt %) contents are depicted in Fig. 4.2. δ^{11}B values mostly range from $\sim +1 - +8$‰. There is an overlap of δ^{11}B values between Minoan pumice, Crystal-rich pumice and scoria clasts (Fig. 4.2). A glass selvage attached to pyroxene in sample SAN58 has the highest δ^{11}B ($\sim +10$‰), while the lowest value was found in a melt inclusion of a plagioclase phenocryst in the Crystal-rich pumice, ~ -1‰ (Pl-3, SAN51-1B). The heavy δ^{11}B signature in glass of Minoan tephra is best explained by a δ^{11}B-enriched slab component. Straub

& Layne (2002) reported $\delta^{11}B$ values as high as $+12\%o$ for Izu arc volcanic rocks and a slab derived origin. Slab derived fluids as a cause for high $\delta^{11}B$ signatures in volcanic glasses are also supported by the works of Marschall *et al.* (2007) and Helbling-Marschall (2011, references therein).

H$_2$O contents vary between $\sim 1 - 7\,wt\%$ in glass of the Minoan pumice (Fig. 4.2). Glass selvages and matrix glass have lower H$_2$O contents, varying between $\sim 1 - 6\,wt\%$ with most analyses between $\sim 2 - 3\,wt\%$, indicating a loss of H$_2$O due to degassing of the magma body. H$_2$O contents in melt inclusions of plagioclase within the Minoan pumice vary between $\sim 2 - 7\,wt\%$ with most analyses in the range of $\sim 5 - 6\,wt\%$. In the Crystal-rich pumice H$_2$O varies between $\sim 4.5 - 5.4\,wt\%$ in plagioclase melt inclusions. An inclusion analyzed in a plagioclase crystal in the more mafic part of sample SAN61-2 had $\sim 5.4\,wt\%$ H$_2$O, and $\sim 4.6\,wt\%$ H$_2$O were analyzed in a melt inclusion in Pl-23 of scoria clast SAN53-4.

Chlorine, Lithium and Boron   Trace element concentrations of chlorine, lithium and boron in melt inclusions and matrix glass of the Minoan pumice, Crystal-rich pumice (included in Minoan D) and scoria samples with glassy matrix are presented in Fig. 4.3. Chlorine concentrations were analyzed by EPMA and lithium and boron concentrations were analyzed by SIMS.

Chlorine concentrations in melt inclusions of phenocrysts found in the Minoan pumice vary between $\sim 1500 - 4000\,\mu g/g$. Inclusions found in the Crystal-rich pumice phenocrysts and in pumice phenocrysts of samples SAN61-1A and SAN61-2 (Minoan Unit B) show lower chlorine concentrations. In the Crystal-rich pumice these vary between $\sim 1300 - 2400\,\mu g/g$ and in the Minoan B samples between $\sim 800 - 1900\,\mu g/g$. Chlorine concentrations in melt inclusions of scoria vary between $\sim 1000 - 2180\,\mu g/g$. One inclusion in a pyroxene of SAN52Agg has chlorine concentrations of $\sim 3400\,\mu g/g$.

Compared to melt inclusions chlorine concentrations in matrix glass of the scoria clasts span a wider range between $\sim 400 - 2800\,\mu g/g$. This is probably due to mingling with the rhyodacitic host magma. A tendency towards lower chlorine concentrations is also observed in the matrix glass of the Minoan pumice ($\sim 1500 - 3900\,\mu g/g$) and the Crystal-rich pumice ($\sim 800 - 2400\,\mu g/g$) which is probably due to degassing of the magma.

Lithium concentrations in melt inclusions of Minoan pumice phenocrysts vary between $\sim 7 - 33\,\mu g/g$. One inclusion found in a plagioclase of the Crystal-rich pumice has a lithium concentration of $\sim 38\,\mu g/g$.

Lithium concentrations in matrix glass and glass selvages vary between $\sim 20 - 37\,\mu g/g$ for the Minoan pumice and show no evident trace of degassing; there

rather seems to be a slight enrichment in lithium. Glass analyzed in the Crystal-rich pumice has lithium concentrations between $\sim 22-26\,\mu\mathrm{g/g}$. These are in the range of the Minoan pumice matrix glass. Matrix glass analyzed in the Minoan scoria samples cover a wider range down to lower lithium concentrations, $\sim 12-31\,\mu\mathrm{g/g}$.

Boron concentrations in the melt inclusions and matrix glass of the Minoan pumice are very similar and vary between $\sim 14-26\,\mu\mathrm{g/g}$, while those of the Crystal-rich pumice vary between $\sim 16-19\,\mu\mathrm{g/g}$. Matrix glass analyzed within the scoria samples has boron concentrations between $\sim 5-23\,\mu\mathrm{g/g}$. The lowest boron concentrations of the scoria samples were analyzed in SAN53-7; these were $\sim 5\,\mu\mathrm{g/g}$. The highest were analyzed in SAN53-3: $\sim 22\,\mu\mathrm{g/g}$.

Average concentrations of all glass analyses are presented in Table 4.1 and Table 4.2.
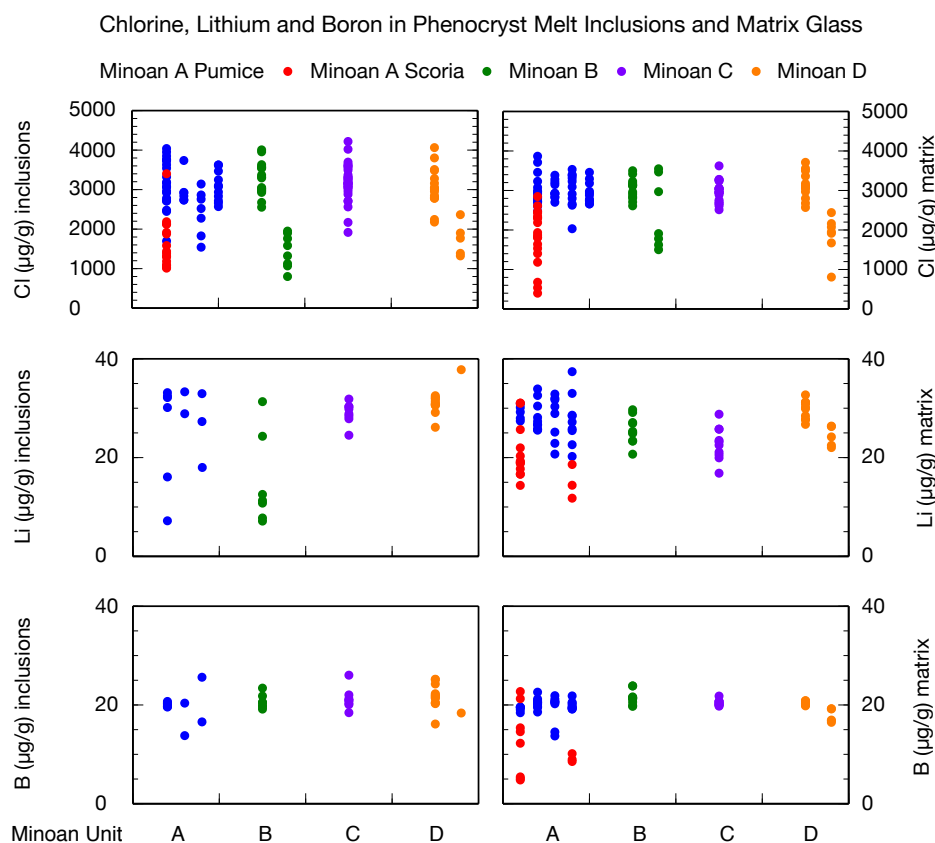
Fig. 4.3. The chlorine concentration is usually lower in inclusions of the Minoan scoria samples, and slightly lower in the Crystal-rich pumice (right orange column of Minoan D) and SAN61 (right green column of Minoan B) phenocryst inclusions. Li shows a high range of concentrations in phenocrysts inclusions compared to matrix glass. B concentrations in melt inclusions and matrix glass seem to be quite similar in the Minoan pumice and Crystal-rich pumice, but vary considerably in the scoria samples. F, Cl and S were analyzed by EPMA.

Table 4.1. EPMA and SIMS Analyses of Melt Inclusions in Plagioclase and Pyroxene

Pl Samples	SAN52	SAN52Agg	SAN54	SAN55	SAN57	SAN58	SAN61-1A	SAN59	SAN50	SAN51
Type	incl	incl	incl	incl	incl	incl	incl	incl	incl	incl
SiO_2	69.77	62.34	71.00	69.88	70.44	69.51	68.25	70.32	69.15	66.63
TiO_2	0.32	0.73	0.28	0.24	0.29	0.32	0.49	0.30	0.30	0.42
Al_2O_3	13.33	14.59	13.30	13.82	12.89	13.29	13.09	13.31	13.54	15.18
FeO	2.05	4.79	1.97	1.83	2.07	2.05	2.90	1.98	2.10	2.84
MnO	0.08	0.15	0.05	0.04	0.07	0.06	0.12	0.07	0.04	0.09
MgO	0.29	1.35	0.28	0.26	0.28	0.31	0.64	0.30	0.33	0.66
CaO	1.31	3.39	1.30	1.53	1.15	1.33	1.57	1.30	1.40	2.59
Na_2O	3.93	3.21	4.52	4.50	3.61	4.26	4.31	3.91	4.50	4.30
K_2O	3.19	2.59	3.11	3.02	3.12	3.11	2.96	3.17	3.18	2.89
P_2O_5	0.04	0.20	0.00	0.07	0.04	0.04	0.18	0.06	0.05	0.10
Total	94.31	93.32	95.82	95.18	93.95	94.28	94.50	94.70	94.59	95.70
F ($\mu g/g$)	NA	1098	NA	NA	NA	1102	NA	NA	NA	919
Cl ($\mu g/g$)	3371	1877	2837	2605	3221	3367	1901	3156	3257	1856
S ($\mu g/g$)	128	250	67	165	103	83	30	107	172	113
Li ($\mu g/g$)	31.3	NA	27.8	NA	18.0	17.6	NA	24.1	NA	34.6
2σ	0.6	NA	0.3	NA	0.4	0.4	NA	0.3	NA	0.9
Be ($\mu g/g$)	1.93	NA	1.98	NA	1.90	1.99	NA	1.94	NA	2.0
2σ	0.08	NA	0.12	NA	0.11	0.11	NA	0.12	NA	0.2
B ($\mu g/g$)	22.3	NA	21.1	NA	20.4	20.7	NA	17.5	NA	18.0
2σ	0.4	NA	0.7	NA	0.4	0.5	NA	0.4	NA	0.7
Sr ($\mu g/g$)	55.4	NA	49.6	NA	55.8	49.5	NA	125	NA	84.6
2σ	1.59	NA	2.2	NA	1.6	1.5	NA	3	NA	5.9
Ba ($\mu g/g$)	386	NA	423	NA	383	421	NA	383	NA	391
2σ	9	NA	8	NA	7	8	NA	8	NA	12
$\delta^{11}B$ (‰)	NA	NA	NA	NA	NA	NA	+5.9	NA	NA	+2.6
2σ	NA	NA	NA	NA	NA	NA	2.0	NA	NA	2.1
H_2O (wt. %)	4.8	NA	4.2	NA	5.7	5.0	NA	4.7	4.0	NA
2σ	0.0	NA	0.0	NA	0.0	0.0	NA	0.0	0.0	NA

Px Samples	SAN52	SAN52Agg	SAN54	SAN55	SAN57	SAN58	SAN61-1A	SAN59	SAN50	SAN51
Type	incl	incl	incl	incl	incl	incl	incl	incl	incl	incl
SiO_2	69.93	65.27	70.49	68.33	70.93	69.30	63.91	70.68	69.19	63.78
TiO_2	0.30	0.47	0.35	0.35	0.29	0.26	0.28	0.31	0.75	0.45
Al_2O_3	13.72	16.30	13.20	14.26	13.55	13.19	16.18	13.39	13.48	15.36
FeO	2.40	2.75	2.56	2.75	2.36	2.15	2.76	2.25	2.73	3.77
MnO	0.10	0.08	0.07	0.13	0.07	0.07	0.11	0.03	0.09	0.19
MgO	0.29	0.41	0.30	0.37	0.24	0.27	1.33	0.19	0.34	4.10
CaO	1.46	2.74	1.40	2.08	1.35	1.41	4.82	1.43	1.47	3.19
Na_2O	3.72	3.82	4.39	4.66	4.16	4.30	4.04	4.37	4.55	3.54
K_2O	3.00	2.86	2.97	2.87	3.06	2.98	1.99	3.10	3.08	1.37
P_2O_5	0.04	0.20	0.01	0.06	0.04	0.05	0.12	0.01	0.03	0.12
Total	94.97	94.90	95.74	95.87	96.05	93.99	95.53	95.77	95.70	95.87
F ($\mu g/g$)	NA	636	NA	NA	NA	NA	450	NA	NA	1238
Cl ($\mu g/g$)	2870	2369	3130	2170	2996	2921	1373	3313	2909	1322
S ($\mu g/g$)	55	240	67	93	207	18	112	62	52	230
Li ($\mu g/g$)	NA	NA	31.6	31.1	30.1	12.5	18.4	30.1	31.6	NA
2σ	NA	NA	0.5	0.4	0.6	1.2	0.8	0.3	0.3	NA
Be ($\mu g/g$)	NA	NA	1.96	1.90	1.71	2.12	1.05	2.24	2.06	NA
2σ	NA	NA	0.10	0.08	0.08	0.13	0.07	0.10	0.06	NA
B ($\mu g/g$)	NA	NA	19.6	15.5	21.1	21.8	5.5	21.5	21.7	NA
2σ	NA	NA	0.4	0.5	0.3	0.5	0.3	0.6	0.5	NA
Sr ($\mu g/g$)	NA	NA	50.6	102	50.8	50.5	117	52.2	57.0	NA
2σ	NA	NA	0.8	2	0.5	1.9	5	0.9	0.9	NA
Ba ($\mu g/g$)	NA	NA	414	498	423	450	260	450	500	NA
2σ	NA	NA	6	6	5	7	11	6	6	NA
$\delta^{11}B$ (‰)	+8.3	NA	+6.7	NA	+1.8	+6.3	NA	+4.5	+6.8	NA
2σ	3.4	NA	1.7	NA	3.4	1.6	NA	1.9	1.5	NA
H_2O (wt. %)	NA	NA	NA	NA	NA	NA	NA	NA	NA	NA
2σ	NA	NA	NA	NA	NA	NA	NA	NA	NA	NA

Average element concentrations of melt inclusions in pl, opx and cpx phenocrysts of the Minoan pumice and the Crystal-rich pumice. Due to space issues, SAN52Agg is listed with the pumice samples. Li, Be, B, Sr, Ba, $\delta^{11}B$ and H_2O were analyzed by SIMS. NA = not analyzed.

Table 4.2. EPMA and SIMS Analyses of Melt Inclusions and Matrix Glass

Sample	SAN52	SAN52Agg	SAN54	SAN55	SAN57	SAN58	SAN61	SAN59	SAN50	SAN51
Type	matrix	matrix	matrix	matrix	matrix	matrix	matrix	matrix	matrix	matrix
SiO_2	71.94	67.50	71.82	71.18	71.88	71.84	67.55	71.42	71.49	68.13
TiO_2	0.30	0.78	0.31	0.33	0.30	0.27	0.35	0.30	0.33	0.48
Al_2O_3	13.68	15.97	13.68	13.64	13.51	13.43	13.48	13.47	13.26	15.46
FeO	2.15	4.37	2.22	2.17	2.19	2.06	2.15	2.05	2.19	3.18
MnO	0.06	0.09	0.06	0.06	0.07	0.09	0.06	0.06	0.07	0.06
MgO	0.29	0.90	0.29	0.33	0.26	0.28	0.33	0.29	0.25	0.65
CaO	1.41	3.05	1.47	1.47	1.38	1.35	1.70	1.38	1.29	2.69
Na_2O	4.64	4.22	4.70	4.63	4.61	4.47	4.30	4.56	4.58	4.55
K_2O	3.18	2.79	3.18	3.17	3.21	3.22	2.87	3.20	3.17	2.86
P_2O_5	0.03	0.23	0.03	0.07	0.05	0.05	0.12	0.03	0.06	0.15
Total	97.68	99.90	97.75	97.05	97.46	97.07	92.93	96.75	96.68	98.22
F (μg/g)	NA	1460	NA	NA	NA	901	896	NA	NA	860
Cl (μg/g)	3004	1762	3016	2998	2937	3044	2614	2976	3127	1894
S (μg/g)	55	200	100	84	40	70	50	53	141	84
Li (μg/g)	28.5	NA	28.5	26.4	30.7	29.4	24.0	24.6	29.0	24.8
2σ	0.4	NA	0.4	0.9	0.3	1.8	1.0	0.3	0.3	0.4
Be (μg/g)	2.11	NA	2.22	2.07	1.99	2.10	2.08	2.08	2.12	2.07
2σ	0.09	NA	0.15	0.10	0.06	0.07	0.13	0.09	0.07	0.1
B (μg/g)	20.3	NA	20.0	17.6	19.4	20.7	12.3	20.3	20.6	17.7
2σ	0.4	NA	0.6	0.4	0.4	0.4	0.3	0.5	0.4	0.5
Sr (μg/g)	51.3	NA	54.8	74.1	54.7	59.1	113	54.1	50.7	69.1
2σ	1.4	NA	1.5	1.2	0.9	2.1	3	1.3	1.2	2.3
Ba (μg/g)	451	NA	460	499	467	472	542	472	460	460
2σ	7	NA	8	6	4	5	9	6	8	9
$\delta^{11}B$ (‰)	NA	NA	NA	+3.9	+3.0	+9.6	NA	NA	+5.3	+4.2
2σ	NA	NA	NA	1.6	1.8	1.6	NA	NA	1.8	3.2
H_2O (wt. %)	1.7	NA	1.5	2.8	NA	2.6	NA	2.6	NA	NA
2σ	0.0	NA	0.0	0.0	NA	0.0	NA	0.0	NA	NA

Sample	SAN56-1	SAN53-4	SAN56-1	SAN53-4	SAN53-4	SAN56-1	SAN53-3	SAN53-4	SAN53-7	SAN56-1
Type	incl	incl	incl	incl	incl	incl	matrix	matrix	matrix	matrix
SiO_2	63.65	62.62	64.11	63.48	66.08	64.97	63.57	70.31	75.79	70.90
TiO_2	0.62	0.33	0.34	0.30	0.27	0.30	0.97	0.34	0.32	0.73
Al_2O_3	13.29	17.86	17.28	18.03	17.37	16.92	15.56	14.18	11.10	13.31
FeO	4.43	2.86	2.44	2.86	3.33	4.41	6.19	2.23	2.04	2.36
MnO	0.08	0.07	0.10	0.10	0.07	0.07	0.17	0.08	0.05	0.09
MgO	1.30	0.54	0.70	0.51	0.75	2.05	1.12	0.36	0.22	0.31
CaO	2.61	4.19	4.11	4.44	2.85	2.40	4.35	2.00	1.21	1.64
Na_2O	3.02	3.75	3.53	3.93	4.71	4.63	4.63	4.03	3.26	3.62
K_2O	2.52	1.85	2.09	1.77	2.11	3.69	2.79	3.09	2.70	3.29
P_2O_5	0.16	0.15	0.14	0.15	0.15	0.15	0.23	0.24	0.11	0.26
Total	91.69	94.23	94.83	95.56	97.69	99.60	99.57	96.84	96.81	96.50
F (μg/g)	NA	303	NA	598	992	NA	1304	1166	532	NA
Cl (μg/g)	1297	1093	1406	1314	1387	2129	2461	2282	1176	1985
S (μg/g)	0	30	143	0	50	0	180	63	37	227
Li (μg/g)	NA	NA	NA	NA	NA	NA	28.4	19.1	18.3	NA
2σ	NA	NA	NA	NA	NA	NA	1.1	0.4	0.3	NA
Be (μg/g)	NA	NA	NA	NA	NA	NA	1.6	2.0	1.2	NA
2σ	NA	NA	NA	NA	NA	NA	0.1	0.1	0.1	NA
B (μg/g)	NA	NA	NA	NA	NA	NA	22.0	14.1	5.1	NA
2σ	NA	NA	NA	NA	NA	NA	05	0.4	0.2	NA
Sr (μg/g)	NA	NA	NA	NA	NA	NA	100	87.6	56.3	NA
2σ	NA	NA	NA	NA	NA	NA	4	5.9	2.3	NA
Ba (μg/g)	NA	NA	NA	NA	NA	NA	205	522	123	NA
2σ	NA	NA	NA	NA	NA	NA	7	10	4	NA
$\delta^{11}B$ (‰)	NA	NA	NA	+3.9	NA	NA	+2.0	+2.6	NA	NA
2σ	NA	NA	NA	4.0	NA	NA	2.9	6.4	NA	NA
H_2O (wt. %)	NA	NA	NA	NA	NA	NA	NA	NA	NA	NA
2σ	NA	NA	NA	NA	NA	NA	NA	NA	NA	NA

Average element concentrations of matrix glass analyses in Minoan pumice/Crystal-rich pumice (upper half of table), as well as melt inclusions and matrix glass of Minoan scoria samples. Li, Be, B, Sr, Ba, $\delta^{11}B$ and H_2O were analyzed by SIMS. NA = not analyzed.

4.2. Phenocryst Analyses

For this study phenocrysts from 10 pumice samples and 11 scoria samples were analyzed by EPMA and SIMS. The main emphasis was put on plagioclase, which will be described in more detail in the following section. Major, minor and trace element geochemistry of orthopyroxene, clinopyroxene and olivine will only be described briefly in this chapter, their profile sheets can be found in the Electronic Appendix.

Plagioclase feldspars form a solid solution series which has two endmembers, albite ($NaAlSi_3O_8$) and anorthite ($CaAl_2Si_2O_8$). The nomenclature for this series is based on six arbitrary divisions of the plagioclase anorthite content, $Ca/(Na+Ca+K)$ (Klein, 2002). The anorthite content is often expressed by the term X_{An} or in the form of $Ab_{1-X}An_X$. The last term is often reduced to An_X. Albite for example covers the composition range between An_{0-10}, oligoclase between An_{10-30}, andesine between An_{30-50}, labradorite between An_{50-70}, bytownite between An_{70-90}, and anorthite between An_{90-100}.

All feldspars analyzed plot within this solution series between the fields of andesine and anorthite (An_{30-90}). Fig. 4.4, Fig. 4.15, and Fig. 4.22 are ternary diagrams, including orthoclase ($KAlSi_3O_8$). These diagrams are used to show the range of anorthite contents found in plagioclase of the Minoan tephra. Ticks are used to mark the approximate positions of the six plagioclase feldspar composition fields.

In the following section the major, minor and trace element characteristics of representative plagioclase crystals are described briefly.

4.2.1. Plagioclase Minoan Pumice: Units A–D

An Average anorthite contents of nine plagioclase crystals of Minoan A–D are shown in Table 4.3. Fig. 4.4 shows the range of anorthite contents analyzed by EPMA for these crystals. Pl-3 (SAN52A), Pl-1 (SAN54A) and Pl-2 (SAN55A) (Table 4.3) plot in the andesine field (An_{30-50}). Pl-3 is the only phenocryst in this group that shows a well developed core visible in the anorthite profile (Fig. 4.6).

All other crystals have cores with higher anorthite content compared to their andesinitic rim composition (normal zoning). Pl-5 (SAN52A, Fig. 4.7) has an extremely patchy core with an anorthite content of up to An_{80}, while the core of Pl-3 (SAN50C) has a maximum anorthite content of An_{76}.

Pl-17 (SAN61-1A, Fig. 4.12) is mostly of bytownitic composition (An_{70-90}). Pl-17's core has the highest anorthite content analyzed of crystals shown in Table 4.3 (An_{84}), and its anorthite content decreases towards the rim to (An_{36}). Pl-1

of SAN61-1A (see Appendix B) covers a similar range of anorthite contents as Pl-17 does.

Fig. 4.5 shows anorthite rim compositions of plagioclase crystals from the different Minoan pumice units. Except for plagioclase crystal Pl-21 found in sample SAN61-2 and crystals of the Crystal-rich pumice (see next subsection), the anorthite rim concentrations hardly vary between the plagioclase phenocrysts analyzed. Sample SAN61-2 includes the transition from a Minoan pumice clast to a scoria clast. Pl-21 is found in the scoria part of SAN61-2 which explains the higher anorthite content of its rim.

Si, Al and Fe^{3+}   Average Si in andesinitic plagioclase crystals varies between $2.60 - 2.63$ cpfu, and Al ranges from $1.37 - 1.39$ cpfu. Average Fe^{3+} is the same, about 0.012 cpfu for all these phenocrysts.

In plagioclase crystals with cores of labradoritic and bytownitic composition Si contents vary between $2.41 - 2.61$ cpfu while Al contents vary between $1.38 - 1.58$ cpfu. Core-to-rim profiles always display lower Si and higher Al contents in cores. Pl-17 (SAN61-1A) shows the lowest average Si and highest average Al contents (Table 4.3). Fe^{3+} tends to be slightly enriched in cores of these plagioclase phenocrysts. Pl-17 (SAN61-1A) shows the most pronounced decrease of Fe^{3+} from core to rim (Fig. 4.12).

Li, Be and B   Average lithium concentrations in all crystals vary between $5.5 - 7.6 \, \mu g/g$ and are therefore quite similar. The lowest lithium concentration was analyzed in Pl-5 (SAN52A, Fig. 4.7). When in a state of equilibrium, lithium usually correlates negatively with anorthite content in all crystals analyzed.

Many crystals however show a rise to higher lithium concentrations towards the rim at a distance of up to $40 \, \mu m$ with a slight drop of lithium concentration on the last $\sim 3 - 5 \, \mu m$ reflecting stages of disequilibrium probably caused by two different events which will be further discussed in Chapter 5 and Chapter 7.

Average beryllium concentrations vary between $1.1 - 1.4 \, \mu g/g$. In well developed cores of lower anorthite content, beryllium concentrations will always be lower compared to crystal rims (see for example Fig. 4.7).

Boron concentrations are usually below $0.3 - 0.4 \, \mu g/g$ in pumice plagioclase. These concentrations will be apparently higher when melt is hit during analyses.
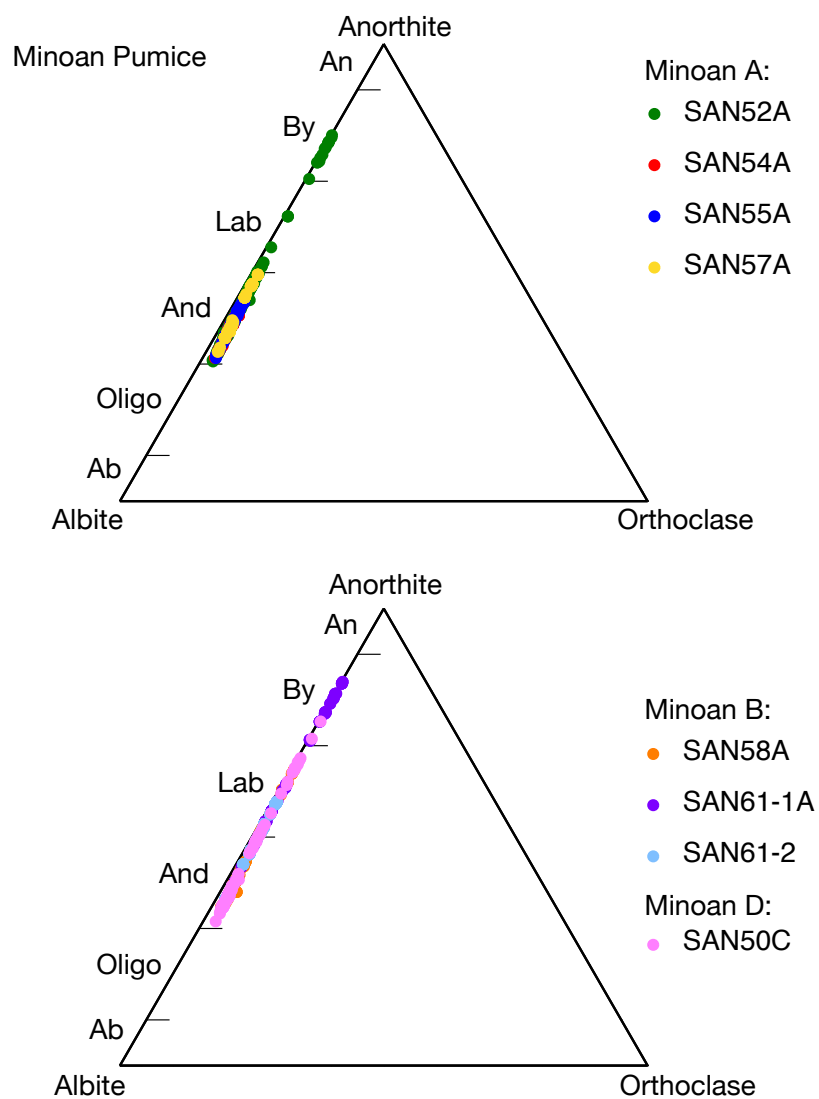
Fig. 4.4. Anorthite contents of Minoan pumice plagioclase. Upper diagram: Minoan A plagioclase. Lower Diagram: Minoan B and D plagioclase. Plagioclase crystals of Minoan C can be found in Appendix B.

Mg, Sr and Ba Average magnesium, strontium and barium concentrations for crystals analyzed are relatively similar. They range from $\sim 117 - 153\,\mu g/g$ for magnesium, $\sim 302 - 372\,\mu g/g$ for strontium and $\sim 63 - 189\,\mu g/g$ for barium. Pl-5 (SAN61-2, Fig. 4.13) has remarkably low average crystal core barium concentrations compared to the other crystals.
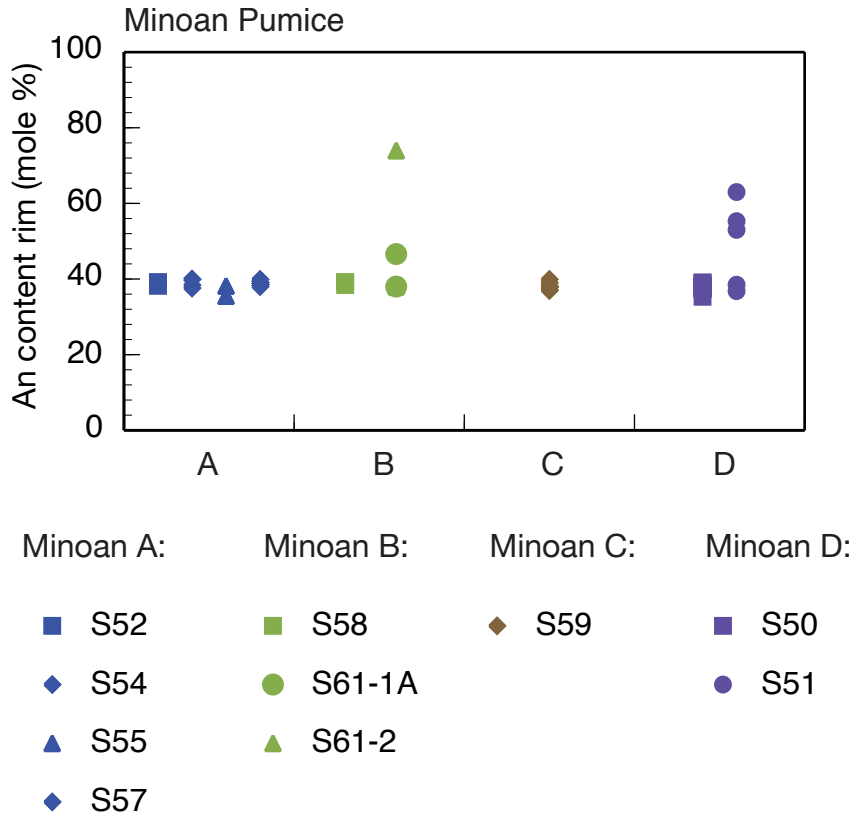
Fig. 4.5. Variations in anorthite rim contents of Minoan pumice and Crystal-rich pumice plagioclase. Except for a plagioclase crystal of SAN61-2 and several crystals in the Crystal-rich pumice, anorthite rim contents are relatively homogeneous. Pl-21 of SAN61-2 belongs to the scoria part of the sample and therefore shows a higher anorthite content at its rim.

Table 4.3. Average Compositions of Plagioclase in Minoan Pumice and Crystal-rich Pumice Samples: Minoan A–D

Sample Crystal	SAN52A Pl-3	SAN52A Pl-5	SAN54A Pl-1	SAN55A Pl-2	SAN57A Pl-3	SAN58A Pl-5	SAN61-1A Pl-17	SAN61-2 Pl-5	SAN50C Pl-3	SAN51-1A Pl-3	SAN51-1A Pl-17	SAN51-1B Pl-2	SAN51-1B Pl-3	SAN51-1B Pl-17
Analysis														
SiO_2	57.96	56.41	58.58	58.45	58.13	57.06	52.63	55.61	56.34	48.72	58.27	48.66	54.70	55.89
Al_2O_3	26.29	27.45	25.90	26.19	26.10	26.97	29.31	28.06	27.31	31.94	25.68	32.31	28.52	27.57
FeO_{tot}	0.32	0.33	0.31	0.33	0.34	0.32	0.40	0.40	0.34	0.80	0.33	0.57	0.39	0.34
CaO	8.29	9.59	7.55	8.04	8.02	8.76	12.12	10.34	9.26	15.43	7.70	15.46	10.59	9.73
Na_2O	6.59	6.05	6.99	6.72	6.70	6.31	4.43	5.63	6.03	2.36	6.86	2.56	5.30	5.79
K_2O	0.31	0.26	0.34	0.32	0.32	0.28	0.16	0.21	0.27	0.16	0.34	0.07	0.21	0.24
Total	99.75	100.10	99.68	100.03	99.61	99.71	99.06	100.24	99.55	99.40	99.77	99.63	99.72	99.57
Calc. to 8 cat.														
Si	2.601	2.533	2.627	2.613	2.611	2.566	2.405	2.499	2.541	2.242	2.627	2.234	2.473	2.523
Al	1.391	1.455	1.369	1.380	1.382	1.430	1.581	1.487	1.453	1.733	1.364	1.749	1.520	1.468
Fe^{3+}	0.012	0.013	0.012	0.012	0.013	0.012	0.015	0.015	0.013	0.031	0.012	0.022	0.015	0.013
Ca	0.399	0.463	0.363	0.385	0.386	0.422	0.595	0.498	0.449	0.761	0.372	0.761	0.513	0.472
Na	0.573	0.526	0.607	0.582	0.583	0.550	0.391	0.490	0.527	0.211	0.600	0.228	0.465	0.506
K	0.018	0.015	0.020	0.018	0.018	0.016	0.009	0.012	0.015	0.009	0.019	0.004	0.012	0.014
Total	4.993	5.004	4.997	4.991	4.993	4.996	4.997	5.001	4.997	4.986	4.995	4.997	4.998	4.996
X_{An}	41.0	46.7	37.4	39.8	39.8	43.4	60.2	50.3	45.9	78.0	38.3	76.9	52.5	48.1
Li (μg/g)	6.5	5.5	7.8	6.4	8.1	7.0	7.1	7.6	6.4	9.2	8.0	6.5	9.5	6.5
2σ	0.1	0.1	0.2	0.2	0.3	0.2	0.2	0.2	0.2	0.3	0.3	0.2	0.2	0.2
Be (μg/g)	1.16	1.20	1.33	1.34	1.40	1.35	1.15	1.08	1.24	0.46	1.34	0.48	1.13	1.13
2σ	0.05	0.05	0.10	0.10	0.15	0.09	0.09	0.10	0.10	0.07	0.13	0.08	0.09	0.10
B (μg/g)	0.21	0.30	0.23	0.23	0.21	0.23	0.23	0.16	0.23	0.101	0.226	0.094	0.153	0.205
2σ	0.03	0.04	0.06	0.06	0.09	0.06	0.06	0.05	0.06	0.045	0.066	0.044	0.046	0.050
Mg (μg/g)	120	119	124	125	123	117	123	153	118	283	118	238	186	119
2σ	2	2	4	4	5	4	4	5	4	8	5	7	5	4
Sr (μg/g)	332	310	317	317	346	302	365	372	302	365	318	344	425	349
2σ	3	3	6	5	8	5	7	6	5	7	6	8	6	6
Ba (μg/g)	170	147	155	176	189	167	157	63	156	46	183	38	131	141
2σ	3	3	6	6	9	6	6	5	5	4	7	3	5	5

EPMA and SIMS analyses of plagioclase of Minoan pumice and Crystal-rich pumice samples. Average values of Si, Al, Fe^{3+}, Ca, Na and K are in cations per formula unit (cpfu).
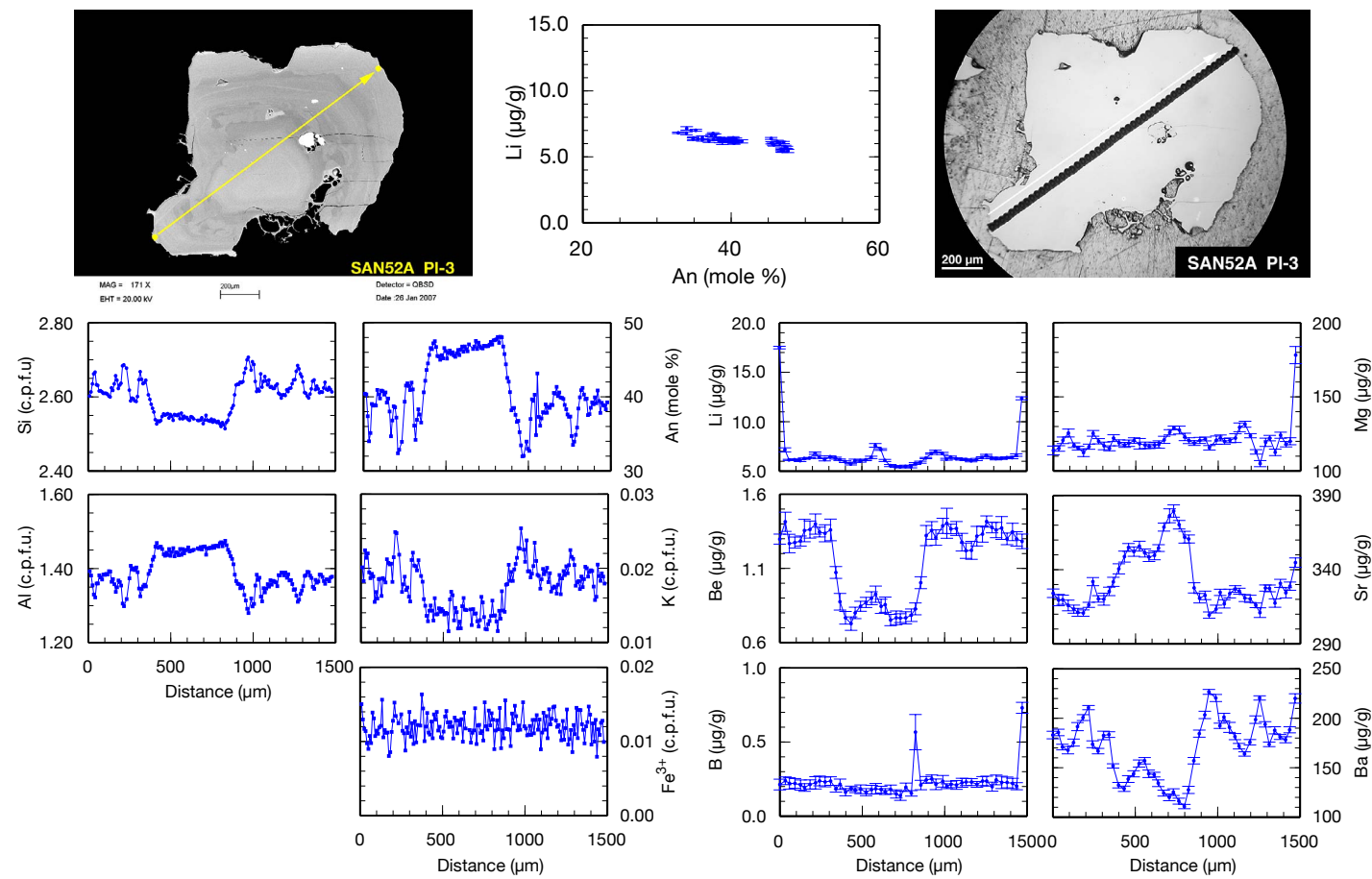
Fig. 4.6. SAN52A Pl-3: This crystal plots in the andesine field. Its core is partly resorbed and surrounded by a low An zone (decrease by > 15 mol%). Error bars of SIMS analyses are 2σ.
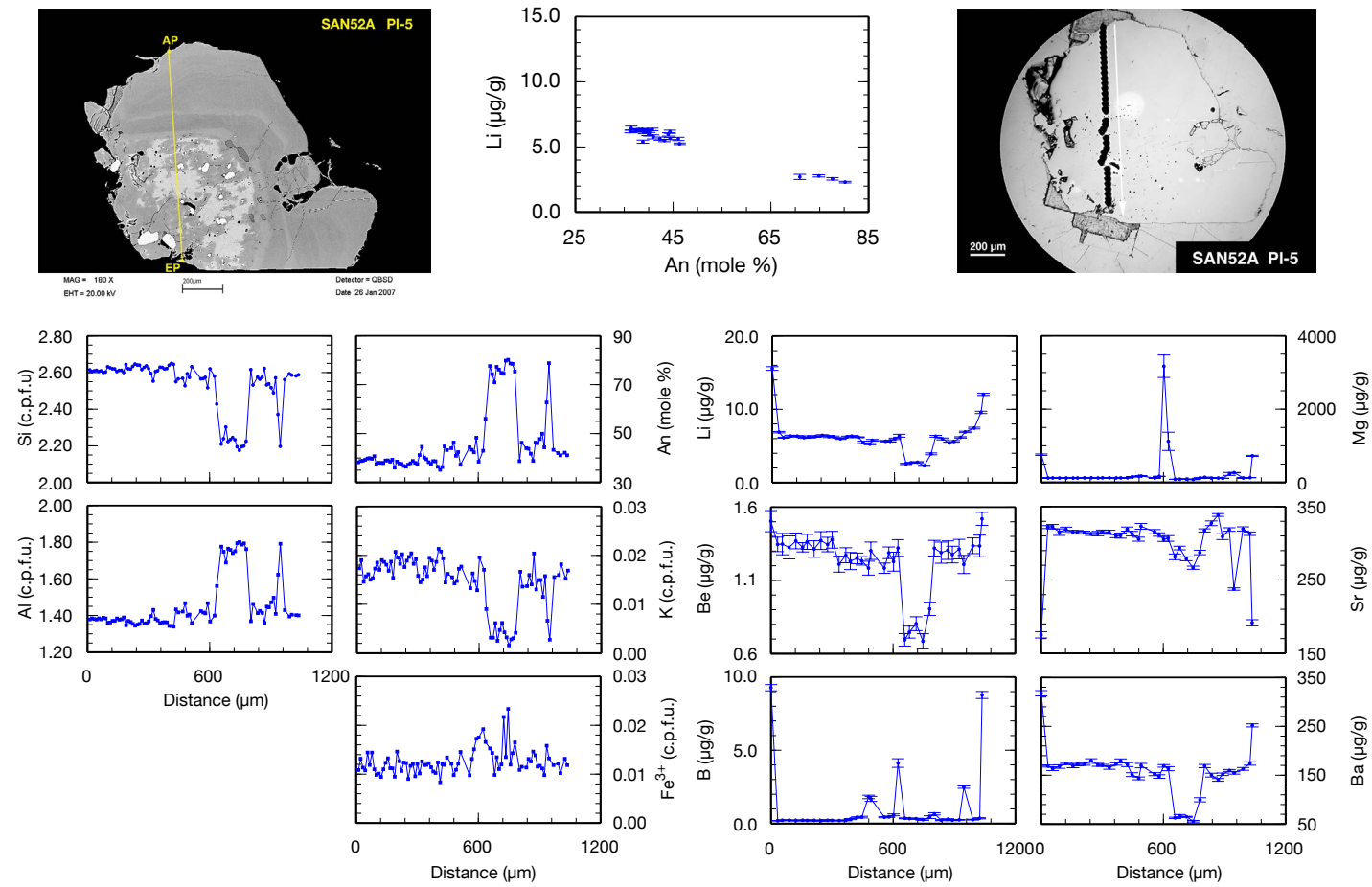
Fig. 4.7. SAN52A Pl-5: This crystal has a patchy core that plots in the bytownite field. Li correlates negatively with An content. Error bars of SIMS analyses are 2σ.
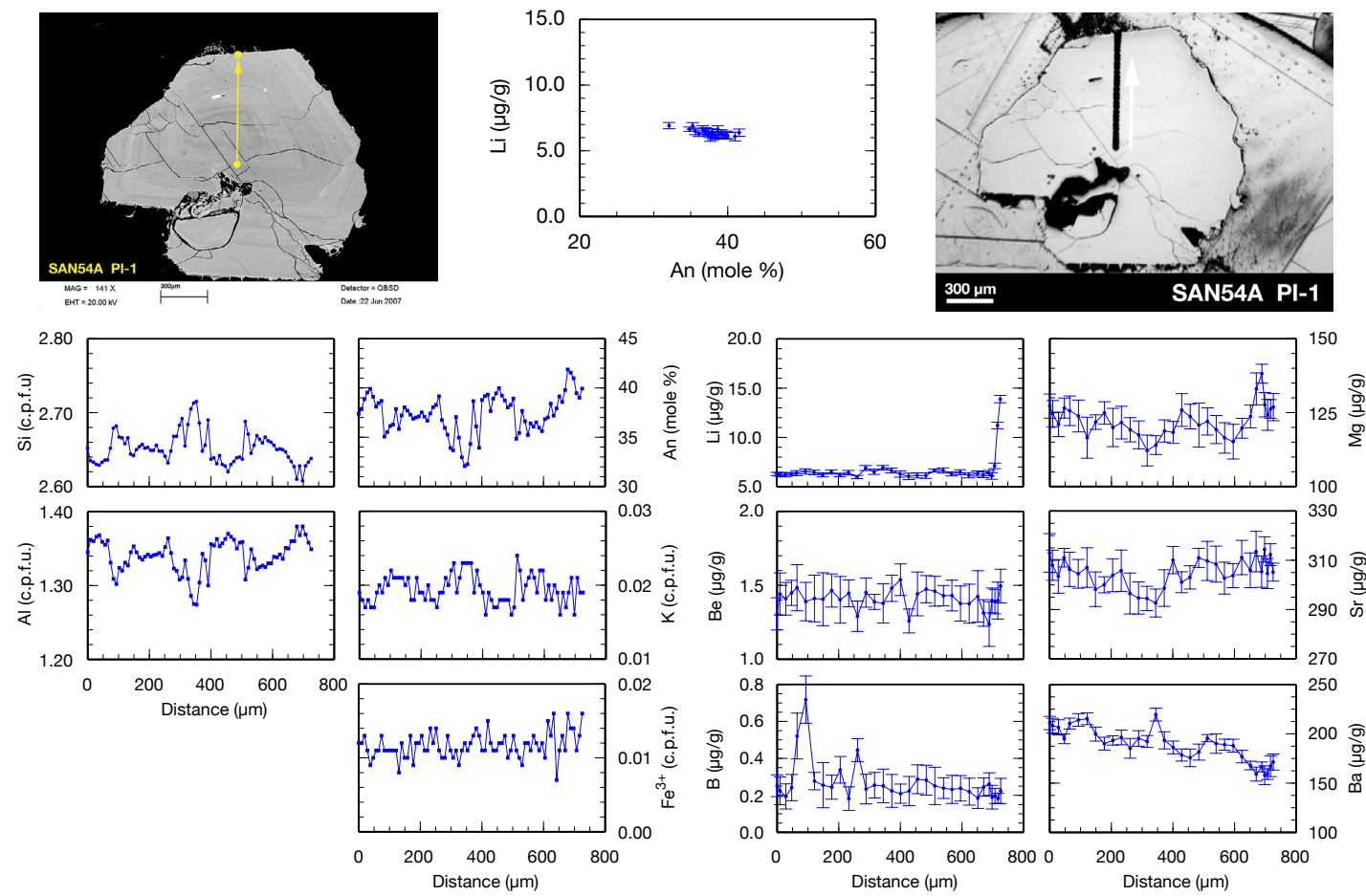
Fig. 4.8. SAN54A Pl-1: This crystal is completely andesinitic and shows oscillatory zoning. Li correlates negatively with An content. Error bars of SIMS analyses are 2σ.
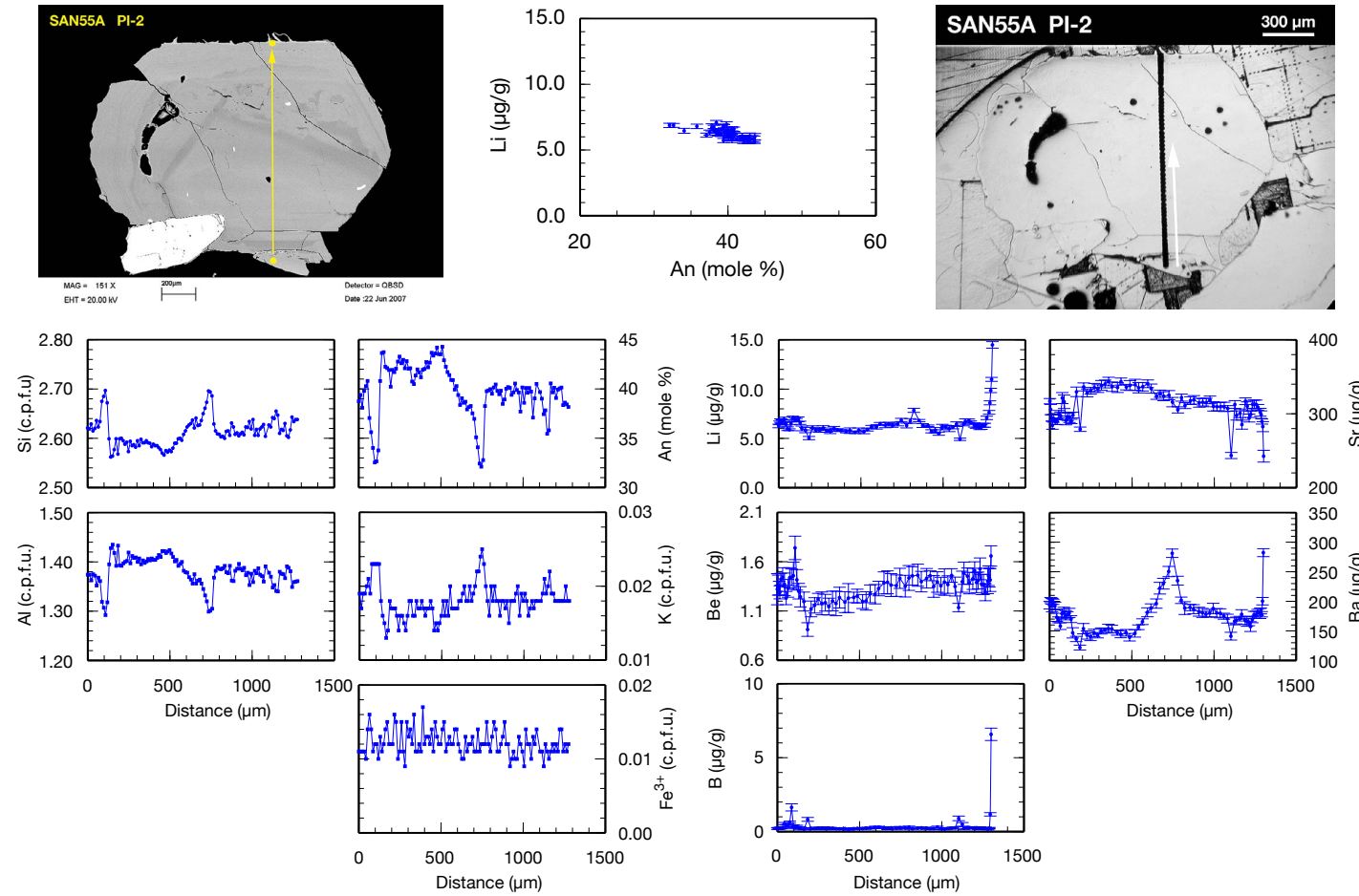
Fig. 4.9. SAN55A Pl-2: This crystal is completely andesinitic in composition. Only parts of the core are visible due to a cutting effect. Li correlates negatively with An content. Error bars of SIMS analyses are 2σ.
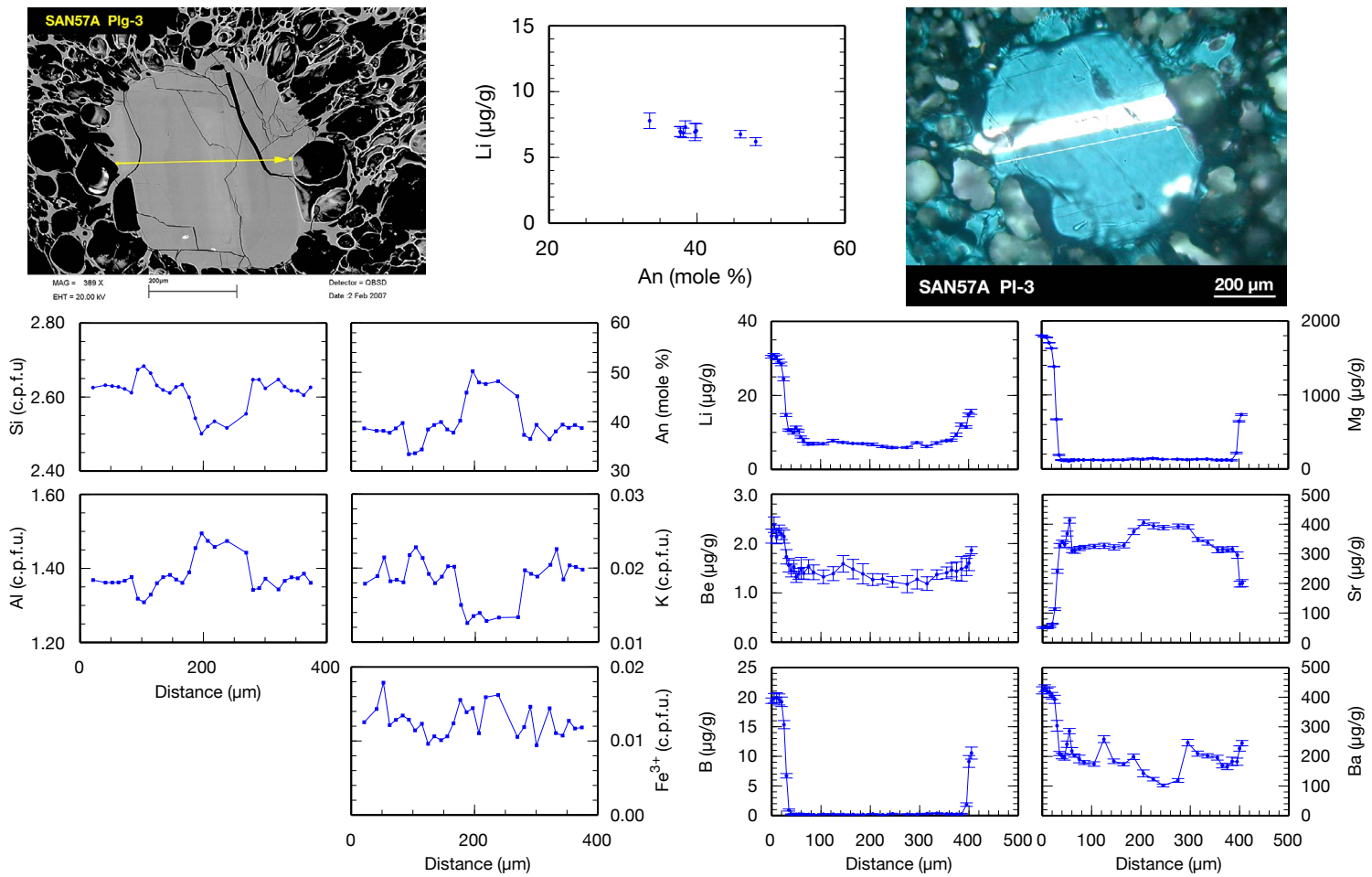
Fig. 4.10. SAN57A Pl-3: The core of this crystal is slightly labradoritic in composition and patchy. The rest of the crystal is andesinitic in composition. Li correlates negatively with An content. Error bars of SIMS analyses are 2σ.
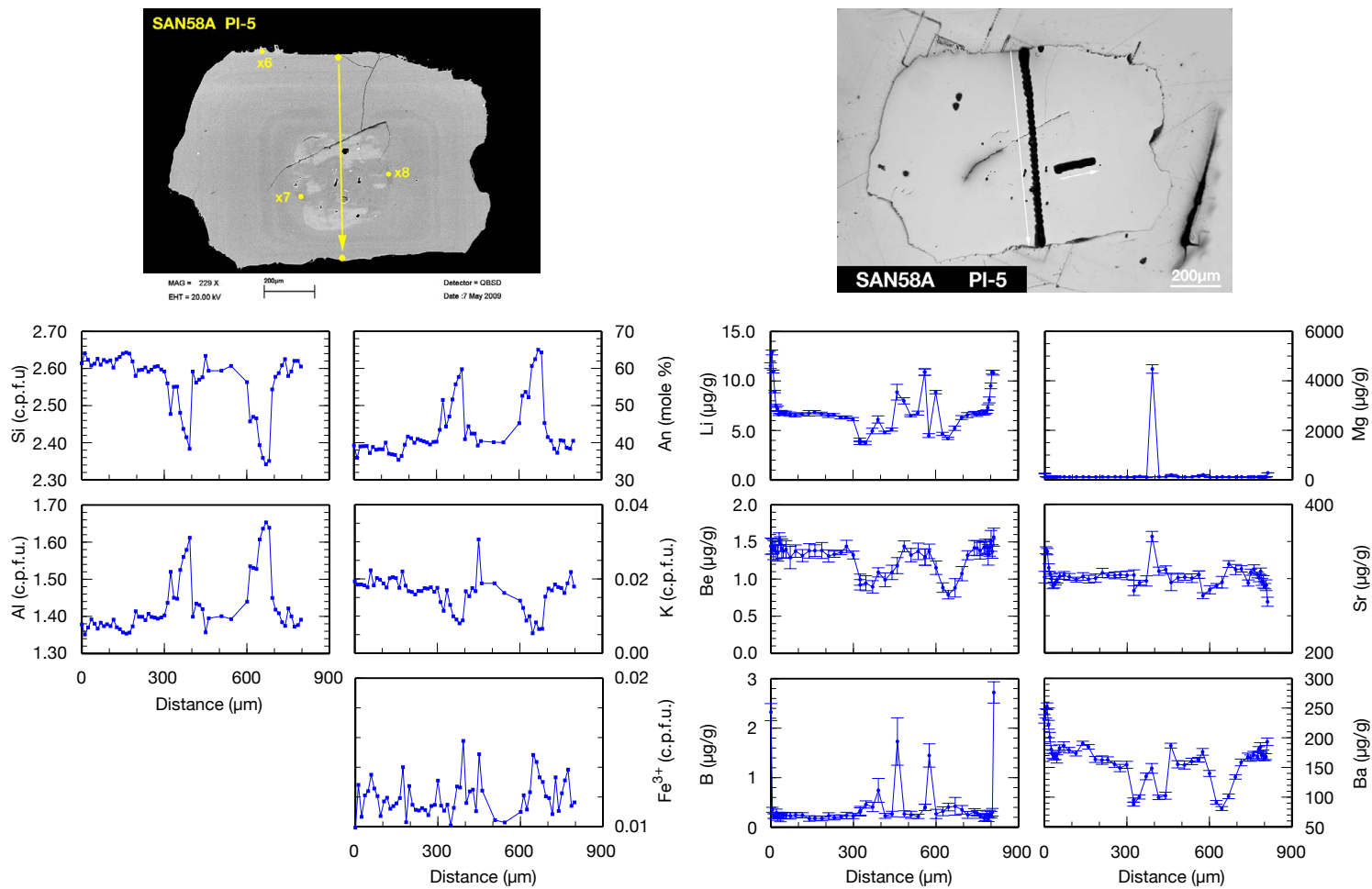
Fig. 4.11. SAN58A Pl-5: This crystal has a patchy core of labradoritic composition. Error bars of SIMS analyses are 2σ.
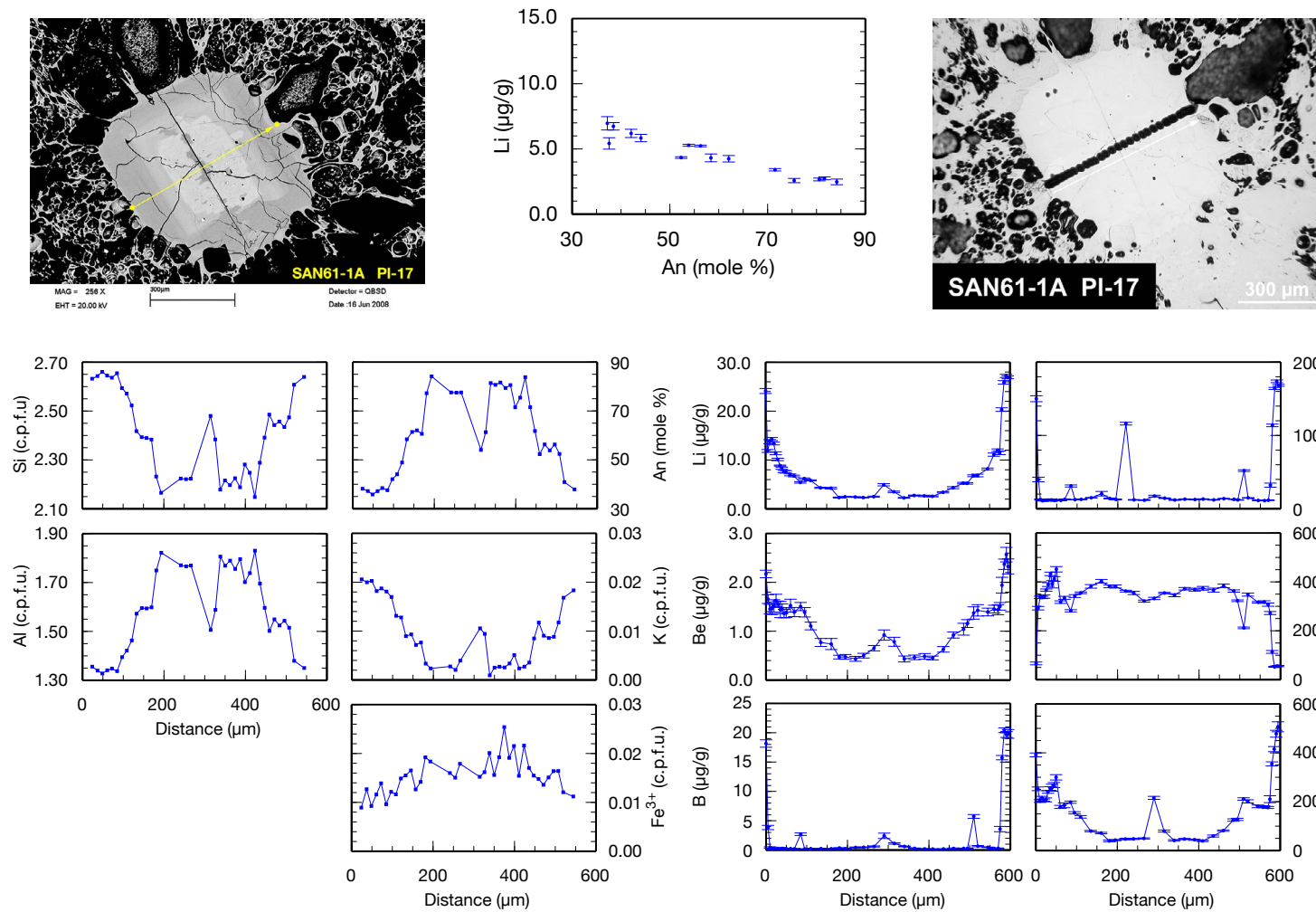
Fig. 4.12. SAN61-1A Pl-17: This pl has a patchy core of bytownitic composition. An content decreases from a labradoritic zone surrounding the core to a more andesinitic composition towards the rim. Li correlates negatively with An content. Error bars of SIMS analyses are 2σ.
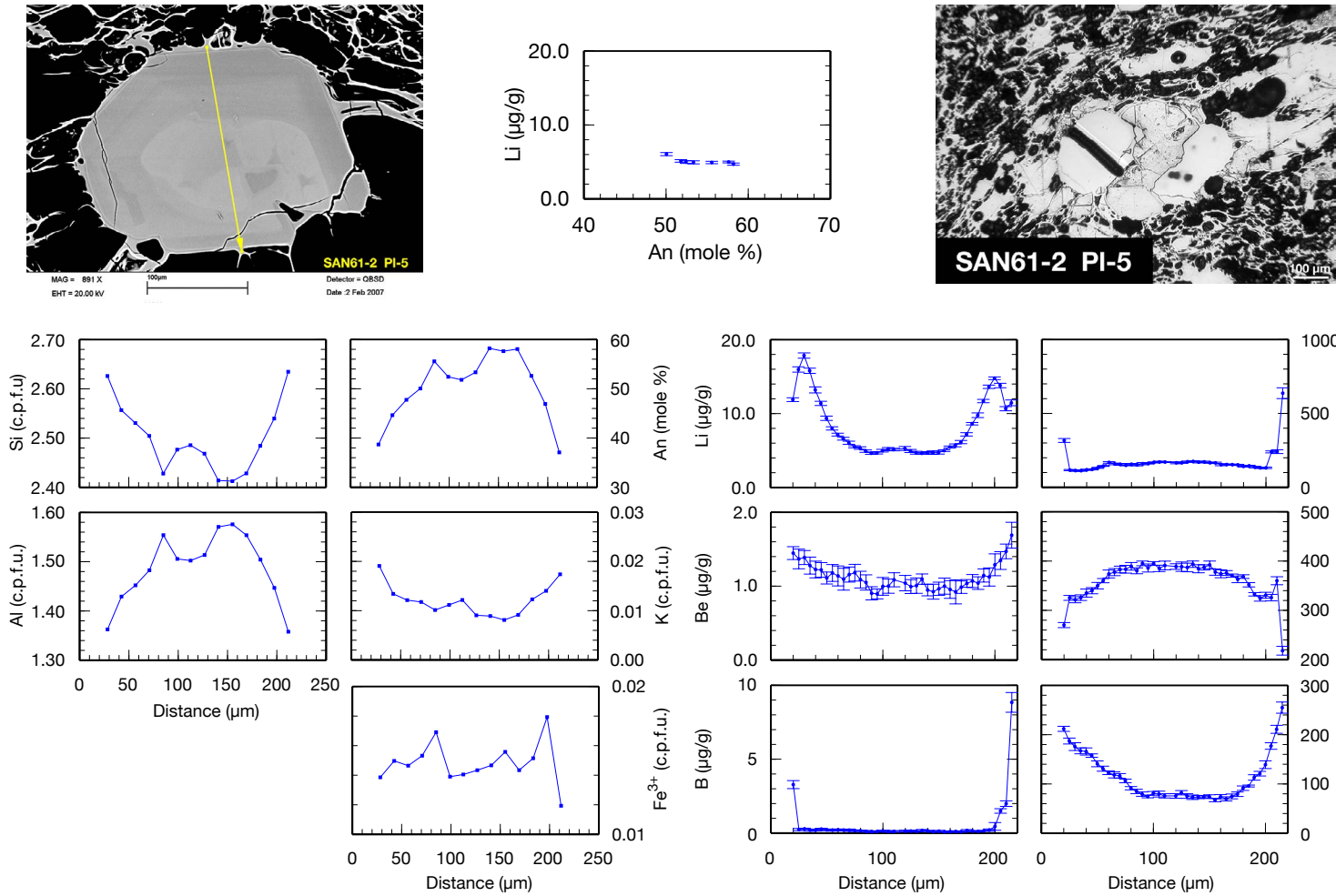
Fig. 4.13. SAN61-2 Pl-5: This pl grain is from Minoan Unit B. The core plots in the labradorite field. There is a decrease of 20 mol% An from core to rim. Error bars of SIMS analyses are 2σ.
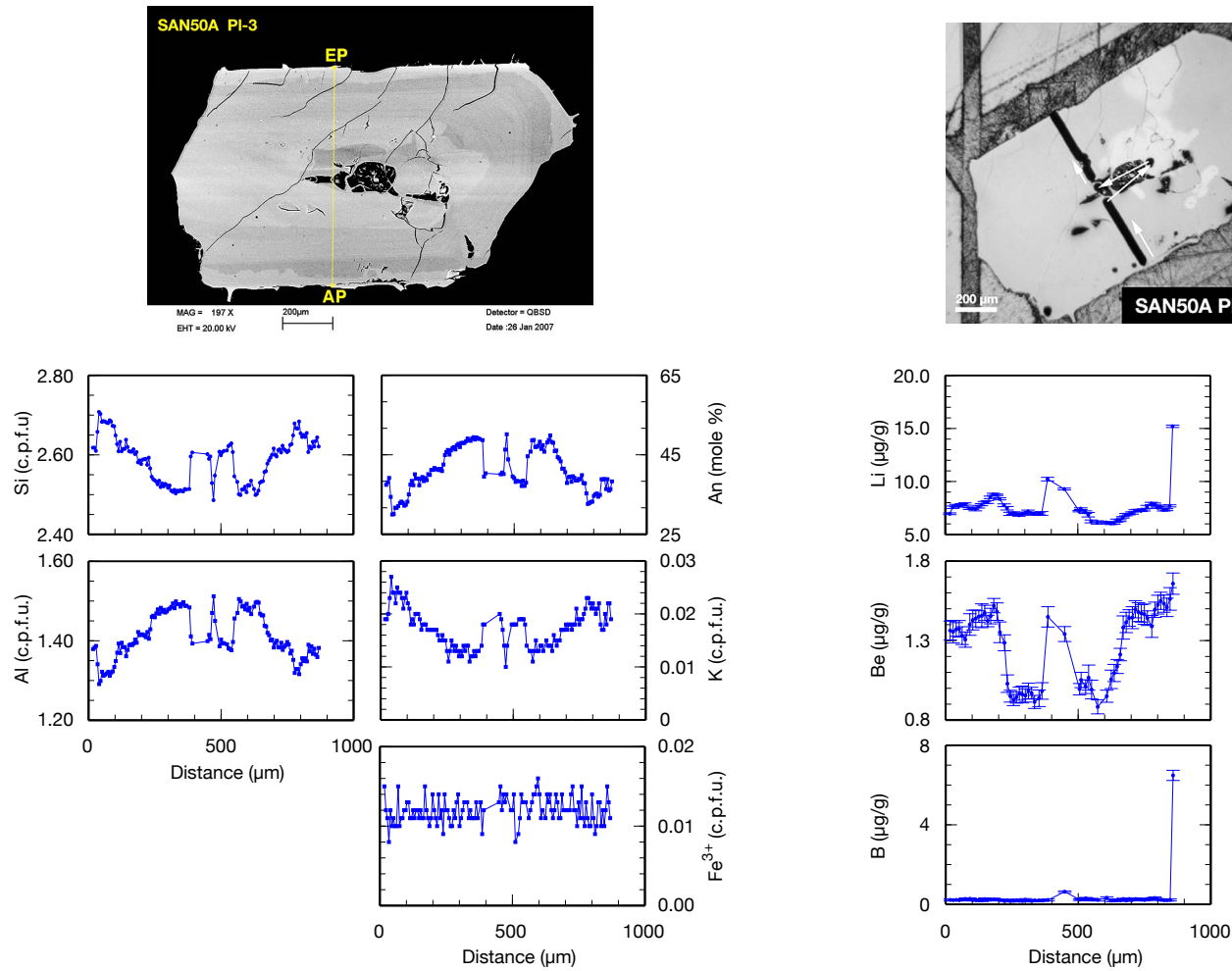
Fig. 4.14. SAN50C Pl-3: This pl grain is from Minoan Unit D and has a patchy core of bytownitic composition. The composition changes from more An-rich zones to An-low zones towards the rim. There is no visible Li diffusion into the crystal. Error bars of SIMS analyses are 2σ.

4.2.2. Crystal-rich Pumice (Minoan D)

An   Table 4.3 on page 76 includes five plagioclase crystals that were sampled from the Crystal-rich pumice. Their range in anorthite content is shown in Fig. 4.15. Pl-17 (SAN51-1A, Fig. 4.17) is completely andesinitic in composition, its average anorthite content is An_{38}. Pl-3 (SAN51-1B, Fig. 4.19) and Pl-17 (SAN51-1B, Fig. 4.20) both have cores of labradoritic composition. Pl-17's core is relatively small with an anorthite content up to An_{70}. Pl-3's core shows a checkerboard pattern with multiple melt inclusions. Maximum anorthite content is An_{63} for the An-rich parts of the core.

Pl-3 (SAN51-1A, Fig. 4.16) and Pl-2 (SAN51-1B, Fig. 4.18) are labradoritic to bytownitic in composition. Their anorthite content varies between An_{55-84}.

The differences in anorthite content of the crystals in this sample as well as the differences in anorthite compositions that can be seen in Fig. 4.5 are a good example for magma mingling. The origin of the Crystal-rich pumice is yet to be discussed.
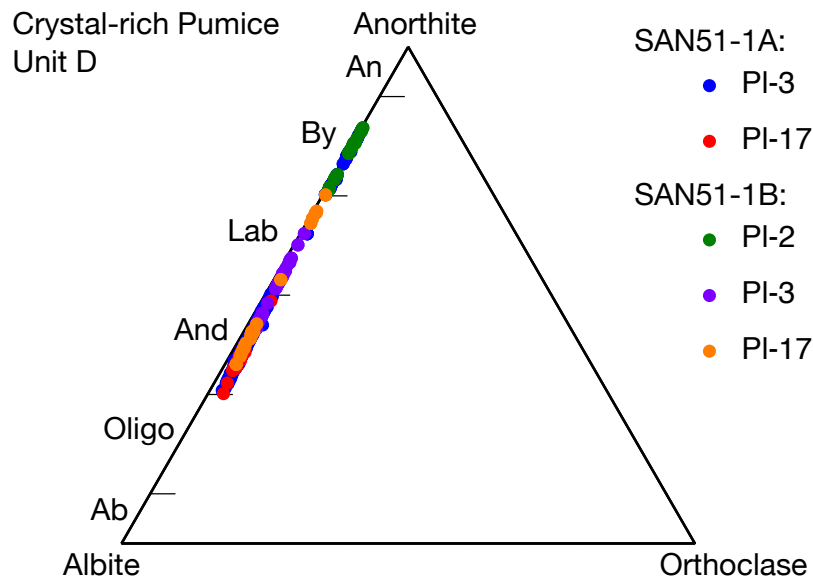
Fig. 4.15. Plagioclase phenocrysts of the Crystal-rich pumice (Minoan D – ignimbrite deposit) cover a wide range of anorthite contents.

Si, Al and Fe^{3+} Average Si for Pl-17 (SAN51-1A) is about 2.63 cpfu. The two crystals with labradoritic cores have average Si contents between $2.47 - 2.52$ cpfu. Average Al contents of these three crystals are: $1.36 - 1.52$ cpfu.

Pl-3 (SAN51-1A) and Pl-2 (SAN51-1B) have the lowest average Si contents: $0.23 - 0.24$ cpfu. Their average Al contents are higher compared to the other crystals, they vary between $1.73 - 1.75$ cpfu. Fe^{3+} is also slightly higher in these crystals, between $0.02 - 0.03$ cpfu.

Li, Be and B Average lithium concentrations of all crystals analyzed vary between $6.5 - 9.5\,\mu g/g$ with Pl-2 and Pl-17 of SAN51-1B having the lowest average lithium concentrations. As already mentioned for the Minoan pumice plagioclase crystals a rise of lithium concentrations followed by a slight drop in lithium concentrations on a short distance towards the rim can be observed. The events that might have lead to higher lithium concentrations close to the rim will be discussed in Chapter 5 and Chapter 7.

Similar to their major and minor element composition beryllium concentrations in crystals with labradoritic to bytownitic composition are much lower compared to the more andesinitic crystals. Average beryllium concentrations in Pl-3 (SAN51-1A) and Pl-2 (SAN51-1B) range from $0.46 - 0.48\,\mu g/g$ while the other crystals have beryllium concentrations $> 1\,\mu g/g$.

Similar to the main Minoan pumice plagioclase crystals, boron concentrations stay below $0.3\,\mu g/g$ unless melt is hit during analyses. Pl-2 (SAN51-1B) shows unusually low average boron concentrations of $\sim 0.1\,\mu g/g$.

Mg, Sr and Ba The anorthite-rich plagioclase crystals Pl-3 (SAN51-1A) and Pl-2 (SAN51-1B) also differ in their average magnesium and barium concentrations (see Table 4.3) with magnesium being higher and barium being much lower. Strontium seems to be more homogeneous ranging from $\sim 318 - 365\,\mu g/g$ with Pl-3 (SAN51-1B) having the highest strontium concentrations, $\sim 425\,\mu g/g$.
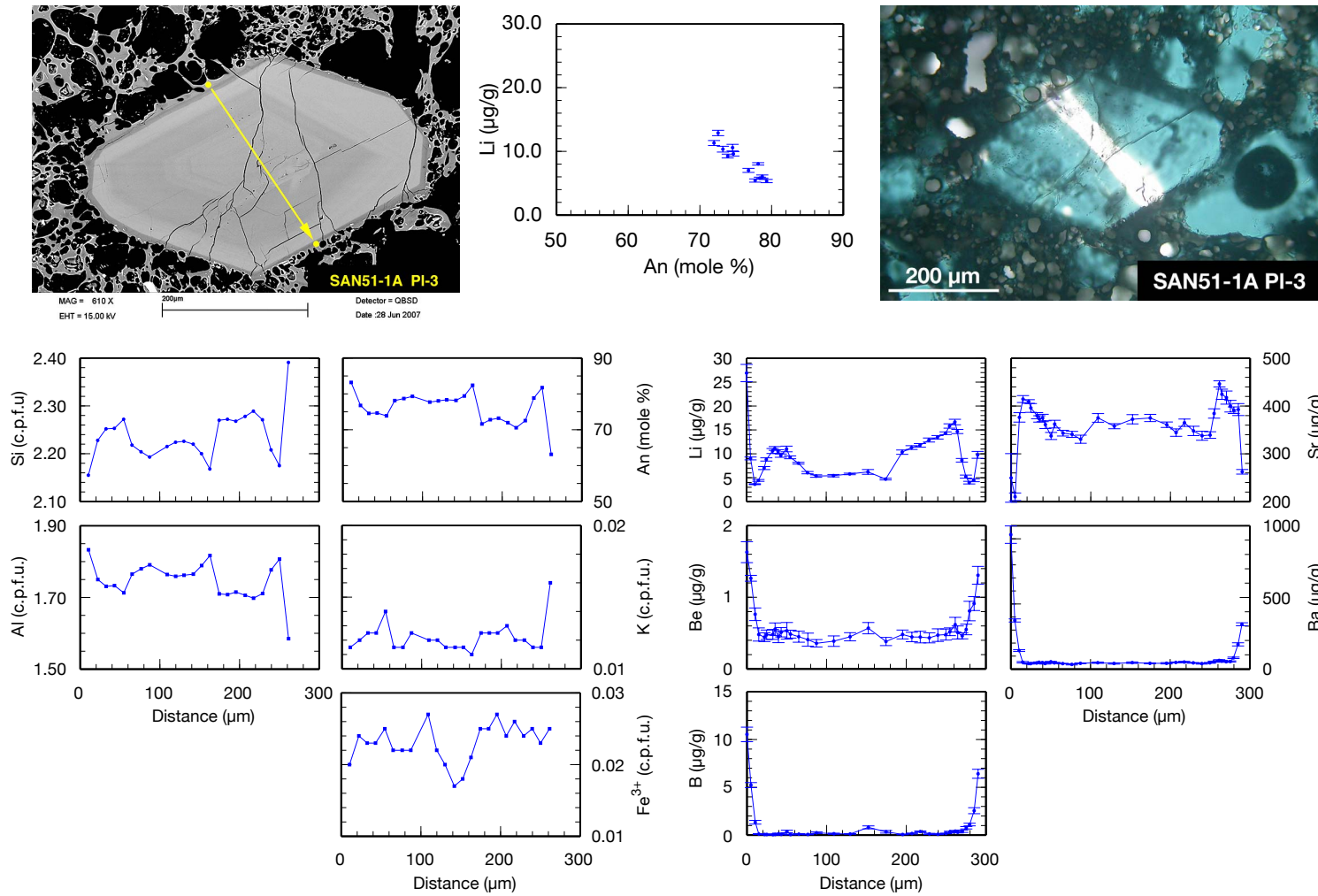
Fig. 4.16. SAN51-1A Pl-3: This pl has a bytownitic core ($X_{An} > 0.7$). The type of zoning is oscillatory with a broad low An zone around the core region. There is a drop of $4.2 - 10.8$ mol% An from core into a low An zone around the rim. Although the crystal is heavily cracked, a negative correlation between An and Li is visible. Li diffusion overprinted the profile at its end due to multiple cracks.
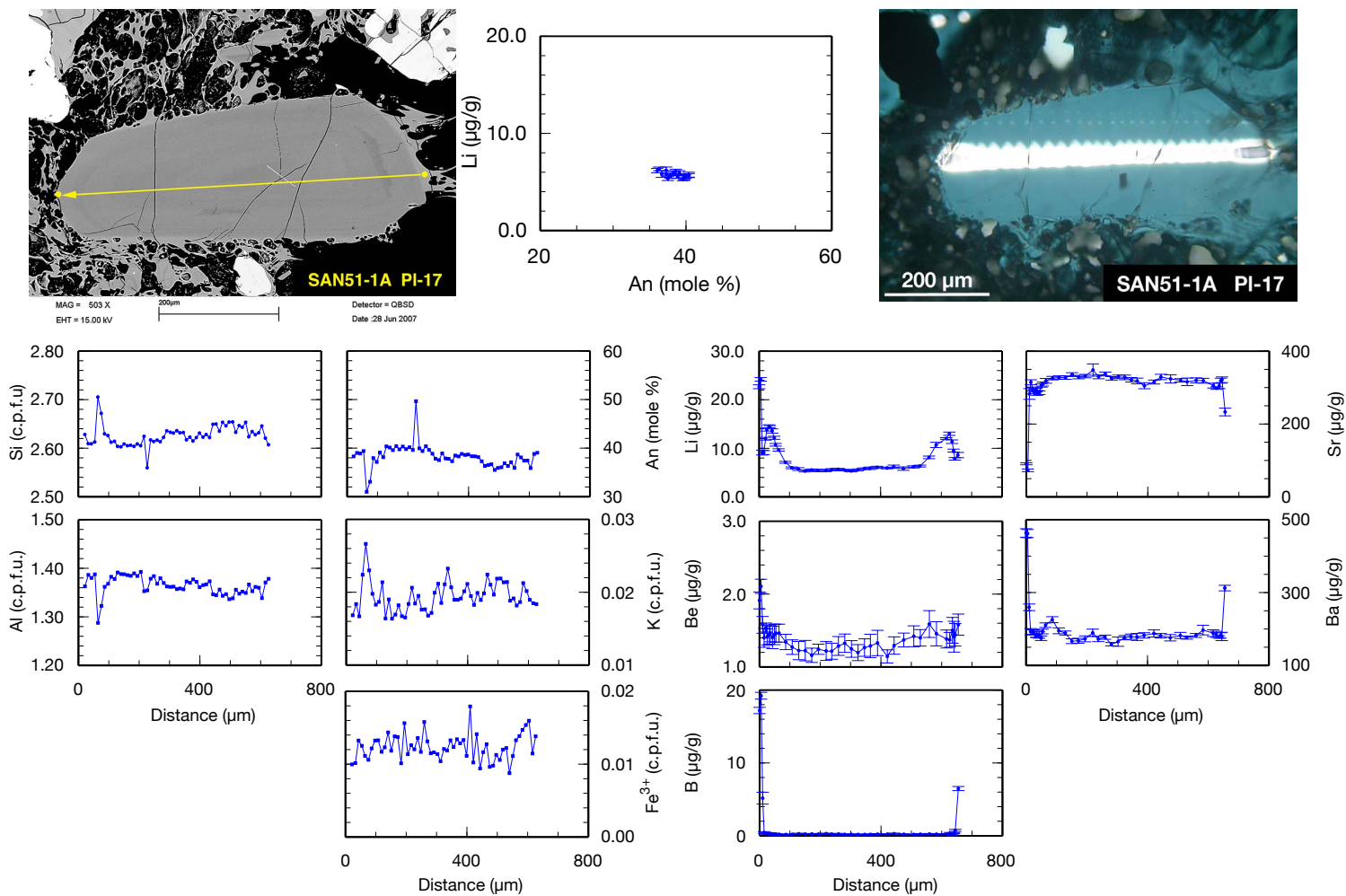
Fig. 4.17. SAN51-1A Pl-17: This andesine has weakly developed oscillatory zoning. Dark, strongly resorbed bands of lower X_{An} are visible. Although the variation in X_{An} within this crystal is relatively small, Li is still negatively correlated with An. The Li profile is overprinted by diffusion at the rim.
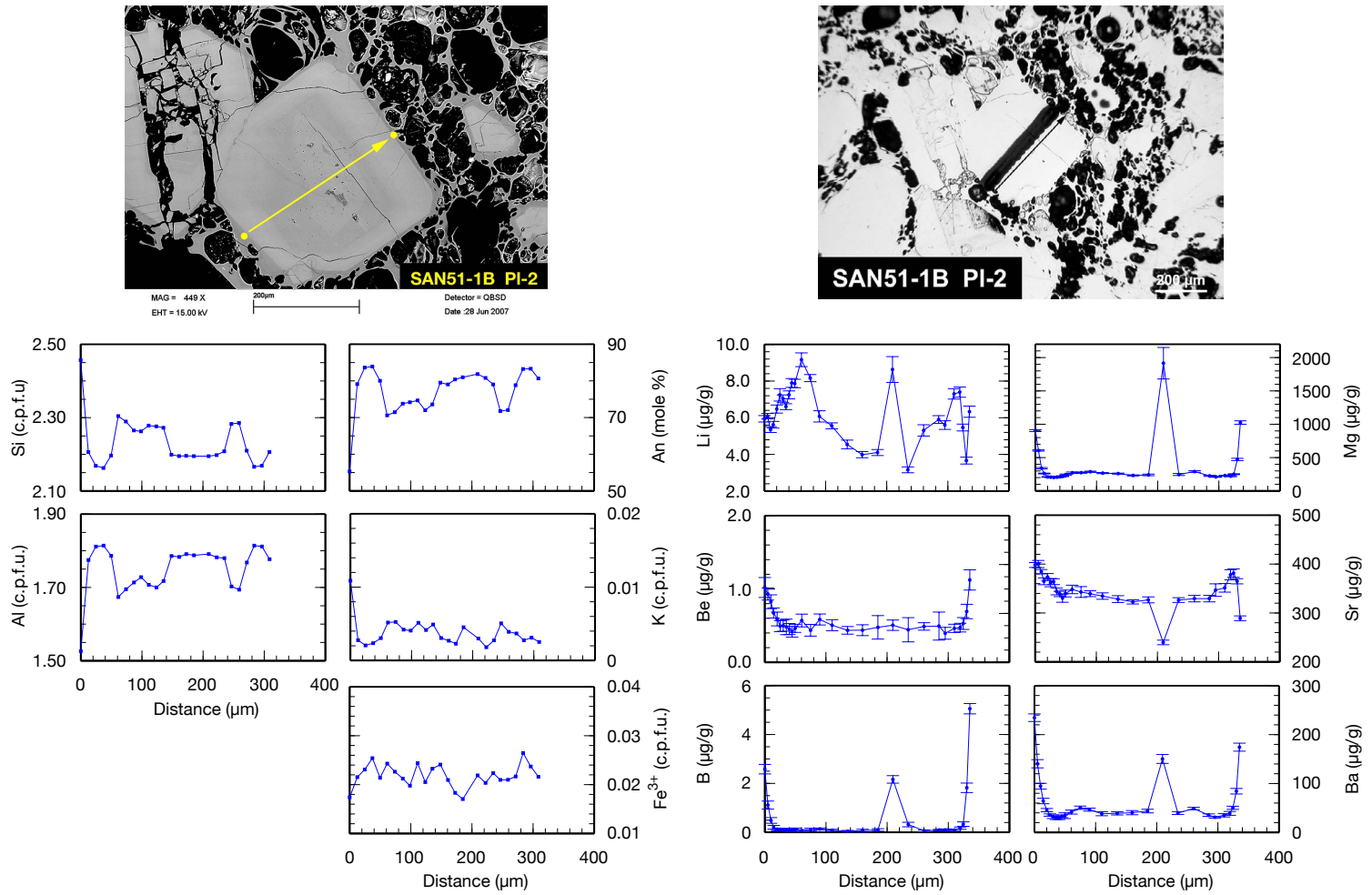
Fig. 4.18. SAN51-1B Pl-2: This crystal is mostly of bytownitic composition. The Li-An correlation is difficult to interpret. It looks like the profile was heavily overprinted by diffusion of Li from cracks into the crystal. Error bars of SIMS analyses are 2σ.
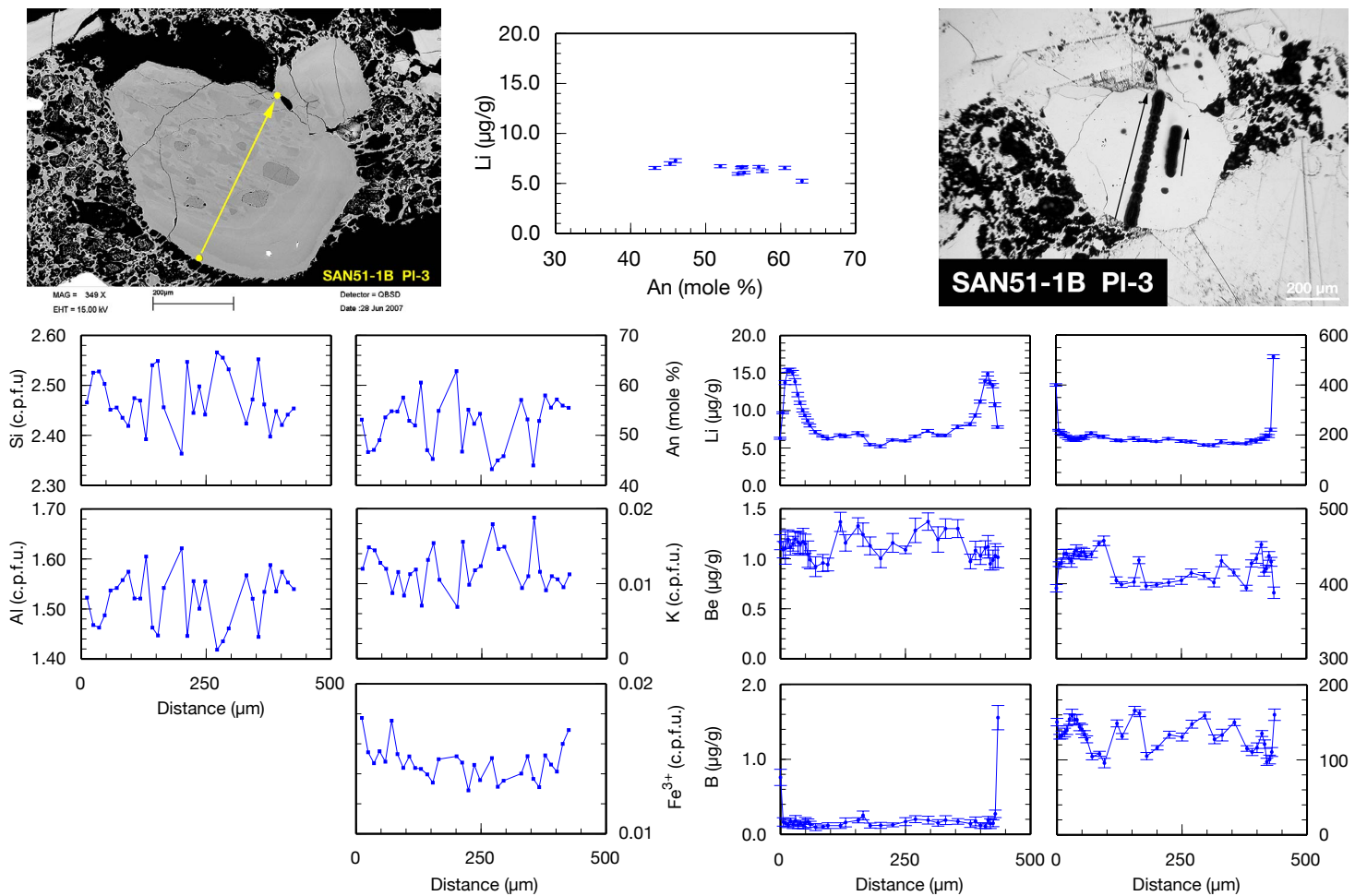
Fig. 4.19. SAN51-1B Pl-3: The core region is strongly resorbed with a checkerboard pattern and multiple melt inclusions (zonation type: relictic sieve-textured). Core remnants are probably of labradoritic composition. The Li profile is overprinted by diffusion into the crystal at its rims.
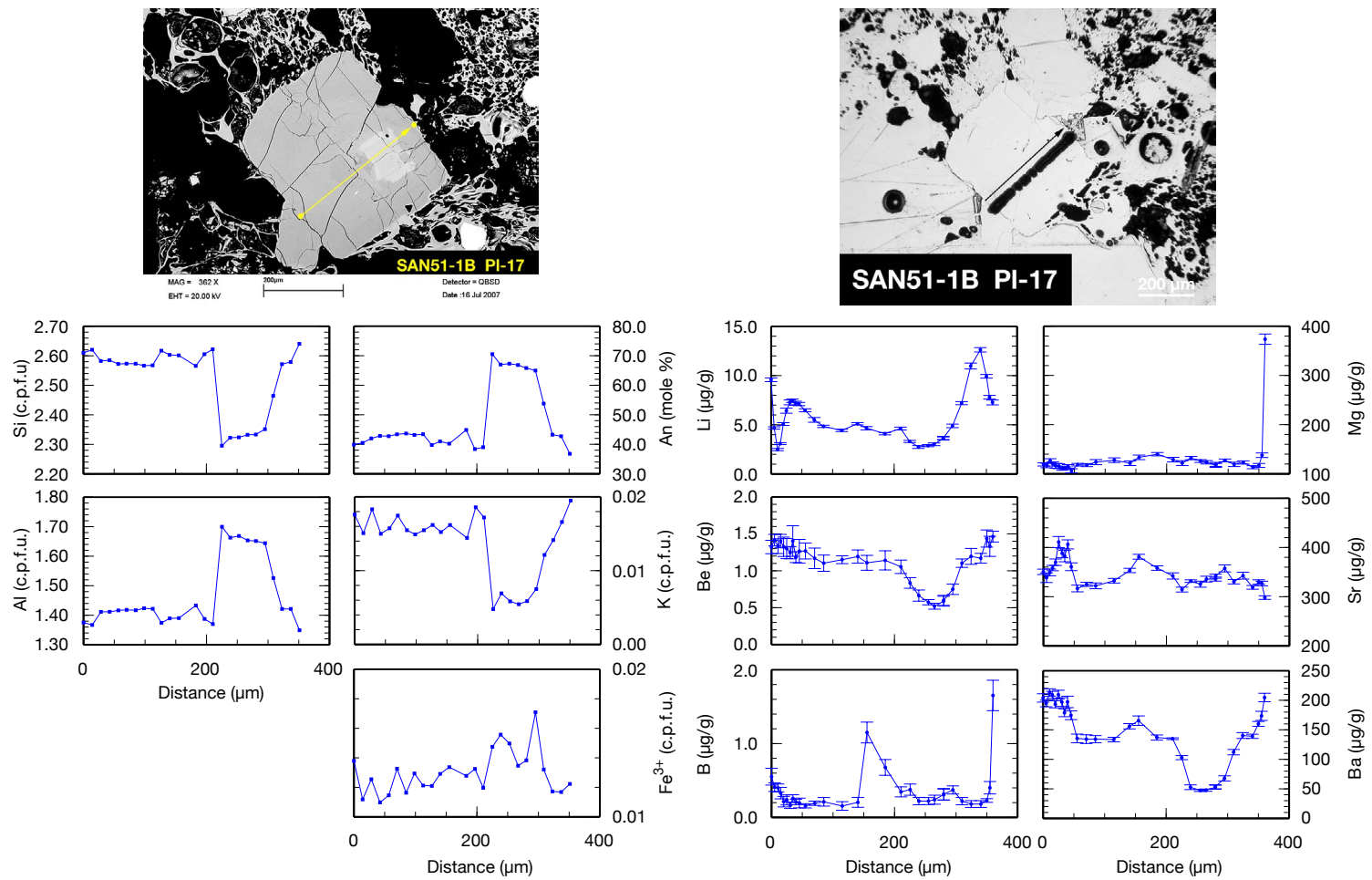
Fig. 4.20. SAN51-1B Pl-17: This crystal has a patchy, resorbed core (patchy Type I) of mostly labradoritic composition. Fe^{3+} is enriched in the crystal's core. The profile is overprinted by diffusion due to multiple cracks.

4.2.3. Scoria Clasts (Minoan A and Minoan B)

30 plagioclase crystals taken from 11 scoria samples were analyzed by EPMA and SIMS. Analyses of 11 of these crystals are shown in Table 4.4. Please note that based on geochemical differences it would be highly arbitrary to sort these crystals into groups; each sample should be studied separately. The following paragraphs will nevertheless be used to shortly describe the geochemical characteristics of the scoria plagioclase crystals and these will be carefully compared to each other and to crystals from the Minoan and Crystal-rich pumice. Many samples are influenced by mingling. For a complete overview of all plagioclase crystals analyzed the reader is referred to Appendix B.
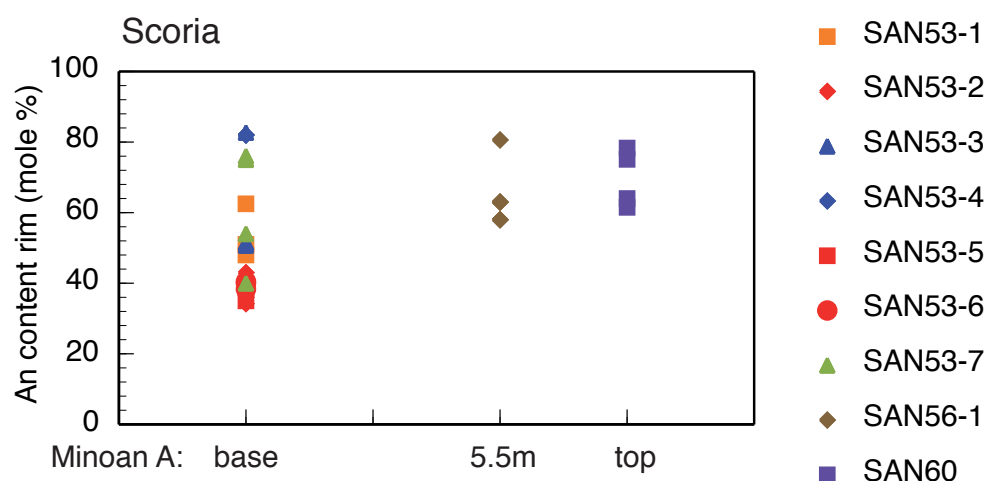
Fig. 4.21. Anorthite compositions of plagioclase rims in Minoan scoria samples show distinctive variations from sample to sample.

An Average anorthite contents of all crystals are shown in Table 4.4. The complete range of anorthite contents is presented in Fig. 4.22. In Table 4.4 plagioclase of samples SAN53-2, SAN53-3, SAN53-5 and SAN53-6 show average anorthite contents that plot in the andesine field between An_{30-50}. Of these plagioclase crystals only Pl-5 (SAN53-2) is completely andesinitic in composition (An_{31-41}). All other crystals have crystal cores of labradoritic composition: up to An_{61}. Pl-6 (SAN53-7, Fig. 4.33) is mostly of labradoritic composition, with a maximum anorthite content of An_{61}. Its rim is andesinitic with an anorthite content of An_{38}.

93

Samples SAN52Agg, SAN53-1, SAN53-3 and SAN56-1 contain plagioclase phenocrysts that are labradoritic to bytownitic in composition. Usually crystal cores with anorthite contents up to An_{88} or anorthite-rich growth zones can be found in these phenocrysts.

SAN53-4, SAN60 and SAN61-2 contain plagioclase crystals that are completely bytownitic in composition with anorthite contents ranging from An_{74-89}.

Rim compositions of plagioclase crystals are similar for those crystals found in samples SAN53-2, SAN53-5 and SAN53-6. Pl-6 of SAN53-7 shows similar anorthite rim compositions compared to the latter crystals. Especially sample SAN53-7 seems to be heavily affected by mingling which was already expressed by several inherited enclaves that included plagioclase phenocrysts (see Chapter 3). Samples SAN53-4, SAN56-1 and SAN60 also show a remarkable spread in anorthite rim compositions.
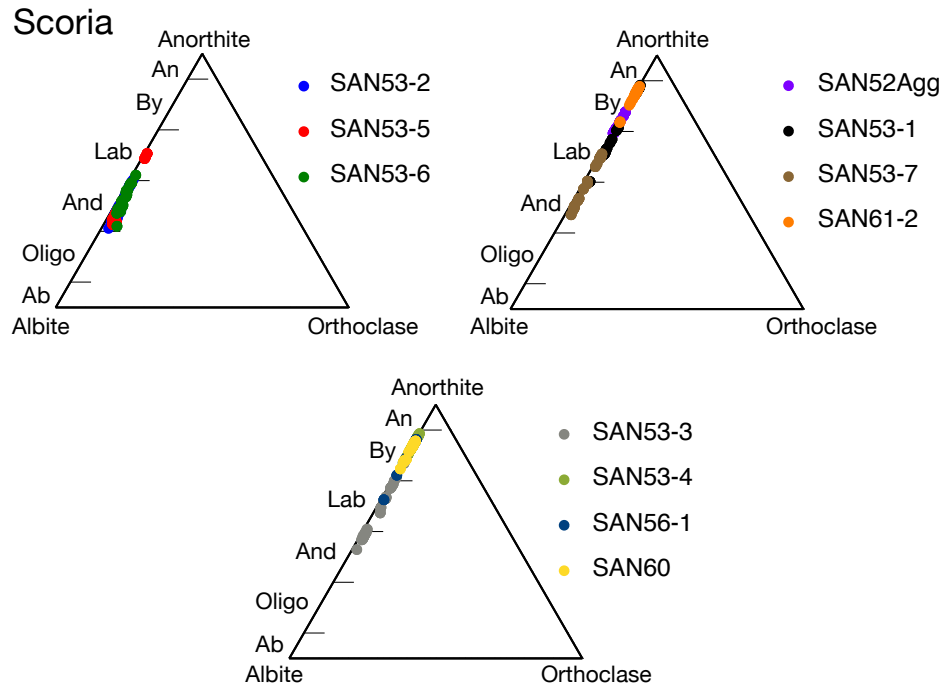
Fig. 4.22. Differences in anorthite content of plagioclase crystals from Minoan scoria clasts.

Si, Al and Fe^{3+}   Average Si contents in plagioclase crystals analyzed vary between $2.14 - 2.63$ cpfu. Phenocrysts of SAN53-2, SAN53-3, SAN53-5 and SAN53-6 have a tendency to higher Si contents.

Average Al contents range from $1.36 - 1.84$ cpfu. The highest Al contents can be found in plagioclase of SAN51-1, SAN56-1, SAN60 and SAN61-2.

Average Fe^{3+} contents of $0.01 - 0.02$ cpfu can be found in plagioclase of samples SAN53-2, SAN53-3, SAN53-5, SAN53-6 and SAN53-7. All other samples are enriched in Fe^{3+} between $0.22 - 0.30$ cpfu.

Li, Be and B SAN53-1 is the sample with the lowest lithium concentrations, these are below $1\,\mu g/g$. Phenocrysts of samples SAN53-2, SAN53-5 and SAN53-6 have remarkably higher lithium concentrations. Average concentrations range from $21.4 - 32.9\,\mu g/g$. All other samples show average lithium concentrations between $2.5 - 6.1\,\mu g/g$.

Average beryllium concentrations are usually below $1\,\mu g/g$, only Pl-14 (SAN53-5), Pl-11 (SAN53-6) and Pl-6 (SAN53-7) have slightly higher average concentrations above $1\,\mu g/g$.

Average boron concentrations in plagioclase of samples SAN53-1, SAN53-2, SAN53-5, SAN53-6 and SAN53-7 vary between $0.1 - 0.3\,\mu g/g$ and are similar to those of plagioclase crystals found in the Minoan pumice and Crystal-rich pumice.

Mg, Sr and Ba The highest average magnesium concentrations can be found in plagioclase crystals of samples SAN53-1, SAN53-4, SAN56-1, SAN60 and SAN61-2. These range from $300 - 469\,\mu g/g$. All the other plagioclase phenocrysts have lower magnesium between $117 - 248\,\mu g/g$.

Average strontium concentrations vary between $\sim 242 - 430\,\mu g/g$ in plagioclase displayed in Table 4.4. Pl-2 (SAN52Agg) and Pl-21 (SAN53-4) have the highest average strontium concentrations ($> 400\,\mu g/g$). Strontium contents below $300\,\mu g/g$ are found in plagioclase phenocrysts of samples SAN53-1, SAN53-3, SAN53-4, SAN56-1, SAN60 and SAN61-2.

Barium concentrations of phenocrysts samples SAN53-2, SAN53-5, SAN53-6 and SAN53-7 are much higher, average concentrations in plagioclase crystals are $\sim 120 - 167\,\mu g/g$.

Comparison to Minoan pumice and Crystal-rich pumice Plagioclase phenocrysts of scoria samples SAN53-2, SAN53-5, SAN53-6 and Pl-6 of SAN53-7 are geochemically closest to the Minoan pumice plagioclase and those crystals similar to the Minoan pumice in the Crystal-rich pumice samples (Pl-17, SAN51-1A). The plagioclase phenocrysts of SAN53-2, SAN53-5 and SAN53-6 have the highest lithium concentrations of all samples analyzed.

Table 4.4. Average Compositions of Plagioclase in Minoan Scoria

Sample Crystal	SAN52Agg Pl-2	SAN53-1 Pl-9	SAN53-1 Pl-16	SAN53-2 Pl-5	SAN53-2 Pl-14	SAN53-3 Pl-1	SAN53-3 Pl-12	SAN53-4 Pl-21	SAN53-5 Pl-14	SAN53-6 Pl-11	SAN53-7 Pl-6	SAN56-1 Pl-13	SAN56-1 Pl-20	SAN60 Pl-29	SAN61-2 Pl-21
Analysis															
SiO_2	49.85	52.10	47.52	58.64	58.62	55.74	51.43	47.31	58.20	57.12	54.92	47.04	47.41	47.63	46.31
Al_2O_3	31.81	30.01	33.29	25.67	26.77	27.53	30.08	33.52	26.43	26.70	28.48	33.48	33.34	33.36	33.64
FeO_{tot}	0.67	0.79	0.73	0.33	0.40	0.42	0.75	0.60	0.36	0.35	0.44	0.71	0.74	0.64	0.56
CaO	14.66	13.09	16.60	7.51	8.59	9.92	13.26	16.88	8.32	8.82	10.74	16.76	16.41	16.68	17.08
Na_2O	3.06	3.93	2.02	6.95	6.61	5.76	3.71	1.83	6.61	6.32	5.29	1.78	1.96	1.96	1.68
K_2O	0.08	0.23	0.09	0.42	0.32	0.23	0.21	0.05	0.38	0.34	0.20	0.05	0.05	0.05	0.04
Total	100.13	100.15	100.25	99.54	101.31	99.60	99.46	100.18	100.30	99.64	100.07	99.82	99.92	100.31	99.30
8 cat.															
Si	2.272	2.365	2.177	2.633	2.593	2.519	2.352	2.169	2.598	2.572	2.475	2.165	2.178	2.173	2.145
Al	1.709	1.606	1.798	1.359	1.396	1.466	1.622	1.811	1.392	1.417	1.513	1.817	1.805	1.807	1.836
Fe^{3+}	0.025	0.030	0.028	0.012	0.013	0.016	0.029	0.023	0.013	0.013	0.017	0.025	0.025	0.025	0.022
Ca	0.716	0.637	0.815	0.362	0.408	0.480	0.650	0.829	0.399	0.426	0.519	0.827	0.808	0.823	0.848
Na	0.271	0.346	0.179	0.605	0.567	0.504	0.329	0.163	0.572	0.552	0.462	0.159	0.175	0.166	0.150
K	0.005	0.013	0.005	0.024	0.018	0.013	0.012	0.003	0.021	0.019	0.011	0.003	0.003	0.003	0.002
Total	4.998	4.997	5.002	4.996	4.995	4.999	4.994	4.997	4.996	4.999	4.997	4.995	4.995	4.996	5.003
X_{An}	72.6	64.8	82.0	37.2	41.8	48.8	66.4	83.6	41.0	43.5	52.9	83.9	82.2	83.2	84.9
Li (μg/g)	5.1	0.7	0.2	32.0	32.9	4.7	4.9	3.5	24.7	21.4	6.1	2.9	3.3	2.7	2.5
2σ	0.2	0.1	0.0	1.0	0.4	0.2	0.2	0.1	0.4	0.3	0.2	0.1	0.1	0.2	0.1
Be (μg/g)	0.52	0.50	0.21	NA	0.81	0.87	0.32	0.26	1.31	1.08	1.03	0.21	0.23	0.24	0.21
2σ	0.07	0.07	0.05	NA	0.07	0.10	0.06	0.04	0.09	0.09	0.09	0.04	0.04	0.06	0.04
B (μg/g)	0.10	0.23	0.06	NA	0.26	0.36	0.18	0.09	0.23	0.24	0.14	0.05	0.06	0.05	0.06
2σ	0.04	0.07	0.04	NA	0.06	0.11	0.06	0.05	0.06	0.06	0.05	0.02	0.03	0.04	0.03
Mg (μg/g)	235	469	300	117	205	248	302	415	118	128	202	449	440	421	421.4
2σ	6	11	7	3	11	6	6	8	4	3	5	7	6	12	9
Sr (μg/g)	430	274	242	NA	407	346	247	290	308	356	385	291	292	294	267
2σ	7	6	5	NA	6	6	4	5	5	5	6	4	5	8	5
Ba (μg/g)	62	42	11	NA	121	74	34	25	167	156	142	23	24	23	22
2σ	4	3	2	NA	5	4	3	2	5	6	5	2	2	2	2

EPMA and SIMS analyses of different plagioclase phenocrysts in Minoan scoria. NA = not analyzed.
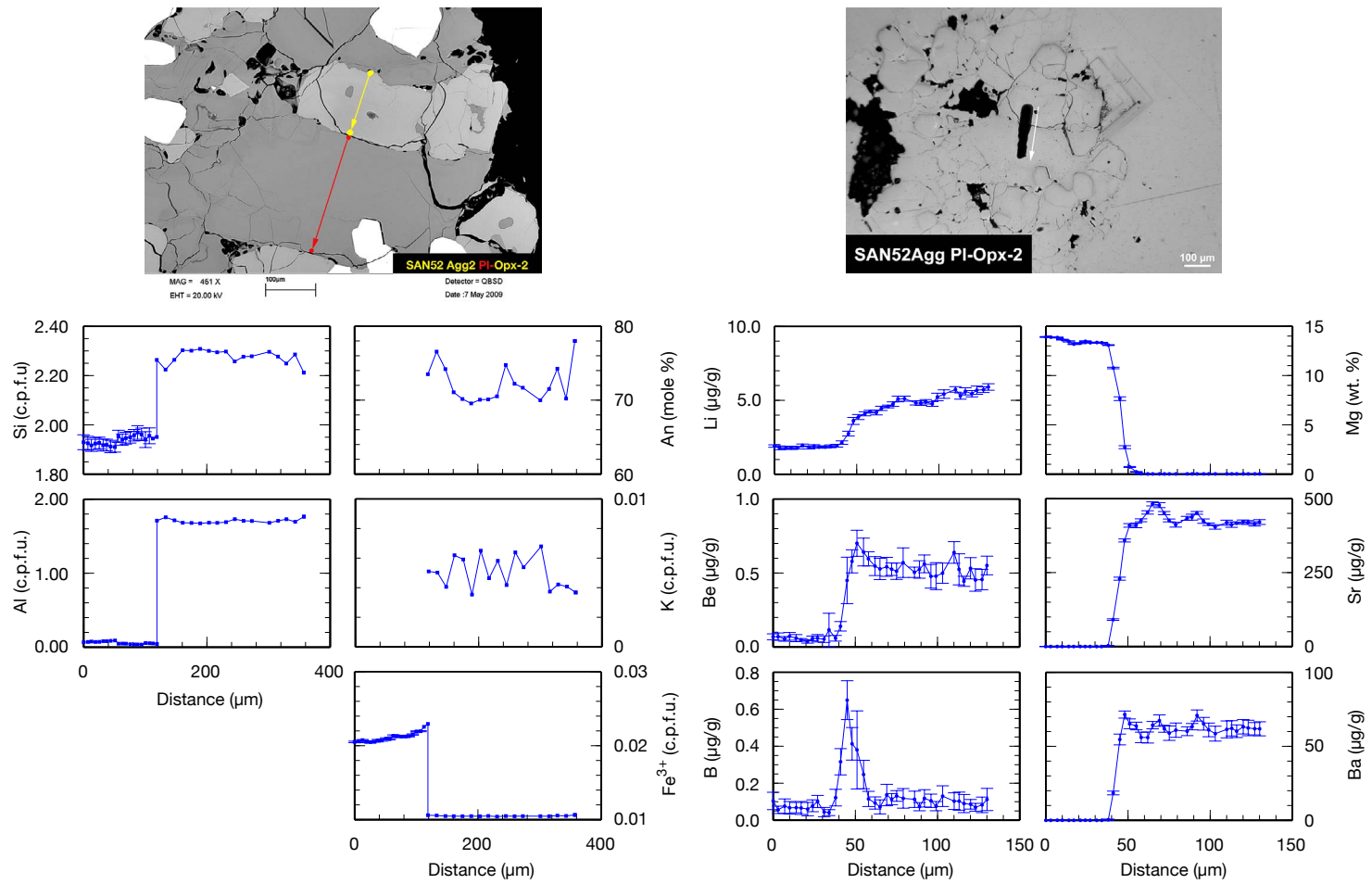
Fig. 4.23. SAN52Agg Pl-2: This crystal's core is bytownitic in composition. An increases by up to 10 mol% at the crystals rims. The Fe^{3+} profile is flat. Li slightly increases along the profile into the crystal. There is no well defined Li diffusion between opx and pl.
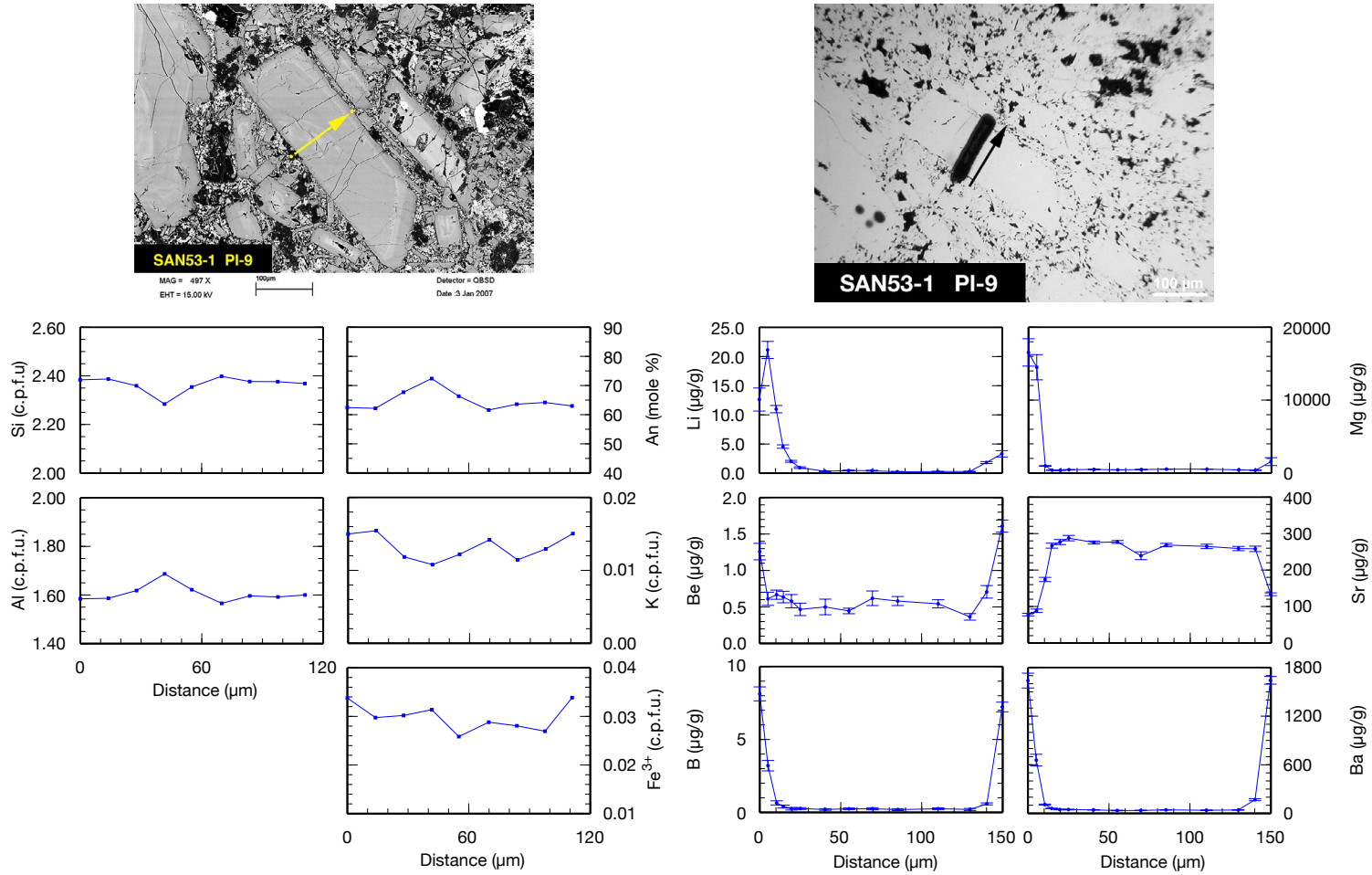
Fig. 4.24. SAN53-1 Pl-9: The profile is too short to gain any good results from it. The small core is strongly resorbed and is settled in the lower bytownite range. There is a high An zone close to the rim that was not hit during analyses. This zone seems to be slightly sieve-textured. An at the rim is approx. $X_{An} = 0.63 - 0.62$.
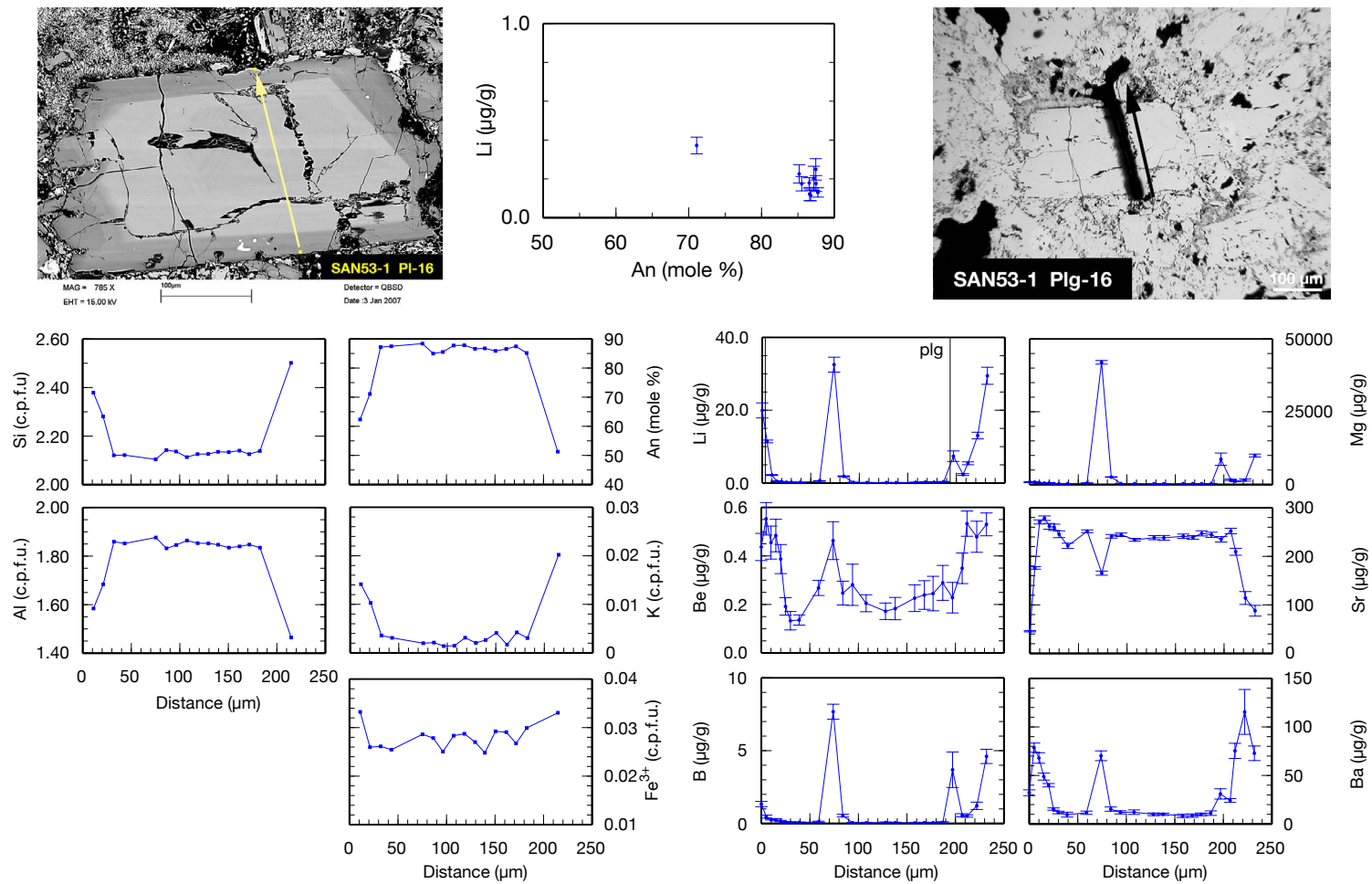
Fig. 4.25. SAN53-1 Pl-16: This crystal has a well developed bytownitic core that is slightly resorbed. The crystal is heavily cracked and the rim strongly resorbed. The drop of An content from core to rim is about 40 mol%. Unfortunately the EPMA profile is too short and the rim area overprinted by Li diffusion so that a clear correlation between An and Li cannot be observed.
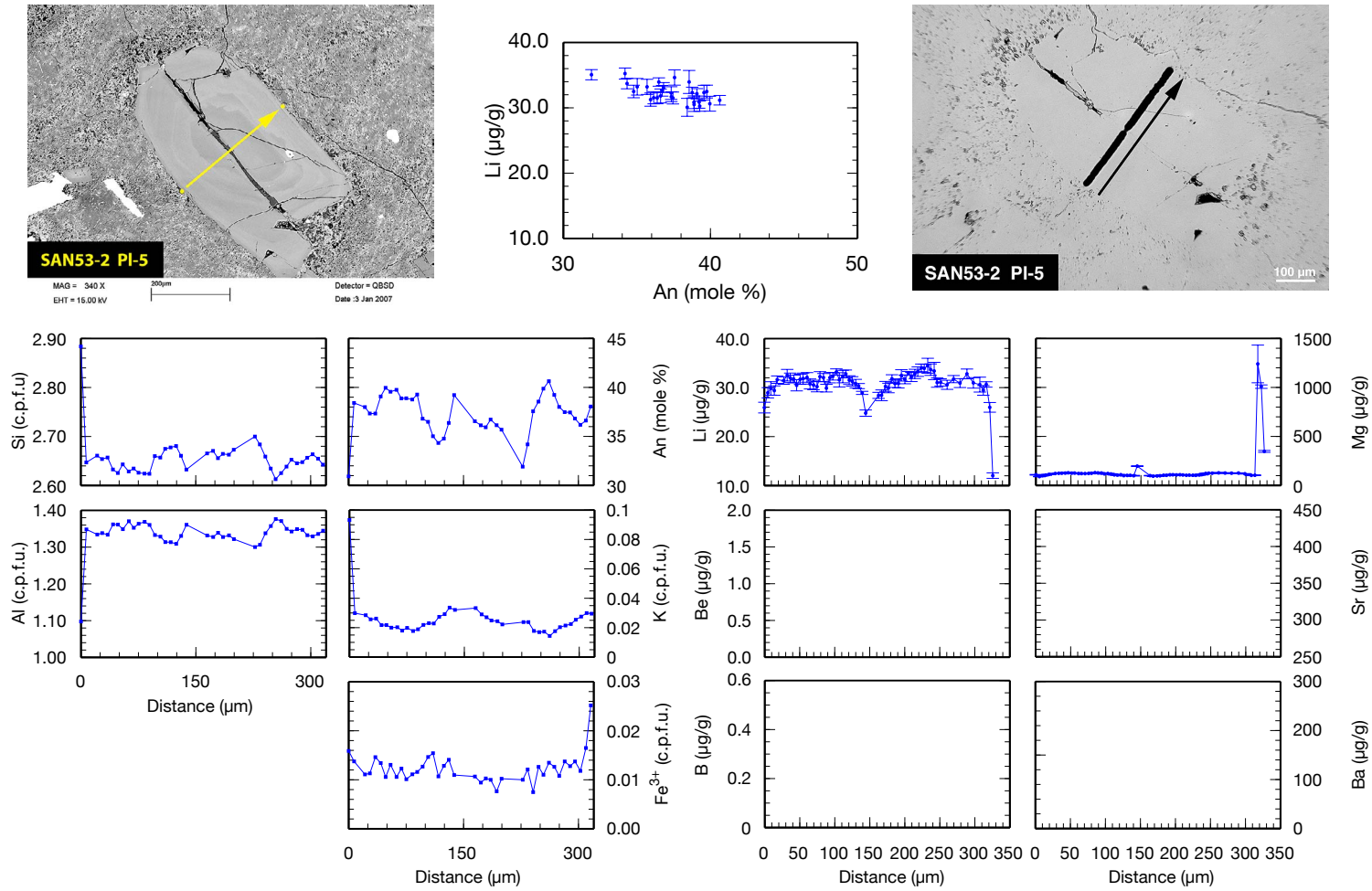
Fig. 4.26. SAN53-2 Pl-5: This crystal has a resorbed core and broad partly resorbed oscillatory zoning bands. X_{An} varies between $0.38 - 30.9$ at the crystal's rim. The Fe^{3+} seems to be rather irregular and does increase at the end of the profile towards the rim. The Li profile shows decreasing concentrations at the profiles' ends, suggesting a possible loss of Li.
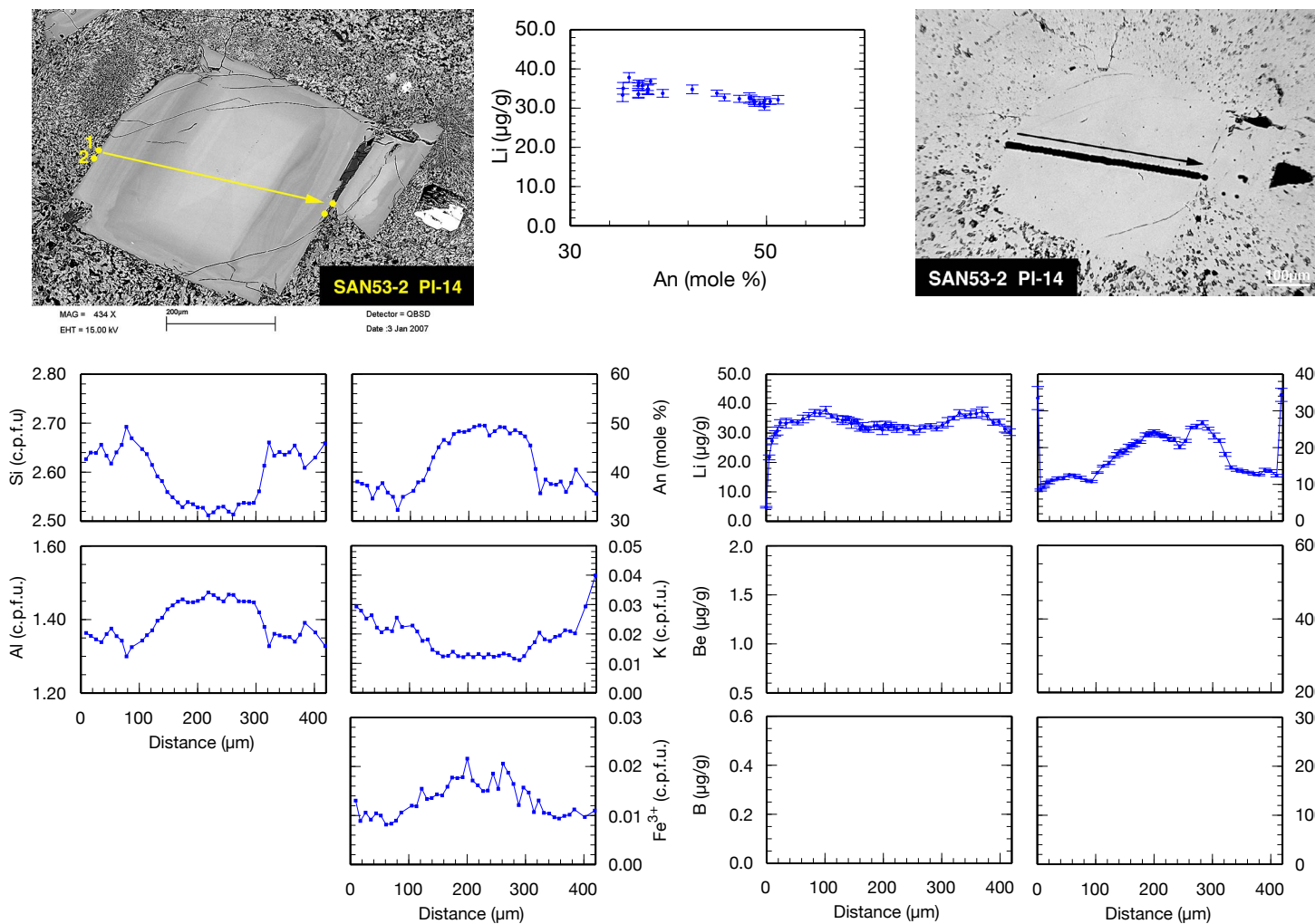
Fig. 4.27. SAN53-2 Pl-14: This crystal has a well developed sector-zoned core with a composition in the range of the andesine-labradorite transition. Oscillatory zoning continues towards the rim with broader low An resorption bands. Fe^{3+} is enriched in the core area and decreases towards the rim. Li is negatively correlated with X_{An}. A loss of Li is visible at the profiles' ends.
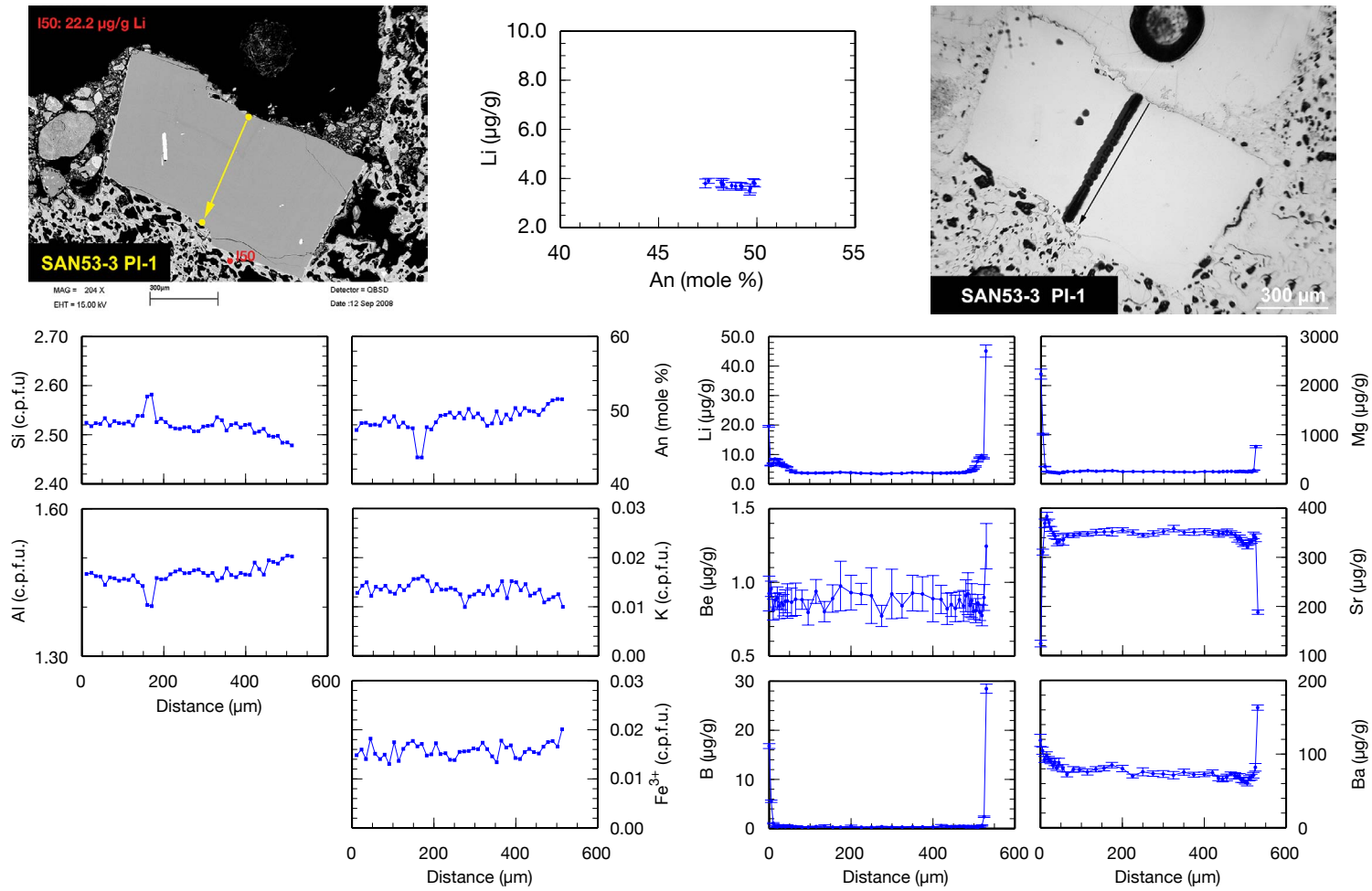
Fig. 4.28. SAN53-3 Pl-1: This crystal has X_{An} in the range of $0.44 - 0.52$. A low An zone of $X_{An}= 0.44$ is visible around the core region. It is obvious that parts of this crystal are missing, still there is Li diffusion into the crystal at the broken rim, indicating that whatever caused the crystal to break up (probably the eruption) happened before Li started to diffuse into the crystal.
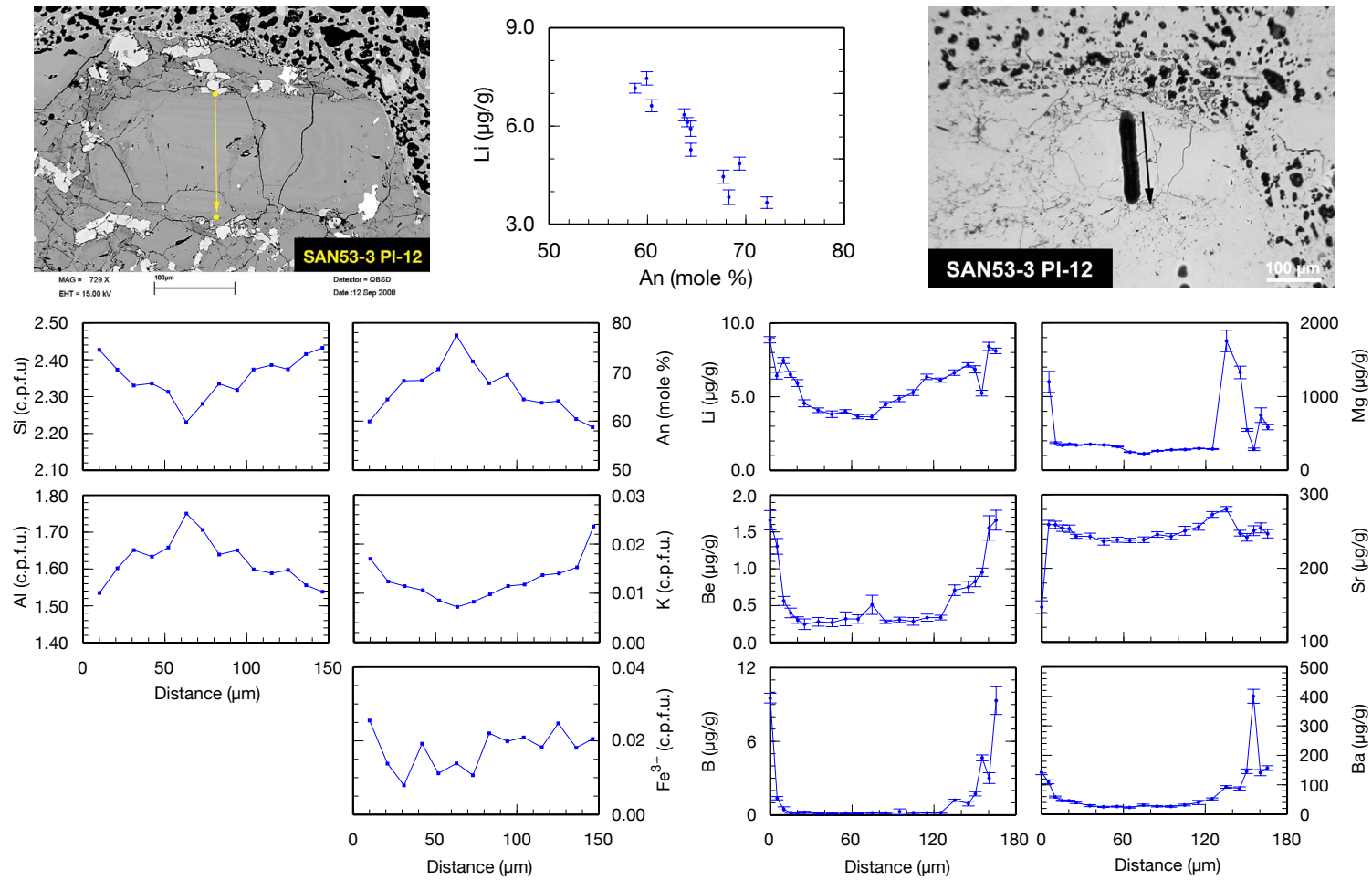
Fig. 4.29. SAN53-3 Pl-12: This pl has an oscillatory zonation with a small bytownitic core. $X_{An} = 0.77 - 0.59$. Rim values range from $X_{An} = 0.60 - 0.59$. Due to the short EPMA profile and the irregular pattern of the Fe^{3+}-profile it is hard to distinguish between core and rim values. Li correlates negatively with An in this crystal.
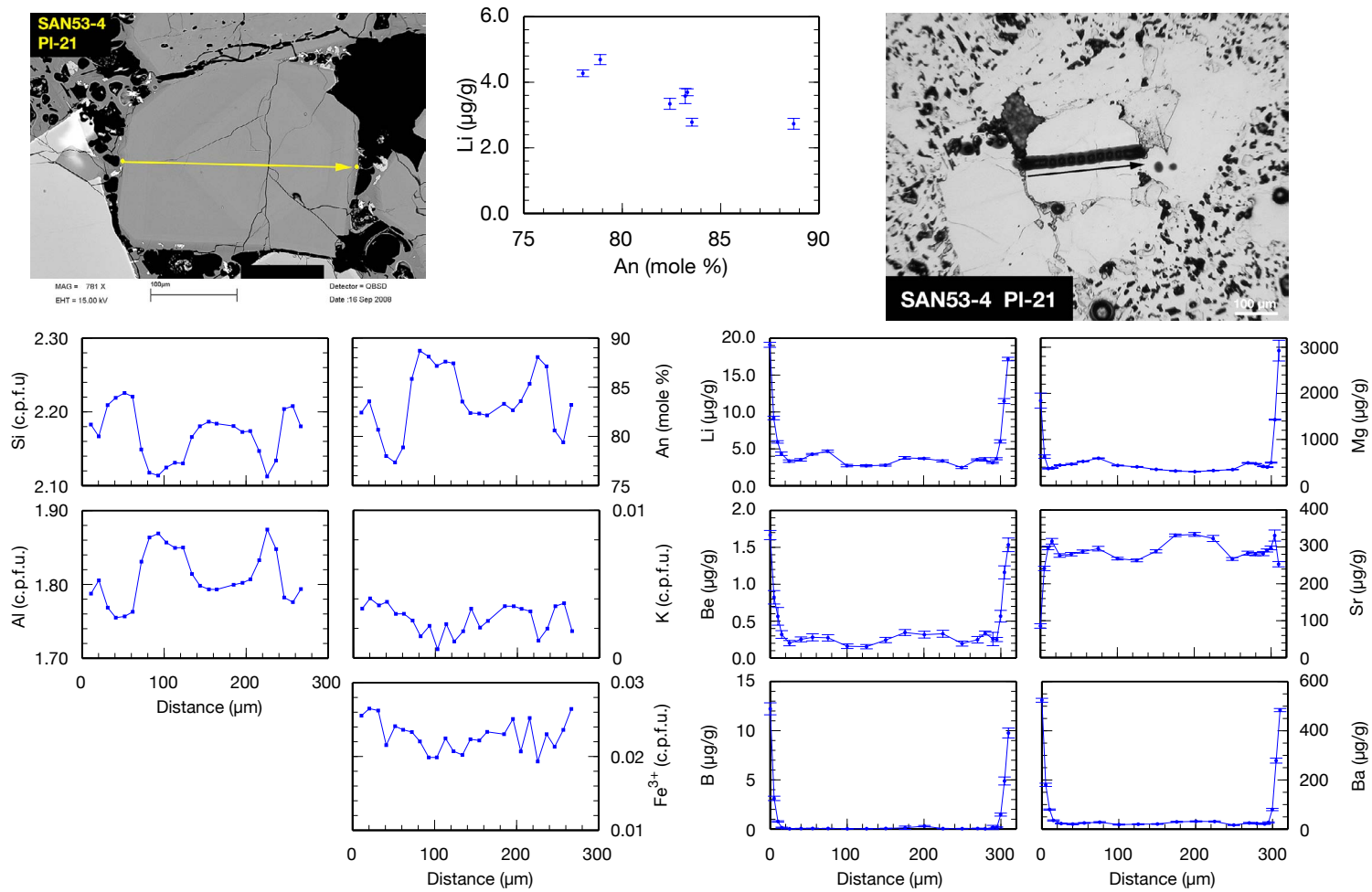
Fig. 4.30. SAN53-4 Pl-21: This pl has a bytownitic core with $X_{An} = 0.82 - 0.83$. The core is hardly visible in the Fe^{3+}-profile. Again the EPMA profile has only a couple of good points that correlate negatively with Li.
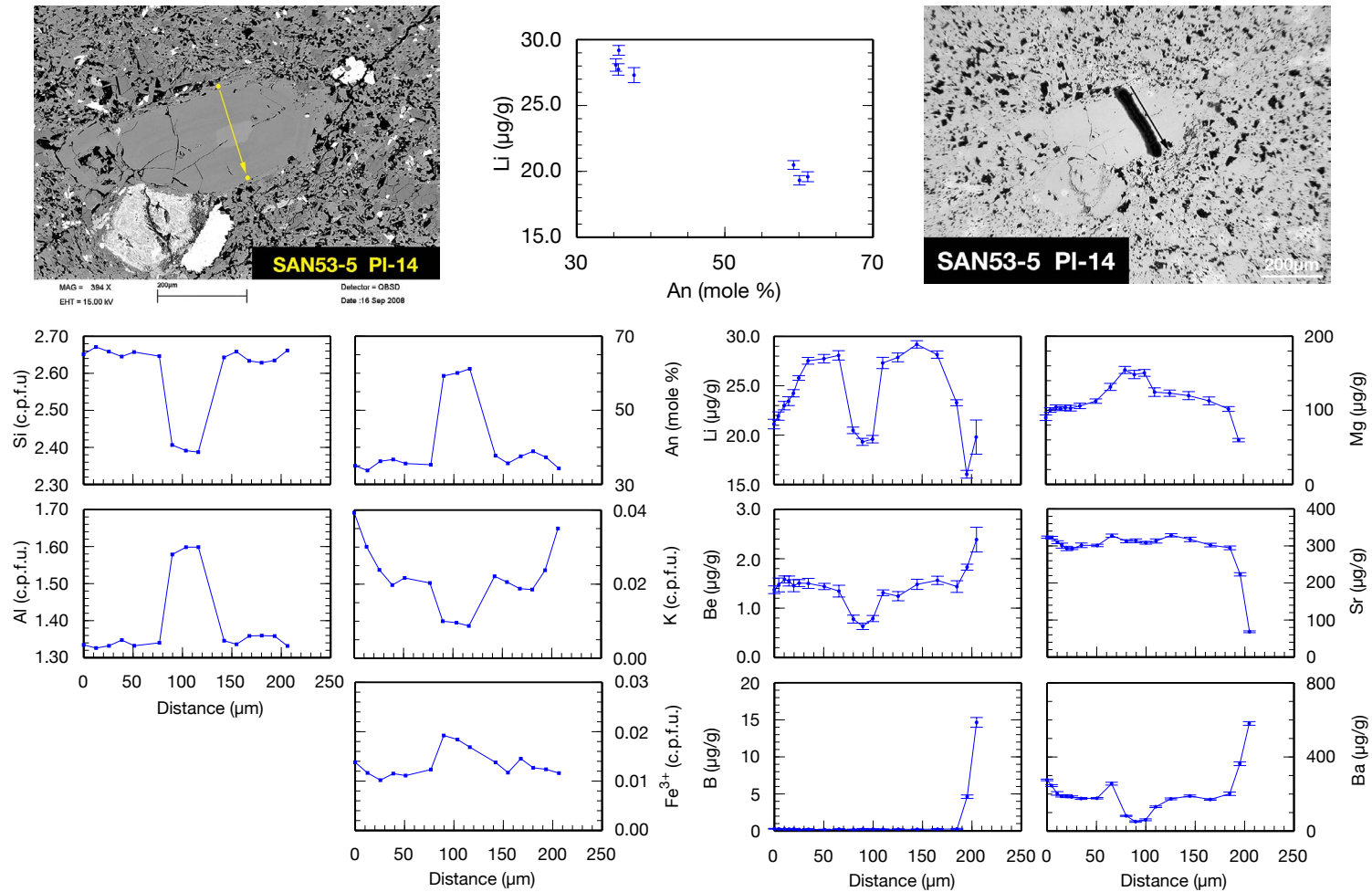
Fig. 4.31. SAN53-5 Pl-14: This phenocryst has a patchy (Type Ic) core of labradoritic composition. Fe^{3+} is slightly enriched in the core. Li correlates negatively with An; its concentrations decrease at the crystal rim. The rim is heavily resorbed.
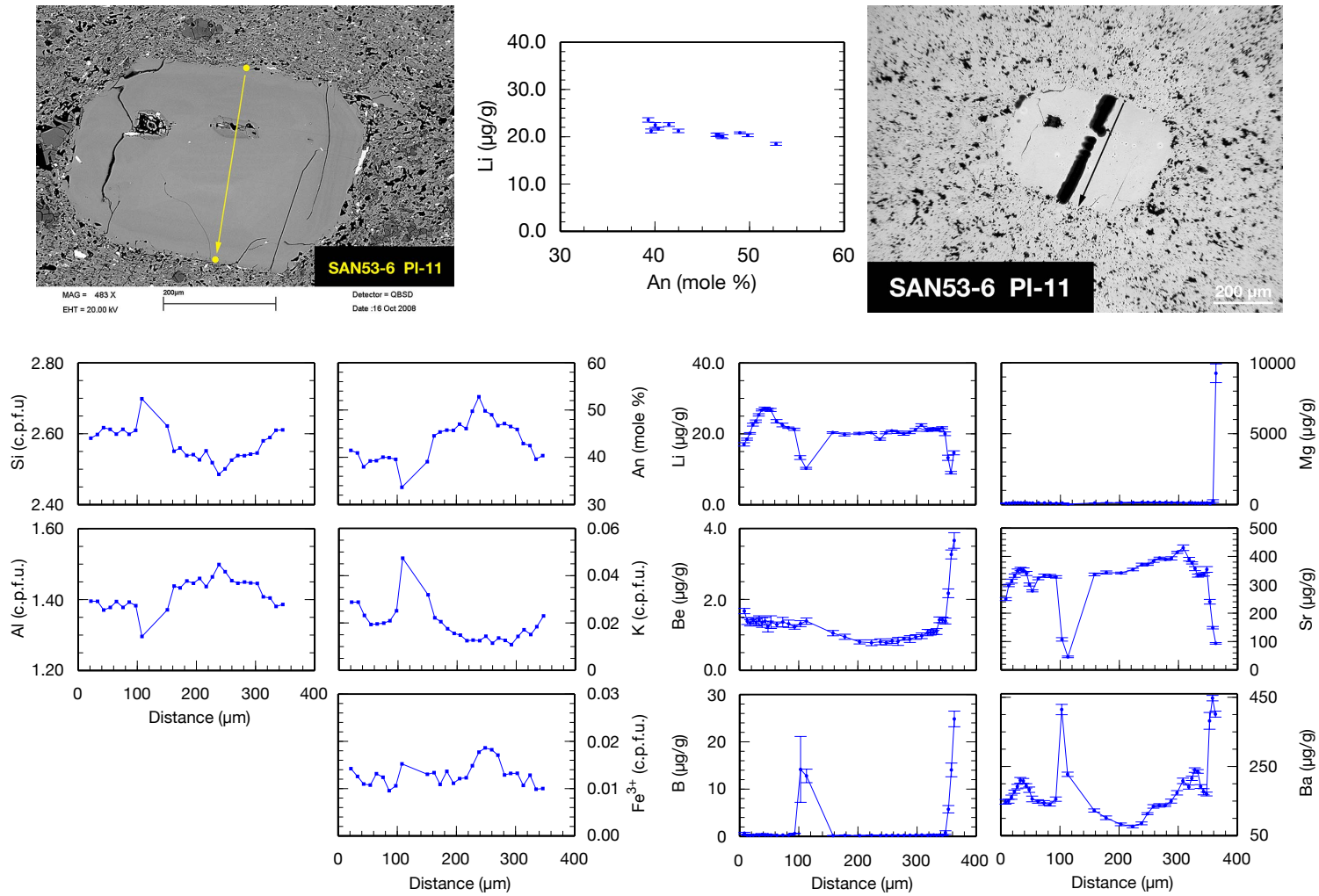
Fig. 4.32. SAN53-6 Pl-11: This pl plots in the andesine field and shows sector zoning in the core area. Fe^{3+} seems to be enriched in the core region. An correlates negatively with Li. There is a decrease in Li towards the crystal's rim.
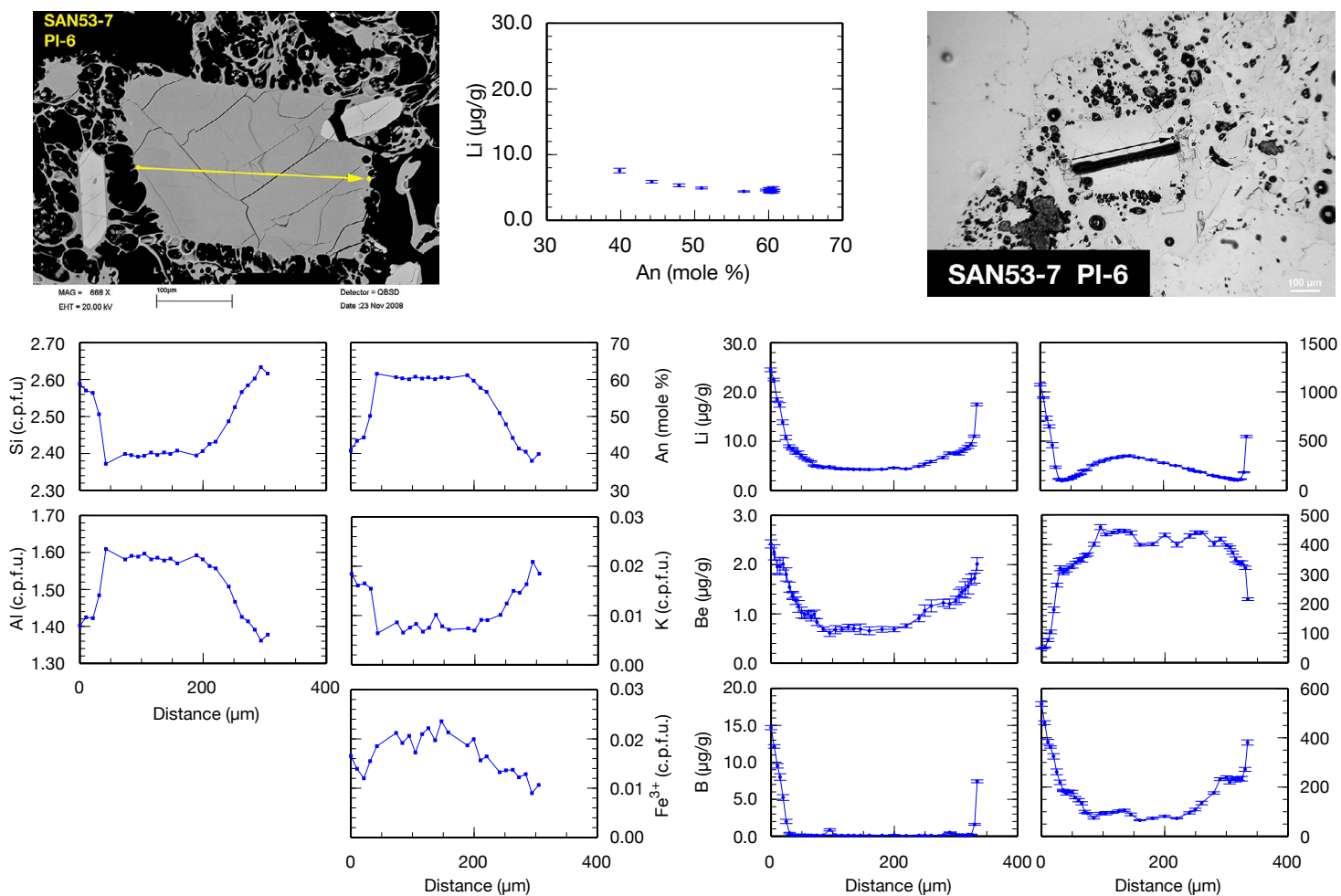
Fig. 4.33. SAN53-7 Pl-6: This crystal has a patchy (type Ic) core of labradoritic composition with a drop of An towards the rim of $\sim 20\,\mathrm{mol\%}$. Fe^{3+} is higher inside the crystal and decreases towards the rim.
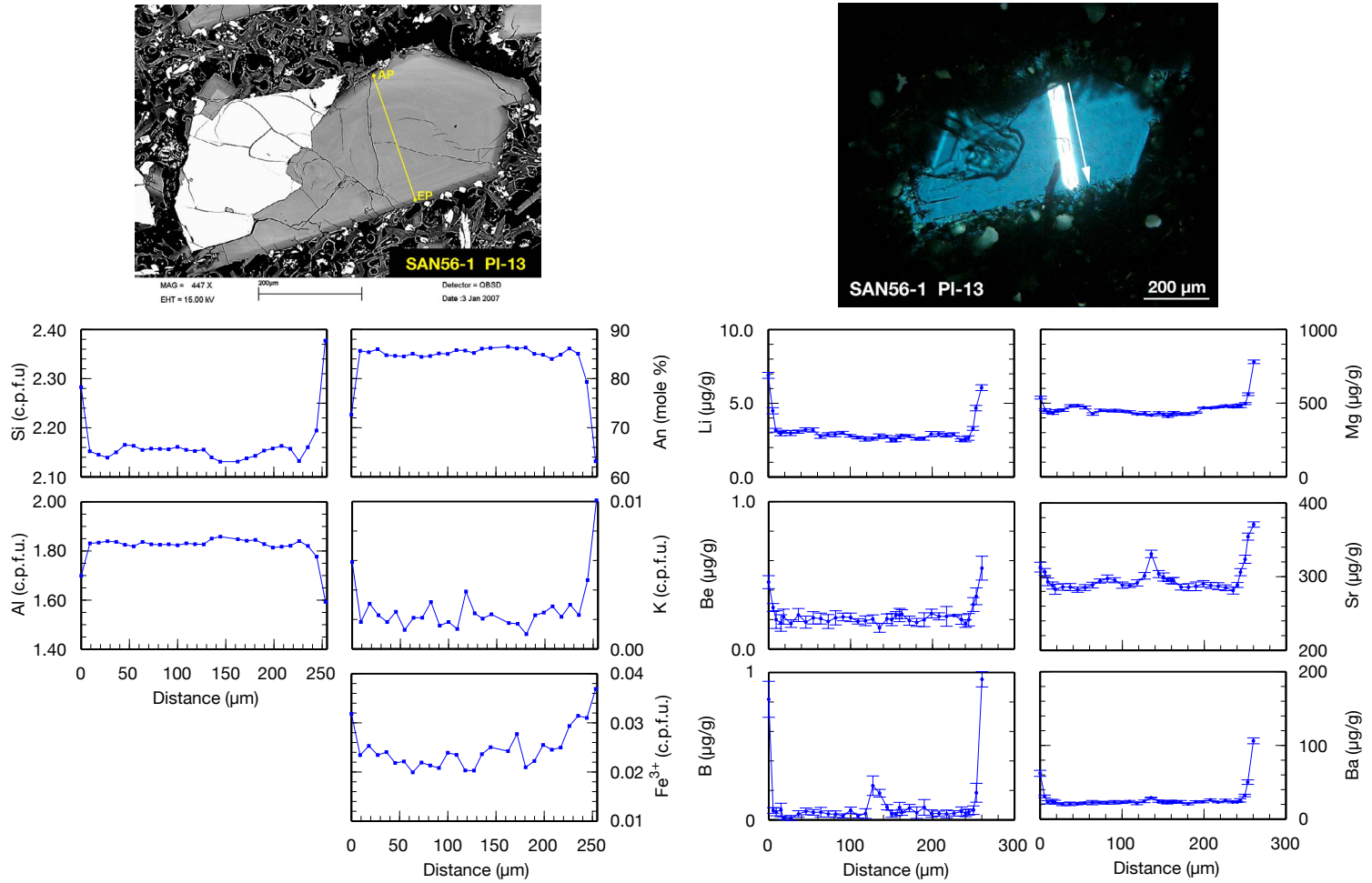
Fig. 4.34. SAN56-1 Pl-13: This pl has an oscillatory zonation and is mostly of bytownitic composition. There is a drop of An towards the rim of $\sim 20\,$mol%. Fe^{3+} slightly increases towards the rim of the crystal. If there is any diffusion of Li into the crystal then it is only on the first five micrometers overprinting the low-An rim. The variation inside the crystal is not high enough for a well developed correlation between Li and An.
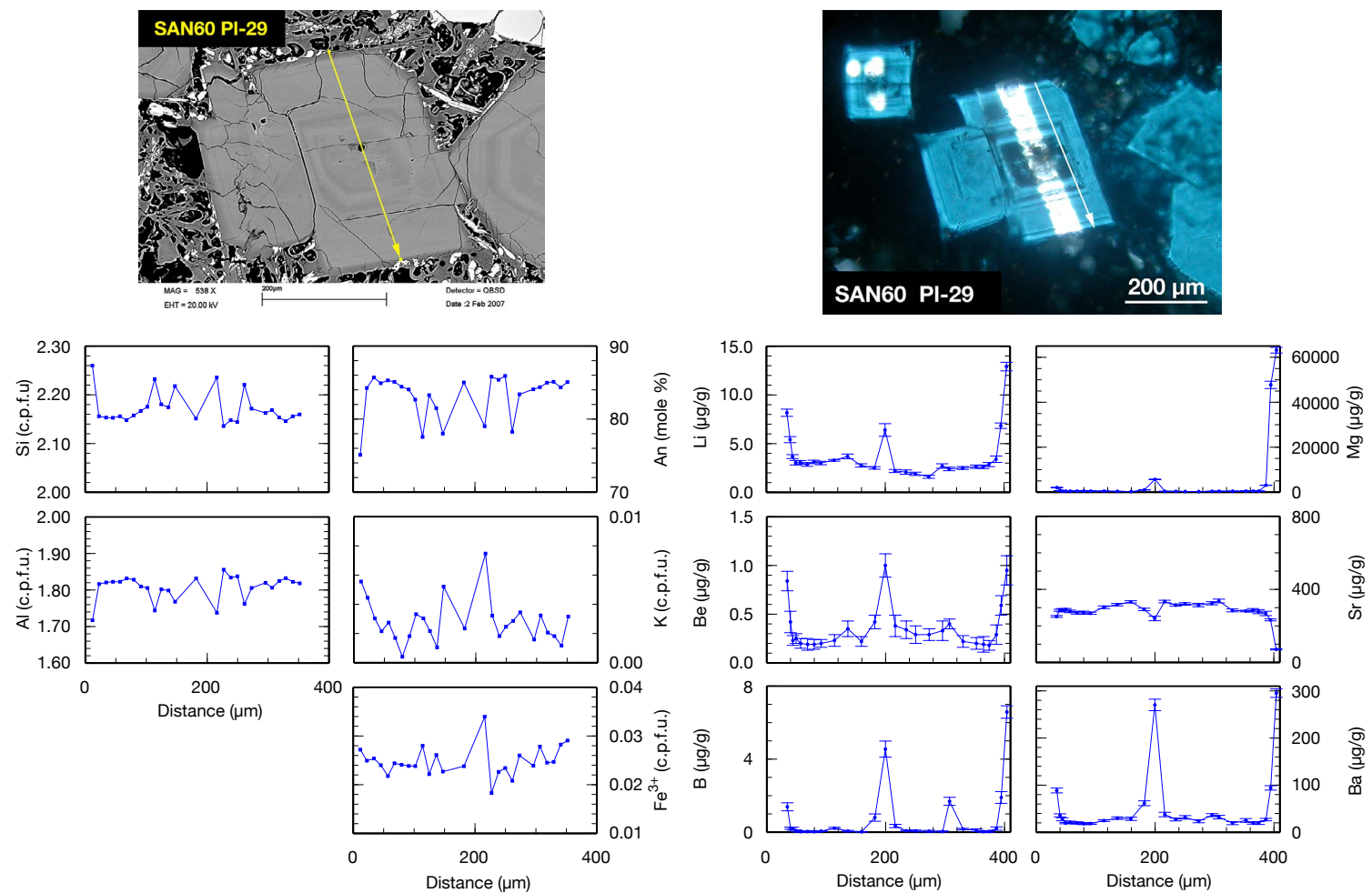
Fig. 4.35. SAN60 Pl-29: This pl crystal has a patchy core and oscillatory zoning towards the rim. It is bytownitic in composition. There is hardly any Li diffusion visible in the SIMS profile.
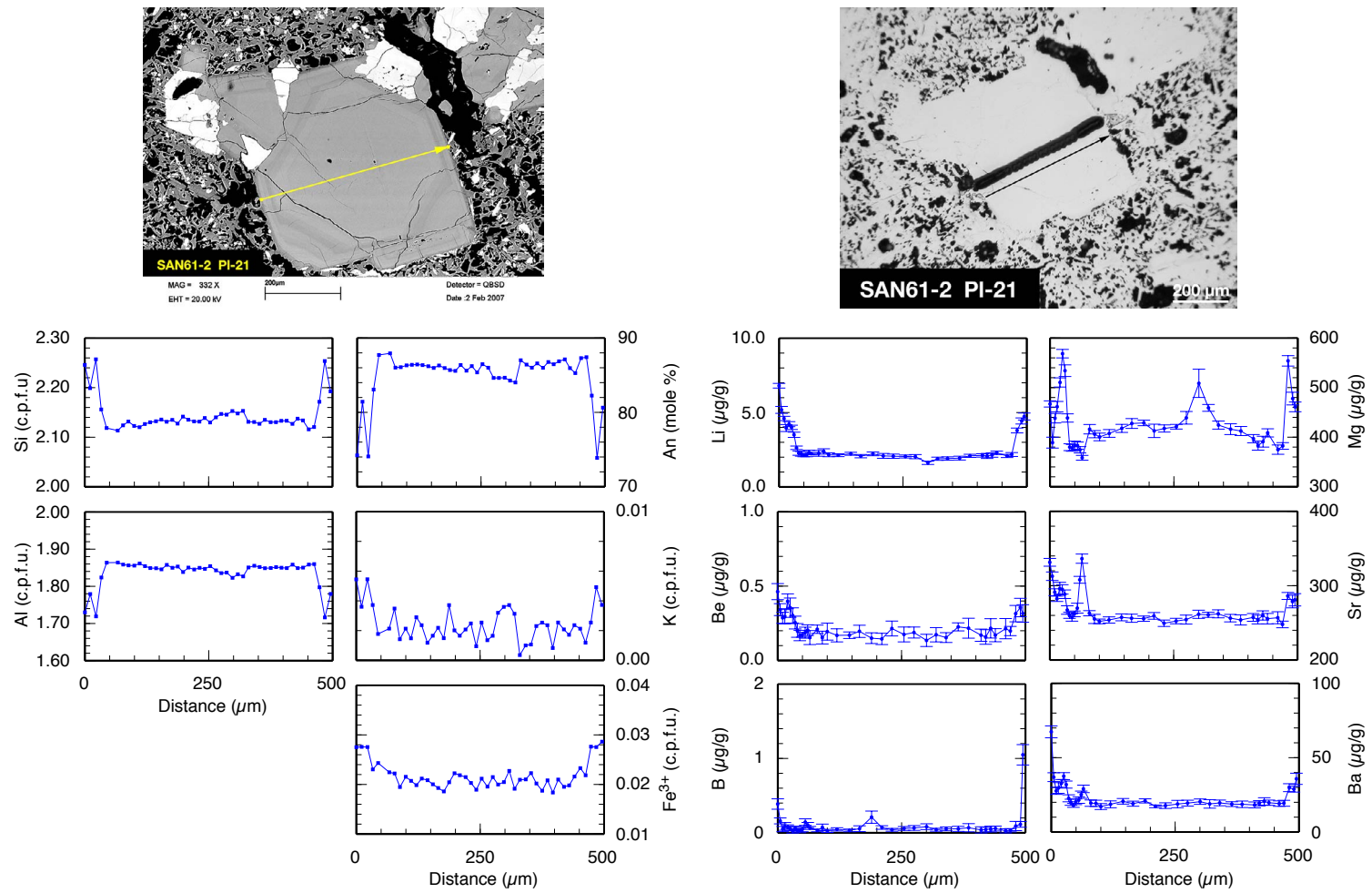
Fig. 4.36. SAN61-2 Pl-21: This crystal has a nicely developed core of $\sim X_{An}$ between $0.84 - 0.88$. Towards the rim there is a lower An zone of $\sim X_{An} = 0.74$.

4.2.4. Orthopyroxene – Minoan Pumice and Crystal-rich Pumice

Clinoenstatite crystals in the Minoan pumice show a wide range of MgO and FeO-Fe_2O_3 compositions Table 4.5 and Fig. 4.37.

X_{Mg} varies between $0.58 - 0.60$ for five of the clinoenstatite crystals in samples SAN52, SAN54, SAN57, SAN58 and SAN61-2. The average X_{Mg} in Opx-10 (SAN61-1A) is the highest with 0.69. Orthopyroxene crystals in SAN59 and SAN55 have X_{Mg} values that fall between Opx-10 and the other crystals.

Opx-1 (Crystal-rich pumice) has the highest MgO contents; X_{Mg} is 0.72. Ca, Mn and Ti contents are similar in all crystals analyzed; CaO for example ranges from $\sim 1.25 - 1.45$ wt% (Table 4.5). Opx-10 (SAN51-1A) has less Mn and slightly more Ti and a higher Al_2O_3 content compared to the other orthopyroxene crystals.

Lithium concentrations range between $\sim 2.6 - 2.9\,\mu g/g$ for most of the Minoan pumice orthopyroxene crystals. Opx-6 (SAN55) and Opx-10 (SAN61-1A) have concentrations below $\sim 2\,\mu g/g$. Opx-1 of the Crystal-rich pumice has the lowest average lithium concentration ($\sim 1.5\,\mu g/g$).

4.2.5. Orthopyroxene – Scoria Units A-B

Orthopyroxene of the Minoan scoria clasts cover a similar range of Mg and Fe contents as the Minoan pumice and Crystal-rich pumice orthopyroxene. Two of the crystals analyzed in Table 4.6 are geochemically very similar to orthopyroxene found in the main Minoan pumice (Fig. 4.37): Opx-15 (SAN53-2) and Opx-19 (SAN53-6). Their average X_{Mg} ranges from $0.59 - 0.60$ (see X_{Mg} values in Table 4.6). The lithium concentration of these orthopyroxene crystals is remarkably different, up to $\sim 17\,\mu g/g$.

Orthopyroxene of SAN52Agg and SAN61-2 is geochemically very similar to the orthopyroxene crystal of the Crystal-rich pumice. The average X_{Mg} value is 0.71. Compared to the crystal group that rather fits with the main Minoan pumice but differs in lithium, this group has lithium concentrations that fit the Crystal-rich pumice orthopyroxene nicely.

Average X_{Mg} of SAN53-3 crystals varies between $0.62 - 0.64$. Their TiO_2 content is similar to the crystal-rich pumice while Al_2O_3 is similar to the main pumice orthopyroxene. Their average lithium concentration is $\sim 2\,\mu g/g$ and therefore similar to crystals found within the main pumice with higher X_{Mg}. Opx-11 (SAN53-2) has a very similar major and minor element composition compared to SAN53-3 crystals and differs from Opx-15 (also SAN53-2). But its lithium concentration is much higher, up to $\sim 19\,\mu g/g$ compared to crystals in SAN53-3.
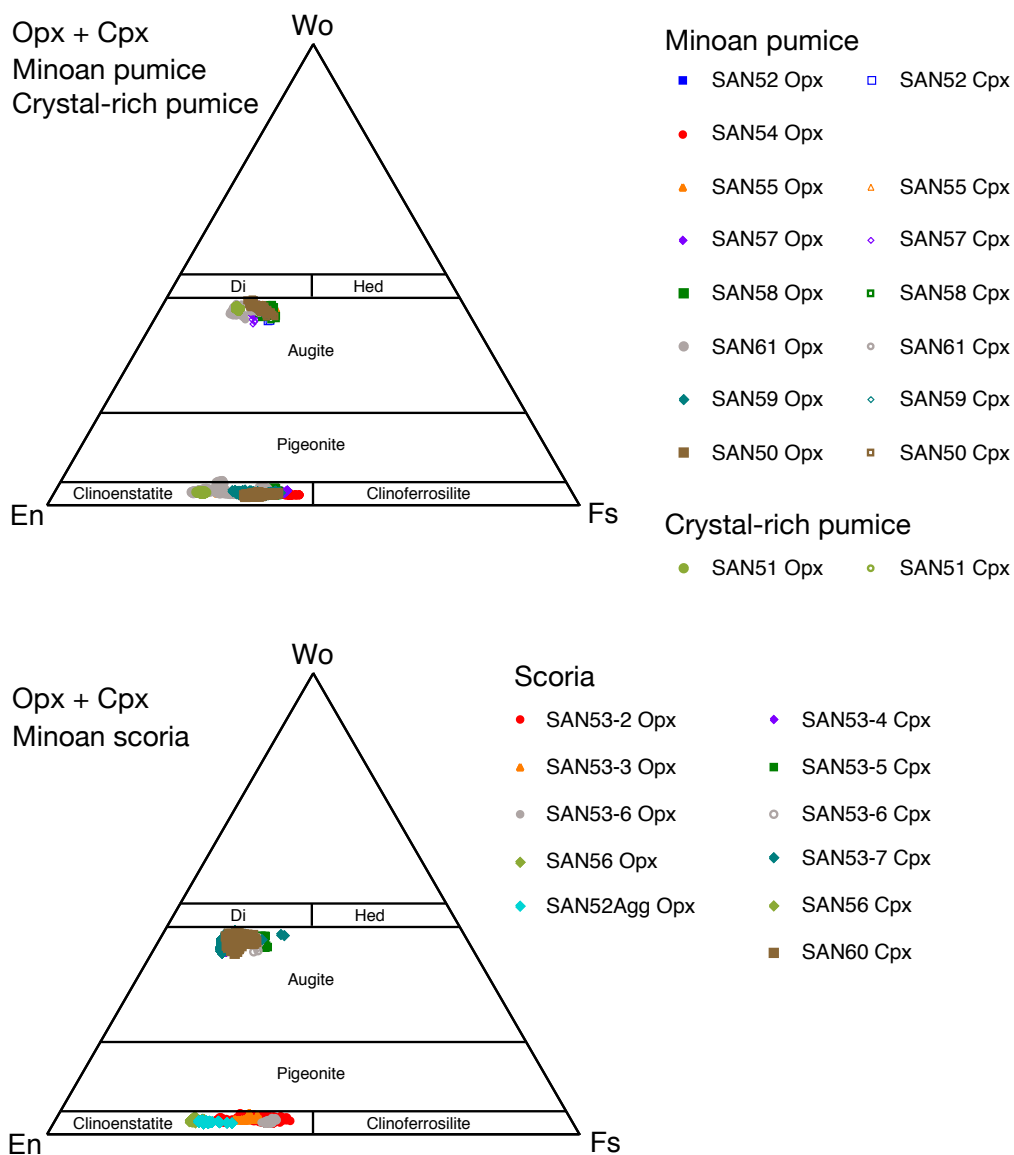
Fig. 4.37. Ternary diagram showing the composition of Minoan pumice, Crystal-rich pumice and Minoan scoria orthopyroxene and clinopyroxene crystals.

4.2.6. Clinopyroxene – Minoan Pumice and Crystal-rich Pumice

Major and minor element concentrations of Minoan pumice clinopyroxene crystals are relatively homogenous (Fig. 4.37, Table 4.5). Crystals plot in the augite field close to the diopside field (Fig. 4.37). Within the Minoan pumice Cpx-12 (SAN57A) has a slightly lower Ca content compared to the other cystals, while it is enriched in Mg, Fe^{3+} and Al. Cpx-1 and Cpx-7 (SAN58D) are also more ferric ($> 1\,wt\%$).

Cpx-2 (SAN51-1A) is geochemically a little different from the main Minoan clinopyroxene crystals. It is enriched in Mg ($> 1.5\,wt\%$), Fe^{3+}, Ti, Al and has less Fe^{2+} and Mn.

Lithium concentrations of Minoan pumice clinopyroxene vary between $\sim 4.0 - 4.4\,\mu g/g$, while beryllium concentrations range from $\sim 0.2 - 0.6\,\mu g/g$ (Table 4.5). Boron concentrations usually stay below $\sim 0.3\,\mu g/g$, unless inclusions are hit during analysis. Clinopyroxene crystals of the main Minoan pumice units have average strontium concentrations of $\sim 8.5 - 10.5\,\mu g/g$. Cpx-2 of the Crystal-rich pumice has about $2\,\mu g/g$ less lithium compared to the Minoan pumice clinopyroxene.

4.2.7. Clinopyroxene – Scoria – Units A–B

EPMA analyses of clinopyroxene crystals from Minoan scoria are presented in Fig. 4.37 and Table 4.6. Fig. 4.37 shows that scoria clinopyroxene crystals are geochemically similar to the main Minoan and Crystal-rich pumice but they do cover a wider range of concentrations.

It is in general difficult to group these crystals, as there are even differences between crystals in each sample. Nevertheless, I will try to divide the crystals of Table 4.6 into five groups for a better comparison.

Ca and Na concentrations in all crystals are quite similar and are comparable to the Minoan pumice and Crystal-rich pumice crystals. Si contents seem to be slightly lower compared to the Minoan pumice clinopyroxene.

The first group comprises clinopyroxene crystals with concentrations similar to the ones of the main Minoan pumice. These are the three crystals of SAN53-5 and SAN53-6. They differ from the Minoan pumice by much higher average lithium concentrations of about $\sim 25\,\mu g/g$ for Cpx-4 (SAN53-6) and $\sim 40\,\mu g/g$ for the SAN53-5 crystals. Note that Cpx-17 has lower Fe^{2+} contents compared to the Minoan pumice. Clinopyroxene crystals of SAN53-5 and SAN53-6 are also affected by rises of lithium towards the rim due to contact with a high lithium phase. Cpx-17 has lithium concentrations that rise up to $\sim 800\,\mu g/g$ at the mineral-matrix transi-

tion (see Chapter 7 for further discussion).

The second group is represented by Cpx-26 (SAN61-2). Compared to all clinopyroxene crystals analyzed, it has the highest Fe^{3+}, Al and Ti and the lowest Fe^{2+} and Mn contents. Its lithium concentration of $\sim 2\,\mu g/g$ is similar to clinopyroxene from the Crystal-rich pumice. Cpx-4 of SAN53-7 fits into this group but has a lower lithium concentration ($\sim 1.3\,\mu g/g$).

Cpx-2 from the same sample has more Fe^{2+} and less Fe^{3+}, although its Fe^{3+} content is still higher compared to the Crystal-rich pumice. Its magnesium content is lower compared to the other two crystals and lies between the Crystal-rich pumice and the Minoan pumice clinopyroxene crystals. It is therefore put into a group of its own.

The fourth group consists of Cpx-4 (SAN56-1) and Cpx-14 (SAN60). These crystals are very similar to each other and their Mg, Fe^{2+} and Mn contents lie between Minoan pumice and Crystal-rich pumice clinopyroxene. Average Fe_2O_3 varies between $\sim 1.6 - 1.7\,wt\%$ and is similar to some of the Minoan pumice clinopyroxene crystals of SAN58.

The fifth group consists of Cpx-3 (SAN53-4). It is geochemically similar to the Crystal-rich pumice, but compared to Cpx-2 of SAN51-1A it has higher Ti, Al and Fe^{3+}. Its Al content is the second lowest of the scoria group.

Table 4.5. Average EPMA and SIMS Analyses of Orthopyroxene and Clinopyroxene in Minoan Pumice and Crystal-rich Pumice

| Sample | S52D | S54D | S55D | S57D | S58D | S61-2 | S61-1A | S59D | S51-1A | S52D | S55D | S57A | S58D | S58D | S61-1A | S59D | S50D |
Crystal	Opx-9	Opx-4	Opx-6	Opx-1	Opx-4	Opx-7	Opx-10	Opx-7	Opx-1	Cpx-7	Cpx-4	Cpx-12	Cpx-1	Cpx-7	Cpx-8	Cpx-11	Cpx-8
Analysis																	
SiO_2	52.45	52.48	53.20	52.38	51.94	51.79	53.28	52.8	53.4	52.43	52.53	52.15	52.22	51.85	52.23	52.39	52.71
TiO_2	0.16	0.18	0.21	0.17	0.20	0.23	0.23	0.2	0.3	0.26	0.25	0.28	0.25	0.25	0.29	0.28	0.25
Al_2O_3	0.44	0.52	0.73	0.47	0.64	0.92	1.15	0.7	1.5	0.96	0.90	1.05	0.93	0.95	1.09	0.96	0.98
Cr_2O_3	0.01	0.01	0.01	0.01	0.01	0.01	0.02	0.0	0.0	0.01	0.01	0.01	0.01	0.01	0.01	0.02	0.01
Fe_2O_3	0.39	0.08	0.60	0.37	0.77	1.80	0.42	0.3	1.9	0.84	0.54	1.45	1.53	1.61	0.87	0.95	0.66
FeO	24.68	24.47	20.15	24.73	23.46	22.72	18.77	22.3	16.0	11.08	10.93	9.62	9.98	10.02	10.34	10.27	10.29
MnO	1.21	1.19	0.85	1.20	1.12	1.01	0.70	0.9	0.5	0.65	0.61	0.58	0.62	0.62	0.59	0.60	0.59
MgO	19.73	19.69	22.97	19.64	20.13	20.42	23.82	21.4	25.6	13.16	13.22	14.09	13.55	13.32	13.53	13.46	13.55
CaO	1.25	1.28	1.32	1.28	1.30	1.45	1.44	1.3	1.4	20.40	20.60	20.26	20.62	20.59	20.40	20.70	20.87
Na_2O	0.02	0.03	0.02	0.02	0.03	0.03	0.02	0.0	0.0	0.34	0.32	0.28	0.32	0.32	0.33	0.32	0.32
Total	100.34	99.93	100.06	100.26	99.60	100.37	99.84	100.0	100.6	100.14	99.90	99.78	100.03	99.54	99.68	99.95	100.22
X_{Mg}	0.58	0.59	0.66	0.58	0.60	0.60	0.69	0.63	0.72	0.66	0.67	0.70	0.68	0.67	0.68	0.68	0.69
Calc. 4 cat.																	
Si	1.982	1.989	1.971	1.98	1.970	1.949	1.964	1.976	1.935	1.972	1.978	1.959	1.962	1.960	1.967	1.969	1.973
Al (IV)	0.016	0.011	0.027	0.02	0.026	0.041	0.036	0.023	0.063	0.028	0.022	0.041	0.036	0.038	0.033	0.031	0.027
Fe^{3+}	0.002	0.000	0.002	0.00	0.004	0.011	0.000	0.001	0.002	0.000	0.000	0.001	0.002	0.002	0.000	0.000	0.000
Total (Tet)	2.000	2.000	2.000	2.00	2.000	2.000	2.000	2.000	2.000	2.000	2.000	2.000	2.000	2.000	2.000	2.000	2.000
Al VI (M1)	0.004	0.012	0.005	0.00	0.003	0.000	0.014	0.010	0.003	0.014	0.018	0.006	0.005	0.005	0.015	0.012	0.017
Ti (M1)	0.005	0.005	0.006	0.00	0.006	0.006	0.006	0.006	0.007	0.007	0.007	0.007	0.008	0.007	0.007	0.008	0.008	0.007
Cr (M1)	0.000	0.000	0.000	0.00	0.000	0.000	0.000	0.000	0.000	0.000	0.000	0.000	0.000	0.000	0.000	0.000	0.000
Fe^{3+} (M1)	0.009	0.002	0.015	0.01	0.018	0.040	0.012	0.008	0.049	0.024	0.015	0.040	0.042	0.044	0.025	0.027	0.018
Mg^{2+}	0.983	0.980	0.974	0.98	0.973	0.953	0.967	0.976	0.941	0.738	0.742	0.789	0.759	0.750	0.760	0.754	0.756
Fe^{2+}	0.000	0.000	0.000	0.00	0.000	0.000	0.000	0.000	0.000	0.216	0.218	0.157	0.187	0.194	0.192	0.199	0.201
Mn	0.000	0.000	0.000	0.00	0.000	0.000	0.000	0.000	0.000	0.000	0.000	0.000	0.000	0.000	0.000	0.000	0.000
Total M1	1.000	1.000	1.000	1.00	1.000	1.000	1.000	1.000	1.000	1.000	1.000	1.000	1.000	1.000	1.000	1.000	1.000
Mg^{2+}	0.129	0.132	0.295	0.13	0.165	0.192	0.341	0.220	0.443	0.000	0.000	0.000	0.000	0.000	0.000	0.000	0.000
Fe^{2+}	0.780	0.776	0.625	0.78	0.744	0.715	0.579	0.697	0.483	0.132	0.126	0.145	0.126	0.123	0.134	0.124	0.121
Mn	0.039	0.038	0.027	0.04	0.036	0.032	0.022	0.029	0.016	0.021	0.019	0.018	0.020	0.020	0.019	0.019	0.019
Ca (M2)	0.050	0.052	0.052	0.05	0.053	0.059	0.057	0.052	0.056	0.822	0.831	0.815	0.830	0.834	0.823	0.833	0.837
Na (M2)	0.002	0.002	0.002	0.00	0.002	0.002	0.001	0.002	0.001	0.025	0.024	0.021	0.024	0.023	0.024	0.024	0.023
Total M2	1.000	1.000	1.000	1.000	1.000	1.000	1.000	1.000	1.000	1.000	1.000	1.000	1.000	1.000	1.000	1.000	1.000
Total	4.000	4.000	4.000	4.000	4.000	4.000	4.000	4.000	4.000	4.000	4.000	4.000	4.000	4.000	4.000	4.000	4.000
Li ($\mu g/g$)	2.6	2.8	1.9	2.8	2.8	2.9	1.6	2.7	1.5	4.3	4.2	NA	4.2	4.0	4.1	4.2	4.1
2σ	0.1	0.1	0.1	0.1	0.1	0.1	0.1	0.1	0.1	0.1	0.2	NA	0.2	0.2	0.2	0.2	0.2
Sr ($\mu g/g$)	0.08	0.13	0.11	0.10	0.09	0.15	0.10	0.19	0.12	9.3	9.5	NA	9.3	8.5	10.0	9.6	9.2
2σ	0.04	0.04	0.04	0.04	0.04	0.11	0.09	0.05	0.10	0.5	0.5	NA	0.5	0.5	1.0	0.5	0.8

Formulas are calculated to 4 cations.

Table 4.6. Average EPMA and SIMS Analyses of Orthopyroxene and Clinopyroxene in Minoan Scoria

Sample Crystal	S52Agg Opx-2	S53-2 Opx-11	S53-2 Opx-15	S53-3 Opx-10	S53-3 Opx-14	S53-6 Opx-19	S61-2 Opx-18	S53-4 Cpx-3	S53-5 Cpx-17	S53-5 Cpx-20	S53-6 Cpx-4	S53-7 Cpx-2	S53-7 Cpx-4	S56-1 Cpx-19	S60 Cpx-14	S61-2 Cpx-26
Analysis																
SiO_2	53.05	52.96	52.37	52.57	52.20	51.94	52.38	51.20	51.97	51.58	52.13	51.56	50.26	52.09	51.79	50.64
TiO_2	0.24	0.32	0.21	0.31	0.30	0.18	0.33	0.58	0.24	0.32	0.25	0.43	0.70	0.41	0.40	0.61
Al_2O_3	1.39	1.48	0.74	0.79	0.75	0.59	1.96	2.88	0.92	1.13	0.99	1.75	3.90	1.68	1.83	3.17
Cr_2O_3	0.01	0.01	0.01	0.02	0.01	0.01	0.01	0.01	0.01	0.02	0.01	0.01	0.03	0.01	0.02	0.03
Fe_2O_3	1.92	0.81	0.22	1.35	1.26	1.18	2.18	2.72	1.85	1.44	0.91	2.34	3.19	1.59	1.72	3.25
FeO	16.59	19.78	24.40	20.57	21.66	23.33	16.22	6.57	8.95	9.98	9.98	7.75	5.28	8.89	8.03	5.82
MnO	0.56	0.78	1.15	0.87	1.02	1.15	0.55	0.29	0.58	0.59	0.59	0.39	0.23	0.44	0.41	0.26
MgO	25.05	22.93	19.71	22.18	21.13	20.18	24.50	15.25	14.01	13.41	13.82	14.48	15.60	14.45	14.71	15.35
CaO	1.37	1.55	1.38	1.59	1.71	1.32	1.85	20.62	20.63	20.28	20.16	20.91	20.56	20.43	20.55	20.62
Na_2O	0.02	0.03	0.03	0.03	0.03	0.02	0.03	0.27	0.31	0.32	0.33	0.28	0.23	0.30	0.28	0.26
Total	100.20	100.66	100.22	100.28	100.06	99.90	100.01	100.39	99.47	99.07	99.18	99.91	99.99	100.28	99.74	100.01
X_{Mg}	0.71	0.66	0.59	0.64	0.62	0.60	0.71	0.75	0.70	0.68	0.69	0.72	0.77	0.71	0.73	0.76
Calc. to 4 cations																
Si	1.938	1.949	1.979	1.956	1.958	1.966	1.919	1.893	1.958	1.957	1.970	1.926	1.859	1.940	1.934	1.877
Al (IV)	0.059	0.051	0.021	0.035	0.033	0.025	0.079	0.107	0.040	0.043	0.030	0.068	0.141	0.060	0.066	0.122
Fe^{3+}	0.004	0.000	0.000	0.009	0.009	0.009	0.002	0.000	0.002	0.000	0.000	0.006	0.000	0.000	0.000	0.000
Total (Tet)	2.000	2.000	2.000	2.000	2.000	2.000	2.000	2.000	2.000	2.000	2.000	2.000	2.000	2.000	2.000	2.000
Al VI (M1)	0.001	0.014	0.011	0.000	0.000	0.001	0.006	0.019	0.001	0.008	0.014	0.010	0.029	0.014	0.015	0.016
Ti (M1)	0.007	0.009	0.006	0.009	0.008	0.005	0.009	0.016	0.007	0.009	0.007	0.012	0.020	0.011	0.011	0.017
Cr (M1)	0.000	0.000	0.000	0.000	0.000	0.000	0.000	0.000	0.000	0.000	0.000	0.000	0.001	0.000	0.000	0.001
Fe^{3+} (M1)	0.049	0.022	0.006	0.028	0.027	0.025	0.058	0.076	0.050	0.041	0.026	0.060	0.089	0.045	0.048	0.091
Mg^{2+}	0.943	0.955	0.976	0.963	0.964	0.969	0.926	0.841	0.787	0.758	0.778	0.806	0.855	0.802	0.818	0.849
Fe^{2+}	0.000	0.000	0.000	0.000	0.000	0.000	0.000	0.049	0.155	0.184	0.174	0.112	0.007	0.128	0.107	0.027
Mn	0.000	0.000	0.000	0.000	0.000	0.000	0.000	0.000	0.000	0.000	0.000	0.000	0.000	0.000	0.000	0.000
Total M1	1.000	1.000	1.000	1.000	1.000	1.000	1.000	1.000	1.000	1.000	1.000	1.000	1.000	1.000	1.000	1.000
Mg^{2+}	0.421	0.302	0.134	0.268	0.217	0.170	0.411	0.000	0.000	0.000	0.000	0.000	0.005	0.000	0.000	0.000
Fe^{2+}	0.507	0.610	0.771	0.640	0.679	0.738	0.497	0.154	0.127	0.133	0.141	0.130	0.157	0.149	0.144	0.154
Mn	0.017	0.024	0.037	0.027	0.032	0.037	0.017	0.009	0.018	0.019	0.019	0.012	0.007	0.014	0.013	0.008
Ca (M2)	0.054	0.061	0.056	0.063	0.069	0.053	0.073	0.817	0.833	0.824	0.816	0.837	0.815	0.815	0.822	0.819
Na (M2)	0.001	0.002	0.002	0.002	0.002	0.002	0.002	0.020	0.023	0.024	0.024	0.020	0.016	0.022	0.020	0.019
Total M2	1.000	1.000	1.000	1.000	1.000	1.000	1.000	1.000	1.000	1.000	1.000	1.000	1.000	1.000	1.000	1.000
Total	4.000	4.000	4.000	4.000	4.000	4.000	4.000	4.000	4.000	4.000	4.000	4.000	4.000	4.000	4.000	4.000
Li ($\mu g/g$)	1.9	18.8	16.9	2.0	2.1	13.8	1.4	1.6	40.9	39.3	25.5	1.5	1.3	1.6	1.5	2.1
2σ	0.1	0.8	0.7	0.1	0.1	0.3	0.1	0.1	0.6	0.9	0.5	0.1	0.1	0.1	0.1	0.1
Sr ($\mu g/g$)	0.12	NA	NA	0.17	0.47	0.11	0.18	15.2	8.9	9.2	9.0	15.0	12.6	12.6	13.8	12.3
2σ	0.12	NA	NA	0.11	0.14	0.09	0.13	1.1	1.0	1.0	1.1	1.4	1.2	0.9	1.3	1.1

Formulas are calculated to 4 cations.

4.2.8. Olivine – Scoria – Minoan A and D

10 olivine crystals were found in six scoria samples. Average contents of major, minor and trace elements analyzed by EPMA and SIMS are shown in Table 4.7. All profiles analyzed can be found in the Electronic Appendix.

EPMA analyses   Olivine crystals analyzed are geochemically very similar. Ol-3 in sample SAN60 (Minoan A – top) is the only one that differs slightly with the lowest average FeO and highest average MgO contents.

SAN53-3: Ol-9 is the only crystal analyzed that shows reverse zoning (Fig. 4.38). Its average Mg ($1.45 - 1.53$ cpfu) and Fe^{2+} ($0.47 - 0.55$ cpfu) contents do hardly differ from olivines discovered in the other scoria samples. Fo content ranges from $72.4 - 76.6$ mol%.

SAN53-4: Ol-9, Ol-12 and Ol-20 are normally zoned crystals. Average Mg ranges from $1.41 - 1.53$ cpfu and Fe^{2+} from $0.47 - 0.58$ cpfu in these crystals. EPMA and SIMS profiles for Ol-9 are displayed in Fig. 4.39.

SAN53-7: Ol-14 is normally zoned with average Mg contents between $1.43 - 1.53$ cpfu and Fe^{2+} concentrations between $0.47 - 0.57$ cpfu.

SAN56-1: Ol-4 and Ol-5 are both normally zoned and average Mg ranges from $1.41 - 1.51$ cpfu and Fe^{2+} varies between $0.50 - 0.59$ cpfu.

SAN60: Ol-3 is normally zoned and has a ferrous core region. Average Fe^{2+} increases to 0.51 cpfu from 0.44 cpfu in the core.

The Mg and Fe^{2+} core profiles of Ol-6 are relatively flat; there is a sharp decrease of Mg at the rim while Fe^{2+} increases. Rim concentrations of Mg and Fe differ from all other samples. The Mg content at the rim is about 1.22 cpfu, and Fe^{2+} content at the rim is about 0.73 cpfu. Both crystals display the widest ranges in Fo content: $62.5 - 73.1$ mol% Fo for Ol-3 and $70.3 - 78.2$ mol% for Ol-6.

SAN61-2: Ol-1 is normally zoned and its average Mg and Fe^{2+} contents are very similar to other olivine crystals analyzed. Mg ranges from $1.41 - 1.51$ cpfu and Fe^{2+} from $0.50 - 5.59$ cpfu.

SIMS analyses   Li concentrations were measured in four olivine crystals and range from $1.71 - 3.07\,\mu g/g$ (Table 4.7).

P was analyzed in Ol-9 (SAN53-3) and Ol-14 (SAN53-7). While minimum concentrations of P ($20\,\mu g/g$) are similar in both crystals, core concentrations differ by more than $110\,\mu g/g$. Ol-9 has core P concentrations of $50\,\mu g/g$, while Ol-14 has core concentrations of $161\,\mu g/g$.

Table 4.7. Average Compositions of Olivine in Minoan Scoria Samples

Sample Crystal Zonation type	SAN53-3 Ol-9 reverse	SAN53-4 Ol-9 normal	SAN53-4 Ol-12 normal	SAN53-4 Ol-20 normal	SAN53-7 Ol-14 normal	SAN56-1 Ol-4 normal	SAN56-1 Ol-5 normal	SAN60 Ol-3 normal + ferrous core	SAN60 Ol-6 flat, decrease at rim	SAN61-2 Ol-1 normal
Analysis										
SiO_2	38.19	38.22	37.87	38.05	38.18	38.22	38.06	38.38	37.65	37.80
TiO_2	0.02	0.02	0.01	0.02	0.02	0.01	0.01	0.01	0.02	0.02
Al_2O_3	0.02	0.02	0.02	0.02	0.02	0.02	0.01	0.02	0.03	0.02
Cr_2O_3	0.01	0.01	0.01	0.02	0.01	0.01	0.01	0.01	0.01	0.01
FeO	23.52	23.35	25.57	24.70	23.33	24.15	25.08	22.70	26.11	24.56
NiO	0.04	0.02	0.02	0.03	0.02	0.03	0.02	*n.d.*	*n.d.*	*n.d.*
MnO	0.37	0.38	0.46	0.42	0.39	0.39	0.44	0.38	0.45	0.43
MgO	38.43	38.64	36.81	37.61	38.58	38.33	37.25	39.32	36.46	37.67
CaO	0.20	0.15	0.17	0.15	0.15	0.15	0.15	0.14	0.15	0.14
Total	100.79	100.81	100.93	101.02	100.70	101.31	101.02	100.97	100.89	100.64
Calc. to 4 ox.										
Si	0.992	0.992	0.992	0.992	0.992	0.990	0.994	0.991	0.990	0.989
Ti	0.000	0.000	0.000	0.000	0.000	0.000	0.000	0.000	0.000	0.000
Al	0.001	0.000	0.001	0.000	0.001	0.000	0.000	0.001	0.001	0.001
Cr	0.000	0.000	0.000	0.000	0.000	0.000	0.000	0.000	0.000	0.000
Fe^{2+}	0.511	0.507	0.560	0.538	0.507	0.534	0.548	0.490	0.574	0.537
Ni	0.001	0.001	0.000	0.001	0.000	0.000	0.000	0.000	0.000	0.000
Mn	0.008	0.008	0.010	0.009	0.009	0.009	0.010	0.008	0.010	0.009
Mg	1.488	1.495	1.438	1.462	1.494	1.471	1.449	1.513	1.429	1.469
Ca	0.006	0.004	0.005	0.004	0.004	0.004	0.004	0.004	0.004	0.004
Total	3.007	3.007	3.007	3.007	3.007	3.009	3.006	3.008	3.009	3.010
Fo (mole%)	74.4	74.7	72.0	73.1	74.7	73.4	72.6	75.5	71.3	73.2
Li (μg/g)	1.91	2.38	NA	NA	NA	2.29	NA	2.09	NA	NA
2σ	0.12	0.13	NA	NA	NA	0.10	NA	0.13	NA	NA
B (μg/g)	0.12	0.10	NA	NA	NA	0.07	NA	0.07	NA	NA
2σ	0.05	0.04	NA	NA	NA	0.03	NA	0.03	NA	NA
Sr ((μg/g)	0.18	0.10	NA	NA	NA	0.30	NA	0.11	NA	NA
2σ	0.13	0.11	NA	NA	NA	0.12	NA	0.10	NA	NA
Ba (μg/g)	0.12	0.05	NA	NA	NA	NA	NA	NA	NA	NA
2σ	0.34	0.21	NA		NA	NA	NA	NA	NA	NA
P (μg/g)	37.6	NA	NA	NA	69.3	NA	NA	NA	NA	NA
2σ	1.7	NA	NA	NA	2.1	NA	NA	NA	NA	NA

Average EPMA and SIMS analyses of olivine crystals in Minoan scoria samples. Formulas were calculated to four oxygens. NA = not analyzed.
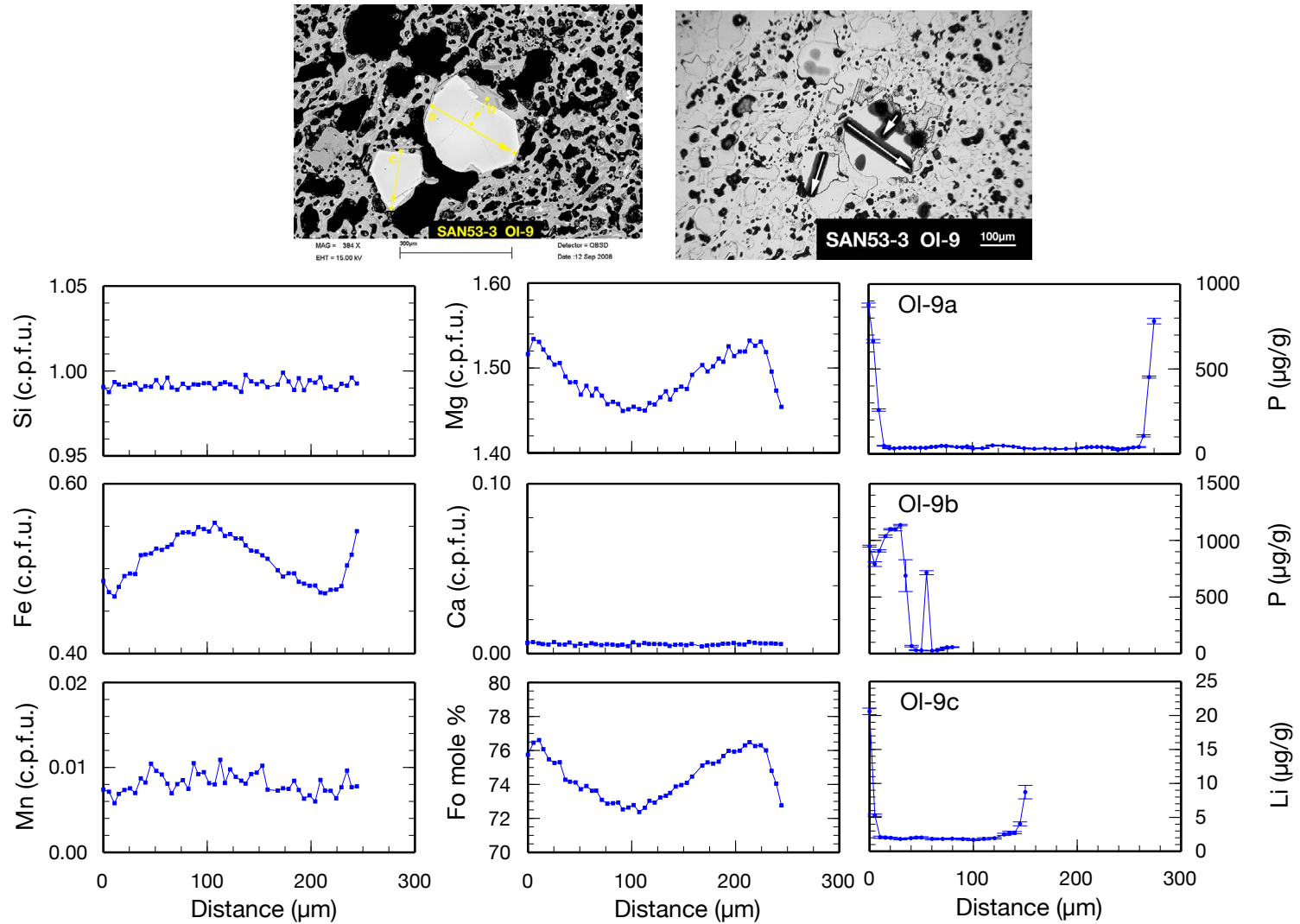
Fig. 4.38. SAN53-3 Ol-9: Formulas are calculated to 4 oxygens. Error bars are 2σ. This crystal is the only reverse zoned ol found in scoria samples. It has P core concentrations of $50\,\mu g/g$.
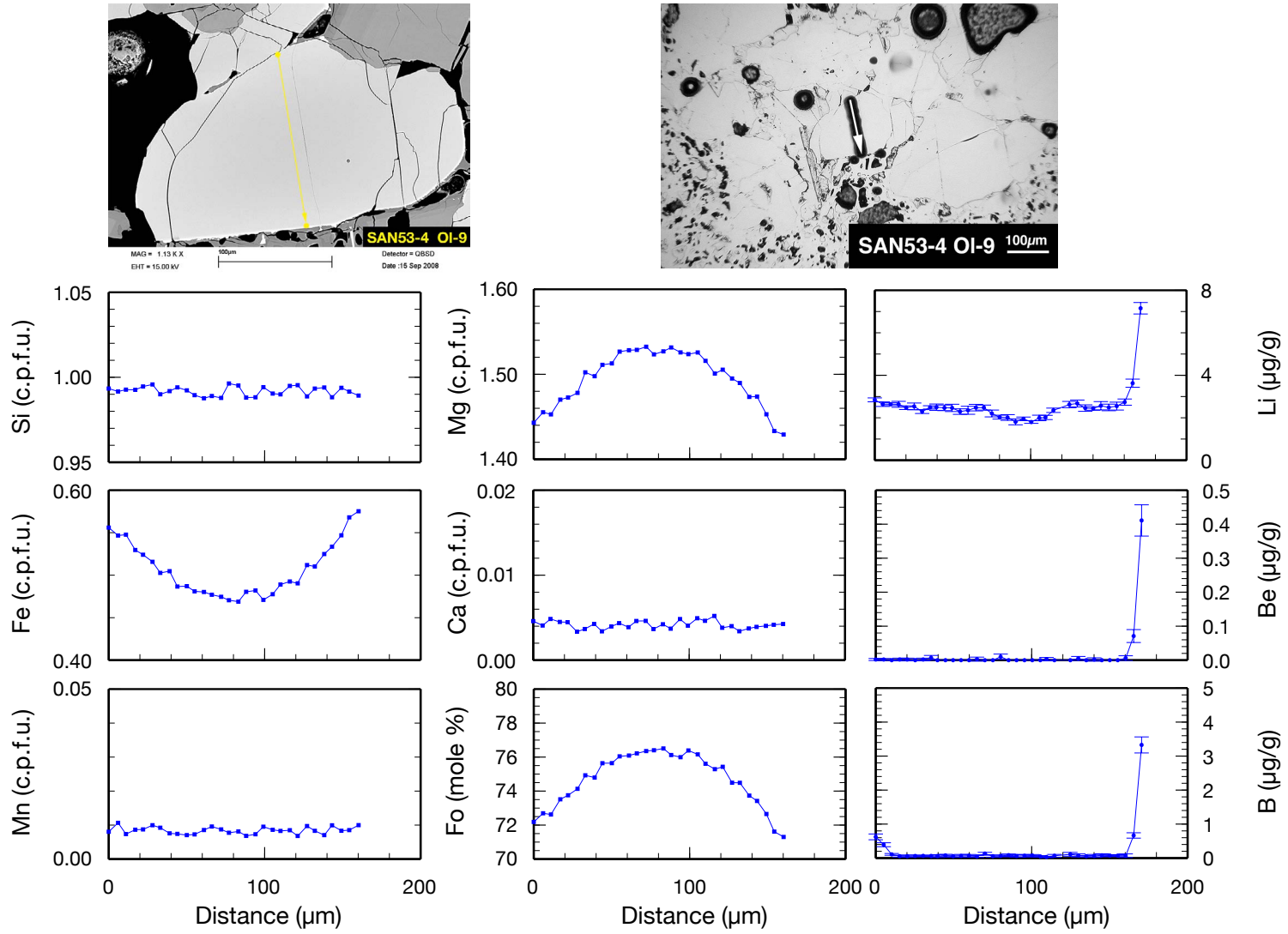
Fig. 4.39. SAN53-4 Ol-9: Formulas are calculated to 4 oxygens. This olivine is normal zoned and is geochemically similar to most of the olivines analyzed.

5. Lithium Diffusion in Minoan Plagioclase

5.1. Introduction

Kinetic modeling of timescales of processes in magmatic systems, i.e. magma generation, the evolution of magma chambers, magma differentiation, magma mingling, residence times of crystals, as well as the assimilation of crustal wall rocks, has become an important tool for geoscientists (e.g. Costa *et al.*, 2003; Costa & Dungan, 2005).

In the past, radioactive decay systems have been used to approach durations of such processes, but geochronological methods work on the basis of determining ages rather than lifetimes of geological events, and they also lack the ability to record short-lived processes (Costa *et al.* (2003), and references therein; Watson & Baxter (2007), Chakraborty (2008)).

Chemical zoning in minerals can be seen as an important archive for magma chamber processes, as growth and resorption zones record changes of intensive variables like temperature, pressure and chemical potential during crystal evolution (Costa & Morgan (2010), and references therein). Trace element diffusion profiles 'frozen' during a stage of disequilibrium in phenocrysts of volcanic rocks have the power to record magmatic processes of very short timescales. Furthermore, the diffusivities of different trace elements in the same mineral phase vary considerably during given magmatic conditions and can therefore record different processes acting on a crystal during its thermal evolution (e.g. Costa *et al.*, 2003; Chakraborty, 2008).

In the first part of this chapter a short introduction to diffusion on a macroscopic and atomic scale is given, while in the second part lithium profiles analyzed in plagioclase crystals of Minoan pumice and scoria samples will be presented. The emphasis will be on lithium and time scales of lithium diffusion in plagioclase, as this was the only element observed to show diffusion in many plagioclase crystals of almost all samples analyzed.

Diffusion Diffusion is the random, thermally driven motion of atoms, ions and molecules with the result of complete mixing of the diffusing particles leading to the homogenization of a heterogeneous substance. It takes place in gases, fluids, melts,

glasses and minerals. The simplest form of diffusion is caused by the Brownian motion of atoms and molecules in fluids and gases.

Adolf Fick developed his famous equations for chemical diffusion in 1855. Based on Fick's first law diffusion is driven by a concentration gradient. The following equations describe diffusion processes in one dimension.

Fick's 1st Law Fick's 1st Law postulates that a diffusive flux of particles (i. e. atoms, ions or molecules) goes from regions of high concentration to low concentration.

$$J = -D\frac{\partial C}{\partial x} \tag{5.1}$$

J is the diffusive flux of particles in mol/m^{2}s, D is the diffusion coefficient (m^2/s), C is the concentration, and x is is the length; $\partial C/\partial x$ is the concentration gradient of particles in the direction of x.

The temperature dependence of the diffusion coefficient D is described through an Arrhenius equation:

$$D = D_0 \exp\left(E_a/RT\right) \tag{5.2}$$

D_0 is the diffusion coefficient at infinite temperature, E_a is the activation energy (J/molK), R is the gas constant (J/molK) and T is the absolute temperature in K.

Fick's 2nd Law Fick's 2nd Law predicts how diffusion changes the concentration with time.

$$\frac{\partial C}{\partial t} = D\frac{\partial^2 C}{\partial x^2} \tag{5.3}$$

C is the concentration (mol/m^3), t is the time (s), D is the diffusion coefficient (m^2/s) and x is the length (m).

The Diffusion Length L is a measure of the distance the concentration of a substance propagates after a certain time. L increases with the square root of time (Wikipedia, 2011).

$$L = 2\sqrt{Dt} \tag{5.4}$$

The equation can be used to estimate the time it takes to gain an observed diffusion profile:

$$t = \frac{x^2}{4D} \tag{5.5}$$

L is the diffusion length (m), D is the diffusion coefficient (m^2/s) and t is the time of diffusion (s).

In this chapter Equation 5.5 was applied to estimate diffusion times of lithium in plagioclase (Table 5.1). For further reading on the topic of diffusion the works of Crank (1975), Mehrer (2007) and Zhang (2010) are recommended.

Diffusion in Crystals Before the process of diffusion in minerals can be addressed, it should be noted that minerals are solid phases in which atoms, ions and molecules are arranged in a regular, periodic pattern. That pattern is repeating itself in three spacial dimensions and builds the crystal lattice. Quasiperiodic crystals however are an exception as their structure is ordered but not periodic (Shechtman *et al.*, 1984). The diffusion of atoms in such a crystal lattice is a relative and random movement that occurs spontaneously.

As crystals are not perfect, different types of crystallographic defects can be found in their lattice structure. These defects play a major role for diffusion processes in minerals. Vacancies in crystals for example are very prominent defects. A vacancy is defined by an atom missing in the crystal structure and therefore allows an adjacent atom to jump onto that empty site.

There are many different defects that occur in crystals, these can be grouped into point defects with no dimension, line defects (one dimensional), planar defects (two dimensional) and bulk defects (three dimensional) (Foell, 2011).

Point defects for example can be—as mentioned above—vacancies where atoms are missing in the mineral's structure or impurities caused by atoms that originally do not belong into the crystal lattice as well as interstitial defects where atoms are occupying sites in a structure where usually no atoms would occur. For further reading the chapter on crystallographic defects at Wikipedia is recommended as well as the AMAT Matwiss-I-Script by Foell (2011).

Fig. 5.1 depicts possible mechanisms by which atoms diffuse in crystals based on Watson & Baxter (2007). The most common mechanism is the diffusion via vacancies where an atom jumps to an adjacent vacancy and therefore moves that vacancy to its former site. Another important mechanism is the diffusion of impurity atoms through interstitial sites. The direct exchange where two adjacent atoms switch sites is another possible mechanism for the movement of atoms within the crystal lattice but it is considered to be energetically disadvantageous and therefore less likely to happen (Costa & Morgan, 2010).

Diffusion mechanisms in crystal phases
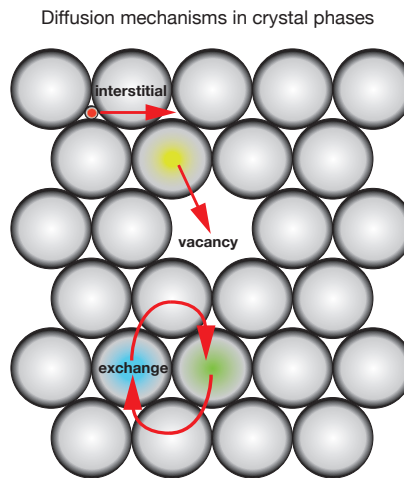
Fig. 5.1. Examples for three diffusion mechanisms that can occur in a crystal lattice based on Watson & Baxter (2007).

For further mechanisms like the indirect impurity mechanism, kick-out mechanism and others which are not depicted in Fig. 5.1 see the script by Foell (2011).

5.2. Lithium Diffusion in Minoan Plagioclase

For the investigation of diffusion processes in phenocrysts of the Minoan pumice and scoria samples, 73 plagioclase (pl) phenocrysts were analyzed with a Cameca ims 3f Secondary Ion Mass Spectrometer at the Institute of Earth Sciences, University of Heidelberg. This spectrometer is equipped with three field apertures. During the first year of the study field aperture #2 was used for analyses (lateral resolution $\sim 12\,\mu m$). Diffusion was hardly observed in samples and in some cases only indicated by a sudden rise of lithium at the crystal rim.

After the SIMS was equipped with a smaller field aperture #3, a higher lateral resolution ($\sim 6\,\mu m$) was gained and it was possible to detect very short diffusion lengths of lithium into plagioclase (Table 5.1), while other trace elements displayed no diffusion (except for Mg in sample SAN53-2 and Pl-6 in SAN53-7). In some samples it was even possible to detect a loss of lithium which overprinted the diffusion profile into the crystal.

5.2.1. Diffusivities of Lithium in Melt and Plagioclase

Lithium is known to diffuse very fast in plagioclase and melt, D is $\sim 2.7 \times 10^{-11} m^2/s$ at $850\,°C$ and $0.1\,MPa$ in anorthite (Giletti & Shanahan, 1997).

The diffusivities of lithium in plagioclase and melt with changing temperature are plotted in Fig. 5.2. It can be seen that at magmatic temperatures the diffusivity of lithium in plagioclase is almost the same as the diffusivity of lithium in melt, while at lower temperatures the diffusivity of lithium in plagioclase is much lower compared to melt.
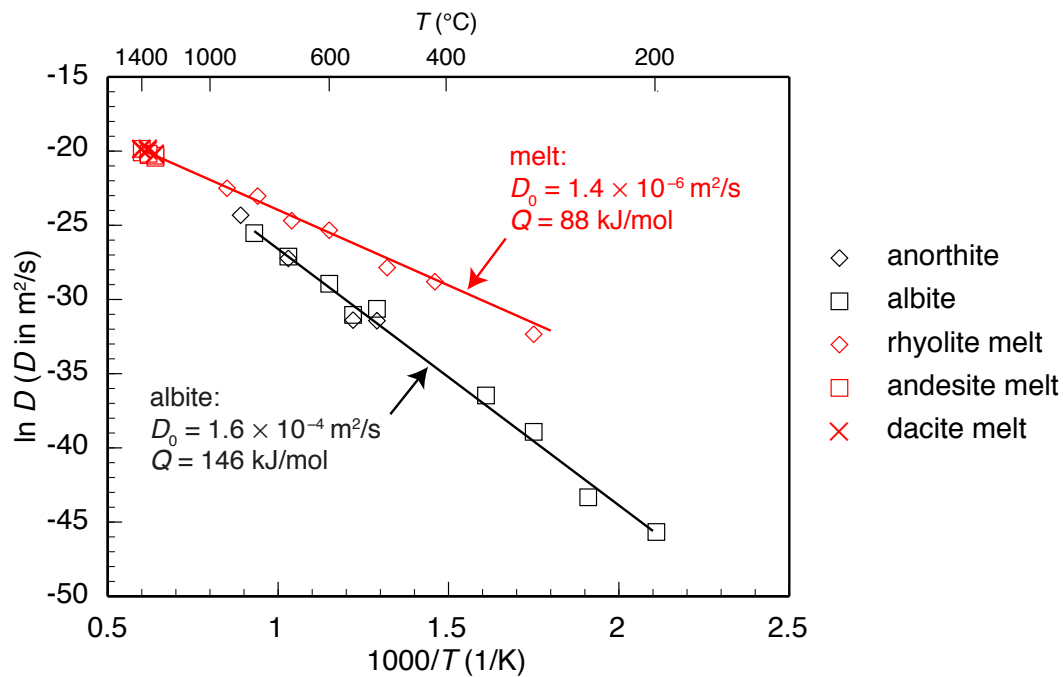
Fig. 5.2. Lithium diffusivities in plagioclase and melt. At magmatic temperatures the diffusivities of lithium in melt and plagioclase are both large. With decreasing temperature the diffusivity of lithium in melt is still large, while it is much lower in plagioclase. Experimental data and the fit for melt are taken from Jambon & Semet (1978) and Cunningham *et al.* (1983). Experimental data for plagioclase and the fit for albite are taken from Giletti & Shanahan (1997).

In order to prove that the observed lithium profiles were caused by diffusion, δ^7Li profiles were analyzed (Fig. 5.12 to Fig. 5.14).

δ^7**Li as an Indicator for Diffusion** A powerful tool to show that lithium concentration profiles are overprinted by (ongoing, 'frozen') diffusion is the analysis of

lithium isotopes. The isotopic composition of lithium is expressed in the form of δ^7Li values (e.g., Hoefs, 2009) referenced to the lithium carbonate standard LSVEC (Flesch *et al.*, 1973):

$$\delta^7\text{Li} = \left(\frac{(\frac{^7Li}{^6Li})_{\text{sample}}}{(\frac{^7Li}{^6Li})_{\text{LSVEC}}} - 1 \right) \cdot 1000 \tag{5.6}$$

The diffusion constants of different isotopes i and j of the same element depend on their masses m_i and m_j (e.g., Richter *et al.*, 2003; Parkinson *et al.*, 2007):

$$\frac{D_i}{D_j} = \left(\frac{m_j}{m_i} \right)^{\beta} \tag{5.7}$$

For the two stable Li isotopes (^{6}Li, $m = 6.015$ u; ^{7}Li, $m = 7.016$ u) β was determined experimentally by Richter *et al.* (2003): $\beta = 0.215$. $D_{^6\text{Li}}$ is therefore 3.4 % higher than $D_{^7\text{Li}}$; ^{6}Li diffuses notably faster than ^{7}Li, which causes fractionation of Li isotopes. A diffusion profile where Li diffuses from phase A with high Li concentration into phase B with lower Li concentration will be characterized by a δ^7Li minimum in phase B, because the ^{6}Li profile extends further into phase B than the ^{7}Li profile.

In order to interpret δ^7Li profiles, it is crucial to understand which parameters influence the length of an observed lithium diffusion profile, and which parameters influence the depth and the width of an observed minimum in the δ^7Li profile. Therefore δ^7Li profiles were modeled with *diff2* (see Appendix A), a program based on numerical diffusion modeling created by Thomas Ludwig (Institute of Earth Sciences, University of Heidelberg).

Parameters chosen to model the profiles shown in Fig. 5.3 were D_0 and E_a for albite taken from Giletti & Shanahan (1997) (based on plagioclase of Minoan pumice being structurally closer to albite, which is discussed in Chapter 7 and shown in Fig. 7.5), and the experimentally determined β value from Richter *et al.* (2003). Diffusion was modeled from an unlimited reservoir with constant concentration c into plagioclase with an initial concentration $c_0 = 1$. The partition coefficient between the reservoir and the plagioclase was assumed to be 1. The temperature was set to 865 °C as calculated for SAN52 (Minoan A) using the plagioclase-liquid thermometer of Putirka (2008) (see Appendix A). Fig. 5.3 shows the effects of varying the concentration ratio c/c_0 (first row), β (second row) and time t (third row). A diffusion time of 3.4 seconds was chosen to obtain a diffusion profile similar to the profile observed in Pl-1 of SAN52A at 865 °C (Chapter 5, Fig. 5.6).

In the first row of Fig. 5.3 the diffusion lengths for the three profiles with initial concentration ratios c/c_0 of 2, 5 and 10 are the same despite the initial differences in

concentration. The δ^7Li profile shows a minimum near the end of the concentration profile in the plagioclase. It can be seen that different initial concentrations of the unlimited reservoir lead to different depths of the δ^7Li minimum, while the width and location of the minimum is hardly influenced.

In the second row of Fig. 5.3 the initial concentration ratio was $c/c_0 = 5$ for all three profiles, while β was different for all three profiles and set to 0.1, 0.215 and 0.4. After 3.4 seconds all three diffusion profiles are virtually identical in length, only the depth of the δ^7Li minimum varies. The variation of β does not affect the width and location of the δ^7Li minimum.

In the third row of Fig. 5.3 the initial concentration ratio again was 5 and $\beta = 0.215$. The time of diffusion was different for all three profiles and set to 1.1, 3.4 and 11.0 s. Due to the different diffusion times the diffusion length L of the concentration profile varies and so does the location of the δ^7Li minimum. The depth of the δ^7Li minimum is *not* influenced by different diffusion times. For a constant β the depth of the δ^7Li minimum ($\Delta\delta^7$Li) depends solely on the concentration ratio c/c_0.

$\Delta\delta^7$Li in an observed δ^7Li profile can therefore be used to estimate c/c_0. Fig. 5.4 shows the variation of $\Delta\delta^7$Li with c/c_0. Data for Fig. 5.4 was obtained by modeling with *diff2* (see Appendix A). The partition coefficient between the reservoir and plagioclase was again assumed to be 1.
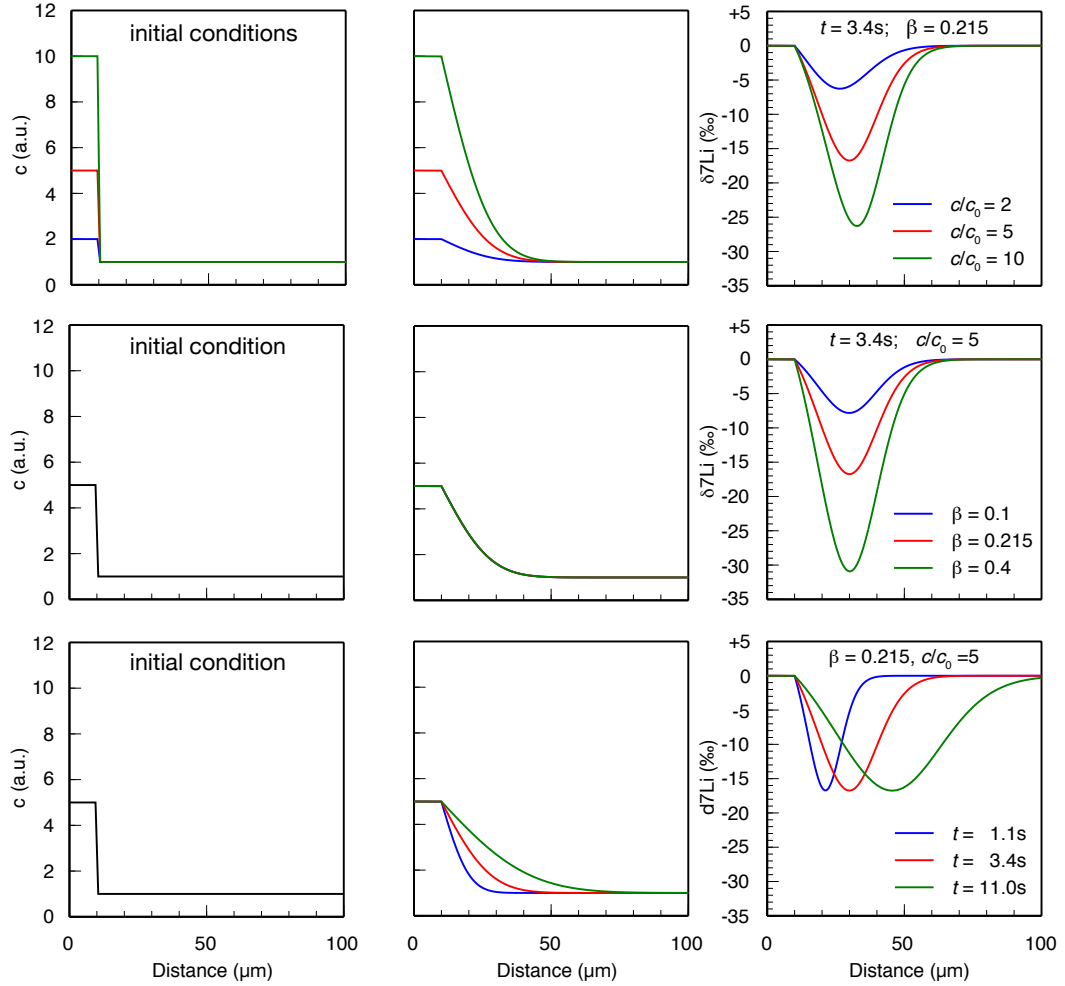
Fig. 5.3. Results of modeling Li diffusion from an unlimited reservoir with constant concentration c into plagioclase with an initial concentration $c_0 = 1$. The following parameters were varied: c/c_0 (first row), β (second row) and the diffusion time t (third row). The first column shows the initial concentration profile. In the second column the concentration profile after the time t is shown while the third column shows the corresponding δ^7Li profile. Please see text for further details.
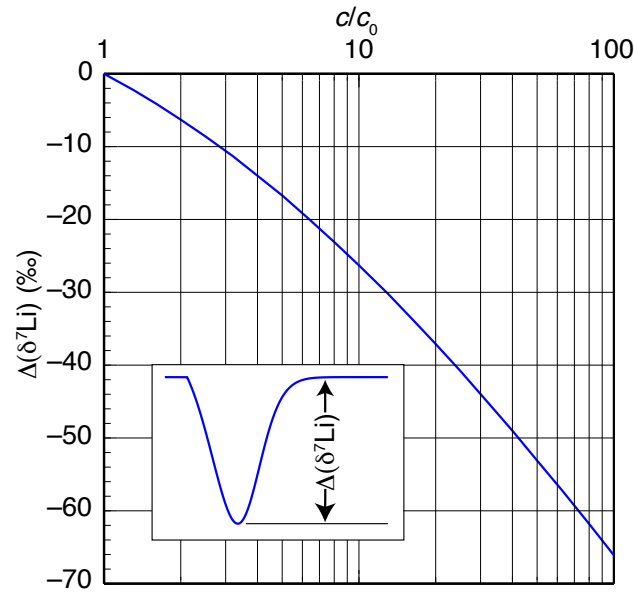
Fig. 5.4. Variation of the depth of the δ^7Li minimum ($\Delta\delta^7$Li) with the concentration ratio c/c_0 for $\beta = 0.215$.

Minoan Pumice and Crystal-rich Pumice   Table 5.1 lists the diffusion lengths L of lithium in plagioclase from the Minoan pumice (Units A to D), the Crystal-rich pumice (Unit D) and Minoan scoria clasts (Units A and B). The diffusion times t for each sample were calculated using Equations 5.2 and 5.5, D_0 and E_a for albite (Giletti & Shanahan, 1997) and temperatures from the plagioclase-liquid thermometer (Putirka, 2008, Appendix A).

The diffusion length L for lithium was determined as follows:

1. Mixed analyses with matrix or inclusions were excluded by taking beryllium, boron, magnesium, strontium and barium concentrations in plagioclase into consideration. Plagioclase is clearly characterized by boron concentrations below $\sim 1\,\mu g/g$ with ideal concentrations inside the plagioclase below $\sim 0.3 - 0.4\,\mu g/g$.

2. The correlation of anorthite with lithium under equilibrium conditions is used to differentiate between analyses not affected by diffusion and those that are (see Fig. 5.5 and Chapter 7). Diffusion of lithium into the crystal will usually be characterized by analyses that plot above the correlation trend (Fig. 5.5).

A loss of lithium would be defined by analyses that plot below the correlation trend.

The estimates for diffusion lengths L gained with this method are reasonable, but the effect of limited lateral resolution, which changes the shape of the profile due to the size of the analysis spot, must still be taken into consideration—mainly for very short profiles ($< 20 \, \mu m$). One should notice that the diffusion length might be stretched by cutting effects, where the direction of diffusion is not parallel to the surface of the polished sample. Especially the long profile of Pl-4 in SAN54A may have its origin in an oblique cut of the crystal.

During the beginning stages of this thesis, profiles were measured with a lateral resolution of $\sim 12 \, \mu m$, and steps between analyses were often as wide as $\sim 30 \, \mu m$ which made it impossible to detect very short diffusion profiles. Especially samples SAN52A, SAN59A, SAN50A, SAN50B, and parts of SAN53-2 were affected by this problem. Therefore, a number of short profiles (up to $\sim 200 \, \mu m$) were analyzed with a higher lateral resolution of $\sim 6 \, \mu m$ in $\sim 5 \, \mu m$ steps (Fig. 5.6 to Fig. 5.7 and Fig. 5.9 to Fig. 5.11). A criterion for these analyses was the start of the profile in glass selvages and the presence of a melt inclusion inside the crystal, which was also analyzed for diffusion. All short profiles analyzed can be be found in Appendix B.
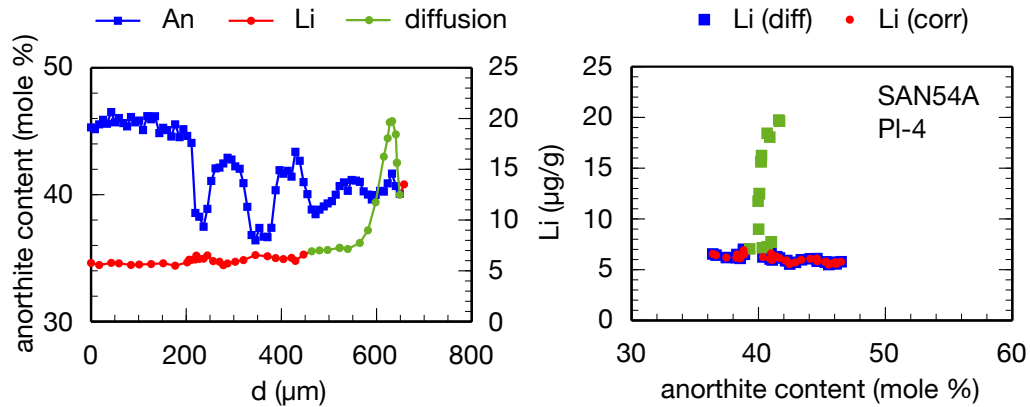
Fig. 5.5. Left: Anorthite and lithium concentration profiles in Pl-4 (SAN54A). The entire diffusion distance is marked in green. **Right:** Correlation diagram for anorthite *vs* lithium. Analyses characterized by diffusion into the crystal plot above the correlation trend (green). Red analyses represent those that were not affected by diffusion. This simple plot can be used to identify the diffusion length L of lithium in plagioclase, in this case $\sim 80 \, \mu m$. In the diagram the entire distance with increased lithium concentration due to diffusion ($\sim 2L$) is highlighted in green.

Crystals of Minoan Units A to D have relatively short diffusion lengths L, many

between $\sim 0-30\,\mu$m with a few exceptions (Table 5.1). Pl-5 (SAN52) displays a lithium diffusion length of $\sim 40\,\mu$m, and Pl-4 in SAN54A shows a diffusion length of up to $\sim 80\,\mu$m into the crystal (Fig. 5.5). Pl-9 (SAN59A) has a lithium diffusion length of $\sim 45\,\mu$m. Crystals of samples from Minoan Unit D seem to be hardly affected by diffusion compared to the other samples. It should be noted that due to a bigger spot size and bigger steps between spots diffusion lengths were not accurately detected in SAN50A and SAN50B. A short profile of higher resolution analyzed in Pl-9 (SAN50A) showed no lithium diffusion (Fig. 5.7). Other crystals analyzed with a lateral resolution of $\sim 12\,\mu$m sometimes had elevated lithium rim concentrations which indicates that diffusion of lithium took also place in the SAN50 samples.

In general, diffusion lengths are short, never exceeding $\sim 100\,\mu$m. The maximum diffusion time is $\sim 50\,$s for Pl-4 (SAN54A). The BSE image however is an indicator that the long distance might have been caused by an oblique cut of the crystal.

Fig. 5.6 and Fig. 5.7 depict diffusion profiles of lithium into plagioclase in the main Minoan pumice in comparison with profiles measured through melt inclusions found inside the same crystal. Shown is the entire distance with increased lithium concentration due to diffusion ($\sim 2L$). Those parts of the profile affected by diffusion are marked in green. Boron (red profiles) is used as an indicator for a better clarification of the transition between matrix glass and plagioclase. Based on most analyses the plagioclase starts when the boron concentration drops below $\sim 0.3-0.4\,\mu$g/g.

Crystals presented in Fig. 5.6 all display diffusion into the crystal. Inclusions inside the crystals show no indication of lithium diffusion into the surrounding plagioclase.

Table 5.1. Li Diffusion Lengths in Minoan Plagioclase

White Pumice Unit	Sample	n	Li Diffusion Length L (μm)	t (s)	T (°C)
Minoan A	SAN52	3	≤ 20 (40)	≤ 3.2 (12.7)	865
	SAN54	4	$10 - 20$ (80)	$0.8 - 3.1$ (48.8)	868
	SAN55	2	$10 - 15$	$0.7 - 1.5$	880
	SAN57	6	$3 - 15$ (25)	$0.1 - 3.2$ (8.8)	824
Minoan B	SAN58	3	$5 - 20$	$0.3 - 4.2$	844
	SAN61-2	6	$5 - 20$	ND	ND
	SAN61-1A	2	$8 - 20$	$0.4 - 2.3$	888
Minoan C	SAN59	7	$3 - 30$ (45)	≤ 11.2 (25.1)	833
Minoan D	SAN50	12	$0 - 3$ (20)	≤ 0.1 (3.3)	862

Crystal-rich Pumice Unit	Sample	n	Li Diffusion Length L (μm)	t (s)	T (°C)
Minoan D	SAN51-1A	2	$35 - 40$	$4.8 - 6.3$	919
	SAN51-1B	3	$35 - 45$	$4.8 - 8.0$	919

Scoria Unit	Sample	n	Li Diffusion Length L (μm)	t (s)	T (°C)
Minoan A	SAN52Agg	2	$0 - 3$	ND	ND
	SAN53-1	4	$5 - 10$	ND	ND
	SAN53-2	8	$3 - 8$	≤ 0.3	896
	SAN53-3	4	$20 - 30$	$0.5 - 1.1$	1022
	SAN53-4	4	$0 - 5$	≤ 0.1	969
	SAN53-5	3	$3 - 15$	ND	ND
	SAN53-6	4	$0 - 15$	ND	ND
	SAN53-7	5	$5 - 8$	≤ 0.6	855
	SAN56-1	4	$3 - 10$	≤ 0.4	923
	SAN60	7	$8 - 15$	ND	ND
Minoan B	SAN61-2 (Pl-21)	1	$3 - 5$	ND	ND

Li diffusion lengths L in pl from the rim into the crystal. Note that a sample can be divided into further subsamples (SAN 50 consists of SAN50A and SAN50C; the crystals in these samples were handpicked from the same clast). n = number of crystals. Diffusion lengths and times in brackets are single crystals that deviate from other crystals of a sample). Diffusion times t of Li were calculated as $t = \frac{x^2}{4D}$. $D = D_0 \exp(-E_a/RT)$. D_0 (m^2/s) = 0.000158 (for albite after Giletti & Shanahan (1997)). E_a (kJ/mol) = 146 $\pm$ 14. Temperatures were calculated after Putirka (2008) (see Appendix A, Table A.5). ND = not determined.
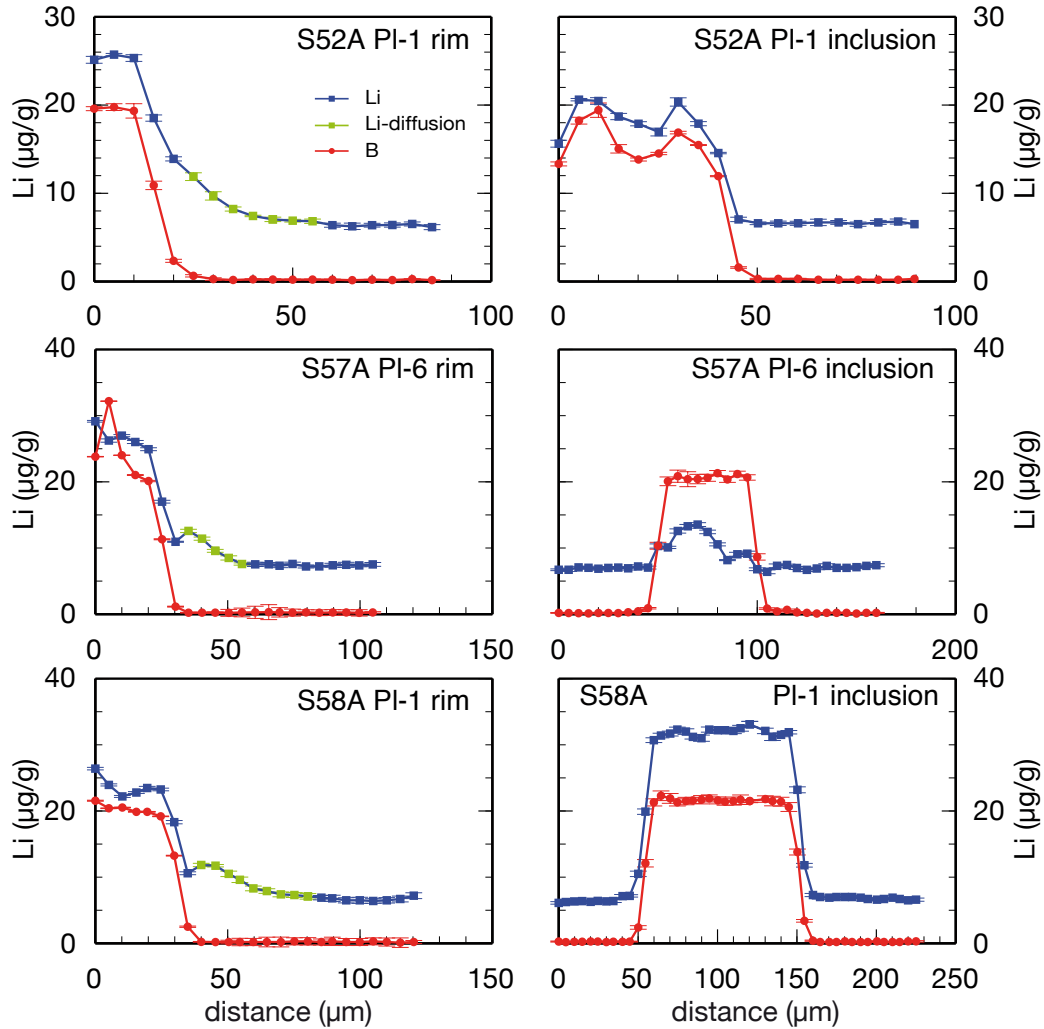
Fig. 5.6. Li and B profiles of pl rims start in glass selvages of pl and were measured perpendicular to the rim into the crystal. B is used as an indicator for the glass–pl transition. The profiles are from pl crystals of Minoan Unit A (SAN52 and SAN57) and Minoan Unit B (SAN58). All crystals show very short Li diffusion distances. There is no diffusion from inclusions into the surrounding pl. Nevertheless, some loss of Li seems to have occurred through cracks in inclusions (S52A Pl-1 and S58A Pl-1). For all crystals the entire distance affected by diffusion is highlighted in green.
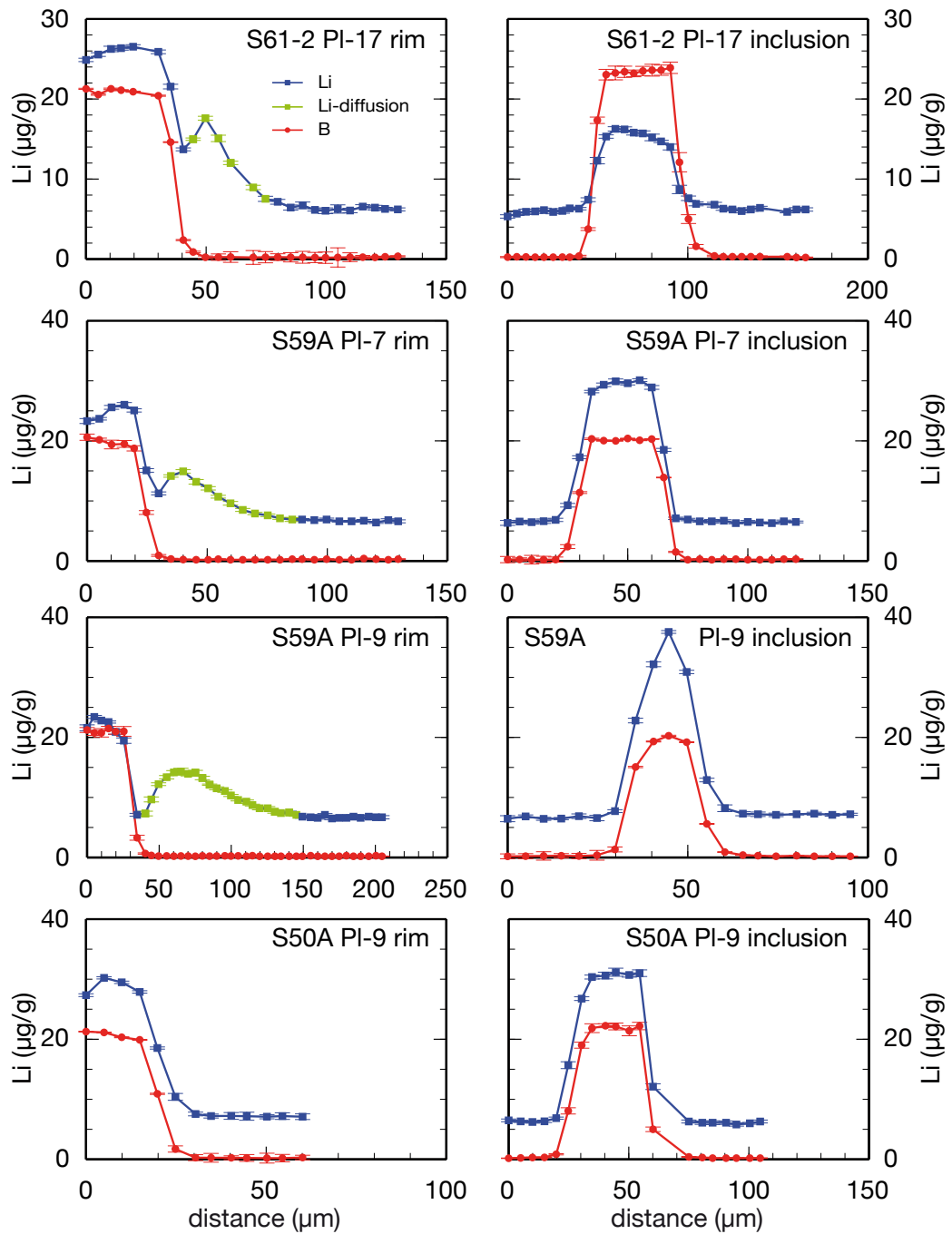
Fig. 5.7. Li and B profiles of pl crystals from Minoan Unit B (SAN61-2), Minoan C (SAN59) and Minoan D (SAN50). Pl-9 (SAN50A) shows no Li diffusion from rim into plagioclase while all the other crystals show Li diffusion into the crystal and a drop of Li concentrations from glass selvages towards the rim. Melt inclusions are not affected by Li diffusion. For all crystals the entire distance affected by diffusion is highlighted in green.

There seems to be a loss of lithium in inclusions that are disrupted by a crack (Pl-1 in SAN52A and Pl-6 in SAN57A, Fig. 5.6). Plagioclase of samples shown in Fig. 5.7 show diffusion into the crystal and a loss of lithium on a short distance towards the rim. This is very well displayed in the lithium profile of Pl-9 (SAN59A). Again, there is no diffusion of lithium from melt inclusions into plagioclase. Pl-17 in SAN61-2 seems to have lost some lithium through a crack. Pl-9 of sample SAN50A shows no diffusion of lithium into the crystal.

Minoan Crystal-rich Pumice Plagioclase of the Crystal-rich pumice (Minoan Unit D) shows lithium diffusion lengths between $\sim 35 - 45\,\mu$m corresponding to diffusion times between 4.8 to 8.0 seconds at 919°C. Diffusion lengths and diffusion times are slightly longer compared to the main amount of plagioclase studied in the Minoan pumice (Table 5.1).

In Fig. 5.8 crystals of sample SAN51-1A are displayed on the left side. The lithium profile of Pl-3 is hard to interpret. In this case the EPMA profile did not match the SIMS profile. The end of the profile hit several cracks and the profile is overprinted by diffusion of lithium into the crystal from these cracks. Pl-17 shows diffusion of lithium into the crystal as well as a loss of lithium that overprints the diffusion profile.

Plagioclase crystals of SAN51-1B show the same phenomena as Pl-17 in SAN51-1A. Similar to melt inclusions of the main Minoan pumice crystals, the one in Pl-3 of SAN51-1B shows no diffusion of lithium into the plagioclase. However, there has been a slight loss of lithium due to a crack.
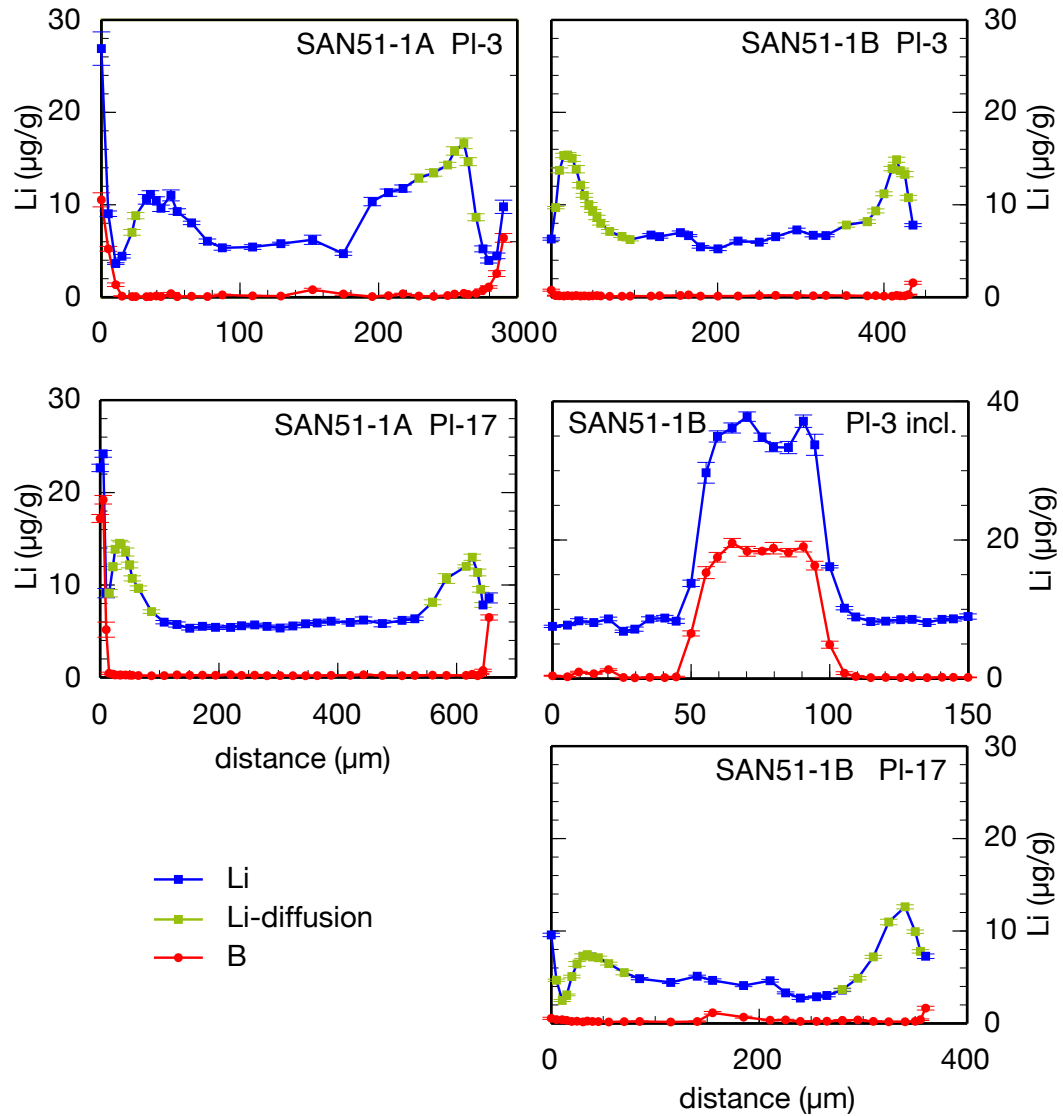
Fig. 5.8. Li and B profiles in plagioclase of the Crystal-rich pumice samples SAN51-1A and SAN51-1B (Minoan Unit D). The profile of Pl-3 (SAN51-1A) does not entirely match the EPMA profile. The end of the profile runs through cracks, so that diffusion of Li from the crack into the crystal is observed. The profiles of Pl-17 (SAN51-1A) and Pl-3 (SAN51-1B) show Li diffusion into the crystal as well as a loss of Li towards the rim. The melt inclusion in Pl-3 (SAN51-1B) was not influenced by Li diffusion into the crystal but might have experienced a slight loss due to a crack running through the inclusion. For all crystals the entire distance affected by diffusion is highlighted in green.

Minoan Scoria Lithium diffusion lengths L are short in scoria samples found in the Minoan pumice (Unit A), $\sim 0 - 30 \, \mu m$. Some crystals show no diffusion and sample SAN53-3 shows the longest diffusion profiles of all scoria samples, $20 - 30 \, \mu m$. Diffusion times and lengths of the main Minoan pumice were not exceeded.

Hardly any diffusion can be found in plagioclase from the crystal clot SAN52Agg and SAN53-4. Especially in SAN52Agg there were not enough crystals analyzed to be representative. The longest diffusion profile of $\sim 30 \, \mu m$ is found in Pl-3 in sample SAN53-3 (see also Chapter 4). For distances and diffusion times of all samples see Table 5.1.

Fig. 5.9 depicts plagioclase crystals of five scoria samples. Plagioclase of SAN53-2 and SAN53-5 show a slight loss of lithium towards the rim. Pl-11 of SAN53-6 shows no indication of lithium diffusion. Pl-16 of SAN53-1—a sample with extremely low lithium concentrations in plagioclase—shows an increase of lithium towards the rim.

Plagioclase crystals of sample SAN53-3 (Fig. 5.10) show lithium diffusion into the crystal and only a slight overprint of lithium loss towards the rim. The melt inclusion found in Pl-3 was not affected by diffusion of lithium into the surrounding plagioclase or a loss of lithium due to a crack. Plagioclase crystals of sample SAN53-4 show hardly any diffusion.

Plagioclase crystals in samples SAN60 and SAN56-1 depicted in Fig. 5.11 only show a weak overprint by lithium diffusion. Melt inclusions found in crystals were extremely small and show no signs of diffusion from the inclusion into the crystal or a loss of lithium through cracks.
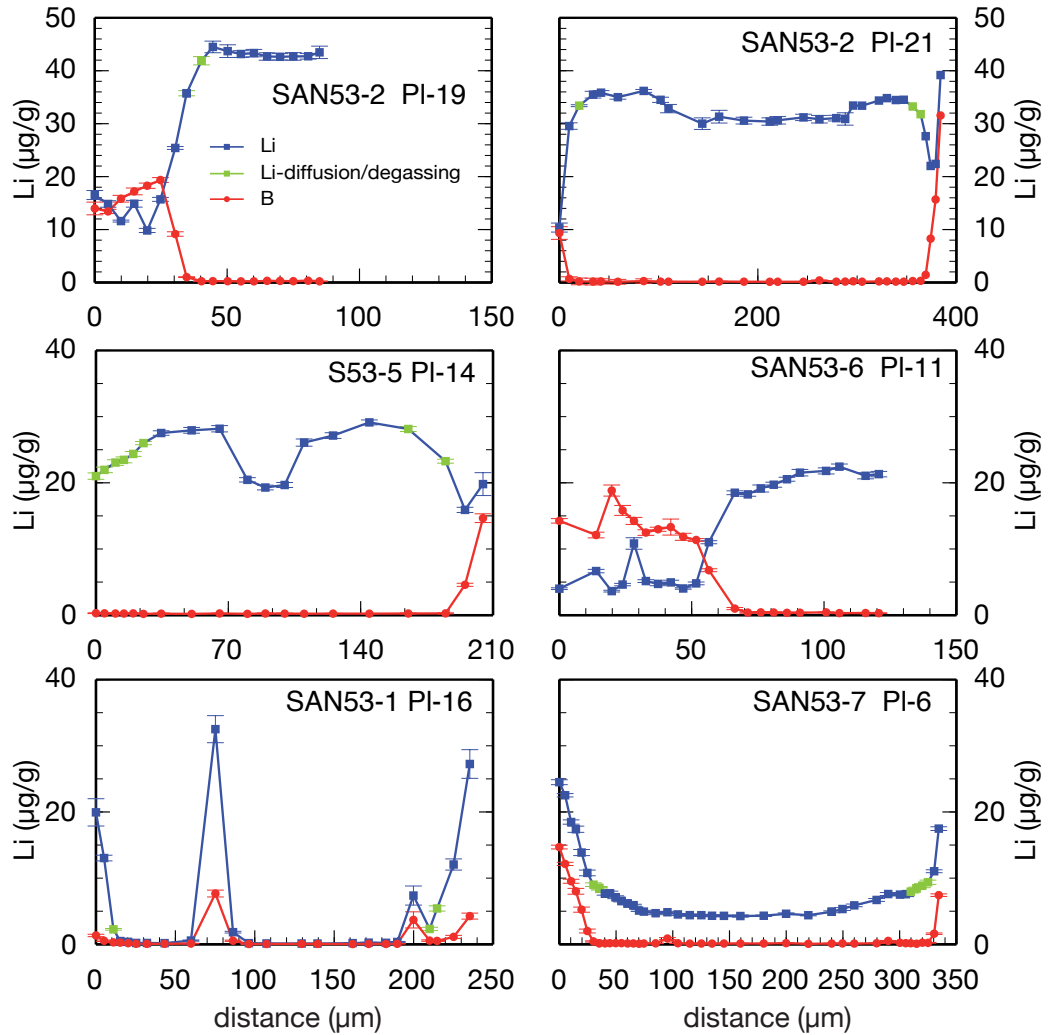
Fig. 5.9. Li and B profiles of pl crystals in different scoria clasts. Samples SAN53-2, SAN53-5 and SAN53-6 contain pl grains with the highest Li concentrations observed in scoria clasts. They experienced a slight loss of Li towards the rim. The left side of Pl-14 (SAN53-5) might have been influenced by a crack. Pl-11 (SAN53-6) doesn't show any Li diffusion. Pl-16 (SAN53-1) has extremely low Li contents. There is less pronounced Li diffusion into the crystal at the rims. High-Li and B peaks within the profile are caused by cracks. Pl-6 (SAN53-7) shows a little diffusion into the crystal. For all crystals the entire distance affected by diffusion is highlighted in green.
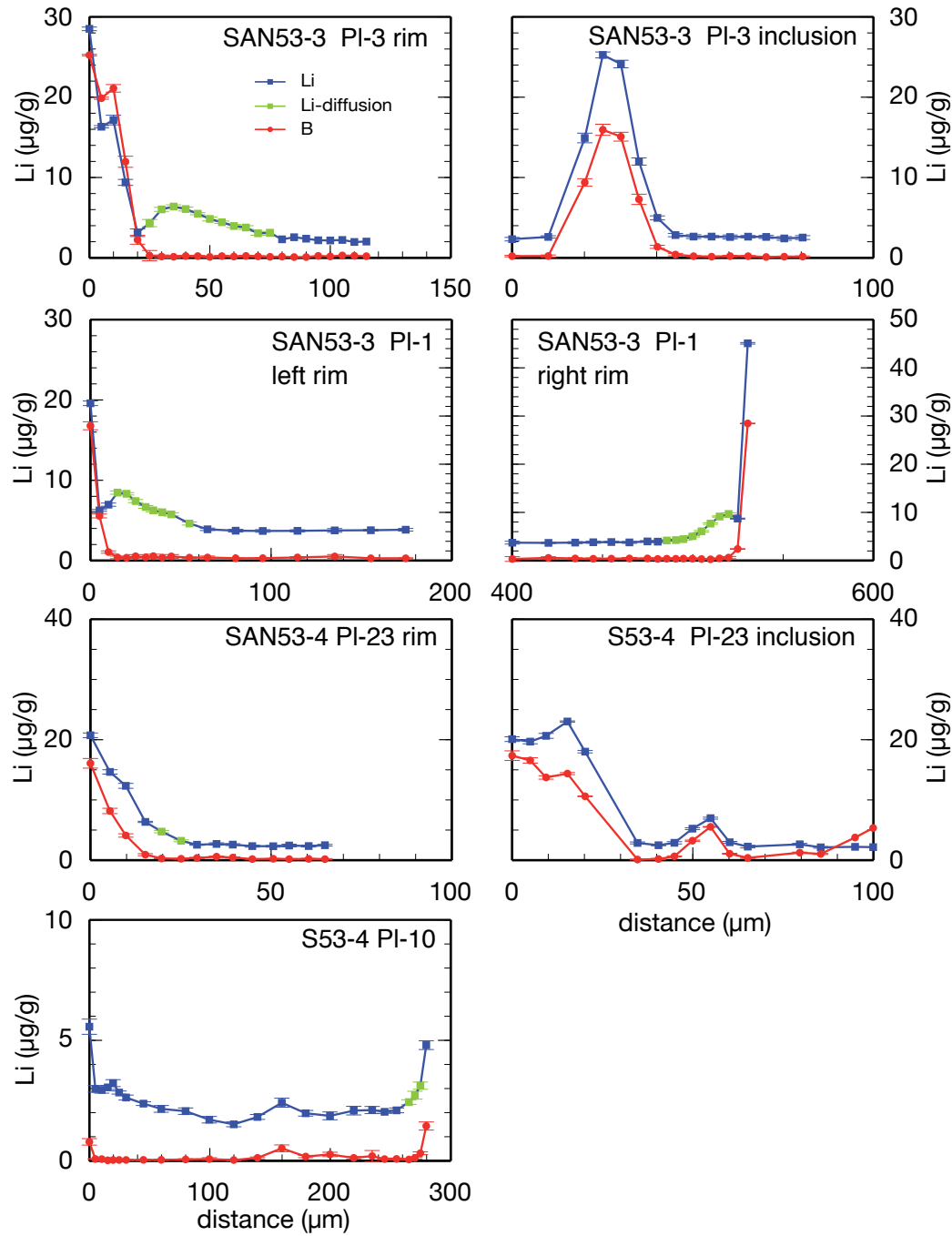
Fig. 5.10. Li and B profiles of pl crystals in different scoria clasts. Pl crystals of sample SAN53-3 show well developed Li diffusion into the crystal. Pl-3 shows a slight loss of Li at the rim. The melt inclusion of Pl-3 is not influenced by Li diffusion. Pl-23 shows little to no Li diffusion. The melt inclusion in Pl-23 has a very low Li concentration and is not influenced by diffusion. For all crystals the entire distance affected by diffusion is highlighted in green.
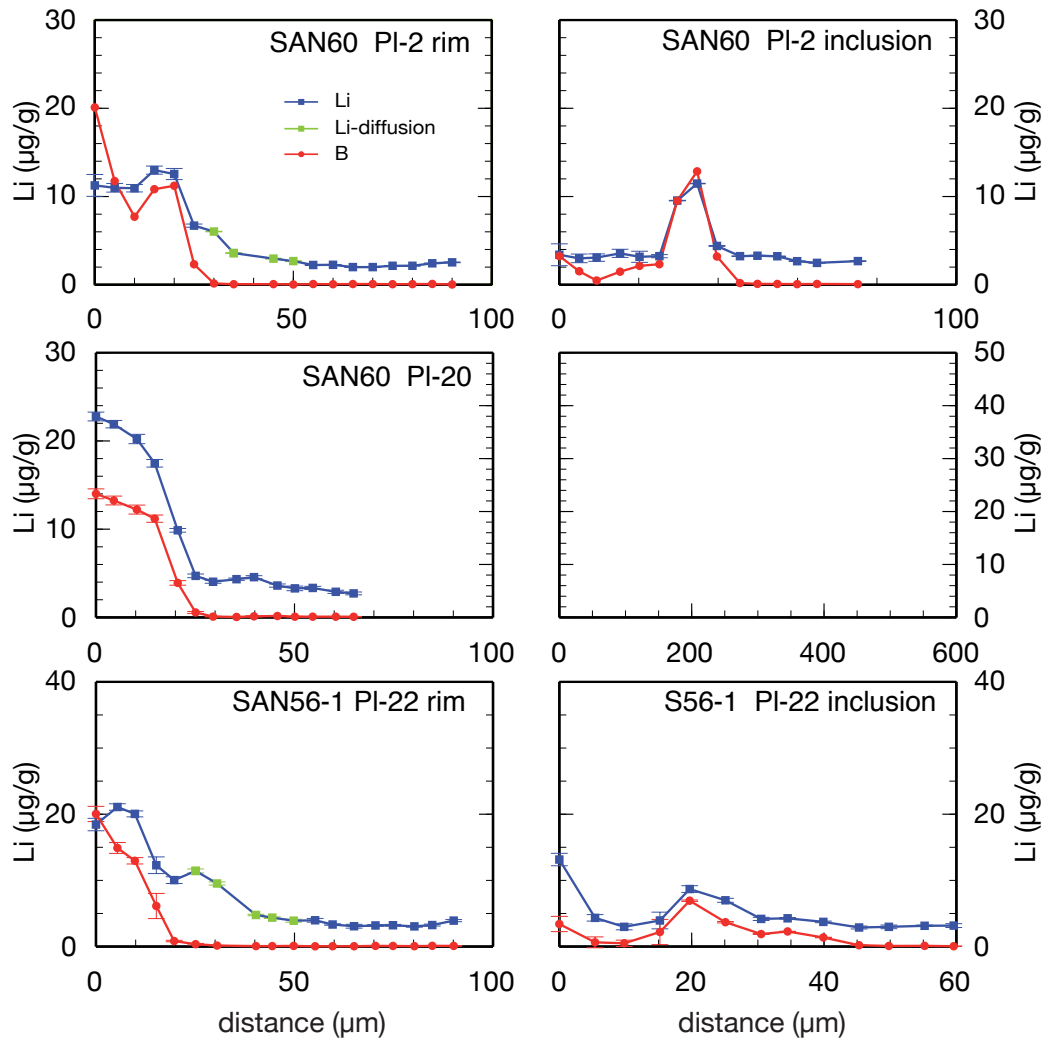
Fig. 5.11. Li and B profiles of pl crystals in different scoria clasts. Pl-2 (SAN60) shows weakly pronounced Li diffusion into the crystal. The melt inclusion found in this pl is not influenced by diffusion. Pl-20 shows no diffusion. Pl-22 (SAN56-1) shows Li diffusion into the crystal. The Li concentration inside the melt inclusion is low and shows no diffusive loss of Li into the surrounding crystal. For all crystals the entire distance affected by diffusion is highlighted in green.

5.2.2. δ^7Li profiles in Minoan Plagioclase

16 δ^7Li short profiles with distances of a maximum of $\sim 300\,\mu$m were analyzed by SIMS with a lateral resolution of $10\,\mu$m, starting in glass selvages of plagioclase and then measured perpendicular into the crystal to prove, whether observed lithium profiles were caused by diffusion or not (Fig. 5.12 to Fig. 5.14). In each diagram of Fig. 5.12, Fig. 5.13 and Fig. 5.14 two profiles are shown; the blue profile is a lithium concentration profile and the red profile is the δ^7Li profile. All plagioclase crystals analyzed in the Minoan pumice show a δ^7Li minimum in their profiles. The observed lithium profiles are therefore indeed diffusion profiles. The flat profile of Pl-7b in SAN59A was measured perpendicular to a broken crystal rim and indicates that the crystal broke up during sample preparation and is therefore lacking any sign of lithium diffusion.

Negative δ^7Li values vary between $\sim -13.9\%_o$ to $\sim -36.6\%_o$ in Minoan pumice plagioclase with Pl-9 (SAN59A) showing the smallest $\Delta\delta^7$Li value ($|\Delta\delta^7$Li$| \approx 15\%_o$) and Pl-3 (SAN51-1B) of the Crystal-rich pumice showing the largest value ($|\Delta\delta^7$Li$| \approx 26\%_o$). Just one distinct minimum was observed in one of the scoria clasts. Pl-1of SAN53-3 shows a minimum with $|\Delta\delta^7$Li$| \approx 23\%_o$.

The widths of δ^7Li minima vary from $\sim 40-130\,\mu$m. Plagioclase Pl-4 (SAN54A) shows the widest distance and Pl-1 (SAN52A) the lowest. All other plagioclase crystals including the scoria crystal Pl-3 (SAN53-3) have distances in between those mentioned above.

The depths ($|\Delta\delta^7$Li$|$) of the observed δ^7Li minima indicates that the source which caused the observed diffusion profiles must have had a much higher lithium concentration as observed in matrix glass and melt inclusions (see Fig. 5.4 and Chapter 4). This observation will be further discussed in Chapter 7.
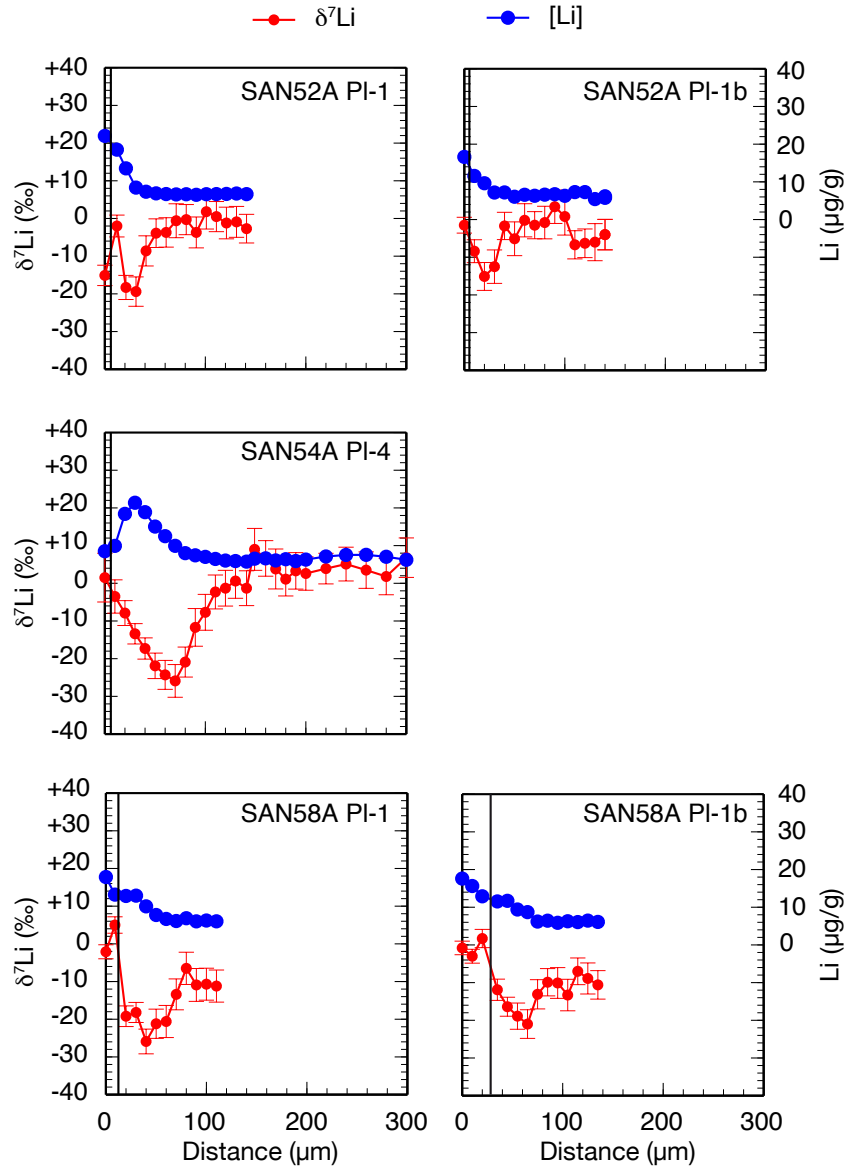
Fig. 5.12. Li concentration and δ^7Li profiles in plagioclase of the Minoan pumice, Unit A (SAN52 and SAN54) and Minoan Unit B (SAN58). The vertical black line marks the glass-plagioclase transition. Li concentration values are derived from count rates of the isotope analyses and are therefore only semi-quantitative.
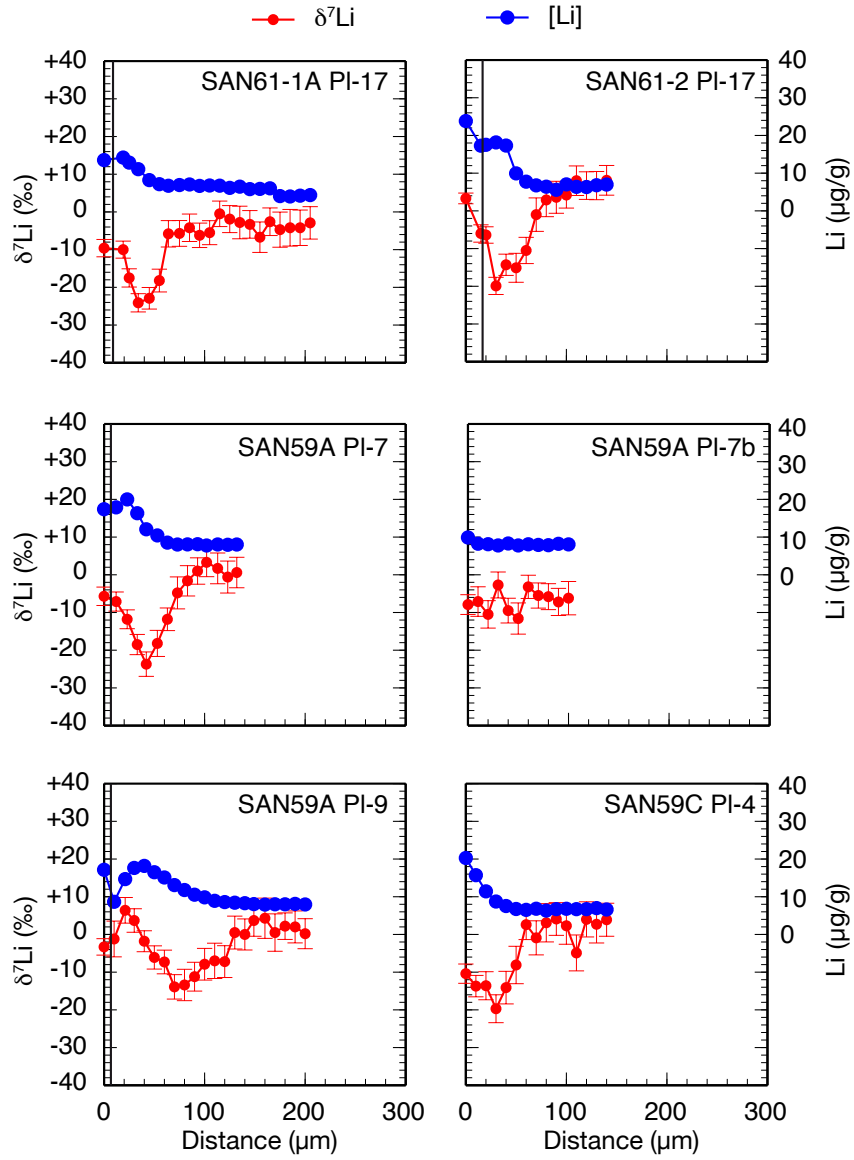
Fig. 5.13. Li concentration and δ^7Li profiles in plagioclase of the Minoan pumice, Unit B (SAN61-1A and SAN61-2) and Minoan Unit C (SAN59). The vertical black line marks the glass-plagioclase transition. Li concentration values are derived from count rates of the isotope analyses and are therefore only semi-quantitative.
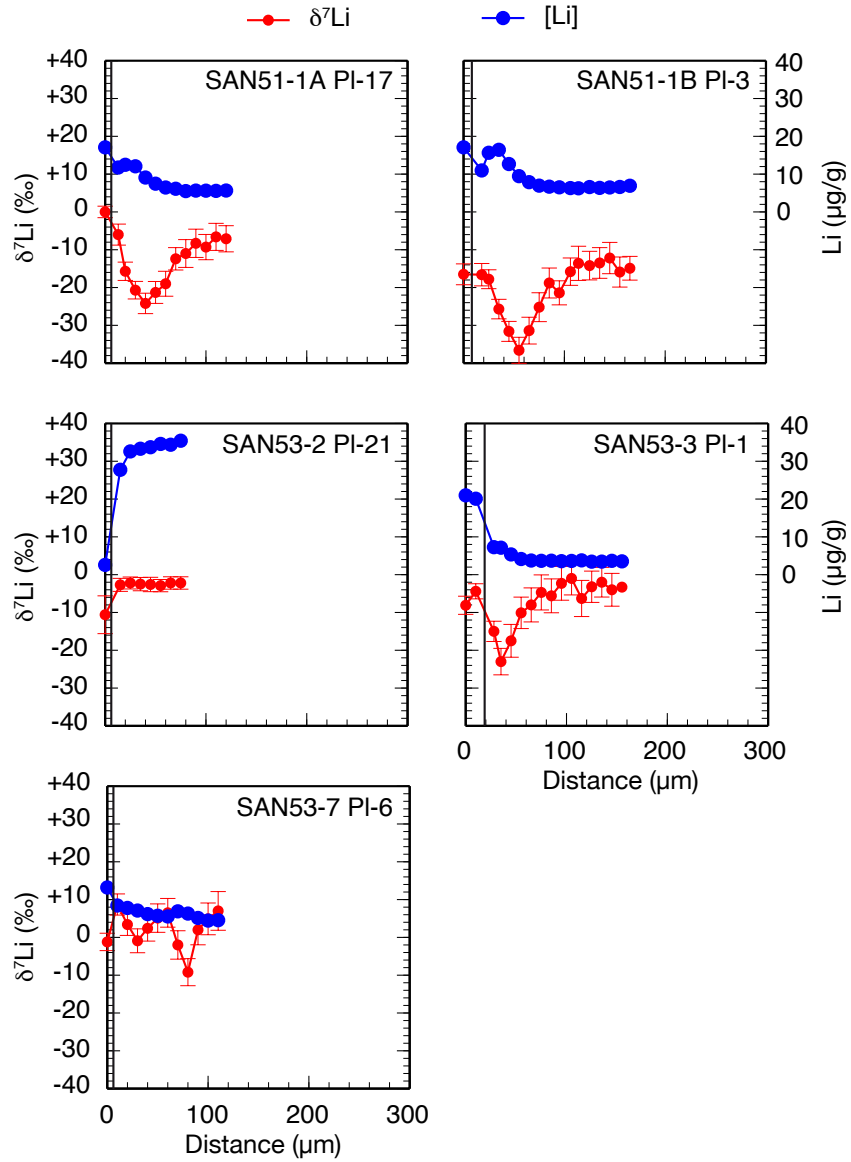
Fig. 5.14. Li concentration and δ^7Li profiles in plagioclase of the Crystal-rich pumice, Minoan Unit D (SAN51) and andesitic scoria of Minoan Unit A (SAN53). The vertical black line marks the glass-plagioclase transition. Li concentration values are derived from count rates of the isotope analyses and are therefore only semi-quantitative.

6. Partition Coefficients

6.1. Introduction

Fig. 6.1 is a theoretical model for the partition coefficient D_i (Equation 6.1) at a constant temperature T under equilibrium conditions for a trace element with the concentration c_1 in melt and c_2 in the crystal.
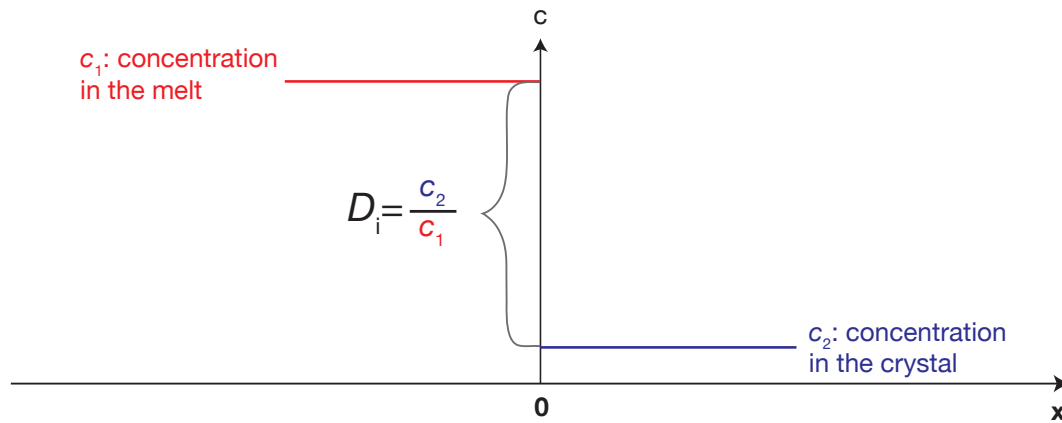
Fig. 6.1. Simple sketch of the distribution of a trace element in two different phases (melt and crystals) at equilibrium and constant T. The ratio for the trace element is given by the Nernst partition coefficient D_i.

$$D_i = \frac{c_2^{crystal}}{c_1^{melt}} \tag{6.1}$$

D_i is known as the Nernst partition coefficient of a trace element i. In many cases partition coefficients calculated from natural samples will be influenced by disequilibrium phenomena.

6.2. Partition Coefficients of Trace Elements in Minoan Plagioclase

Crystals from Minoan pumice samples were handpicked and prepared carefully (no ultrasonic cleaning) to avoid a loss of attached glass selvages. In thin sections of scoria samples glass selvages were often well preserved. In many samples SIMS profiles were started or ended in glass selvages and run perpendicular to the plagioclase rims. These analyses allowed to calculate partition coefficients for many plagioclase crystals analyzed in all pumice samples and in some of the scoria clasts. Partition coefficients were calculated using the last point measured in the glass selvage and the last point analyzed in the plagioclase (Equation 6.1).

This method is fairly easy but one may realize that natural profiles are not always showing such a nice state of equilibrium as the profile in Fig. 6.1 . Profiles are often overprinted by diffusion into or out of the crystal representing a stage of disequilibrium when the concentration in one phase changes (also seen in plagioclase crystals in Chapter 5). In magma chambers this might happen when repeated intrusions of new magma enter a magma chamber. Crystals are often not idiomorphic but deformed due to resorption processes inside the magma chamber. Even in a state of equilibrium concentrations of trace elements inside plagioclase are not necessarily homogeneous; their concentrations may also depend on the compositional zoning of crystals. Another important factor is the limited lateral resolution created by the size of the spot during analyses. This will have an influence on the shape of the profile; a profile not influenced by diffusion like the one measured through the glass inclusion in Pl-7 (SAN52A, Fig. 6.2) should have sharp transitions like observed in Fig. 6.1. The limited lateral resolution will lead to a more smooth transition between inclusion and plagioclase.

In this section different ways for calculating partition coefficients will be presented. The emphasis is based on lithium as this element shows the most significant diffusion phenomena and drastic variations in partition coefficients. Table 6.1 presents all measured partition coefficients for lithium, beryllium, boron, magnesium, strontium and barium between plagioclase and glass selvages in Minoan pumice, Crystal-rich pumice and scoria samples. Partition coefficients of scoria samples were difficult to calculate as there often was not enough glass attached to the crystal. For that reason we will focus on the calculation of partition coefficients in Minoan pumice and the Crystal-rich pumice samples.

Table 6.1. Trace Element Partition Coefficients in Minoan Plagioclase

Pumice	T (°C)	An$_{Xrim}$	D_{Li} (B < 0.3)	D_{Li} (B 0.3 − 1.0)	D_{Li} (B > 1.0)	D_{Be} (B < 0.3)	D_{Be} (B 0.3 − 1.0)	D_{Be} (B > 1.0)	D_{B} (B < 0.3)	D_{B} (B 0.3 − 1.0)	D_{B} (B > 1.0)
SAN52	865	38 − 39	0.24 − 0.45	0.28 − 0.47	0.41 − 0.55	0.66	0.62	0.77	0.01	0.01 − 0.03	0.09 − 0.12
SAN54	868	38 − 40	0.51 − 0.6	0.57	0.59	0.60 − 0.88	0.61	0.86	0.01 − 0.02	0.03	0.18
SAN55	880	36 − 38	0.31	0.34	ND	0.64	0.71	ND	0.01	0.02	ND
SAN57	824	38 − 39	0.35 − 0.44	0.35 − 0.61	0.38 − 0.60	0.54 − 0.68	0.63 − 0.73	0.66	0.01	0.02 − 0.05	0.05
SAN58	844	38 − 39	0.38 − 0.51	0.47	0.48 − 0.49	0.74	ND	0.71	0.01	0.02	0.06 − 0.09
SAN61-2	ND	38 − 74	0.28 − 0.68	0.35 − 0.68	ND	0.60 − 0.66	0.65 − 0.71	ND	0.01	0.01 − 0.04	ND
SAN61-1A	888	38 − 47	0.39 − 0.59	0.36 − 0.57	ND	0.50 − 67	0.64 − 0.67	ND	0.01	0.02 − 0.03	ND
SAN59	833	37 − 40	0.33 − 0.73	0.39 − 0.75	0.48 − 0.55	0.68 − 0.70	0.66 − 0.70	0.65 − 0.72	0.01	0.02 − 0.03	0.05 − 0.09
SAN50	862	35 − 39	0.30 − 0.35	ND	ND	ND	ND	ND	0.01	ND	ND
SAN51	919	37 − 63	0.16 − 0.57	0.49	ND	0.30 − 0.67	0.73	ND	0.01	0.02	0.02
Scoria											
SAN52Agg	ND	ND	0.15	0.19	ND	ND	ND	ND	0.01	0.02	ND
SAN53-3	1022	51 − 83	0.22 − 0.43	0.18	ND	0.95	ND	ND	0.005 − 0.02	0.01	ND
SAN53-4	969	82	0.14 − 0.23	ND	ND	ND	ND	ND	0.01 − 0.02	ND	ND
SAN53-7	855	40 − 76	0.35	0.37	ND	0.57	0.64	ND	0.01	0.03	ND
SAN56-1	923	58 − 63	0.35 − 0.52	ND	ND	0.29	ND	ND	0.01 − 0.03	ND	ND
SAN60	ND	62 − 78	0.2 − 0.54	ND	ND	ND	ND	ND	0.01	ND	ND

Pumice	T (°C)	An$_{rim}$	D_{Mg} (B < 0.3)	D_{Mg} (B 0.3 − 1.0)	D_{Mg} (B > 1.0)	D_{Sr} (B < 0.3)	D_{Sr} (B 0.3 − 1.0)	D_{Sr} (B > 1.0)	D_{Ba} (B < 0.3)	D_{Ba} (B 0.3 − 1.0)	D_{Ba} (B > 1.0)
SAN52	865	38 − 39	0.07	0.09	0.17	4.7	4.7	4.7	0.50	0.50	0.59
SAN54	868	38 − 40	0.07 − 0.12	ND	ND	2.4 − 5.5	6.1	2.2	0.42 − 0.49	0.52	0.57
SAN55	880	36 − 38	0.08	0.10	ND	5.1	4.8	ND	0.67	0.52	ND
SAN57	824	38 − 39	0.07	0.08 − 0.11	0.1	5.9 − 6.8	5.7	5.5	0.38 − 0.48	0.44 − 0.50	0.44
SAN58	844	38 − 39	0.08	ND	0.08	6.0	ND	6.0	0.41	ND	0.41
SAN61-2	ND	38 − 74	0.07 − 0.09	0.08 − 0.10	ND	4.1 − 7.9	4.6 − 7.6	ND	0.35 − 0.51	0.37 − 0.59	ND
SAN61-1A	888	38 − 47	0.07 − 0.11	0.08 − 0.13	ND	5.1 − 8.5	5.1 − 8.1	ND	0.23 − 0.55	0.27 − 0.52	ND
SAN59	833	37 − 40	0.07	0.07 − 0.08	0.07 − 0.14	ND	ND	ND	ND	ND	ND
SAN50	862	35 − 39	ND	ND	ND	ND	ND	ND	ND	ND	ND
SAN51	919	37 − 63	0.04 − 0.06	0.04	ND	1.7 − 4.0	4.1	ND	0.05 − 0.41	ND	ND
Scoria											
SAN52Agg	ND	ND	ND	ND	ND	ND	ND	ND	ND	ND	ND
SAN53-3	1022	51 − 83	0.11	ND	ND	3.1	ND	ND	0.82	ND	ND
SAN53-4	969	82	ND	ND	ND	ND	ND	ND	ND	ND	ND
SAN53-7	855	40 − 76	0.09	0.11	ND	6.4	6.6	ND	0.35	0.41	ND
SAN56-1	923	58 − 63	0.38	ND	ND	1.6	ND	ND	0.14	ND	ND
SAN60	ND	62 − 78	ND	ND	ND	ND	ND	ND	ND	ND	ND

Partition coefficients of Li, Be, B, Mg, Sr and Ba between pl and matrix glass/glass selvages. The three columns based on B concentration show how partition coefficients change depending on the choice of analysis for calculation. Due to the limited lateral resolution the partition coefficients can vary significantly when the wrong analyses are chosen for calculation. Boron is used as an indicator for the glass-pl transition. The most accurate partition coefficients can be calculated with B concentrations below $0.3 − 0.4 \, \mu g/g$. ND = not determined. Temperatures are calculated based on Putirka (2008). Anorthite rim contents are based on on crystals found in samples. Large variations are due to mingling of crystals with different X_{An}.

It is not possible to determine the first analyses inside the plagioclase by considering lithium alone because plagioclase rims are almost always overprinted by diffusion of lithium from rim into crystal (see Chapter 5).

The partition coefficients in Table 6.1 are calculated from SIMS profiles started in glass selvages and run perpendicular to plagioclase crystal rims. Representative lithium and boron profiles are shown in Fig. 6.2. Boron is used as an indicator for the glass-plagioclase transition because boron profiles are not affected by diffusion, and they have a very small D due to the large concentration difference between melt and crystal.

It can also be helpful to take Ca or other trace elements into consideration when trying to determine the beginning of plagioclase in a profile that was started in a glass selvage. Boron however showed the most stable values for distribution coefficients and concentrations in glass and plagioclase and was therefore considered being the best indicator for determining whether an analysis represents a mixed analysis of plagioclase and glass.

Based on observations for most analyses the first analyses not influenced by mixing were those with boron concentrations below $0.3\,\mu g/g$. However, there were cases were boron concentrations higher than $0.3\,\mu g/g$ seemed to be a better fit. For comparison partition coefficients calculated from analyses with different boron rim concentrations (< 0.3, between $0.3 - 1.0$ and $> 1.0\,\mu g/g$) are shown in Table 6.1.

In Fig. 6.2 short lithium profiles are presented to demonstrate how partition coefficients will change when lithium diffusion is involved.

For Pl-2 (SAN59A) a short lithium profile from the rim into the plagioclase is shown. The green colored points show the best analyses for the last point analyzed in the glass selvage and the first point in the plagioclase along the profile. The effect of lithium diffusion into the crystal is minor in this case. The analyses marked in orange give the partition coefficient for the last point analyzed in the selvage and the first point analyzed in the crystal not influenced by diffusion. Both partition coefficients are nearly equal.

This is in contrast to the profile of Pl-1 (SAN52A), which is influenced by lithium diffusion into the crystal. The partition coefficient calculated from the first point analyzed in the plagioclase crystal is much higher ($D_{Li}^{pl/glass} = 0.38$ at $d = 60\,\mu m$) than the partition coefficient based on an analysis of the plagioclase that was not influenced by diffusion ($D_{Li}^{pl/glass} = 0.25$). Note that the latter is already far away from the crystal rim and the melt and therefore should not be taken into account for the calculation of a partition coefficient.
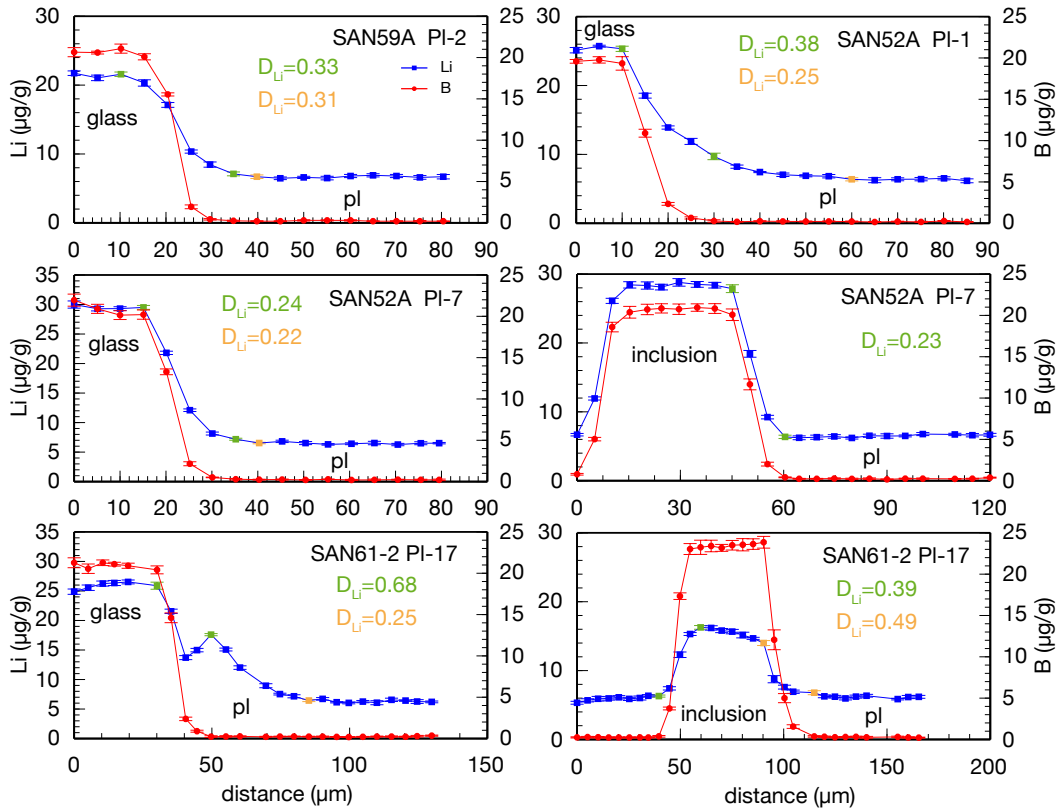
Fig. 6.2. The choice of analyses for calculating partition coefficients of lithium from a SIMS profile is often difficult and will lead to considerable differences in partition coefficients when an diffusion overprint is involved. Note the difference between lithium partition coefficients of the rim profile in Pl-2 (SAN59A). It is hardly influenced by diffusion, while Pl-17 (SAN61-2) has a profile strongly influenced by diffusion. If the partition coefficient in Pl-17 (SAN61-2) is calculated from the green analyses it will be too high. This kind of calculation leads to false partition coefficients as the source that lead to the diffusion of lithium into pl is unknown (further discussed in Chapter 7).

Fig. 6.2 also shows a rim profile analyzed in Pl-7 (SAN52A) and a profile that was measured through a melt inclusion within the same crystal. There is hardly any diffusion of lithium into the crystal; the melt inclusion shows a homogeneous lithium concentration. The differences in calculated partition coefficients are relatively small in all three cases.

This is not always the case, as demonstrated by Pl-17 (SAN61-2). A rim profile and a profile through a melt inclusion were analyzed. The rim profile shows a drop of lithium from glass into the crystal and a slight increase before the beginning of the crystal is marked by the boron concentration. Diffusion of lithium into the crystal is well visible. The orange point marks the end of the diffusion profile. Again we see the difference in the partition coefficients analyzed. The partition coefficient calculated from the diffusion profile is $D_{Li}^{pl/glass} = 0.68$. In Chapter 7 it will be shown that this partition coefficient is most likely not meaningful. The lithium concentration within the melt inclusion is not homogeneous. This phenomenon is often observed when a crack runs through the inclusion or adjacent to it. It is assumed that cracks lead to a loss of lithium from the melt inclusion. The process behind that loss is not entirely understood (see Chapter 7). However, if partition coefficients are calculated from both rims of the inclusion these vary significantly from each other and those calculated at the rim.

Table 6.2 shows partition coefficients calculated from lithium short profiles (glass selvage/plagioclase crystal) and profiles running through inclusions in the same plagioclase crystal. Column **D-Diff** is based on those calculations for partition coefficients marked in green in Fig. 6.2 for the rim profiles. Column **D-no-Diff** was calculated the same way as the analyses marked in orange in Fig. 6.2. Column **D – no-Diff-Incl** is a special case, where D was calculated from the first analyses not influenced by diffusion (orange analyses in pl) and the lithium concentration of the melt inclusion. These D-values are similar to those in column **D-inclusion** that were calculated from the lithium concentration in plagioclase closest to the melt inclusion and the lithium inclusion inside the melt inclusion.

It can also be seen that plagioclase-melt inclusion partition coefficients for lithium are often similar to those calculated between glass selvage and the first point in the plagioclase crystal that was not influenced by lithium diffusion (analyses marked in orange). This will be further discussed in Chapter 7.

Table 6.2. Trace Element Partition Coefficients of Short Profiles and Melt Inclusions

Sample T (°C)	Pl	An$_X$	D-Diff	D – no-Diff	D – no-Diff-Incl	D-inclusion	Li Diff rim (µm)	Li-loss in inclusion
Min A								
SAN52A	Pl-1 (rim 1)	39	0.38	0.25	0.31		yes	
865 °C	Pl-1 (rim 2)	39	0.45	0.25			yes	
	Pl-1 incl.	40				0.32		yes, crack
SAN52A	Pl-7 (rim 1)	NA	0.24	0.22	0.23		yes	
	Pl-7 (rim 2)	NA	0.44	0.36	0.22			
	Pl-7 incl.	NA				0.23		no
SAN57A	Pl-6	38	0.50	0.30	0.56		yes	
824 °C	Pl-6 incl.	41				0.52		yes, crack
Min B								
SAN58A	Pl-1 (rim 1)	NA					yes	
844 °C	Pl-1 (rim 2)	NA	0.51	0.30	0.22			
	Pl-1 incl.	NA				0.23		no
SAN58A	Pl-5	39	0.38	0.29	0.32		yes	
	Pl-5 incl.	40				0.29		no
SAN61-2	Pl-5	38	0.28	0.19			yes	no incl
SAN61-2	Pl-9	NA	0.45	0.31			yes	no incl
SAN61-2	Pl-13	NA	0.65	0.36			yes	no incl
SAN61-2	Pl-17	NA	0.68	0.25	0.40		yes	
T = ND	Pl-17 incl.	NA				0.37		yes, crack
Min C								
SAN59A	Pl-2	38	0.33	0.31	0.55		yes	
833 °C	Pl-2 incl.	41				0.54		yes, very close to rim
SAN59A	Pl-7 (rim 1)	38	0.48	0.37	0.30		yes	
	Pl-7 (rim 2)	38	0.54	0.26	0.24			
	Pl-7 incl.	41				0.24		no
SAN59A	Pl-9 (rim 1)	37	0.63	0.37	0.19		yes	
	Pl-9 (rim 2)	37	0.40	0.26	0.18			
	Pl-9 incl.	42				0.19		no
SAN59A	Pl-10	39	0.45	0.23	0.33		yes	
	Pl-10 incl.	37				0.34		yes, crack
Min D								
SAN50A	Pl-1	38	0.35	0.32	0.21		yes	
862 °C	Pl-1 incl.	40				0.18		no
SAN50A	Pl-2	NA	0.30	0.29	0.36		yes	
	Pl-2 incl.	NA				0.36		no
SAN50A	Pl-8	39	0.33	0.31	0.23		yes	
	Pl-8 incl.	42				0.19		no
SAN50A	Pl-9	NA		0.27			no diff	
	Pl-9 incl.	NA				0.20		no
Crystal-rich SAN51-1B 919 °C	Pl-3 incl.	44-45				0.24		yes, crack

Variations in partition coefficients based on Fig. 6.2. **D-Diff:** Partition coefficient between the last analysis in the glass selvage and the first analysis in pl (usually influenced by diffusion; Fig. 6.2 – green analysis in Pl-2 of S59A). **D – no-Diff:** Partition coefficient calculated from the last point in the glass selvage and the first analysis in the pl not influenced by diffusion (Fig. 6.2 – orange analysis in Pl-2 of S59A). **D – no-Diff-Incl:** Partition coefficient calculated from the first point not influenced by diffusion in the profile with the Li concentration of the melt inclusion. **D-inclusion:** Partition coefficient for the melt inclusion as shown in Fig. 6.2 for Pl-7 (SAN52A). Temperatures are calculated based on Putirka (2008). Anorthite contents are only given for crystals analyzed by EPMA. Anorthite contents next to inclusions were estimated based on the EPMA profile. NA = not analyzed.

7. Discussion: Lithium Distribution in Minoan Plagioclase

7.1. The Lithium *vs* Anorthite Correlation Phenomenon

In her studies on phenocrysts from the Nea Kameni dacites and Thera andesites, Cabato (2006) suggested that an investigation of a possible correlation between lithium and anorthite content in plagioclase should be taken into further consideration. Sonntag (2007) detected a negative correlation between lithium and anorthite content in plagioclase from volcanic rocks of Nisyros, and Coogan (2011) was able to show experimentally that lithium does correlate with anorthite content in plagioclase (An_{60-89} at 1000°C) under equilibrium conditions. In this study, a clear Li *vs* X_{An} correlation was observed in plagioclase of the Minoan pumice, the Crystal-rich pumice and scoria clasts found within the Minoan pumice (Fig. 7.1).

This correlation is often overprinted by diffusion, as lithium diffusion is very fast in plagioclase at magmatic temperatures (Giletti & Shanahan, 1997), and therefore it might be easily overlooked. Minoan plagioclase crystals show relatively short diffusion profiles, often only in the range of $\sim 40\,\mu m$ with a few exceptions (Chapter 5) and make it therefore easy to observe this correlation trend, especially in pumice plagioclase grains up to $\sim 2\,mm$ in length and with broad anorthite zoning bands.

To detect the correlation, the Li concentration profile has to be purged of data points affected by diffusion (see Fig. 5.5 on p.130), matrix material or any kind of inclusions. As the Li and Ca concentration data is taken from profiles that were acquired using different techniques (Ca: EPMA; Li: SIMS), it is necessary to check whether both profiles match exactly. Offsets between the profile have to be corrected before plotting the data points. In total 71 plagioclase crystals were analyzed and corrected and the best analyses are presented in Fig. 7.1. Some profiles were excluded due to a lack of EPMA or SIMS data points or because the zoning was too narrow to be properly detected during analyses. This is especially difficult because EPMA profiles and SIMS profiles are usually analyzed with different lateral resolutions, $\sim 10\,\mu m$ for EPMA and $\sim 6\,\mu m$ for SIMS. All corrected profiles are included on the CD.

Data points of Minoan pumice samples clearly show a correlation with anorthite content (Fig. 7.1). Anorthite contents are usually below An_{60} with two exceptions:

(1) Pl-5 in SAN52A (Minoan A) has a patchy core with a high anorthite content (An_{60-80}) surrounded by a rim of An_{30-50} and (2) anorthite contents of Pl-1 and Pl-17 (SAN61-1A) vary between An_{37-85} (Chapter 4 and Appendix B).

Plagioclase of scoria clasts can be divided into two groups, Scoria A and Scoria B (Fig. 7.1). Crystals with high lithium concentrations between $\sim 20-40\,\mu g/g$ and gentle slopes in the Li *vs* anorthite content plot (Scoria A: SAN53-2, SAN53-5 and SAN53-6) and crystals with low lithium concentrations ($< \sim 10\,\mu g/g$) and steeper slopes (Scoria B: SAN53-3, SAN53-4 and SAN56-1). Sample SAN53-3 contains plagioclase crystals with different anorthite contents. Pl-12 has anorthite contents higher than An_{60} and shows a steep slope (Fig. 7.1). Pl-1 has anorthite contents below An_{60}. The variation in anorthite content is very small in Pl-1, nevertheless the slope of the correlation trend is flat.
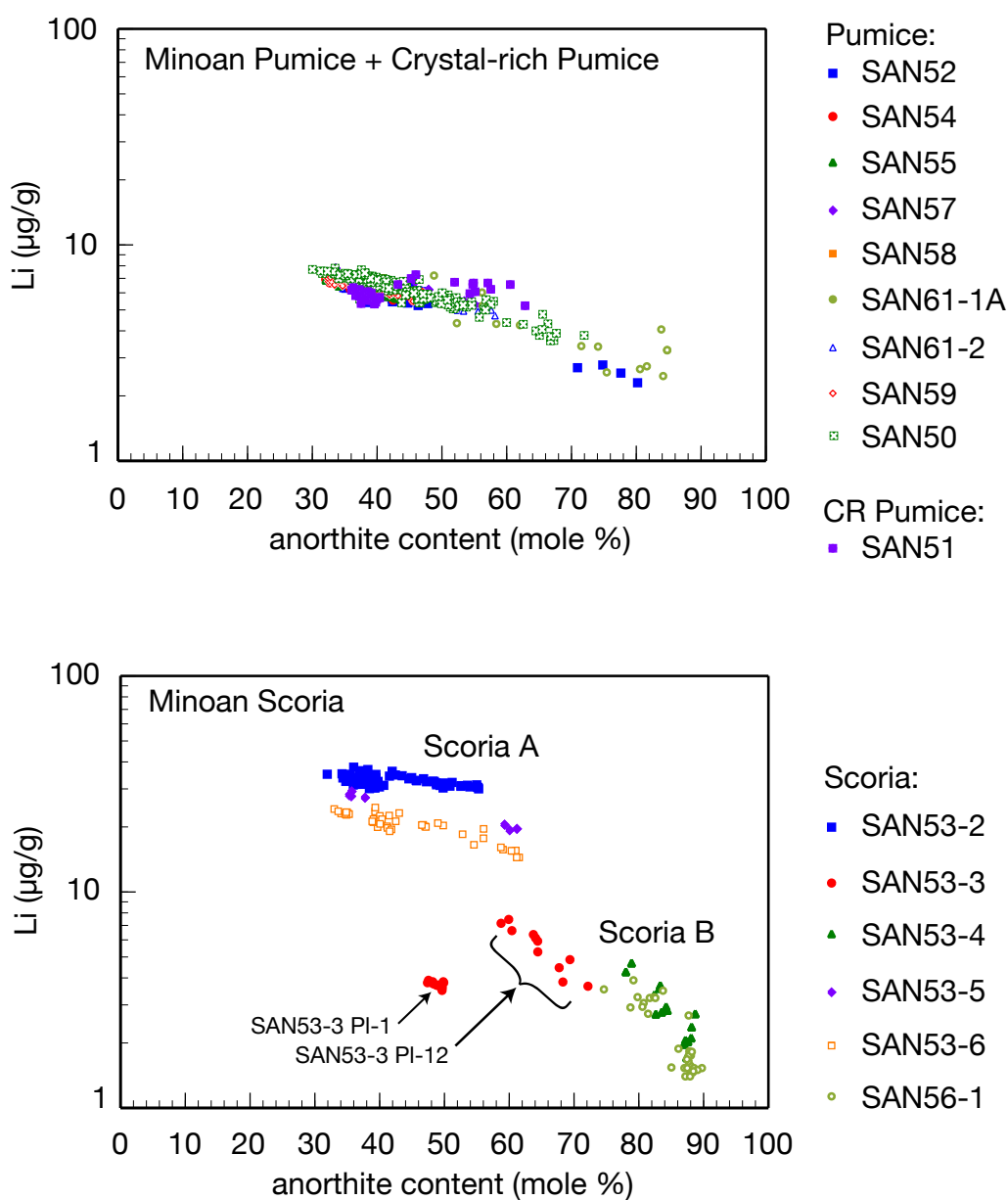
Fig. 7.1. Anorthite content *vs* Li plot of plagioclase sampled from Minoan pumice, Crystal-rich (CR) pumice and scoria clasts. Data points show a negative correlation between lithium ($\mu g/g$) and anorthite content (mole%). There is a noticeable difference in the slopes for different crystals. Plagioclase with anorthite contents higher than An_{60} shows steeper slopes. For a better visibility of the data points error bars were not plotted, but can be found in the SIMS data sheets on the CD.

7.1.1. Models for the Distribution of Lithium in Plagioclase

Physical Model Blundy & Wood (1994) developed a model to predict partition coefficients based on physical characteristics of cation sites in crystals, namely the size and elasticity of the crystal lattice site of interest. They used an equation developed by Brice (1975) that relates the mechanical strain energy around a homovalent cation defect to the Young's modulus E of the host crystal. Blundy & Wood (1994) used this equation to calculate the partition coefficient D_a of an isovalent cation 'a' of radius r_a at the pressure P, temperature T and composition X of a phase of interest:

$$D_i(P,T,X) = D_a(P,T,X) \exp \left(\frac{-4\pi E N_A \left[\frac{r_0}{2}(r_a^2 - r_i^2) + \frac{1}{3}(r_i^3 - r_a^3) \right]}{RT} \right) \quad (7.1)$$

r_i is the radius of the substituent cation, and r_0 is the optimum radius of the lattice site.

In order to model the distribution of lithium in plagioclase with variable anorthite content X_{An} we assume that the Young's modulus E and r_0 vary linearly with X_{An}:

$$r_0 = r_{0,Ab} + X_{An} \left(r_{0,An} - r_{0,Ab} \right) = r_{0,Ab} + X_{An} \Delta r_{Pl} \quad (7.2)$$

$$E = E_{Ab} + X_{An} \left(E_{An} - E_{Ab} \right) = E_{Ab} + X_{An} \Delta E_{Pl} \quad (7.3)$$

Since we are not interested in partitioning between melt and plagioclase here, Eq. 7.1 can be simplified:

$$c = c_0 \exp \left(\frac{-4\pi E N_A \left[\frac{r_0}{2}(r_a^2 - r_i^2) + \frac{1}{3}(r_i^3 - r_a^3) \right]}{RT} \right) \quad (7.4)$$

Substitution of E and r_0 yields:

$$c(X_{An}) = c_0 \exp \left(\frac{-4\pi (E_{Ab} + X_{An}\Delta E_{Pl}) N_A \left[\frac{r_{0,Ab} + X_{An}\Delta r_{Pl}}{2}(r_a^2 - r_i^2) + \frac{1}{3}(r_i^3 - r_a^3) \right]}{RT} \right)$$

$$(7.5)$$

Table 7.1. Parameters for Equation 7.5 taken from Blundy & Wood (1994)

E_{Ab} (kbar)	E_{An} (kbar)	$r_{0,Ab}$ (Å)	$r_{0,An}$ (Å)	r_a (Ca) (Å)	r_i (Li) (Å)
516 ± 39	673 ± 70	1.237 ± 0.016	1.216 ± 0.031	1.12	0.92[1]

[1] The radius of lithium for 8-fold coordination was taken from Shannon (1976). The uncertainties are 1σ standard deviation.

Exponential Model   The lithium concentration as a function of X_{An} may also be described by a simple exponential model:

$$c(X_{An}) = c_0 \exp\left(\ln K_D \, X_{An}\right) \tag{7.6}$$

K_D is the partition coefficient between albite and anorthite and c_0 is the concentration in albite. Coogan (2011) used this model to fit his experimental data and reported $\ln K_D = -6.5 \pm 0.5$ for lithium in anorthite and An_{60-89} at $1000\,°C$.

7.1.2. Least Square Fits of the Models

Both models were fit to the observed data by performing a least squares fit using the Solver in Microsoft Excel. For the physical model the following variables were varied in order to find the best fit (lowest sum of squared errors): c_0, ΔE_{Pl} and Δr_{Pl} (Equation 7.5). The variables for the fit of the exponential model were c_0 and $\ln K_D$ (Equation 7.6). For all variables of the fit, the range of variation was *not* restricted. Both fits are shown in Fig. 7.2. The resulting values for the variables ΔE_{Pl}, Δr_{Pl} and $\ln K_D$ are presented in Fig. 7.3 (physical and exponential model) and Table 7.2 (exponential model only).

The results (less one outlier) fall in two distinct groups:

1. Weak correlation of Li *vs* anorthite: $\overline{X}_{An} < 0.60$, $\Delta r_{Pl} \leq 0.1\text{Å}$, $\Delta E_{Pl} \leq 250\,\text{kbar}$ and $\ln K_D > -2.5$. Samples that belong to this group are: Minoan Pumice, CR Pumice, Scoria A and Nisyros (NIS). The mean value of $\Delta E_{Pl} = 172 \pm 56\,\text{kbar}$ is in good agreement with the value of $157 \pm 80\,\text{kbar}$ reported by Blundy & Wood (1994). The agreement is not as good for $\Delta r_{Pl} = 0.080 \pm 0.044\,\text{Å}$ compared to $-0.021 \pm 0.035\,\text{Å}$ (Blundy & Wood, 1994, uncertainties are 1 s.d.). It should be noted, though, that Δr_{Pl} is very small compared to r_0 (see Table 7.1).

2. Strong correlation of Li *vs* anorthite: $\overline{X}_{An} > 0.60$, $\Delta r_{Pl} > 0.2\text{Å}$, $\Delta E_{Pl} > 400\,\text{kbar}$ and $\ln K_D \leq -5$. All samples in this group are Scoria B samples. The experimental data from Coogan (2011) also fall in this group.
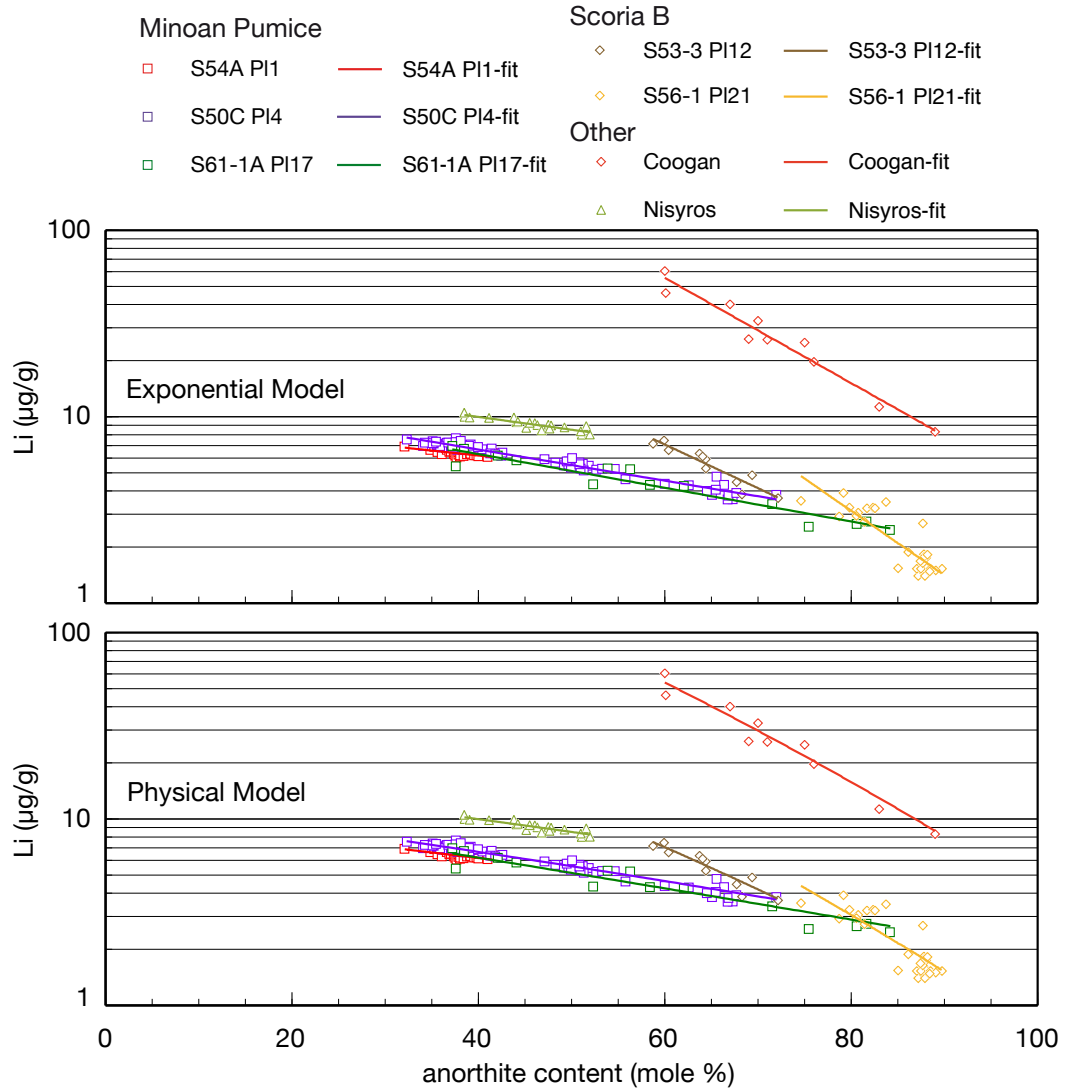
Fig. 7.2. Fits of the exponential model and the physical model (Blundy & Wood, 1994) for lithium *vs* anorthite were applied to pl crystals of the Minoan pumice (S54A, S50C and S61-1A), Minoan scoria (SAN53-3 and SAN56-1), a pl from Nisyros (Pl-1, NIS21) and the data of Coogan (2011). Both models fit the data well; the difference between the two fits is barely visible. The physical model fit is nearly exponential because for the given parameters ΔE_{Pl} dominates over Δr_{Pl} in Equation 7.5 (see Fig. 7.3 for the values of ΔE_{Pl} and Δr_{Pl}). Excel sheets for both model fits are included on the CD.
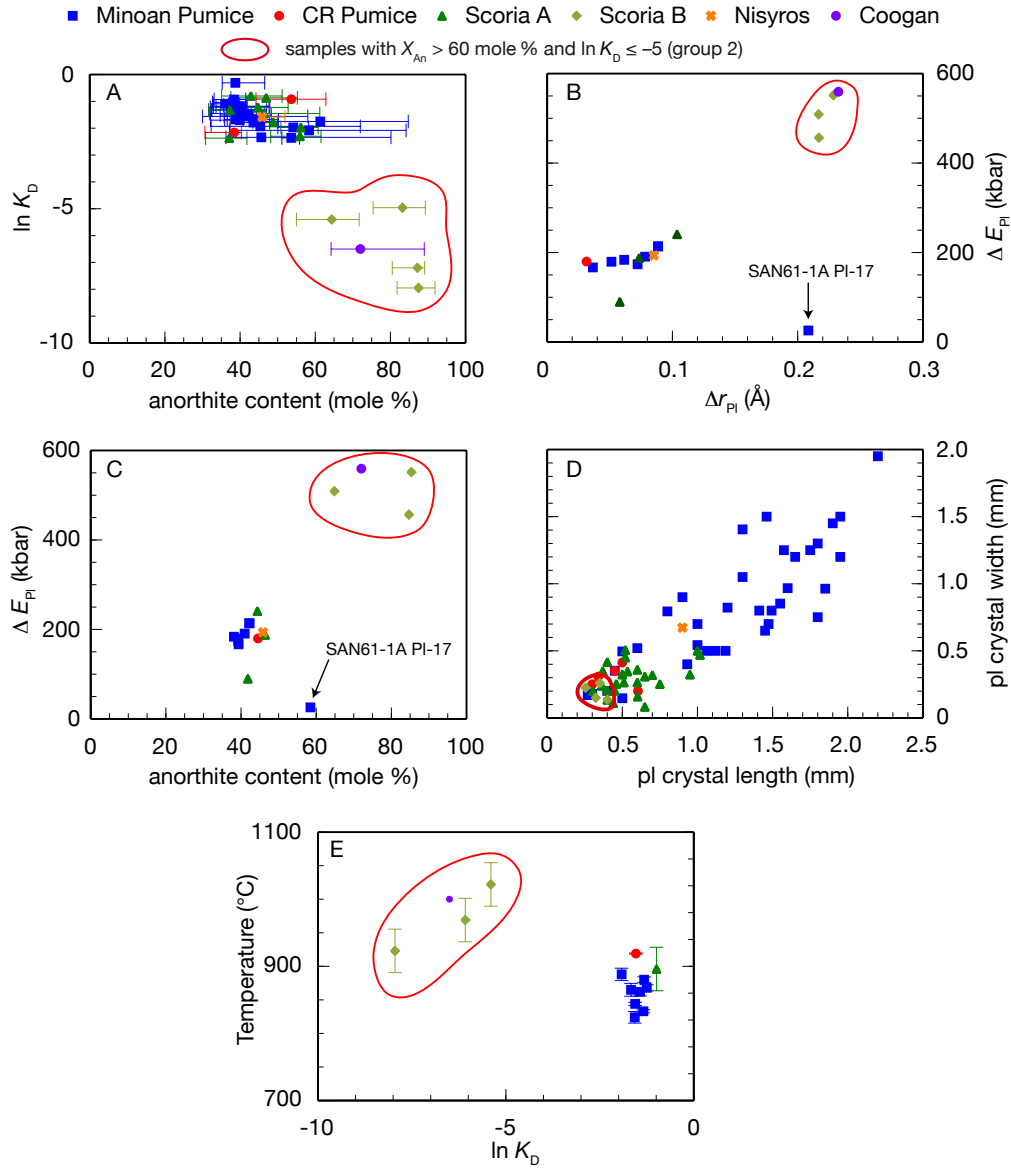
Fig. 7.3. A: ln K_D *vs* average anorthite content (exponential model). The horizontal error bars denote the anorthite content range of the sample. **B:** ΔE_{Pl} *vs* Δr_{Pl} (physical model). **C:** ΔE_{Pl} *vs* average anorthite content. **D:** Pl crystal length *vs* pl crystal width. **E:** Temperature (°C) *vs* ln K_D (exponential model). The temperatures were calculated based on Putirka (2008). Minoan Pumice: SAN52–SAN50; Crystal-rich Pumice: SAN51; Scoria A: SAN53-2, SAN53-5, SAN53-6; Scoria B: SAN53-3, SAN53-4, SAN56-1; Nisyros: NIS21 (Sonntag (2007); Coogan: Coogan (2011). See also Table 7.2.

159

Table 7.2. Anorthite content and results of the exponential model fit

Sample	An_{min}	An_{max}	An_{mean}	An_{median}	$\ln K_D$	K_D	T (°C)
Minoan Pum.							
SAN52	34.6	58.7	42.6	40.4	−1.7	0.19	865
SAN54	35.7	43.3	39.3	39.4	−1.3	0.29	868
SAN55	32.6	42.5	39.2	39.7	−1.3	0.27	880
SAN57	40.1	48.5	43.9	43.2	−1.6	0.21	824
SAN58	33.9	46.6	41.9	42.2	−1.6	0.21	844
SAN61-1A	41.6	84.5	59.9	53.3	−1.9	0.15	888
SAN59	34.1	42.7	38.1	37.9	−1.3	0.26	833
SAN50	34.1	53.5	41.8	40.5	−1.4	0.24	862
CR Pum.							
SAN51	39.6	51.6	46.0	46.6	−1.5	0.21	919
Scoria A							
SAN53-2	34.7	49.0	42.4	42.0	−1.0	0.37	896
SAN53-5	35.3	61.2	46.4	37.7	−1.5	0.23	896
SAN53-6	37.2	52.1	45.9	46.9	−2.0	0.14	896
Scoria B							
SAN53-4	80.3	88.4	84.4	85.2	−6.1	0.0023	969
SAN53-3 (Pl12)	58.7	72.1	64.8	64.4	−5.4	0.0045	1022
SAN56-1	74.6	89.7	85.3	87.5	−8.0	0.0004	923
NIS	38.5	52.0	45.8	46.2	−1.6	0.21	905
Coogan	60.0	89.0	72.0	70.5	−6.5	0.0015	1000

Coogan: Data based on Coogan (2011). **NIS:** Pl sample from Nisyros (Sonntag, 2007). The temperatures calculated are based on Putirka (2008)

The outlier is Pl-17 of SAN61-1A which covers a wide range of anorthite content (An_{37-84}) and plots away from both groups.

In Fig. 7.3D the crystal length is plotted against the crystal width. All crystals of group 2 are smaller than 0.5 mm. But especially the low anorthite samples of the Scoria A group and also some crystals of the main pumice group (all belonging to group 1) plot within the group of small crystals. The scatter of the main pumice crystals is large, which is mainly caused by broken crystals. But it can clearly be seen that crystal size can be ruled out as an explanation for the observed difference in slopes.

Fig. 7.3E shows $\ln K_D$ *vs* temperature. Temperatures for different samples are presented in Chapter A. Due to mingling between scoria samples and Minoan pumice some of the temperatures for plagioclase in scoria clasts were difficult to calculate. For SAN53-3, which was probably not only affected by mingling processes, but also shows traces of palagonitization, it was especially difficult to calculate temperatures. Good results for pumice temperatures were gained from the plagioclase-liquid thermometer by Putirka (2008). For the Scoria A group a temperature could

be calculated for a single plagioclase grain with the clinopyroxene-orthopyroxene thermometer of Putirka (2008). Due to similarity of the samples the temperature was also used for SAN53-5 and SAN53-6. Therefore the temperatures for the Scoria A group are not ideal. Minoan pumice samples have a trend to lower temperatures, while Scoria B and the Crystal-rich pumice samples have elevated temperatures. SAN53-2 (Scoria A) with plagioclase geochemically similar to the Minoan pumice has a tendency to plot closer to the Minoan pumice group.

Samples of group 2 (including the experimental data from Coogan (2011)) also form a distinct group in the $\ln K_D$ *vs* temperature plot, but at $\sim 900\,°C$ both groups (1 and 2) overlap, so that temperature is most likely not the cause of the observed phenomenon.
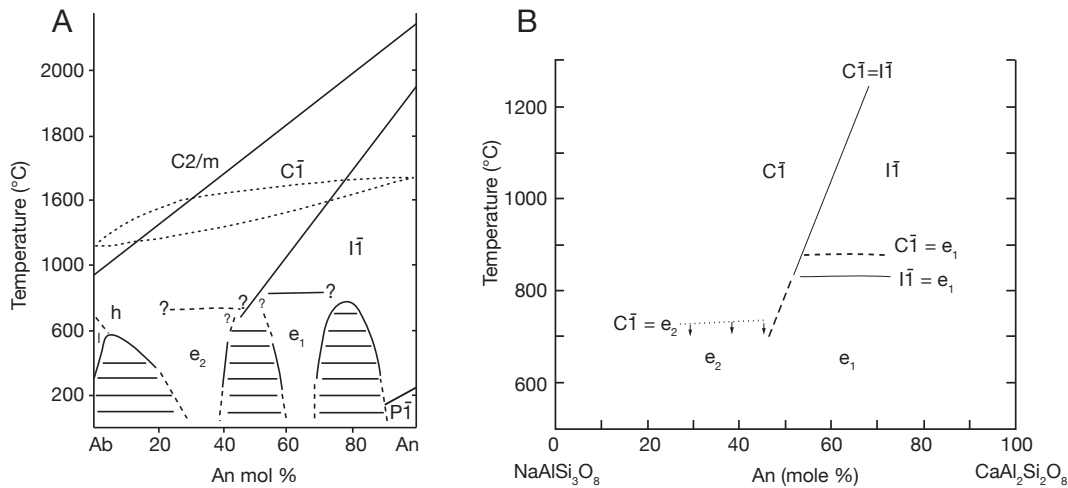
Fig. 7.4. A: This schematic phase diagram for plagioclase was taken from Carpenter (1988) and is slightly modified. It shows the $C\bar{1} \rightleftharpoons I\bar{1}$ transition line, the position of the C2/m $\rightleftharpoons C\bar{1}$ transition line, the position of the $C\bar{1} \rightleftharpoons e_2$ and $I\bar{1} \rightleftharpoons e_1$ transition lines and the transition from high to low albite. Miscibility gaps are represented by horizontal lines (for more information on data background see Carpenter (1988)). **B:** Temperature-composition limits for the ordering of different superlattice types are taken from Carpenter (1986). Shown are the $C\bar{1} \rightleftharpoons I\bar{1}$ transition line, the $C\bar{1} \rightleftharpoons e_1$, $C\bar{1} \rightleftharpoons e_2$ and $I\bar{1} \rightleftharpoons P\bar{1}$ transition lines as well as the fields for e_1 and e_2 ordering. Note that the C2/m $\rightleftharpoons I\bar{1}$ and the $C\bar{1} \rightleftharpoons I\bar{1}$ transition lines have been extrapolated into the stability field of liquid.

Crystallographic and Miscibility Effects in Plagioclase It is well known that the plagioclase series between albite and anorthite does not represent a continuous solid solution (Holland & Powell, 1992; Carpenter, 1985, and references therein).

Plagioclase is composed of a $C\bar{1}$ region ranging from albite to $\sim An_{50}$ at $\sim 700\,°C$ (see Fig. 7.4) and an $I\bar{1}$ region ranging to more anorthitic compositions (Orville,

1972). With increasing temperature this phase transition moves to more calcic compositions, which can be expressed by an equation from Carpenter & McConnell (1984). Albite, one of the end members in the plagioclase feldspar series, is monoclinic; when cooled it transforms to a triclinic structure ($C\bar{1}$) (Carpenter, 1988). The $C\bar{1}$ region is defined by a disordered distribution of AlO_4 and SiO_4 tetrahedra that becomes more ordered with decreasing temperature (Carpenter, 1988) while $I\bar{1}$ plagioclase is defined by partial to high degrees of order (Carpenter, 1988; Holland & Powell, 1992). In between there is a region called e plagioclase which is defined by curious ordering behavior on cooling to temperatures below $\sim 700 - 800\,°C$. This ordering behavior leads to the development of an incommensurate structure (thin slabs with albite-like and anorthite-like ordering patterns alternate with a periodicity that is out of step ('incommensurate') with the overall lattice (Parsons, 2010), which is not well understood (Carpenter, 1986).

Anorthite is the other end member in the plagioclase feldspar series. Close to $510\,K$ it undergoes a change in symmetry of $I\bar{1}$ to $P\bar{1}$ with falling temperature.

Of particular interest is the $C\bar{1} \rightleftharpoons I\bar{1}$ transition line which is located near An_{55-60} at magmatic temperatures typical for the plagioclase crystals of this study. Fig. 7.5 shows average anorthite contents of the plagioclases plotted against temperature. All group 1 plagioclase crystals ($\overline{X}_{An} < 0.60$) plot in the $C\bar{1}$ phase field while group 2 plagioclase crystals ($\overline{X}_{An} > 0.60$) plot in the $I\bar{1}$ field. Therefore the observed phenomenon of huge differences in $\ln K_D$ might have its origin in the symmetry of the crystal lattice which in this case is given by Si/Al ordering and disordering structures.

Scoria B sample SAN53-3 is interesting in that it features a group 1 plagioclase (Pl-1) that falls in the $C\bar{1}$ phase field and a group 2 plagioclase (Pl-12) which plots in the $I\bar{1}$ field. Li vs X_{An} data points of these plagioclases are plotted and highlighted in Fig. 7.1.

Pl-17 from SAN61-1A (the 'outlier') with An_{32-84} which belongs neither to group 1 nor to group 2 has a $\ln K_D > -2.5$ but plots in the $I\bar{1}$ field. As the plot is based on average anorthite contents and the ordering within the phase field is temperature dependent (Carpenter, 1986), the observed $\ln K_D$ might have been caused by cooling. From other studies it is known that plagioclase crystals with anorthite contents of An_{66-70} that were quenched during a volcanic eruption, retained $I\bar{1}$ ordering (McLaren & Marshall, 1974; Carpenter, 1986, references therein), but there is also evidence of e ordering in plagioclase from cooled volcanic rocks that had seen a history of higher temperatures with $I\bar{1}$ ordering that turned into e ordering during cooling to lower temperatures (Carpenter, 1986). Both crystals, Pl-1 and Pl-17 of SAN61-1A have heavily resorbed high anorthite cores surrounded by broad low anorthite zones and rims which clearly demonstrate that the cores are of

xenocrystic origin. The core of the 'outlier' may have grown at higher temperature in the $C\bar{1}$ field and its transition to $I\bar{1}$ may have been inhibited by the surrounding low-An plagioclase.
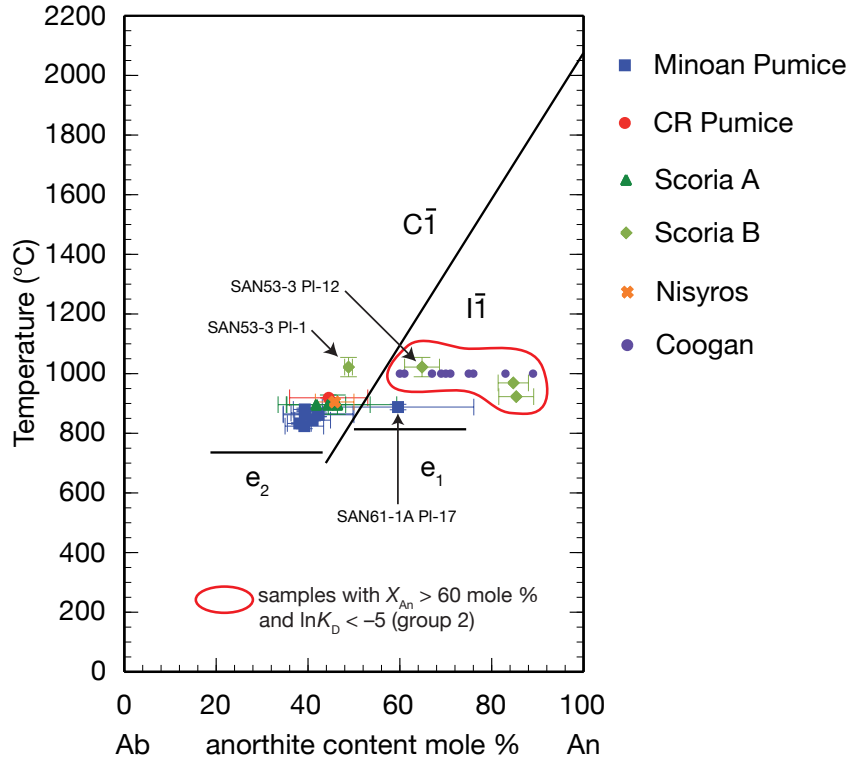
Fig. 7.5. Anorthite content *vs* temperature plot based on Carpenter (1988). The extensions of the $C\bar{1} \rightleftharpoons e_2$ and $I\bar{1} \rightleftharpoons e_1$ transition lines are not exactly known, and the $C\bar{1} \rightleftharpoons e_2$ transition might also be at lower temperatures (see Carpenter (1988)). Each separate sample from Coogan (2011) was plotted, instead of one data point with an average anorthite content. Minoan pumice, Crystal-rich pumice (low An pl); and Scoria A samples (all group 1) plot in the $C\bar{1}$ phase field, while Coogan and Scoria B data (all group 2) plot on the $I\bar{1}$ field. Pl-12 of SAN53-3 (Scoria B, group 2) plots in the $I\bar{1}$ phase field, while Pl-1 (group 1) of the same sample falls in the $C\bar{1}$ phase field. Pumice sample SAN61-1A (An$_{32-84}$, the 'outlier') plots in the $I\bar{1}$ phase field but has a $\ln K_D > -2.5$. Note that the $C\bar{1} \rightleftharpoons I\bar{1}$ transition line has been extrapolated into the stability field of liquid.

7.2. The Origin of Lithium Diffusion in Minoan Plagioclase

With the help of δ^7Li analyses it was shown that the observed lithium rim profiles in many plagioclase feldspars of the Minoan tephra were caused by diffusion of lithium into the crystal (Chapter 5). The depth of the δ^7Li minima suggests that the concentration of Li in the plagioclases was increased by a factor of $6-10$ during diffusion (Chapter 5, Fig. 5.12 to Fig. 5.14). Diffusion times for these profiles are typically $< 12\,\mathrm{s}$ for most of the crystals (Chapter 5, Table 5.1, page 132).

The difference in lithium concentrations observed in plagioclase of pumice and scoria samples of the Minoan eruption suggests a complex origin and history of these samples. Average lithium concentrations of all samples are depicted in Fig. 7.6. Plagioclase crystals of the Minoan pumice and the Crystal-rich pumice have average lithium concentrations of $5.1-7.3\,\mathrm{\mu g/g}$ throughout all Minoan Units therefore reflecting a rather homogeneous magma chamber composition, despite traces of mingling represented by the presence of crystal clots similar to sample SAN52Agg (Chapter 3). Single crystals like Pl-3 (SAN51-1A) reach slightly higher average lithium concentrations ($8.1\,\mathrm{\mu g/g}$) or lower concentrations of $\sim 4.3\,\mathrm{\mu g/g}$ (Pl-17, SAN61-1A).

The lithium concentrations of plagioclase found in the andesitic scoria clasts represent different histories and stages of mingling and differentiation. High lithium plagioclase crystals have average lithium concentrations of $19.4-42.9\,\mathrm{\mu g/g}$ (Fig. 7.6). Further distinctive characteristics of these scoria clasts are plagioclase crystals with anorthite contents below An_{60} and the lack of a glassy matrix.

The low lithium plagioclase crystals have varying lithium concentrations between $0.3-5.0\,\mathrm{\mu g/g}$. Except for SAN53-1, which is the sample with lithium concentrations below $1\,\mathrm{\mu g/g}$, all these samples have a glassy matrix.

A characteristic feature of the high lithium samples is a slight loss of lithium at the rims on a very short distance ($\sim 5\,\mathrm{\mu m}$), while all other crystals show different degrees of lithium diffusion into the crystal (see Chapter 5). The high lithium concentrations found in samples SAN53-2, SAN53-5 and SAN53-6 indicate that these plagioclase phenocrysts had been in contact with a lithium-rich phase before the eruption.

The origin of these samples is not clear. They could represent lithium-rich magma batches that inherited Minoan pumice plagioclase. The dense matrix of the clasts suggests a different degree of undercooling compared to those scoria clasts with a glassy matrix and possibly a longer residence time in the magma chamber (Martin *et al.*, 2006) which must have been only a few days prior to eruption because otherwise hornblende found in matrix glass of scoria clasts (also found in SAN53-2) would have suffered a breakdown if stored for a longer time at $50\,\mathrm{MPa}$ (Cottrell
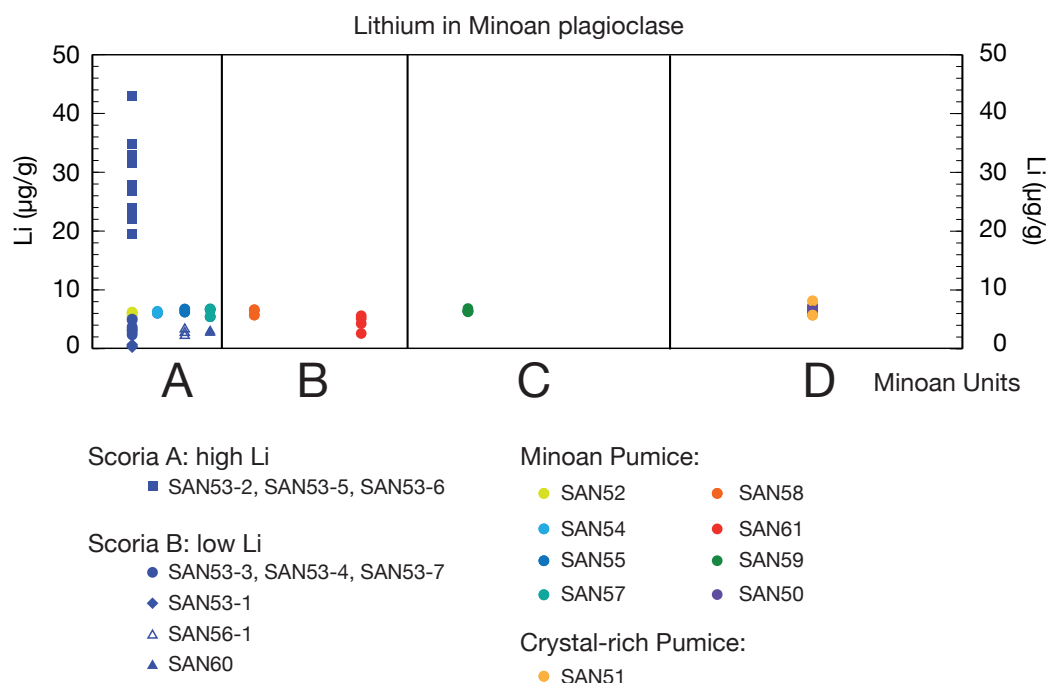
Fig. 7.6. Average Li concentrations of Minoan pumice, Crystal-rich pumice and Minoan scoria plagioclase phenocrysts. Average Li concentrations in Minoan pumice and Crystal-rich pumice plagioclase crystals through all Units vary between $4.3 - 8.1\,\mu\text{g/g}$. Pl-21 (SAN61-2) has average lithium concentrations of $2.6\,\mu\text{g/g}$, it does not belong to the Minoan pumice, but to the andesitic part of the sample. Most scoria clasts were sampled from the base of Minoan Unit A along with Minoan pumice sample SAN52. Li concentrations in pl of these scoria clasts vary considerably. High-Li pl have average concentrations of $19.4 - 42.9\,\mu\text{g/g}$, and low-Li pl have average concentrations of $0.3 - 5.0\,\mu\text{g/g}$.

et al., 1999). The dense matrix makes it also more difficult to lose lithium due to diffusion which would have been fast in melt (Chapter 5, Fig. 5.2).

Geochemically the high-Li plagioclase phenocrysts found in the clasts are similar to the plagioclase crystals found in the Minoan pumice. Anorthite rim contents are in the same range as those plagioclase crystals found in SAN52 suggesting that they might have mingled with a lithium-rich phase and have been in contact with that phase prior to the eruption. Traces of lithium enrichment were also found in the matrix of SAN53-2. A SIMS profile was run through the matrix adjacent to Pl-21. A single peak showed lithium concentrations of $\sim 61\,\mu\text{g/g}$. The mineral phase carrying this amount of lithium could be hornblende.

Extraordinary high lithium concentrations were analyzed at rim-matrix interfaces
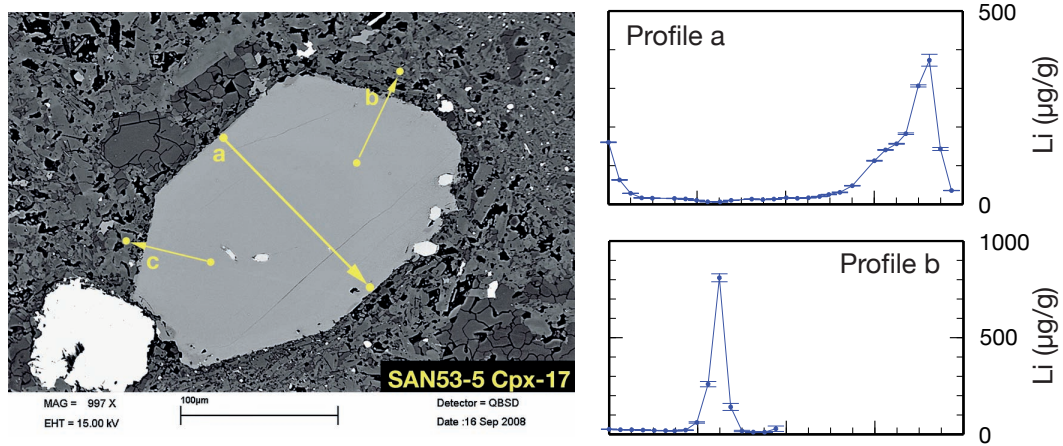
Fig. 7.7. High lithium concentrations along the grain boundaries of Cpx-17 (SAN53-5). Profile 'a' shows significant diffusion of lithium into the crystal. The crystal core shows lithium concentrations of $6\,\mu g/g$. Profile 'b' shows lithium concentrations of up to $800\,\mu g/g$ at the grain boundary.

of clinopyroxenes in sample SAN53-5, up to $800\,\mu g/g$ (Fig. 7.7). Diffusion into Cpx-17 is strong with core values of $6\,\mu g/g$ and rim values of $183\,\mu g/g$. As lithium diffusion in clinopyroxene is a lot slower compared to plagioclase (Giletti & Shanahan, 1997; Coogan *et al.*, 2005) this might be another indicator that crystals were mingled into a lithium-rich magma batch. Due to the faster diffusion of lithium in plagioclase it is not obvious when enrichment occurred, but the diffusion profile of Cpx-17 might be an indicator for enrichment prior to the eruption.

Next to samples with high-lithium phenocrysts only one other scoria clast, SAN53-3, was found with an interesting high lithium feature that may represent altered glass (palagonite). It can be seen in Fig. 7.8 as a crust like feature which builds an interface between non-altered glass and mineral debris. The debris carrying agent might have been a hot vapor phase that leached SiO_2, CaO, K_2O and Na_2O from the matrix glass and lead to an enrichment of lithium ($123\,\mu g/g$) and B ($53\,\mu g/g$) in the palagonitic crust. Mineral debris seems to be unaltered while Pl-6 was altered by the same phase; the darker parts of the crystal are enriched in sodium. Lithium increases up to $136\,\mu g/g$ at the end of Pl-6's SIMS profile, represented by the yellow arrow. Lithium diffusion into the crystal is well visible.
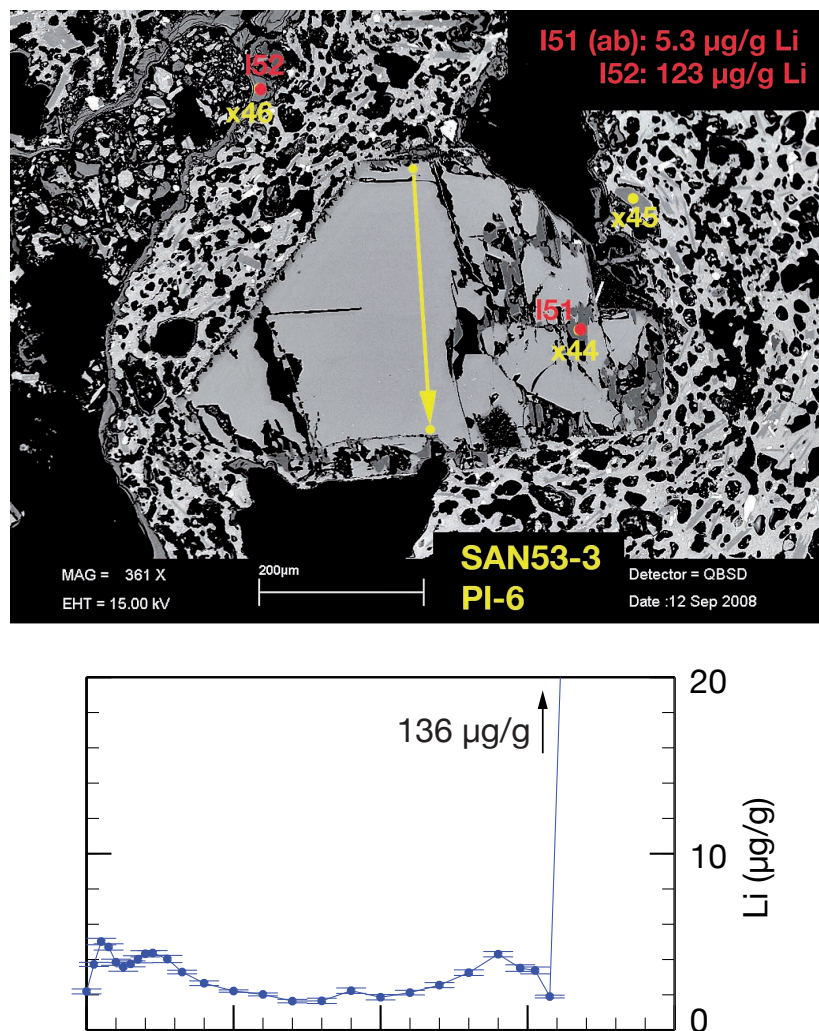
Fig. 7.8. The left side of the BSE image, especially the upper left shows a substance that formed a crust, which shields debris that may have been carried along by a vapor phase after deposition. 'x46' marks the EPMA spot which shows that the crust is depleted in SiO_2, CaO, K_2O and Na_2O and enriched in FeO and Al_2O_3 (see Excel Data Sets on CD for glass analyses). It is also enriched in Li ($123\,\mu g/g$) and B ($53\,\mu g/g$). In thin section the color of this phase is a dark brown, sometimes with yellowish or reddish hues. The crust is probably palagonite; except for the enrichment in Al_2O_3 the analysis is similar to those described in Stroncik & Schmincke (2002).

7.2.1. Time Constraints on the Contact with a Lithium-rich Phase

Significant enrichment of lithium in melt inclusions was reported from Mount St. Helens cryptodome samples (Blundy *et al.*, 2008; Kent *et al.*, 2007; Berlo *et al.*, 2004). The enrichment is supposed to have been caused by transfer of a lithium-rich vapor phase from deeper parts of the Mount St. Helens plumbing system and happened at the top of the main magma chamber where the separation of the vapor phase eventually occurred and lead to the formation of a Li-rich brine (Blundy *et al.*, 2008; Kent *et al.*, 2007). Berlo *et al.* (2004) explain that the longer a magma batch is stored at low pressures, the greater is the lithium enrichment of melt. When magma rises above the level of lithium enrichment, degassing leads to a loss of lithium in the melt but preserves the enrichment of lithium in melt inclusions and plagioclase phenocrysts. Mount St. Helens plagioclase inclusions show lithium contents as high as $\sim 270\,\mu g/g$, while quenched matrix glass kept lithium concentrations of $\sim 25 - 30\,\mu g/g$ (Blundy *et al.*, 2008).
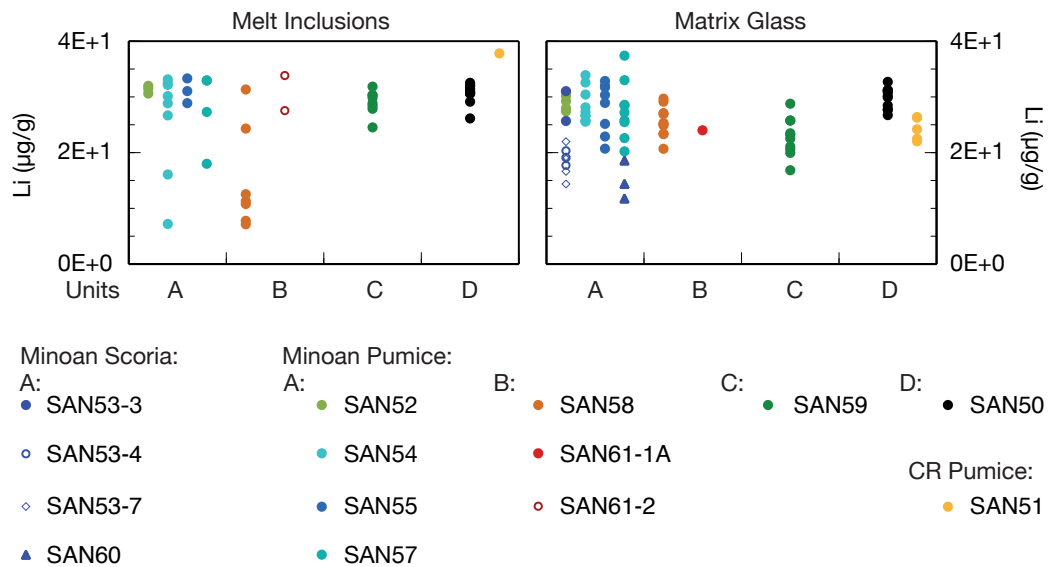
Fig. 7.9. A comparison of lithium concentrations in melt inclusions of phenocrysts and matrix glass in Minoan samples. Lithium concentrations in inclusions below $20\,\mu g/g$ seem to be affected by cracks running through the phenocryst and the inclusion. Lithium contents in inclusions and in matrix glass cover a similar range of concentrations. Matrix glass lithium contents of the mafic scoria clasts are lower in general. Matrix glass close to palagonitisized glass in SAN53-7 has lithium contents similar to those of the pumice matrix glass.

Lithium concentrations in melt inclusions of Minoan phenocrysts and matrix glass from Minoan samples draw a very different picture compared to Mount St. Helens (Fig. 7.9). Lithium concentrations in melt inclusions cover a broader range of $\sim 7 - 38 \, \mu g/g$ in all samples investigated. A closer investigation of melt inclusions revealed that especially those inclusions with lithium contents below $20 \, \mu g/g$ were affected by cracks (Fig. 7.10). The loss of lithium obviously occurred after deposition due to degassing as water contents were not affected. Escape of H_2O however was observed in melt inclusions of Mount St. Helens and attributed to rupturing of inclusions during ascent (Blundy *et al.*, 2008). Differences in water content of melt inclusions in Minoan phenocrysts suggest that degassing was already taking place prior to sealing of inclusions rather than being caused by rupturing, although this might also be the case for some inclusions.
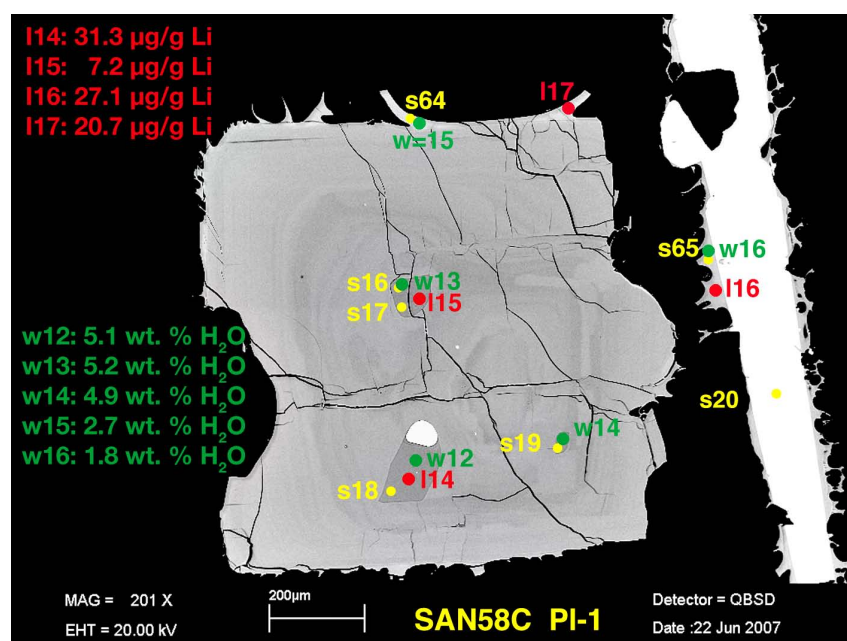
Fig. 7.10. Melt inclusions in Minoan plagioclase that are ruptured by cracks show decreased lithium concentrations below $20 \, \mu g/g$. Analysis 'l15' has a lithium concentration of $7.1 \, \mu g/g$. While lithium concentrations seem to be affected by cracks, water contents stay the same. Compare analysis 'w13' to 'w12', the latter was analyzed in a melt inclusion that did not rupture. This may indicate that lithium loss in inclusions happened after deposition. **Red:** SIMS analyses of Li. **Green:** SIMS analysis of H_2O. **Yellow:** EPMA analyses. All analyses can be found in the Electronic Appendix.

The contact of plagioclase grains with a lithium-rich phase must therefore have happened after sealing of the melt inclusions. Blundy *et al.* (2008) suggest that the sealing point for melt inclusions in Mount St. Helens plagioclase corresponds

closely to the onset of the event that lead to eruption. Cottrell *et al.* (1999), however, demonstrated a three stage development for the Minoan magma, where it first crystallized at $\sim 200\,\text{MPa}$ and $\sim 825\,°\text{C}$; it rose to $\sim 50\,\text{MPa}$ where it was heated to $\sim 885\,°\text{C}$ due to the intrusion of multiple batches of hotter, mafic magma. They argued that melt inclusions where trapped at higher pressures and lower temperatures, and that the low sulfur contents in inclusions of $112\,\mu\text{g/g}$ would support this assumption based on sulfur solubilities in silicate melt.

If the latter were the case, there would have been sufficient time for a lithium-rich phase to interact with the Minoan magma and pumice phenocrysts, so that despite of degassing or other distribution phenomena, all phenocrysts in the Minoan pumice should have elevated lithium concentrations. This leads to the assumption that the very short interaction between a lithium-rich phase and the Minoan pumice phenocrysts must have taken place very shortly prior to the eruption.

Decompression-driven Growth Strikingly similar lithium profiles with a short diffusion distance into the crystal and a slight loss of lithium that overprinted the profile at a distance of only a couple of micrometers towards the rim were documented by Genareau *et al.* (2009) and Genareau & Clarke (2010) from plagioclase of Soufrière Hills volcano, Montserrat by SIMS depth profiling. They state that lithium is a good indicator for decompression-induced growth, even better than anorthite content due to lithium's high diffusivity. The short growth zone is thought to have been caused by decompression. These growth zones correspond to the short distance of diffusive loss of lithium in Minoan plagioclase profiles (for example Fig. 5.7, Pl-9 of SAN59, Chapter 5).

Genareau *et al.* (2009) and Genareau & Clarke (2010) show that their growth zone is marked by an inflection point in the lithium profiles analyzed. Genareau & Clarke (2010) analyzed ten phenocrysts and detected average growth rates of $2.7\,\mu\text{m}$ corresponding to a growth rate of $G = 8.3 \times 10^{-8}\,\text{mm/s}$. Therefore it would take approximately 32 seconds to create a growth zone of $2.7\,\mu\text{m}$. As the rapid diffusion times for lithium based on Giletti & Shanahan (1997) would contradict their results and they also did not manage to simulate their observed lithium profiles based on the data of Giletti & Shanahan (1997), Genareau & Clarke (2010) argued that lithium diffusion is slower than reported by Giletti & Shanahan (1997).

Coogan (2011) was able to show that the lithium depth profiles analyzed by Genareau *et al.* (2009); Genareau & Clarke (2010) cannot have been caused by decompression-driven growth, but are diffusive. Coogan (2011) was able to model these profiles based on Giletti & Shanahan (1997). He reported that the profiles must have occurred over a time span of 1–12 seconds at magmatic temperatures but

also said that if diffusion profiles were gained at lower temperatures due to cooling, then it would take tens of minutes to gain these profiles at temperatures of $600\,^\circ$C.

Unfortunately, there is no data available on lithium content of plagioclase, plagioclase hosted melt inclusions or matrix glass from eruption products of Soufrière Hills volcano, nor were δ^7Li profiles analyzed. This makes it extremely difficult to compare the observed phenomena to those found in Minoan tephra.

Temperature Development of Minoan Pumice Clasts During Eruption For phenocrysts of the Minoan eruption it is still striking to observe the diffusion profiles in almost all phenocrysts analyzed. Due to temperature development in pumice clasts from the moment when magma gets erupted, there is still sufficient time for pumice clasts to react with a lithium-rich vapor phase in the eruption column to cause the observed diffusion phenomena (Tait *et al.*, 1998).

Unfortunately, little is known about the time frame of the Minoan eruption. It might have occurred within hours or could have lasted a couple of days. Products were also not erupted from a single vent but probably from multiple vents. The first vent during the first two phases (A and B) was probably close to the Kameni Line and might have developed into a fissure, while the vent of phase three (Minoan C) was probably closer to the Columbo Line and might also have developed into a fissure (see Chapter 2, Fig. 2.4 and Pfeiffer (2001)). It is also not entirely clear if and how sea water during phases $2-4$ has contributed to the observed phenomena.

A short contact with a lithium-rich phase inside the eruption column that lasted only a couple of seconds may have been possible but probably not for all samples. Tait *et al.* (1998) showed that Minoan pumice of the plinian fallout phase (Minoan A) with a 10 cm radius can keep a core temperature of $890\,^\circ$C for several hundreds of seconds counted from the moment when ejected from the vent. Especially larger pumice clasts had enough permeability to react with air which is shown by their pink interiors. These interiors developed due to oxidation when air entered the pumice. Fig. 6 in Tait *et al.* (1998) shows that even clasts with a hypothetical radius of 3 cm can keep a core temperature of $830\,^\circ$C for 2 minutes, while clasts of 10 cm can keep a core temperature of $830\,^\circ$C for 17 minutes.

Pumice clasts smaller than 5 cm do not show any signs of oxidation, meaning that they were too cold to be oxidized by air entering the pumice interior. Therefore smaller pumice clasts and rims of larger pumice clasts should not contain plagioclase affected by diffusion. The location of plagioclase inside the pumice or the size of pumice clasts was not considered prior to preparation of phenocrysts. At least one plagioclase crystal not affected by diffusion was found in sample SAN50A, Pl-1 (Minoan D), which could have been located closer to the rim of the pumice clast

analyzed.

Lithium Diffusion into Plagioclase after Emplacement of Deposits Fig. 7.11 is a temperature – time plot that shows how a change in temperature affects the diffusion time for a given profile with a diffusion length of $L = 20\,\mu m$ in plagioclase. On the right side in orange is the time frame for magmatic temperatures based on the plagioclase – liquid thermometer of Putirka (2008) and representing those temperatures when plagioclase in the Minoan pumice and Crystal-rich pumice last equilibrated with the melt.

The gray field in Fig. 7.11 shows the range of minimum welding temperatures for ignimbrites taken from Giordano *et al.* (2005). In this range of temperatures it would have taken minutes to hours to produce the observed profiles. As no welding was observed in the Minoan D ignimbrite the emplacement temperatures must have been below the minimum welding temperatures.

Emplacement temperatures (green field in Fig. 7.11) for Minoan deposits were gained from Bardot *et al.* (1996) and Druitt *et al.* (1999) and range from $150 - 350\,°C$ with Minoan A–C falling in the range of $150 - 250\,°C$ and Minoan D (ignimbrite) having emplacement temperatures of $300 - 350\,°C$. At these low temperatures the time required to get the observed Li profiles is between 1 month and several years. Li Diffusion in the matrix glass would be a couple orders of magnitude faster (see Fig. 5.2, Chapter 5).

For lithium diffusion to occur after emplacement, the deposit must keep its temperature for a significant period of time after deposition. Torres *et al.* (1996) were able to show that pyroclastic deposits from Mount Pinatubo kept elevated temperatures for many years. The ignimbrite deposited by the eruption of June 15, 1991 still had temperatures up to $390\,°C$ one meter below the surface of the deposit after 18 months.

Fossil fumaroles reported from the Minoan D ignimbrite by Druitt *et al.* (1989) support that at least the ignimbrite deposit kept higher temperatures for some time and that significant vapor flow took place through pipes. Some vapor flow must have also taken place in deposit Minoan A as supported by the palagonitization of glass in scoria clast SAN53-3 (Fig. 7.8). But vapor flow has obviously been minor because none of the other samples shows traces of alteration in matrix glass or phenocrysts phases.
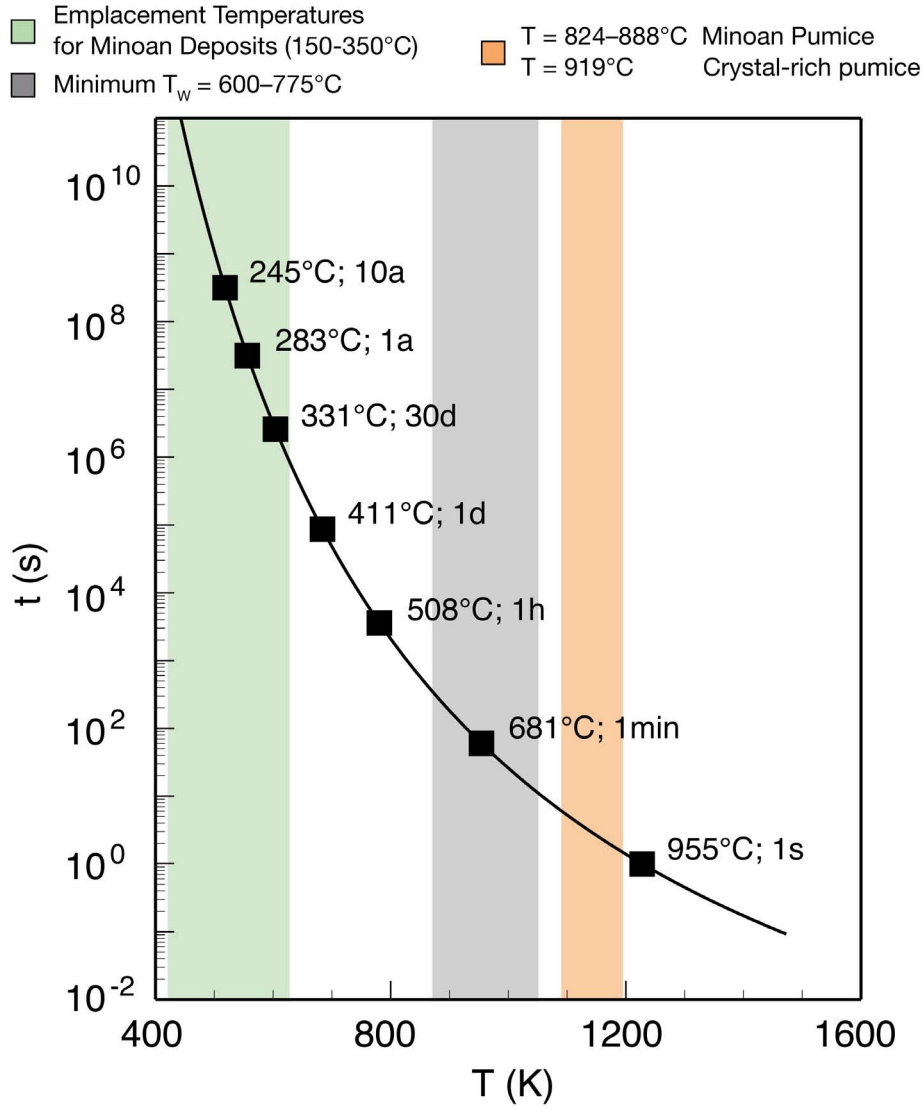
Fig. 7.11. Temperature – time diagram for a Li diffusion profile in a plagioclase with a length *L* of 20 μm. Based on the facts (no welding of the deposits) known for the Minoan eruption the profile could have been caused at magmatic conditions ($\sim 865\,°C$) or after deposition below $400\,°C$ (non-welded deposits, Druitt *et al.* (1999)). Emplacement temperatures are based on Bardot *et al.* (1996) and Druitt *et al.* (1999), temperatures for minimum welding were taken from Giordano *et al.* (2005). According to Thomas & Sparks (1992) welding requires temperatures above $585\,°C$.

Another characteristic feature of vapor flow dependent lithium diffusion into plagiocalse crystals along grain boundaries would be diffusion not only from crystal rims but also from syn-eruptive cracks. Diffusion of lithium from cracks into crystals is not observed in most cases. In the few cases where diffusion is visible from cracks, it is relatively weak, with more pronounced diffusion from cracks into crystal occurring only in the Crystal-rich pumice (see profiles in Chapter 5, Fig. 5.8).

One might argue that cracks were caused during preparation of the samples, especially hand crushing of pumice clasts, but it can actually be shown that most cracks were created before deposition and therefore during eruption. Cracks inside crystals almost never continue into the matrix clasts but are exclusively in phenocrysts ruling out crack development during preparation, as the pumice clasts still had been hot when rupturing had occurred.

A Model for the Observed Diffusion Profiles δ^7Li profiles revealed that the plagioclase phenocrysts had been in contact with a lithium-rich phase which had much higher lithium concentration than observed in matrix glass and melt inclusions. Based on the diffusion lengths the contact with the lithium-rich phase was short, typically < 12 s (Chapter 5, Table 5.1). Additionally, many plagioclase crystals show a decrease in Li very close to the rim. The diffusion of Li into the crystal from a Li-rich phase must have been followed by a reverse process: Li diffusion out of the crystal. As the initial diffusion profiles are still preserved a few µm away from the rim, the diffusion lenghts of the reverse diffusion are much shorter. Therefore the reverse diffusion must have lasted for an even shorter time or it must have taken place at lower temperatures than the initial diffusion. A valid model should reproduce these complex profiles. Since no significant inhomogeneities of Li were found in the matrix glass, it should also reproduce (nearly) constant Li concentrations therein.

The profiles observed can be reproduced with a two-step model, which was simulated using the *diff2* software (see Appendix A):

1. Diffusion from a high-lithium phase 'X' (e.g., a vapor phase) into melt and plagioclase at magmatic temperatures:

   At $860\,°$C the diffusivity of lithium in melt is $1.2 \times 10^{-10}\,\mathrm{m^2/s}$ and $3.0 \times 10^{-11}\,\mathrm{m^2/s}$ in plagioclase, which means that diffusion in melt and plagioclase is nearly equally fast. The lithium-rich phase 'X' for this model is assumed to be an infinite reservoir with a constant lithium concentration of $240\,\mathrm{µg/g}$, and the partitioning coefficients are assumed to be $D_{\mathrm{Li}}^{\mathrm{melt/X}} = 1$ and $D_{\mathrm{Li}}^{\mathrm{pl/X}} = 0.25$. The results are shown in the top half of Fig. 7.12. After $8\,$s the diffusion

lengths are $\sim 20\,\mu$m in plagioclase and $\sim 40\,\mu$m in the melt, and the δ^7Li profile in plagioclase has a minimum of $-26‰$. Since the melt—in opposite to the plagioclase crystals—can be percolated by phase 'X', it is justified to assume that at the end of step 1 the melt will have gained a high lithium concentration which will be distributed homogeneously.

Because of the temperature and the very short time span, step 1 must have taken place right before or in the first few seconds of the eruption.

2. Degassing and diffusion at $300\,°$C after deposition:

   At $300\,°$C the diffusivity of lithium is $1.3 \times 10^{-14}\,$m^2/s in glass and $7.8 \times 10^{-18}\,$m^2/s in plagioclase, which means that diffusion in glass is *much* faster than in plagioclase. The partitioning coefficient between plagioclase and glass is assumed to be $D_{\text{Li}}^{\text{pl/glass}} = 0.07$. This step was simulated as follows (see bottom half of Fig. 7.12): The glass degasses at $x = -100\,\mu$m; the degassing is simulated by a layer with a constant lithium concentration of $30\,\mu$g/g. The glass layer with an initial lithium concentration of $240\,\mu$g/g and a thickness of $100\,\mu$m is in contact with the plagioclase, which has the lithium profile gained in step 1. After 40 days the glass layer has lost most of its lithium and has reached a nearly homogeneous distribution of lithium, while the plagioclase has lost lithium only at its rim over a length of $\sim 10\,\mu$m. The δ^7Li minimum produced in step 1 is well preserved. The resulting complex concentration and δ^7Li profiles are very similar to the observed profiles. Please see, e.g., SAN59A Pl-9 in Fig. 5.12.

The high-lithium phase 'X' might be a vapor from deeper parts of the Minoan storage system (similar to vapor fluxes observed at Mt St. Helens by Berlo *et al.* (2004); Kent *et al.* (2007) and Blundy *et al.* (2008)) that entered the magma chamber prior to or at the onset of eruption and lead to the observed diffusion into plagioclase. After deposition lithium loss based on degassing was much faster in pumice glass compared to plagioclase at $300\,°$C. Therefore the contact with phase 'X' was not preserved in glass and only traceable in plagioclase through lithium isotopes. Loss of lithium due to degassing after emplacement may be common in pyroclastic deposits and was also postulated by Helbling-Marschall (2011) for ignimbrite deposits of Lesbos Island, Greece. The two-step model also shows that high $D_{\text{Li}}^{\text{pl/melt}} = 0.68$ (Chapter 6) are arbitrary. The high-lithium phase 'X' that lead to enrichment is gone, and the analyzed lithium concentration in pumice glass does not represent the concentration of lithium at magmatic temperatures but the concentration after emplacement and degassing at lower temperature.
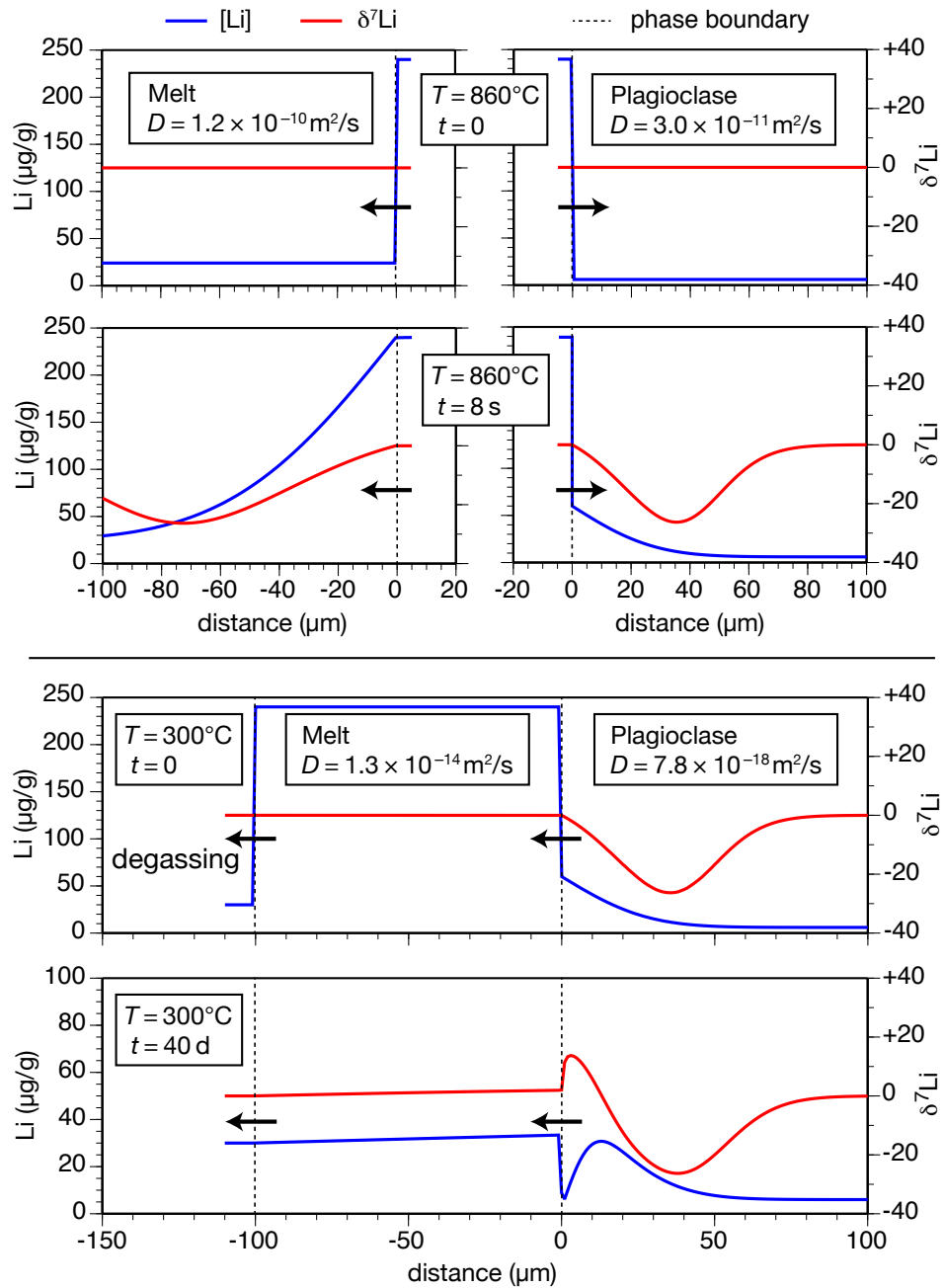
Fig. 7.12. A two-step model for the observed lithium diffusion profiles in plagioclase. Black arrows indicate the direction of diffusion. **First step:** Diffusion profiles for lithium concentration (blue) and δ^7Li (red) at 860 °C and 8 s. Diffusion into melt and into pl caused by contact to an infinite reservoir with constant concentration. Observed profiles are similar to the profiles observed in Pl-1 (SAN52A). **Second step:** Diffusion after deposition at T = 300 °C and 40 d. Lithium distribution in melt + degassing of melt leads to decrease of lithium in melt. Pl starts to equilibrate with melt, leading to observed lithium decrease at pl rim.

Degassing and the Influence of Water on Partition Coefficients   The presence of water is common during most magmatic processes. The effects of water on partition coefficients are not well understood but will certainly influence major and trace element activities (Fig. 7.13). Wood & Blundy (2002) state that the relative enthalpies of fusion ΔH_f of major and trace elements govern the increase or decrease of partition coefficients with the addition of water and developed two different models where $\Delta H_f^{\text{trace}} > \Delta H_f^{\text{major}}$ leads to an increase of D_{trace} with H_2O addition, and $\Delta H_f^{\text{trace}} < \Delta H_f^{\text{major}}$ leads to a decrease of D_{trace} with H_2O addition. They applied their model to REE in pyroxene and garnet. For this thesis it was unfortunately not possible to calculate ΔH_f for lithium and to study the effect that changing water content in the melt—for example by degassing of magma—may have on partition coefficients.

Fig. 7.13 which was taken from Wood & Blundy (2002) suggests that degassing of water will lead to an increase in the observed partition coefficients. Therefore it should be mentioned that abrupt degassing of water during the Minoan eruption may also cause a sudden increase in lithium partition coefficients between plagioclase and melt, maybe even driving partition coefficients to values of 1 and higher. This might be another possible explanation for the diffusion of lithium into plagioclase.
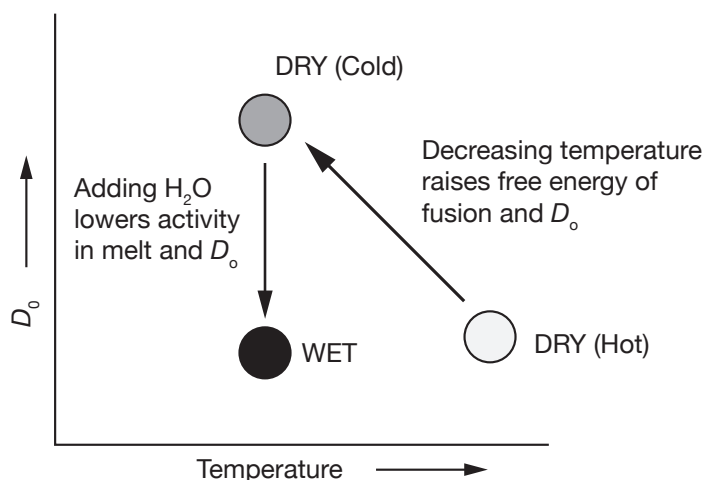
Fig. 7.13. The diagram shows the change in D_0 at dry and wet conditions and was taken from Wood & Blundy (2002).

Scoria Clasts   The high lithium contents of phenocrysts in scoria clasts, especially in SAN53-2, SAN53-5, SAN53-6 suggest late stage interaction with a lithium-rich

magma and intense mingling of pumice phenocrysts with this magma. Lithium diffused into these phenocrysts and could be retained in plagioclase much better after deposition due to the lack of a glassy matrix. These batches of lithium-rich magma stem from upmoving magma in the deeper parts of the storage system shortly before eruption. Degassing of the magma from deeper storage regions may have caused overpressure in the magma chamber—next to lithium enrichment of the magma body—leading to the onset of the Minoan eruption.

The origin of palagonitization in the matrix of SAN53-3 might be contributed to post-emplacement vapor fluxes.

The Crystal-rich Pumice   The Crystal-rich pumice described in this thesis is different from the Crystal-rich pumice described by Druitt *et al.* (1999) and Martin *et al.* (2010). The latter was exclusively sampled in a single layer in deposit Minoan A. The Crystal-rich pumice (SAN51) reported here was sampled from deposit Minoan D and therefore is part of the ignimbrite deposit like sample SAN50. Both differ in crystal content, with pumice clasts from SAN50 being more similar to the other deposits, Minoan A–C. An increase of crystals in the ignimbrite deposit was however reported from Druitt *et al.* (1989); Heiken & McCoy (1984); Druitt *et al.* (1999) and might be attributed to differences in eruption style during phase D. Differences in anorthite content of erupted plagioclase crystals in SAN51 can also be attributed to mingling during the eruption. As the ignimbrite was erupted during the last stage of the Minoan eruption it is also possible that crystals with higher anorthite content were entrained from a crystal mush zone at the bottom of the main magma chamber.

The Need for Further Investigation of Minoan Samples   Based on the results gained from this thesis there is still a need to further study the nature of lithium-rich source(s), e.g., vapor fluxes prior to eruptions and after emplacement. δ^7Li profiles were mainly measured from crystal rim into the the plagioclase. For future works δ^7Li profiles should also include cracks running through crystals as well as broken rim areas of crystals. If the onset of crack development could be determined properly, δ^7Li profiles might shed further light on the time frame of lithium diffusion phenomena. For a better consistency of the observed diffusion lengths in phenocrysts, crystals need to be properly oriented prior to analysis.

Of further interest should also be a thorough investigation of the matrix and phenocrysts of lithium-rich samples like SAN53-2, SAN53-5 and SAN53-6. What is the amount of lithium enriched clasts within deposit Minoan A compared to other scoria clasts? Can these clasts also be found in other Minoan deposits?

Traces of palagonitization were only discovered in SAN53-3. It is also of interest to study more scoria clasts showing traces of alteration in matrix glass.

What is the origin of scoria clast SAN53-1 which contains plagioclase phenocrysts with lithium concentrations below $1\,\mu g/g$? Are the low concentrations due to degassing?

8. Conclusions

Minoan plagioclase crystals were of great value for this thesis as both equilibrium and disequilibrium behavior were detected in single crystals.

Under equilibrium conditions lithium shows a negative correlation with anorthite content that was observed in all phenocrysts after purging data from diffusive overprints. Furthermore two distinct correlation trends were observed which made it possible to divide plagioclase phenocrysts into two groups:

1. Plagioclase crystals with a weak correlation trend and $\overline{X}_{An} < 0.60$.

2. Plagioclase crystals with a strong correlation trend and $\overline{X}_{An} > 0.60$.

It was possible to apply a physical model based on Blundy & Wood (1994) and a simple exponential model to the observed correlation trend. For plagioclase with $\overline{X}_{An} < 0.60 \ln K_D > -2.5$ was calculated while plagioclase with $\overline{X}_{An} > 0.60$ yielded $\ln K_D \leq -5$.

This phenomenon may have its origin in structural differences of plagioclase feldspar. The albite-anorthite feldspar series is not a continuous solid solution but defined by phase transitions and miscibility gaps. At magmatic temperatures and at approximately An_{55-60} the phase field of $C\overline{1}$ plagioclase feldspar is divided from the $I\overline{1}$ phase field by a phase transition line. Plagioclase crystals with $\overline{X}_{An} < 0.60$ plot in the $C\overline{1}$ phase field while plagioclase crystals with $\overline{X}_{An} > 0.60$ plot in the $I\overline{1}$ phase field (except one outlier). The difference in Si/Al ordering in both phase fields may have an important effect on the incorporation of lithium into the plagioclase crystal structure leading to the observed differences in $\ln K_D$.

Lithium disequilibrium in Minoan plagioclase phenocrysts is characterized by diffusion of lithium into the crystal on very short diffusion lengths L which hardly exceed $20-40\,\mu m$. These diffusion profiles are often overprinted by a diffusive loss of lithium from the crystal on a distance of a few μm. $\delta^7 Li$ profiles revealed that diffusion into the crystal was caused by a high lithium phase—probably a lithium-rich vapor. It was possible to recreate the observed lithium profiles by numerical diffusion modeling. Diffusion profiles were calculated using a two-stage approach, which yielded the following results:

1. Lithium diffusion into the crystal took place at magmatic temperatures of $\sim 860\,^{\circ}C$ prior to or during the eruption at time scales of seconds.

181

2. Diffusive loss of lithium took $\sim 40\,\mathrm{d}$ at $\sim 300\,^\circ\mathrm{C}$ and must have happened after emplacement due to degassing of lithium. Higher temperatures can be ruled out for the second profile as increased lithium diffusivity would have smoothed out the observed profiles in plagioclase.

If the results gained from diffusion modeling are correct, all partition coefficients with high values of up to 0.7 calculated from plagioclase rims with disequilibrium lithium concentrations and matrix glass are incorrect. The amount of lithium that is left in matrix glass does not represent the lithium concentration in melt at magmatic temperatures and after enrichment with a lithium-rich vapor. Due to its high diffusivity in glass at emplacement temperatures, lithium was lost from the pumice glass due to degassing. To gain partition coefficients at magnatic temperatures it might be better to calculate lithium partition coefficients between melt inclusions that were not influenced by cracks and adjacent plagioclase.

The results demonstrate that the use of lithium concentration and isotope ($\delta^7\mathrm{Li}$) profiles with high lateral resolution has the potential to trace lithium-rich vapor fluxes from deeper parts of volcanic plumbing systems even when there is no apparent lithium enrichment in matrix glass or melt inclusions. The low diffusivity of lithium in plagioclase at emplacement temperatures supports the idea of Coogan *et al.* (2005); Sonntag (2007) and Coogan (2011) to use lithium as a tracer for short time geologic processes such as cooling and degassing of volcanic deposits.

Bibliography

altamaresantorini.com (2011) www.altamaresantorini.com. `http://www.altamaresantorini.com/santorini-island-info.htm`

Altherr R, Siebel W (2002) I-Type plutonism in a continental back-arc setting: Miocene granitoids and monzonites from the central Aegean Sea, Greece. *Contributions to Mineralogy and Petrology* 143: 397–415

Altherr R, Okrusch M, Seidel E, Kreuzer H, Harre W, Lenz H, Wendt I, Wagner GA (1979) Geochronology of high-pressure rocks on Sifnos (Cyclades, Greece). *Contributions to Mineralogy and Petrology* 70: 245–255

Altherr R, Kreuzer H, Wendt I, Lenz H, Wagner G, Keller J, Harre W, Hoehndorf A (1982) A late Oligocene/early Miocene high temperature belt in the Attic-Cycladic crystalline complex (SE Pelagonian, Greece). *Geologisches Jahrbuch, Reihe E: Geophysik* 23: 97–164

Altherr R, Kreuzer H, Lenz H, Wendt I, Harre W, Dürr S (1994) Further evidence for a late Cretaceous low-pressure/high temperature terrane in the Cyclades, Greece. *Chemie der Erde* 54: 319–328

Anderson AT (1984) Probable relations between plagioclase zoning and magma dynamics, Fuego Volcano, Guatemala. *American Mineralogist* 69: 660–676

Antonopoulos J (1992) The great Minoan eruption of Thera volcano and the ensuing tsunami in the Greek Archipelago. *Natural Hazards* 5: 153–168

Bardot L, Thomas R, McClelland E (1996) *Palaeomagnetism and Tectonics of the Mediterranean Region*, vol. 105, chap. Emplacement temperatures of pyroclastic deposits on Santorini deduced from palaeomagnetic measurements: constraints on eruption mechanisms, 345–358. Geological Society of London Special Publication

Bebout GE, Ryan JG, Leeman WP, Bebout AE (1999) Fractionation of trace elements by subduction-zone metamorphism - effect of convergent-margin thermal evolution. *Earth and Planetary Science Letters* 171: 63–81

Bédard JH (2006) Trace element partitioning in plagioclase feldspar. *Geochimica et Cosmochimica Acta* 70: 3717–3742

Berlo K, Blundy J, Turner S, Chashman K, Hawkesworth C, Black S (2004) Geochemical Precursors to Volcanic Activity at Mount St. Helens, USA. *Science* 306: 1167–1169

Berlo K, Gardner JE, Blundy JD (2010) *Timescales of Magmatic Processes - From Core to Atmosphere*, chap. 11 Timescales of Magma Degassing, 231–255. Wiley-Blackwell

Bindeman IN, Davis AM, Drake MJ (1998) Ion microprobe study of plagioclase-basalt partition experiments at natural concentration levels of trace elements. *Geochimica et Cosmochimica Acta* 62: 1175–1193

Blundy J, Wood B (1994) Prediction of crystal-melt partition coefficients from elastic moduli. *Nature* 372: 452–454

Blundy J, Wood B (2003) Partitioning of trace elements between crystals and melts. *Earth and Planetary Science Letters* 210: 383–397

Blundy J, Chashman KV, Berlo K (2008) *A Volcano Rekindled: The Renewed Eruption of Mount St. Helens, 2004-2006*, chap. 33: Evolving Magma Storage Conditions Beneath Mount St. Helens Inferred from Chemical Variations in Melt Inclusions from the 1980-1986 and Current (2004-2006) Eruptions, 755–790. U.S. Geological Survey

Blundy JD, Dalton J (2000) Experimental comparison of trace element partitioning between clinopyroxene and melt in carbonate and silicate systems, and implications for mantle metasomatism. *Contributions to Mineralogy and Petrology* 139: 356–371

Blundy JD, Wood BJ (1991) Crystal-chemical controls on the partitioning of Sr and Ba between plagioclase feldspar, silicate melts, and hydrothermal solutions. *Geochimica et Cosmochimica Acta* 55: 193–209

Blundy JD, Robinson JAC, Wood BJ (1998) Heavy REE are compatible in clinopyroxene on the spinell lherzolite solidus. *Earth and Planetary Science Letters* 160: 493–504

Blundy JD, Cashman KV, Humphreys MCS (2006) Magma heating by decompression-driven crystallization beneath andesite volcanoes. *Nature* 443: 76–80

Bond A, Sparks RSJ (1976) The Minoan eruption of Santorini, Greece. *Journal of the Geological Society* 132: 1–16

Bottinga Y, Kudo A, Weill D (1966) Some observations on oscillatory zoning and crystallization of magmatic plagioclase. *American Mineralogist* 51: 792–806

Brenan JM, Neroda E, Lindstrom CC, Shaw HF, Ryerson FJ, Phinney DL (1998a) Behavior of boron, beryllium and lithium during melting and crystallization: constraints from mineral-melt partitioning experiments. *Geochimica et Cosmochimica Acta* 62: 2129–2141

Brice JC (1975) Some thermodynamic aspects of the growth of strained crystals. *Journal of Crystal Growth* 28: 249–253

Bröcker M, Franz L (1998) Rb-Sr isotope studies on Tinos Island (Cyclades, Greece): additional time constraints for metamorphism, extent of infiltration-controlled overprinting and deformational activity. *Geological Magazine* 135: 369–382

Bröcker M, Kreuzer H, Matthews A, Okrusch M (1993) ^{40}Ar/^{39}Ar and oxygen isotope studies of polymetamorphism from Tinos island, Cycladic blueschist belt, Greece. *Journal of Metamorphic Geology* 11: 223–240

Cabato EJA (2006) *Abundances of Lithium, Beryllium and Boron in the Phenocrysts from Santorini Volcano (Greece): Implications on Magma Genesis and Eruption Mechanisms*. Dr. rer. nat. thesis, University of Heidelberg, Germany

Callender G (1999) *The Minoans and the Mycenaeans: Aegean Society in the Bronze Age*. Oxford University Press

Carpenter MA (1985) *Reviews in Mineralogy: Microscopic to Macroscopic: Atomic Environments to Mineral Thermodynamics*, chap. Order-disorder transformations in mineral solid solutions, 187–223. 14, Mineralogical Society of America

Carpenter MA (1986) Experimental Delineation of the $e \rightleftharpoons I\bar{1}$ and $e \rightleftharpoons C\bar{1}$ Transformations in Intermediate Plagioclase Feldspars. *Physics and Chemistry of Minerals* 13: 119–139

Carpenter MA (1988) *Physical Properties and Thermodynamic Behaviour of Minerals*, chap. Thermochemistry of Aluminium/Silicon Ordering In Feldspar Minerals, 265–315. D. Reidel Publishing Company

Carpenter MA, McConnell JD (1984) Experimental delineation of the $C\bar{1} \rightleftharpoons I\bar{1}$ transformation in intermediate plagioclase feldspars. *American Mineralogist* 69: 112–121

Chacko T, Cole DR, Horita J (2001) *Stable Isotope Geochemistry*, vol. Bd. 1, chap. Equilibrium oxygen, hydrogen and carbon isotope fractionation factors applicable to geologic systems, 1–81. Mineralogical Society of America

Chakraborty S (2008) Diffusion in Solid Silicates: A Tool to Track Timescales of Processes Comes of Age. *Annual Reviews of Earth and Planetary Sciences* 36: 90–153

Chaussidon M, Jambon A (1994) Boron content and isotopic composition of tourmalines from the 3.8-Ga-old Isua supracrustals, West Greenland: implications on the δ^{11}B value of early Archean seawater. *Chemical Geology* 136: 171–180

Chen J (1999) *Encyclopedia of Geochemistry*, chap. Lithium: Element and Geochemistry, 369. Kluwer Academic Publishers

Cherniak DJ, Watson EB (1994) A study of strontium diffusion in plagioclase using Rutherford backscattering spectroscopy. *Geochimica et Cosmochimica Acta* 58: 5179–5190

Chertkoff DG, Gardner JE (2004) Nature and timing of magma interactions before, during and after the caldera-forming eruption of Volcán Ceboruco, Mexico. *Contributions to Mineralogy and Petrology* 146: 715–735

Coogan LA (2011) Preliminary experimental determination of the partitioning of lithium between plagioclase crystals of different anorthite contents. *Lithos* 125: 711–715

Coogan LA, Kasemann SA, Chakraborty S (2005) Rates of hydrothermal cooling of new oceanic upper crust derived from lithium-geospeedometry. *Earth and Planetary Science Letters* 240: 415–424

Coombs ML, Eichelberger JC, Rutherford MJ (2000) Magma storage and mixing conditions for the 1953-1974 eruptions of Southwest Trident volcano, Katmai National Park, Alaska. *Contributions to Mineralogy and Petrology* 140: 99–118

Costa F, Dungan M (2005) Short time scales of magmatic assimilation from diffusion modeling of multiple elements in olivine. *Geology* 33: 837–840

Costa F, Morgan D (2010) *Timescales of Magmatic Processes - From Core to Atmosphere*, chap. 7 Time Constraints from Chemical Equilibration in Magmatic Crystals, 125–159. Wiley-Blackwell

Costa F, Singer B (2002) Evolution of the Holocene Dacite and Compositionally Zoned Magma, Volcán San Pedro, Southern Volcanic Zone, Chile. *Journal of Petrology* 42: 1571–1593

Costa F, Chakraborty S, Dohmen R (2003) Diffusion coupling between trace and major elements and a model for calculation of magma residence times using plagioclase. *Geochimica et Cosmochimica Acta* 67: 2189–2200

Cottrell E, Gardner JE, Rutherford MJ (1999) Petrologic and experimental evidence for the movement and heating of the pre-eruptive Minoan rhyodacite (Santorini, Greece). *Contributions to Mineralogy and Petrology* 135: 315–331

Crabtree SM, Lange RA (2011) Complex Phenocryst Textures and Zoning Patterns in Andesites and Dacites: Evidence of Degassing-Induced Rapid Crystallization? *Journal of Petrology* 52: 3–38

Crank J (1975) *The Mathematics of Diffusion*. Oxford Science

Cunningham GJ, Henderson P, Lowry RK, Nolan J, Reed SJB, Long JVP (1983) Lithium diffusion in silicate melts. *Earth and Planetary Science Letters* 65: 203–205

Davidson JP, De Silva S (1999) *Encyclopedia of Volcanoes*, chap. Explosive Volcanism: Composite Volcanoes. Academic Press

Davidson JP, Tepley III FJ (1997) Recharge in Volcanic Systems: Evidence from Isotope Profiles of Phenocrysts. *Science* 275: 826–829

Domanik KJ, Hervig RL, Peacock SM (1993) Beryllium and boron in subduction zone minerals: An ion microprobe study. *Geochimica et Cosmochimica Acta* 57: 4997–5010

Druitt TH, Francaviglia V (1992) Caldera formation on Santorini and the physiography of the islands in the late Bronze Age. *Bulletin of Volcanology* 54: 484–493

Druitt TH, Mellors, Pyle DM, Sparks RSJ (1989) Explosive volcanism on Santorini, Greece. *Geological Magazine* 126: 95–126

Druitt TH, Edwards L, Mellors RM, Pyle DM, Sparks RSJ, Lanphere M, Davies M, Barriero B (1999) *Santorini Volcano*. 165 pp., The Geological Society

Dürr S (1986) *Geologie von Griechenland*, chap. Das Attisch-Kykladische Kristallin. Jacobshagen, V.

Dürr S, Altherr R, Keller J, Okrusch M, Seidel E (1978) The median Aegean crystalline belt: stratigraphy, structure, metamorphism, magmatism, Alps, Appennines, Hellenides. In: *Inter-union Commission on Geodynamics Scientific report*, vol. 38 of *537-564*, Closs, H. and Roeder, D. and Schmidt, K.

Dyar MD, Wiedenbeck M, Robertson D, Cross LR, Delaney JS, Ferguson K, Francis CA, Grew ES, Guidotti CV, Hervig RL, Hughes JM, Husler J, Leeman W, McGuire AV, Rhede D, Rothe H, Paul RL, Richards L, Yates M (2001) Reference minerals for the microanalysis of light elements. *Geostandards Newsletter: The Journal of Geostandards and Geoanalysis* 25: 441–463

Eichelberger JC (1978) Andesitic volcanism and crustal evolution. *Nature* 275: 21–27

Evensen JM, London D (2002) Experimental silicate mineral/melt partition coefficients for beryllium and the crustal Be cycle from migmatite to pegmatite. *Geochimica et Cosmochimica Acta* 66: 2239–2265

Evensen JM, London D (2003) Experimental partitioning of Be, Cs and other trace elements between cordierite and felsic melt, and the chemical signature of S-type granite. *Contributions to Mineralogy and Petrology* 144: 739–757

Faccenna C, Jolivet L, Piromallo C, Morelli A (2003) Subduction and the depth of convection in the Mediterranean mantle. *Journal of Geophysical Research* 108: 2099–2112

Flesch GD, Anderson AR, Svec HJ (1973) A Secondary Isotopic Standard For ^{6}Li/^{7}Li Determinations. *International Journal of Mass Spectrometry and Ion Physics* 12: 265–272

Foell H (2011) Einführung in die Materialwissenschaft I. `http://www.tf.uni-kiel.de/matwis/amat/`

Fouqué F (1879) *Santorin et ses éruptions*. Masson

Friedrich WL, Kromer BK, Friedrich M, Heinemeier J, Pfeiffer T, Talamo S (2006) Santorini Eruption Radiocarbon Dated to 1627-1600 B.C. *Science* 312: 548

Fytikas M, Marinelli G (1976) Geology and geothermics of the island of Milos (Greece). *Proceedings of Geothermal Energy* 1: 516–524

Fytikas M, Mazzuoli P, Peccerillo A, Villari L (1984) Tertiary to Quaternary evolution of volcanism in the Aegean region. *The Geological Evolution of the Eastern Mediterranean, Special Publications* 17: 687–699

Fytikas M, Kolios N, Vougioukalakis G (1990a) Post-Minoan volcanic activity of the Santorini volcano. Volcanic hazard and risk, forecasting possibilites. In: Hardy DA (ed.) *Thera and the Aegean World III*, chap. 2, 183–198, The Thera Foundation

Genareau K, Clarke AB (2010) *In situ* measurements of plagioclase growth using SIMS depth profiles of ^{7}Li/^{30}Si: A means to acquire crystallization rates during short-duration decompression events. *American Mineralogist* 95: 592–601

Genareau K, Clarke AB, Hervig RL (2009) New insight into explosive volcanic eruptions: Connecting crystal-scale chemical changes with conduit-scale dynamics. *Geology* 37: 367–370

Ghiorso MS, Sack RO (1991) Fe-Ti oxide geothermometry: thermodynamic formulation and the estimation of intensive variables in silicic magmas. *Contributions to Mineralogy and Petrology* 108: 485–510

Giletti BJ, Casserly JED (1994) Strontium diffusion kinetics in plagioclase feldspars. *Geochimica et Cosmochimica Acta* 58: 3785–3793

Giletti BJ, Shanahan TM (1997) Alkali diffusion in plagioclase feldspar. *Chemical Geology* 139: 3–20

Ginibre C, Wörner G, Kronz A (2002) Minor- and trace element zoning in plagioclase: implications for magma chamber processes at Parinacota volcano, northern Chile. *Contributions to Mineralogy and Petrology* 143: 300–315

Giordano D, Nichols ARL, Dingwell DB (2005) Glass transition temperatures of natural hydrous melts: a relationship with shear viscosity and implications for the welding process. *Journal of Volcanology and Geothermal Research* 142: 105–118

greeka.com (2011) www.greeka.com. `http://www.greeka.com/cyclades/santorini/santorini-map.htm`

Grove TH, Baker MB, Kinzler RJ (1984) Coupled CaAl-NaSi diffusion in plagioclase feldpsar: Experiments and applications to cooling rate speedometry. *Geochimica et Cosmochimica Acta* 48: 2113–2121

Hammer CU, Clausen HB, Friedrich WL, Tauber H (1987) The Minoan eruption of Santorini in Greece dated to 1645 B. C. *Nature* 328: 517–519

Hawthorne FC, Huminicki DMC (2002) *Reviews in Mineralogy*, chap. The crystal chemistry of beryllium, 333–403. 50, Mineralogical Society of America

Heiken G, McCoy F (1990) Precursory activity to the Minoan eruption, Thera, Cyclades, Greece. In: *Thera and the Aegean World III*, The Thera Foundation

Heiken G, McCoy FJ (1984) Caldera development during the Minoan eruption, Thira, Cyclades, Greece. *Journal of Geophysical Research* 89: 8441–8462

Helbling-Marschall AH (2011) *Lithium, Beryllium and Boron in high-K Rhyolites from Lesbos Island, Greece*. Dr. rer. nat. thesis, Ruprecht-Karls-Universität Heidelberg

van Hinsbergen DJJ, Hafkenscheid E, Spakman W, Meulenkamp JE, Wortel R (2005) Nappe stacking resulting from subduction of oceanic and continental lithosphere below Greece. *Geology* 33: 325–28

Hoefs J (2009) *Stable Isotope Geochemistry*. Springer-Verlag, 6 edn.

Holland T, Powell R (1992) Plagioclase feldspars: Activity-composition relations based upon Darken's quadratic formalism and Landau theory. *American Mineralogist* 77: 53–61

Homma VF (1932) Über das Ergebnis von Messungen an zonaren Plagioklasen aus Andesiten mit Hilfe des Universaldrehtisches. *Schweizerische Mineralogische und Petrographische Mitteilungen* 12: 345–352

Huchon P, Lybéris N, Angelier J, Le Pichon X, Renard V (1982) Tectonics of the Hellenic trench: A synthesis of sea-beam and submersible observations. *Tectonophysics* 86: 69–74

Huijsmans JPP, Barton M (1989) Polybaric Geochemical Evolution of Two Shield Volcanoes from Santorini, Aegean Sea, Greece: Evidence for Zoned Magma Chambers from Cyclic Compositional Variations. *Journal of Petrology* 30: 583–625

190

Humphreys MCS, Blundy JD, Sparks RSJ (2006) Magma Evolution and Open-System Processes at Shiveluch Volcano: Insights from Phenocryst Zoning. *Journal of Petrology* 47: 2303–2334

Innocenti F, Manetti P, Peccerillo A, Poli G (1979) Inner arc volcanism in NW Aegean arc, geochemical and geochronological data. *Neues Jahrbuch für Mineralogie* 4: 145–158

Innocenti F, Manetti P, Peccerillo A, Poli G (1981) South Aegean volcanic arc: geochemical variations and geotectonic implications. *Bulletin of Volcanology* 44: 377–391

Ishikawa T, Nakamura E (1994) Origin of the slab component in arc lavas from across-arc variation of B and Pb isotopes. *Nature* 370: 205–208

Jackson J (1994) Active tectonics of the Aegean region. *Annual Reviews of Earth and Planetary Sciences* 22: 239–271

Jambon A, Semet MP (1978) Lithium Diffusion In Silicate Glasses Of Albite, Orthoclase, And Obsidian Composition: An Ion-Microprobe Determination. *Earth and Planetary Science Letters* 37: 445–450

Jochum KP, Willbold M, Raczek I, Stoll B, Herwig K (2005) Chemical characterisation of the USGS reference glasses GSA-1G, GSC-1G, GSD-1G, GSE-1G, BCR-2G, BHVO-2G and BIR-1G using EPMA, ID-TIMS, ID-ICPMS and LA-ICPMS. *Geostandards and Geoanalytical Research* 29: 285–302

Jochum KP, Wilson SA, Abouchami W, Amini M, Chmeleff J, Eisenhauer A, Hegner E, Iaccheri LM, Kieffer B, Krause J, McDonough WF, Mertz-Kraus R, Raczek I, Rudnick RL, Scholz D, Steinhoefel G, Stoll B, Stracke A, Tonarini S, Weis U, Woodhead JD (2011) GSD-1G and MPI-DING Reference Glasses for In Situ and Bulk Isotopic Determination. *Geostandards and Geoanalytical Research* 35: 193–226

Kahl M, Chakraborty S, Costa F, Pompilio M (2011) Dynamic plumbing system beneath volcanoes revealed by kintetic modeling, and the connection to monitoring data: An example from Mt. Etna. *Earth and Planetary Science Letters* 308: 11–22

Kaliwoda M, Marschall HR, Marks MAW, Ludwig T, Altherr R, Markl G (2011) Boron and boron isotope systematics in the peralkaline Ilímaussaq intrusion

(South Greenland) and its granitic country rocks: A record of magmatic and hydrothermal processes. *Lithos* 125: 51–64

Kent AJR, Blundy J, Cashman KV, Cooper KM, Donnelly C, Pallister JS, Reagan M, Rowe MC, Thornber CR (2007) Vapor transfer prior to the October 2004 eruption of Mount St. Helens, Washington. *Geology* 35: 231–234

Kessel R, Schmidt MW, Ulmer P, Pettke T (2005) Trace element signature of subduction-zone fluids, melts and supercritical liquids at 120-180 km depth. *Nature* 437: 724–727

Klein C (2002) *Mineral Science*. John Wiley and Sons, Inc.

Klug C, Cashman KV, Bacon CR (2002) Structure and physical characteristics of pumice from the climactic eruption of Mount Mazama/Crater Lake), Oregon. *Bulletin of Volcanology* 64: 486–501

Kuritani T (1998) Boundary Layer Crystallization in a Basaltic Magma Chamber: Evidence from Rishiri Volcano, Northern Japan. *Journal of Petrology* 39: 1619–1640

Kuscu GG, Floyd PA (2001) Mineral compositional and textural evidence for magma mingling in the Saraykent volcanics. *Lithos* 56: 207–230

Lamoreaux PE (1995) Worldwide environmental impacts from the eruption of Thera. *Environmental Geology* 26: 172–181

Loomis TP, Welber PW (1982) Crystallization Processes in the Rocky Hill Granodiorite Pluton, California: An Interpretation Based on Compositional Zoning of Plagioclase. *Contributions to Mineralogy and Petrology* 81: 230–239

Ludwig T, Stalder R (2007) A new method to eliminate the influence of *in situ* contamination in SIMS analysis of hydrogen. *Journal of Analytical Atomic Spectrometry* 22: 1415–1419

Luhr JF (2000) The geology and petrology of Volcán San Juan (Nayarit, México) and the compositionally zoned Tepic Pumice. *Journal of Volcanology and Geothermal Research* 95: 109–156

Luhr JF, Carmichael ISE (1980) Colima Volcanic Complex, Mexico. 1. Post-caldera andesites from Volcán Colima. *Contributions to Mineralogy and Petrology* 71: 343–373

Makris J (1978) The crust and upper mantle of the Aegean region from deep seismic soundings. *Tectonophysics* 46: 269–284

Manning S, Ramsey CB, Kutschera W, Higham T, Kromer BK, Steier P, Wild EM (2006) Chronology for the Aegean Late Bronze Age 1700-1400 B.C. *Science* 312: 565–569

Marchev P, Raicheva R, Downes H, Vaselli O, Chiaradia M, Moritz R (2004) Compositional diversity of Eocene-Oligocene basaltic magmatism in the Eastern Rhodopes, SE Bulgaria: implications for genesis and tectonic setting. *Tectonophysics* 393: 301–28

Marinatos S (1939) The volcanic destruction of Minoan Crete. *Antiquity* 13: 425–439

Marschall H, Ludwig T (2004) The low-boron contest: minimising surface contamination and analysing boron concentrations at the ng/g-level by secondary ion mass spectrometry. *Mineralogy and Petrology* 81

Marschall HR, Altherr R, Rüpke L (2007) Squeezing out the slab - modelling the release of Li, Be and B during progressive high-pressure metamorphism. *Chemical Geology* 239: 323–335

Martin VM, Holness MB, Pyle DM (2006) Textural analysis of magmatic enclaves from the Kameni Islands, Santorini, Greece. *Journal of Volcanology and Geothermal Research* 154: 89–102

Martin VM, Davidson J, Morgan D, Jerram DA (2010) Using the Sr isotope compositions of feldspars and glass to distinguish magma system components and dynamics. *Geology* 38: 539–542

McKenzie D (1970) Plate tectonics of the Mediterranean region. *Nature* 226: 239–243

McKenzie D (1978) Active tectonics of the Alpine-Himalayan belt: the Aegean Sea and surrounding regions. *Geophysical Journal of the Royal Astronomy Society* 55: 217–254

McLaren AC, Marshall DB (1974) Transmission Electron Microscope Study of the Domain Structures Associated with *b*-, *c*-, *d*-, *e*- and *f*-Reflections in Plagioclase Feldspars. *Contributions to Mineralogy and Petrology* 44: 237–249

Mehrer H (2007) *Diffusion in Solids*. Springer-Verlag

Michaud V, Clocchiatti R, Sbrana S (2000) The Minoan and post-Minoan eruptions, Santorini (Greece), in the light of melt inclusions: chlorine and sulphur behaviour. *Journal of Volcanology and Geothermal Research* 99: 195–214

Mittlefehldt DW (1999) *Encyclopedia of Geochemistry*, chap. Magnesium, 379. Kluwer Academic Publishers

Nakamura M, Shimakita S (1997) Kinetic constraints on the mode of magma mixing and ascent in the 1991 Unzen eruption. In: *Proc Unzen International Workshop: Decade Volcano and Scientific Drilling*, 83–85

Nelson ST, Montana A (1992) Sieve-textured plagioclase in volcanic rocks produced by rapid decompression. *American Mineralogist* 77: 1242–1249

Nicholls IA (1971) Petrology of Santorini Volcano, Cyclades, Greece. *Journal of Petrology* 12: 67–119

Okay AI, Kelley SP (1994) Tectonic setting, petrology and geochronology of jadeite + glaucophane and chloritoid + glaucophane schists from north-west Turkey. *Journal of Metamorphic Geology* 12: 455–466

Olsher U, Izatt RM, Bradshaw JS, Dalley NK (1991) Coordination chemistry of lithium ion: a crystal and molecular structure review. *Chemical Reviews* 91: 137–164

Orville PM (1972) Plagioclase Cation Exchange Equilibria With Aqueous Chloride Solution: Results at 700 °C and 2000 Bars In The Presence Of Quartz. *American Journal of Science* 272: 234–272

Palmer MR, Swihart GH (2002) *Boron: mineralogy, petrology and geochemistry*, vol. Bd. 33, chap. Boron isotope geochemistry: an overview, 709–744. Mineralogical Society of America

Papazachos BC, Panagiotopoulos DG (1993) Normal faults associated with volcanic activity and deep rupture zones in the southern Aegean volcanic arc. *Tectonophysics* 220: 301–308

Pareschi M M T Favalli, Boschi E (2006) Impact of the Minoan tsunami of Santorini: Simulated scenarios in the eastern Mediterranean. *Geophysical Research Letters* 33

Parkinson I, Hammond S, James R, Rogers N (2007) High-temperature lithium isotope fractionation: Insights from lithium isotope diffusion in magmatic systems. *Earth and Planetary Science Letters* 257: 609–621

Parsons I (2010) Feldspars defined and described: a pair of posters published by the Mineralogical Society. Sources and supporting information. *Mineralogical Magazine* 74: 529–551

Pe-Piper G, Piper DJW (2002) *The Igneous Rocks of Greece: The Anatomy of an Orogen*. Berlin: Gebrüder Borntraeger

Pearce NJG, Perkins WT, Westgate JA, Gorton MP, Jackson SE, Neal CR, Chenery SP (1997) A compilation of new and published major and trace element data for NIST SRM 610 and NIST SRM 612 glass reference materials. *Geostandards Newsletter* 21: 115–144

Pearce TH, Russel JK, I W (1987) Laser-interference and Nomarski interference imaging of zoning profiles in plagioclase phenocrysts from the May 18, 1980, eruption of Mount St. Helens, Washington. *American Mineralogist* 72: 1131–1143

Pfeiffer T (2001) Vent development during the Minoan eruption (1640 BC) of Santorini, Greece, as suggested by ballistic blocks. *Journal of Volcanology and Geothermal Research* 106: 229–242

Pichler H, Friedrich WL (1980) Mechanism of the Minoan eruption of Santorini. In: *Thera and the Aegean World II*, The Thera Foundation

Pichler H, Pichler T (2007) *Vulkangebiete der Erde*. Elsevier - Spektrum Akademischer Verlag

Pouchou JL, Pichoir F (1984) A new model for quantitative analyses. I. Application to the analysis of homogeneous samples. *La Recherche Aérospatiale* 3: 13–38

Pouchou JL, Pichoir F (1985) PAP correction procedure for improved quantitative microanalysis. *Microbeam Analysis* 104–106

Price RC, Gamble JA, Smith IEM, Stewart RB, Eggins S, Wright IC (2005) An integrated model for the temporal evolution of andesites and rhyolites and crustal development in New Zealand's North Island. *Journal of Volcanology and Geothermal Research* 140: 1–24

Putirka KD (2008) *Minerals, Inclusions and Volcanic Processes*, vol. 69, chap. Thermometers and Barometers for Volcanic Systems, 61–120. Mineralogical Society of America

Pyle DM (1997) The global impact of the Minoan eruption of Santorini, Greece. *Environmental Geology* 30: 59–61

von Quadt A, Moritz R, Peytcheva I, Heinrich CA (2005) Geochronology and geodynamics of Late Cretaceous magmatism and Cu-Au mineralization in the Panagyurishte region of the Apuseni-Banat-Timok-Srednogorie belt, Bulgaria. *Ore Geology Reviews* 27: 95–126

Reck H (1936) *Santorin; Der Werdegang eines Inselvulkans und sein Ausbruch 1925-28*. Dietrich Reimer

Reubi O, Blundy J (2008) Assimilation of plutonic roots, formation of high-K 'exotic' melt inclusions and genesis of andesitic magmas at Volcán de Colima, Mexico. *Journal of Petrology* 49: 2221–2243

Richter F, Davis A, DePaolo D, Watson E (2003) Isotope fractionation by chemical diffusion between molten basalt and rhyolite. *Geochimica et Cosmochimica Acta* 67: 3905–3923

Ricou LE, Burg JP, Godfriaux I, Ivanov Z (1998) Rhodope and Vardar: the metamorphic and the olistostromic paired belts related to the Cretaceous subduction under Europe. *Geodinamica Acta* 11: 285–309

Ring U, Glodny J, Will T, Thomson S (2010) The Hellenic Subduction System: High-Pressure Metamorphism, Exhumation, Normal Faulting, and Large-Scale Extension. *Annual Reviews of Earth and Planetary Sciences* 38: 45–76

Robertson AHF, Dixon JE (1984) Aspects of the geological evolution of the Eastern Mediterranean. In: Robertson AHF, Dixon JE (eds.) *The Geological Evolution of the Eastern Mediterranean*, vol. 17, 1–74, Geological Society of London Special Publication

Rosner M, Wiedenbeck M, Ludwig T (2008) Composition-Induced Variations in SIMS Instrumental Mass Fractionation during Boron Isotope Ratio Measurements of Silicate Glasses. *Geostandards and Geoanalytical Research* 32: 27–38

Ruprecht P, Wörner G (2007) Variable regimes in magma systems documented in plagioclase zoning patterns: El Misti stratovolcano and Andahua monogenetic cones. *Journal of Volcanology and Geothermal Research* 165: 142–162

Ryan GR (1999) *Encyclopedia of Geochemistry*, chap. Barium, 29–30. Kluwer Academic Publishers

Ryan JG, Langmuir CH (1987) The systematics of lithium abundances in young volcanic rocks. *Geochimica et Cosmochimica Acta* 51: 1727–1741

Ryan JG, Langmuir CH (1988) Beryllium systematics in young volcanic rocks: implications for ^{10}Be. *Geochimica et Cosmochimica Acta* 52: 237–244

Ryan JG, Langmuir CH (1993) The systematics of boron abundances in young volcanic rocks. *Geochimica et Cosmochimica Acta* 57: 1489–1498

Shannon RD (1976) Revised effective ionic radii in halides and chalcogenides. *Acta Crystallographica* A32: 751–767

Shechtman D, Blech I, Gratias D, Cahn J (1984) Metallic Phase with Long-Range Orientational Order and No Translational Symmetry. *Physical Review Letters* 53: 1951–1953

Siivola J, Schmid R (2007) *List of Mineral Abbreviations*. Recommendations by the IUGS Subcommission on the Systematics of Metamorphic Rocks: Web version 01.02.07

Simmons EC (1999) *Encyclopedia of Geochemistry*, chap. Strontium: Element and Geochemistry, 598–599. Kluwer Academic Publishers

Singer BS, Pearce TH, Kolisnik A, Myers JD (1993) Plagioclase zoning in mid-Pleistocene lavas from the Seguam volcanic center, central Aleutian arc, Alaska. *American Mineralogist* 78: 143–1576

Singer BS, Dungan MA, Layne GD (1995) Textures and Sr, Ba, Mg, Fe, K, and Ti compositional profiles in volcanic plagioclase: clues to the dynamics of calc-alkaline magma chambers. *American Mineralogist* 80: 776–798

Smith VC, Blundy JD, Arce JL (2009) A Temporal Record of Magma Accumulation and Evolution beneath Nevado de Toluca, Mexico, Preserved in Plagioclase Phenocrysts. *Journal of Petrology* 50: 405–426

Sonntag I (2007) *Die Verteilung von Lithium, Beryllium und Bor in Phänokristallen von kalkalkalischen Gesteinen am Beispiel der Insel Nisyros (Ägäis)*.Dr. rer. nat. thesis, Ruprecht-Karls-Universität Heidelberg

Sparks RSJ (2003) Forecasting volcanic eruptions. *Earth and Planetary Science Letters* 210: 1–15

Sparks RSJ, Marshall LA (1986) Thermal and mechanical constraints on mixing between mafic and silicic magmas. *Journal of Volcanology and Geothermal Research* 29: 99–124

Sparks RSJ, Wilson CJN (1990) The Minoan deposits: a review of their characteristics and interpretation. In: Hardy DA (ed.) *Thera and the Aegean World III*, chap. 2, 89–99, The Thera Foundation

Stamatelopoulou-Seymour K, Vlassopoulos D, Pearce TH, Rice C (1990) The record of magma chamber processes in plagioclase phenocrysts at Thera Volcano, Aegean Volcanic Arc, Greece. *Contributions to Mineralogy and Petrology* 104: 73–84

Stewart ML, Pearce TH (2004) Sieve-textured plagioclase in dacitic magma: Interference imaging results. *American Mineralogist* 89: 348–351

Stiros S, Chasapis A, Kontogianni V (2003) Geodetic evidence for slow inflation of the Santorini caldera. In: *11th FIG Symposium on Deformation Measurements, Santorini, Greece*

Straub SM, Layne GD (2002) The systematics of boron isotopes in Izu arc front volcanic rocks. *Earth and Planetary Science Letters* 198: 25–39

Stroncik NA, Schmincke HU (2002) Palagonite - a review. *International Journal of Earth Sciences (Geologische Rundschau)* 91: 680–697

Sullivan D (1988) The discovery of Santorini Minoan tephra in western Turkey. *Nature* 333: 552–554

Taddeucci J, Wohletz KH (2001) Temporal evolution of the Minoan eruption (Santorini, Greece), as recorded by its Plinian fall deposit and interlayered ash flow beds. *Journal of Volcanology and Geothermal Research* 109: 299–317

Tait S, Thomas R, Gardner J, Jaupart C (1998) Constraints on cooling rates and permeabilities of pumice in an explosive eruption jet from colour and magnetic mineralogy. *Journal of Volcanology and Geothermal Research* 86: 79–91

Tatsumi Y, Isoyama H (1988) Transportation of beryllium with H_2O at high pressures; implication for magma genesis in subduction zones. *Geophysical Research Letters* 15: 180–183

Teng FZ, McDonough W, Rudnick RL, Walker R, Sirbescu ML (2006b) Lithium isotopic systematics of granites and pegmatites from the Black Hills, South Dakota. *American Mineralogist* 91: 1488–1498

Tepley III FJ, Davidson JP, Clynne MA (1999) Magmatic Interactions as Recorded in Plagioclase Phenocrysts of Chaos Crags, Lassen Volcanic Center, California. *Journal of Petrology* 40: 787–806

Thomas N, Jaupart C, Vergniolle S (1994) On the vesicularity of pumice. *Journal of Geophysical Research* 99: 15 633–15 644

Thomas RME, Sparks RSJ (1992) Cooling of tephra during fallout from eruption columns. *Bulletin of Volcanology* 54: 542–553

Tomascak PB (2004) *Geochemistry of non-traditional stable isotopes*, vol. Bd. 55, chap. Developments in the Understanding and Application of Lithium Isotopes in the Earth and Planetary Science, 153–189. Mineralogical Society of America

Tomascak PB, Tera F, Helz T, Walker R (1999) The absence of lithium isotope fractionation during basalt differentiation: New measurements by multicollector sector ICP-MS. *Geochimica et Cosmochimica Acta* 63: 907–910

Tonarini S, Pennisi M, Adorni-Braccesi A, Dini A, Ferrara G, Gonfiantini R, Wiedenbeck M, Gröning M (2003) Intercomparison of boron isotope and concentrations measurements. Part I: Selection, preparation and homogeneity tests of the intercomparison materials. *Geostandards Newsletter: The Journal of Geostandards and Geoanalysis* 27: 21–39

Torres RC, Self S, Martinez MML (1996) *Fire and Mud: Eruptions and Lahars of Mount Pinatubo, Philippines*, chap. Secondary Pyroclastic Flows from the June 15, 1991, Ignimbrite of Mount Pinatubo. University of Washington Press

Tsuchiyama A (1985) Dissolution kinetics of plagioclase in the melt of the system diopside-albite-anorthite and origin of dusty plagioclase in andesites. *Contributions to Mineralogy and Petrology* 101: 232–244

Wallace PJ, Carmichael ISE (1994) Petrology of Volcán Tequila, Jalisco, Mexico: disequilibrium phenocrysts assemblages and evolution of the subvolcanic magma system. *Contributions to Mineralogy and Petrology* 117: 345–361

Watkins ND, Sparks RSJ, Sigurdsson H, Huang TC, Federman A, Carey S, Ninkovich D (1978) Volume and extent of the Minoan tephra from Santorini Volcano: new evidence from deep-sea sediment cores. *Nature* 271: 122–126

Watson EB, Baxter EF (2007) Diffusion in solid-Earth systems. *Earth and Planetary Science Letters* 253: 307–327

Webster JD, Holloway JR, Hervig RL (1987) Partitioning of lithophile trace elements between H_2O and $H_2O + CO_2$ fluids and topaz rhyolite melt. *Economic Geology* 84: 116–134

Wenger M, Armbruster T (1991) Crystal chemistry of lithium; oxygen coordination and bonding. *European Journal of Mineralogy* 3: 387–399

Wijbrans JR, McDougall I (1988) Metamorphic evolution of the Attic-Cycladic metamorphic belt on Naxos (Cyclades, Greece) utilizing $^{40}Ar/^{39}Ar$ age spectrum measurements. *Journal of Metamorphic Geology* 6: 571–594

Wikipedia (2011) www.wikipedia.org. `http://en.wikipedia.org/wiki/Fick% 27s_laws_of_diffusion`

Wilson CJN, Houghton BF (1990) Eruptive mechanisms in the Minoan eruption: Evidence from pumice vesicularity. In: Hardy D (ed.) *Thera and the Aegean World III*, vol. 2, The Thera Foundation

Wood BJ, Blundy JD (2002) The effect of H_2O on crystal-melt partitioning of trace elements. *Geochimica et Cosmochimica Acta* 66: 3647–3656

Zellmer GF, Annen C (2008) *Dynamics of Crustal Magma Transfer, Storage and Differentiation*, vol. 304. Geological Society of London Special Publication

Zellmer GF, Sparks RSJ, Hawkesworth CJ, Wiedenbeck M (2003) Magma Emplacement and Remobilization Timescales Beneath Montserrat: Insights from Sr and Ba Zonation in Plagioclase Phenocrysts. *Journal of Petrology* 44: 1413–1431

Zhang Y (2010) *Diffusion in Minerals and Melts*, vol. 72, chap. Diffusion in minerals and melts: theoretical background, 5–59. Mineralogical Society of America

A. Methods

A.1. Sample Preparation

Nine rhyodacitic pumice clasts were carefully hand crushed with an agate mortar and pestle to avoid contamination; phenocrysts of plagioclase and pyroxene, as well as pieces of matrix glass were handpicked.

Grains and matrix glass were then embedded in epoxy and polished to gain a flat surface for further geochemical analyses with EPMA and SIMS. Ultrasonic cleaning of phenocrysts before embedding was avoided to preserve glass selvages.

Polished thin sections with a thickness of about $50\,\mu m$ were prepared from nine mafic scoria clasts and the Crystal-rich pumice (SAN51). These clasts were too dense for hand crushing and handpicking. Thin sections were then pre-analyzed with a polarized microscope (Type Leitz LaborLux 12 Pol-S). The most interesting samples where chosen for further analytical treatment.

A.2. Scanning Electron Microscope – SEM

Petrographic studies on all samples investigated were carried out on a LEO 440 scanning electron microscope at the Institute of Earth Sciences, University of Heidelberg. For SEM analyses samples were cleaned with isopropanol, dried under a heat lamp and coated with carbon. Back-scattered images were made of plagioclase, orthopyroxene, clinopyroxene, olivine, magnetite and ilmenite pheno- and microcrysts. Operating conditions were an $15-20\,kV$ accelerating voltage, a working distance of $11-13\,mm$, and a beam current of $5-7\,nA$ for all samples. The beam current was slightly increased for better visibility of zonation patterns in phenocrysts, but kept below $10\,nA$ to avoid sample damage.

A.3. Electron Probe Microanalysis – EPMA

Major and minor element compositions of phenocrysts and glass were determined using a Cameca SX51 at the Institute of Earth Sciences, University of Heidelberg. The EPMA is equipped with five wavelength-dispersive spectrometers; operating conditions were a $20\,nA$ beam current and a $15\,kV$ acceleration voltage. A $1\,\mu m$

beam was used for the analyses of orthopyroxene, clinopyroxene, olivine and oxides. The beam was defocused to $10\,\mu m$ for plagioclase and glass analyses to avoid loss of alkalis and halogens. In general, profiles were run through plagioclase, orthopyroxene, clinopyroxene and olivine phenocrysts while point analyses were performed for magnetite and ilmenite crystals and the analyses of glass inclusions and matrix glass. PAP correction was applied to the raw data (Pouchou & Pichoir, 1984, 1985). Table A.2 shows analytical parameters and setups used for EPMA.

A.3.1. Formula Calculations

Table A.1 gives a brief overview of formula calculations applied to plagioclase, orthopyroxene, clinopyroxene, olivine and oxide analyses. All formulas were calculated based on methods taught in the course *Arbeitsmethoden in der Mineralogie (Working Methods in Mineralogy)* by Hans-Peter Meyer (Institute of Earth Sciences, University of Heidelberg). A Si-Al-test was applied to several analyses of plagioclase phenocrysts (see Table A.1). Due to problems with the sample stage some profiles were analyzed slightly out of focus. When possible profile analyses of plagioclase crystals were corrected using the Si-Al-test by shifting of the values into the range between ± 0.025 while applying a factor between 1.01 to 1.02 to SiO_2 or Al_2O_3 analyses (also see formula calculation sheets on the CD.)

Table A.1. Formula Calculations and Formula Corrections

Mineral	Calculation Method	Corrections
Pl	calculated to 8 oxygens	Multiplier for Fe_2O_3: 1.111; Si-Al-Test (Si-2-Na-K and Al+Fe3+-1-Ca between ± 0.025)
Opx	calculated to 4 cations	-
Cpx	calculated to 4 cations	-
Ol	calculated to 4 oxygens	-
Mag	calculated to 3 cations	$V_2O_3 = V_2O_{3meas} - 0.0036 \times TiO_2$
Ilm	calculated to 2 cations	$V_2O_3 = V_2O_{3meas} - 0.0036 \times TiO_2$

All formulas were calculated based on methods taught in the course *Arbeitsmethoden in der Mineralogie* by Hans-Peter Meyer (Institute of Earth Sciences, University of Heidelberg).

Table A.2. Analytical Parameters and Setups used for Electron Probe Microanalyses

Atomic number	Element	Spectral line	Crystal	Spectrometer	Minerals/glass analyzed	Standard	Element concentration (wt %)	Integration time (s)	Detection limit* at 15 kV, 20 nA (wt % Oxide)
9	F	K_α	PC0	5	glass	topaz	20.65	40	0.05 % F
11	Na	K_α	TAP	1	pl, opx, cpx, ol, glass, mag, ilm	albite	8.71	10	0.04
12	Mg	K_α	TAP	5	pl, opx, cpx, ol, glass, mag, ilm	MgO	60.31	10	0.07
13	Al	K_α	TAP	1	pl	anorthite	19.07	10	0.04
		K_α	TAP	1	opx, cpx, ol, glass, mag, ilm	Al_2O_3	52.93	10	0.04
14	Si	K_α	TAP	5	pl, opx, cpx, ol, glass, mag, ilm	wollastonite	24.08	10	0.03
15	P	K_α	PET	2	glass	apatite	18.43	10	0.18
16	S	K_α	PET	2	glass	$BaSO_4$	13.74	20	0.09
17	Cl	K_α	PET	3	glass	scapolite	1.43	30	0.01 % Cl
19	K	K_α	PET	3	pl, opx, cpx, ol, glass, mag, ilm	orthoclase	12.18	10	0.03
20	Ca	K_α	PET	3	pl	anorthite	13.64	10	0.03
		K_α	PET	3	opx, cpx, ol, glass, mag, ilm	wollastonite	34.12	10	0.04
22	Ti	K_α	PET	2	opx, cpx, ol, glass, mag, ilm	TiO_2	59.95	10	0.06
23	V	K_α	LiF	4	mag, ilm	V	100	20	0.05
24	Cr	K_α	PET	2	opx, cpx, ol, mag, ilm	Cr_2O_3	68.42	10	0.07
25	Mn	K_α	LiF	4	opx, cpx, ol, glass, mag, ilm	rhodonite	33.68	10	0.08
26	Fe	K_α	LiF	4	pl, opx, cpx, ol, glass, mag, ilm	Fe_2O_3	69.94	10	0.11
28	Ni	K_α	LiF	4	ol	NiO	78.58	10	0.10
30	Zn	K_α	LiF	4	mag, ilm	gahnite	34.14	30	0.09
38	Sr	L_α	PET	3	pl	celestine	47.7	20	0.14
56	Ba	L_α	PET	3	pl	baryte	58.84	20	0.09

*3 RSD - relative standard deviation of background. Corrections were applied to F and Zn analyses. Abbreviations used for mineral phases are based on the *List of Mineral Abbreviations* by Siivola & Schmid (2007).

A.4. Secondary Ion Mass Spectrometry – SIMS

Concentrations of elements shown in Table A.1 were measured by secondary ion mass spectrometry (SIMS) with a modified Cameca IMS 3f ion microprobe at the the Institute of Earth Sciences, University of Heidelberg.

For analysis with SIMS thin sections were cleaned with acetone and polished to remove scratches and residues of carbon coating. Afterwards thin sections were subjected twice to ultrasonic cleaning for $\sim 10\,\mathrm{min}$; first in deionized water, and then in fresh ultra pure (Millipore) filtered water to minimize boron surface contamination (Marschall & Ludwig, 2004). Thin sections were then dried under a heat lamp and then coated with a gold layer $50\,\mathrm{nm}$ thick.

Analyses were performed using a $14.5\,\mathrm{keV}/20\,\mathrm{nA}$ $^{16}O^-$ primary ion beam and positive secondary ions were nominally accelerated to $4.5\,\mathrm{keV}$. Analytical parameters for the analyses of Li, Be, B, Mg, Sr, Ba, P, H_2O, $\delta^{11}B$ and δ^7Li can be found in Table A.1. Please see these papers for further details of analytical methods: Ludwig & Stalder (2007) for H_2O, Kaliwoda *et al.* (2011) for Li, Be, B and Rosner *et al.* (2008) for $\delta^{11}B$.

Table A.3. Analytical Parameters used for Secondary Ion Mass Spectrometry

Elements analyzed Minerals analyzed	Li, Be, B, (Mg), Sr, Ba, (U, Th) pl, opx, cpx and ol	P ol	H_2O glass incl./matrix	$\delta^{11}B$ glass incl./matrix	δ^7Li pl
Beam current	$5-20\,nA$	$20\,nA$	$10\,nA$	$40\,nA$	$8\,nA$
Reference isotope	^{30}Si	^{30}Si	^{30}Si	—	—
Reference material	NIST SRM-610 [2]	BCR-2G [3]	Elbaite 98144 Schorl 112566 Dravite 108796 [4]	B6 obsidian [5]	GSD1G [6]
Energy window (eV)	40	40	40	100	100
Offset (eV)	75	50	75	0	0
Mass Resolution (10%)	~ 1000	~ 2600	~ 400	~ 1100	~ 750
Image field	25	25	25	25	25
Field aperture	2 or 3	3	2 or 3	2	3
Diameter of area analyzed [1]	12 or 6 μm	6 μm	12 or 6 μm	12 μm	6 μm

Mg was not measured in pyroxenes. U and Th were measured in pl of samples SAN50B. P was analyzed in Ol grains of the scoria clasts. [1] The diameter of the area analyzed is limited by the size of the field aperture and the secondary magnification (image field). [2] Pearce *et al.* (1997) [3] Jochum *et al.* (2005) [4] Dyar *et al.* (2001) [5] Tonarini *et al.* (2003) [6] Jochum *et al.* (2011)

A.5. Numerical Modeling of Diffusion

One-dimensional numerical diffusion modeling was performed with the computer program *diff2* written in 'C' using Xcode from Apple. *diff2* was written by Thomas Ludwig (Institute of Earth Sciences, University of Heidelberg).

diff2 solves one-dimensional diffusion problems by calculating finite differences in space and time. The following equation (Crank, 1975) is repeatedly solved for each point with the concentration $c_{i,j}$ in space X (i is the space index) and T (see Fig. A.1):

$$c_{i,j+1} = c_{i,j} + r \left(c_{i-1,j} - 2c_{i,j} + c_{i+1,j} \right), \tag{A.1}$$

with $r = \delta T / (\delta X)^2$. δT and δX are both dimensionless variables:

$$X = x/l, \quad T = Dt/l^2 \tag{A.2}$$

D, l and t are the 'real world' variables diffusion constant D (m^2/s), step size l (m) and time step t (s).

r controls the stability of the solution; stable solutions are achieved for $r < 0.5$. *diff2* chooses the time steps t automatically to achieve $r = 0.45$.
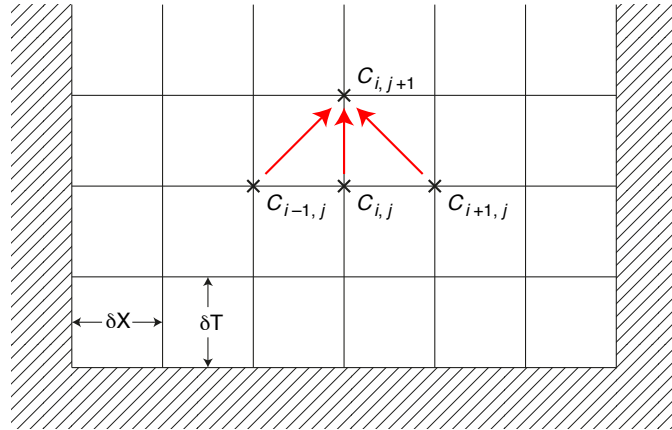
Fig. A.1. is modified after Crank (1975).

A.6. Geothermometers

A.6.1. Magnetite-Ilmenite Thermometer

Oxides analyzed for magnetite-ilmenite geothermometry were: TiO_2, Al_2O_3, V_2O_3, Cr_2O_3, FeO, MnO, MgO, CaO, ZnO. EPMA data for Vanadium was corrected based on the formula: $V_2O_3 = V_2O_{3meas} - (0.0036 \times TiO_2)$. Temperatures and log f_{O_2} were determined from magnetite-ilmenite pairs found as inclusions in orthopyroxene crystals of the Minoan pumice using the Fe-Ti oxide geothermometer of Ghiorso & Sack (1991). The temperatures calculated shown in Table A.5 were gained from crystal rims adjacent to each other. Core temperatures were $\sim 22 - 45\,°C$ lower than rim temperatures (see Table A.4).

A.6.2. Plagioclase-Liquid Thermometer

Temperatures of the Minoan pumice, Crystal-rich pumice and scoria samples SAN53-3, SAN53-4, SAN53-7 and SAN56-1 were calculated using Equation 24a of Putirka (2008). The calculated temperatures are presented in Table A.5.

The temperatures for a sample were calculated from the following data pairs based on EPMA analyses:

1. Glass inclusion in plagioclase + anorthite content adjacent to glass inclusion.

2. Glass inclusion in plagioclase + average element composition of the plagioclase profile.

3. Glass selvage + average element composition of the plagioclase profile.

H_2O contents of glass inclusions in plagioclase or glass selvages were analyzed by SIMS. If possible the value analyzed for a glass inclusion was matched with the anorthite content of the crystal next to the inclusion. Average H_2O contents for a sample or a sample with similar geochemical characteristics were used when no glass inclusion analyses were available for a sample. H_2O contents in glass inclusions of plagioclase within the white Minoan pumice vary between $\sim 2 - 7\,wt\%$ with most analyses in the range of $\sim 5 - 6\,wt\%$. The input parameter for the pressure was $0.5\,GPa$ ($0.25 - 0.5\,GPa$, Michaud *et al.* (2000)).

Temperatures gained were matched with Equation 26 from Putirka (2008) to test for plagioclase equilibrium. Equation 26 gives the temperature at which a liquid will require plagioclase saturation. All temperatures calculated were in the range of $\pm 38\,°C$ of the saturation temperature as suggested by Putirka (2008) and are shown in Table A.5. Given are the average temperature of a sample based on all

Table A.4. Average Compositions of Mag-Ilm Pairs of Minoan Pumice Samples

No.	30	31	34	35	36	37	42	43	46	47
Location	rim	core	rim	core	core	rim	rim	core	rim	core
Mag Analysis	S50D-Px5	S50D-Px5	S50D-Px8	S50D-Px8	S52D-Px4	S52D-Px4	S54D-Px10	S54D-Px10	S55D-Px9	S55D-Px9
SiO_2	0.07	0.05	0.07	0.07	0.03	0.04	0.07	0.06	0.08	0.05
TiO_2	13.41	12.61	12.92	12.65	12.63	12.96	13.27	12.70	12.90	12.66
Al_2O_3	1.80	1.74	1.77	1.75	1.79	1.78	1.80	1.77	1.77	1.76
V_2O_3	0.32	0.39	0.35	0.36	0.38	0.37	0.31	0.30	0.38	0.36
Cr_2O_3	0.00	0.00	0.03	0.04	0.06	0.03	0.00	0.03	0.02	0.08
Fe_2O_3										
FeO	78.34	76.99	77.25	77.22	78.14	77.68	77.41	77.60	77.35	78.08
MnO	0.61	0.61	0.56	0.62	0.60	0.63	0.66	0.72	0.68	0.68
MgO	1.32	1.29	1.24	1.25	1.23	1.27	1.31	1.30	1.29	1.27
CaO	0.01	0.01	0.07	0.11	0.01	0.03	0.02	0.01	0.02	0.03
ZnO	0.10	0.17	0.13	0.10	0.10	0.10	0.11	0.19	0.10	0.09
Total	95.96	93.86	94.39	94.17	94.98	94.87	94.95	94.69	94.58	95.05

No.	29	28	33	32	39	38	40	41	44	45
Location	rim	core	rim	core	core	rim	rim	core	rim	core
Ilm Analysis	S50D-Px5	S50D-Px5	S50D-Px8	S50D-Px8	S52D-Px4	S52D-Px4	S54D-Px10	S54D-Px10	S55D-Px9	S55D-Px9
TiO_2	45.76	46.43	45.82	46.11	46.41	45.84	45.96	46.38	46.31	46.42
Al_2O_3	0.14	0.15	0.14	0.13	0.15	0.14	0.15	0.15	0.14	0.14
V_2O_3	0.19	0.07	0.05	0.08	0.07	0.01	0.11	0.11	0.09	0.06
Cr_2O_3	0.00	0.00	0.01	0.04	0.01	0.01	0.02	0.00	0.06	0.03
FeO	47.46	47.45	47.73	47.87	47.01	48.00	47.56	47.44	47.73	46.90
MnO	0.86	0.84	0.90	0.77	0.90	0.87	0.86	0.87	0.86	0.90
MgO	2.29	2.29	2.26	2.20	2.26	2.34	2.28	2.33	2.24	2.26
CaO	0.01	0.02	0.08	0.09	0.05	0.04	0.03	0.03	0.02	0.05
ZnO	0.03	0.03	0.05	0.04	0.02	0.05	0.04	0.00	0.05	0.04
Total	96.72	97.24	96.98	97.28	96.86	97.25	96.97	97.31	97.44	96.75

T (°C)	898	868	898	882	858	903	895	872	882	856
$\log f_{O_2}$	−11.83	−12.43	−11.77	−12.08	−12.68	−11.64	−11.88	−12.34	−12.15	−12.74

Temperatures were determined from mag-ilm pairs that were found in opx crystals and calculated after Ghiorso & Sack (1991). Shown are rim and core temperatures. There were no single mag-ilm pairs discovered in the Minoan glass matrix. Mag-ilm pairs analyzed by Cottrell *et al.* (1999) yield temperatures of $885 \pm 7\,°C$ and a $\log f_{O_2}$ of $−11.7 \pm 0.2$.

calculations and the standard deviation of the average temperature when more than one temperature was calculated for a sample.

Several samples were heavily affected by magma mingling, therefore sample SAN61-2 was divided into areas that are texturally and chemically similar to the Minoan pumice (P) and those that belong to Minoan scoria (S). SAN51 (Crystal-rich pumice) consists of plagioclase crystals with anorthite contents below An_{60} and higher than An_{60}. Therefore two different temperatures were calculated for those plagioclase crystals. Sample SAN53-3 consists of several enclaves and different pumiceous parts. It was not possible to calculate a temperature for Pl-12 (SAN53-3) which was found in an enclave, but a temperature was calculated from a plagioclase in the fine pumiceous areas of the sample.

Temperatures for samples SAN53-1, SAN53-2, SAN53-5 and SAN53-6 could not be calculated with this thermometer because these samples lack a glassy matrix.

Table A.5. Geothermometers used for Temperature Calculations in Minoan Pumice, Crystal-rich Pumice and Scoria Samples

Sample	Pl-Liq - Mean T (°C)	SD (°C)	Cpx-Opx - T(°C)	SD (°C)	Mag-Ilm (T°C)	SD (°C)
Minoan Pumice						
SAN52	865	9.6	–	–	904	–
SAN54	868	4.6	–	–	895	–
SAN55	880	4.3	882	–	882	–
SAN57	824	8.6	–	–	–	–
SAN58	844	2.3	–	–	–	–
SAN61-1A	888	9.2	1145	–	–	–
SAN61-2 P	846	–	–	–	–	–
SAN61-2 S	902	–	–	–	–	–
SAN59	833	2.2	–	–	–	–
SAN50	862	6.0	–	–	898	0.5
			–	–	–	–
CR Pumice			–	–	–	–
SAN51 < An60	919	0.8	–	–	–	–
SAN51 >An60	974	–	–	–	–	–
			–	–	–	–
Scoria			–	–	–	–
SAN53-1	–	–	–	–	–	–
SAN53-2	–	–	896	–	–	–
SAN53-3 (fine)	1022	–	–	–	–	–
SAN53-4	969	32.4	–	–	–	–
SAN53-5	–	–	–	–	–	–
SAN53-6	–	–	–	–	–	–
SAN53-7	855	–	–	–	–	–
	–	–	–	–	–	–
SAN56-1	923	–	–	–	–	–
SAN60	–	–	–	–	–	–

Temperatures calculated based on Putirka (2008) (Pl-Liquid Thermometer + Cpx-Opx Thermometer) and Ghiorso & Sack (1991) (Mag-Ilm Thermometer - rim analyses only).

A.6.3. Two-Pyroxene Thermometer (Putirka, 2008)

For samples that lack a glassy matrix the two-pyroxene thermometer (Equation 37, Putirka (2008)) was applied. Results were tested for equilibrium conditions based on K_D (Fe-Mg)$^{cpx-opx}$ as suggested by Putirka (2008). Those results that were in agreement with the equation are presented in Table A.5. The temperature for SAN53-2 was included as it was almost in agreement with K_D (Fe-Mg)$^{cpx-opx}$ (in this case ± 0.17 instead of ± 0.14). The temperature of SAN61-1A is a lot higher compared to the plagioclase-liquid thermometer.

B. Sample Overview

B.1. SAN52 to SAN57 – Minoan A

Sample positions Minoan A

up to 40 m — D

up to 55 m — C

up to 12 m — B

up to 6 m — A

just underneath B: SAN-57
ca. 5.50 m: SAN-55
ca. 2.10 m: SAN-54
basal position: SAN-52
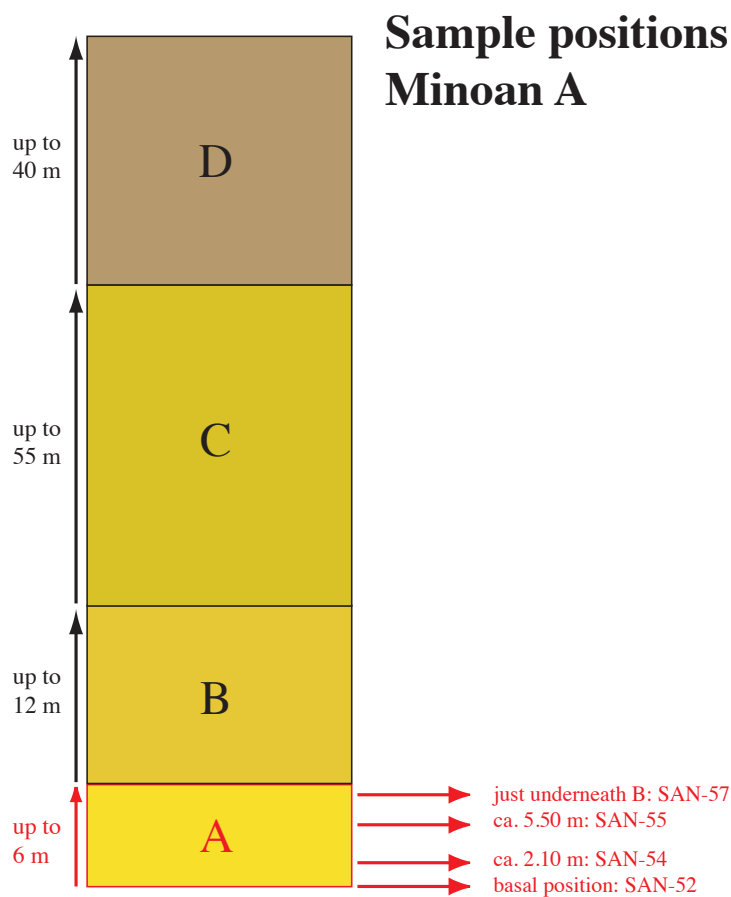
Fig. B.1. Positions of pumice samples taken from Minoan Unit A.
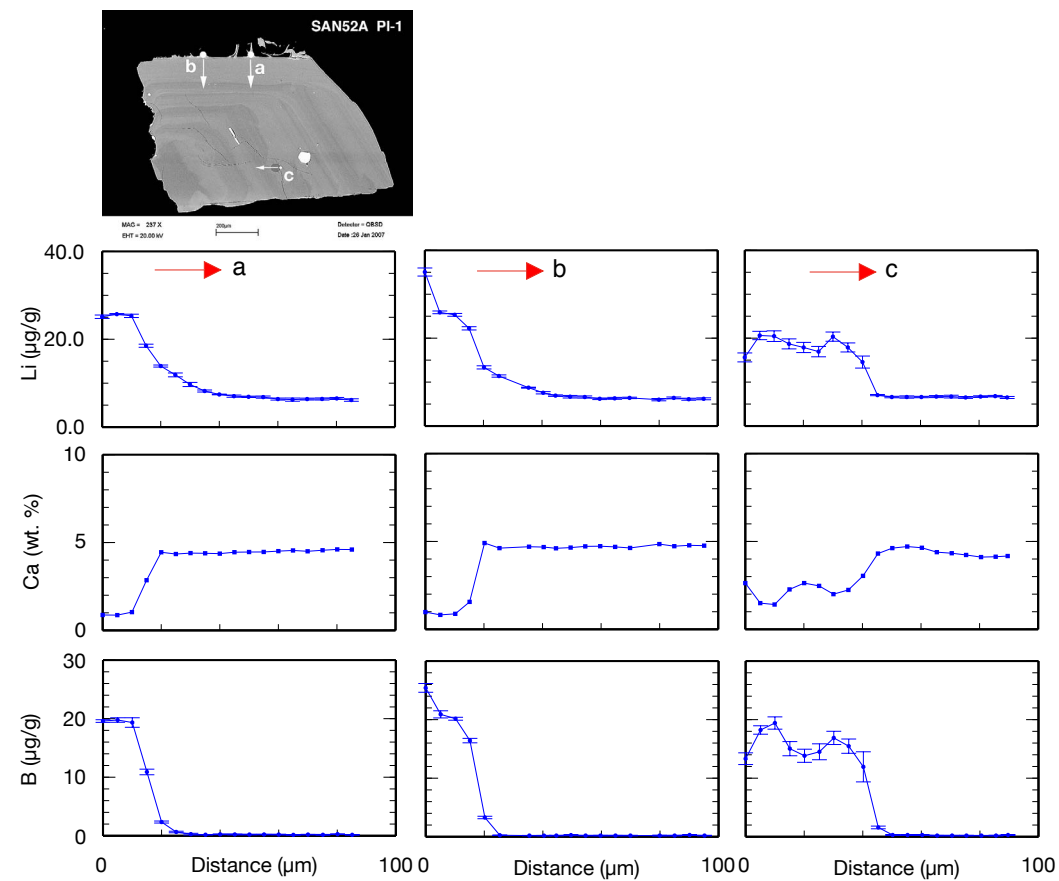
Fig. B.2. SAN52A: Pl-1. Short SIMS profiles to detect/exclude diffusion of Li from melt selvage into pl crystal or from inclusion into pl.

Fig. B.3. SAN52A: Pl-1. Short δ^7Li SIMS profile. The blue arrow marks the δ^7Li profiles; the red or white arrows mark the regular Li short profiles. A yellow arrow usually marks the EPMA profile (not all pl crystals were analyzed by EPMA). Li concentration values are derived from count rates of the isotope analyses and are therefore only semi-quantitative.
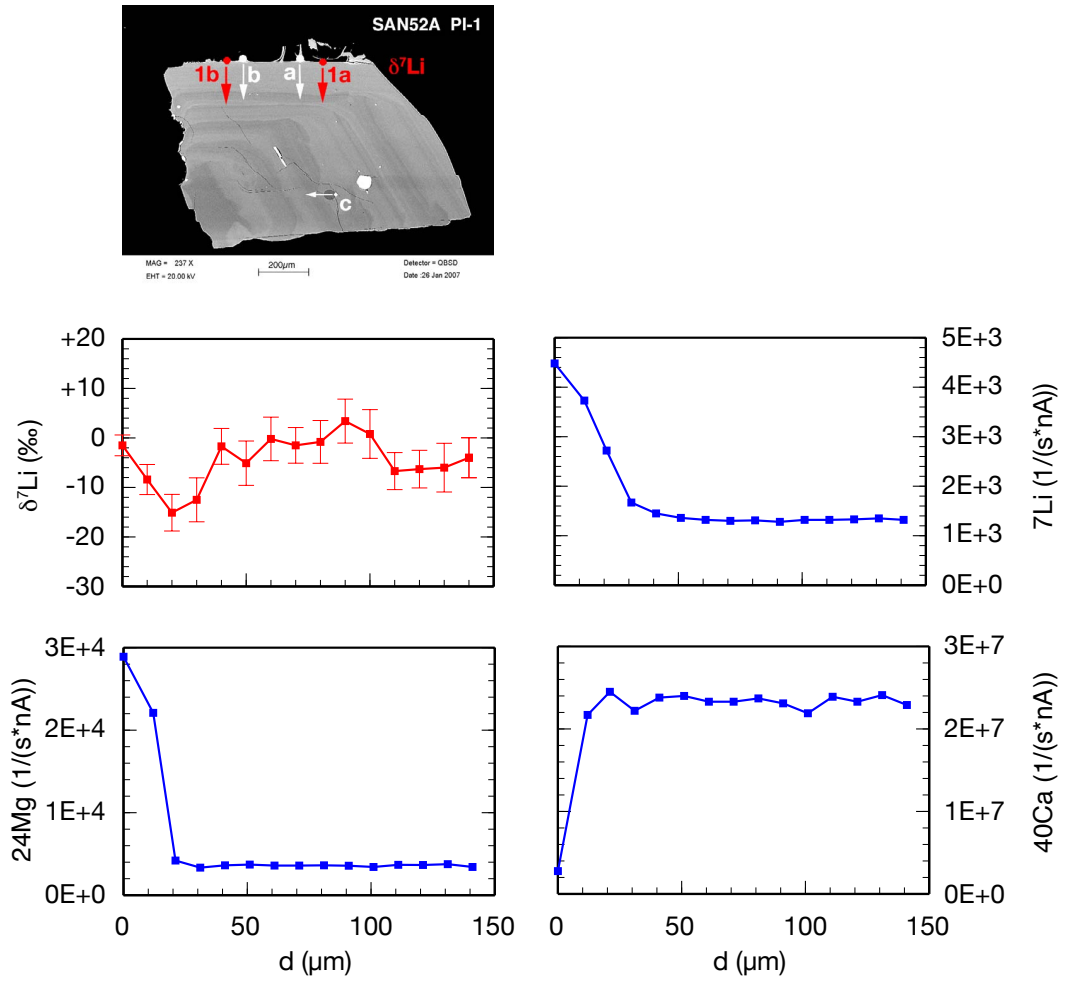
Fig. B.4. SAN52A: Pl-1. Short δ^7Li SIMS profile. The blue arrow marks the δ^7Li profiles; the red or white arrows mark the regular Li short profiles. A yellow arrow usually marks the EPMA profile (not all pl crystals were analyzed by EPMA). Li concentration values are derived from count rates of the isotope analyses and are therefore only semi-quantitative.

Fig. B.5. SAN52A: Pl-3. EPMA and SIMS profiles. Formulas of EPMA analyses are calculated to 8 oxygens.
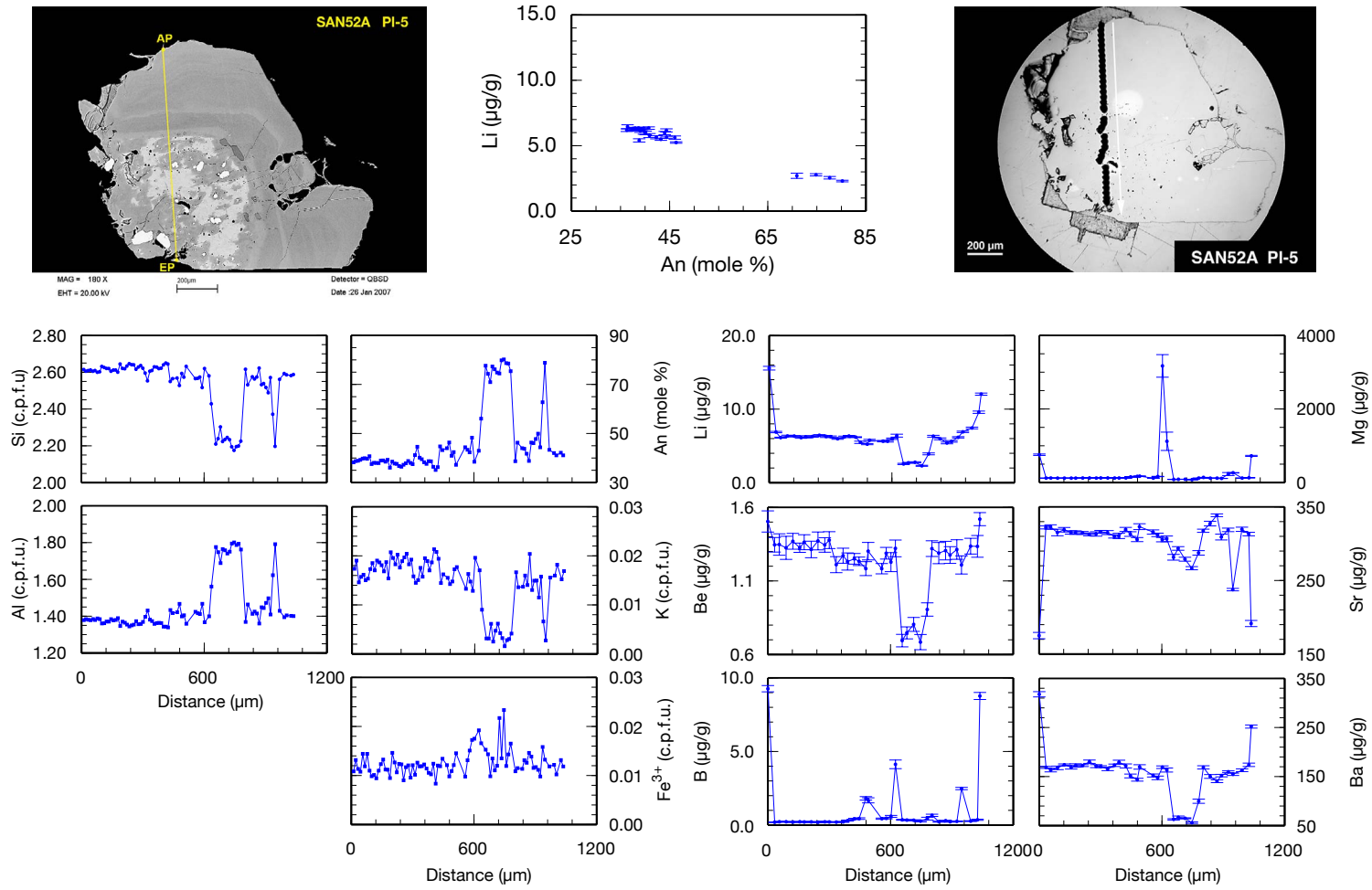
Fig. B.6. SAN52A: Pl-5. EPMA and SIMS profiles. Formulas of EPMA analyses are calculated to 8 oxygens.
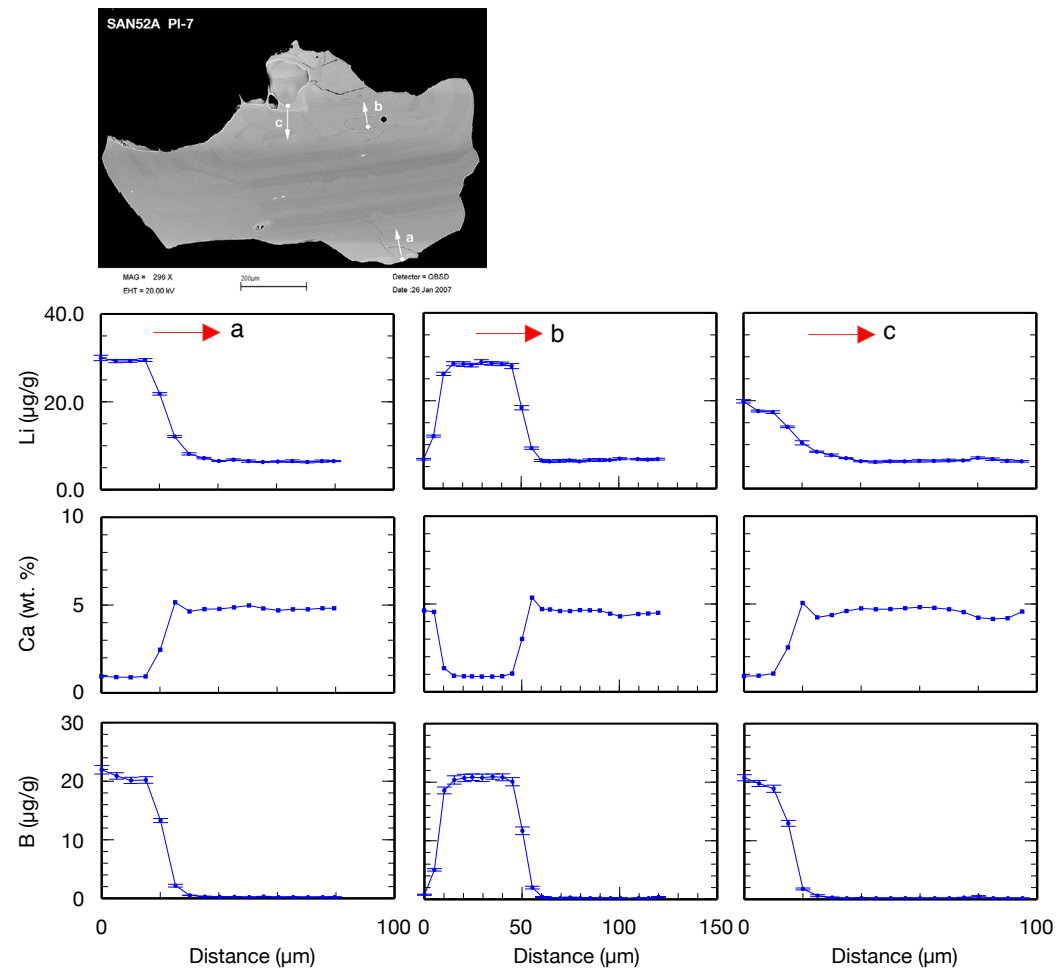
Fig. B.7. SAN52A: Pl-7. Short SIMS profiles to detect/exclude diffusion of Li from melt selvage into pl crystal or from inclusion into pl.
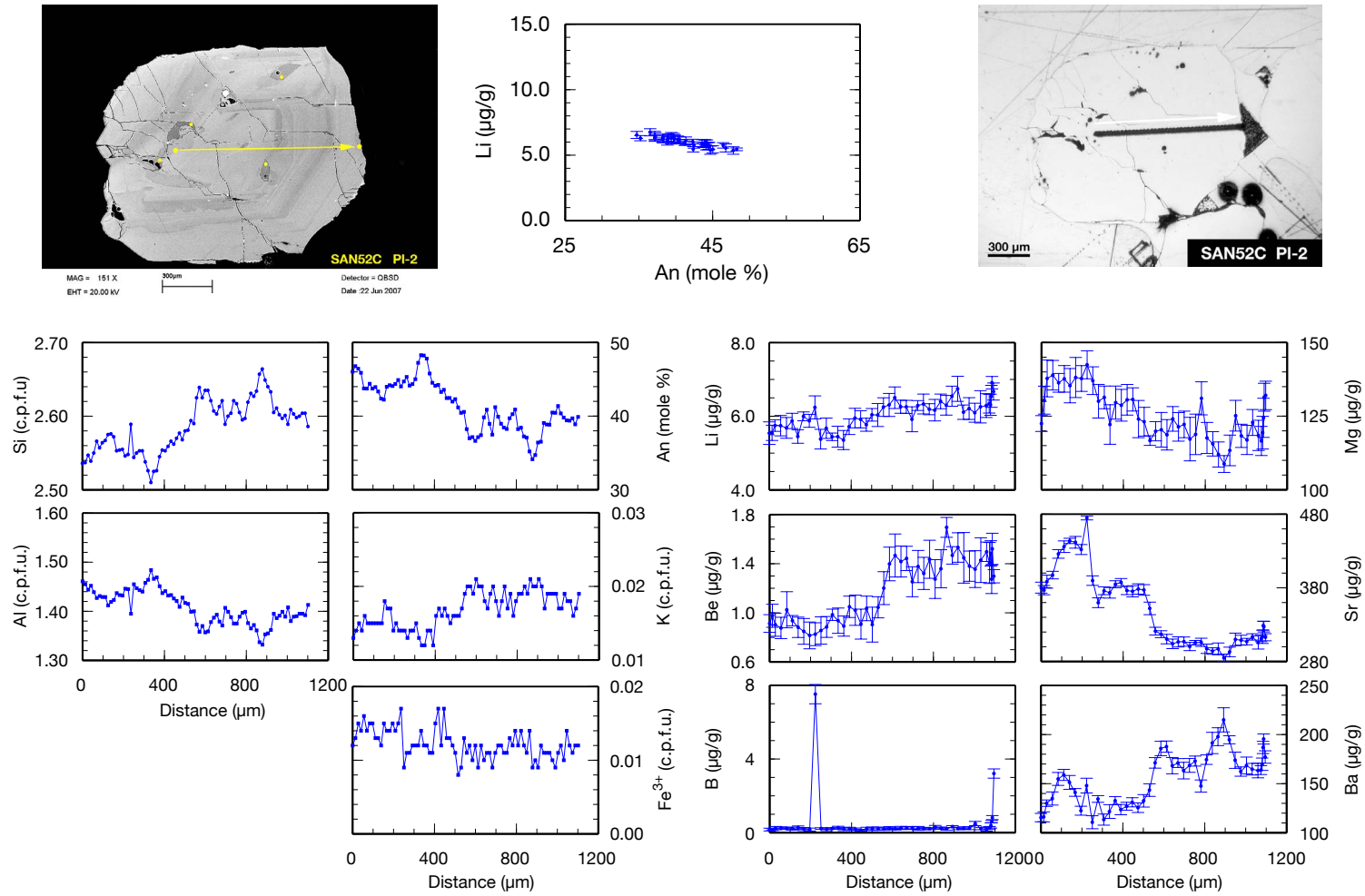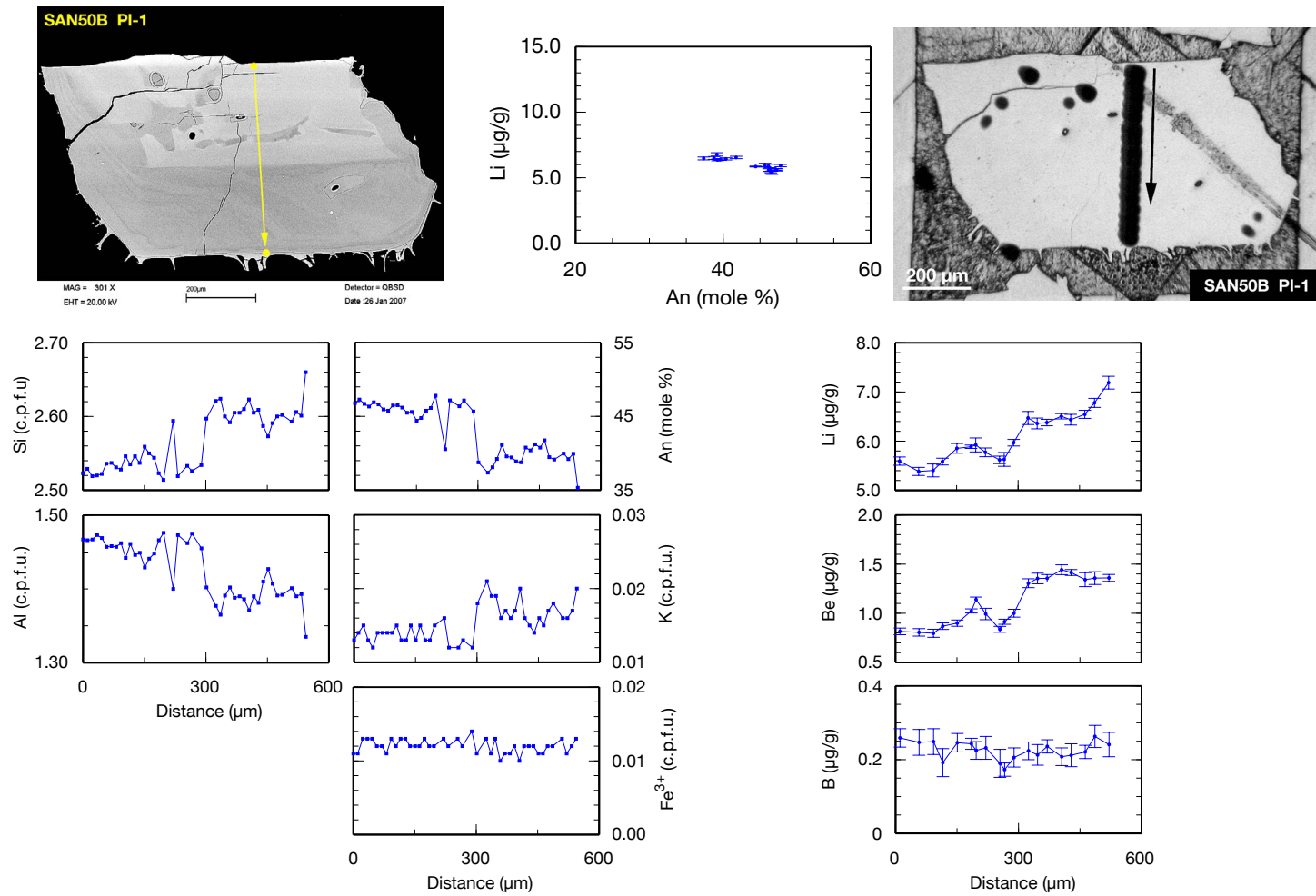
Fig. B.8. SAN52C: Pl-2. EPMA and SIMS profiles. Formulas of EPMA analyses are calculated to 8 oxygens.

Fig. B.9. SAN54A: Pl-1. EPMA and SIMS profiles. Formulas of EPMA analyses are calculated to 8 oxygens.
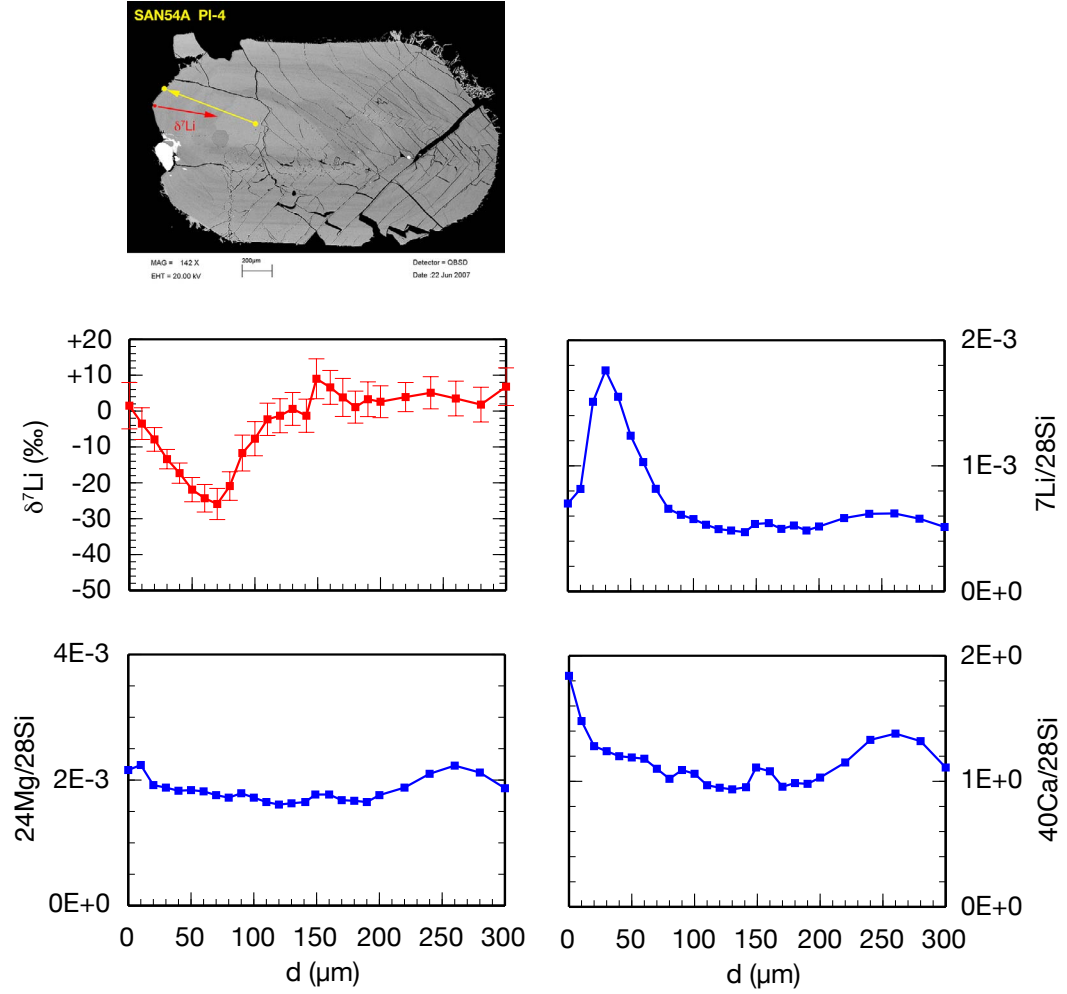
Fig. B.10. SAN54A: Pl-4. Short δ^7Li SIMS profile. The blue arrow marks the δ^7Li profiles; the red or white arrows mark the regular Li short profiles. A yellow arrow usually marks the EPMA profile (not all pl crystals were analyzed by EPMA). Li concentration values are derived from count rates of the isotope analyses and are therefore only semi-quantitative.

Fig. B.11. SAN54A: Pl-4. EPMA and SIMS profiles. Formulas of EPMA analyses are calculated to 8 oxygens.
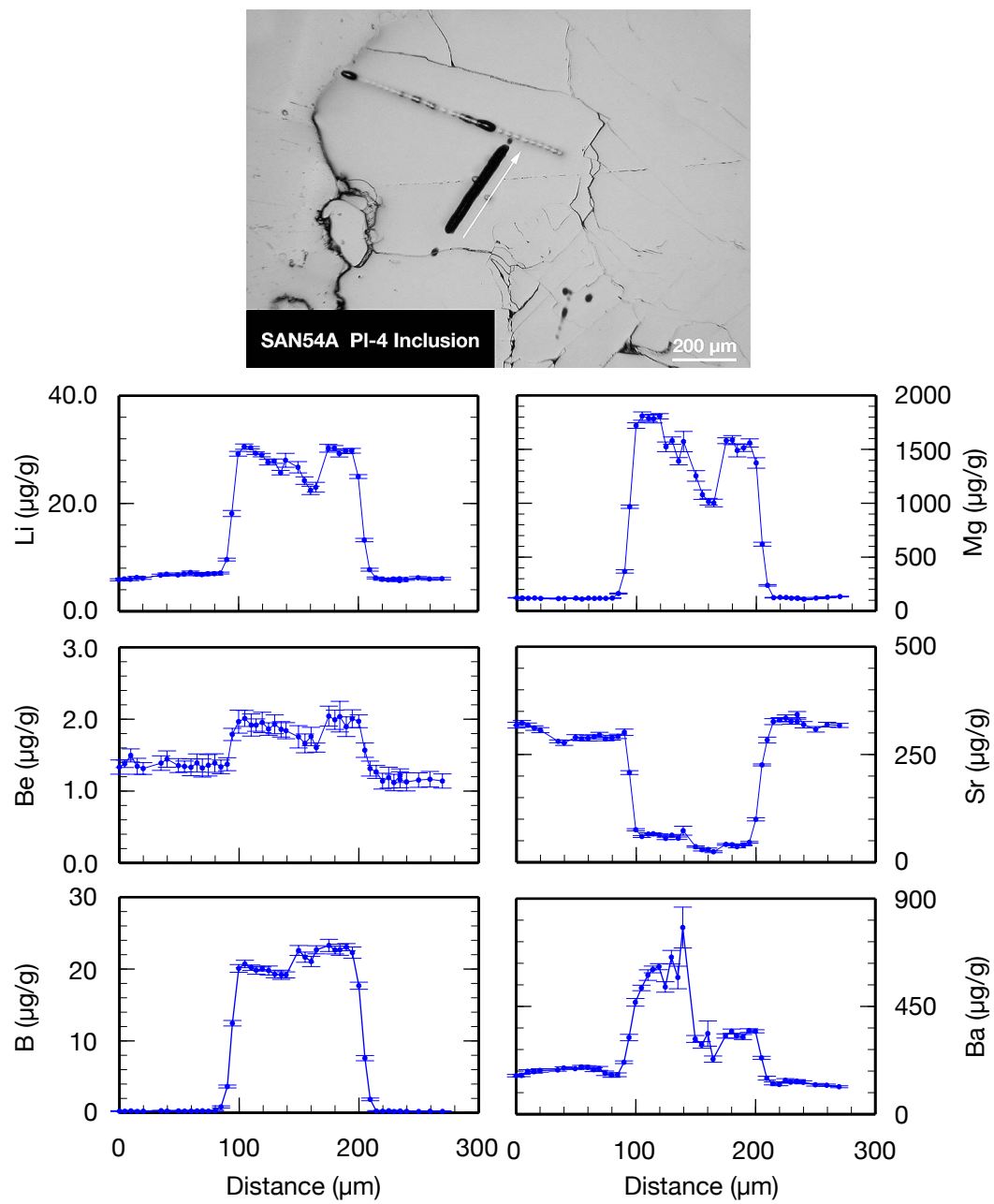
**Fig. B.12.** SAN54A: Pl-4. SIMS profile through glass inclusion.
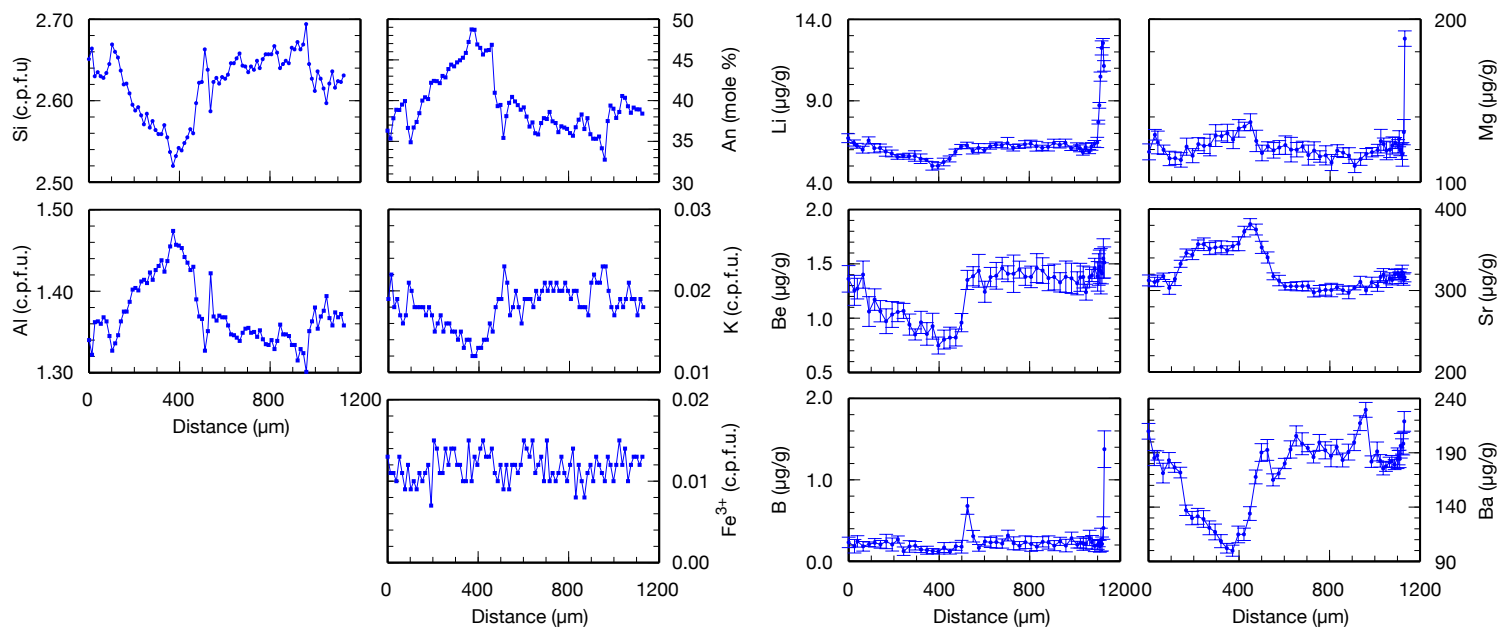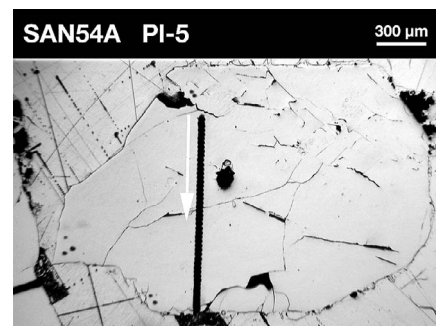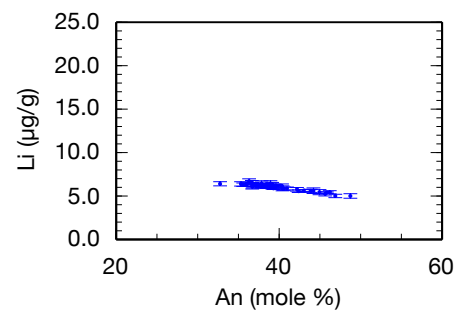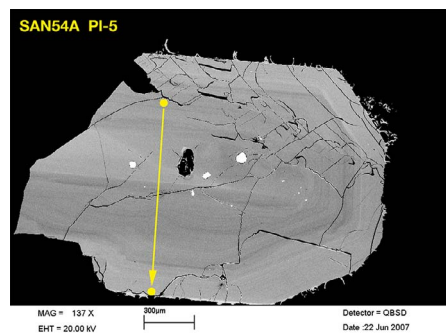
Fig. B.13. SAN54A: Pl-5. EPMA and SIMS profiles. Formulas of EPMA analyses are calculated to 8 oxygens.
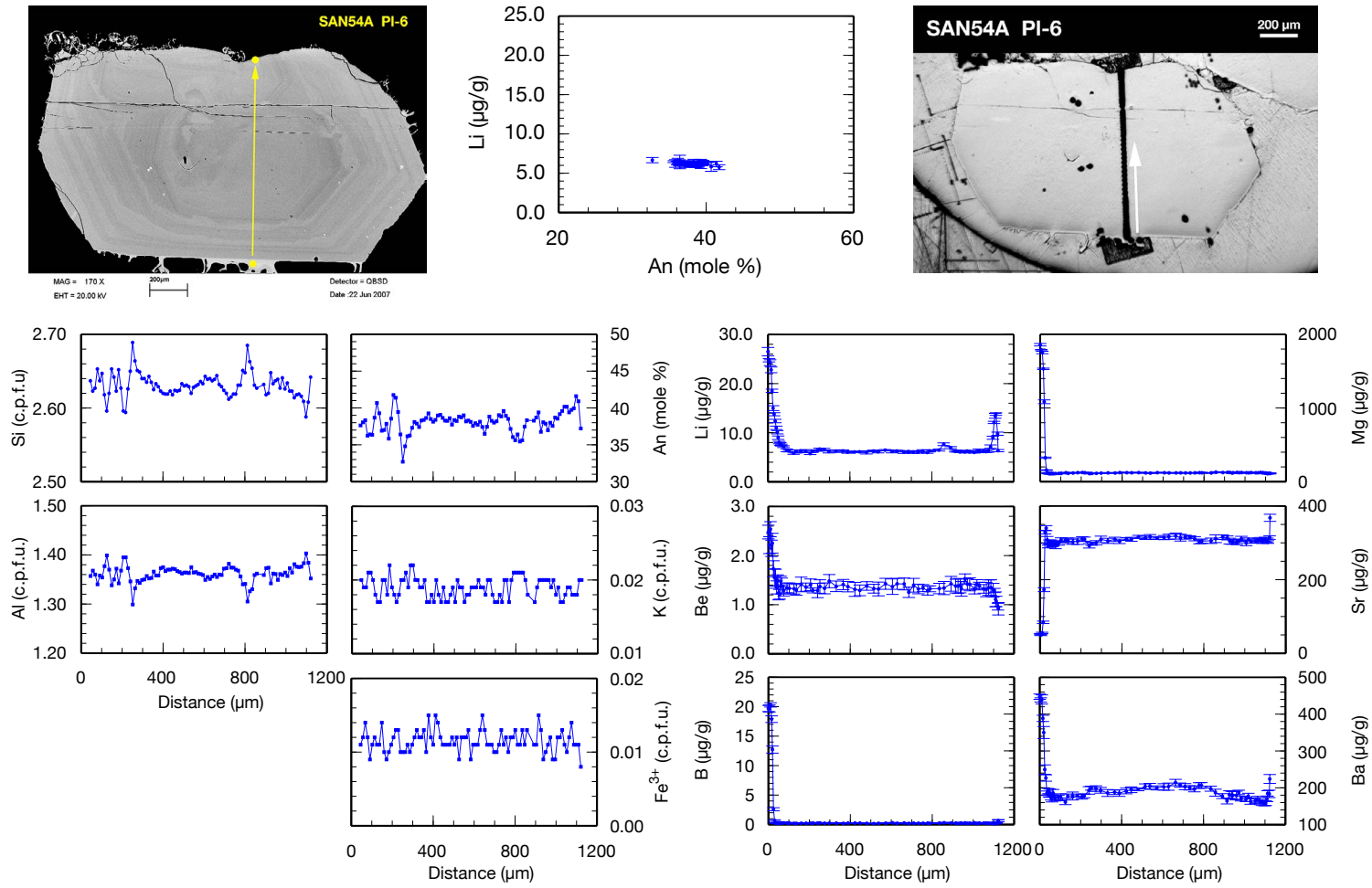
Fig. B.14. SAN54A: Pl-6. EPMA and SIMS profiles. Formulas of EPMA analyses are calculated to 8 oxygens.
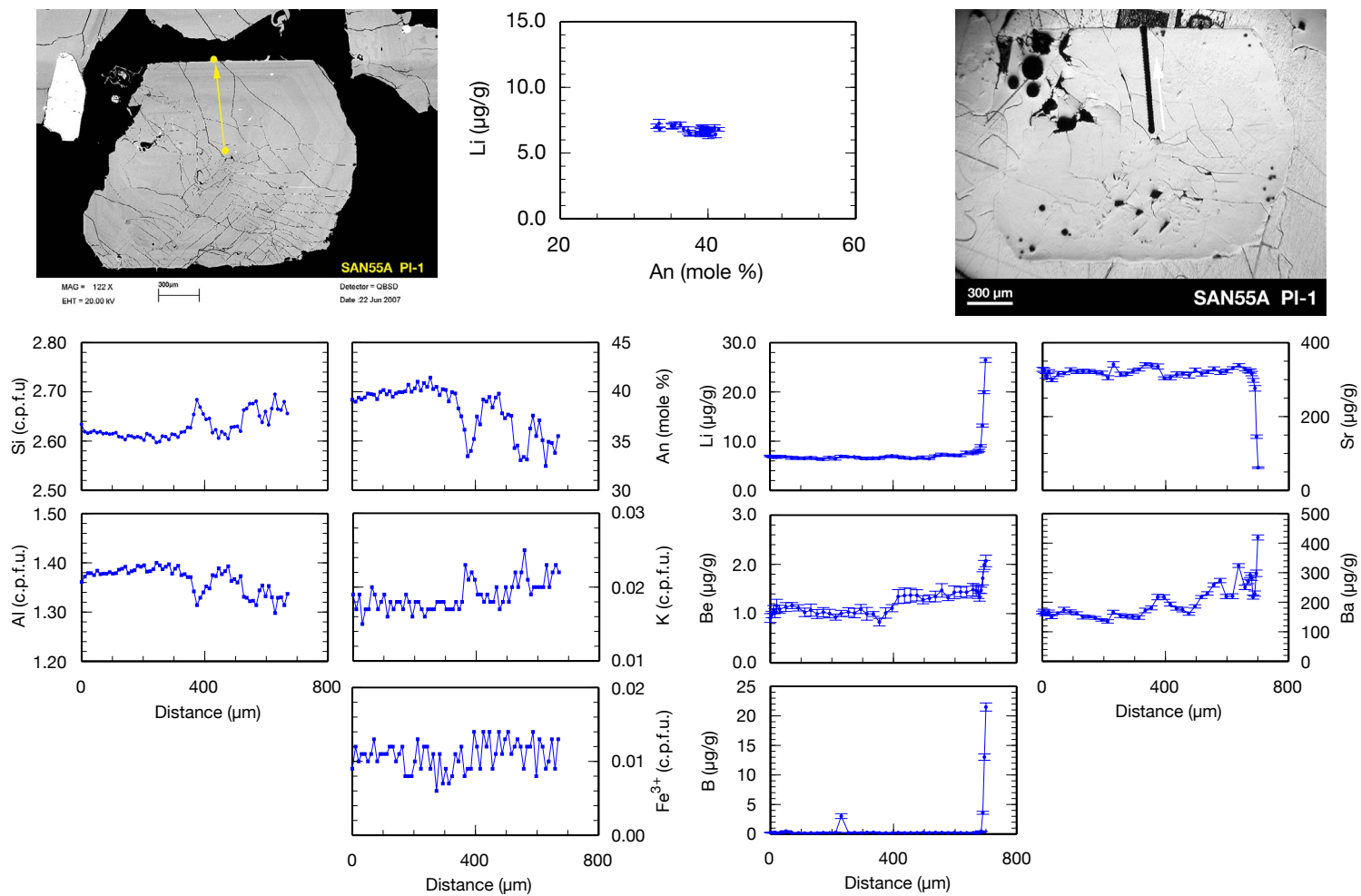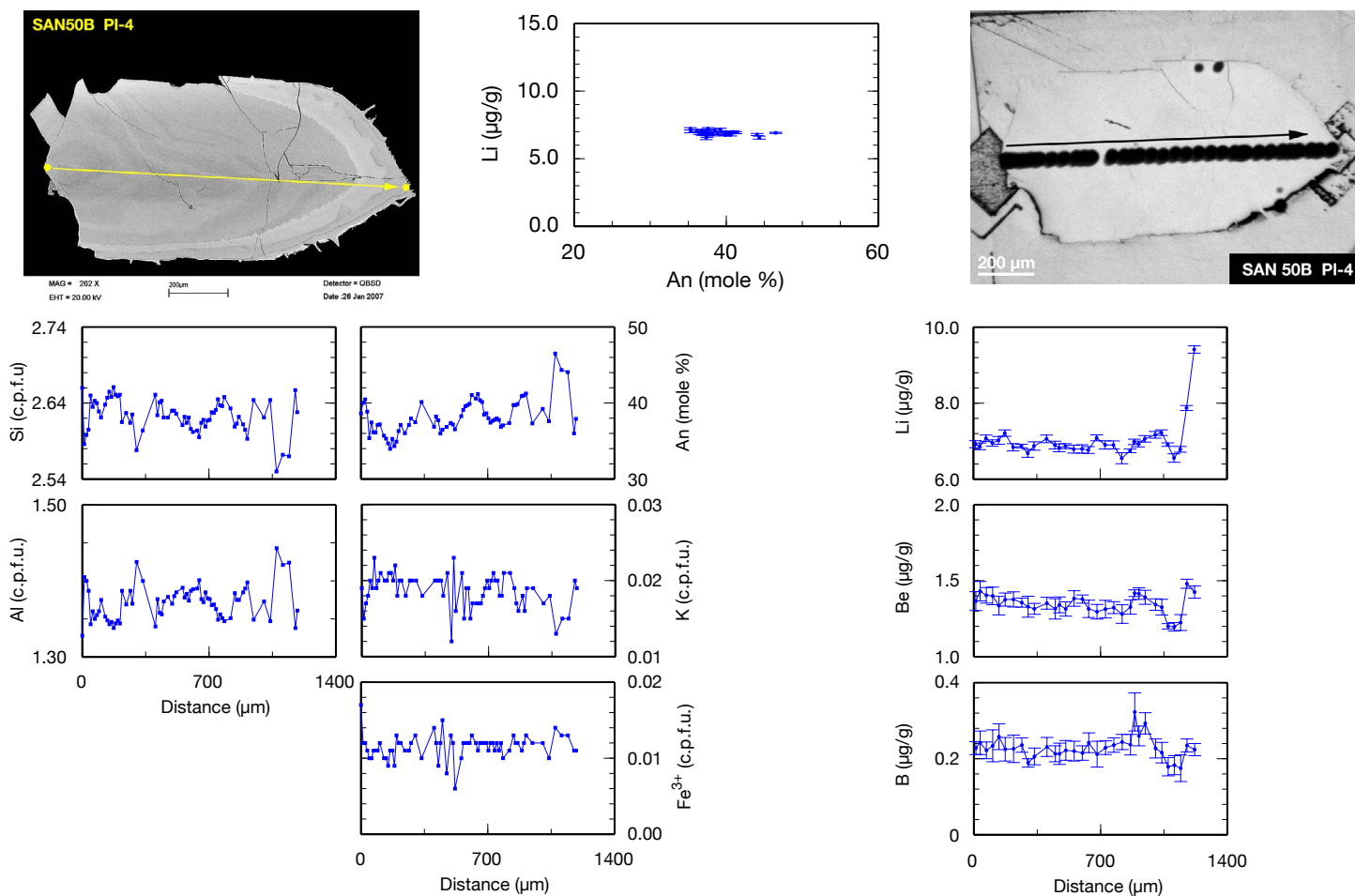
Fig. B.15. SAN55A: Pl-1. EPMA and SIMS profiles. Formulas of EPMA analyses are calculated to 8 oxygens.
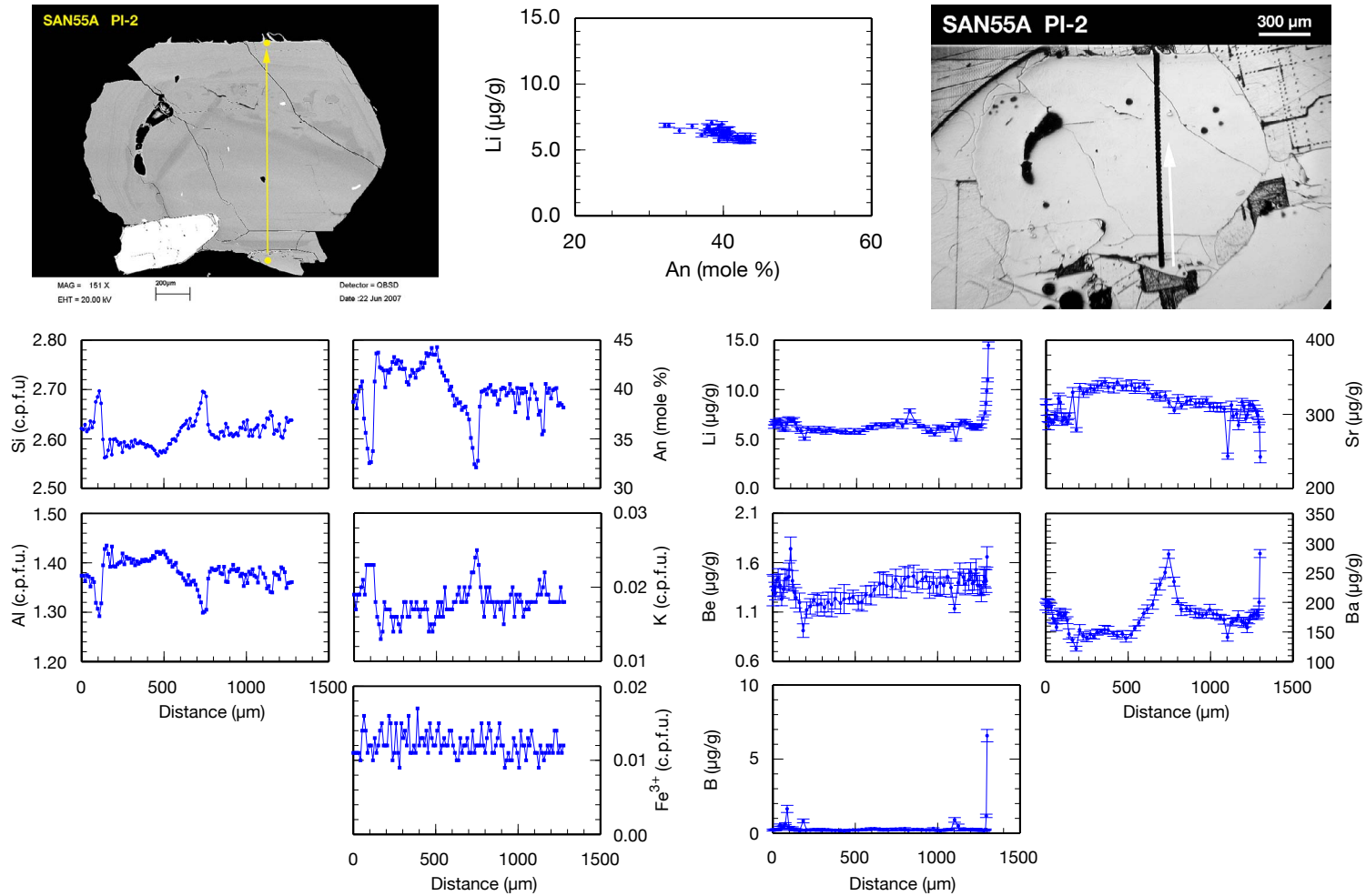
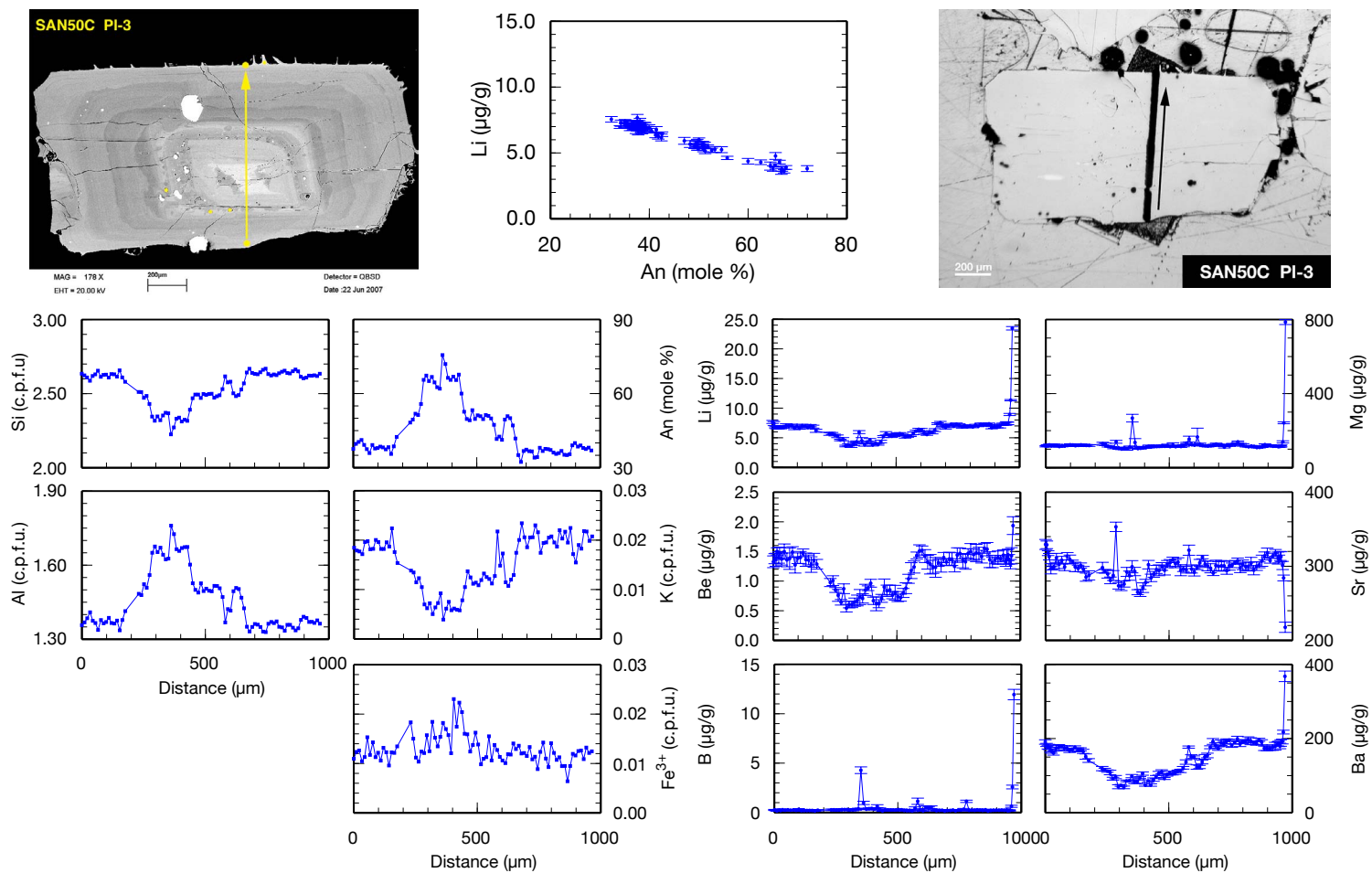**Fig. B.16.** SAN55A: Pl-2. EPMA and SIMS profiles. Formulas of EPMA analyses are calculated to 8 oxygens.

Fig. B.17. SAN57A: Pl-2. EPMA and SIMS profiles. Formulas of EPMA analyses are calculated to 8 oxygens.
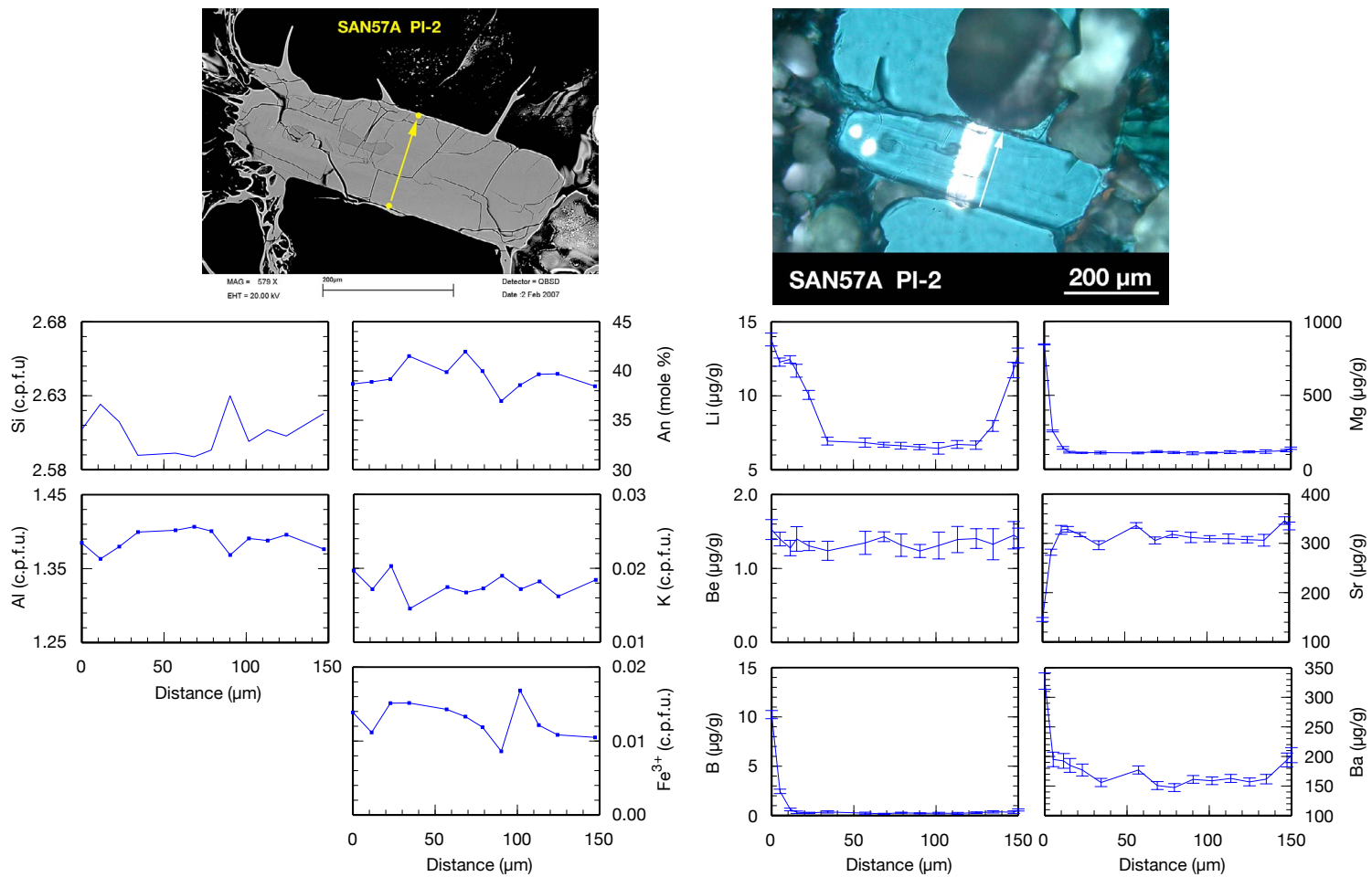
Fig. B.18. SAN57A: Pl-3. EPMA and SIMS profiles. Formulas of EPMA analyses are calculated to 8 oxygens.
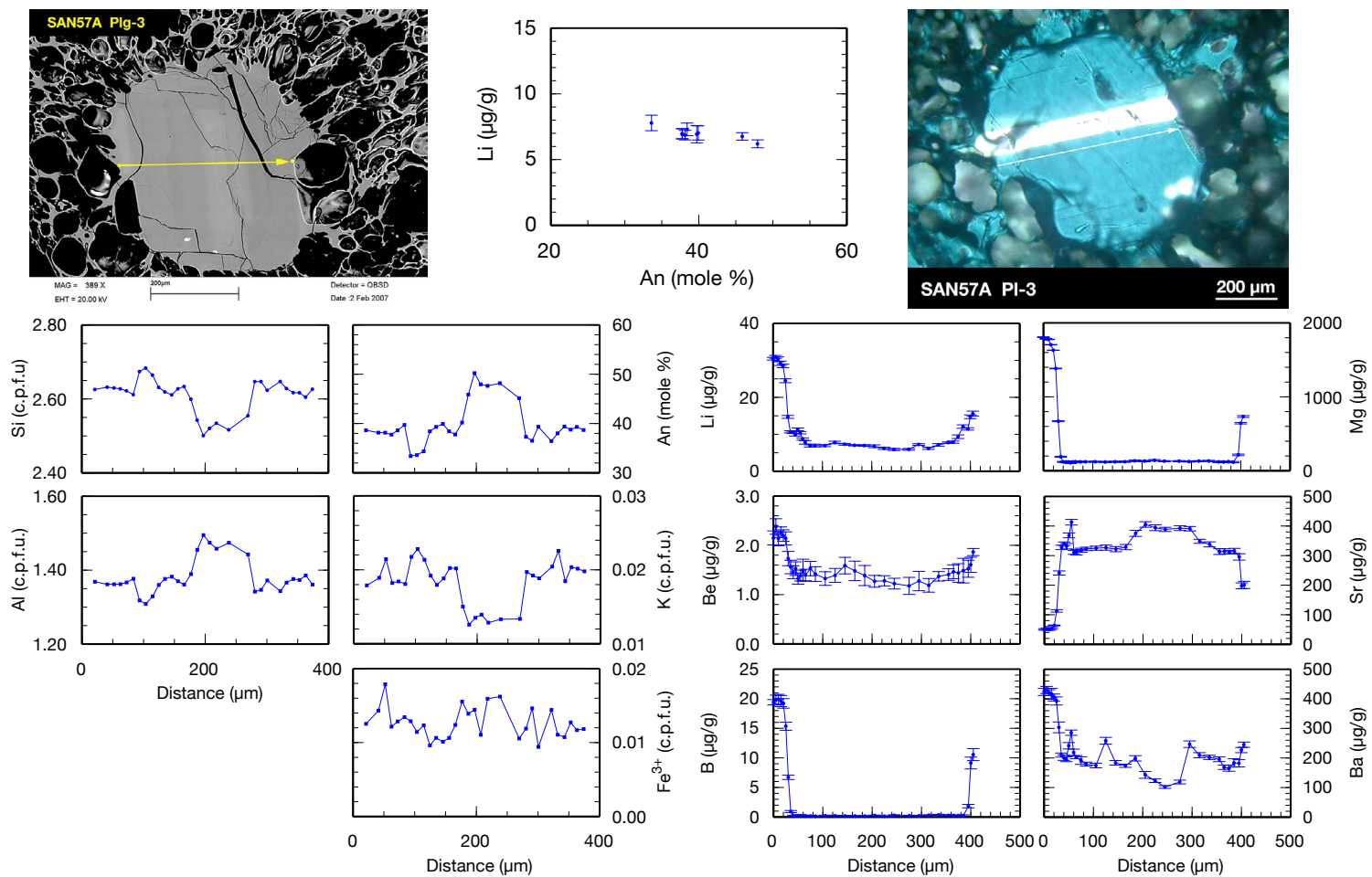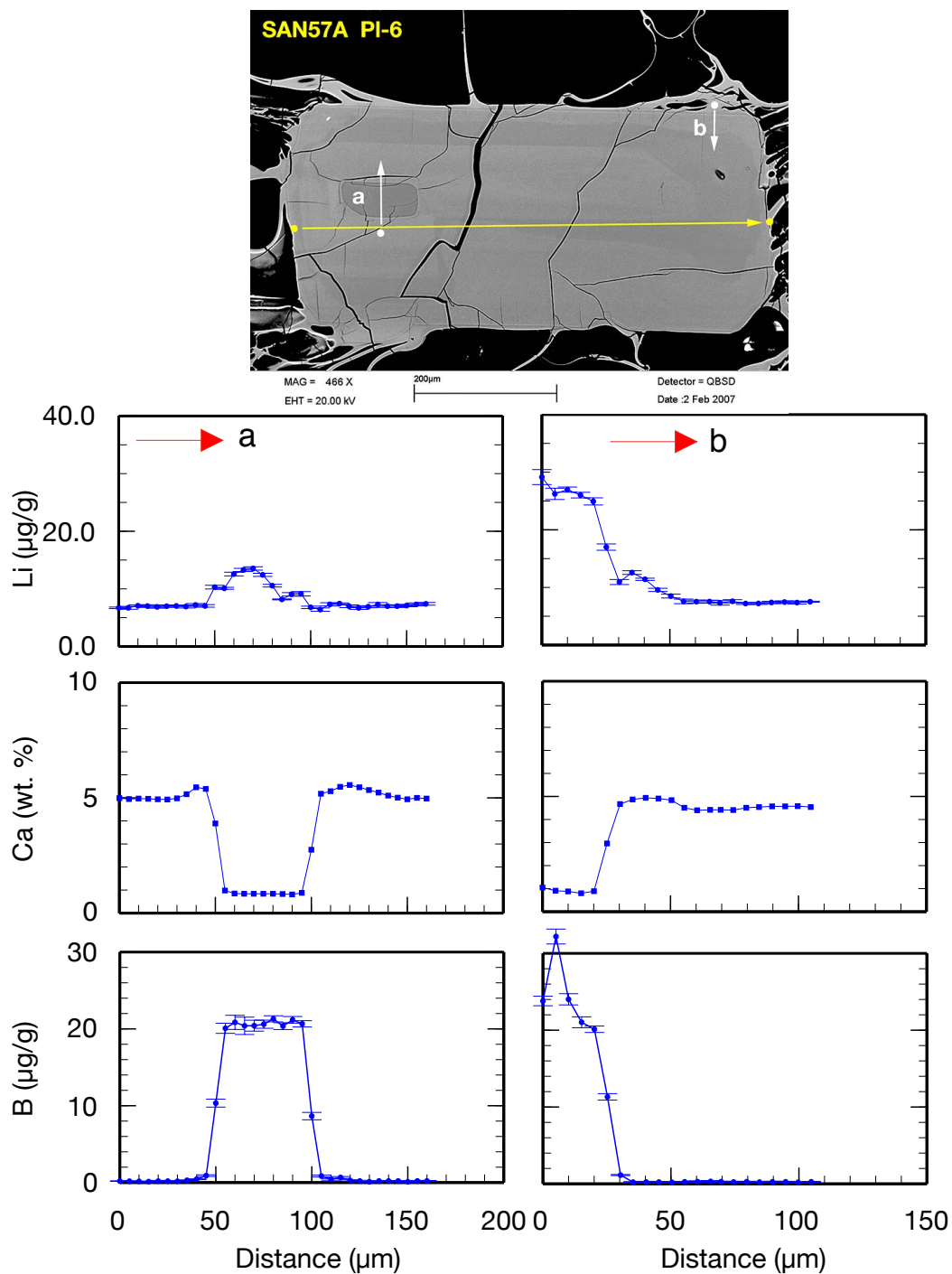
Fig. B.19. SAN57A Pl-6: Short SIMS profiles to detect/exclude diffusion of Li from melt selvage into pl crystal or from inclusion into pl.
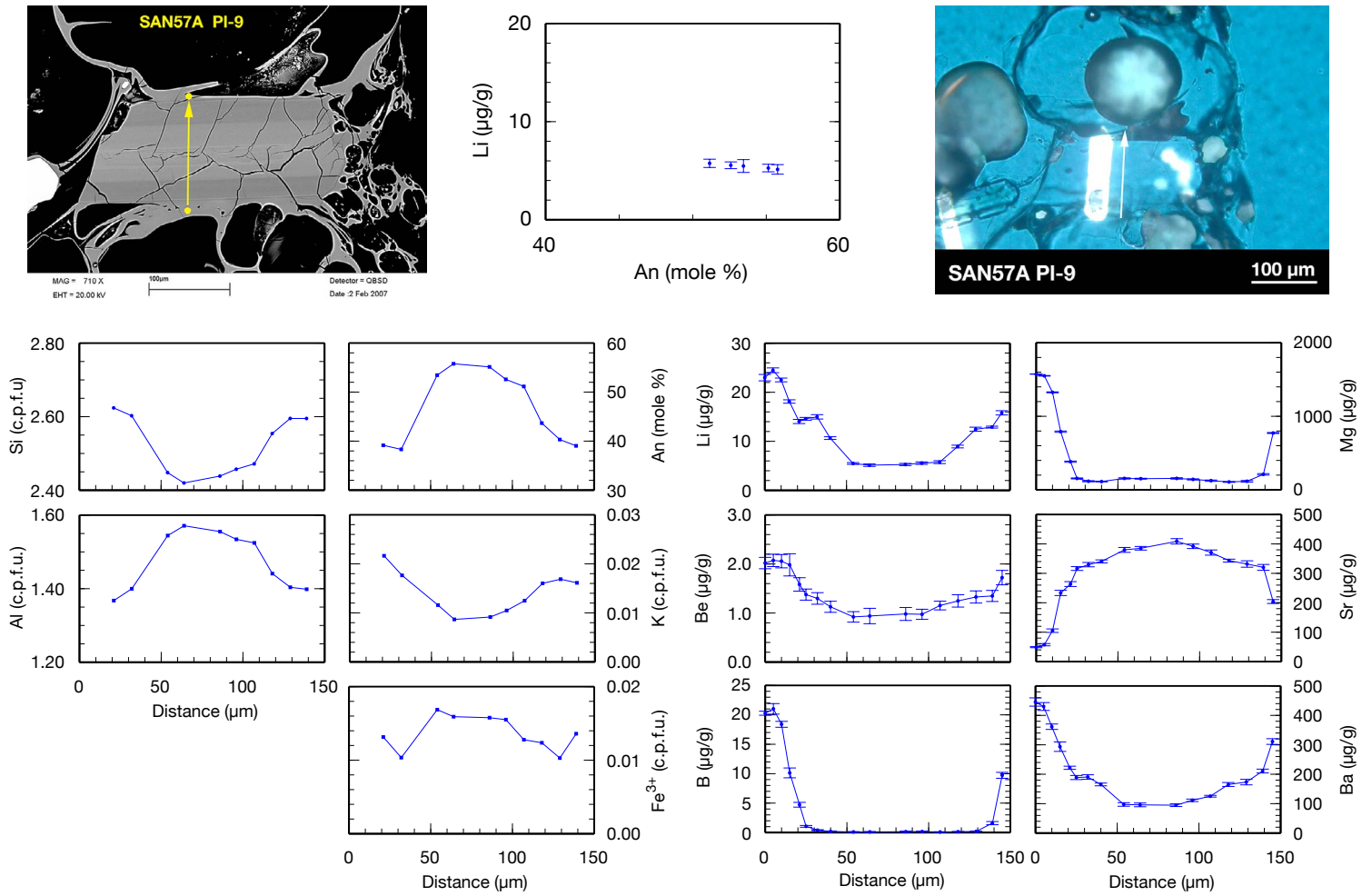
Fig. B.20. SAN57A: Pl-9. EPMA and SIMS profiles. Formulas of EPMA analyses are calculated to 8 oxygens.
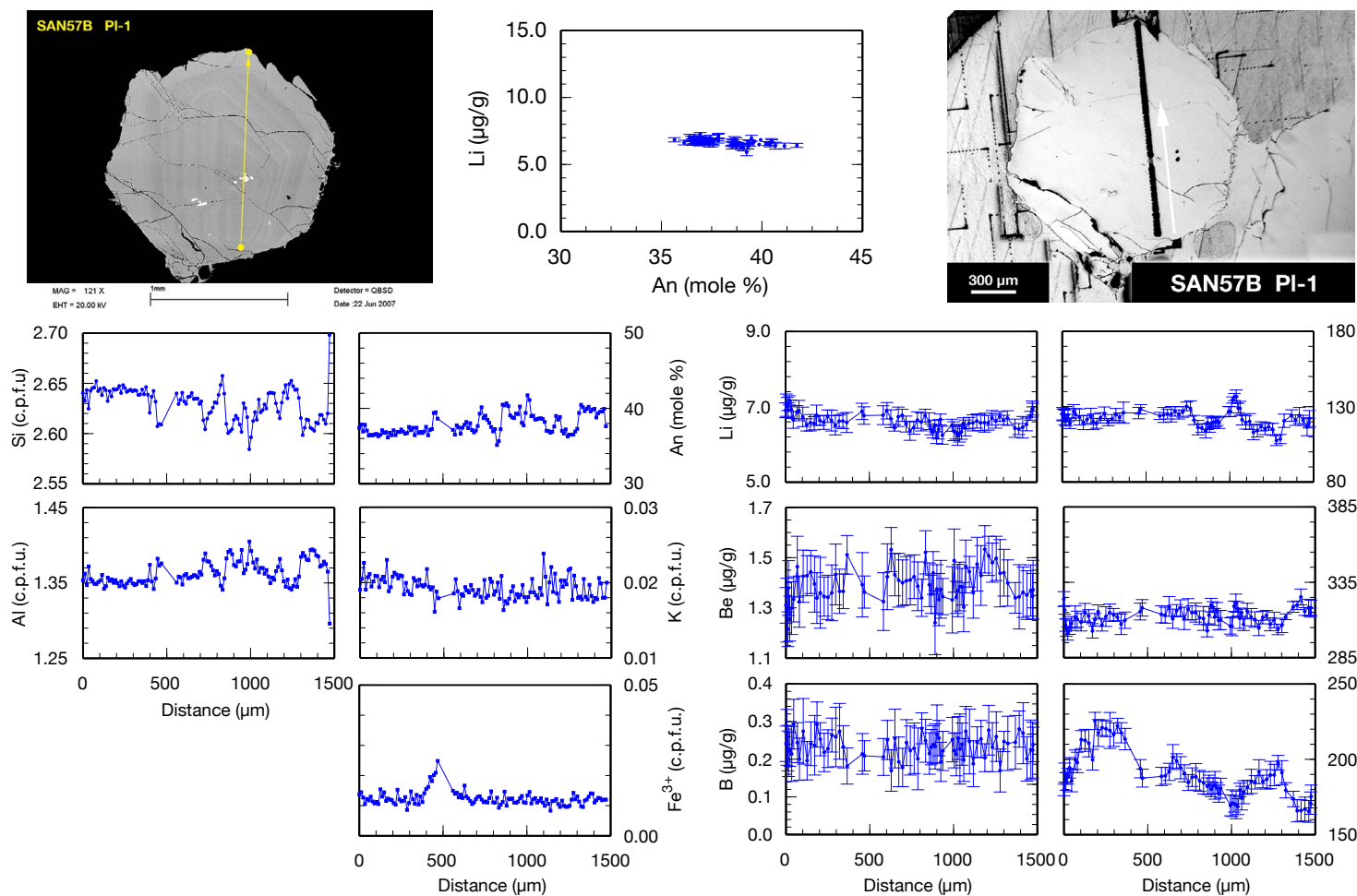
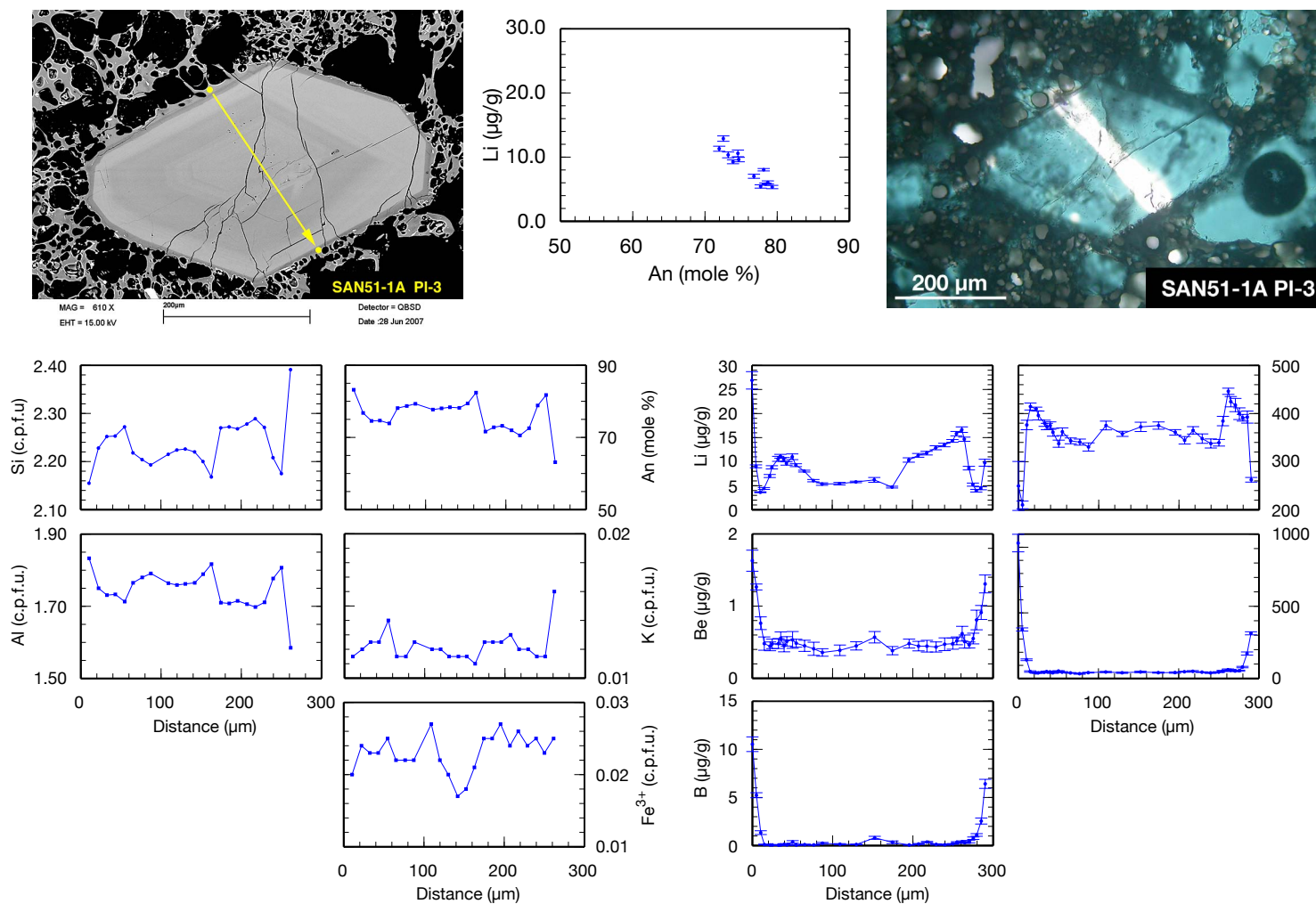**Fig. B.21.** SAN57B: Pl-1. EPMA and SIMS profiles. Formulas of EPMA analyses are calculated to 8 oxygens.
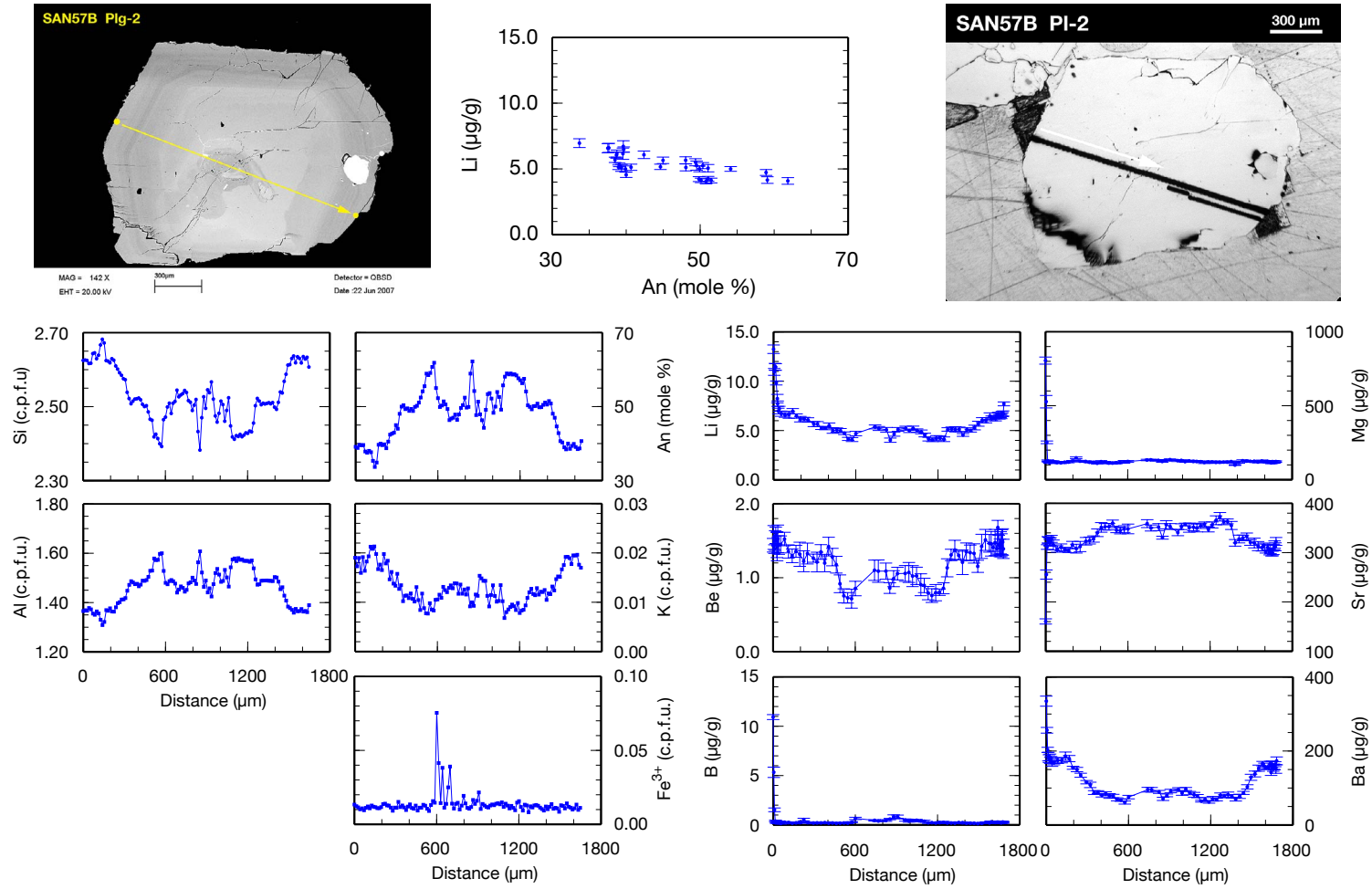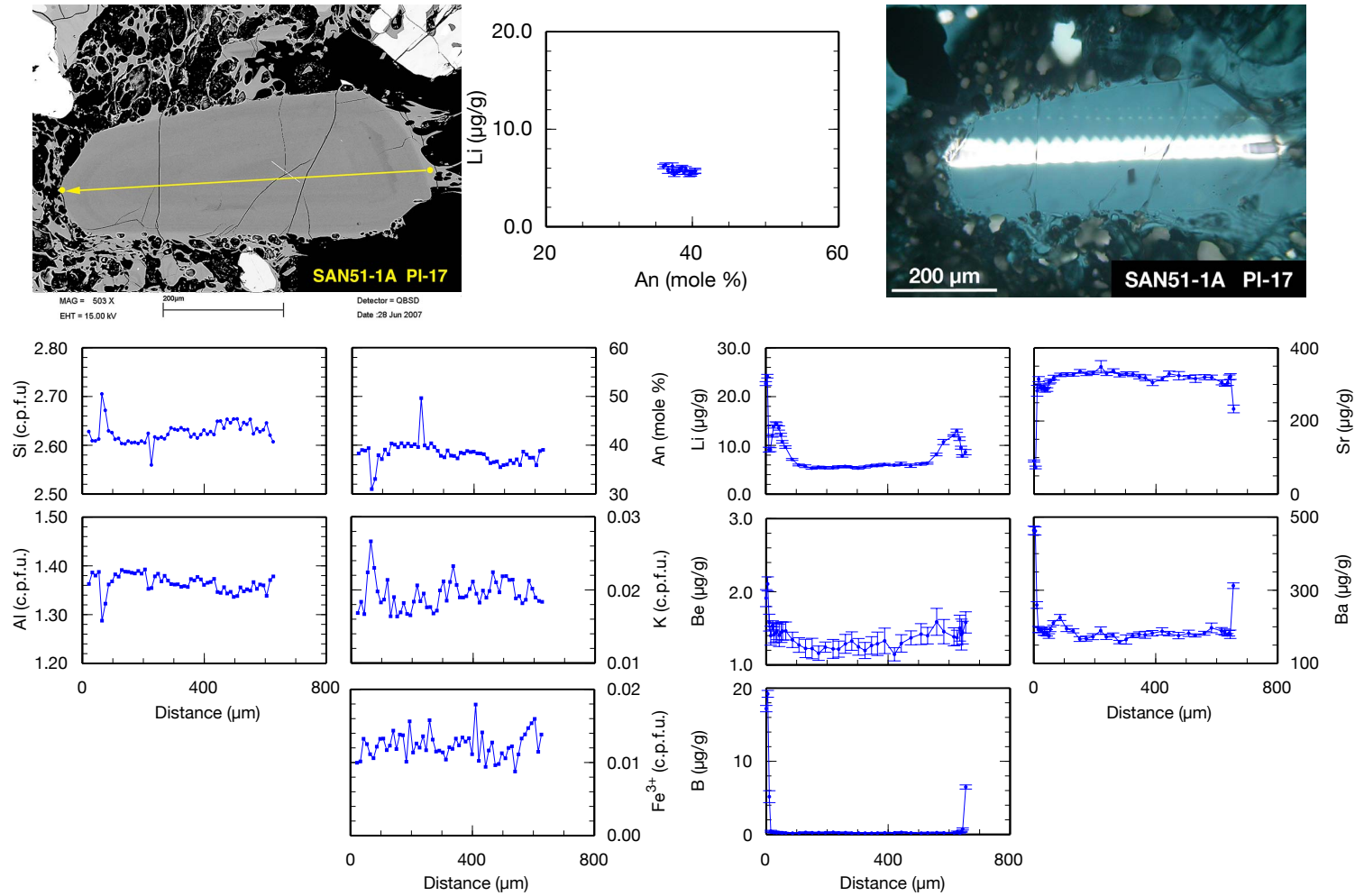
Fig. B.22. SAN57B: Pl-2. EPMA and SIMS profiles. Formulas of EPMA analyses are calculated to 8 oxygens.

B.2. SAN58 & SAN61 – Minoan B

**Sample positions
Minoan B**

up to
40 m

D

up to
55 m

C

up to
12 m

B

top area → SAN - 61

SAN - 58
ca. 2 m

up to
6 m

A
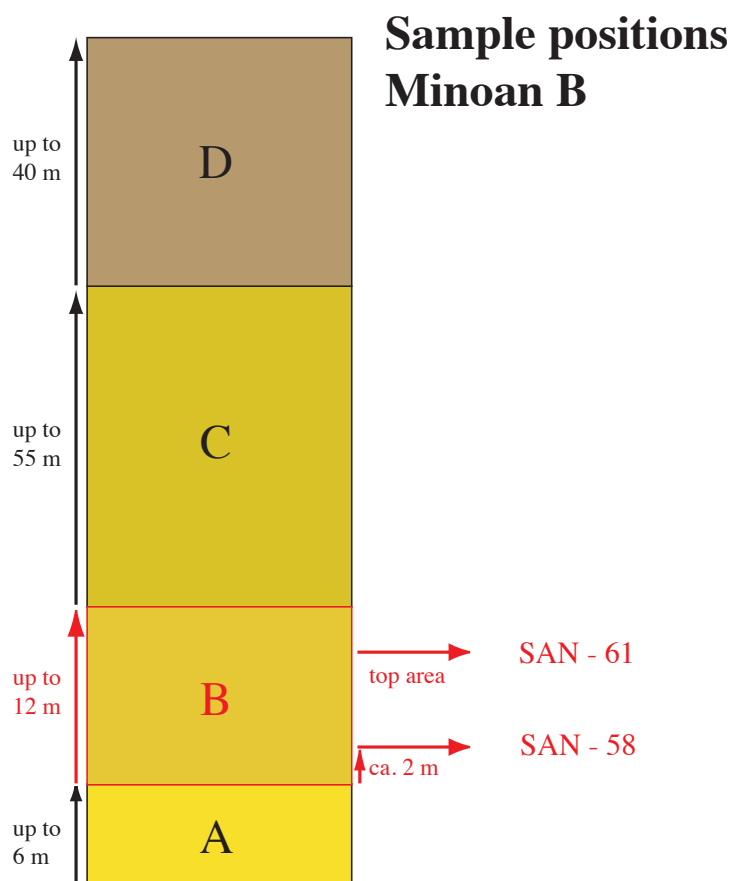
Fig. B.23. Positions of pumice samples taken from Minoan Unit B.
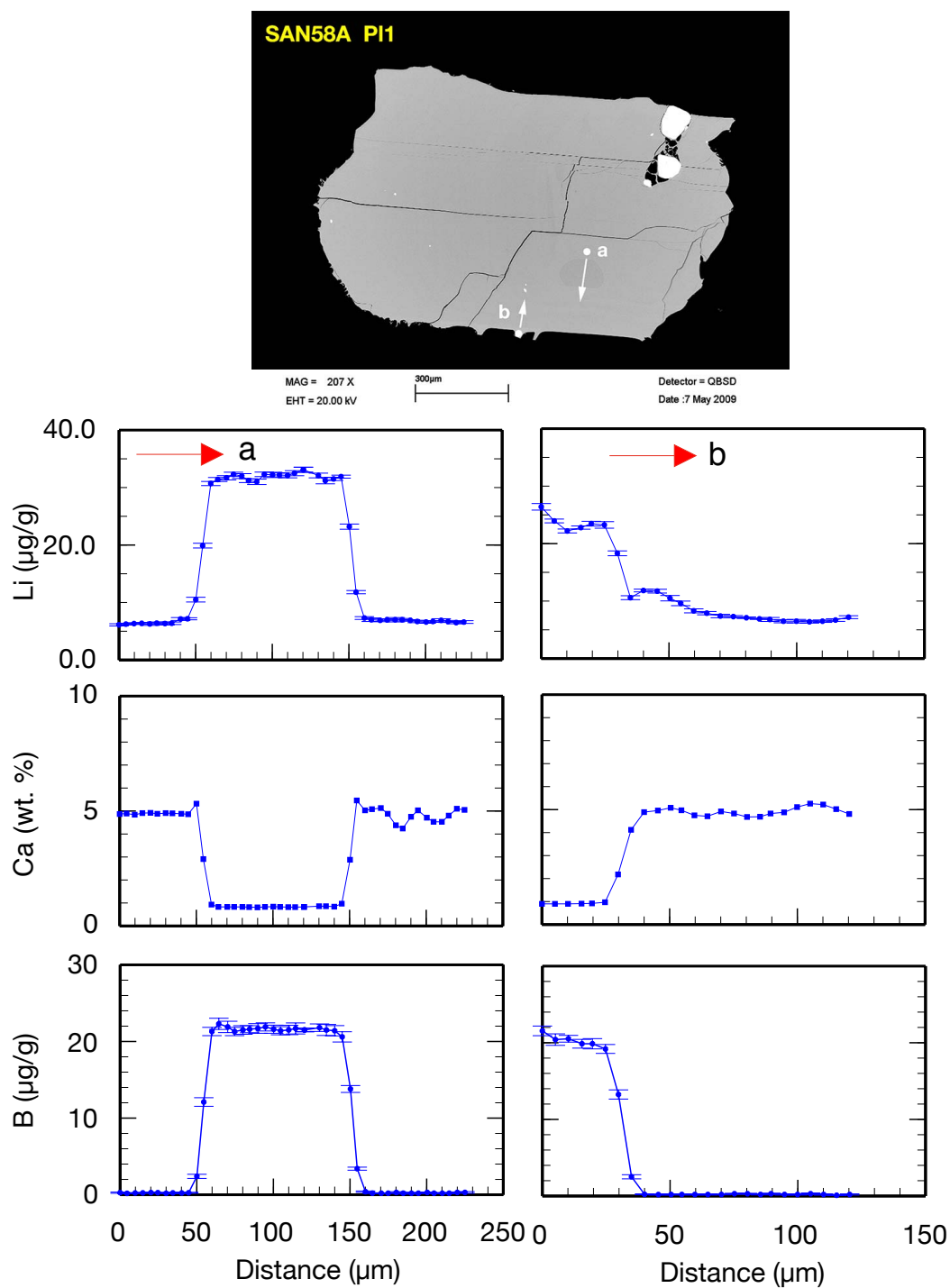
Fig. B.24. SAN58A: Pl-1. A short SIMS profile was analyzed to detect or exclude diffusion of Li from glass selvages or inclusions into plagioclase.
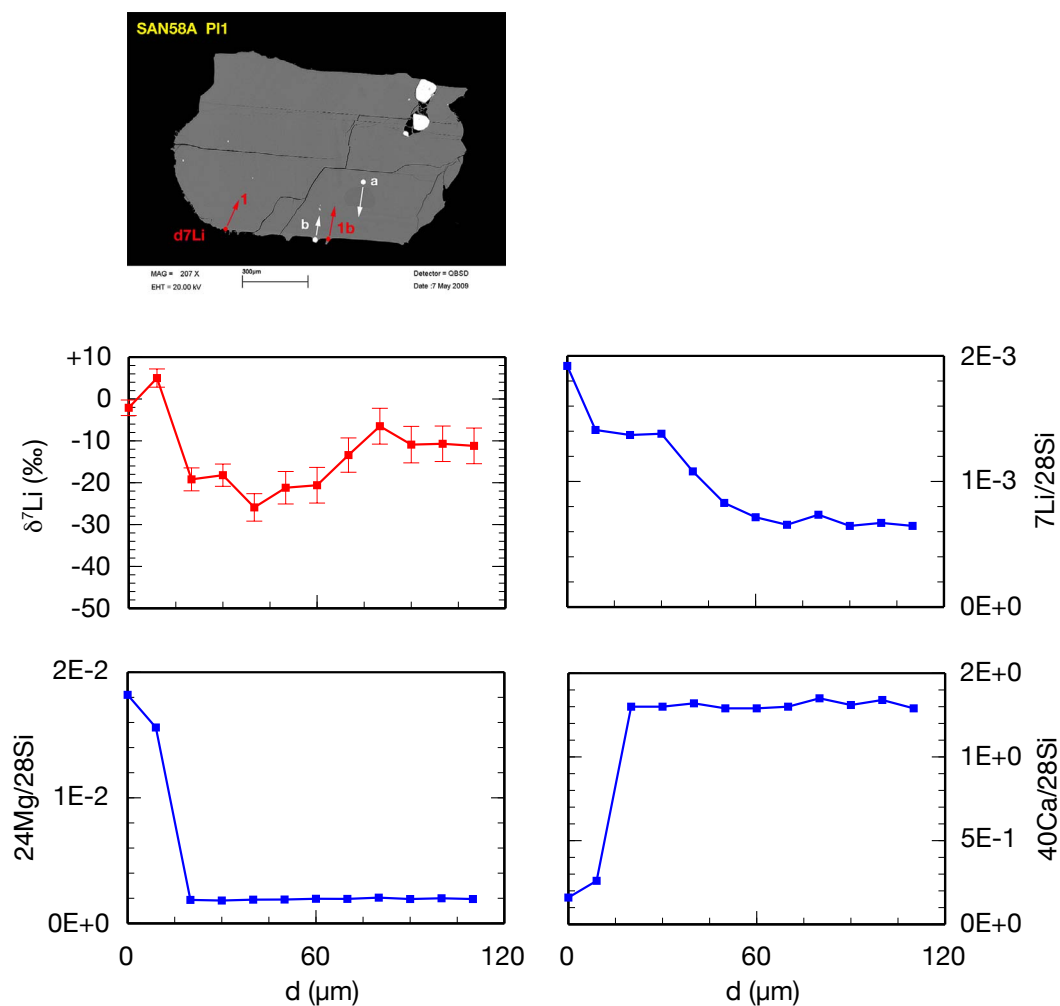
Fig. B.25. SAN58A: Pl-1. Short δ^7Li SIMS profile. The blue arrow marks the δ^7Li profiles; the red or white arrows mark the regular Li short profiles. A yellow arrow usually marks the EPMA profile (not all pl crystals were analyzed by EPMA). Li concentration values are derived from count rates of the isotope analyses and are therefore only semi-quantitative.
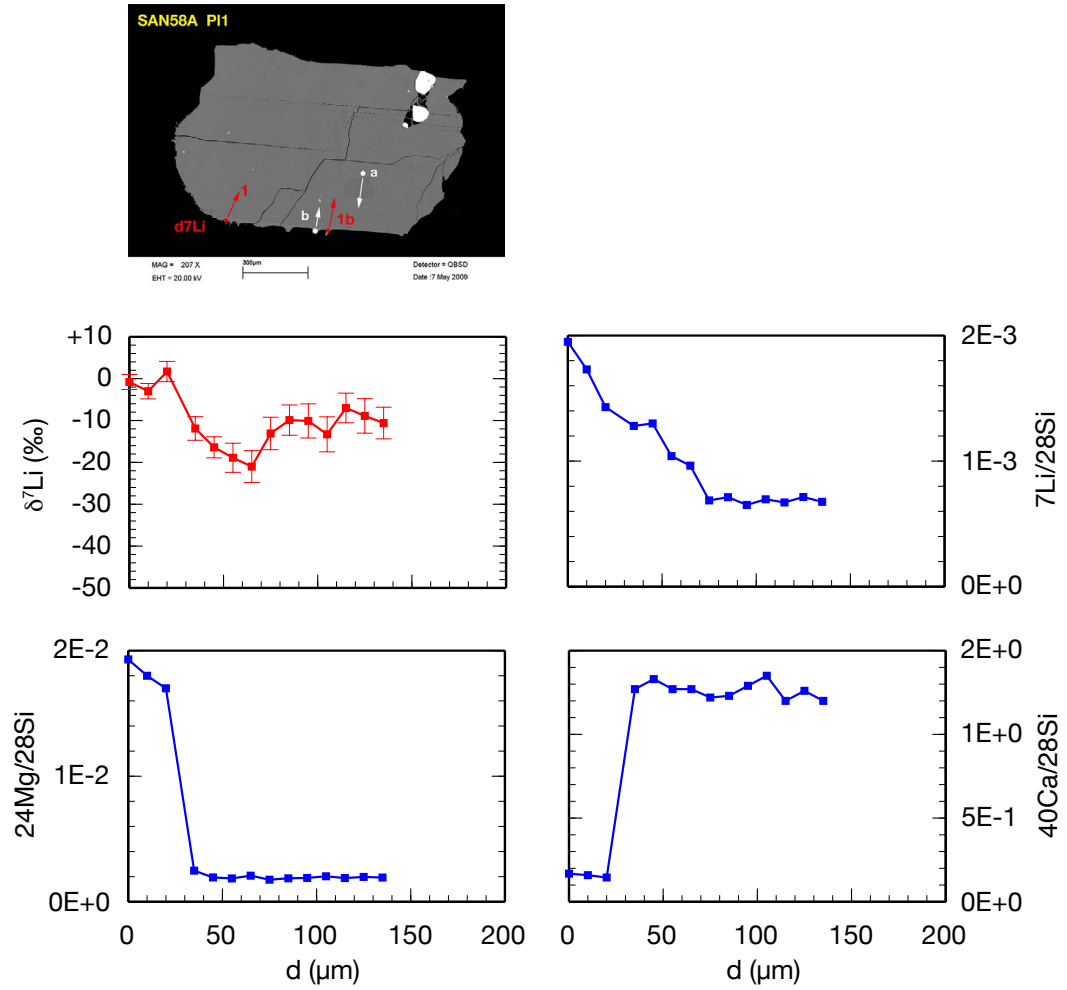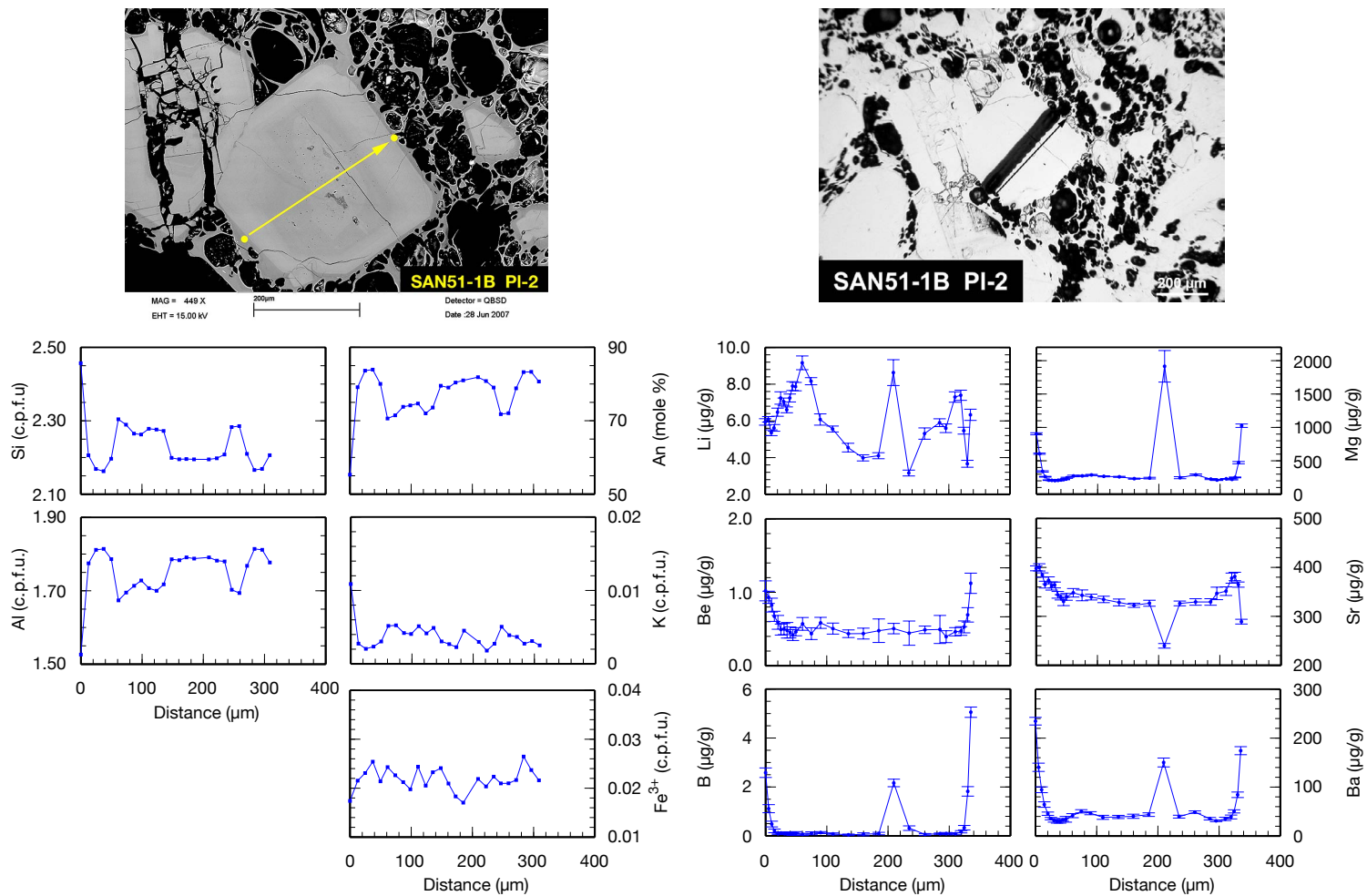
Fig. B.26. SAN58A: Pl-1b. Short δ^7Li SIMS profile. The blue arrow marks the δ^7Li profiles; the red or white arrows mark the regular Li short profiles. A yellow arrow usually marks the EPMA profile (not all pl crystals were analyzed by EPMA). Li concentration values are derived from count rates of the isotope analyses and are therefore only semi-quantitative.
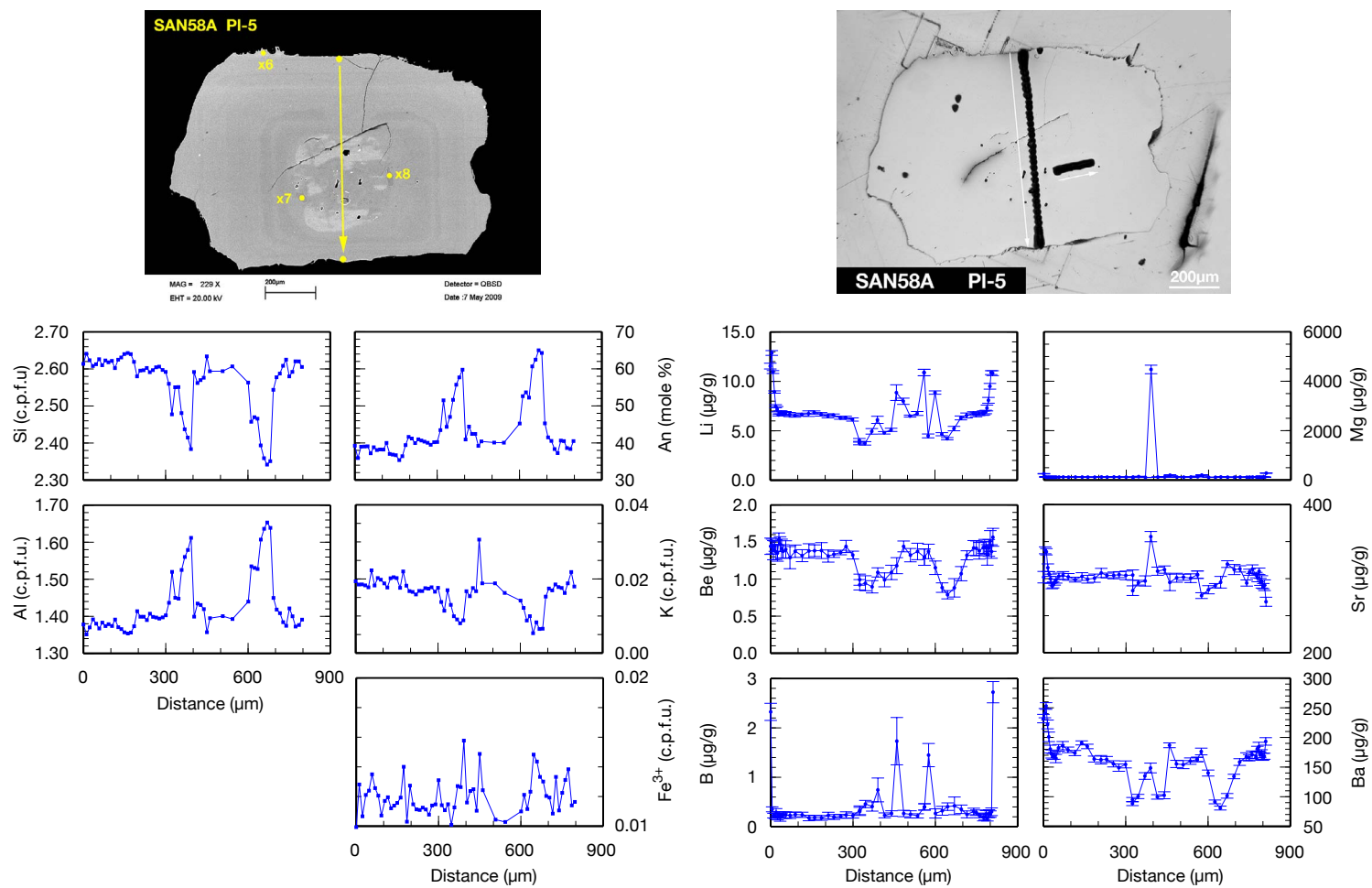
Fig. B.27. SAN58A: Pl-5. EPMA and SIMS profiles. Formulas of EPMA analyses are calculated to 8 oxygens.
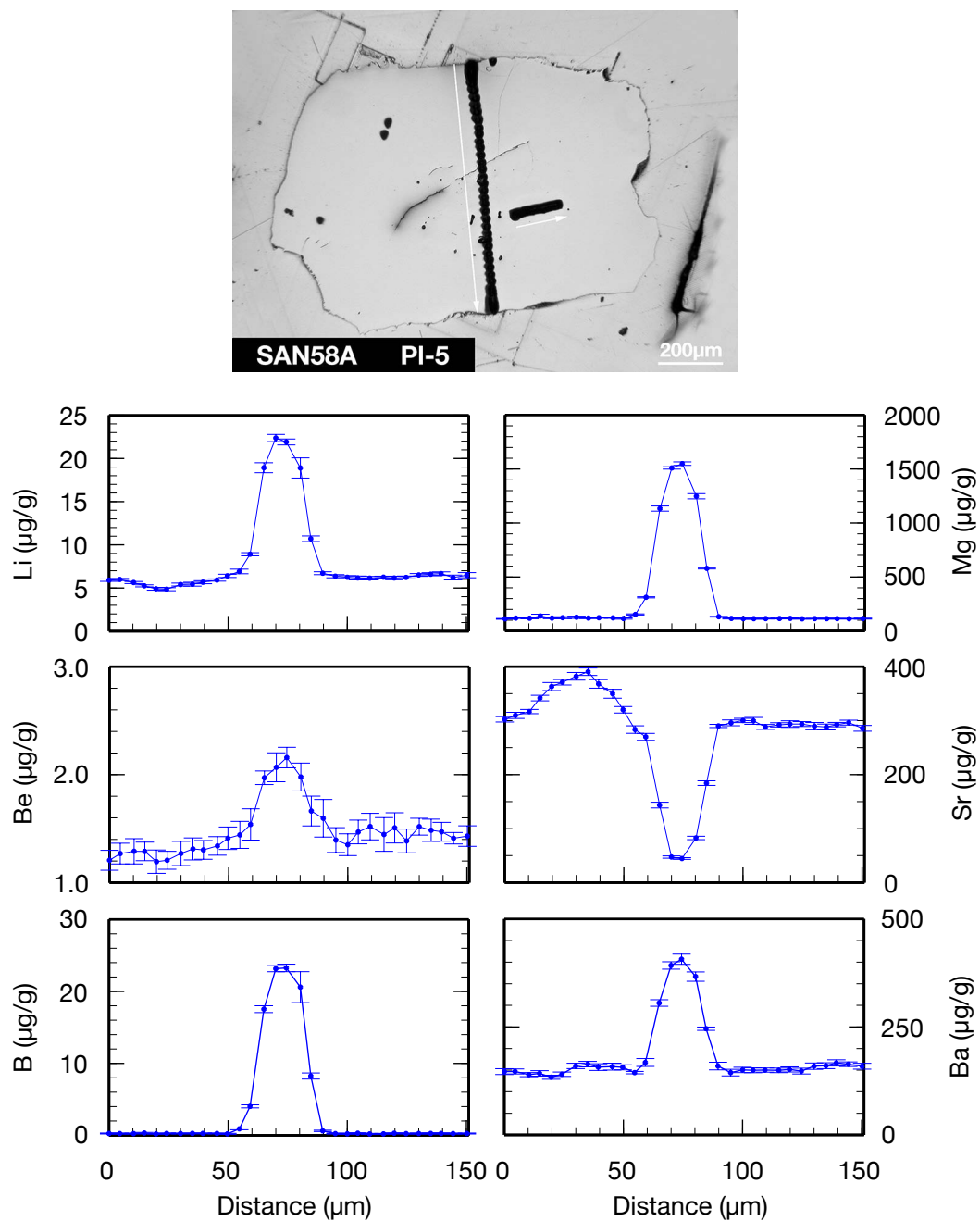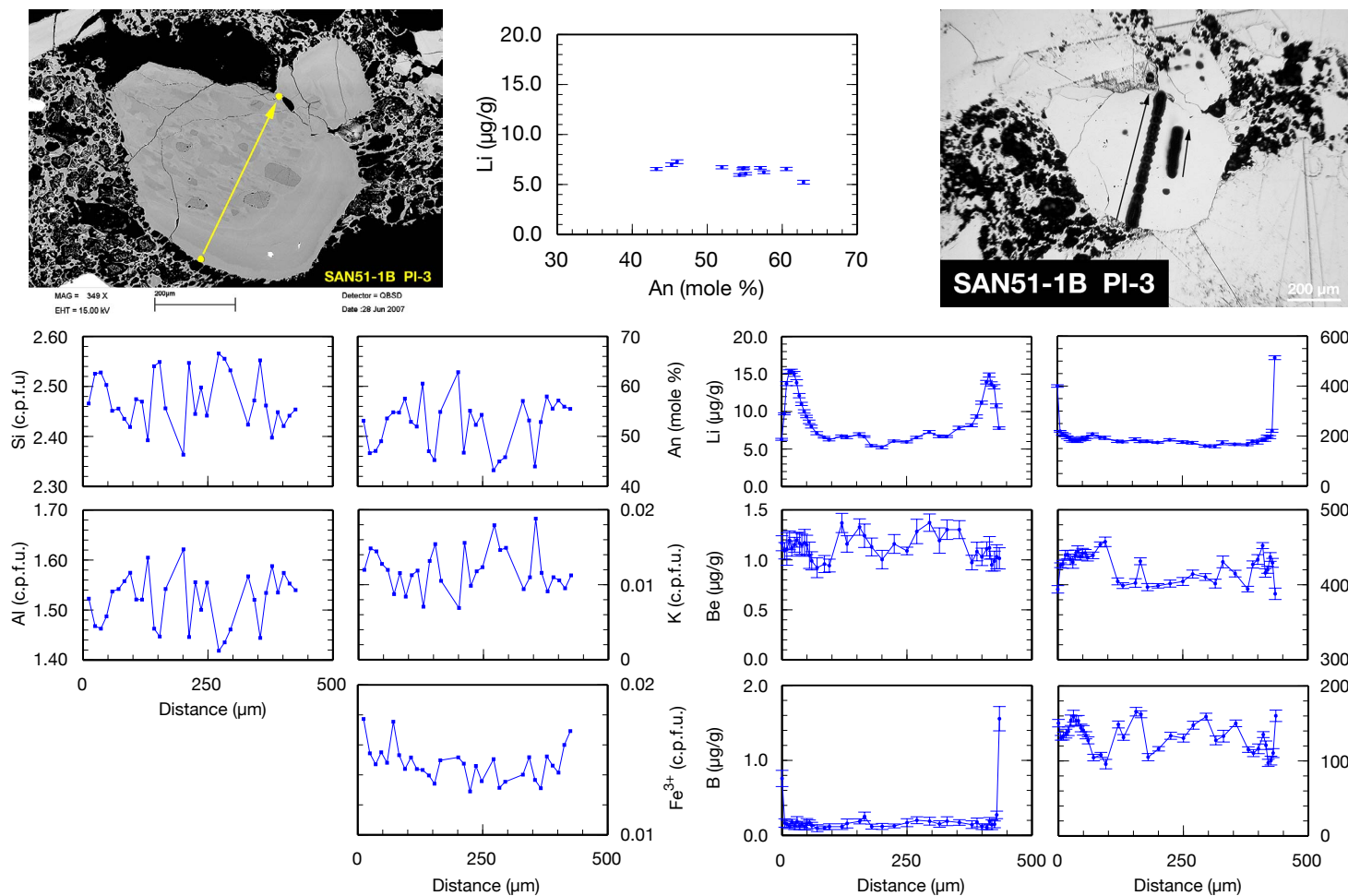
**Fig. B.28.** SAN58A: Pl-5. SIMS profile through glass inclusion.
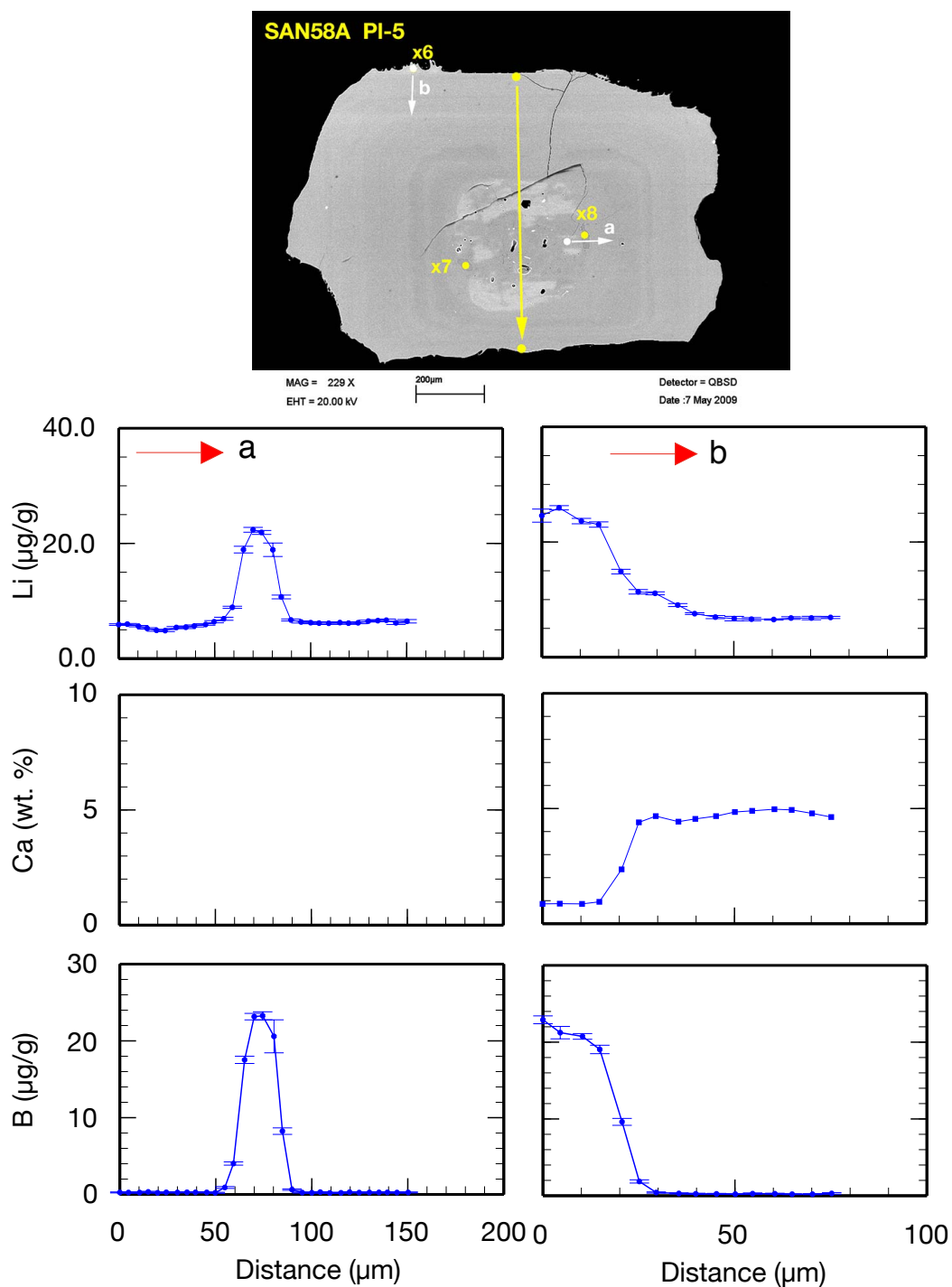
Fig. B.29. SAN58A: Pl-5. A short SIMS profile was analyzed to detect or exclude diffusion of Li from glass selvages or inclusions into plagioclase..
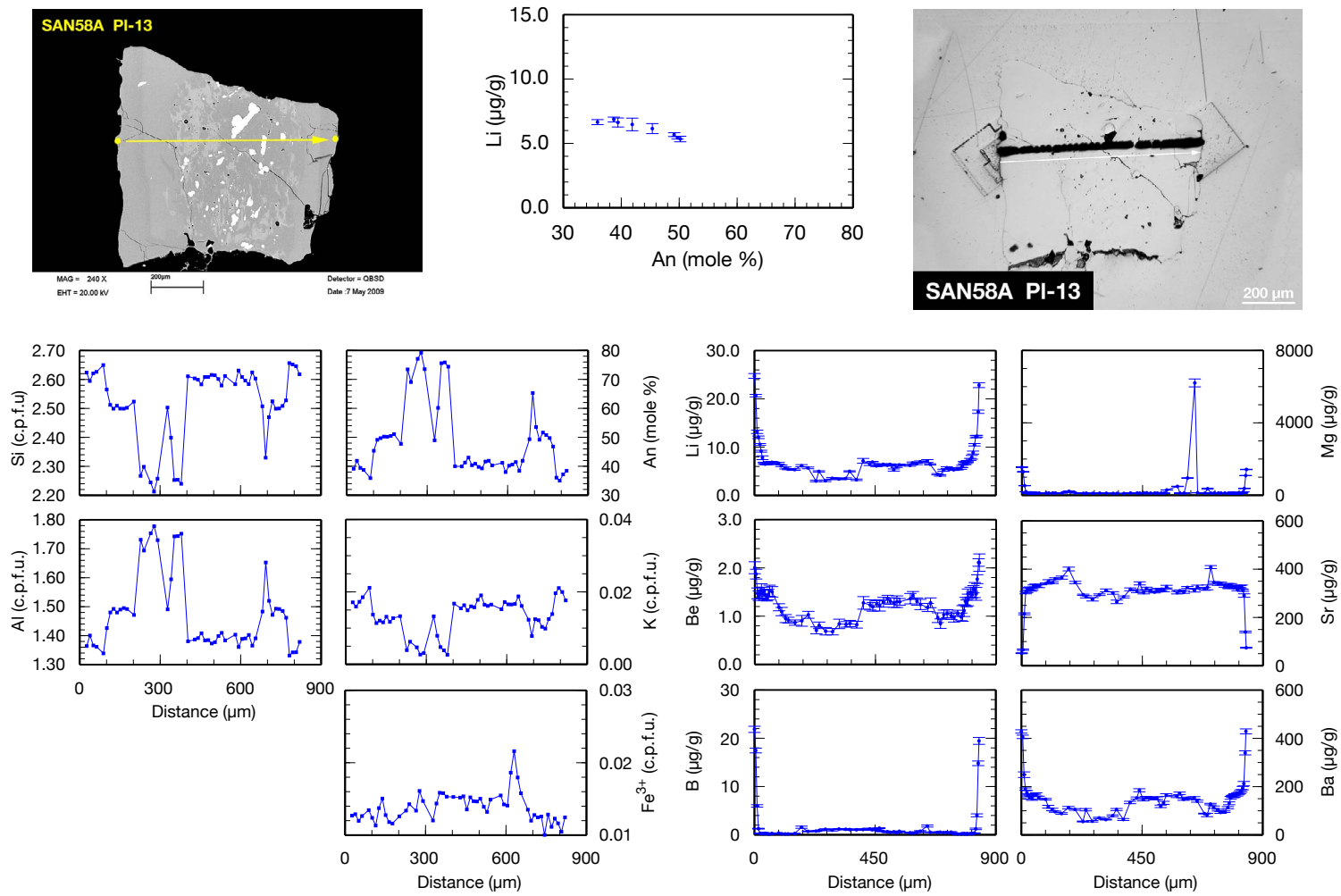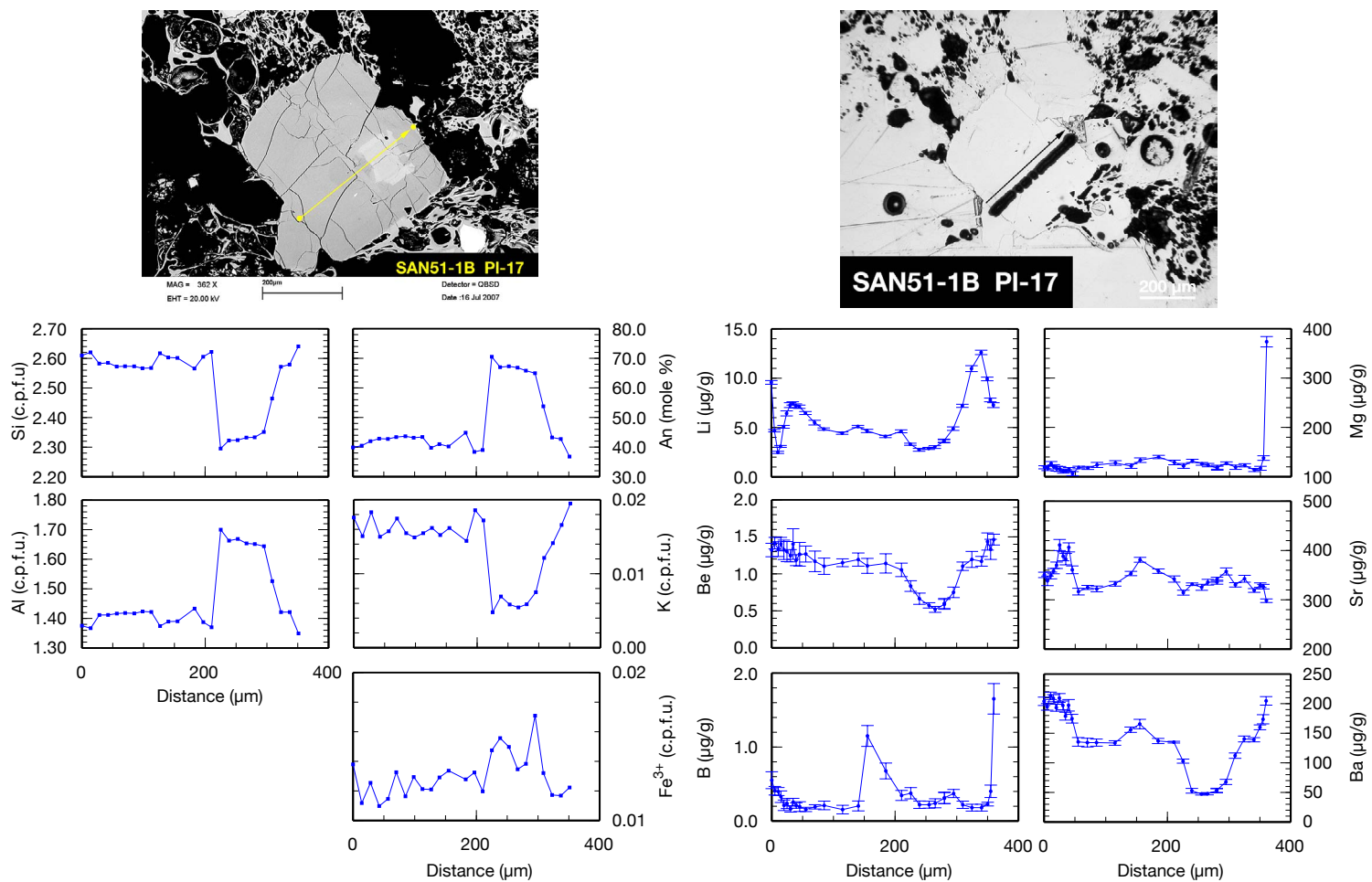
Fig. B.30. SAN58A: Pl-13. EPMA and SIMS profiles. Formulas of EPMA analyses are calculated to 8 oxygens.
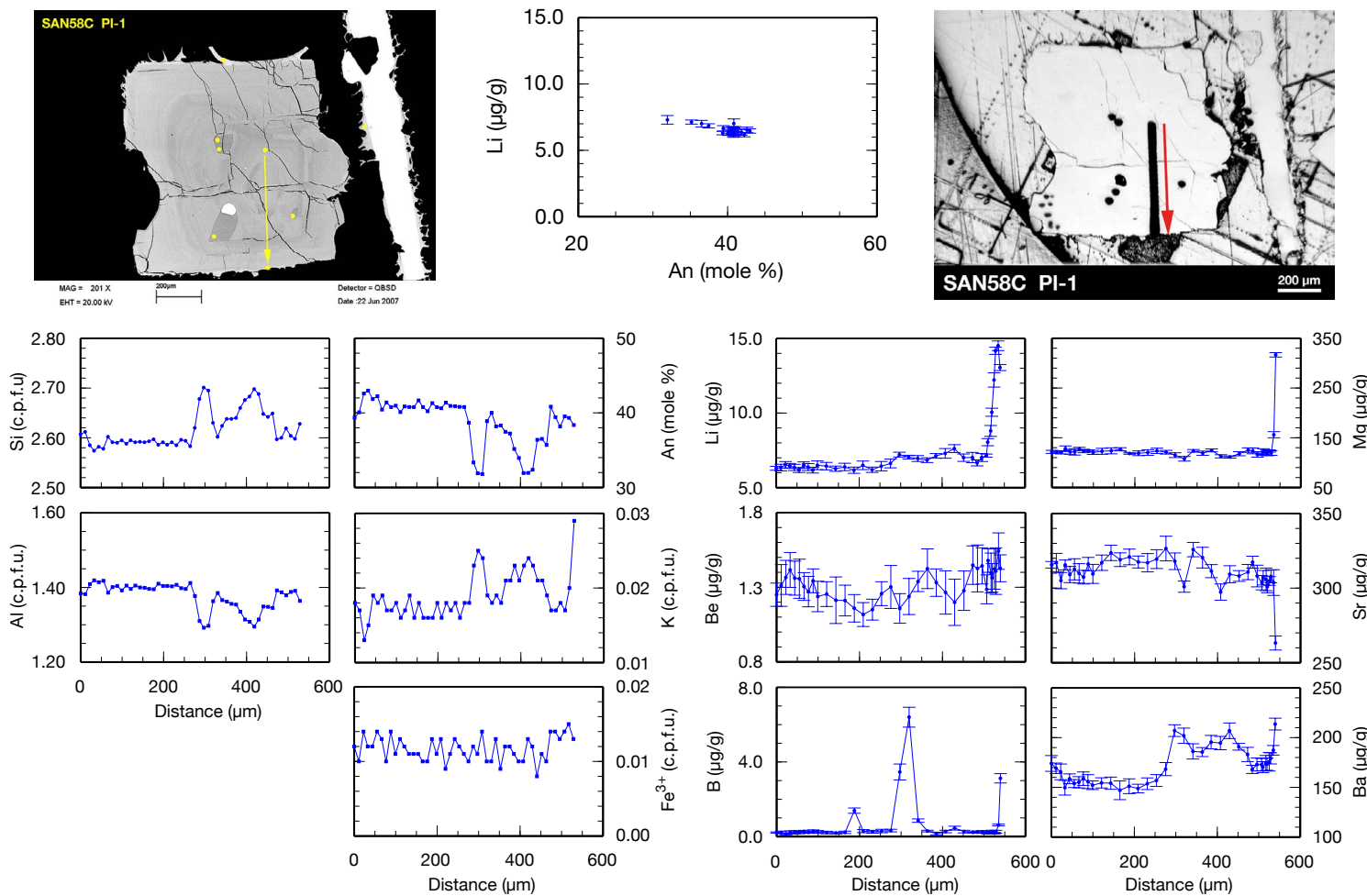
Fig. B.31. SAN58C: Pl-1. EPMA and SIMS profiles. Formulas of EPMA analyses are calculated to 8 oxygens.
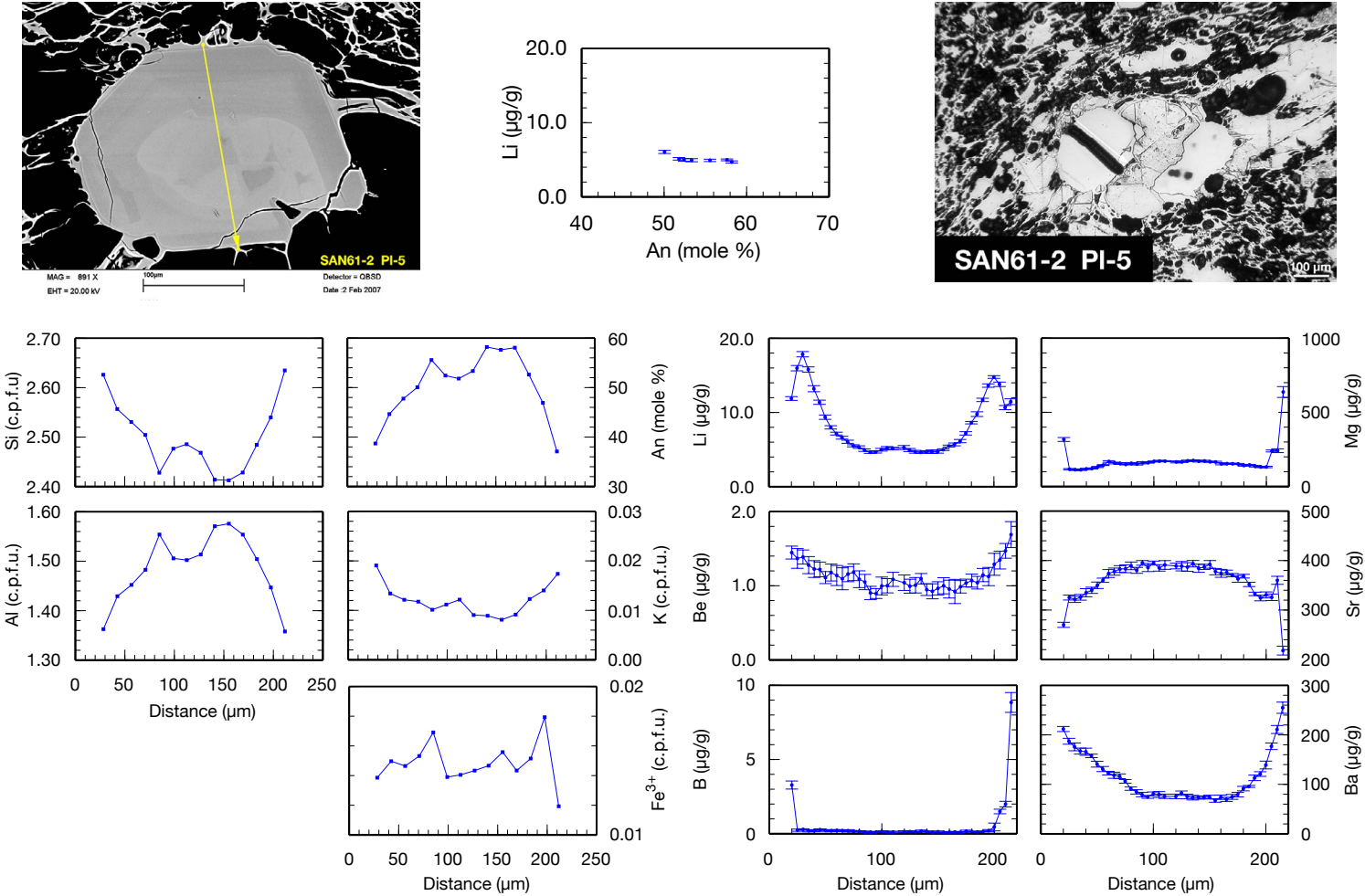
Fig. B.32. SAN61-2: Pl-5. EPMA and SIMS profiles. Formulas of EPMA analyses are calculated to 8 oxygens.
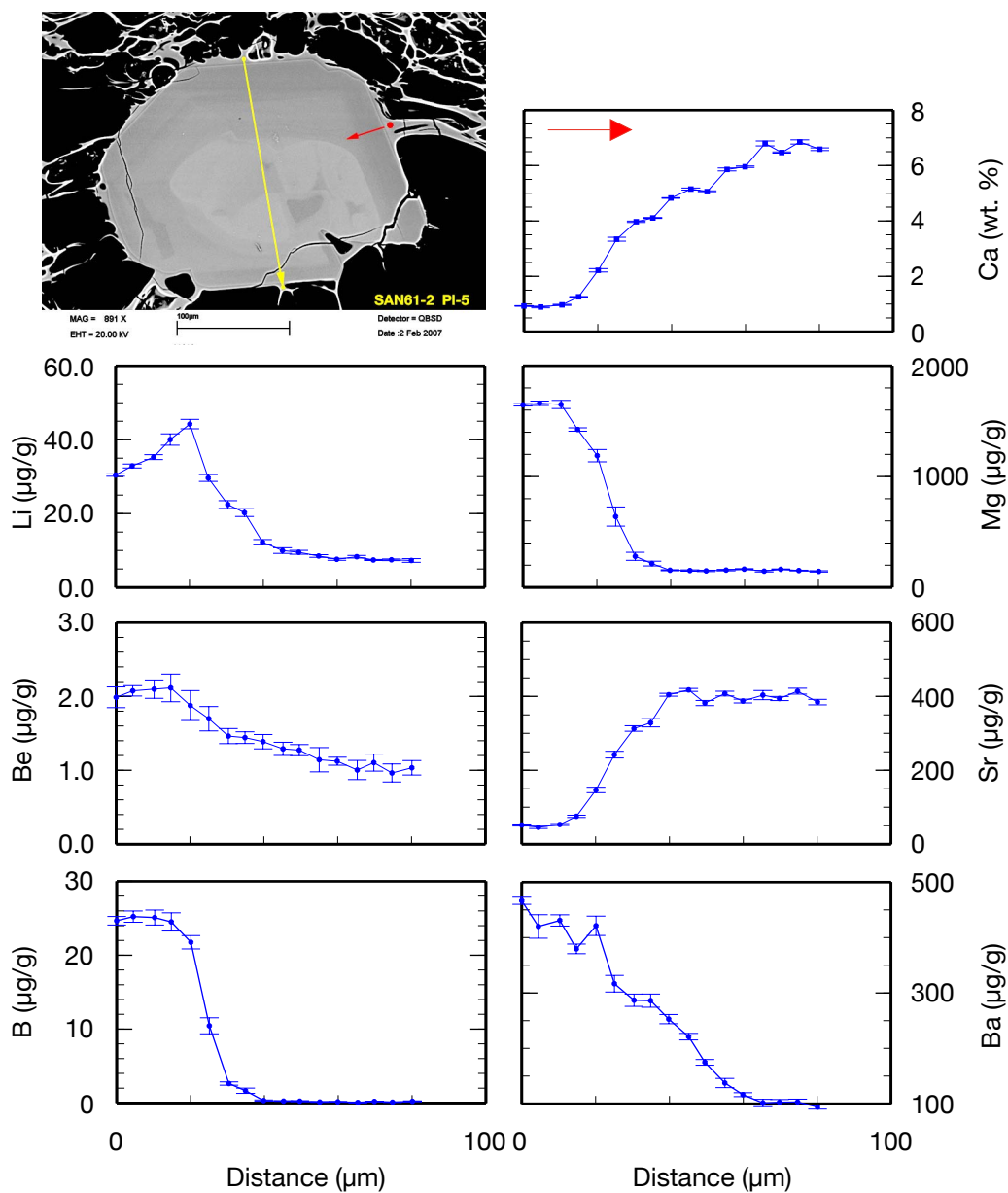
Fig. B.33. SAN61-2: Pl-5. A short SIMS profile was analyzed to detect or exclude diffusion of Li from glass selvages into plagioclase.
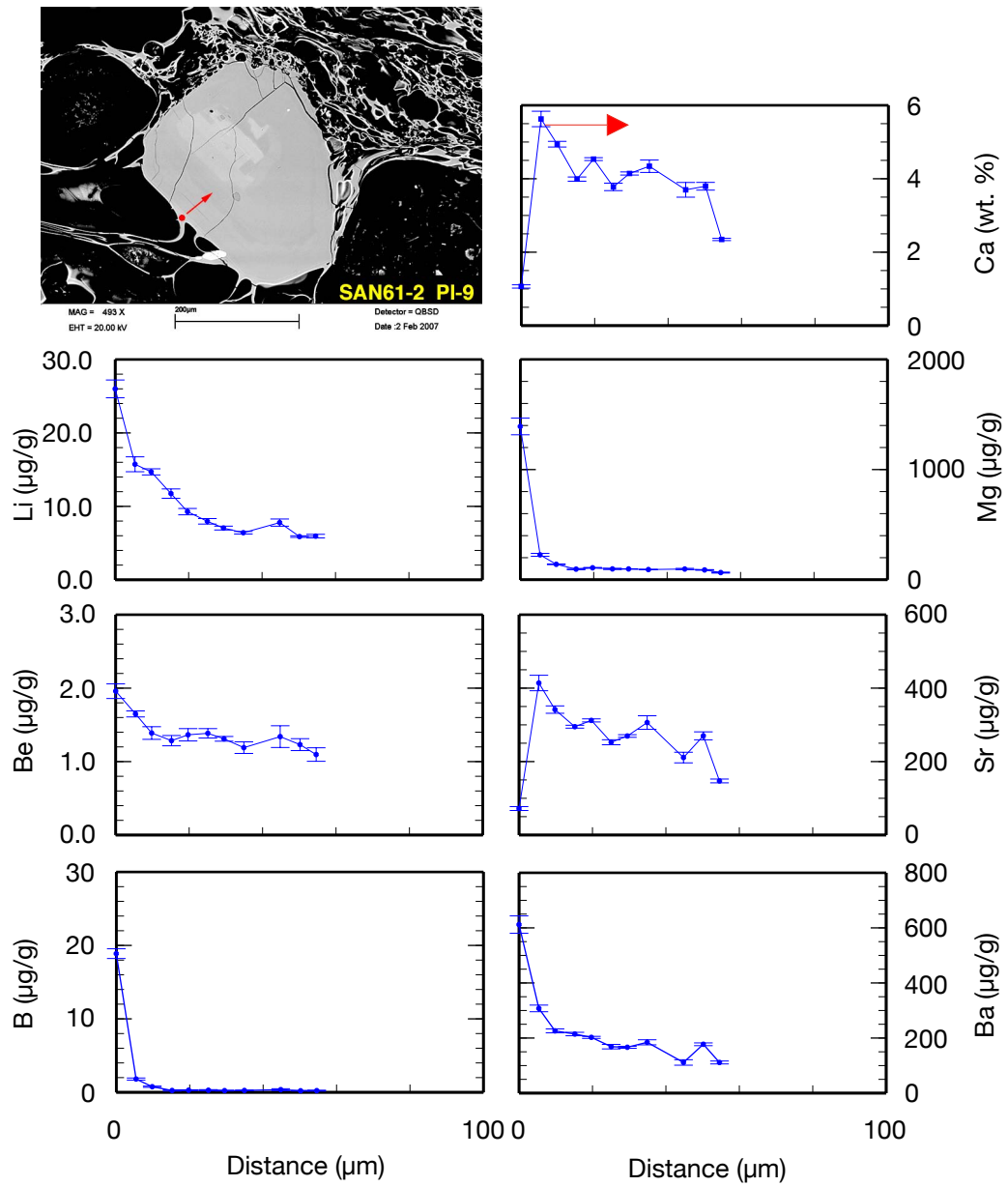
Fig. B.34. SAN61-2: Pl-9. A short SIMS profile was analyzed to detect or exclude diffusion of Li from glass selvages into plagioclase.
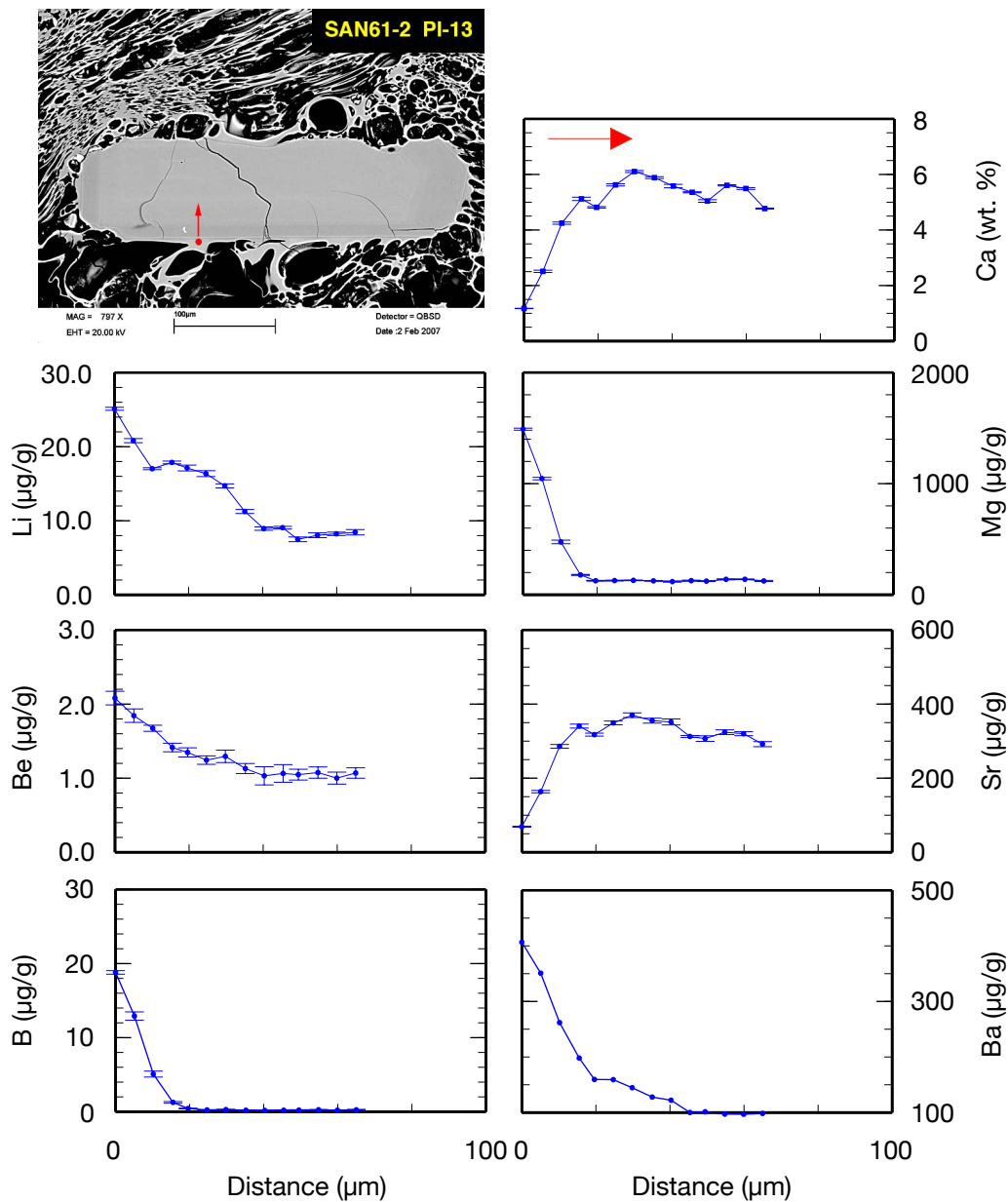
Fig. B.35. SAN61-2: Pl-13. A short SIMS profile was analyzed to detect or exclude diffusion of Li from glass selvages into plagioclase.
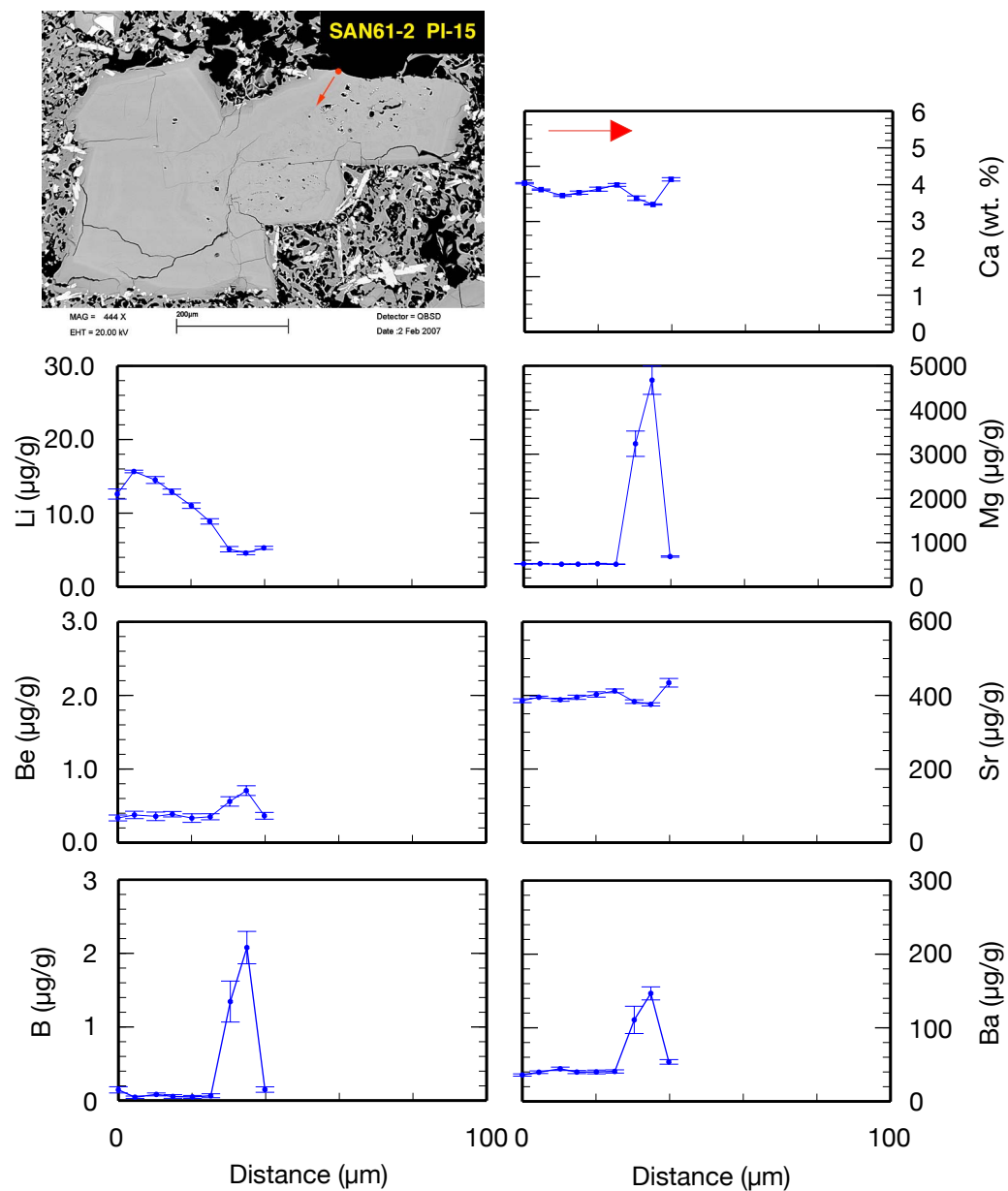
Fig. B.36. SAN61-2: Pl-15. A short SIMS profile was analyzed to detect or exclude diffusion of Li from a broken rim into plagioclase.
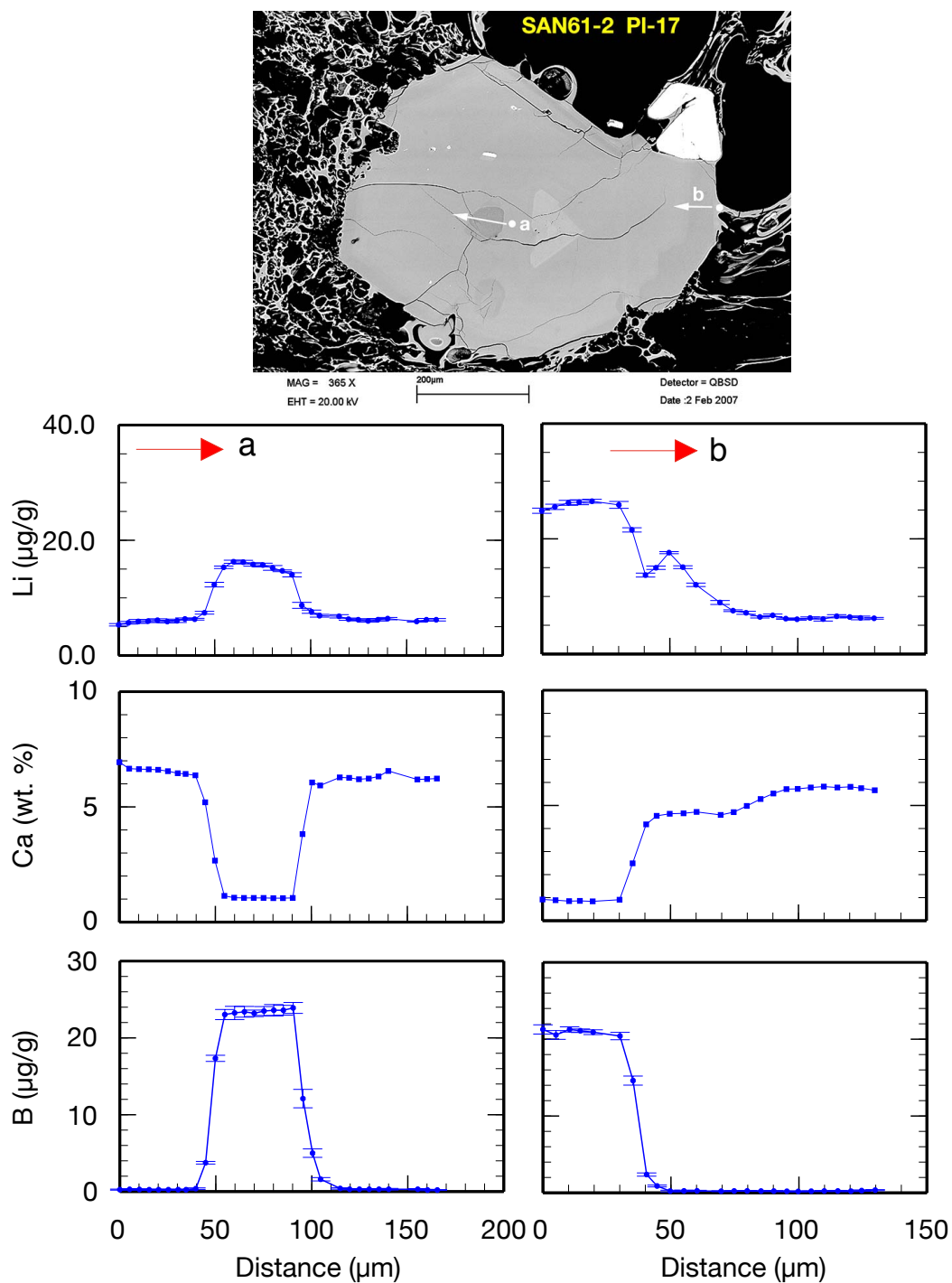
Fig. B.37. SAN61-2: Pl-17. A short SIMS profile was analyzed to detect or exclude diffusion of Li from a broken rim into plagioclase.
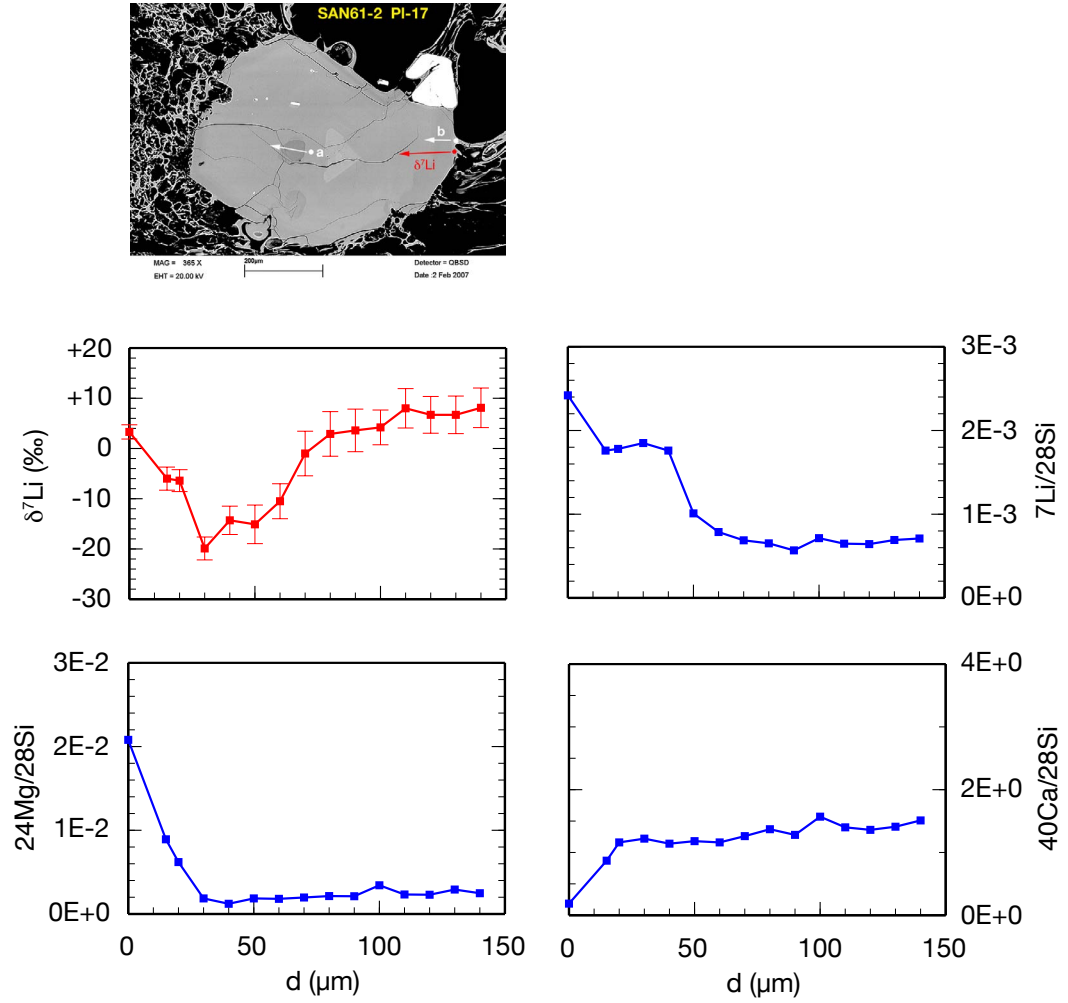
Fig. B.38. SAN61-2: Pl-17. Short δ^7Li SIMS profile. The blue arrow marks the δ^7Li profiles; the red or white arrows mark the regular Li short profiles. A yellow arrow usually marks the EPMA profile (not all pl crystals were analyzed by EPMA). Li concentration values are derived from count rates of the isotope analyses and are therefore only semi-quantitative.

Fig. B.39. SAN61-2: Pl-19. A short SIMS profile was analyzed to detect or exclude diffusion of Li from a broken rim into plagioclase
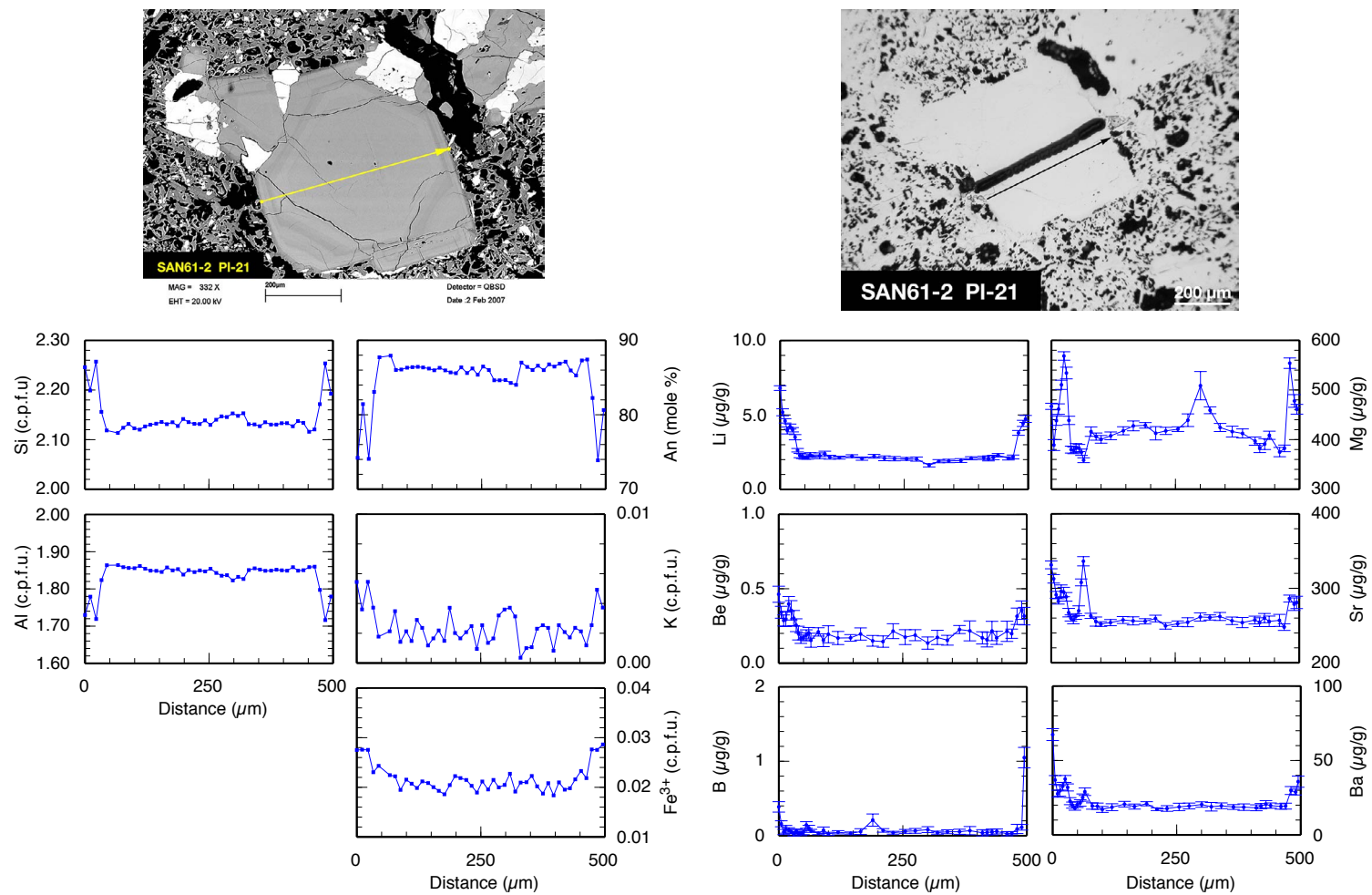
Fig. B.40. SAN61-2: Pl-21. EPMA and SIMS profiles. Formulas of EPMA analyses are calculated to 8 oxygens.
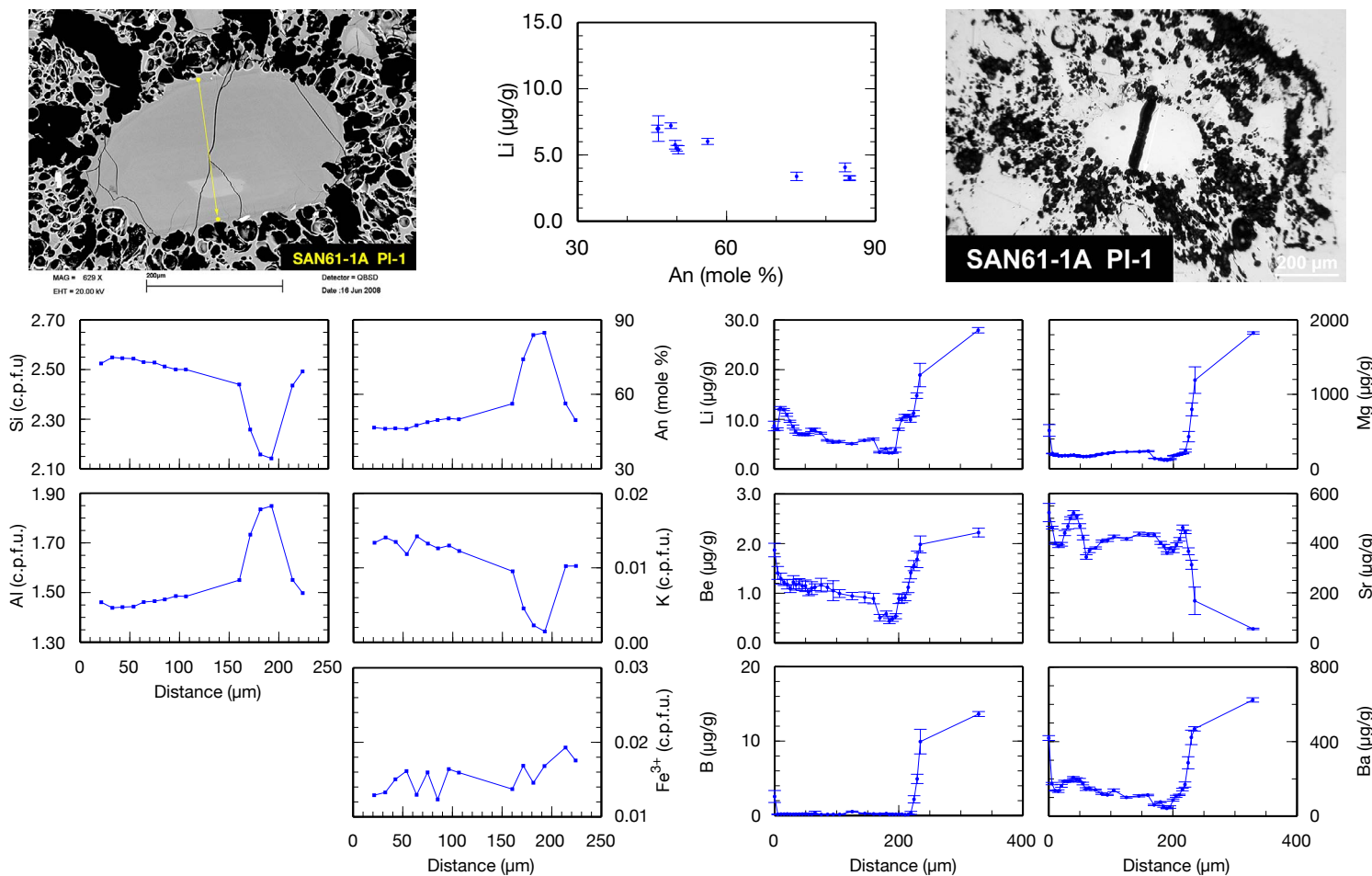
Fig. B.41. SAN61-1A: Pl-1. EPMA and SIMS profiles. Formulas of EPMA analyses are calculated to 8 oxygens.
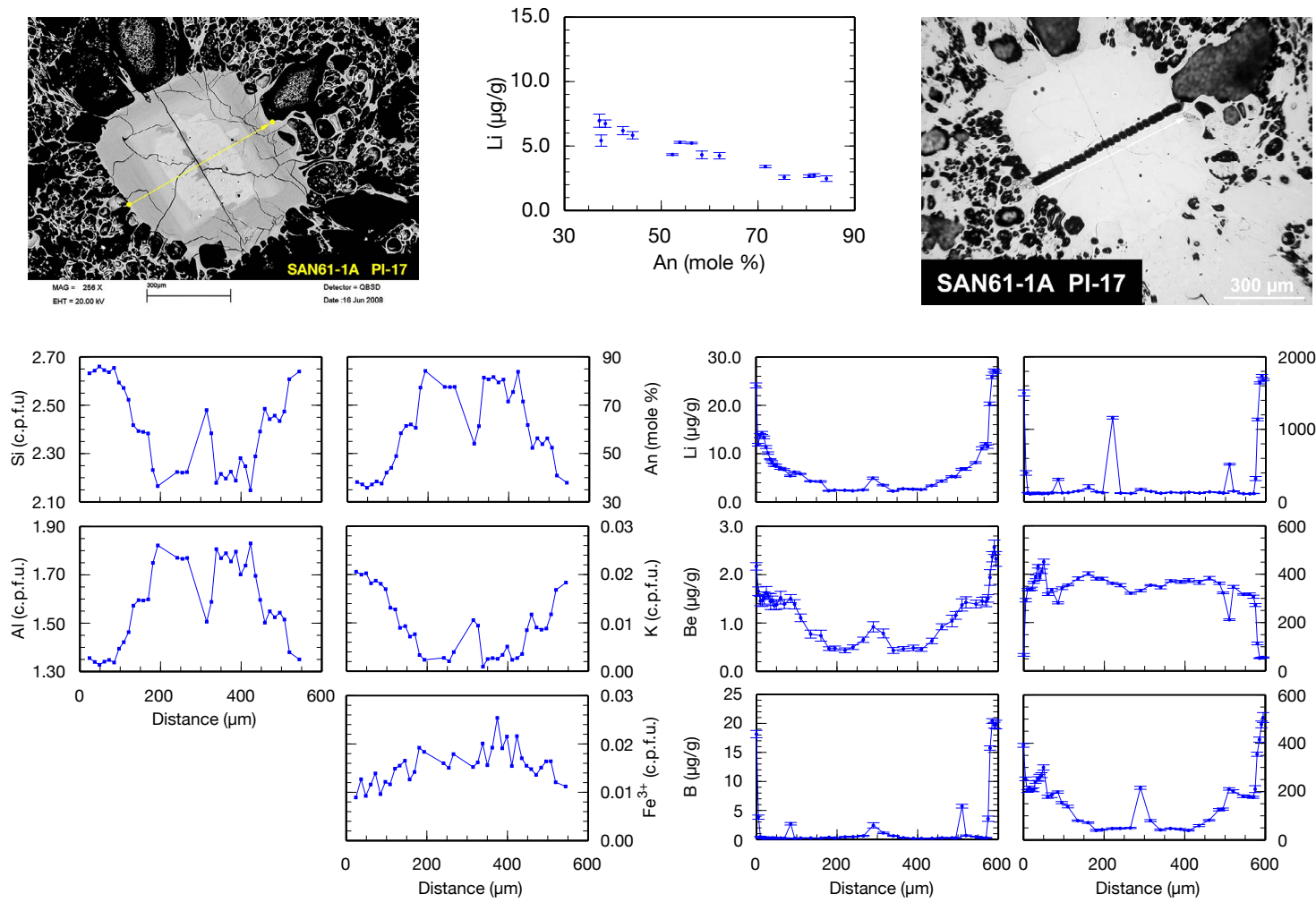
Fig. B.42. SAN61-1A: Pl-17. EPMA and SIMS profiles. Formulas of EPMA analyses are calculated to 8 oxygens.
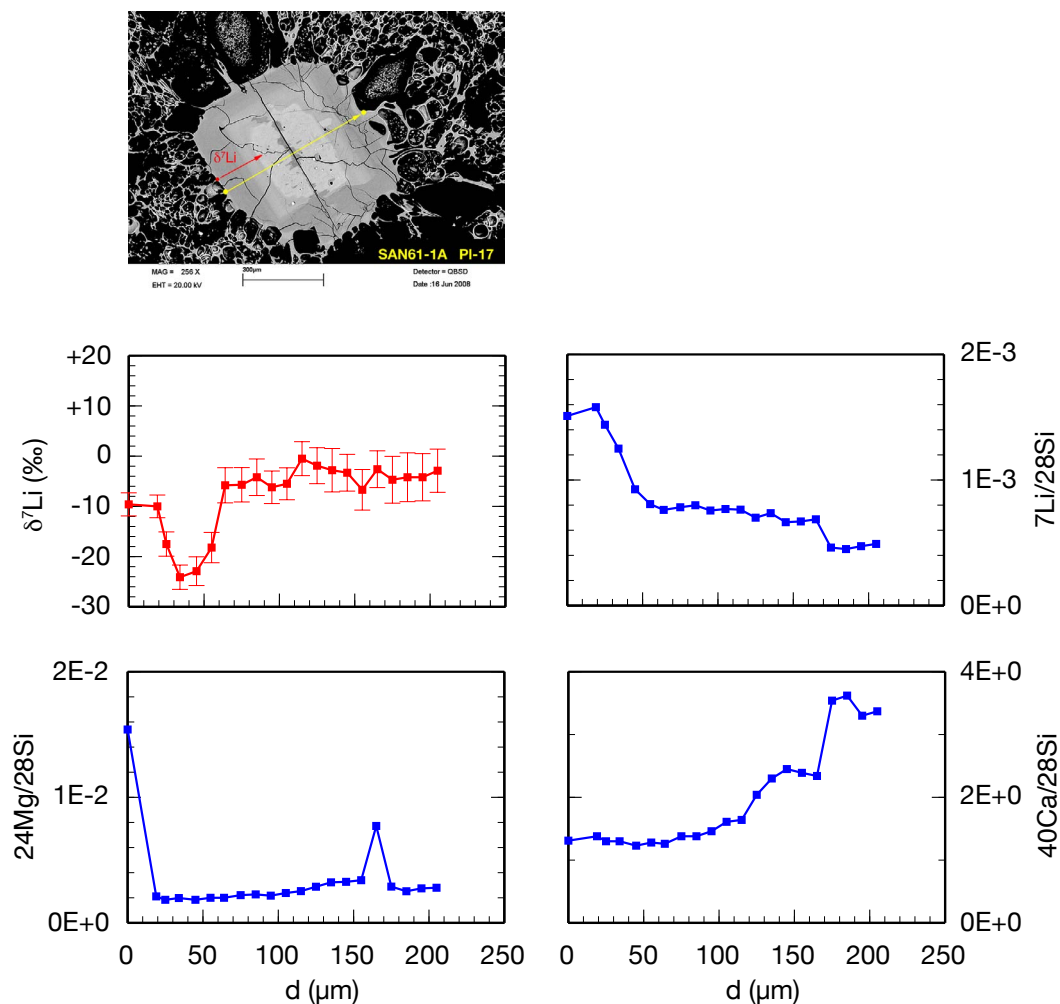
Fig. B.43. SAN61-1A: Pl-17. Short δ^7Li SIMS profile. The blue arrow marks the δ^7Li profiles; the red or white arrows mark the regular Li short profiles. A yellow arrow usually marks the EPMA profile (not all pl crystals were analyzed by EPMA). Li concentration values are derived from count rates of the isotope analyses and are therefore only semi-quantitative.

B.3. SAN59 – Minoan C
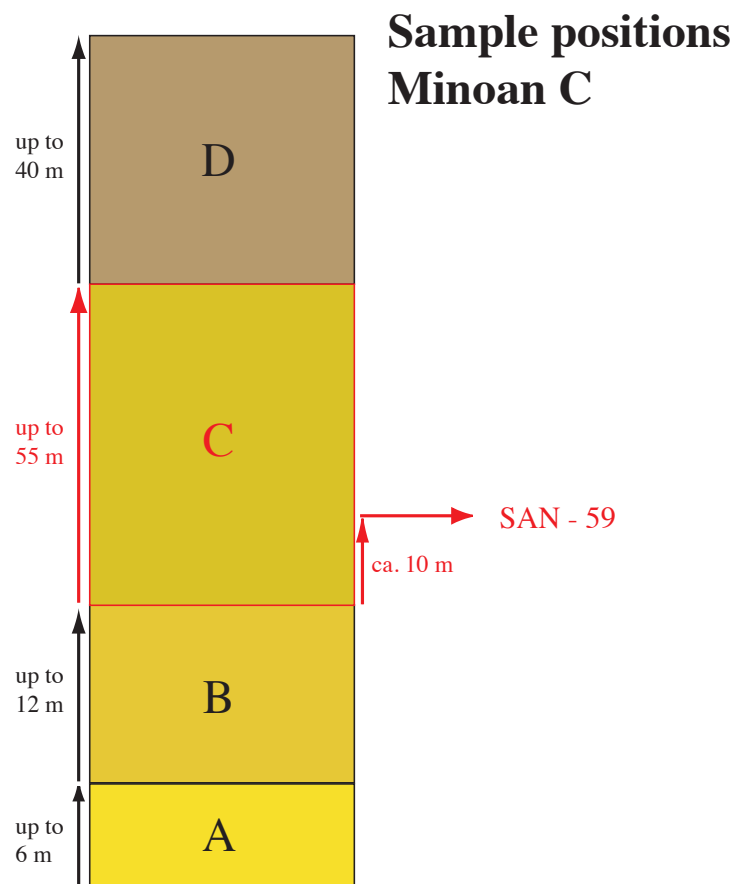
Fig. B.44. Positions of pumice samples taken from Minoan Unit C.
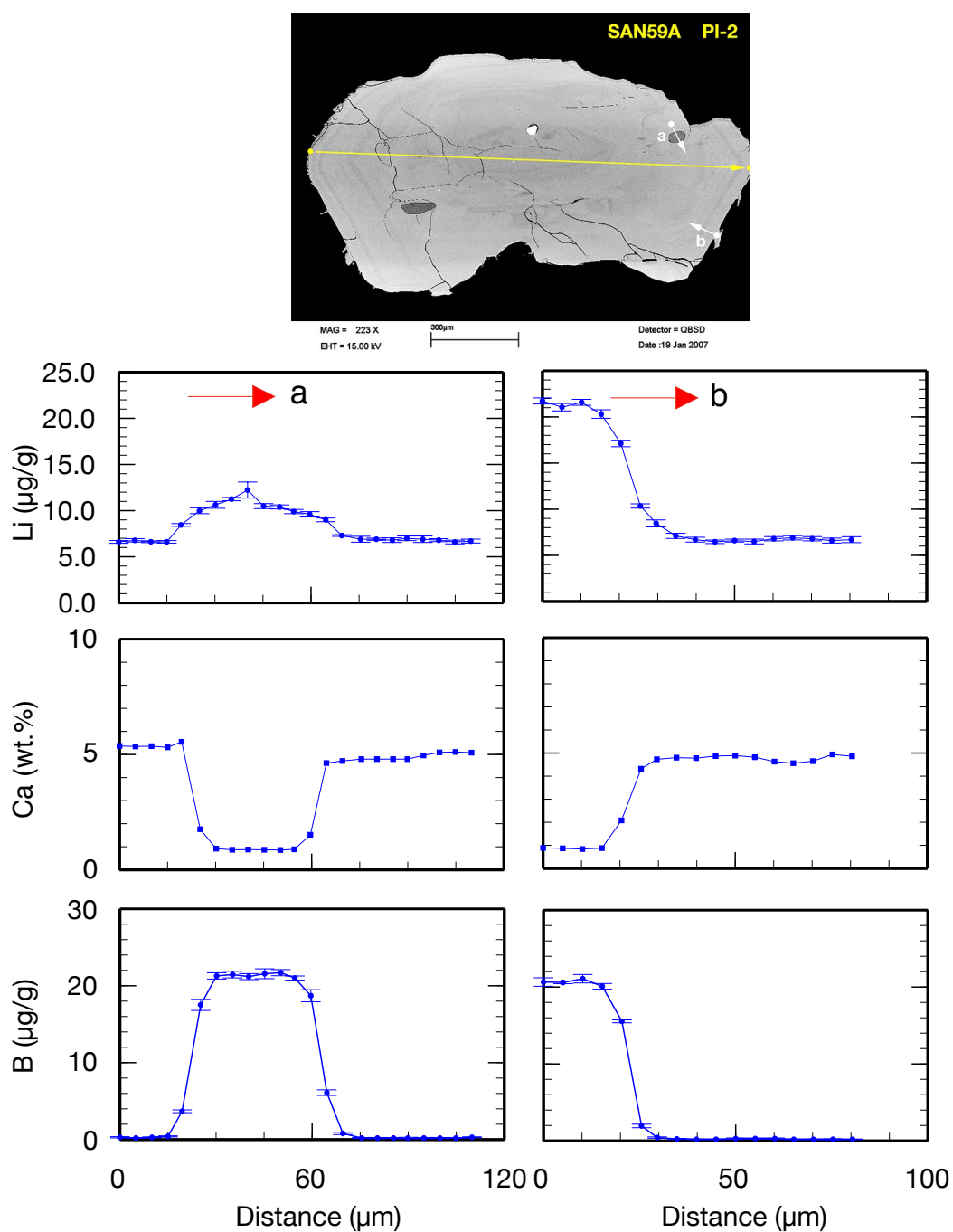
Fig. B.45. SAN59A: Pl-2. A short SIMS profile was analyzed to detect or exclude diffusion of Li from glass selvages or inclusions into plagioclase.
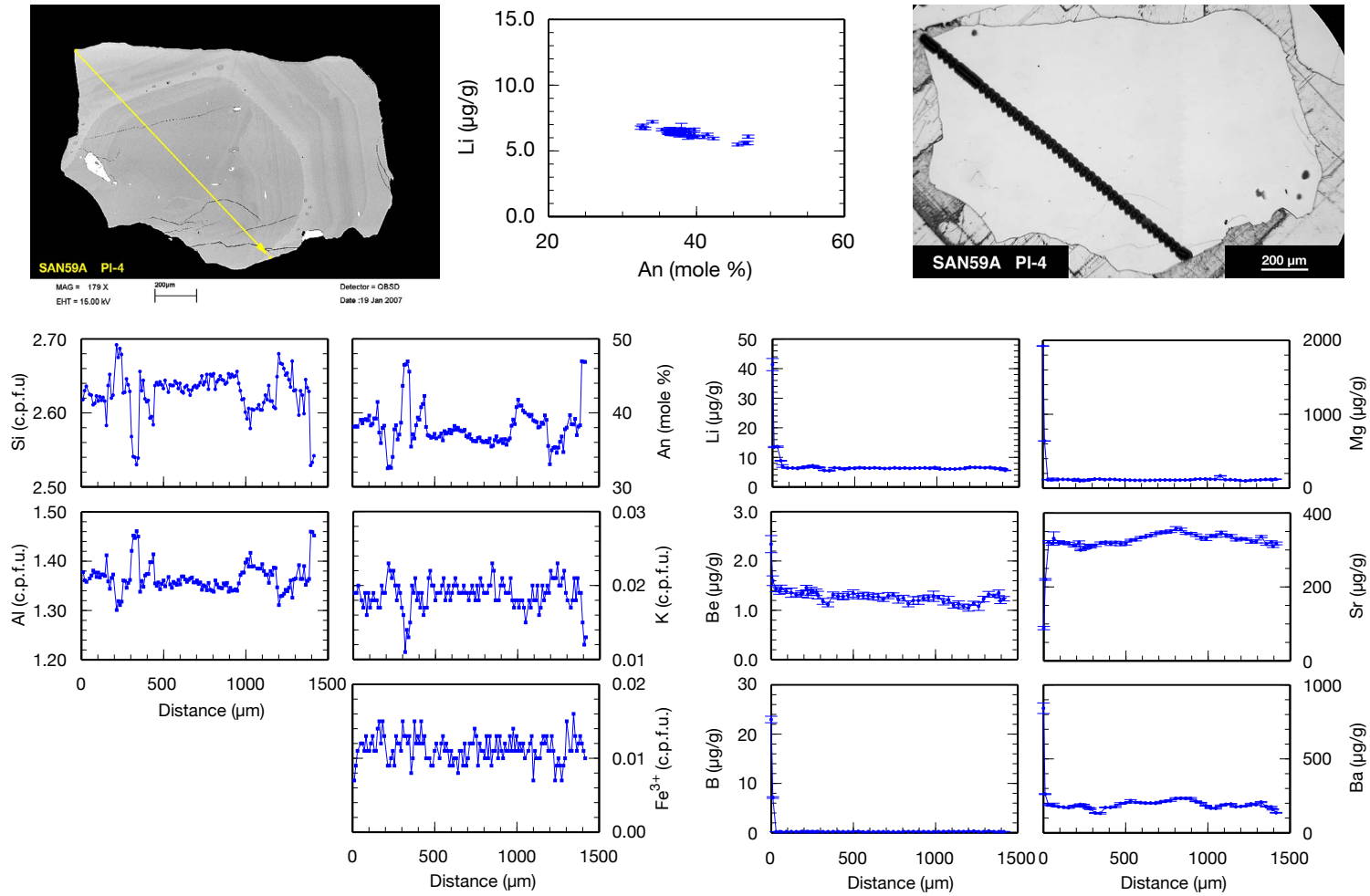
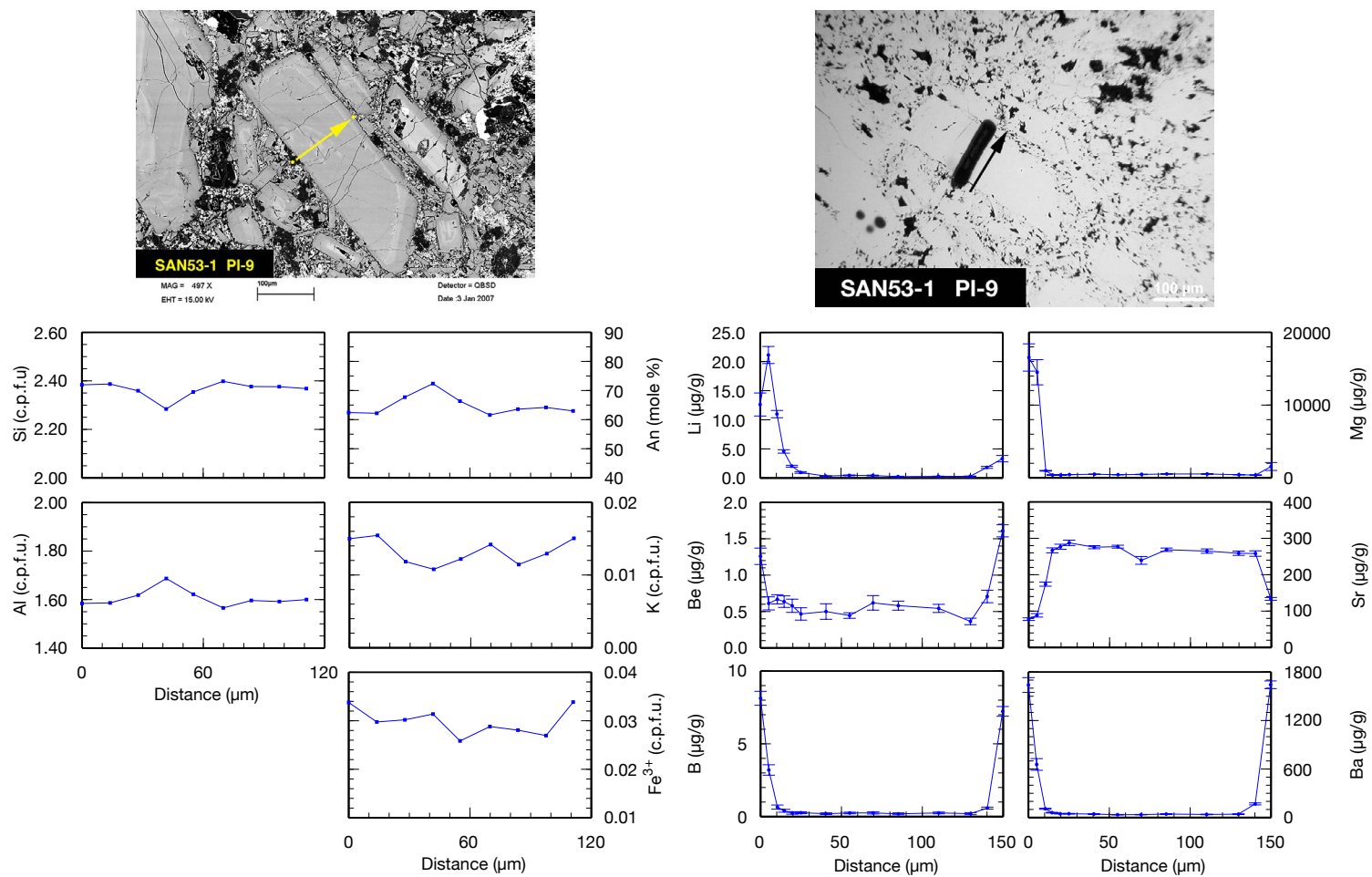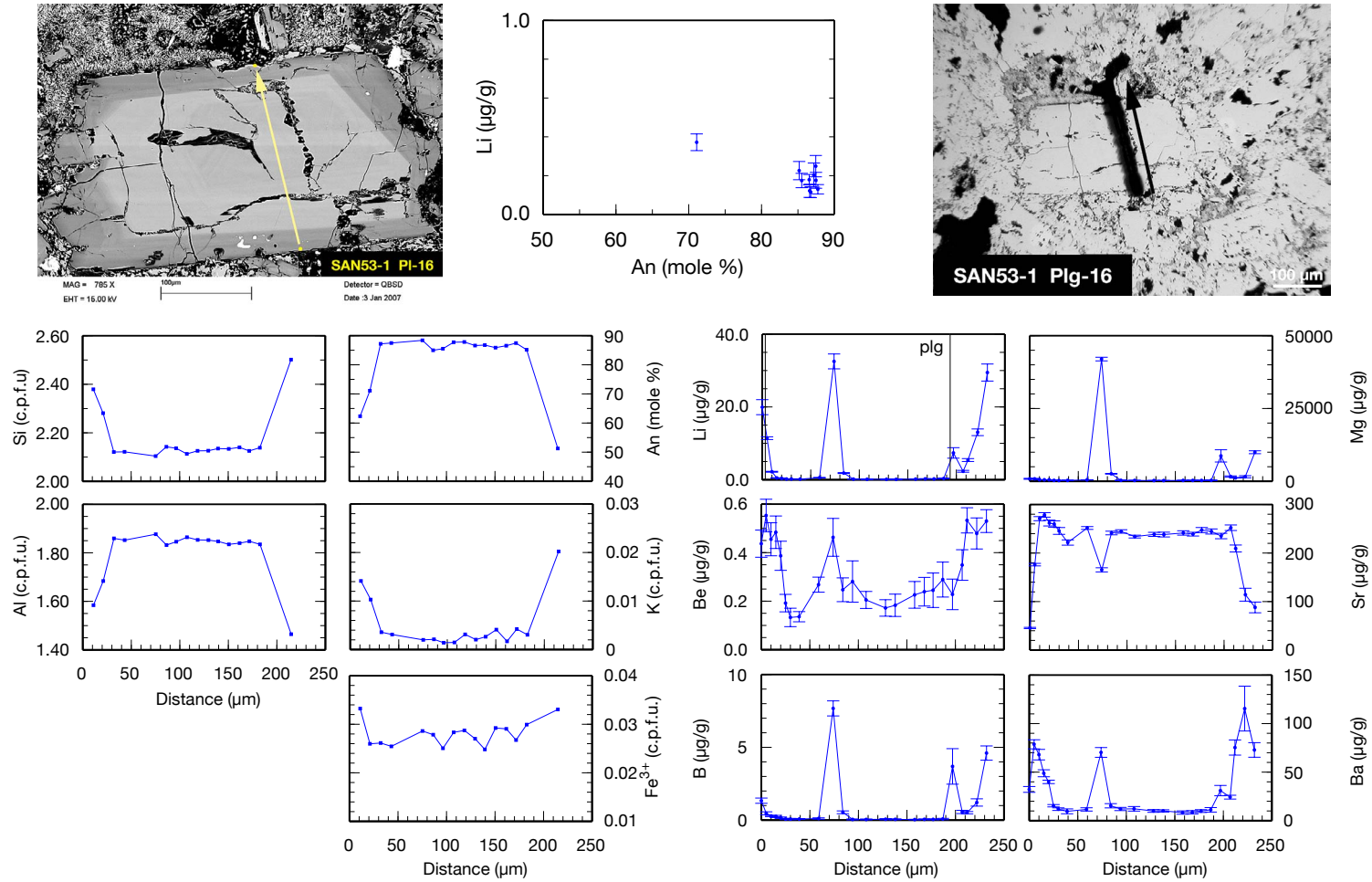**Fig. B.46.** SAN59A: Pl-4. EPMA and SIMS profiles. Formulas of EPMA analyses are calculated to 8 oxygens.
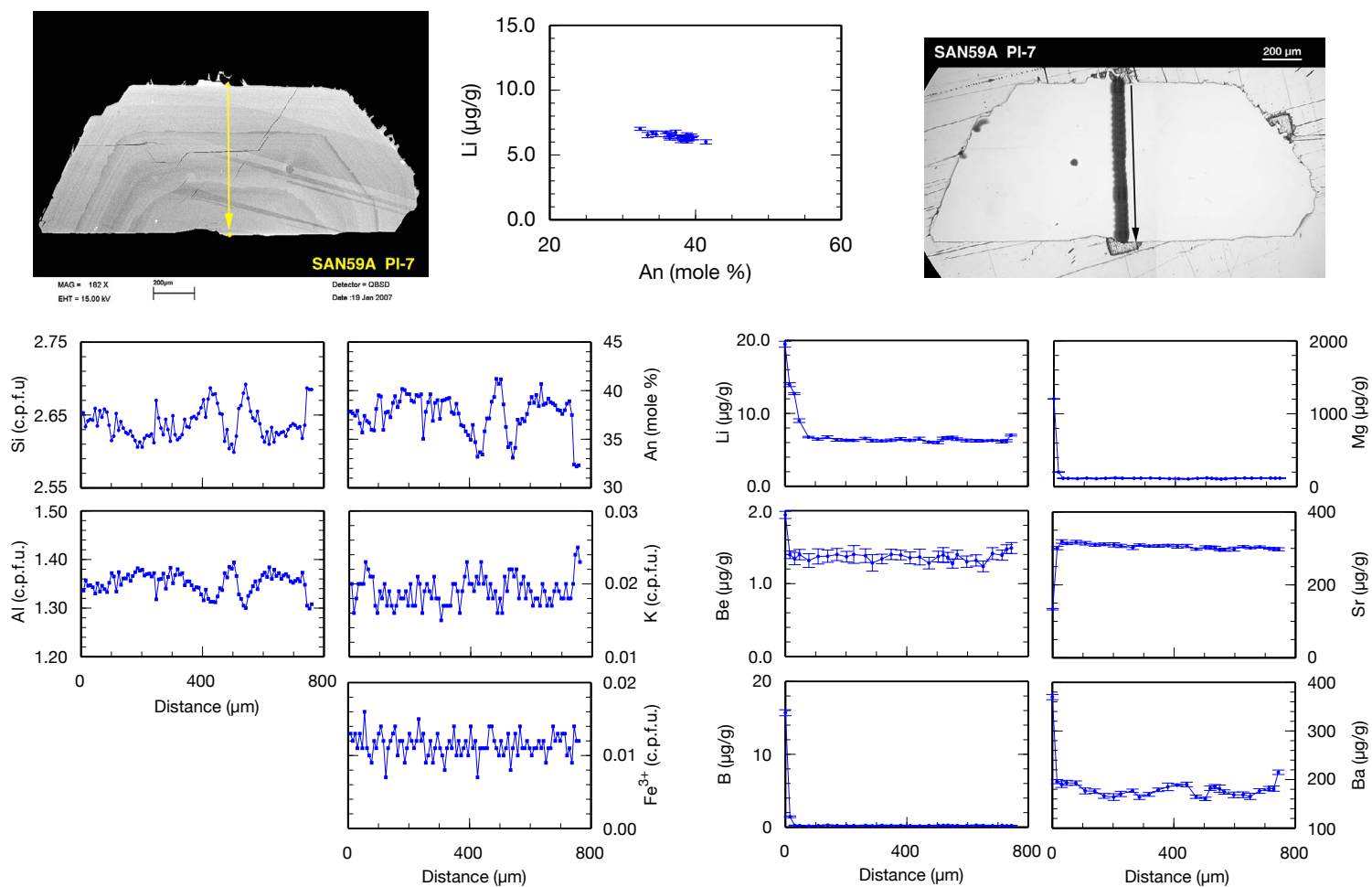
Fig. B.47. SAN59A: Pl-7. EPMA and SIMS profiles. Formulas of EPMA analyses are calculated to 8 oxygens.
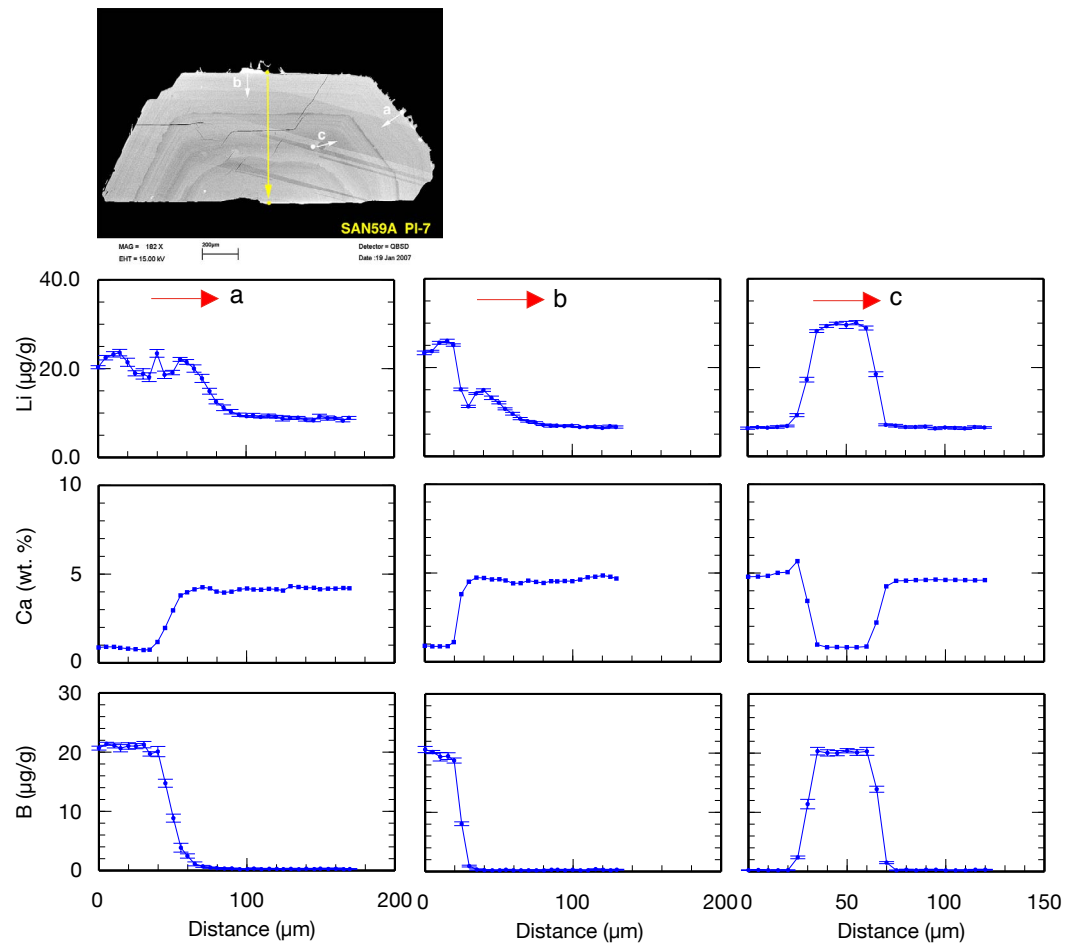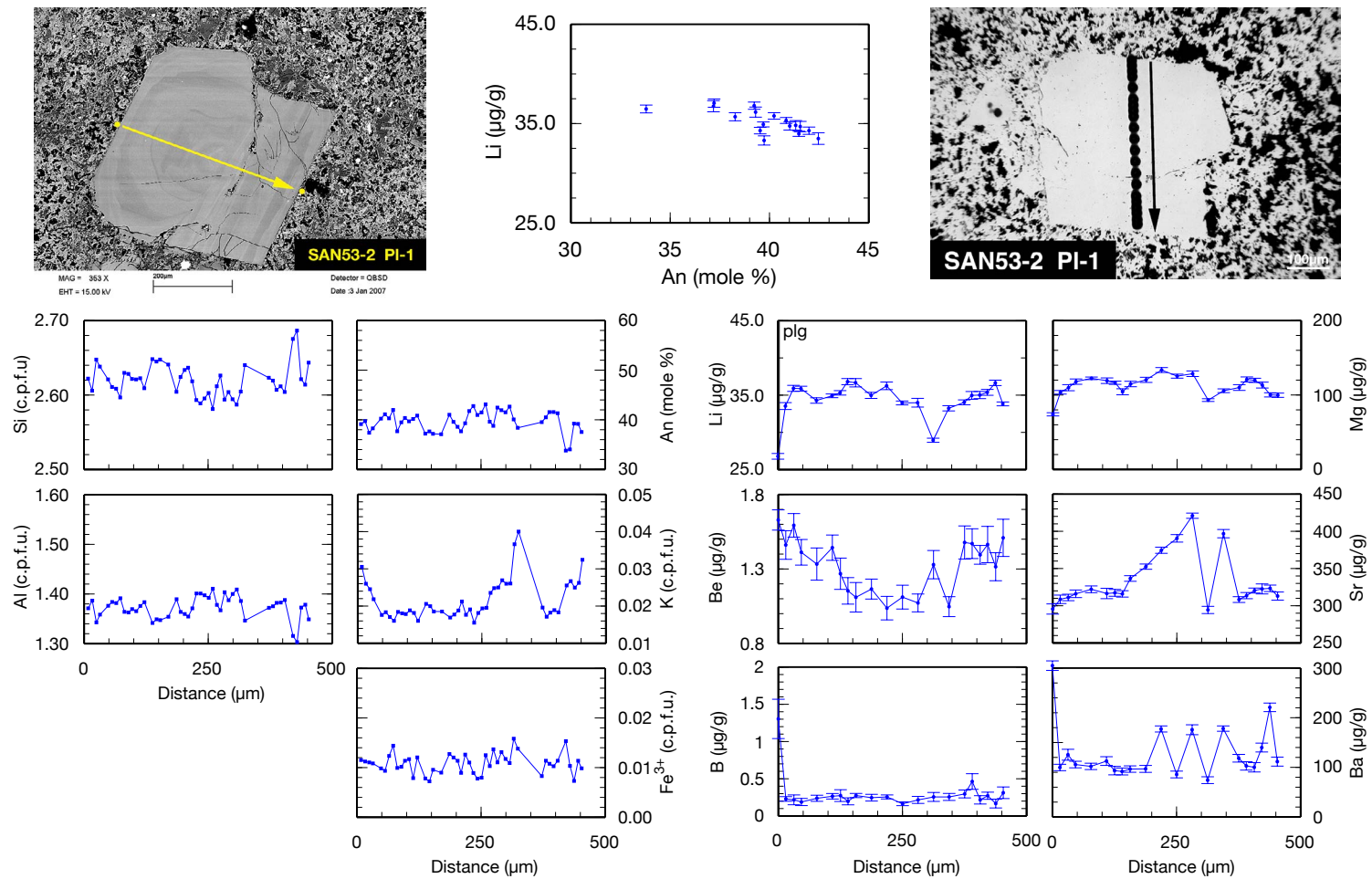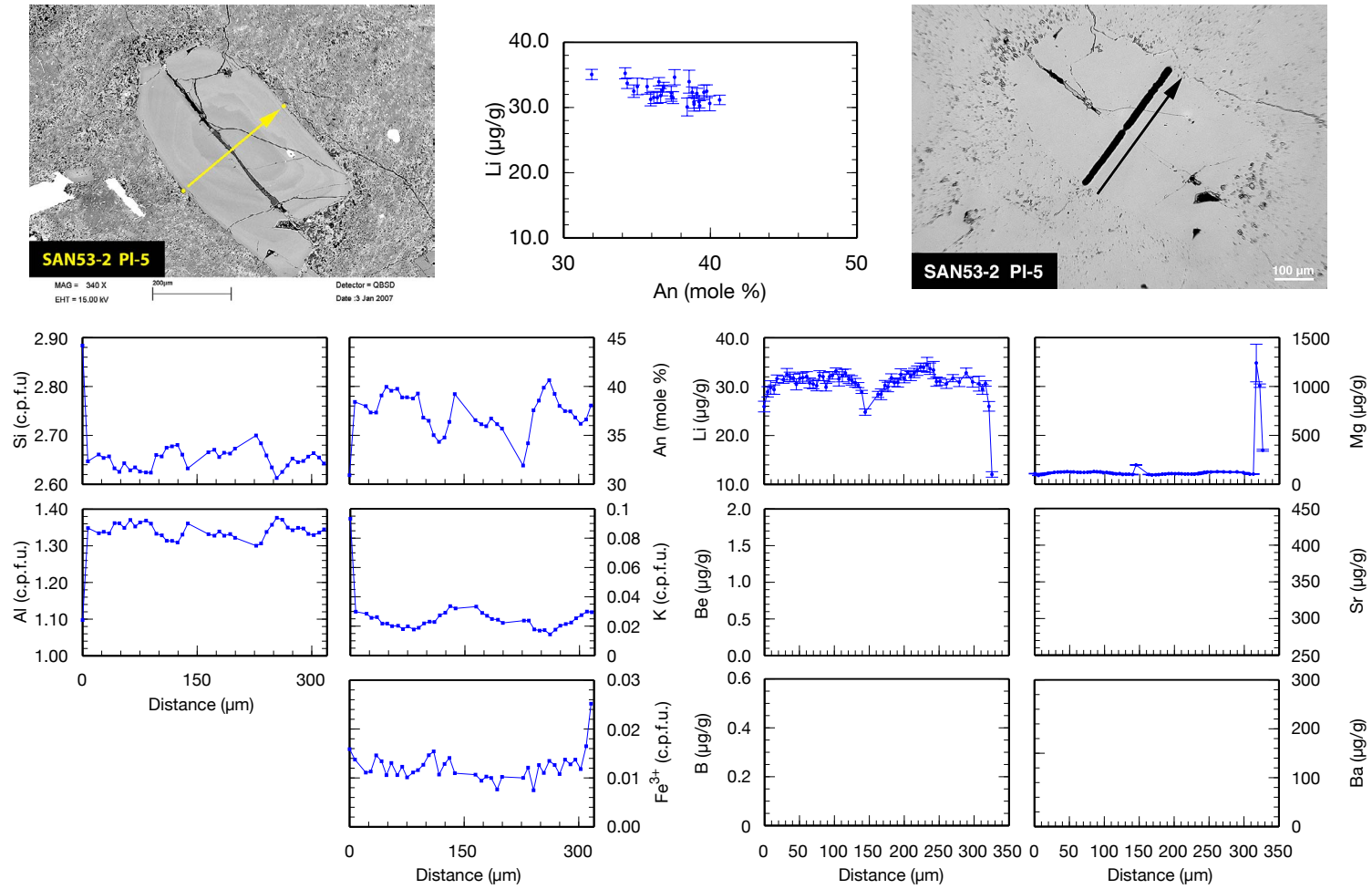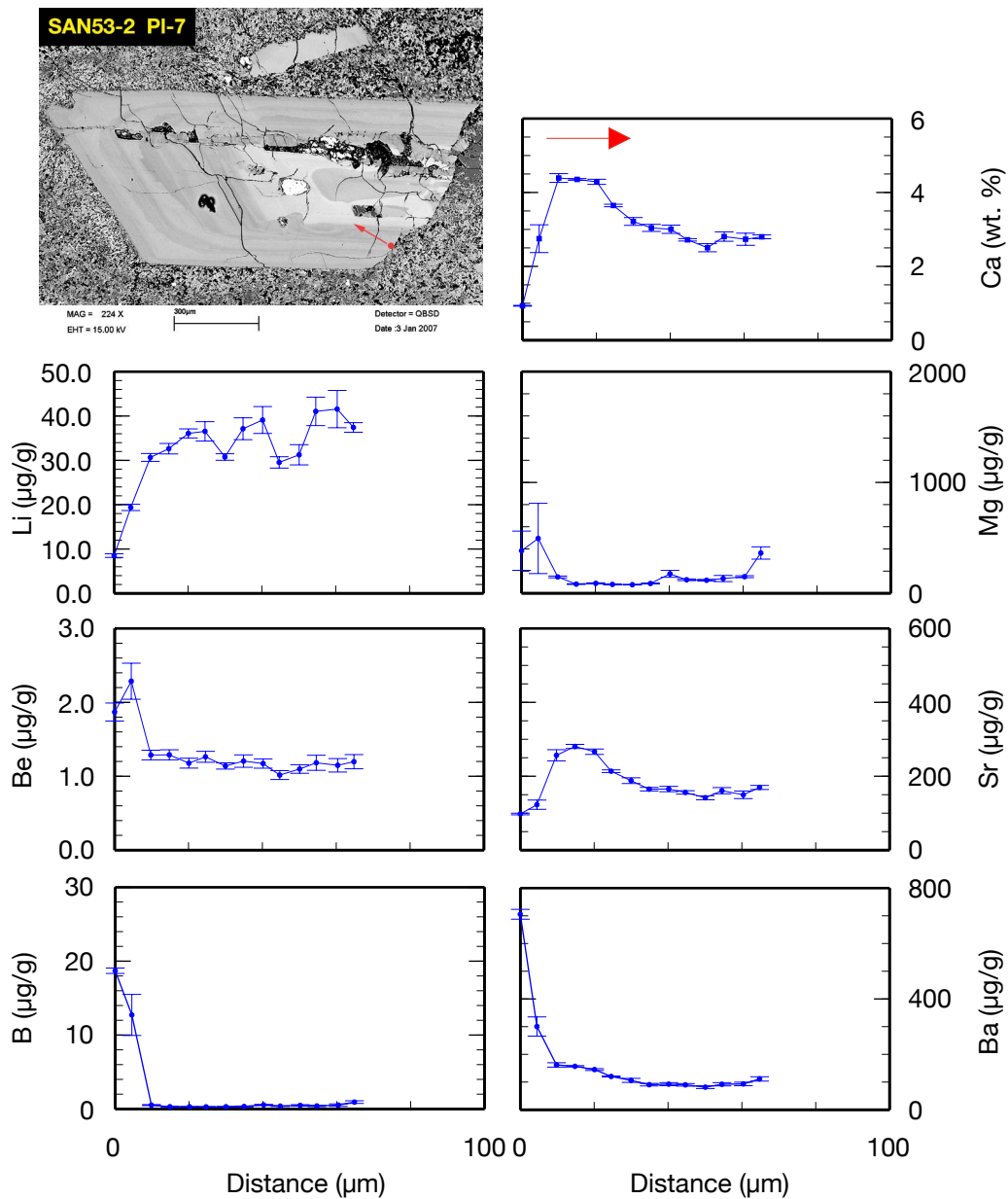
Fig. B.48. SAN59A: Pl-7. A short SIMS profile was analyzed to detect or exclude diffusion of Li from glass selvages or inclusions into plagioclase.

Fig. B.49. SAN59A: Pl-7. Short δ^7Li SIMS profile. The blue arrow marks the δ^7Li profiles; the red or white arrows mark the regular Li short profiles. A yellow arrow usually marks the EPMA profile (not all pl crystals were analyzed by EPMA). Li concentration values are derived from count rates of the isotope analyses and are therefore only semi-quantitative.
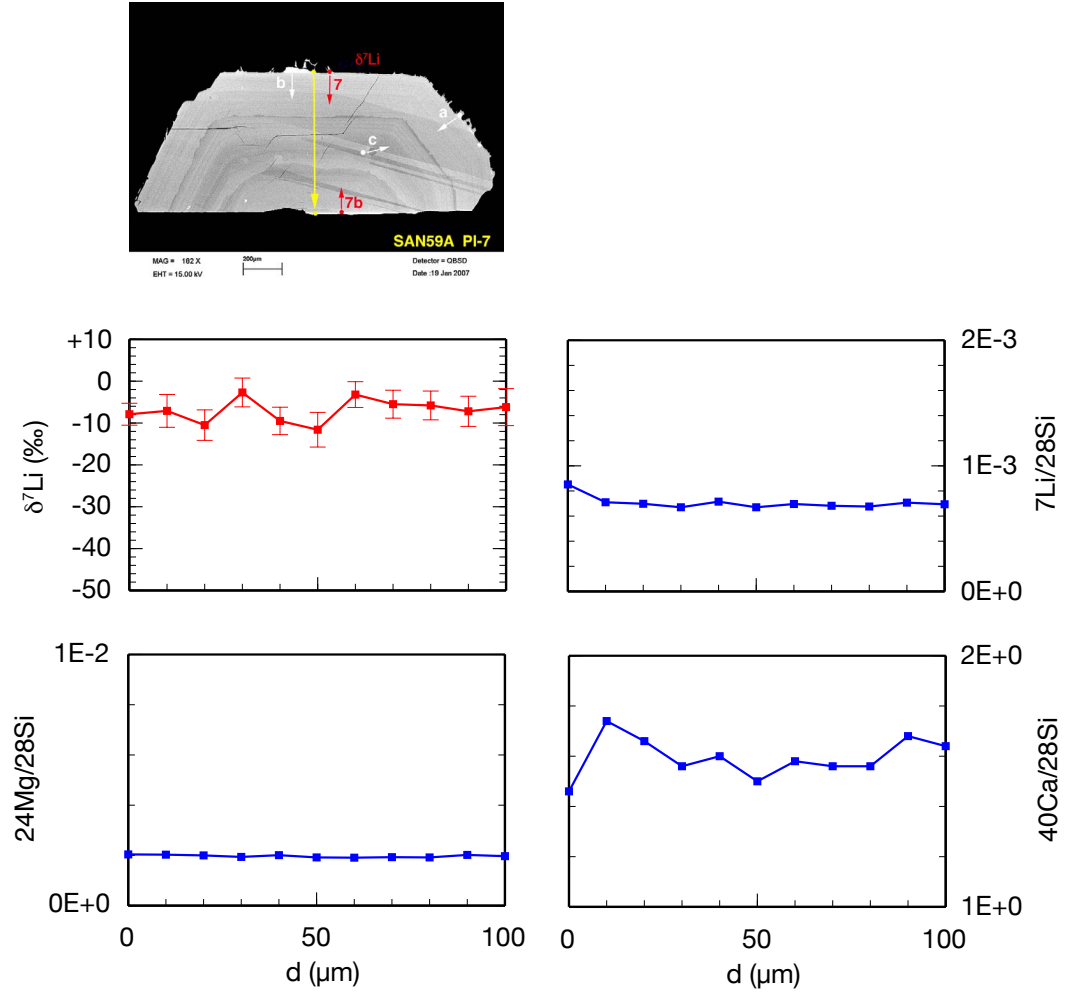
Fig. B.50. SAN59A: Pl-7b. Short δ^7Li SIMS profile. The blue arrow marks the δ^7Li profiles; the red or white arrows mark the regular Li short profiles. A yellow arrow usually marks the EPMA profile (not all pl crystals were analyzed by EPMA). Li concentration values are derived from count rates of the isotope analyses and are therefore only semi-quantitative.
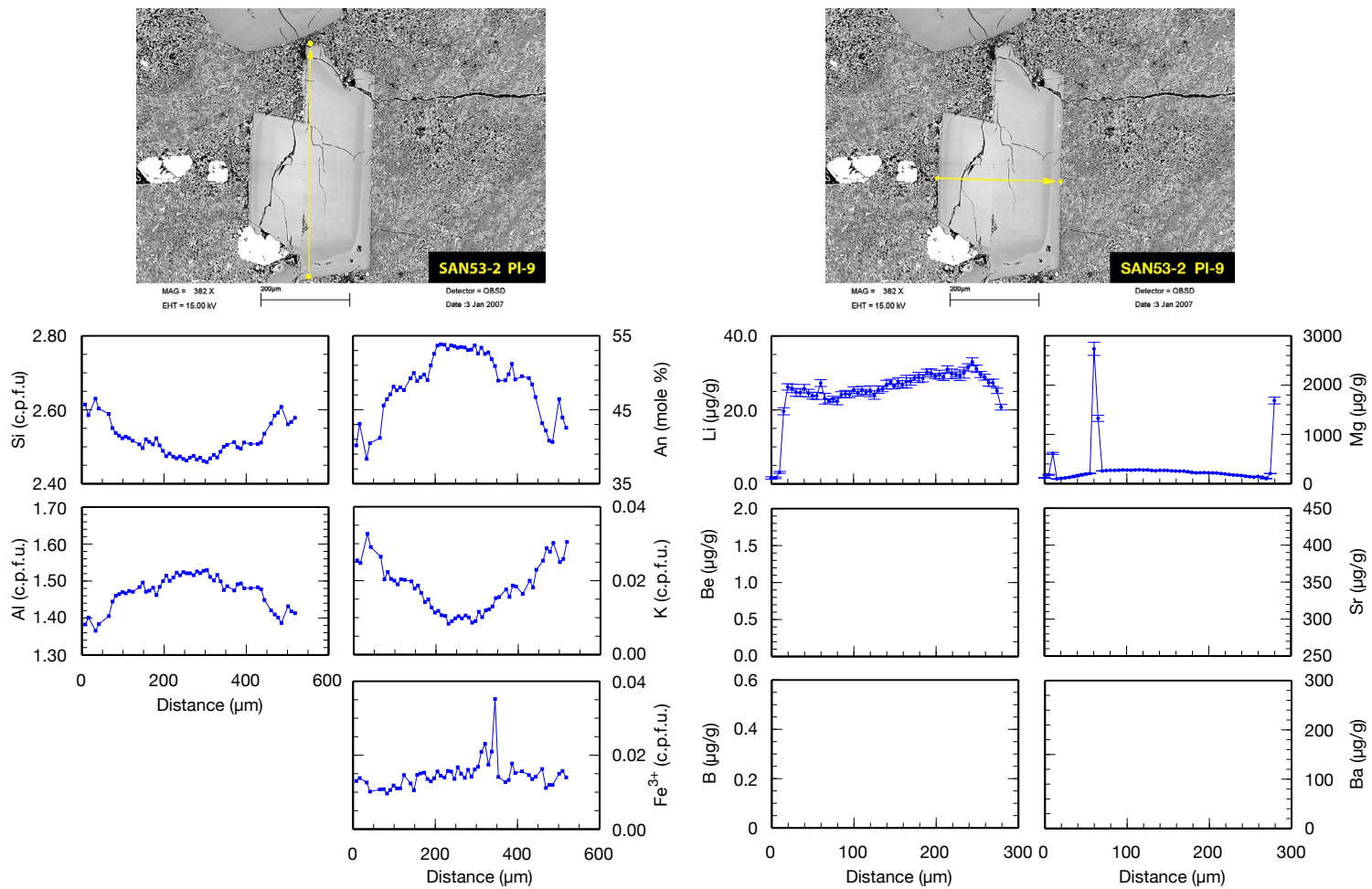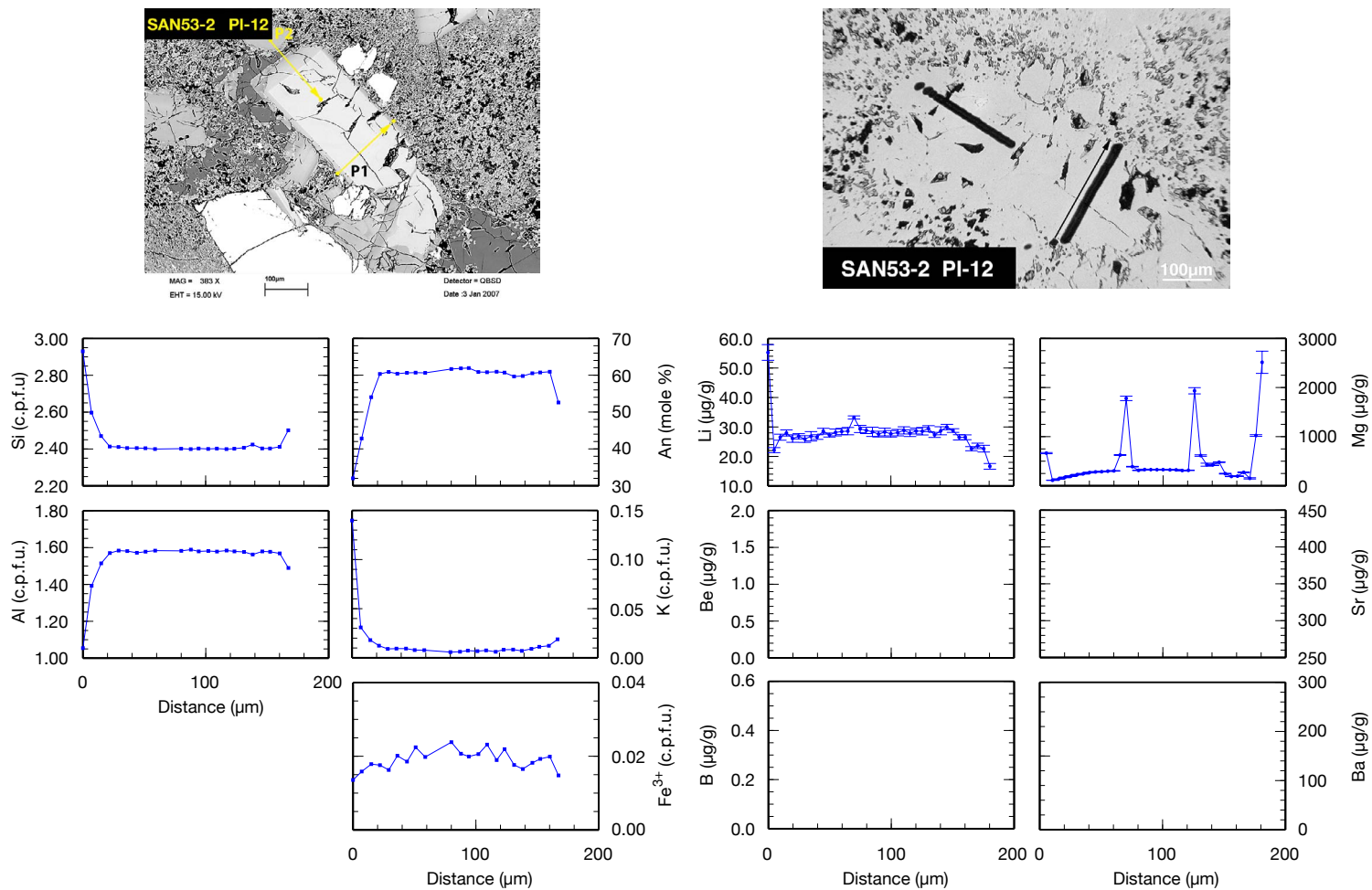
Fig. B.51. SAN59A: Pl-8. EPMA and SIMS profiles. Formulas of EPMA analyses are calculated to 8 oxygens.
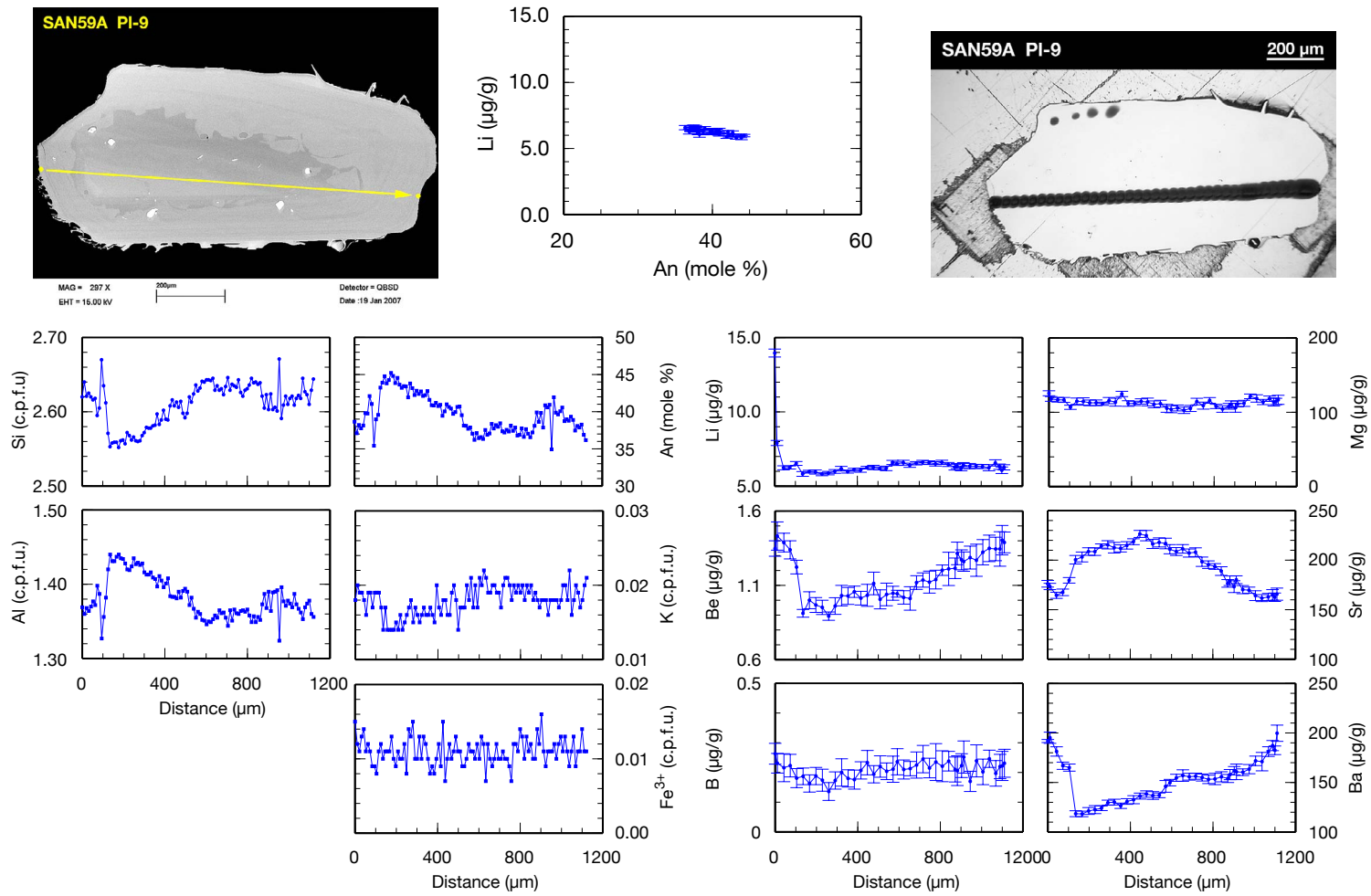
Fig. B.52. SAN59A: Pl-9. EPMA and SIMS profiles. Formulas of EPMA analyses are calculated to 8 oxygens.
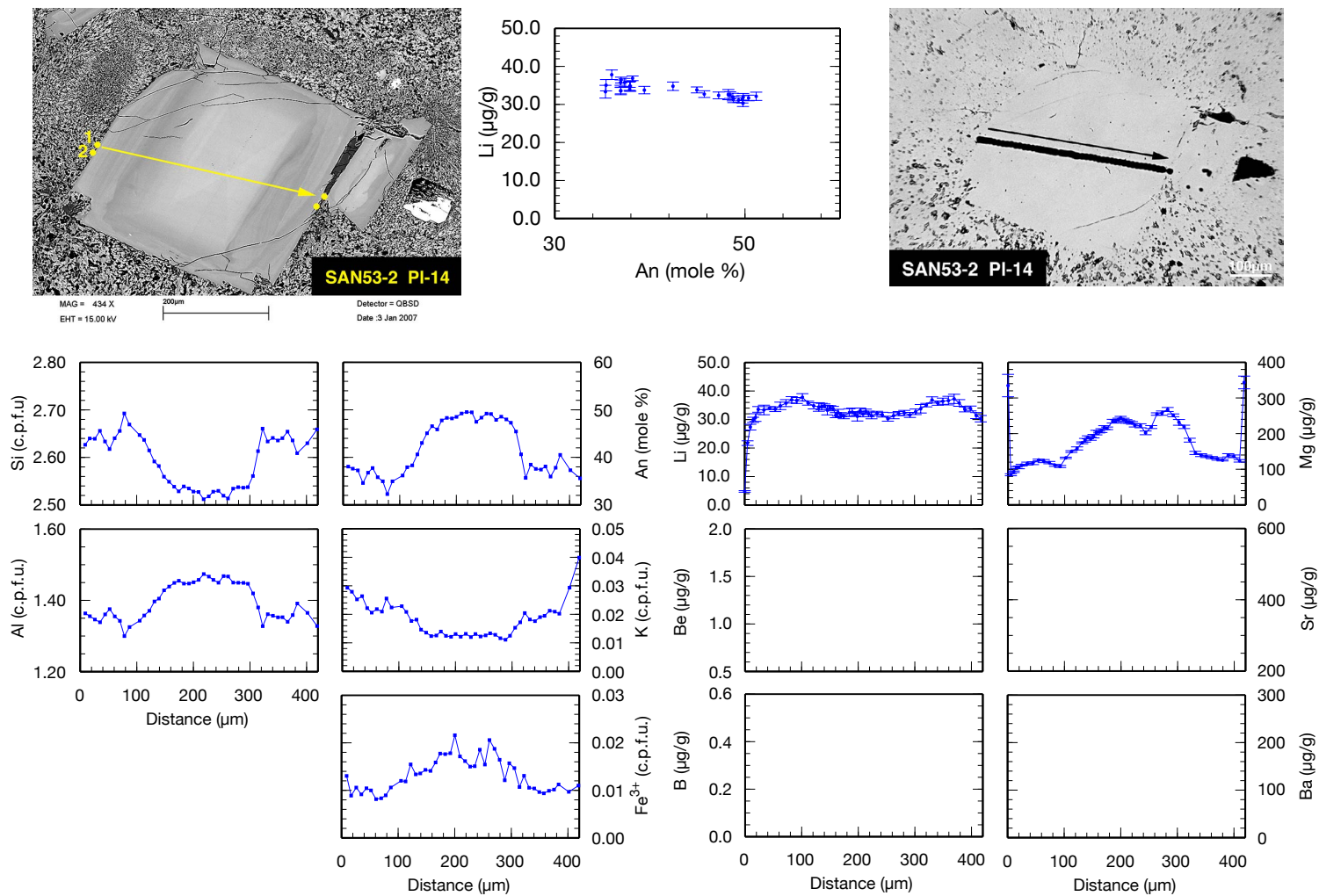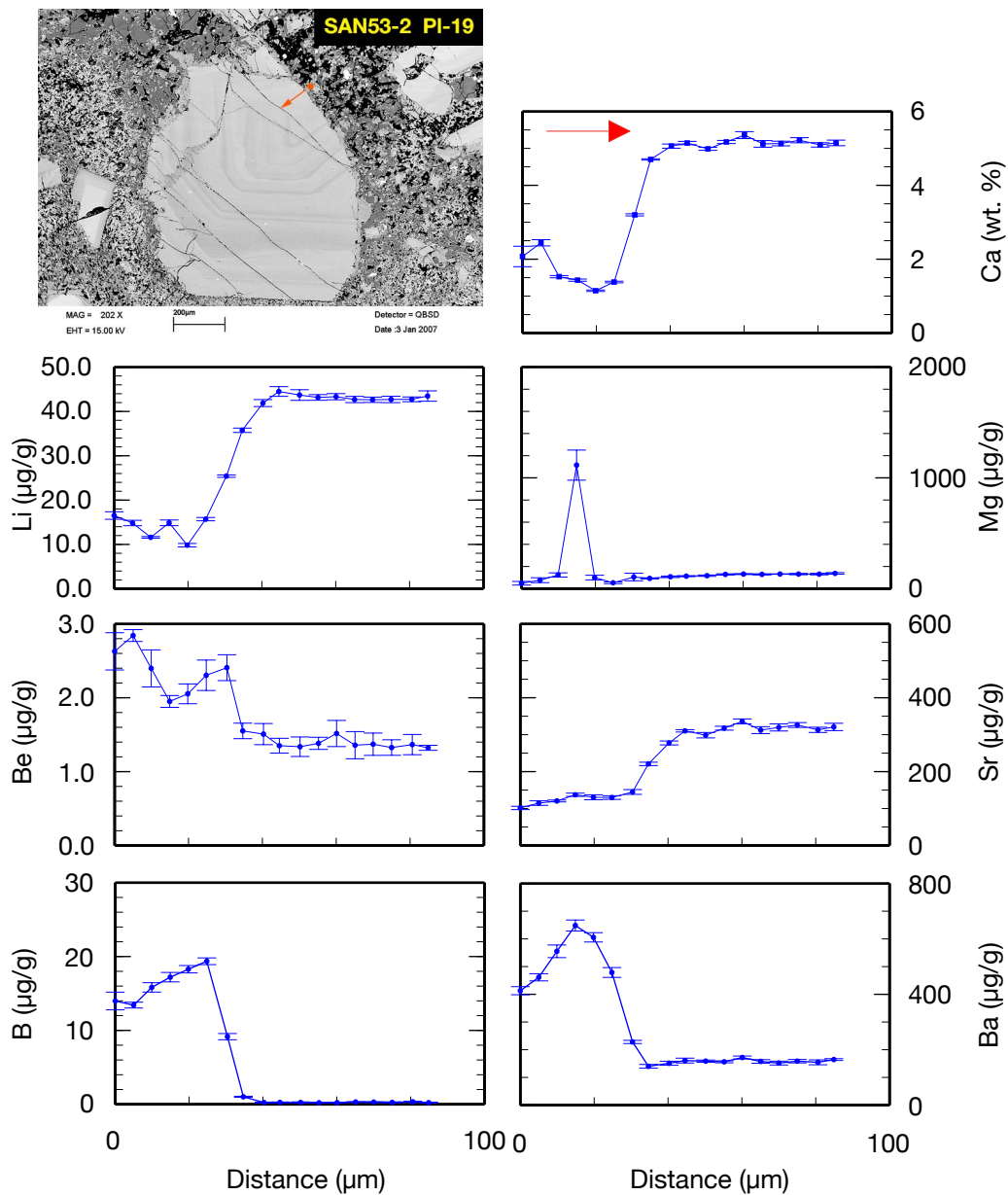
Fig. B.53. SAN59A: Pl-9. A short SIMS profile was analyzed to detect or exclude diffusion of Li from glass selvages or inclusions into plagioclase.
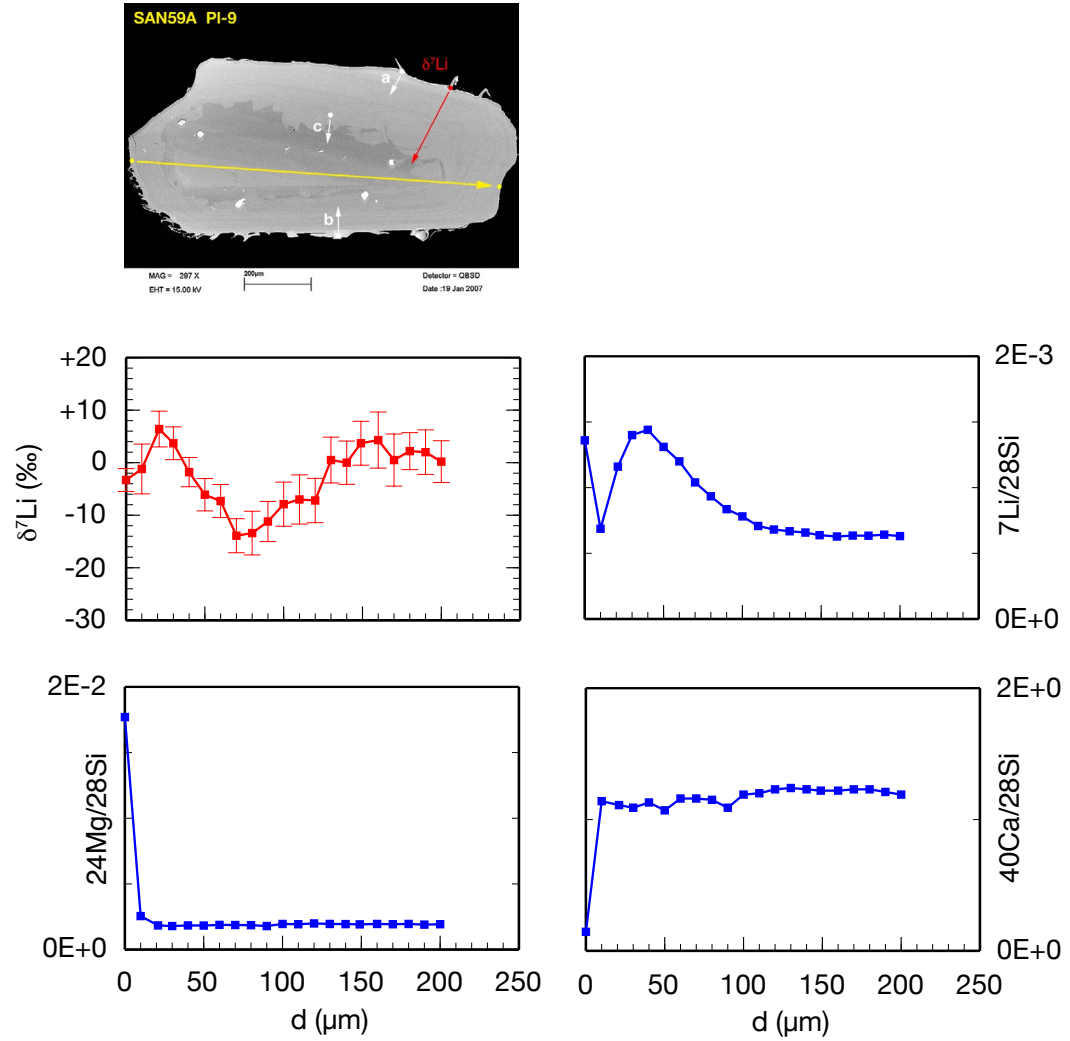
Fig. B.54. SAN59A: Pl-9. Short δ^7Li SIMS profile. The blue arrow marks the δ^7Li profiles; the red or white arrows mark the regular Li short profiles. A yellow arrow usually marks the EPMA profile (not all pl crystals were analyzed by EPMA). Li concentration values are derived from count rates of the isotope analyses and are therefore only semi-quantitative.

Fig. B.55. SAN59A: Pl-10. A short SIMS profile was analyzed to detect or exclude diffusion of Li from glass selvages or inclusions into plagioclase.
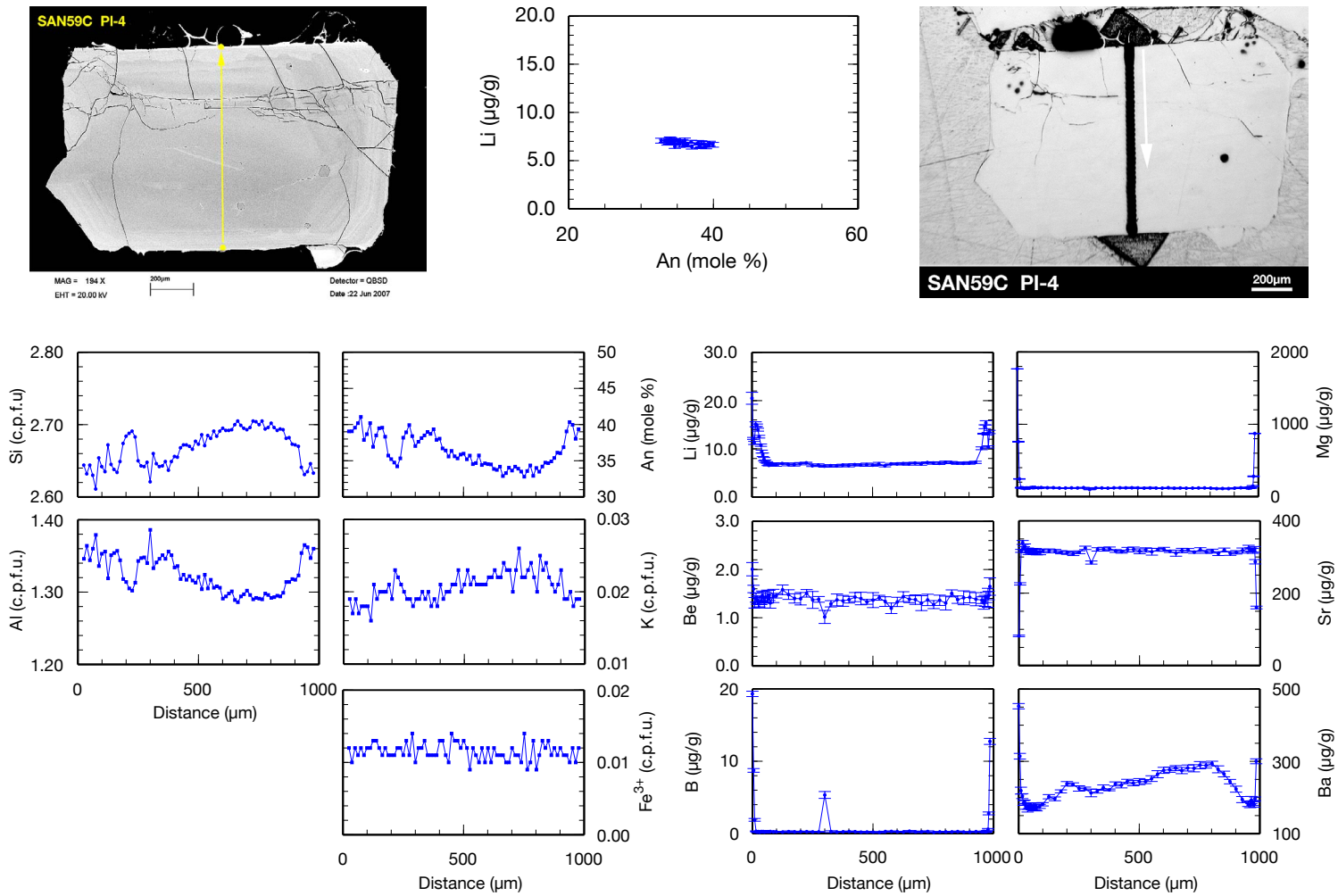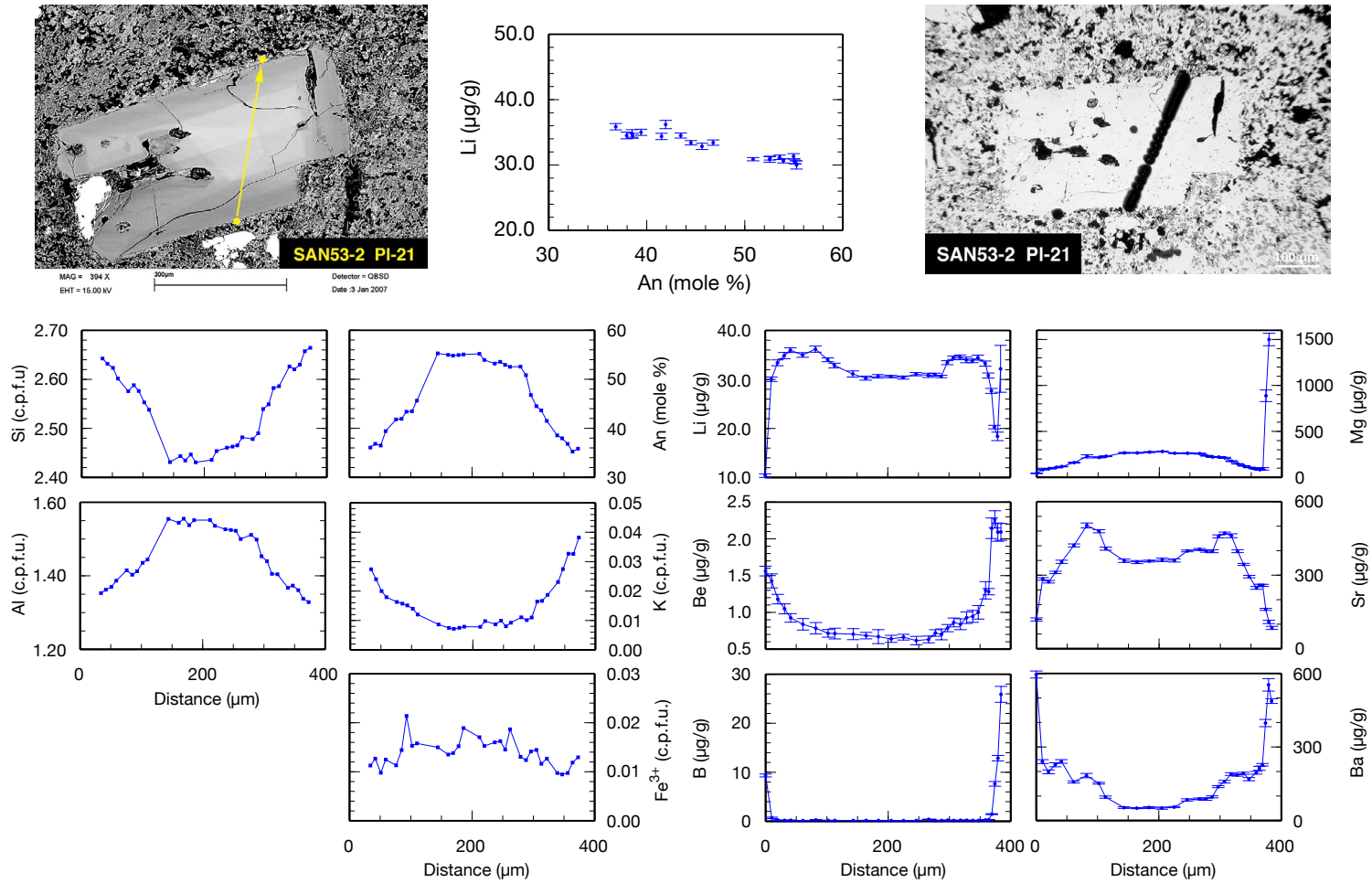
Fig. B.56. SAN59C: Pl-4. EPMA and SIMS profiles. Formulas of EPMA analyses are calculated to 8 oxygens.
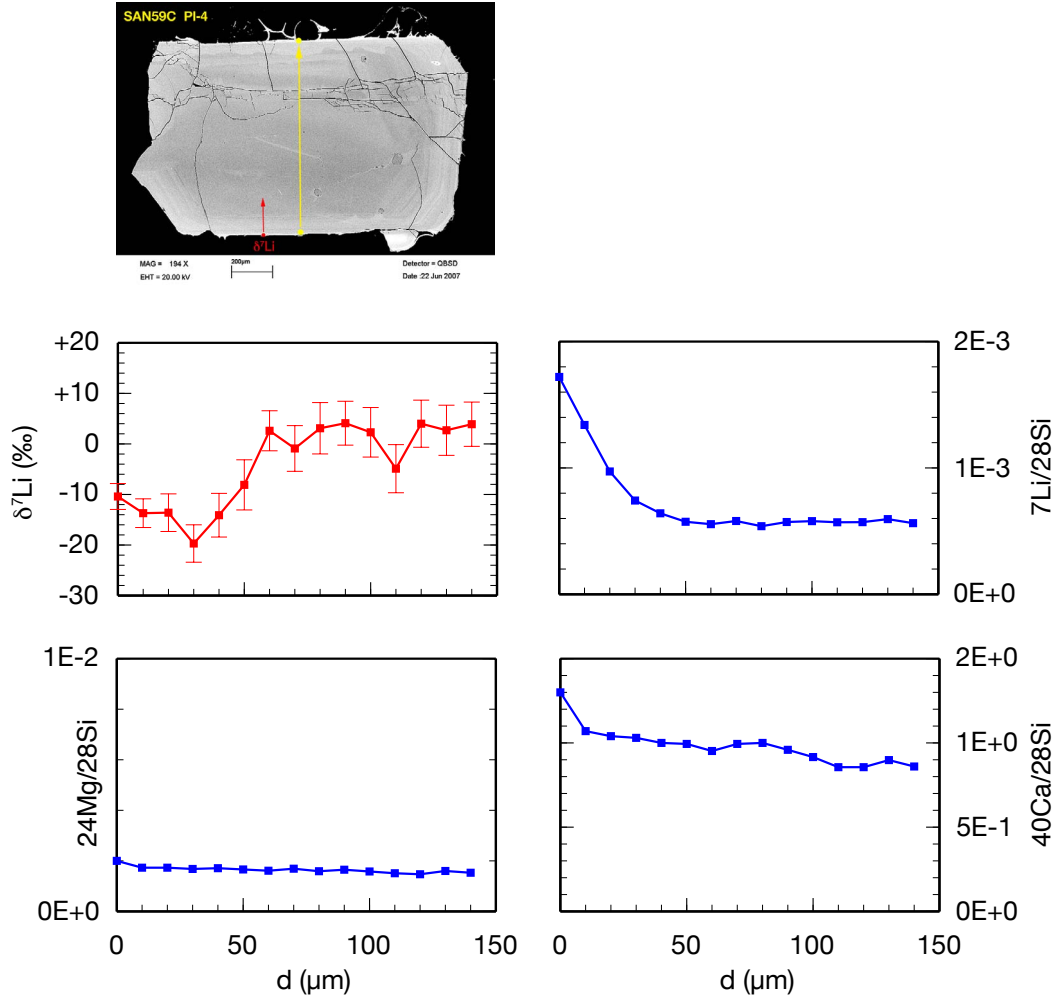
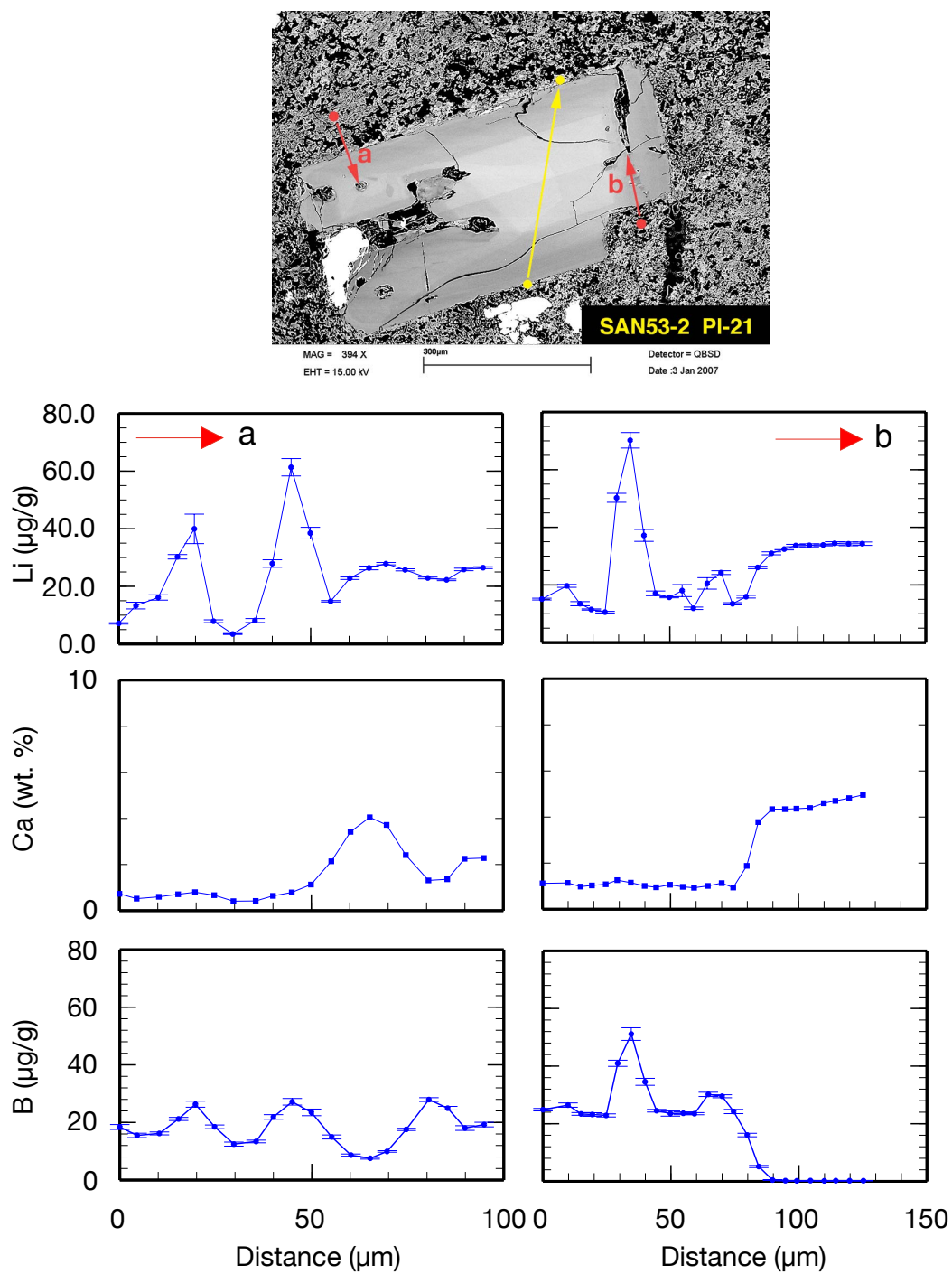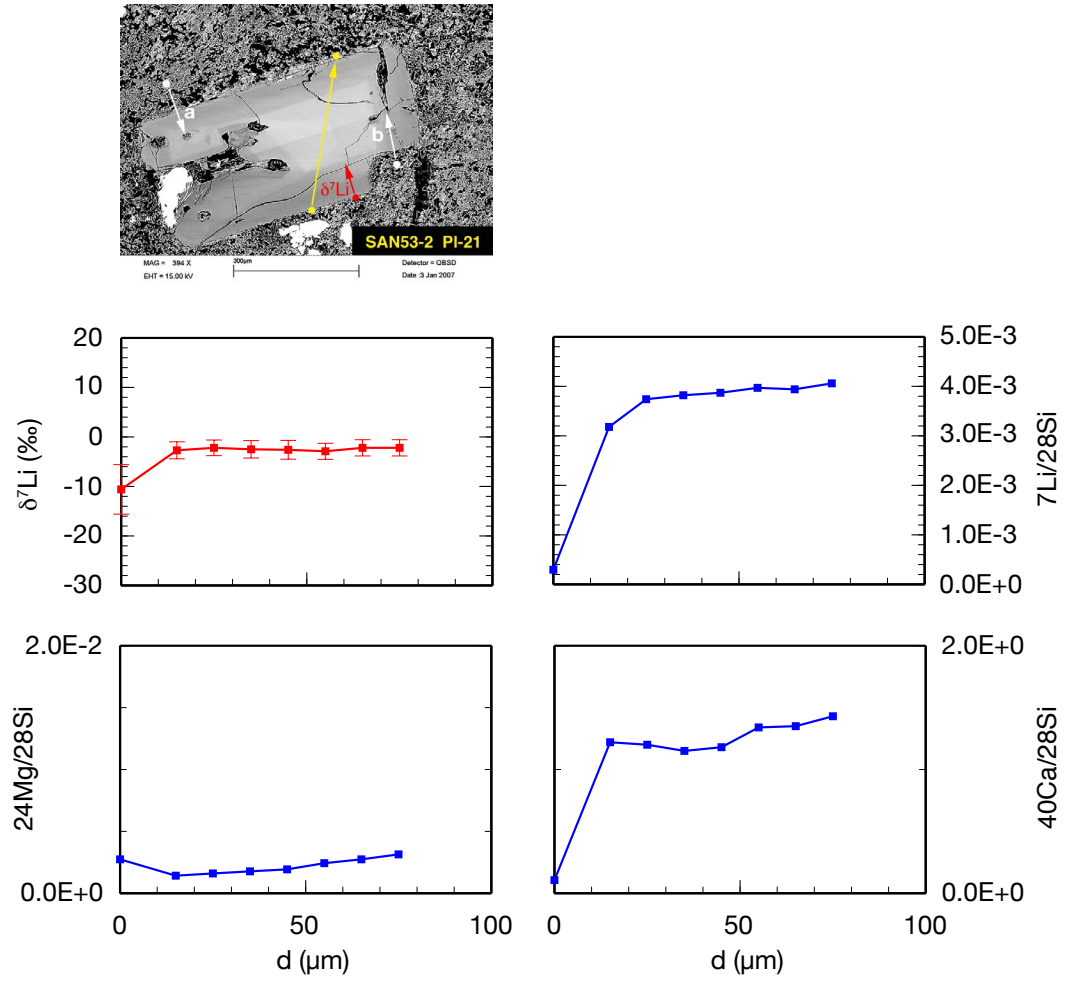**Fig. B.57.** SAN59C: Pl-4. Short δ^7Li SIMS profile. The blue arrow marks the δ^7Li profiles; the red or white arrows mark the regular Li short profiles. A yellow arrow usually marks the EPMA profile (not all pl crystals were analyzed by EPMA). Li concentration values are derived from count rates of the isotope analyses and are therefore only semi-quantitative.

B.4. SAN50 & SAN51 (Crystal-rich pumice) – Minoan D
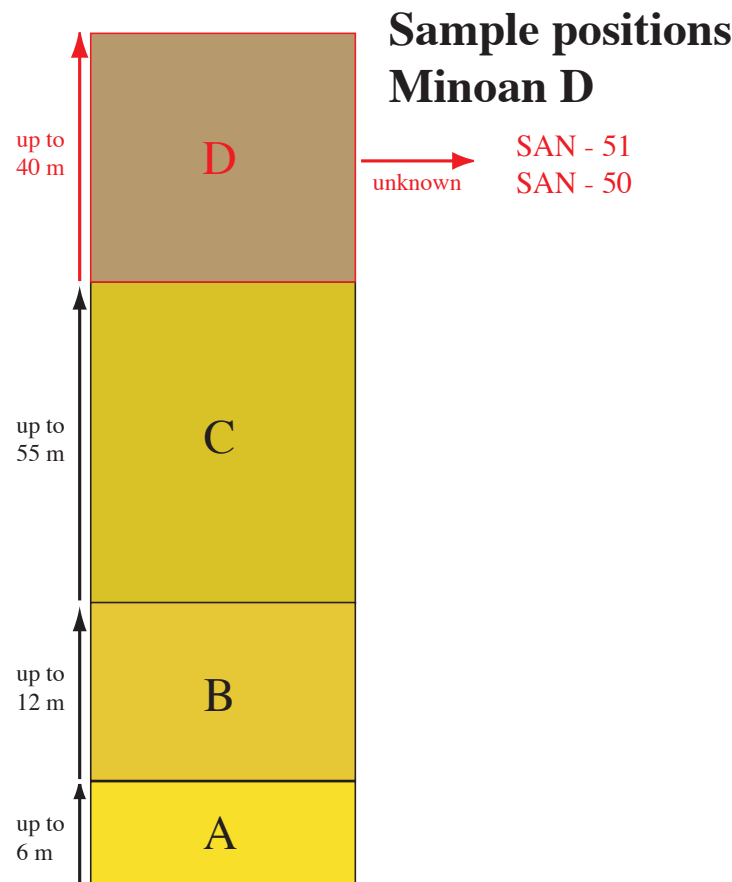
Fig. B.58. Positions of pumice samples taken from Minoan Unit D.
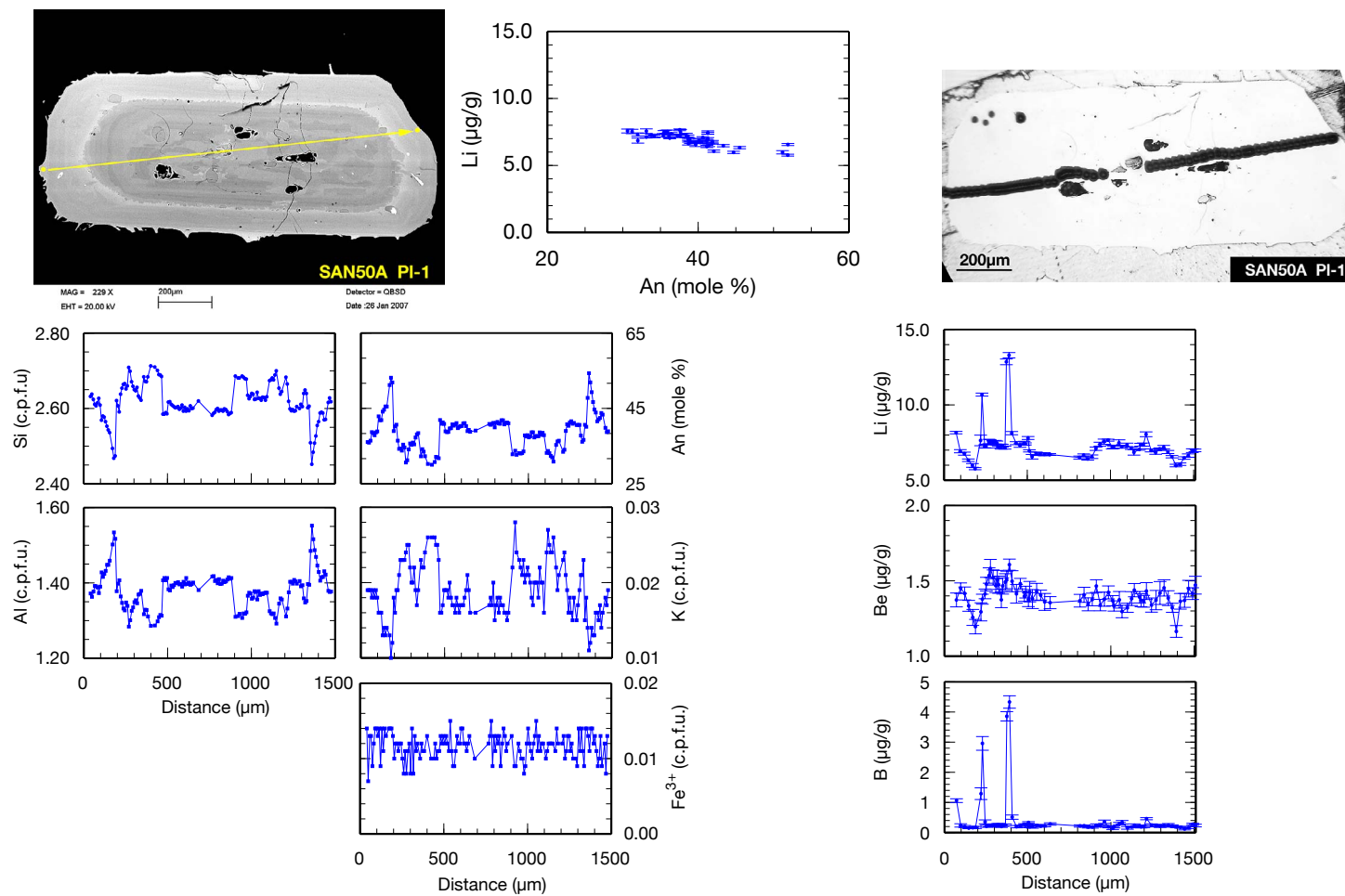
Fig. B.59. SAN50A: Pl-1. EPMA and SIMS profiles. Formulas of EPMA analyses are calculated to 8 oxygens.
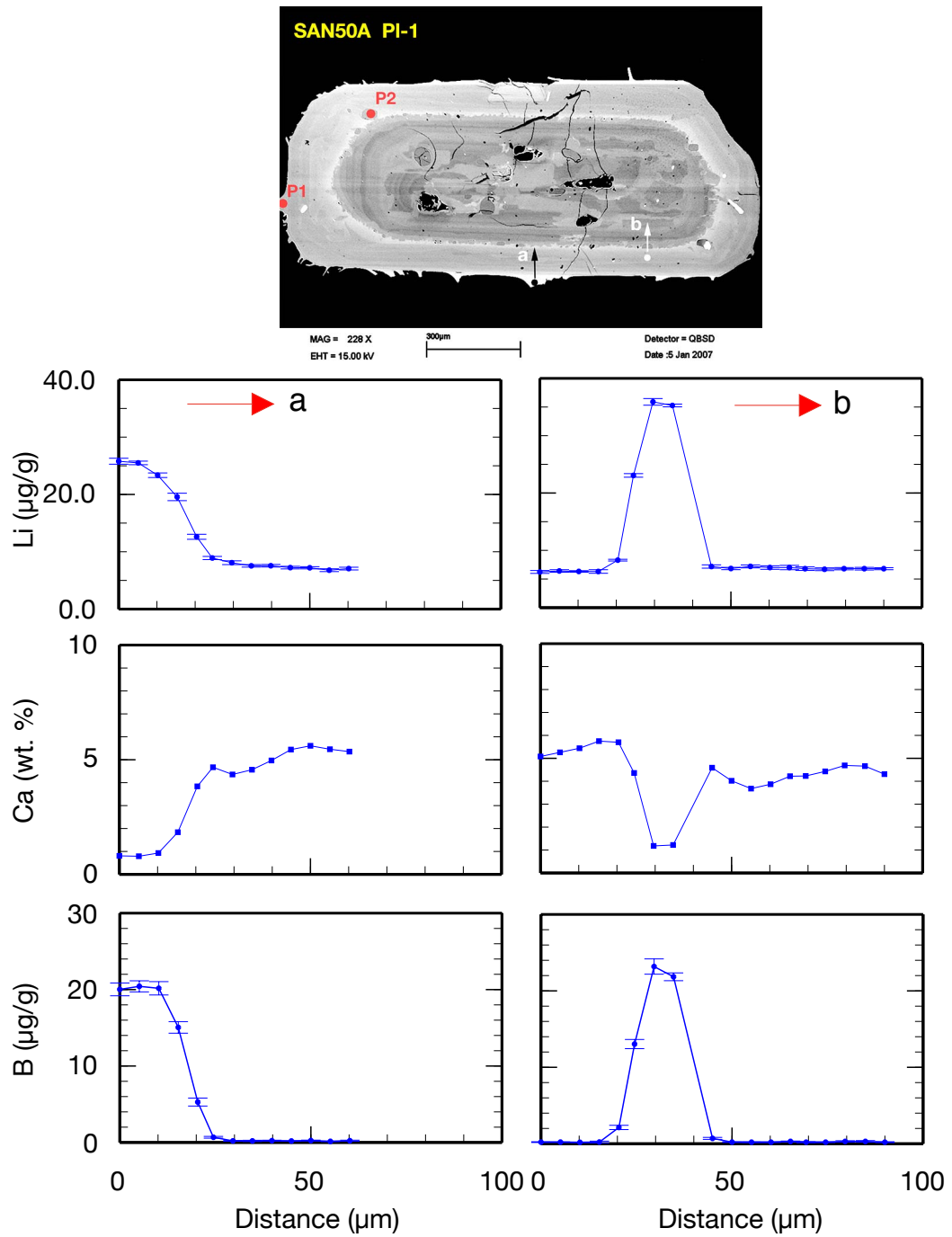
Fig. B.60. SAN50A: Pl-1. A short SIMS profile was analyzed to detect or exclude diffusion of Li from glass selvages or inclusions into plagioclase.
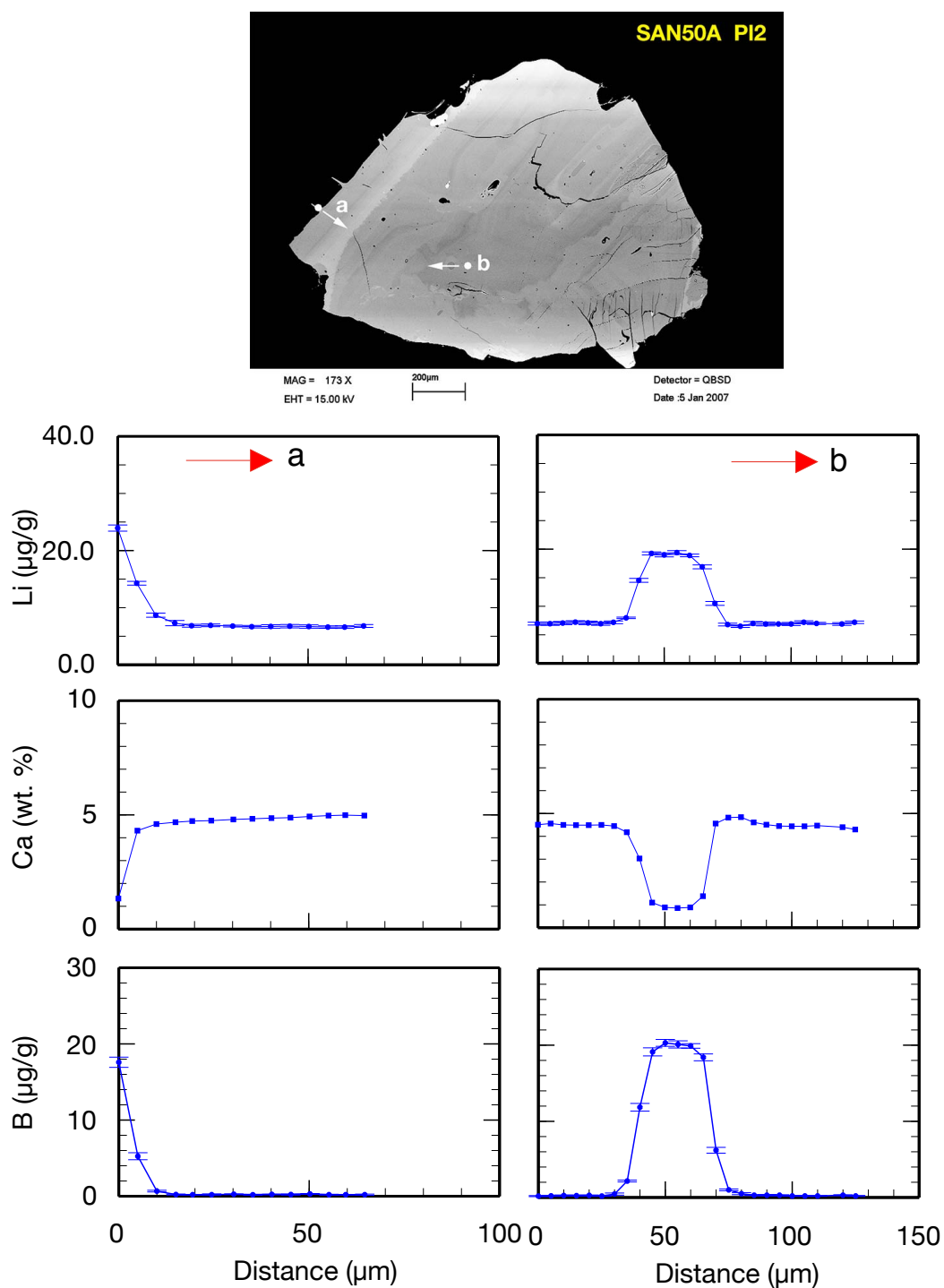
Fig. B.61. SAN50A: Pl-2. A short SIMS profile was analyzed to detect or exclude diffusion of Li from glass selvages or inclusions into plagioclase.
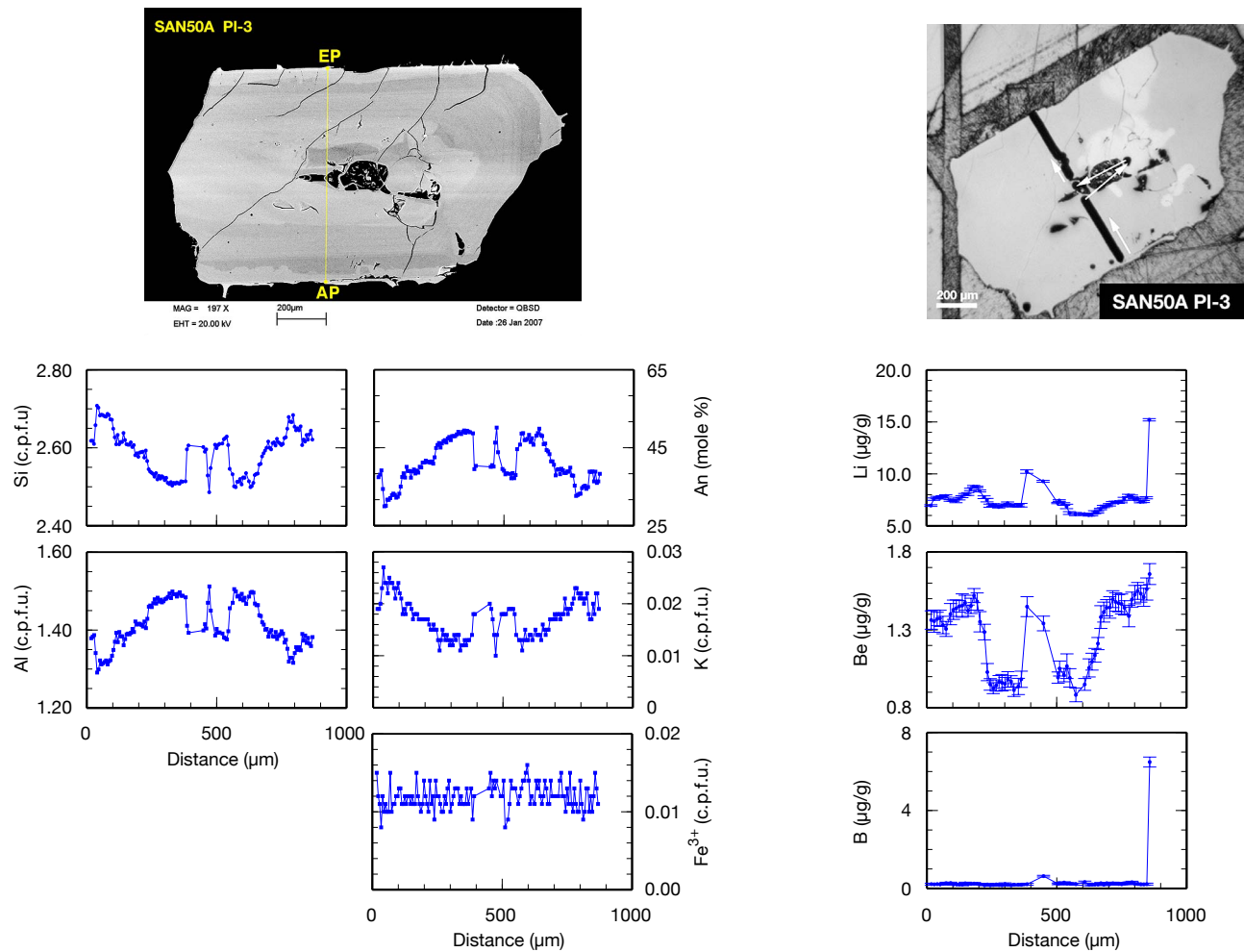
Fig. B.62. SAN50A: Pl-3. EPMA and SIMS profiles. Formulas of EPMA analyses are calculated to 8 oxygens.
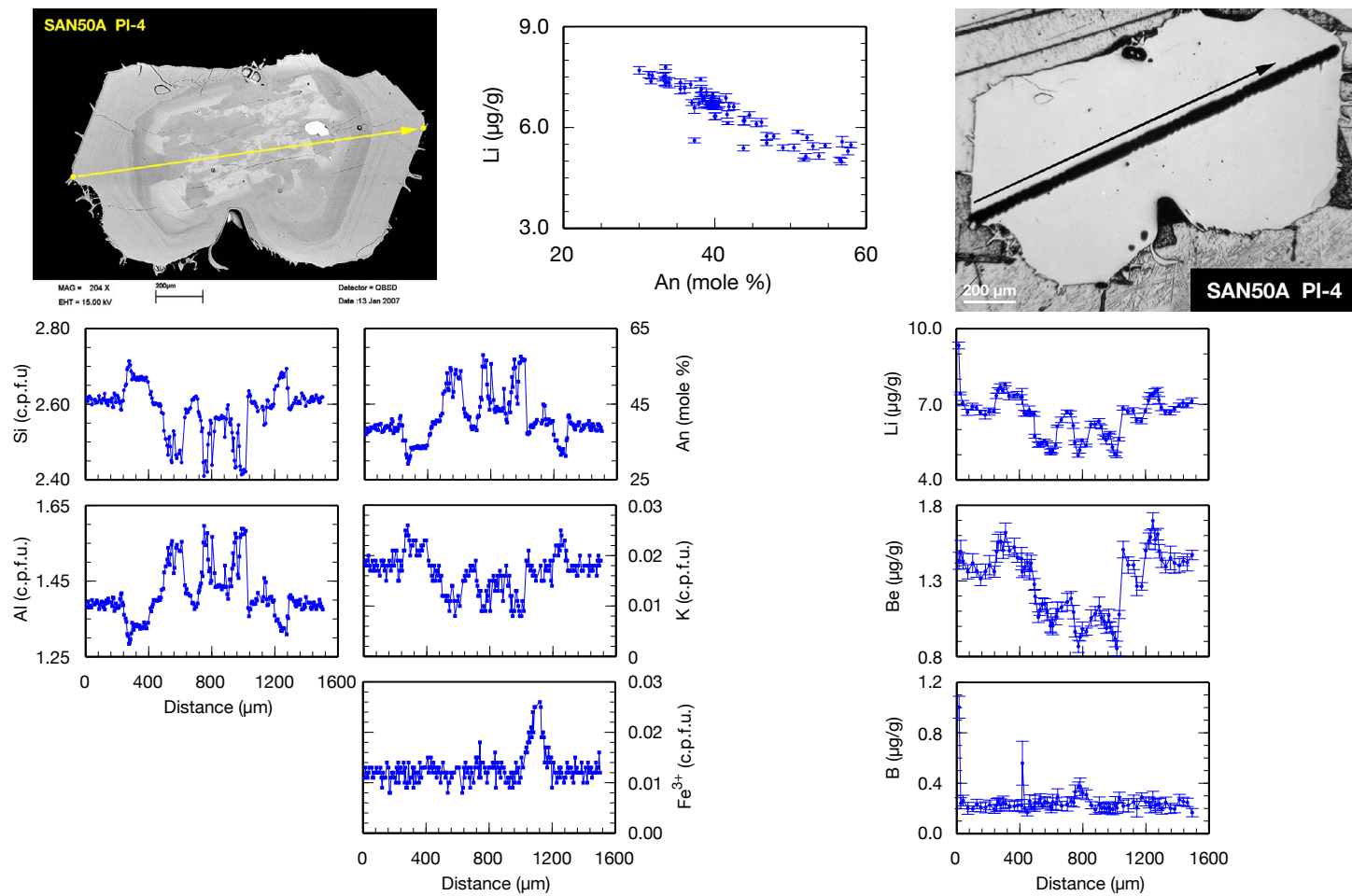
Fig. B.63. SAN50A: Pl-4. EPMA and SIMS profiles. Formulas of EPMA analyses are calculated to 8 oxygens.
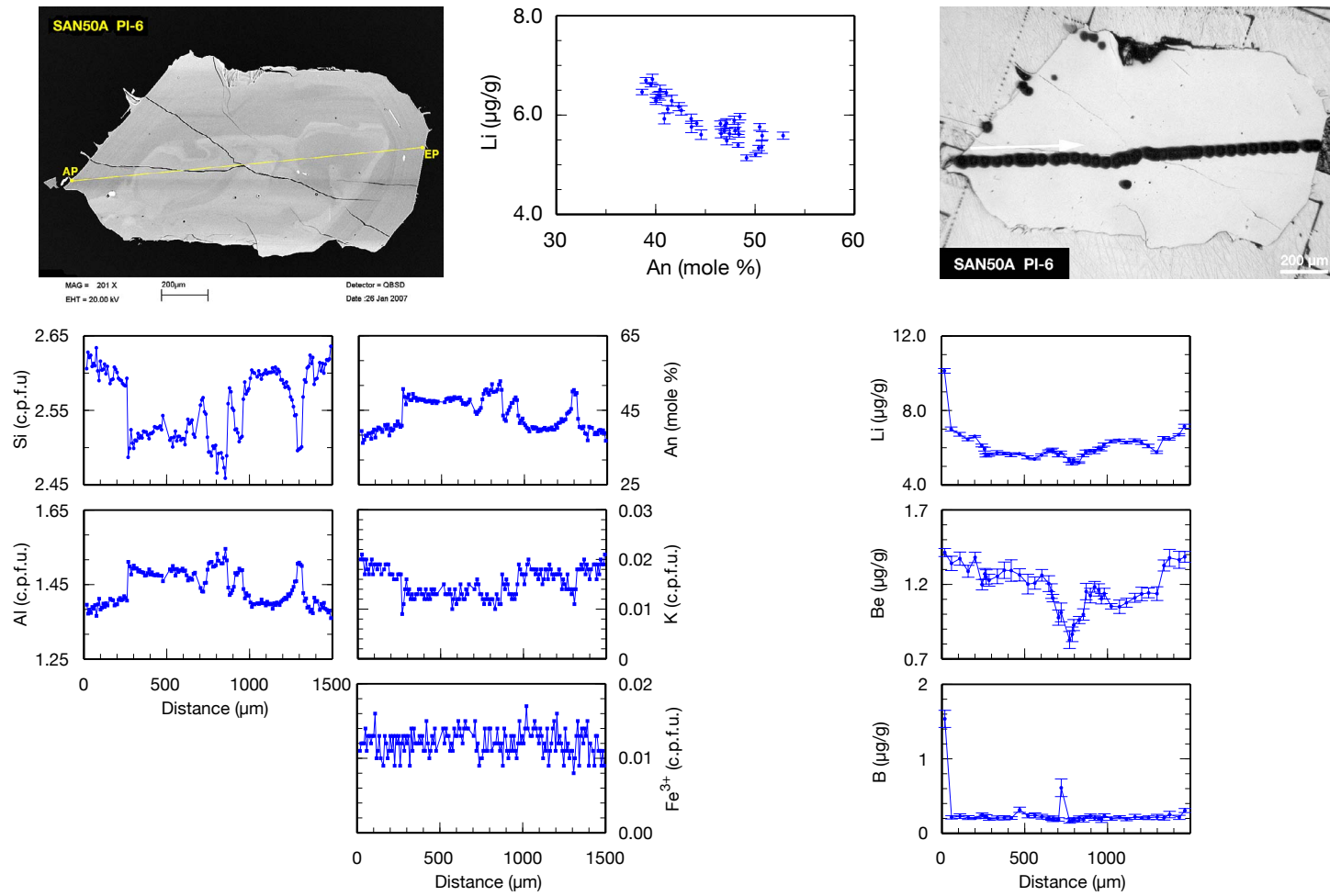
Fig. B.64. SAN50A: Pl-6. EPMA and SIMS profiles. Formulas of EPMA analyses are calculated to 8 oxygens.
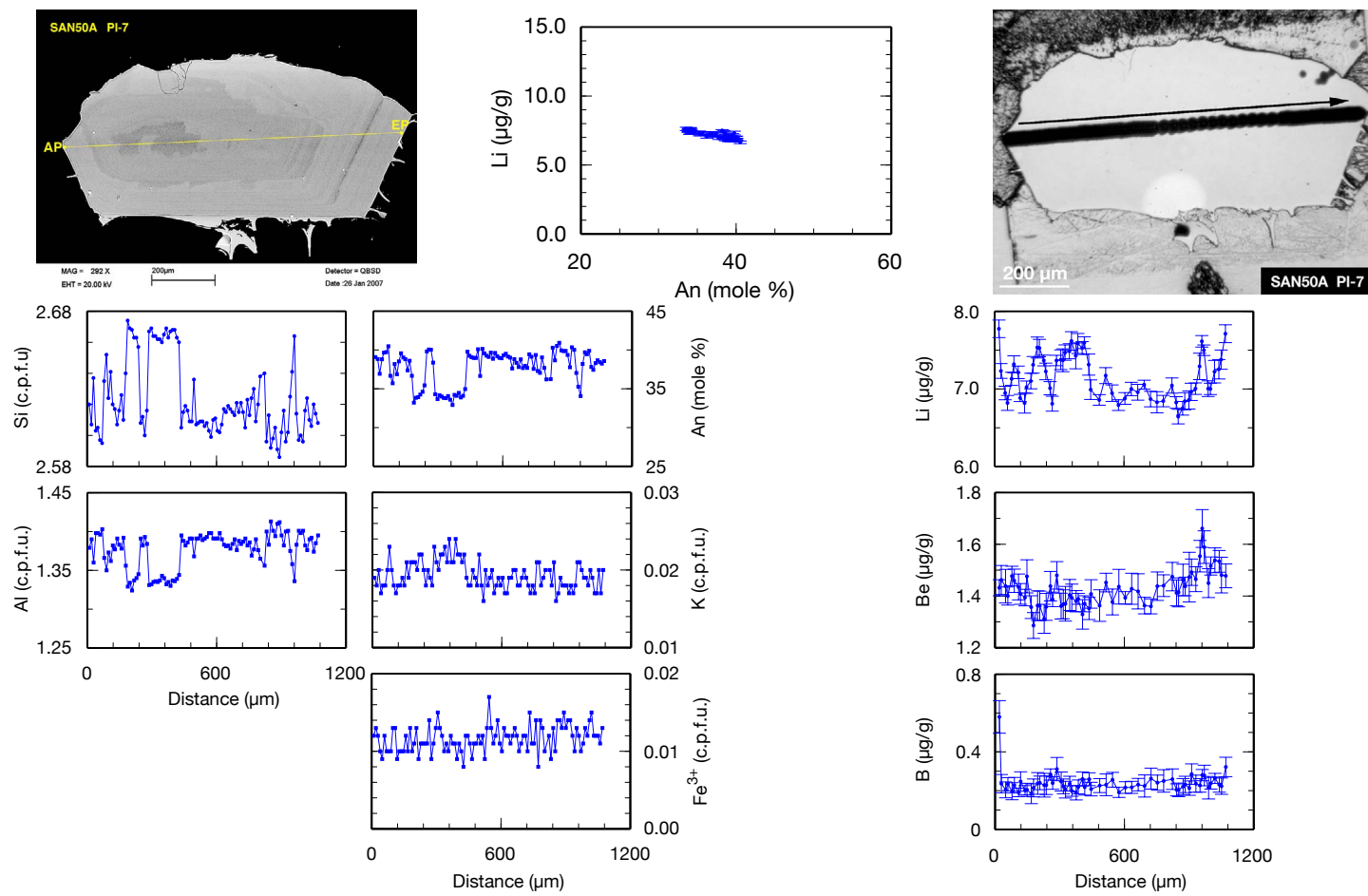
Fig. B.65. SAN50A: Pl-7. EPMA and SIMS profiles. Formulas of EPMA analyses are calculated to 8 oxygens.
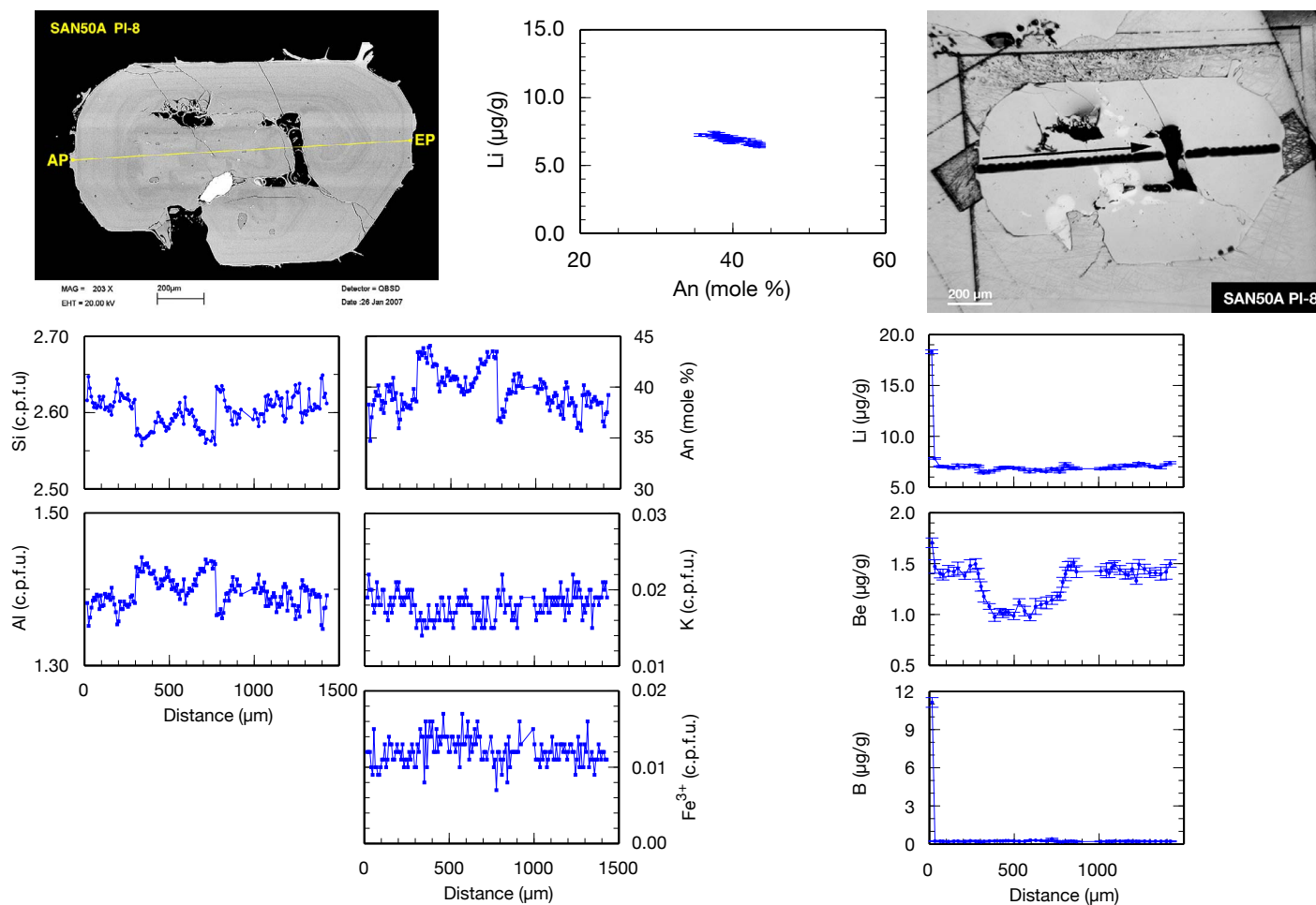
Fig. B.66. SAN50A: Pl-8. EPMA and SIMS profiles. Formulas of EPMA analyses are calculated to 8 oxygens.
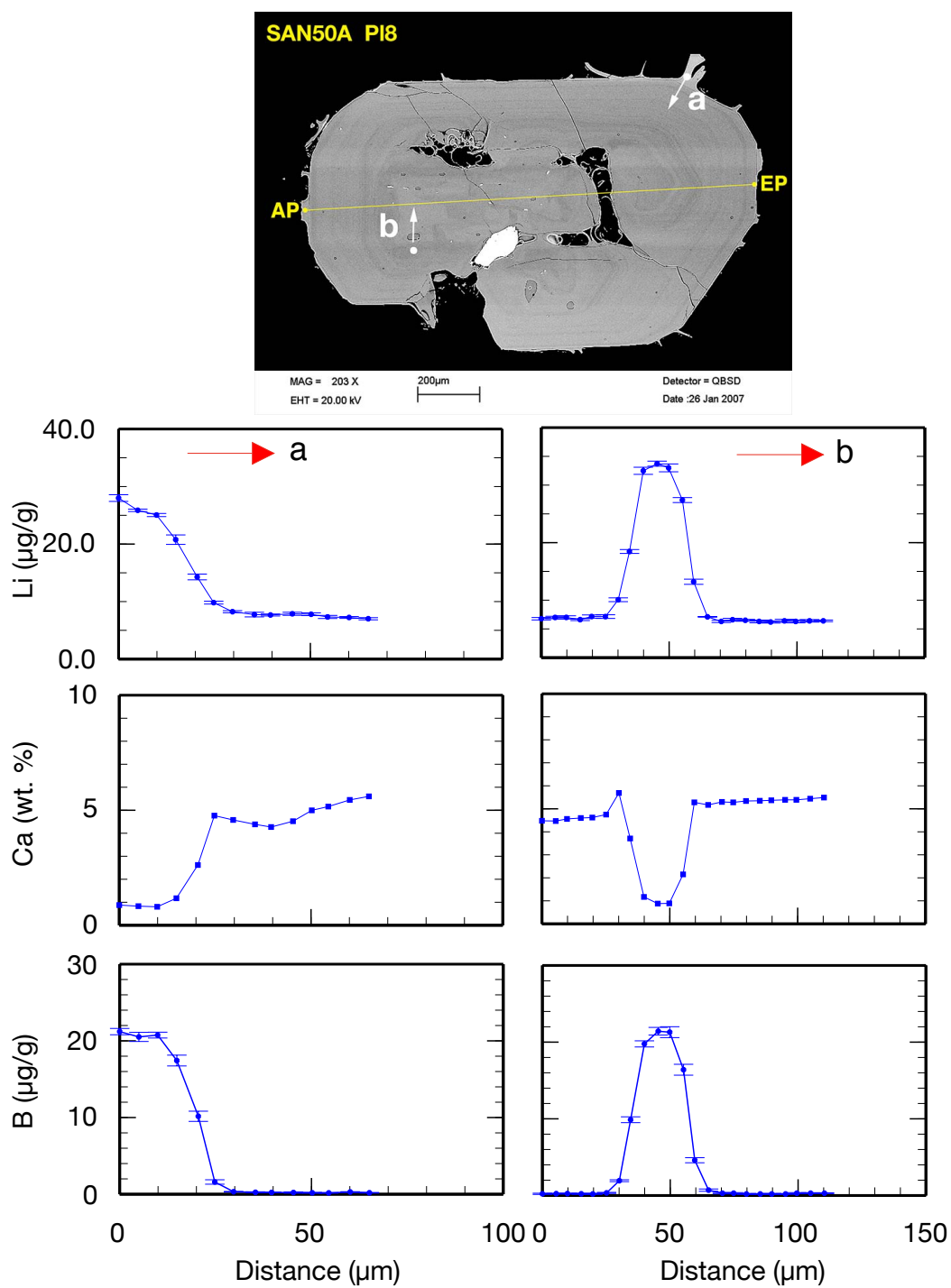
Fig. B.67. SAN50A: Pl-8. A short SIMS profile was analyzed to detect or exclude diffusion of Li from glass selvages or inclusions into plagioclase.
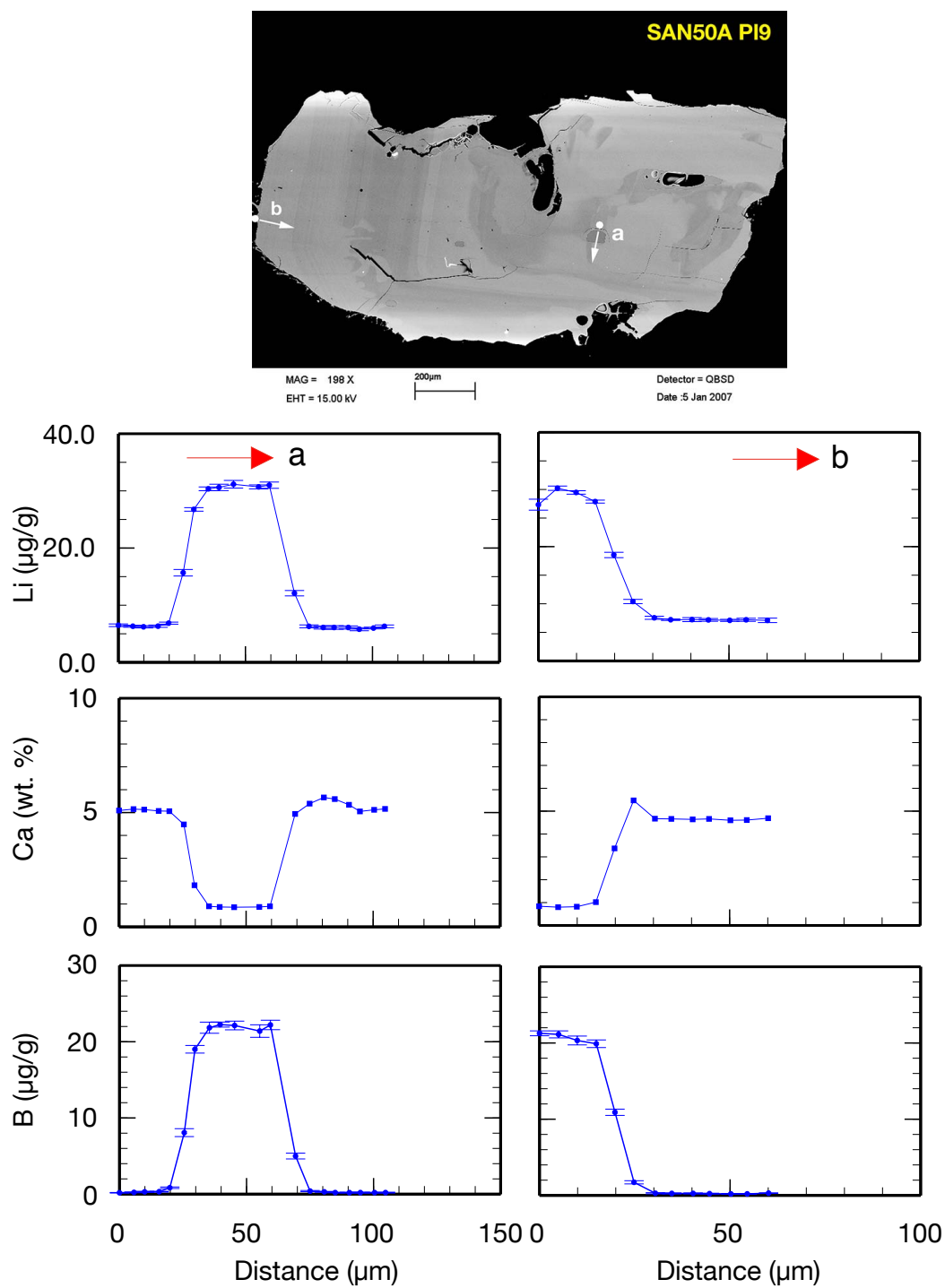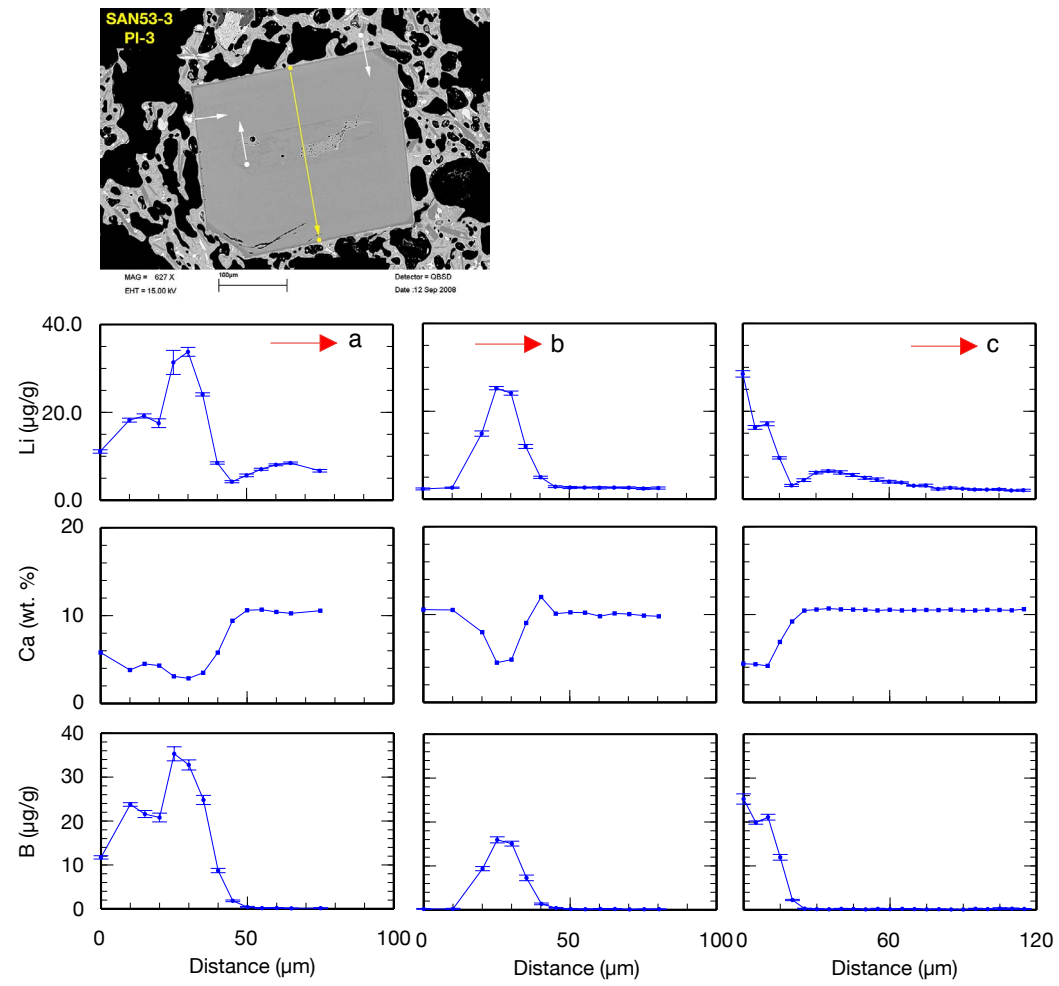
Fig. B.68. SAN50A: Pl-9. A short SIMS profile was analyzed to detect or exclude diffusion of Li from glass selvages or inclusions into plagioclase.

Fig. B.69. SAN50B: Pl-1. EPMA and SIMS profiles. Formulas of EPMA analyses are calculated to 8 oxygens.
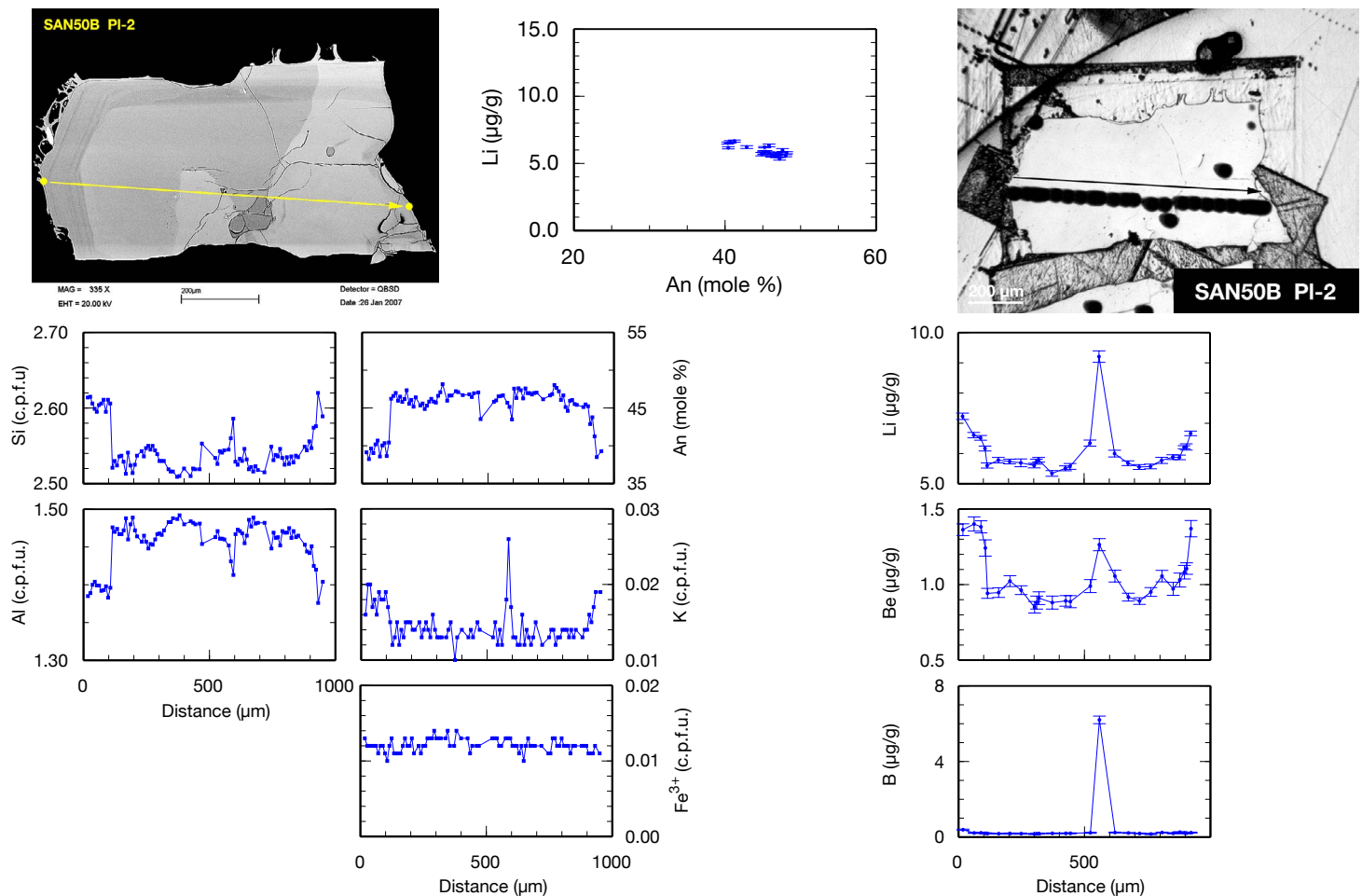
Fig. B.70. SAN50B: Pl-2. EPMA and SIMS profiles. Formulas of EPMA analyses are calculated to 8 oxygens.

Fig. B.71. SAN50B: Pl-4. EPMA and SIMS profiles. Formulas of EPMA analyses are calculated to 8 oxygens.

Fig. B.72. SAN50C: Pl-3. EPMA and SIMS profiles. Formulas of EPMA analyses are calculated to 8 oxygens.
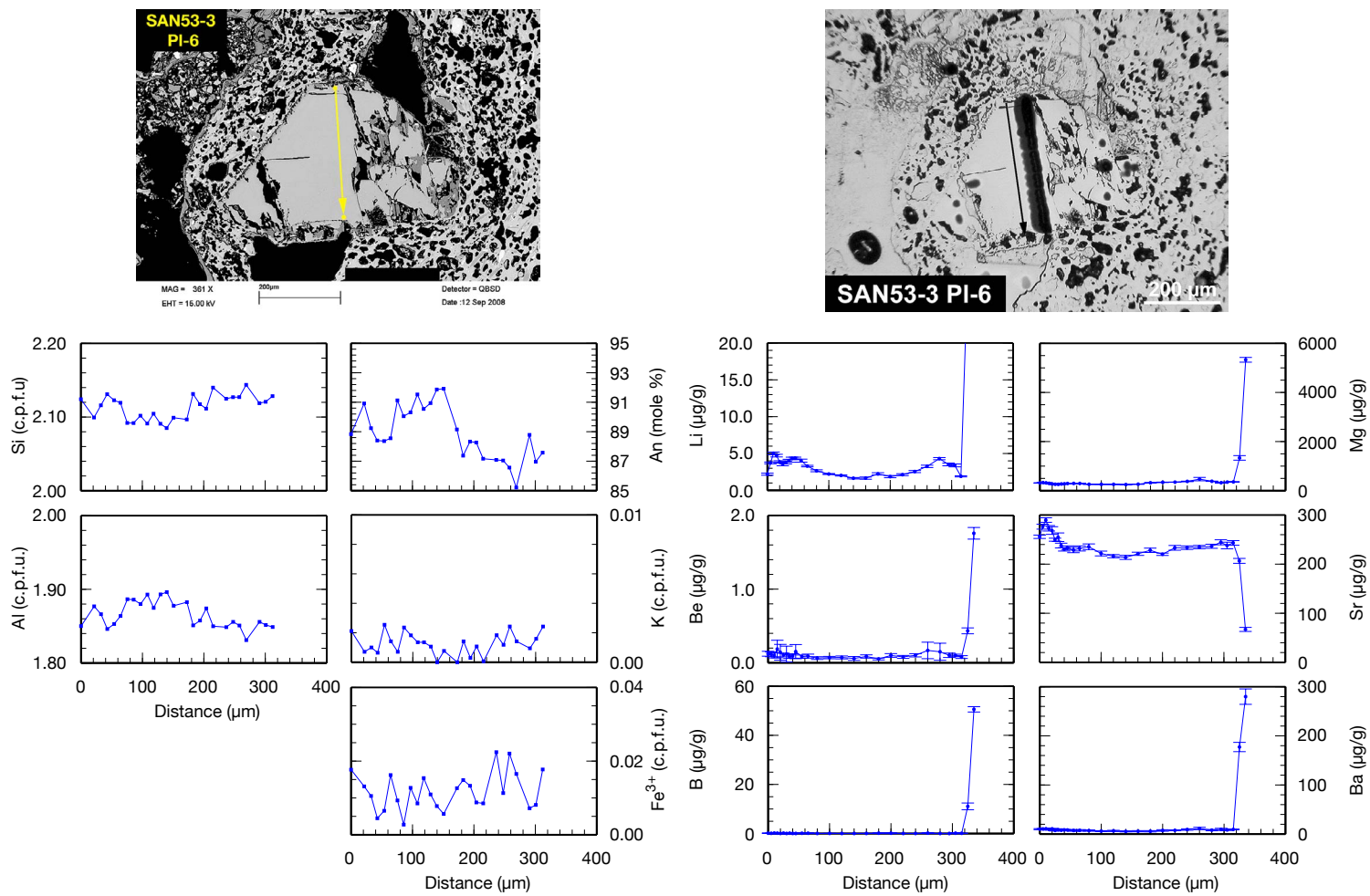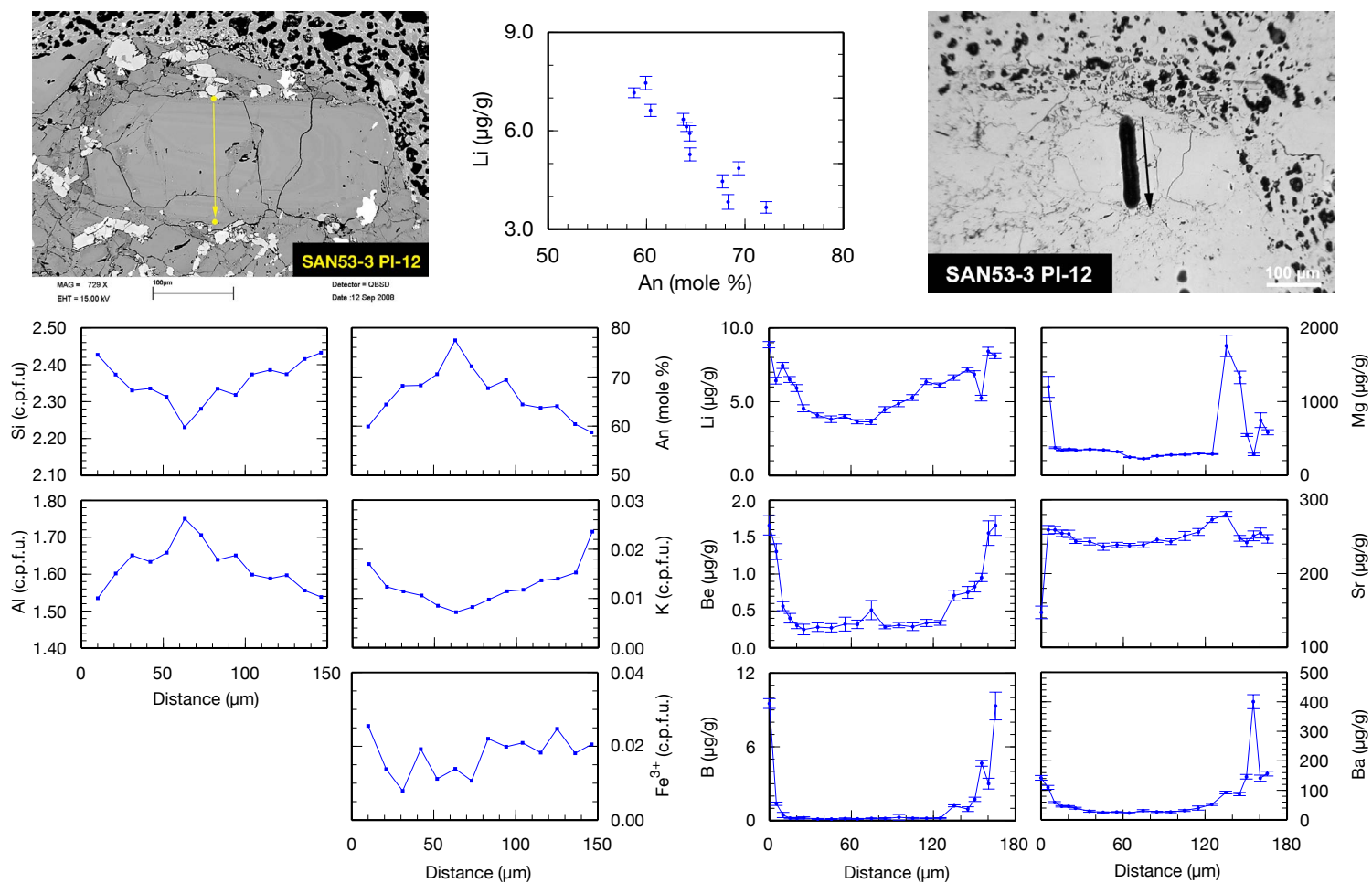
Fig. B.73. SAN51-1A: Pl-3. EPMA and SIMS profiles. Formulas of EPMA analyses are calculated to 8 oxygens.

Fig. B.74. SAN51-1A: Pl-17. EPMA and SIMS profiles. Formulas of EPMA analyses are calculated to 8 oxygens.
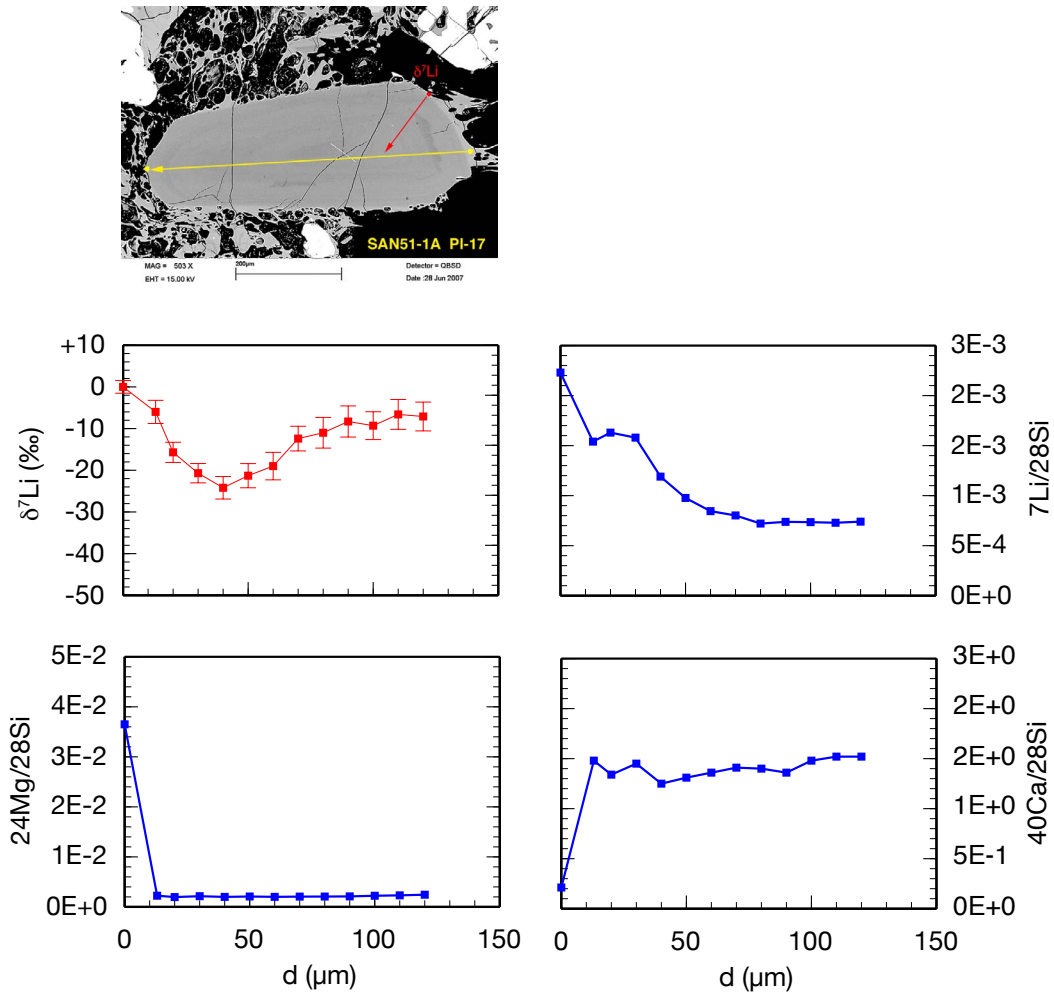
Fig. B.75. SAN51-1A: Pl-17. Short δ^7Li SIMS profile. The blue arrow marks the δ^7Li profiles; the red or white arrows mark the regular Li short profiles. A yellow arrow usually marks the EPMA profile (not all pl crystals were analyzed by EPMA). Li concentration values are derived from count rates of the isotope analyses and are therefore only semi-quantitative.

Fig. B.76. SAN51-1B: Pl-17. EPMA and SIMS profiles. Formulas of EPMA analyses are calculated to 8 oxygens.

Fig. B.77. SAN51-1B: Pl-3. EPMA and SIMS profiles. Formulas of EPMA analyses are calculated to 8 oxygens.
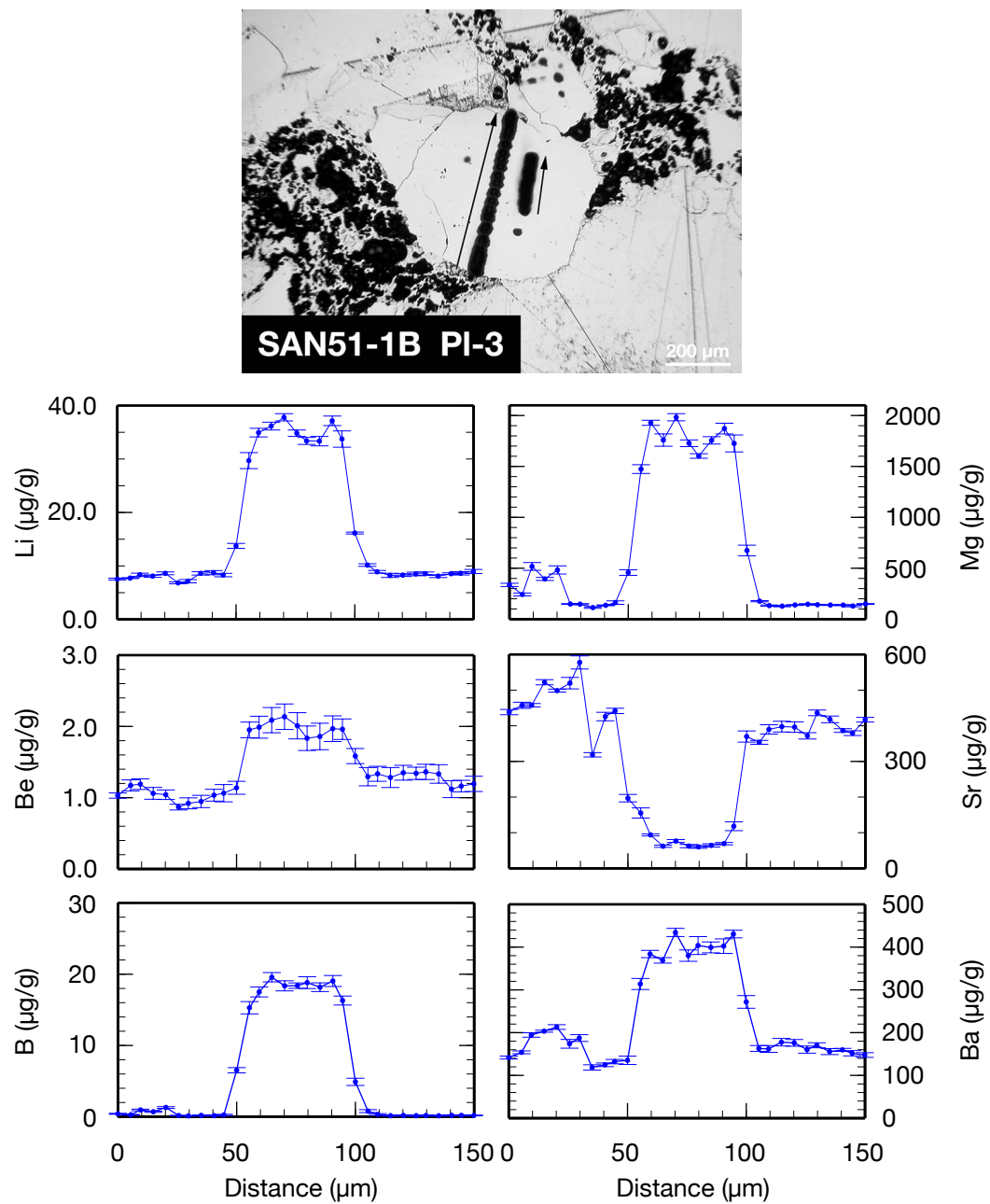
Fig. B.78. SAN51-1B: Pl-3. Profile through glass inlcusion.
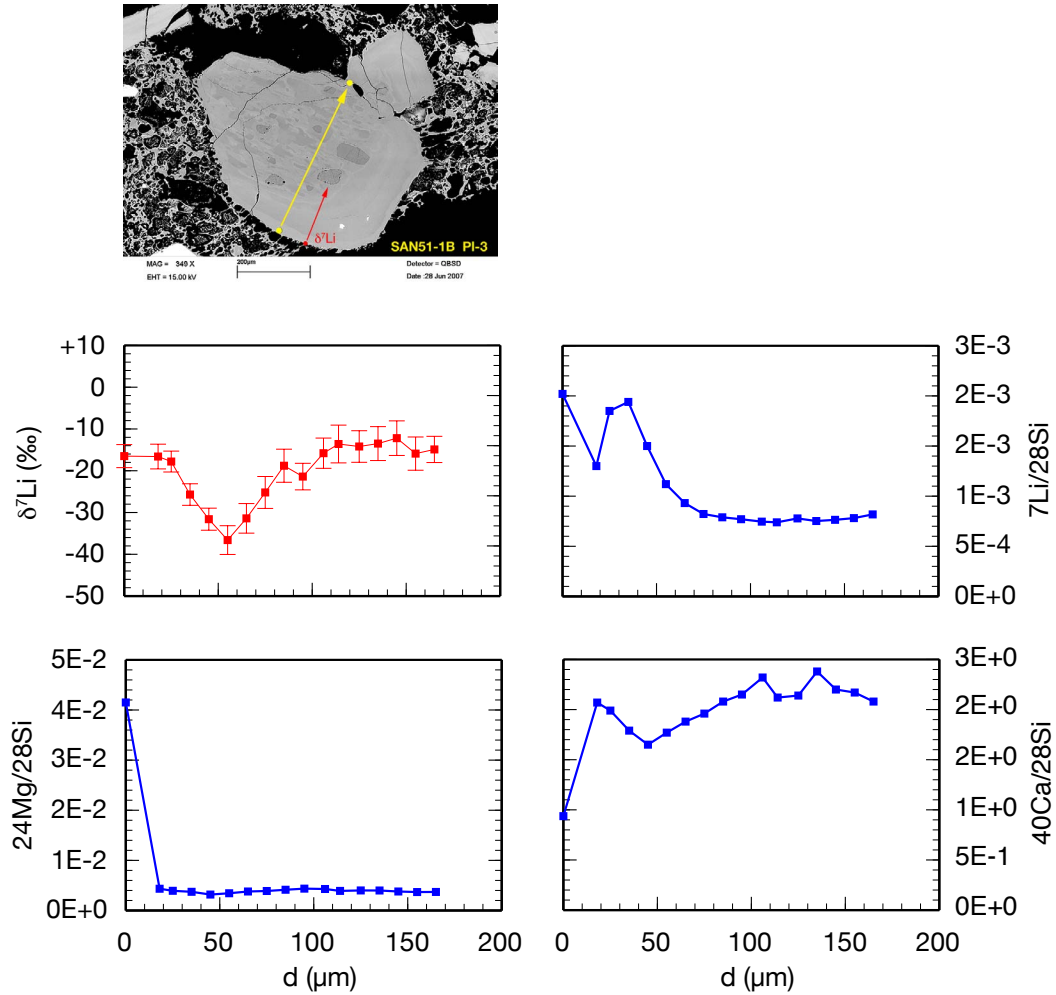
Fig. B.79. SAN51-1AB: Pl-3. Short δ^7Li SIMS profile. The blue arrow marks the δ^7Li profiles; the red or white arrows mark the regular Li short profiles. A yellow arrow usually marks the EPMA profile (not all pl crystals were analyzed by EPMA). Li concentration values are derived from count rates of the isotope analyses and are therefore only semi-quantitative.

Fig. B.80. SAN51-1B: Pl-17. EPMA and SIMS profiles. Formulas of EPMA analyses are calculated to 8 oxygens.
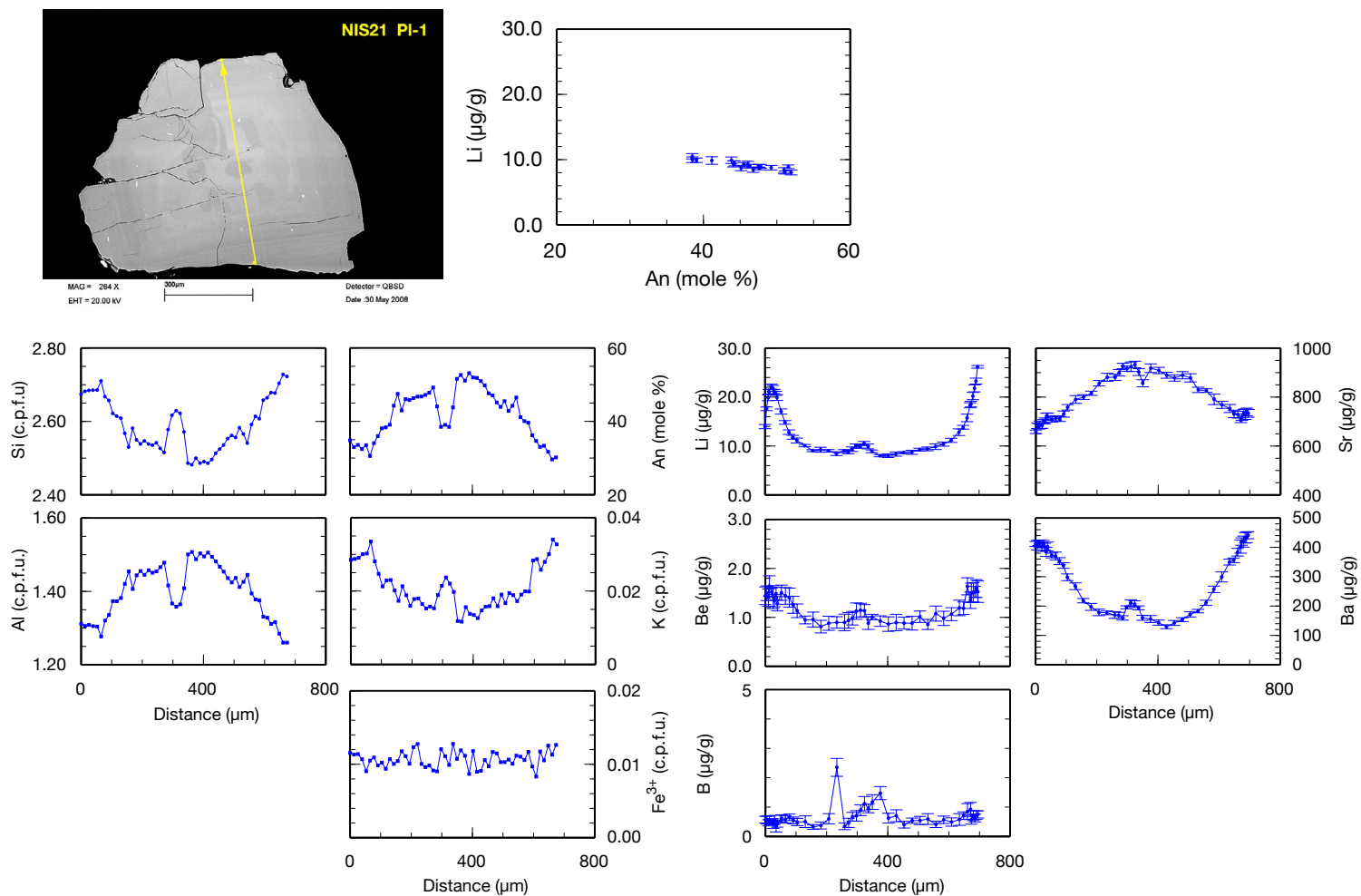
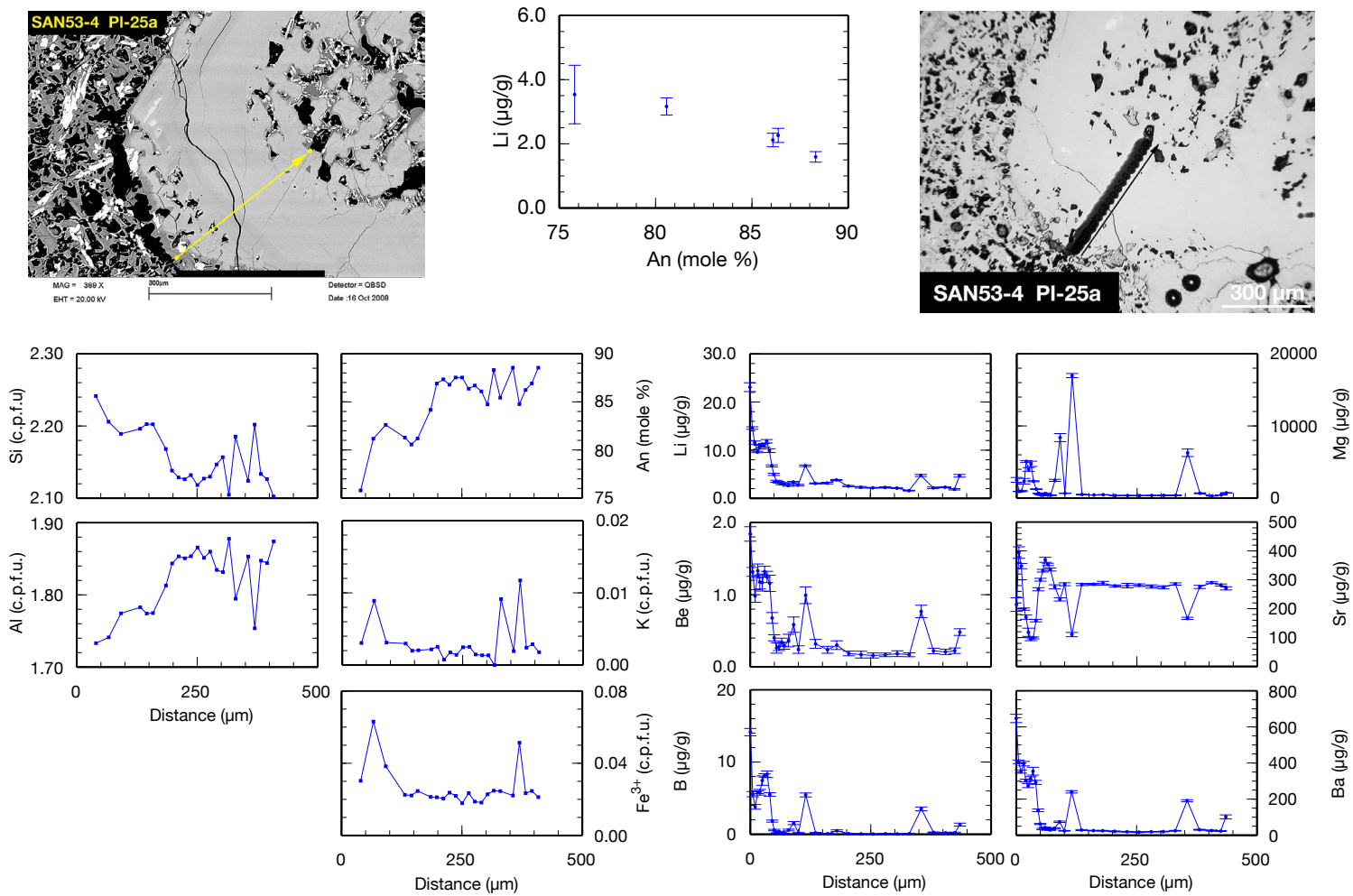**Fig. B.81.** NIS21: Pl-1. EPMA and SIMS profiles. Formulas of EPMA analyses are calculated to 8 oxygens.

B.5. SAN52Agg – SAN53 – SAN56 – SAN60 – Minoan Scoria
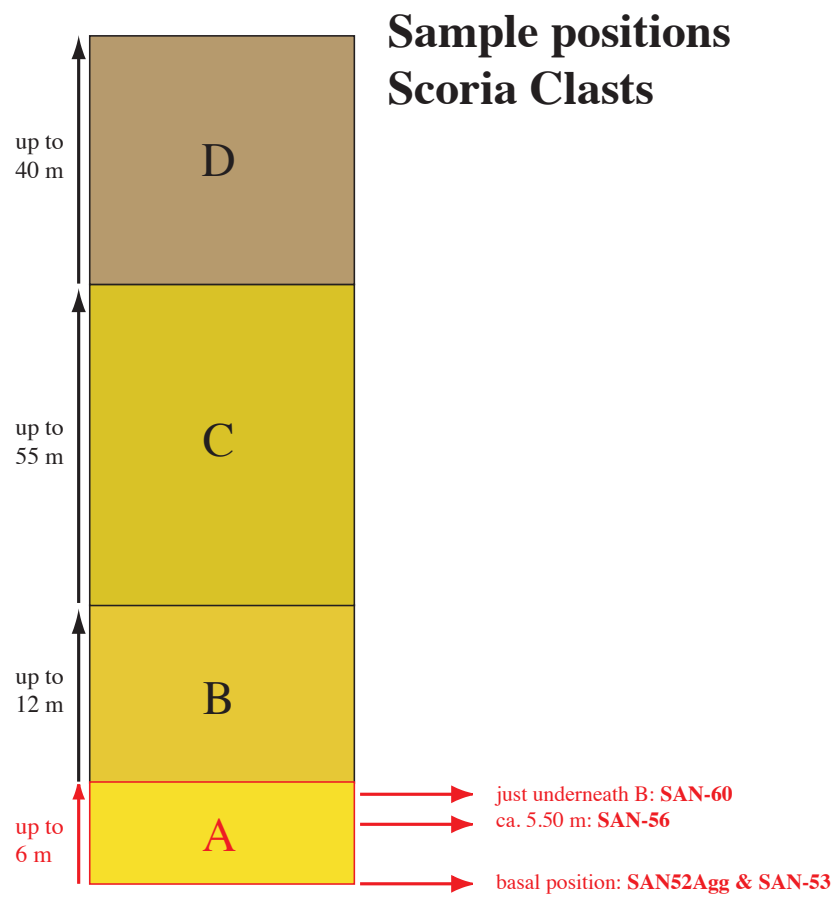
Fig. B.82. Positions of scoria samples taken from Minoan Unit A.
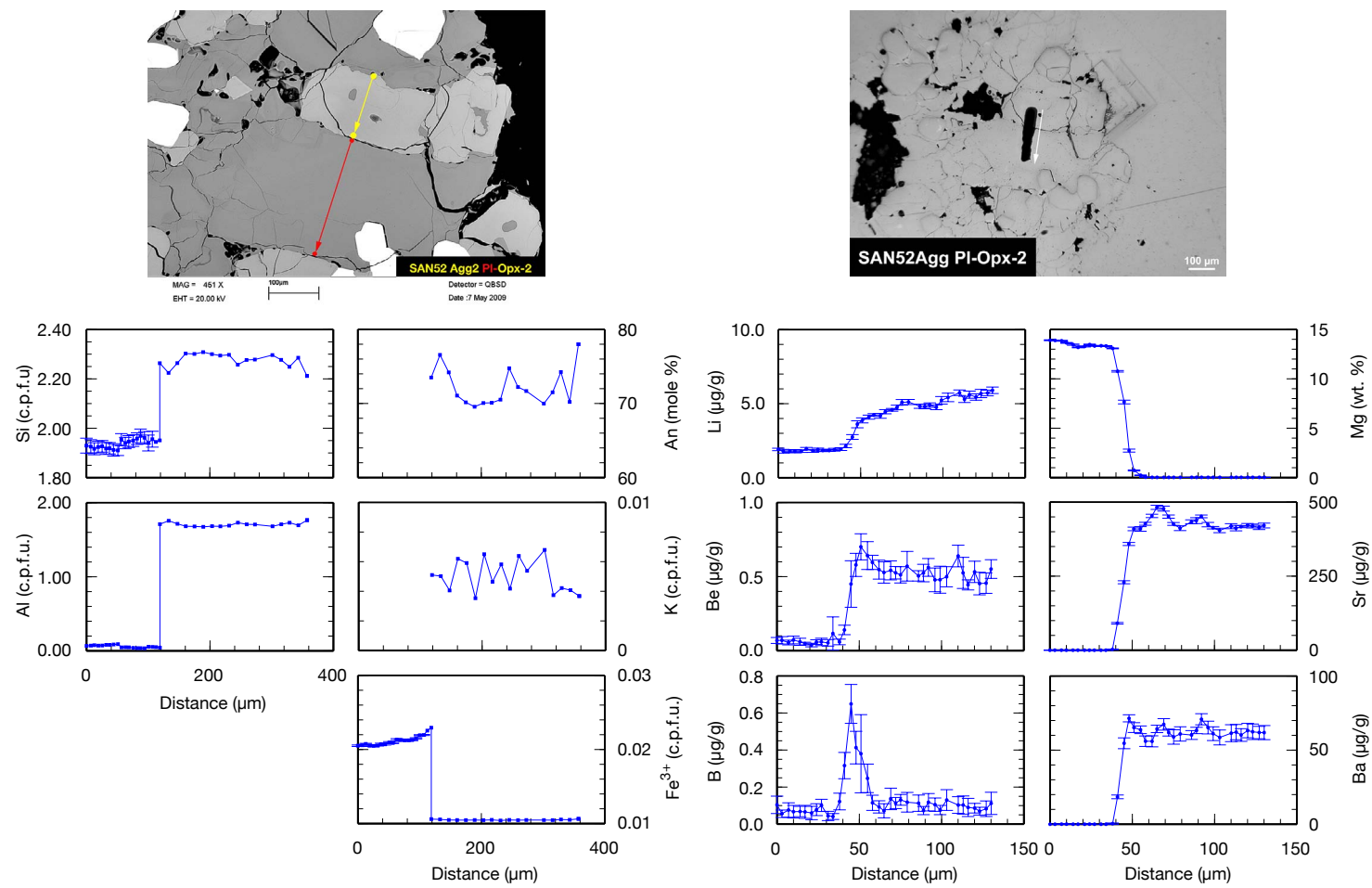
Fig. B.83. SAN52D: Pl-Opx-2. EPMA and SIMS profiles. Formulas of EPMA analyses for px are calculated to 4 cations; EPMA analyses for pl are calculated to 8 oxygens.
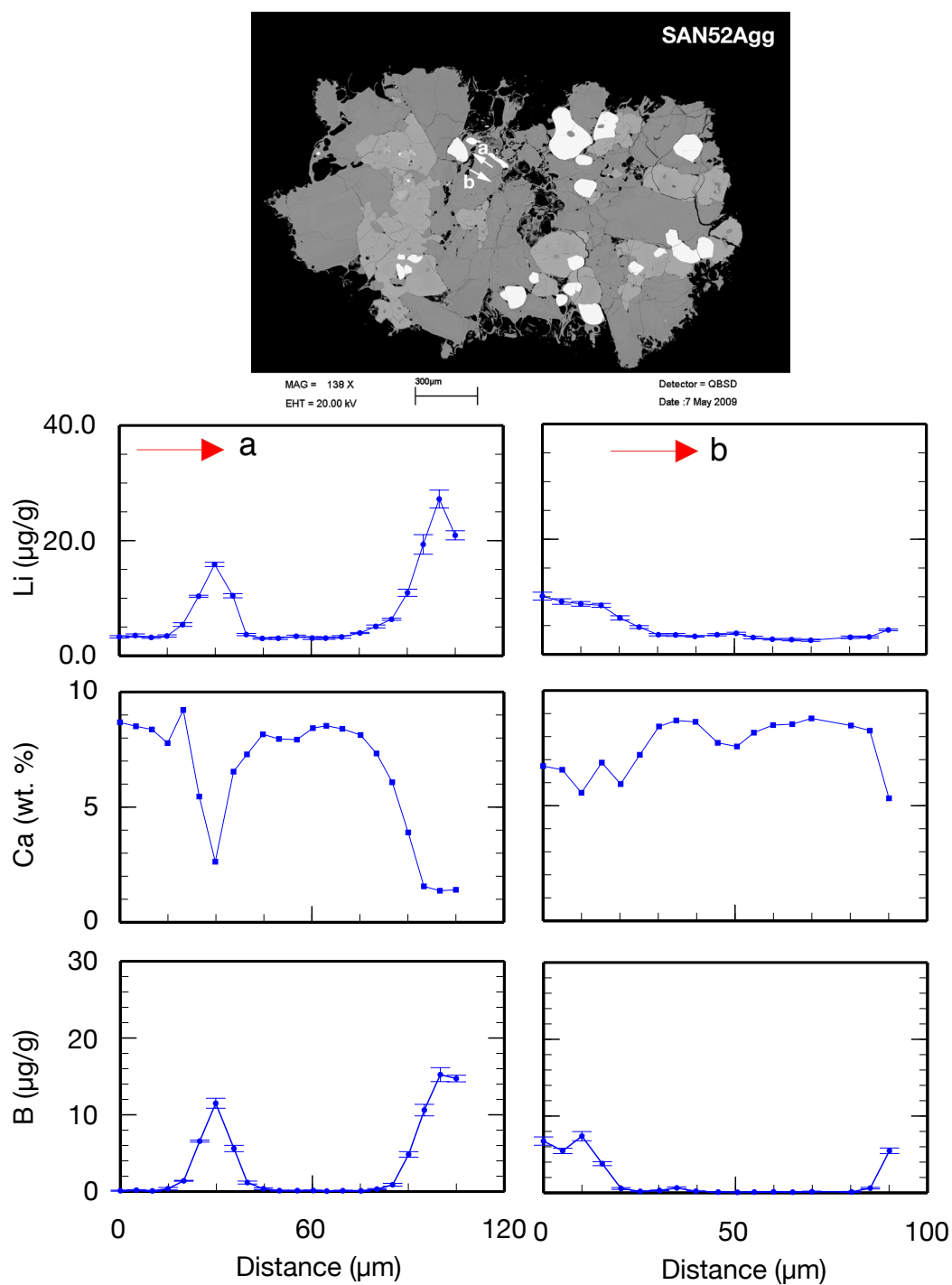
Fig. B.84. SAN52Agg: Short SIMS profiles to detect/exclude diffusion of Li from melt selvage into pl crystal or from inclusion into pl.
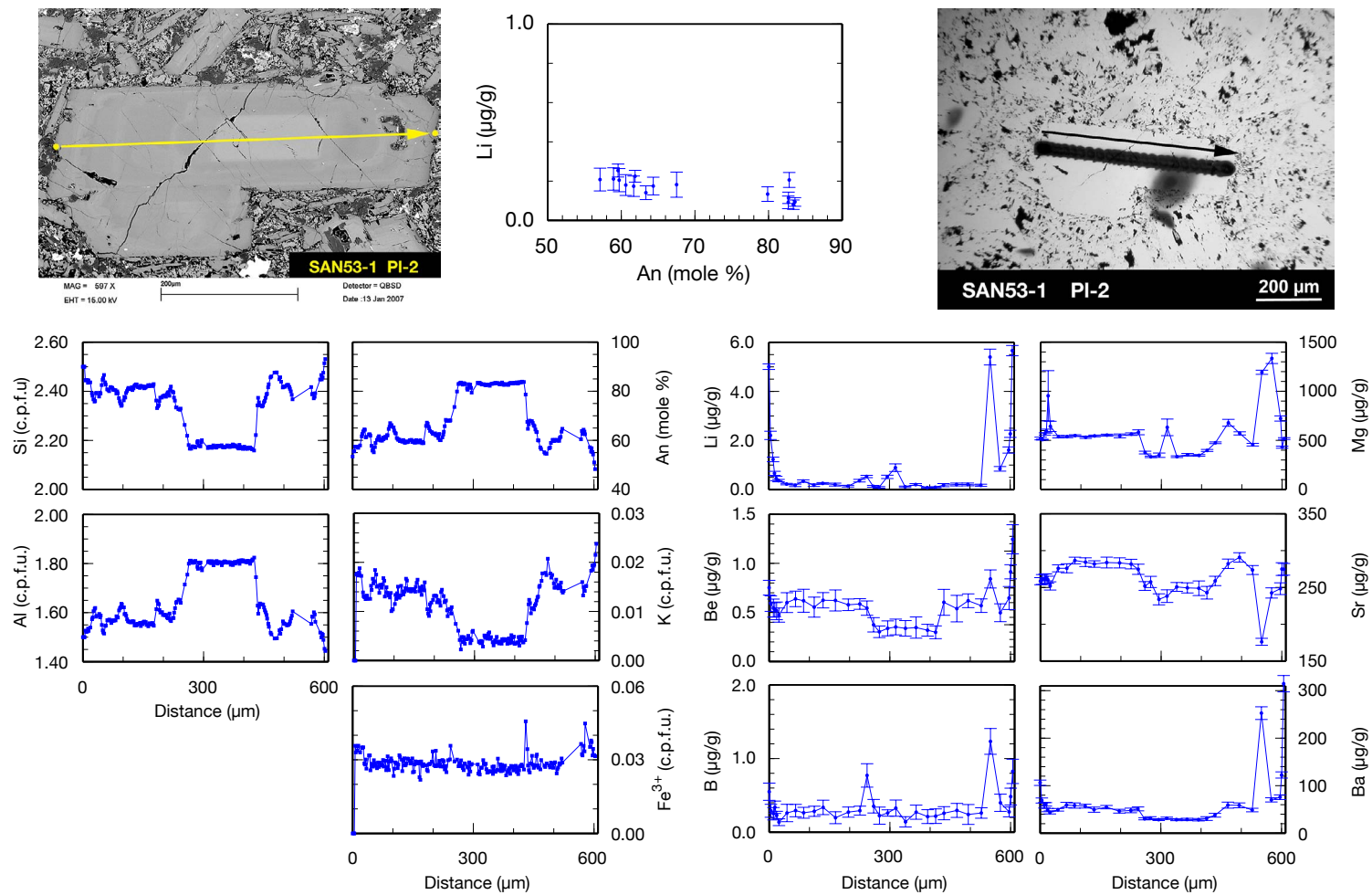
Fig. B.85. SAN53-1: Pl-2. EPMA and SIMS profiles. Formulas of EPMA analyses are calculated to 8 oxygens.
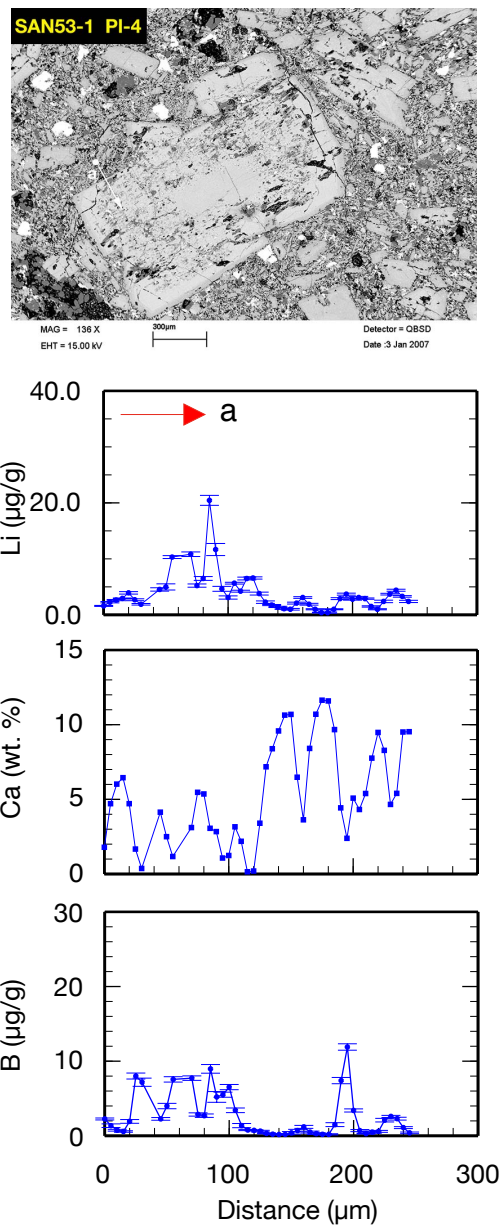
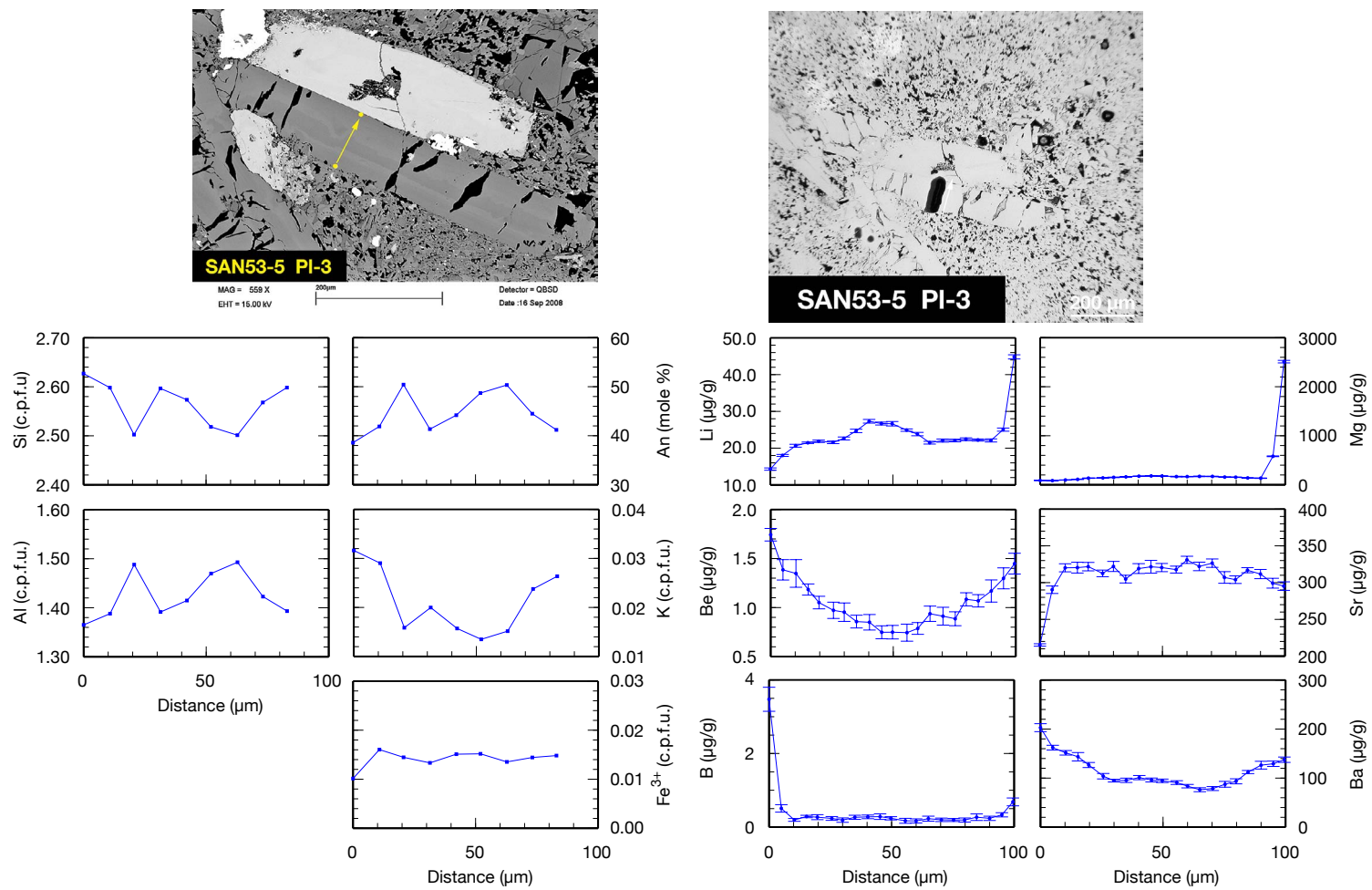**Fig. B.86.** SAN53-1: Pl-4. A short SIMS profile was analyzed to detect Li concentrations in matrix adjacent to plagioclase.

Fig. B.87. SAN53-1: Pl-9. EPMA and SIMS profiles. Formulas of EPMA analyses are calculated to 8 oxygens.

Fig. B.88. SAN53-1: Pl-16. EPMA and SIMS profiles. Formulas of EPMA analyses are calculated to 8 oxygens.

Fig. B.89. SAN53-2: Pl-1. EPMA and SIMS profiles. Formulas of EPMA analyses are calculated to 8 oxygens.
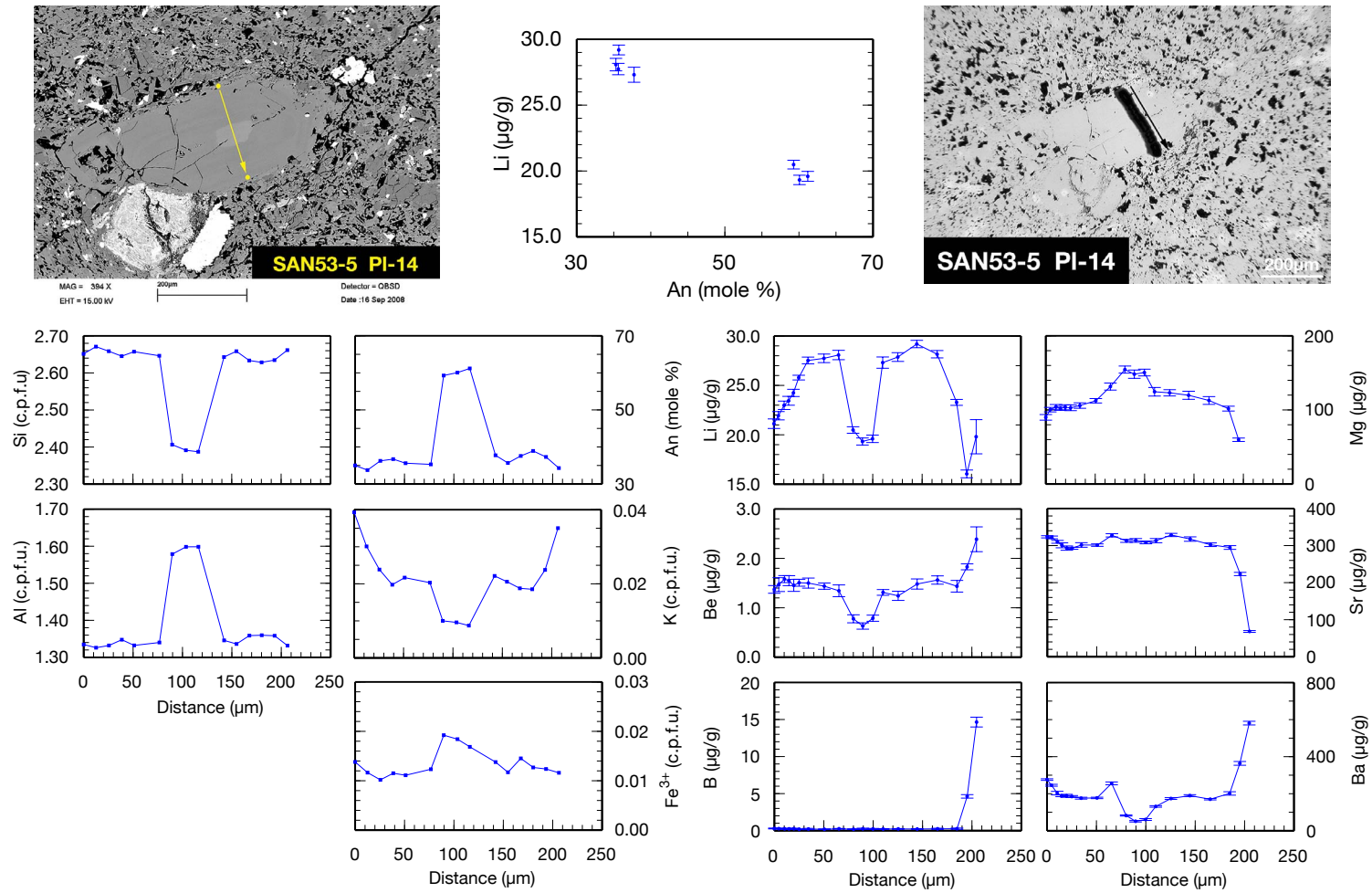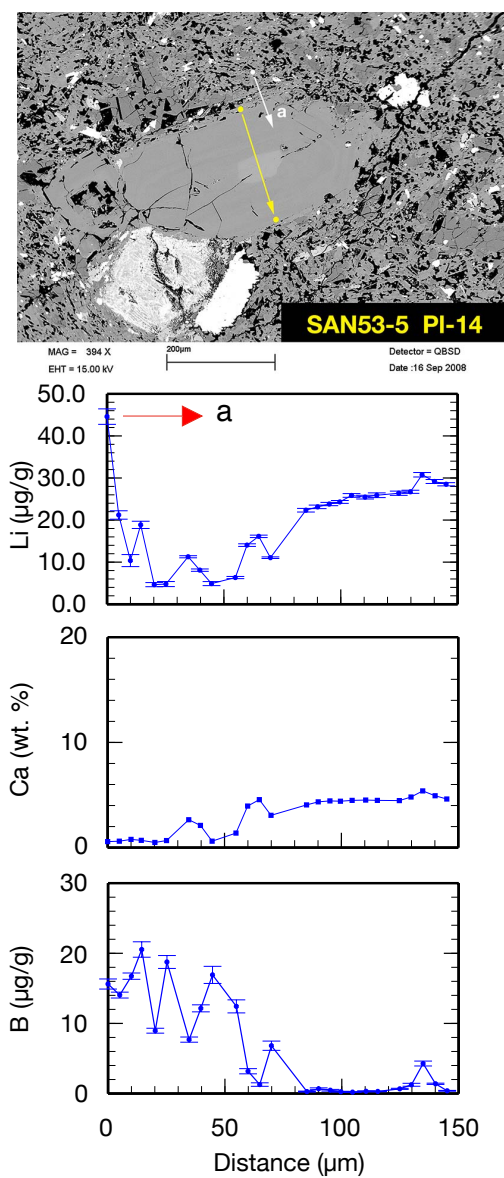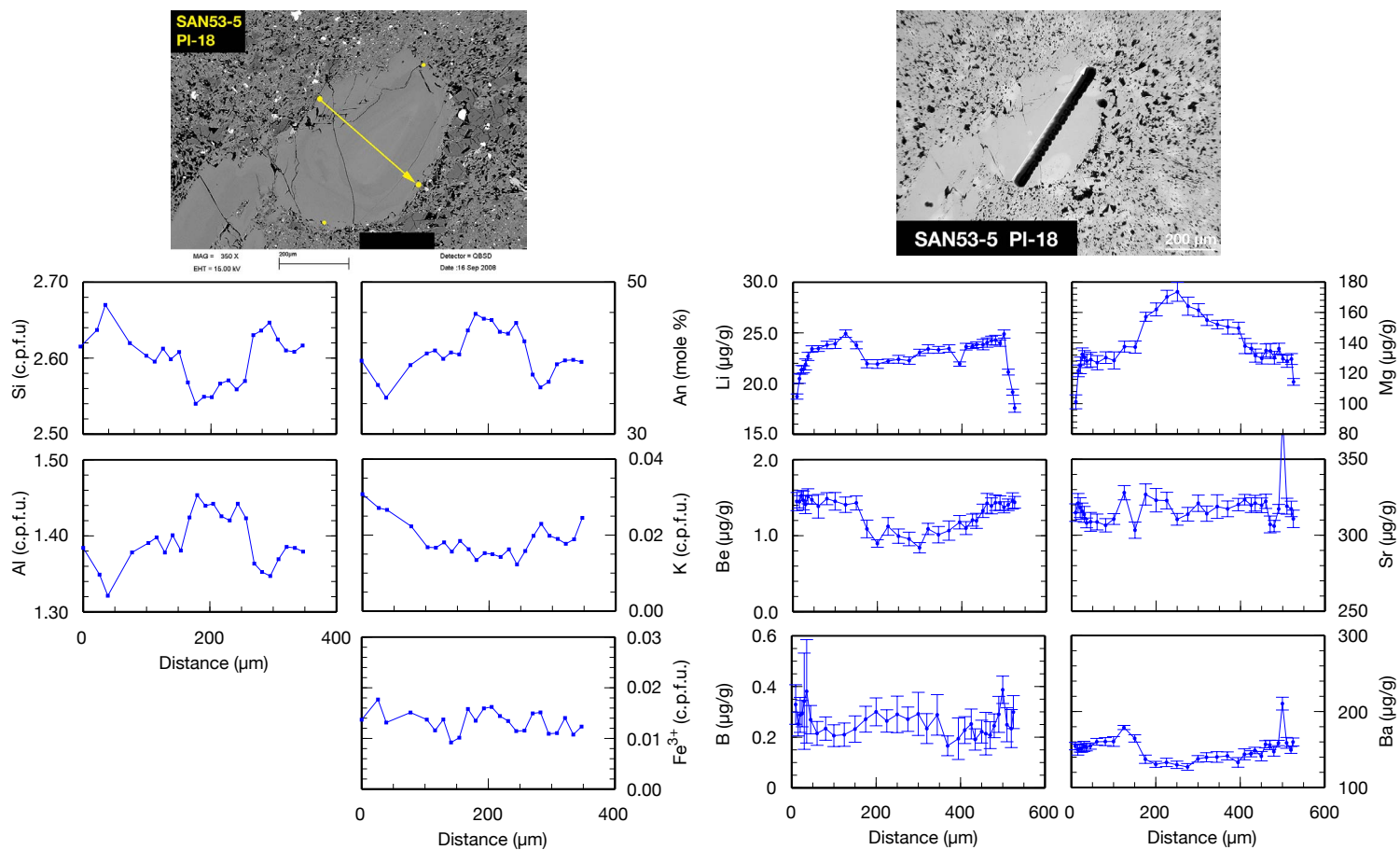
Fig. B.90. SAN53-2: Pl-5. EPMA and SIMS profiles. Formulas of EPMA analyses are calculated to 8 oxygens.

Fig. B.91. SAN53-2: Pl-7. A short SIMS profile was analyzed to detect or exclude Li diffusion from broken rims into plagioclase.

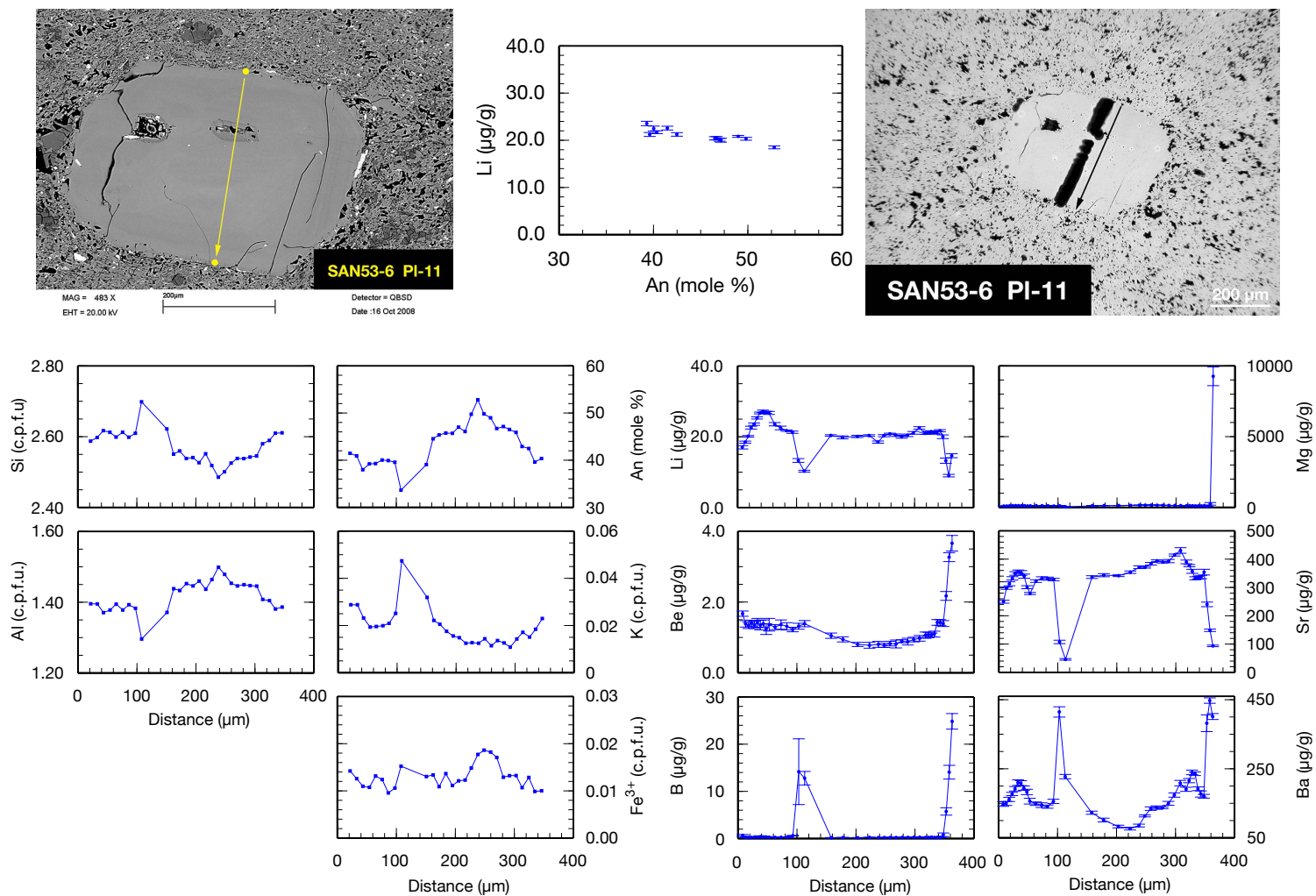**Fig. B.92.** SAN53-2: Pl-9. EPMA and SIMS profiles. Formulas of EPMA analyses are calculated to 8 oxygens.

Fig. B.93. SAN53-2: Pl-12. EPMA and SIMS profiles. Formulas of EPMA analyses are calculated to 8 oxygens.

Fig. B.94. SAN53-2: Pl-14. EPMA and SIMS profiles. Formulas of EPMA analyses are calculated to 8 oxygens.

Fig. B.95. SAN53-2: Pl-19. A short SIMS profile was analyzed to detect or exclude Li diffusion from broken rims into plagioclase.

Fig. B.96. SAN53-2: Pl-21. EPMA and SIMS profiles. Formulas of EPMA analyses are calculated to 8 oxygens.
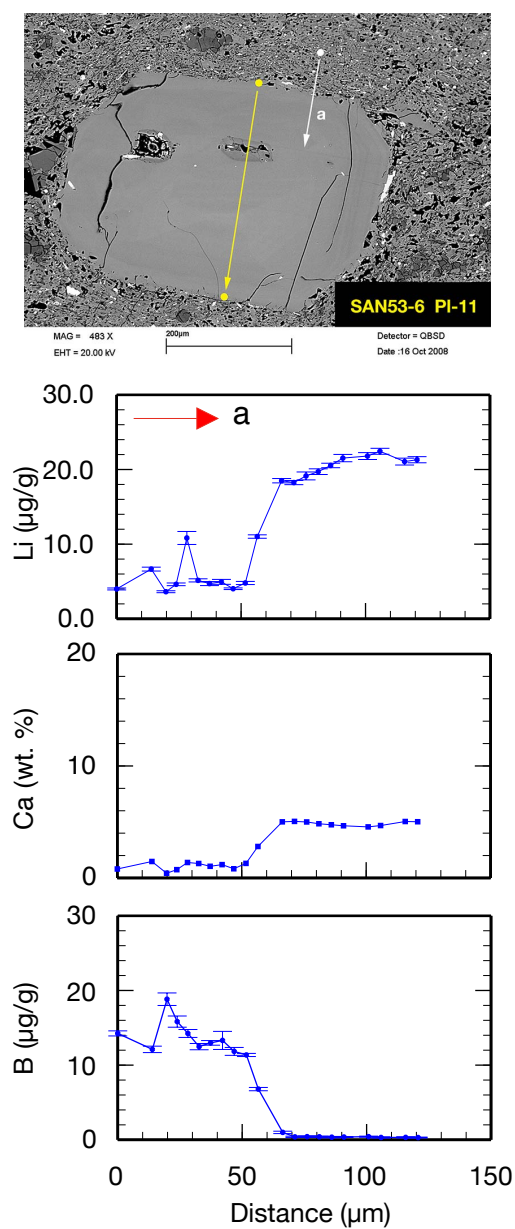
Fig. B.97. SAN53-2: Pl-21. A short SIMS profile was analyzed to detect Li concentrations in matrix adjacent to plagioclase.

**Fig. B.98.** SAN53-2: Pl-21. Short δ^7Li SIMS profile. The blue arrow marks the δ^7Li profiles; the red or white arrows mark the regular Li short profiles. A yellow arrow usually marks the EPMA profile (not all pl crystals were analyzed by EPMA). Li concentration values are derived from count rates of the isotope analyses and are therefore only semi-quantitative.

Fig. B.99. SAN53-3: Pl-1. EPMA and SIMS profiles. Formulas of EPMA analyses are calculated to 8 oxygens.
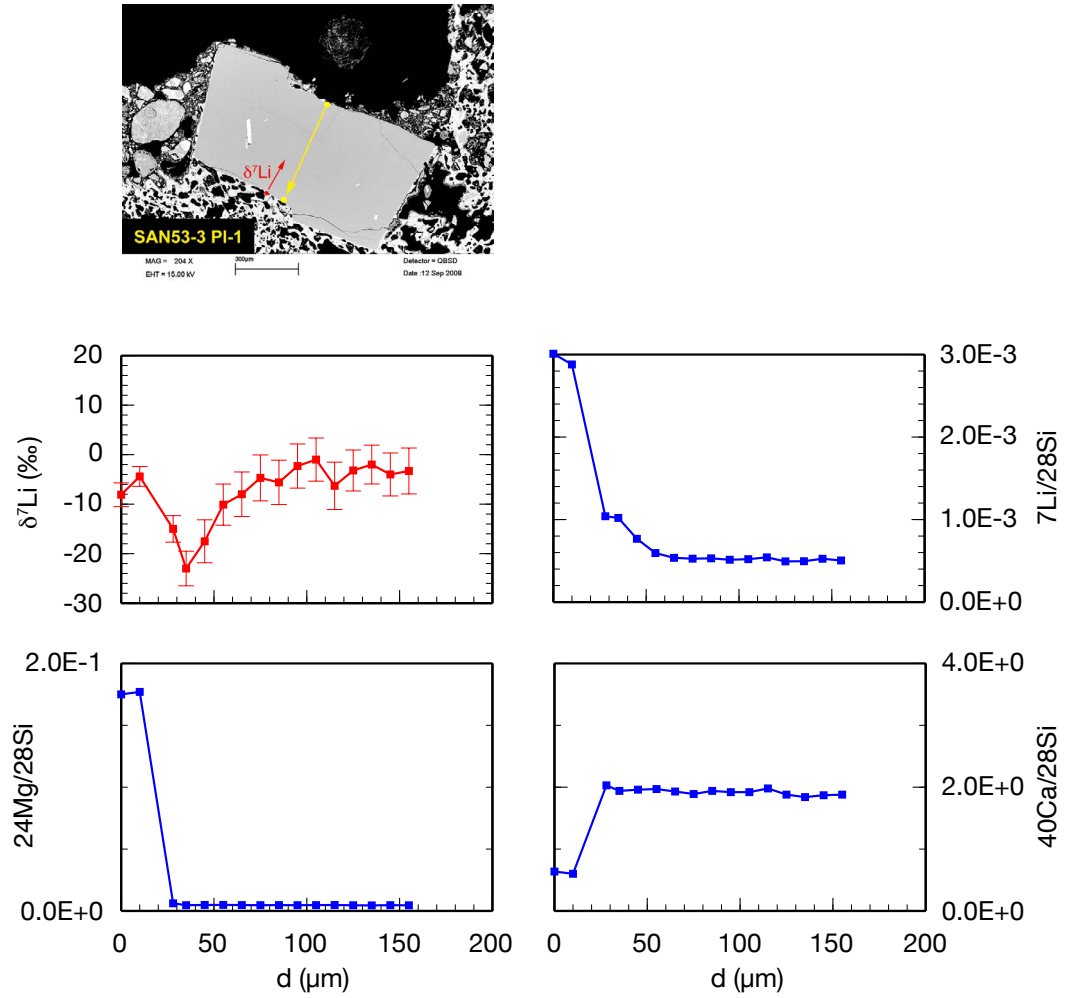
Fig. B.100. SAN53-3: Pl-1. Short δ^7Li SIMS profile. The blue arrow marks the δ^7Li profiles; the red or white arrows mark the regular Li short profiles. A yellow arrow usually marks the EPMA profile (not all pl crystals were analyzed by EPMA). Li concentration values are derived from count rates of the isotope analyses and are therefore only semi-quantitative.

Fig. B.101. SAN53-3: Pl-3. A short SIMS profile was analyzed to detect or exclude diffusion of Li from glass selvages or inclusions into plagioclase.

Fig. B.102. SAN53-3: Pl-6. EPMA and SIMS profiles. Formulas of EPMA analyses are calculated to 8 oxygens.

Fig. B.103. SAN53-3: Pl-12. EPMA and SIMS profiles. Formulas of EPMA analyses are calculated to 8 oxygens.
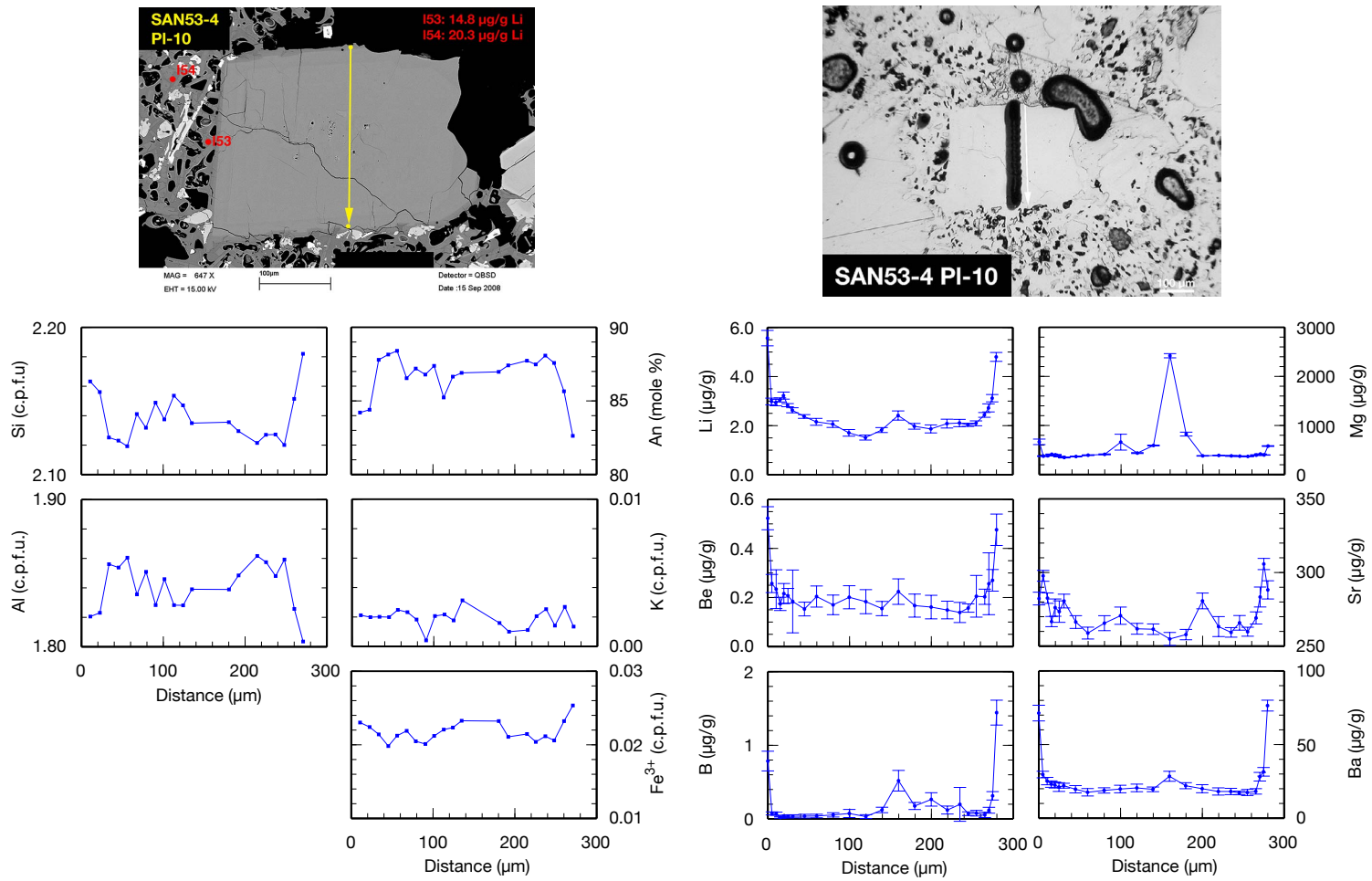
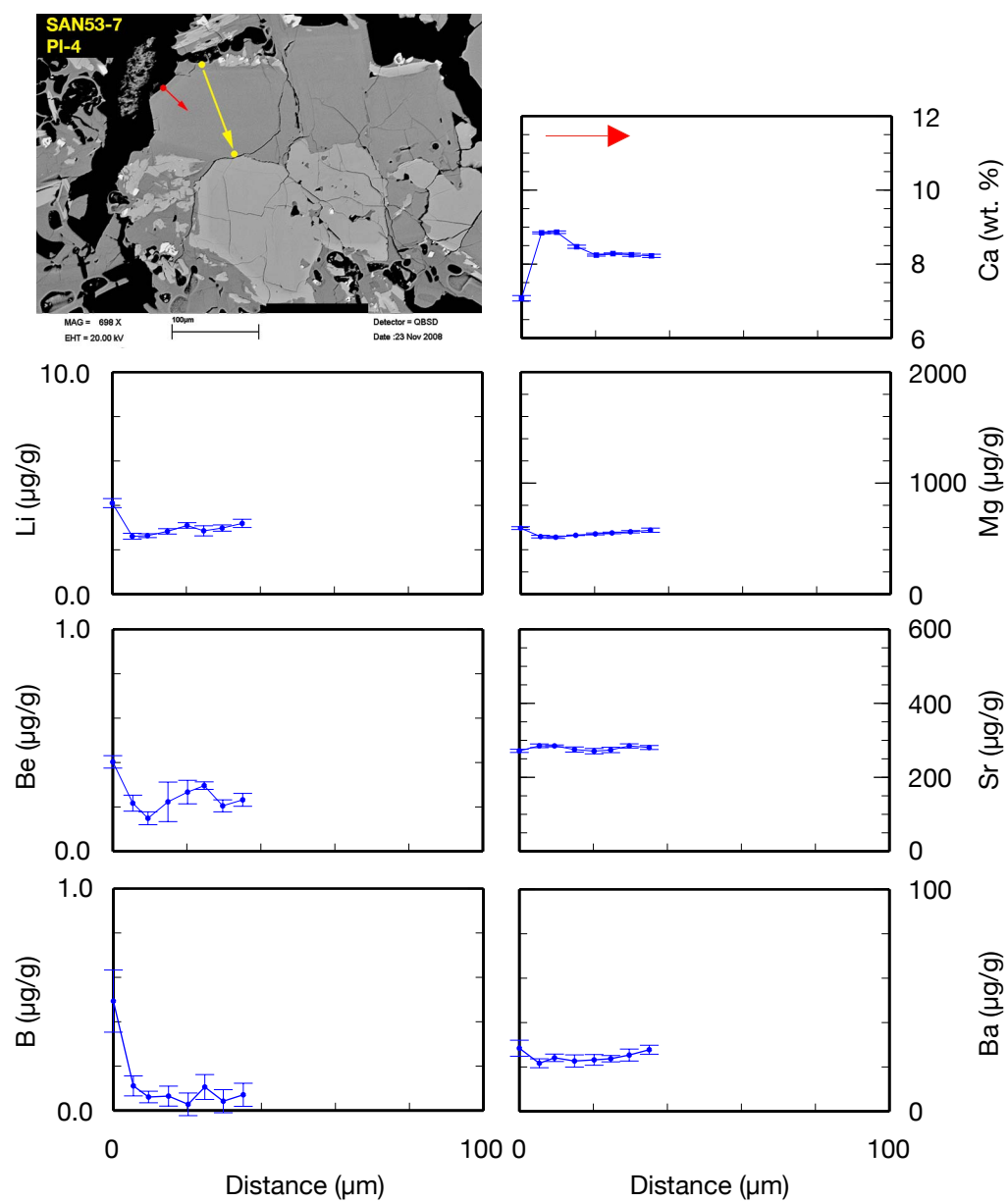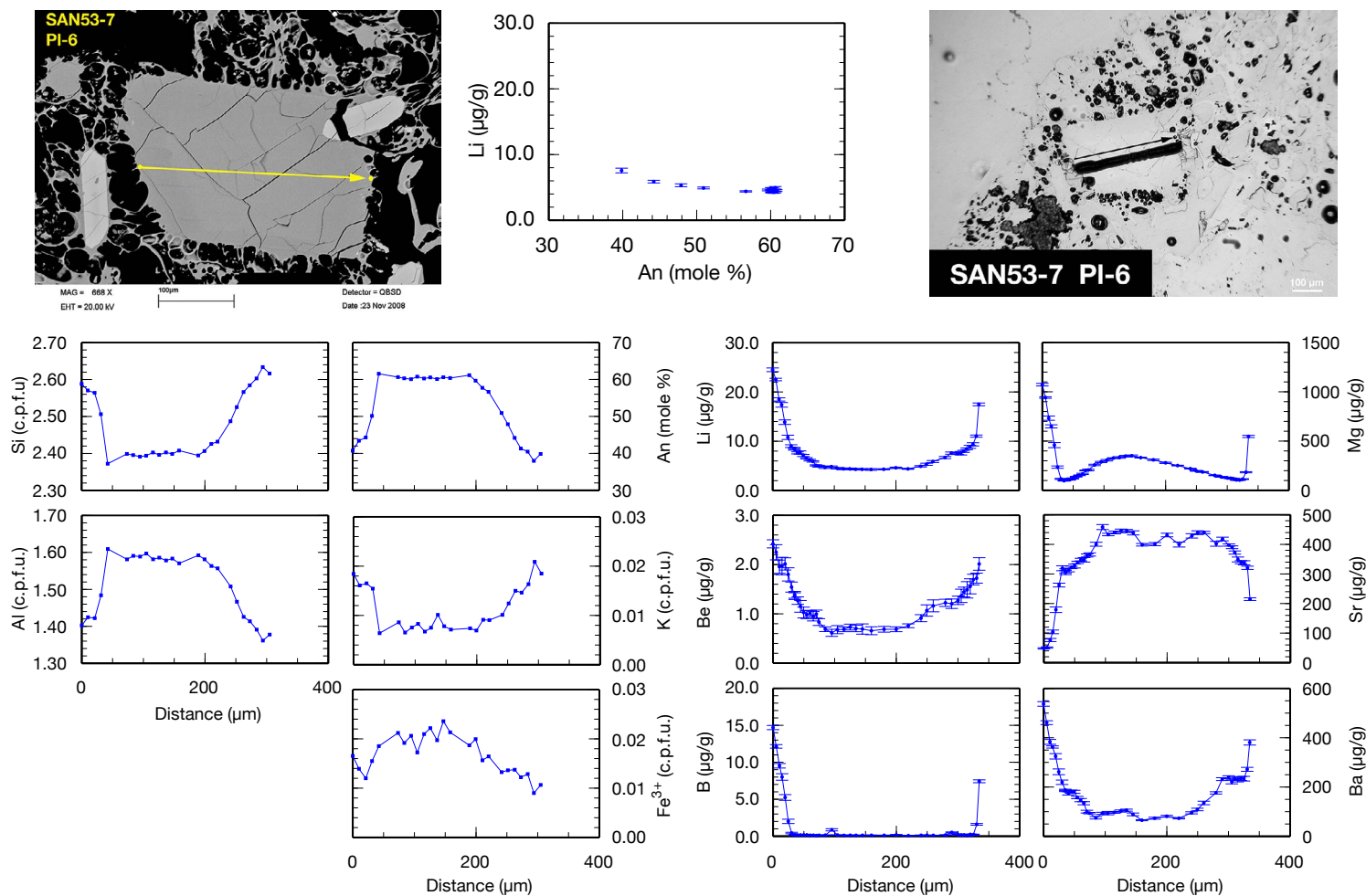**Fig. B.104.** SAN53-4: Pl-10. EPMA and SIMS profiles. Formulas of EPMA analyses are calculated to 8 oxygens.
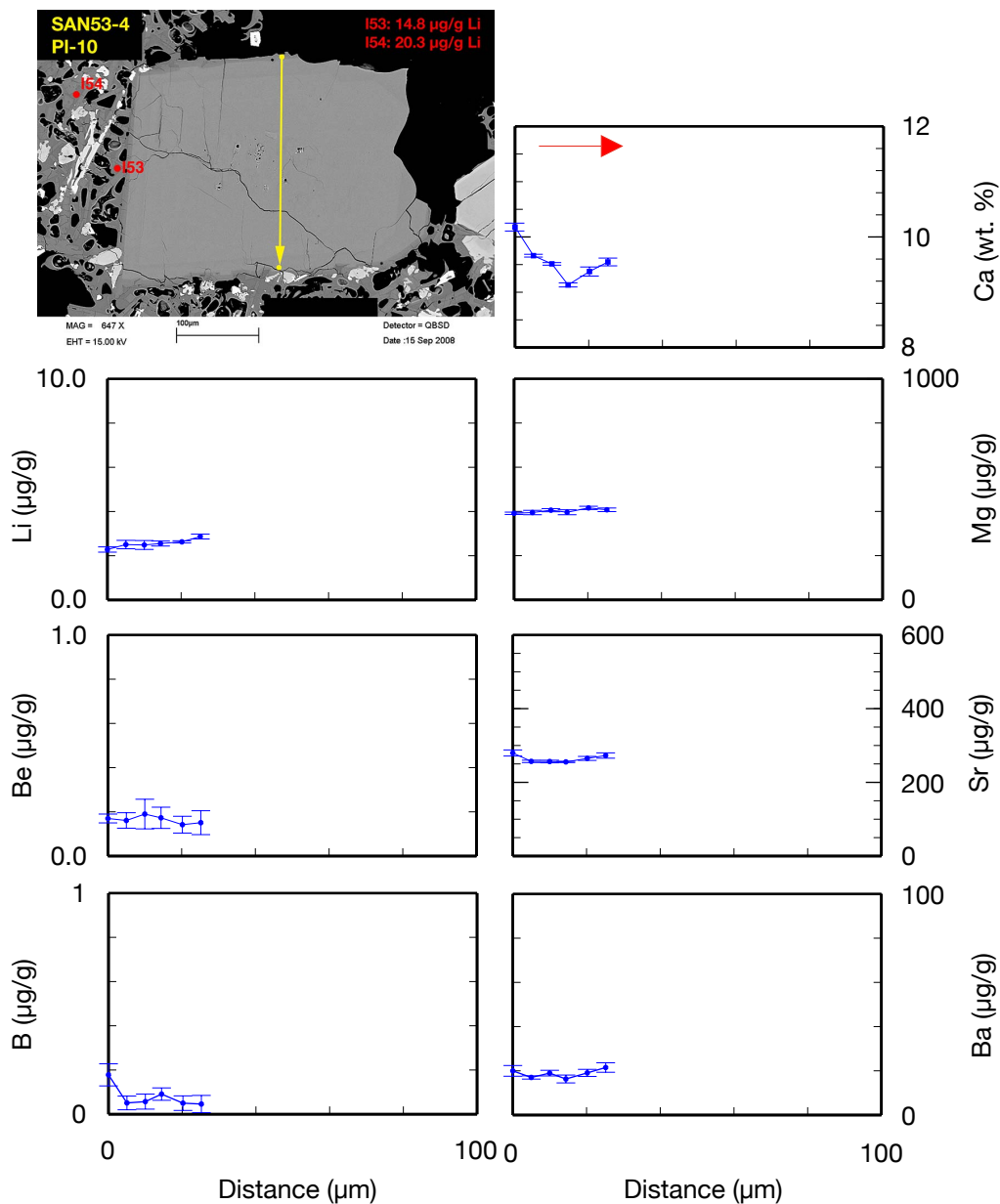
Fig. B.105. SAN53-4: Pl-10. A short SIMS profile was analyzed to detect or exclude diffusion of Li from glass selvages or broken rims into plagioclase.
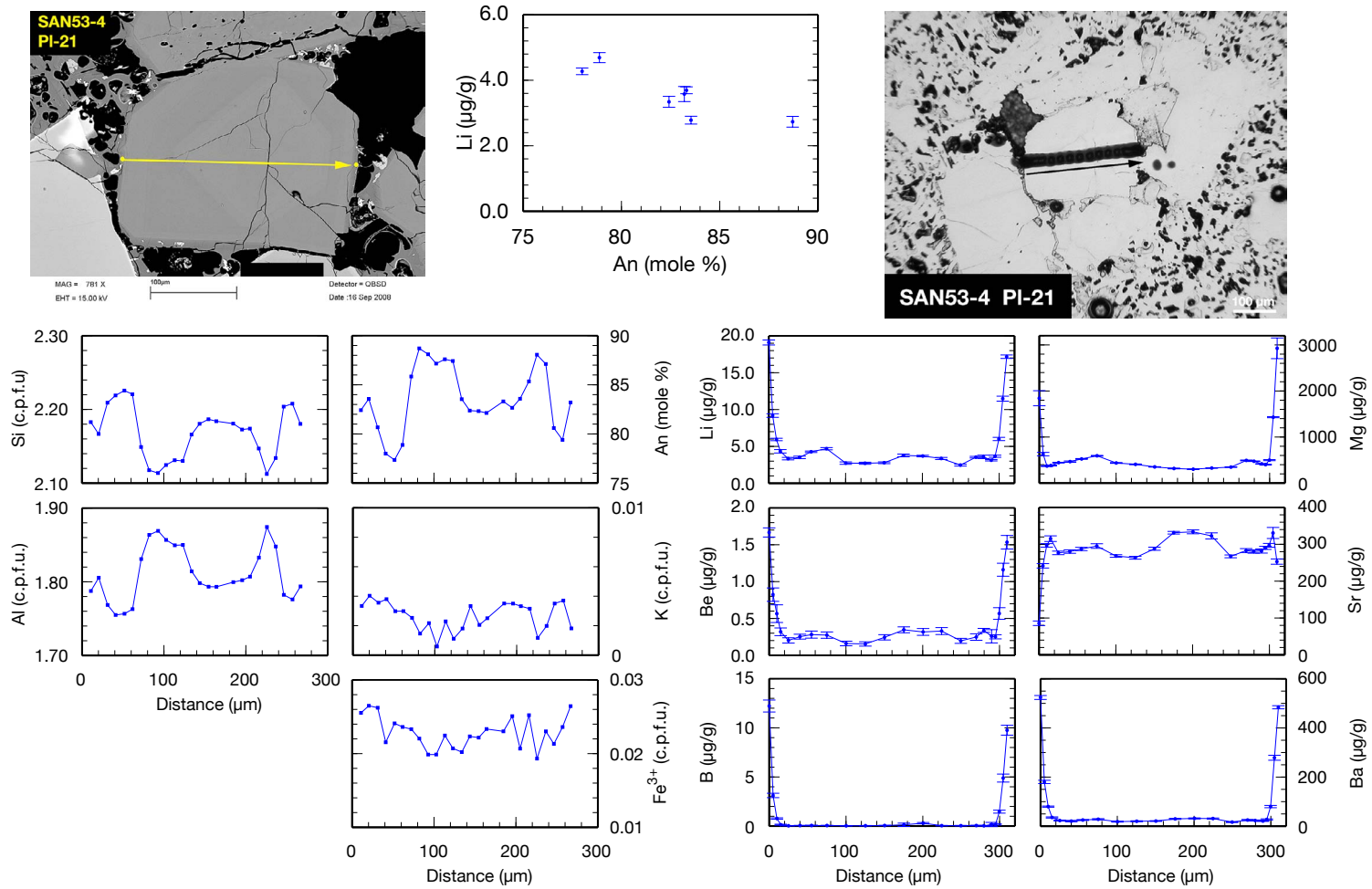
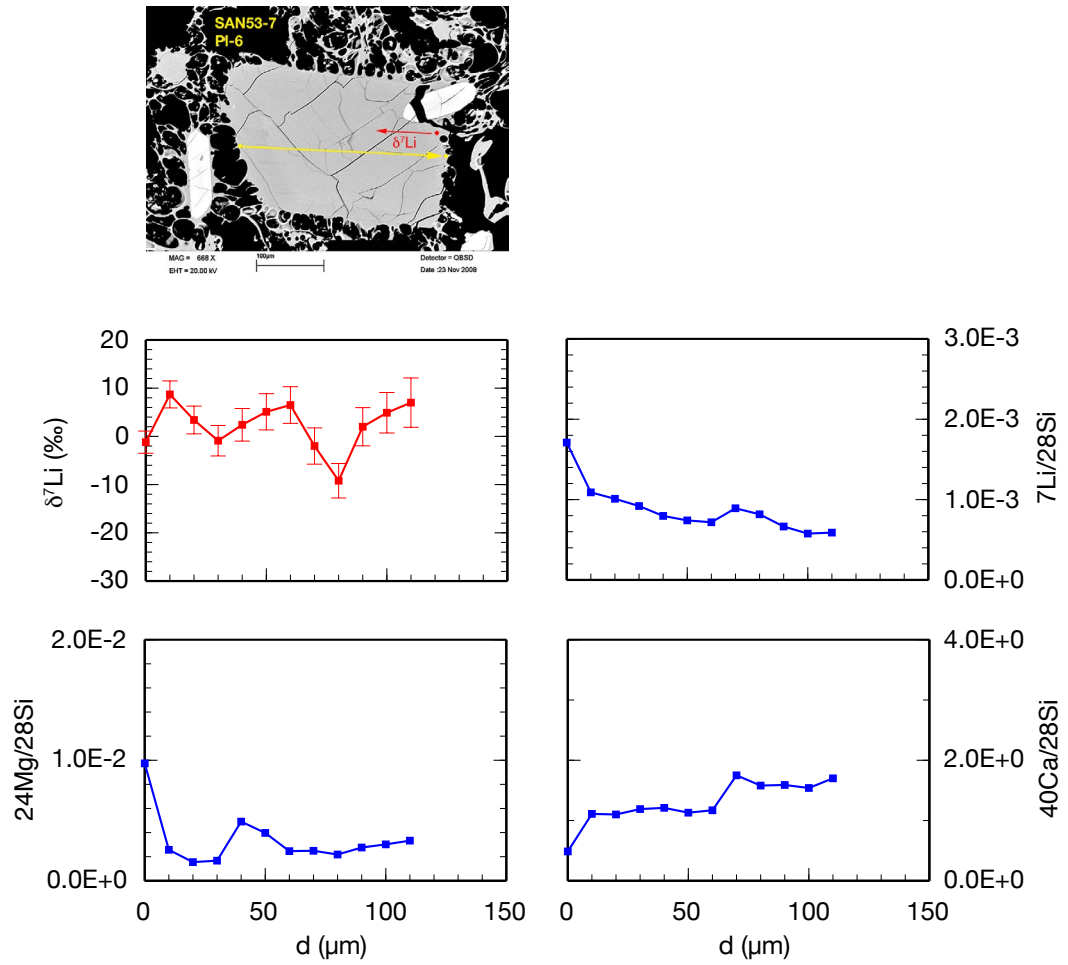**Fig. B.106.** SAN53-4: Pl-21. EPMA and SIMS profiles. Formulas of EPMA analyses are calculated to 8 oxygens.
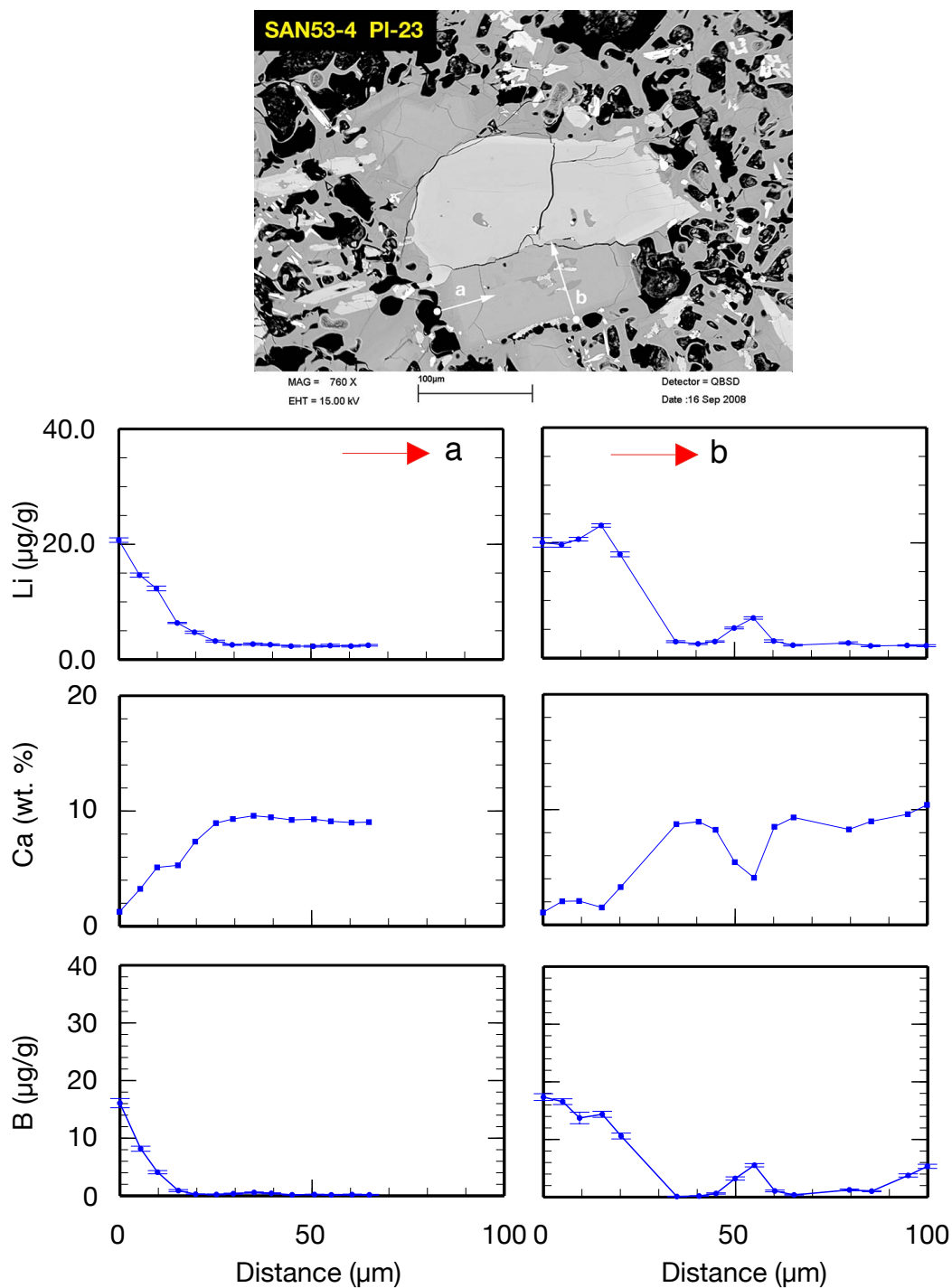
Fig. B.107. SAN53-4: Pl-23. A short SIMS profile was analyzed to detect or exclude diffusion of Li from glass selvages or inclusions into plagioclase.
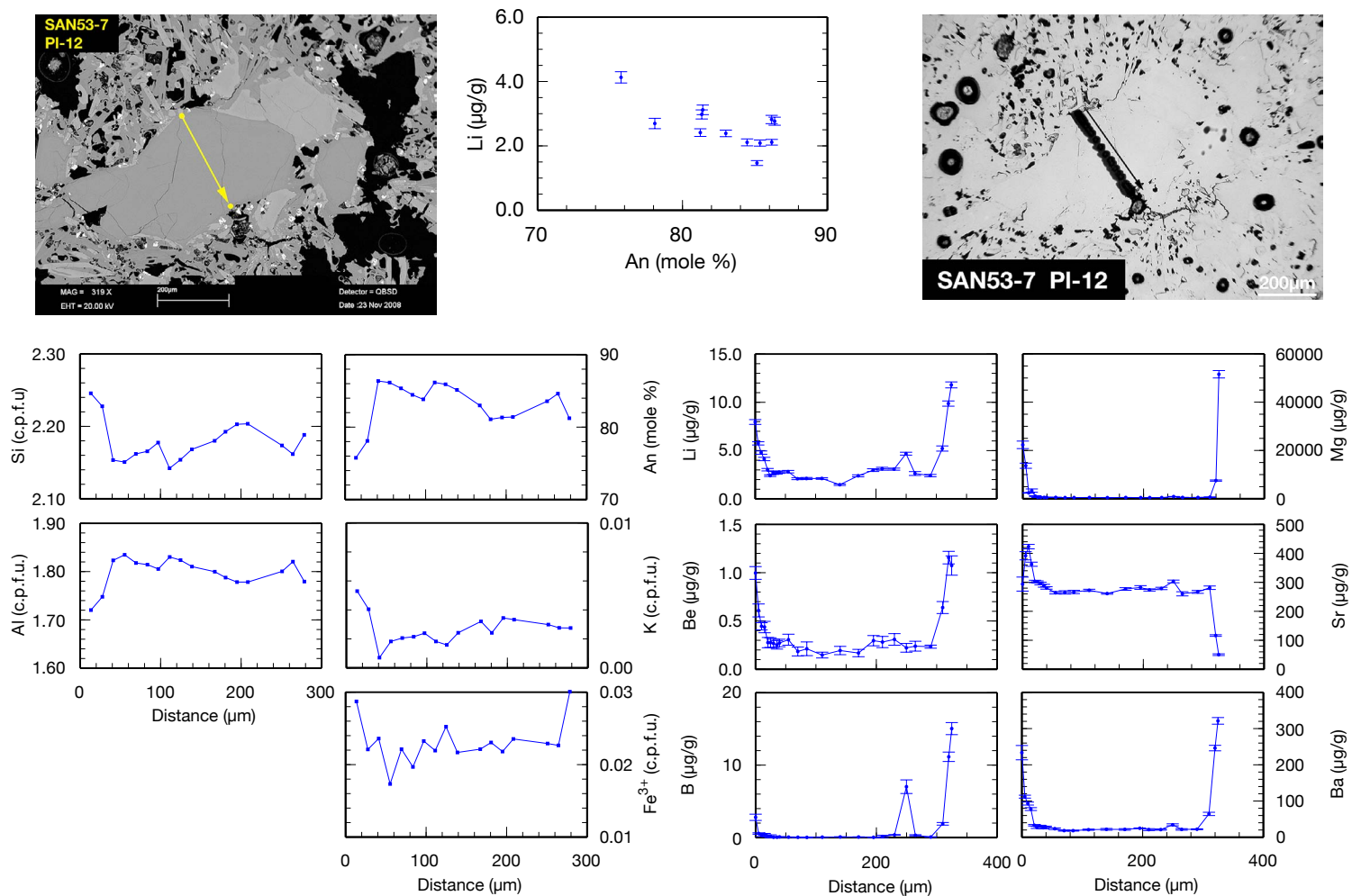
Fig. B.108. SAN53-4: Pl-25. EPMA and SIMS profiles. Formulas of EPMA analyses are calculated to 8 oxygens.

Fig. B.109. SAN53-5: Pl-3. EPMA and SIMS profiles. Formulas of EPMA analyses are calculated to 8 oxygens.

Fig. B.110. SAN53-5: Pl-14. EPMA and SIMS profiles. Formulas of EPMA analyses are calculated to 8 oxygens.

Fig. B.111. SAN53-5: Pl-14. A short SIMS profile was analyzed to detect Li concentrations in matrix adjacent to plagioclase.
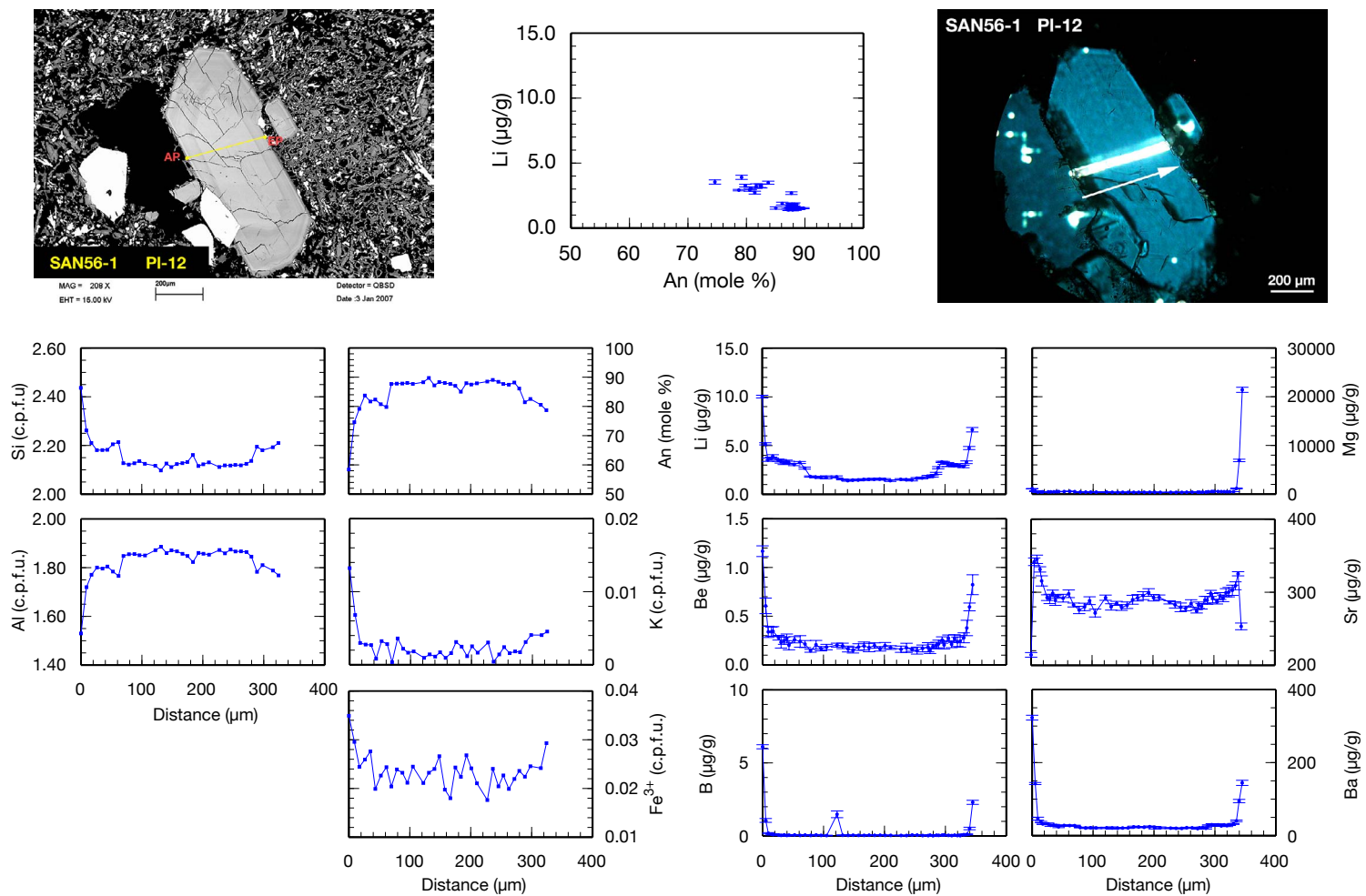
Fig. B.112. SAN53-5: Pl-18. EPMA and SIMS profiles. Formulas of EPMA analyses are calculated to 8 oxygens.

Fig. B.113. SAN53-6: Pl-11. EPMA and SIMS profiles. Formulas of EPMA analyses are calculated to 8 oxygens.

Fig. B.114. SAN53-6: Pl-11. A short SIMS profile was analyzed to detect Li concentrations in matrix adjacent to plagioclase.
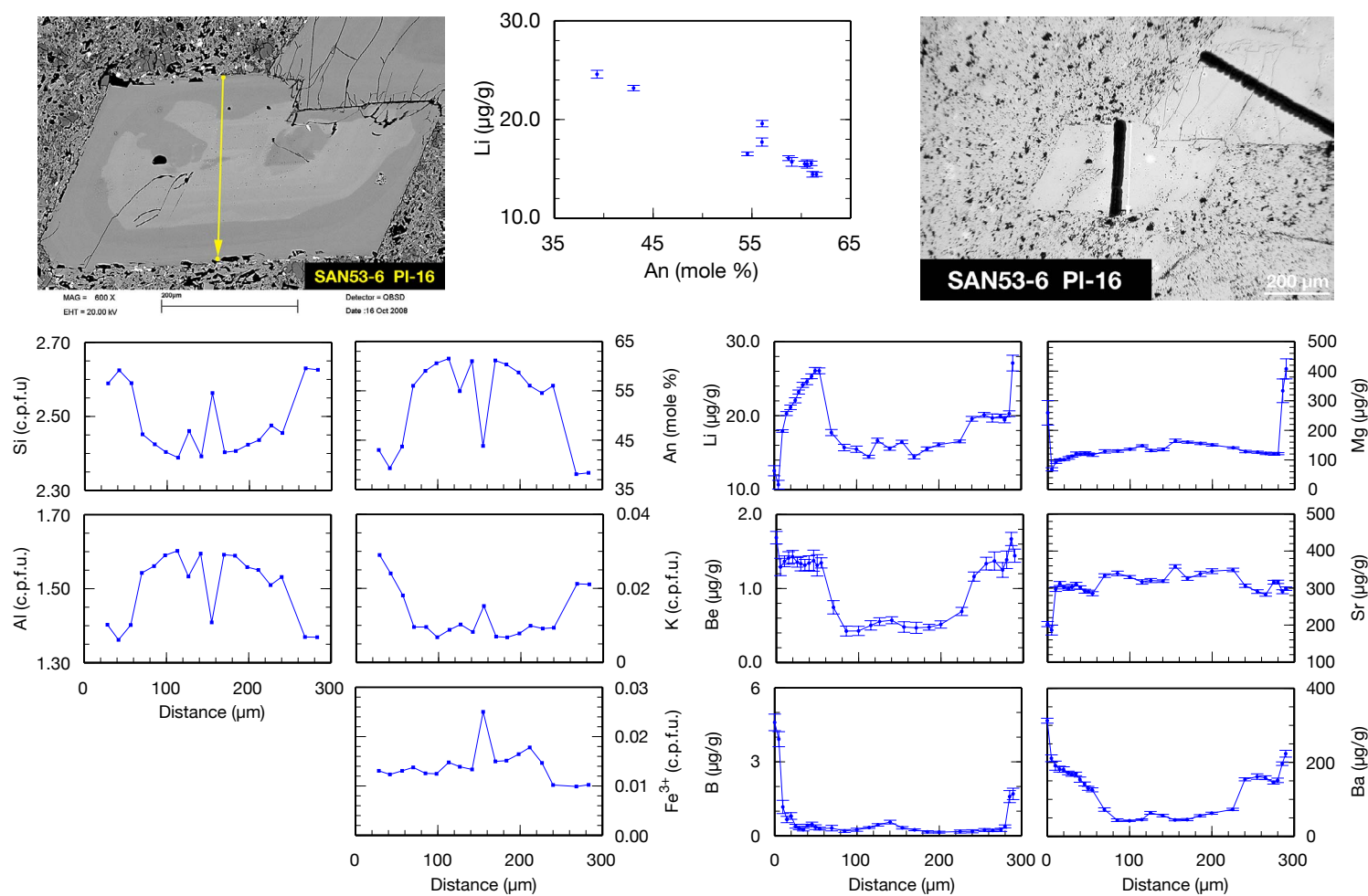
Fig. B.115. SAN53-6: Pl-16. EPMA and SIMS profiles. Formulas of EPMA analyses are calculated to 8 oxygens.
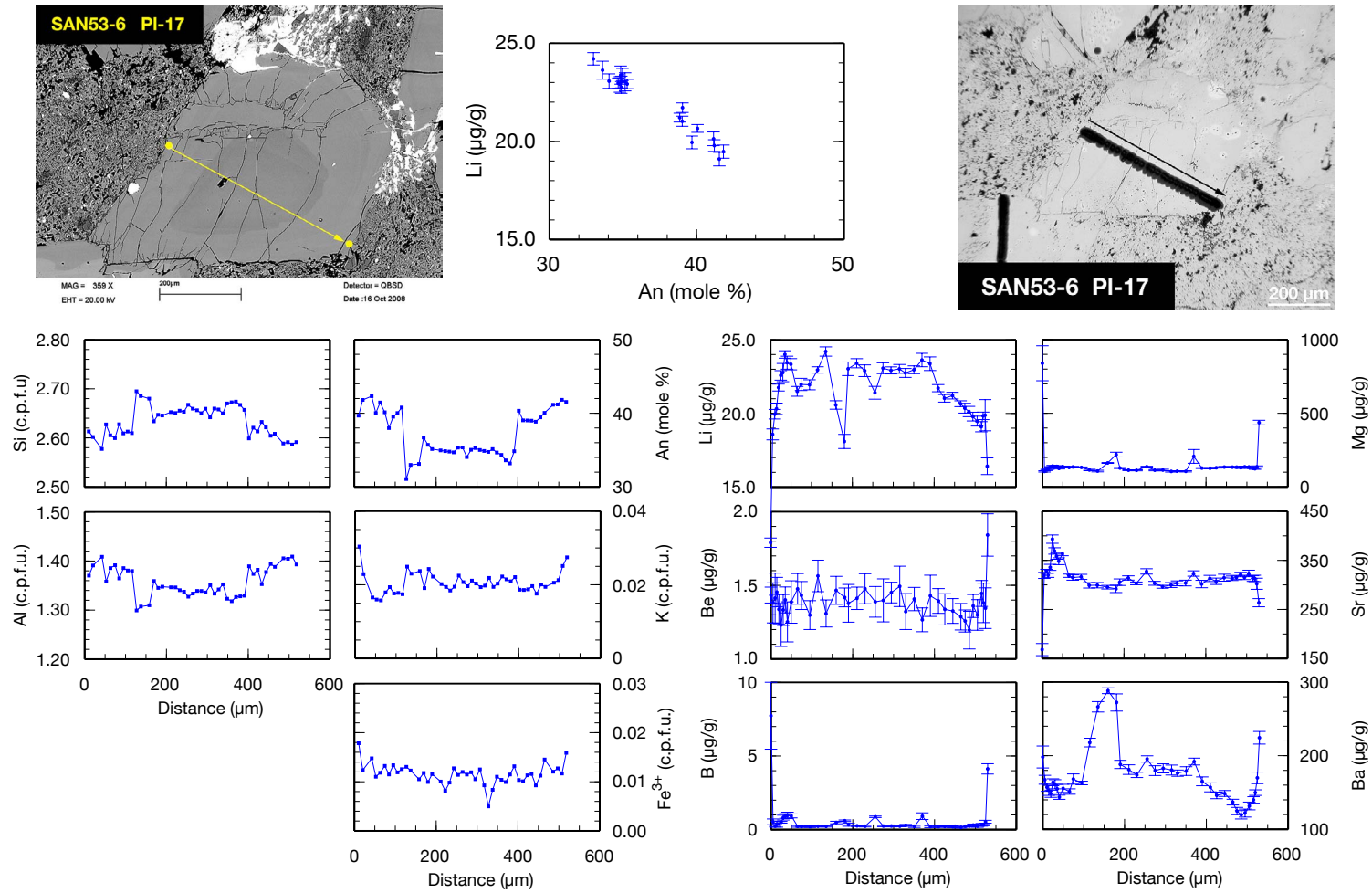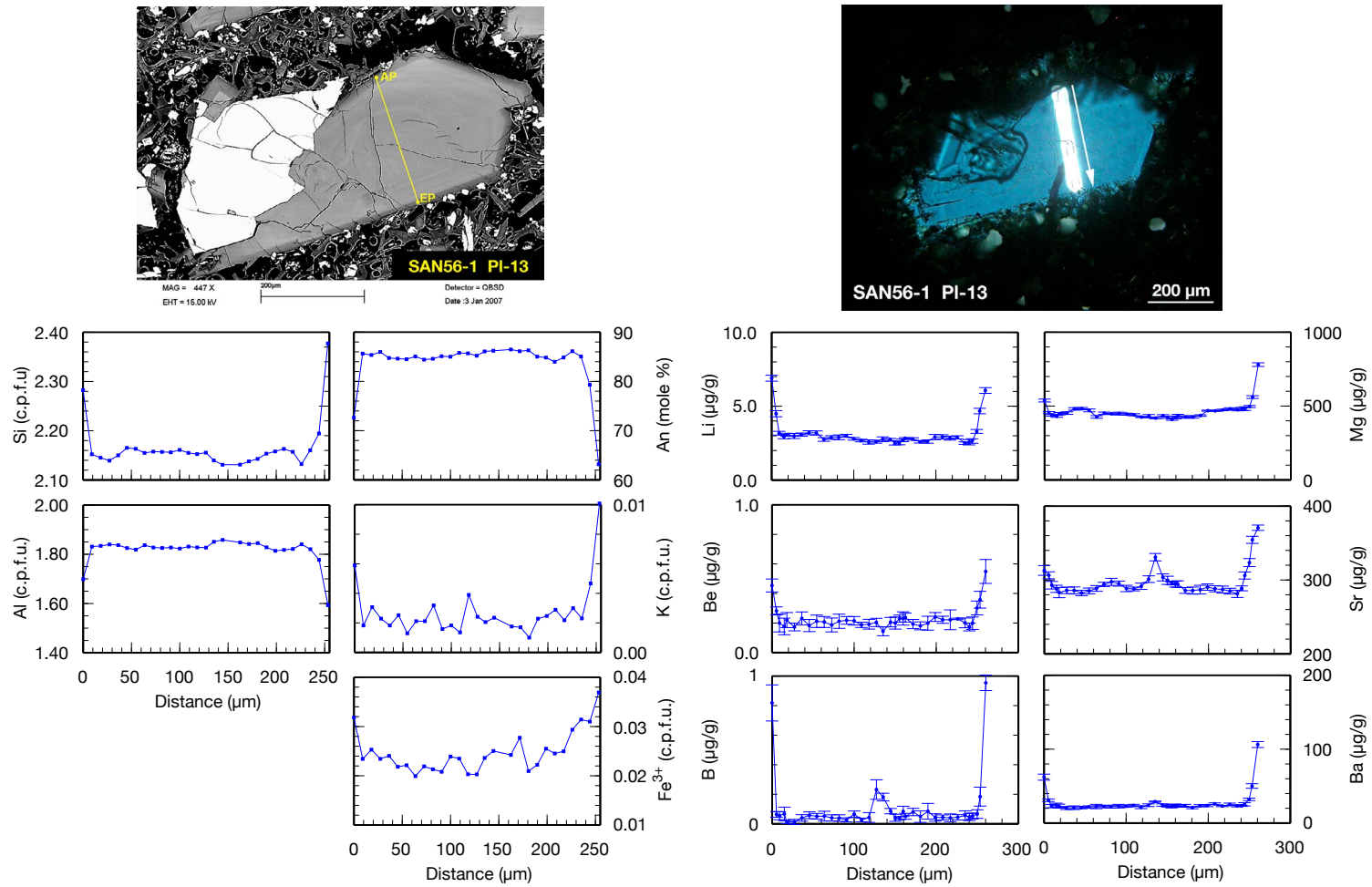
Fig. B.116. SAN53-6: Pl-17. EPMA and SIMS profiles. Formulas of EPMA analyses are calculated to 8 oxygens.
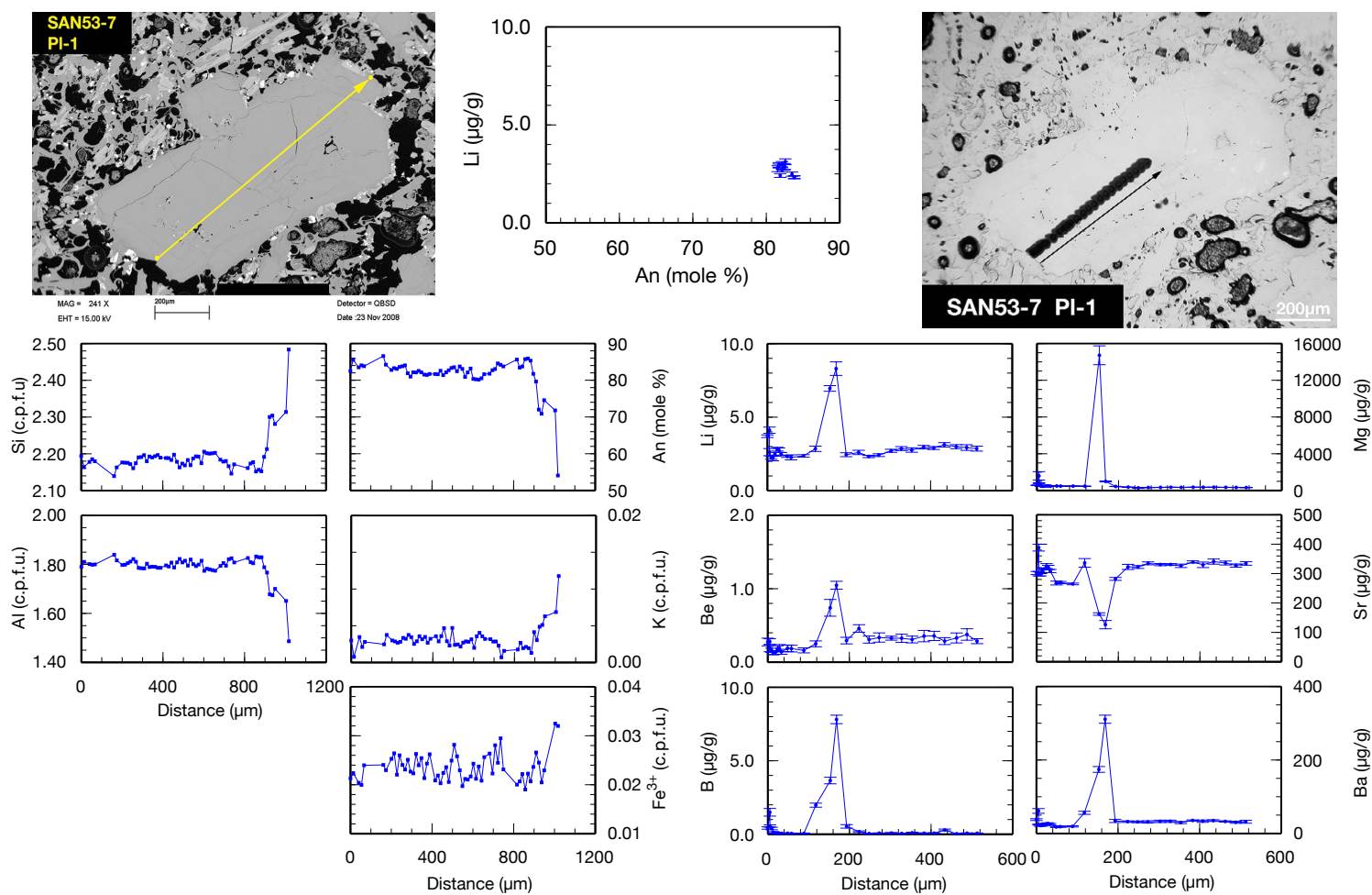
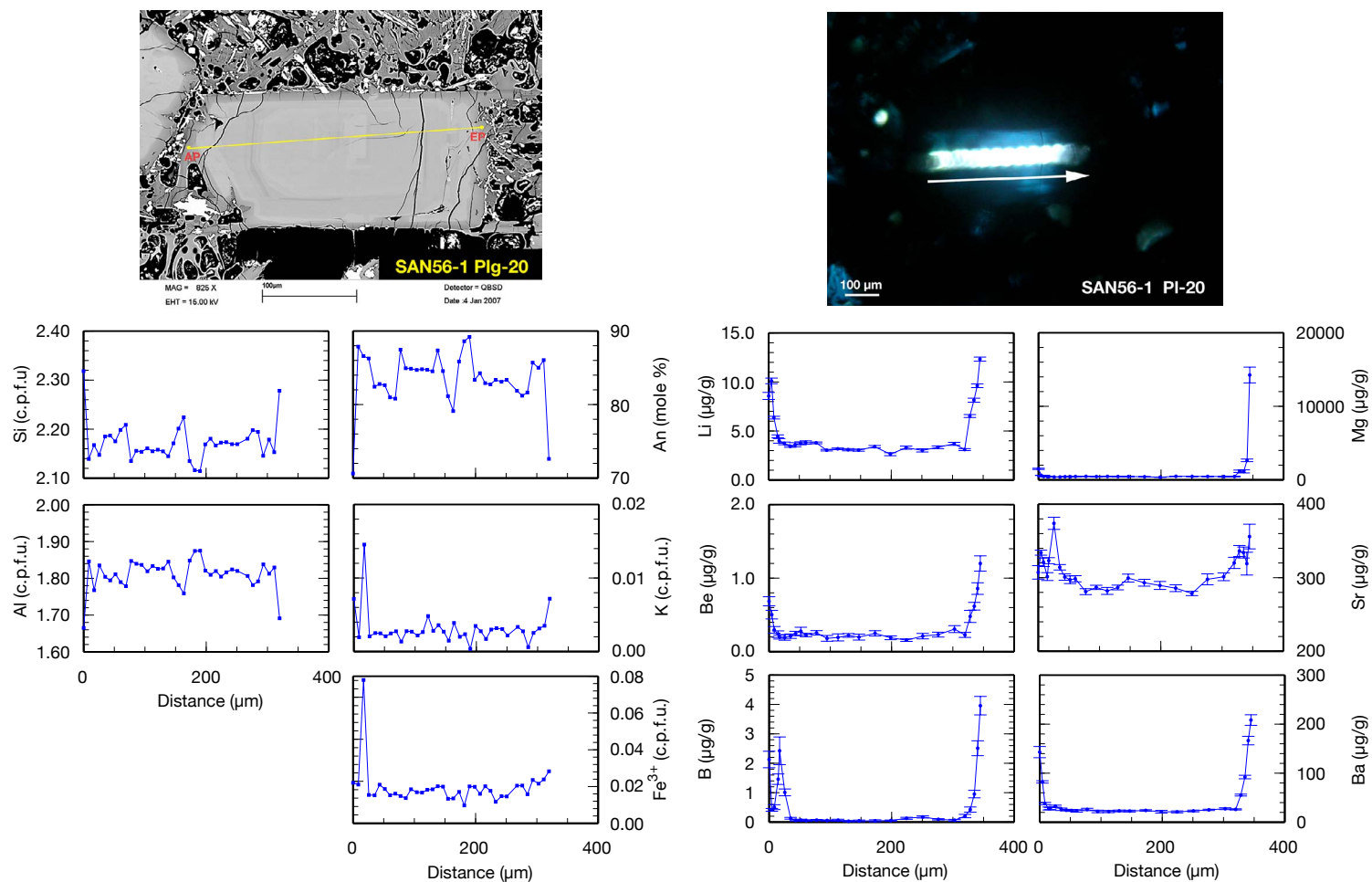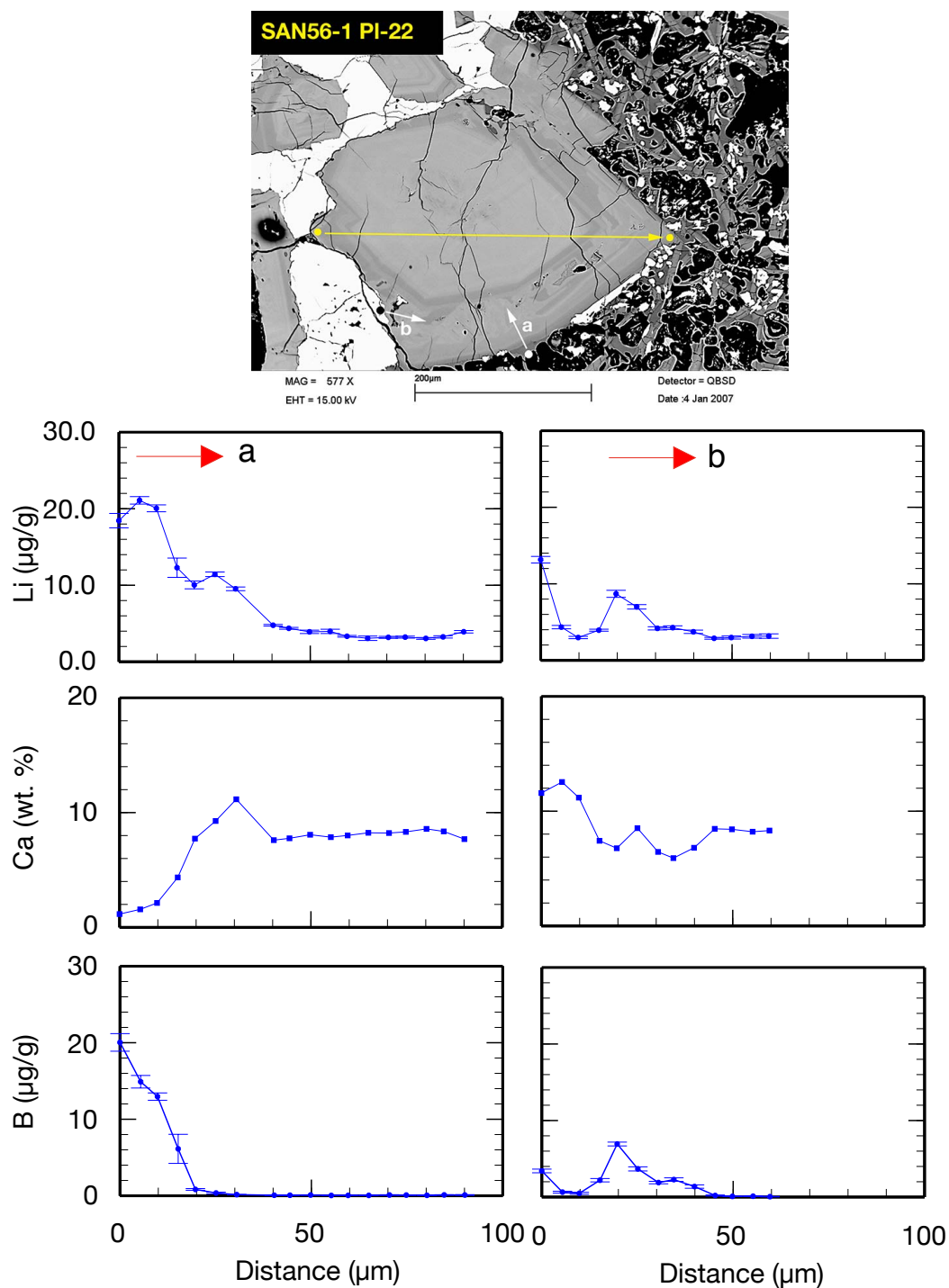**Fig. B.117.** SAN53-7: Pl-1. EPMA and SIMS profiles. Formulas of EPMA analyses are calculated to 8 oxygens.

Fig. B.118. SAN53-7: Pl-4. A short SIMS profile was analyzed to detect or exclude Li diffusion from broken rims into plagioclase.

Fig. B.119. SAN53-7: Pl-6. EPMA and SIMS profiles. Formulas of EPMA analyses are calculated to 8 oxygens.

Fig. B.120. SAN53-7: Pl-6. Short δ^7Li SIMS profile. The blue arrow marks the δ^7Li profiles; the red or white arrows mark the regular Li short profiles. A yellow arrow usually marks the EPMA profile (not all pl crystals were analyzed by EPMA). Li concentration values are derived from count rates of the isotope analyses and are therefore only semi-quantitative.

Fig. B.121. SAN53-7: Pl-12. EPMA and SIMS profiles. Formulas of EPMA analyses are calculated to 8 oxygens.
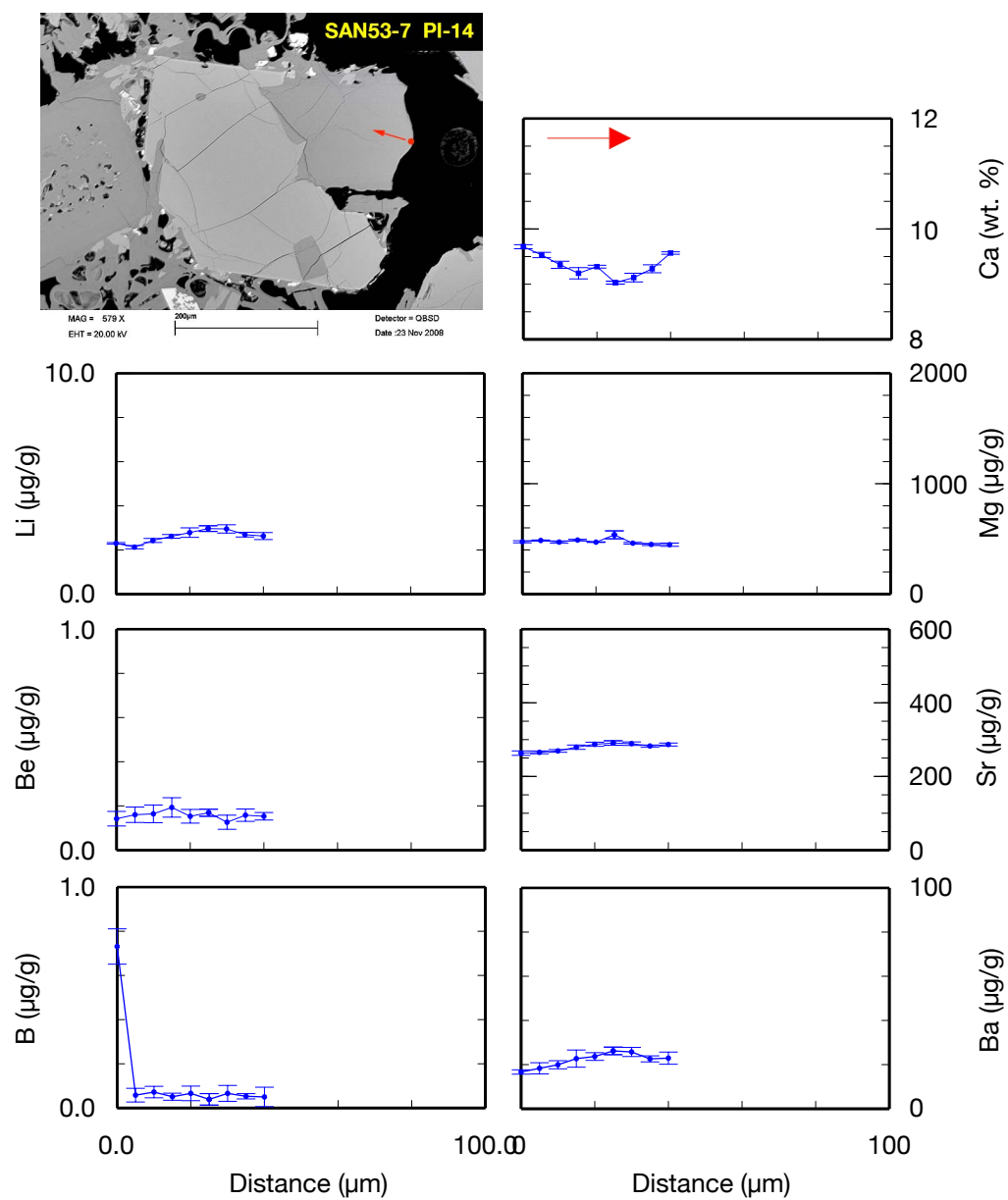
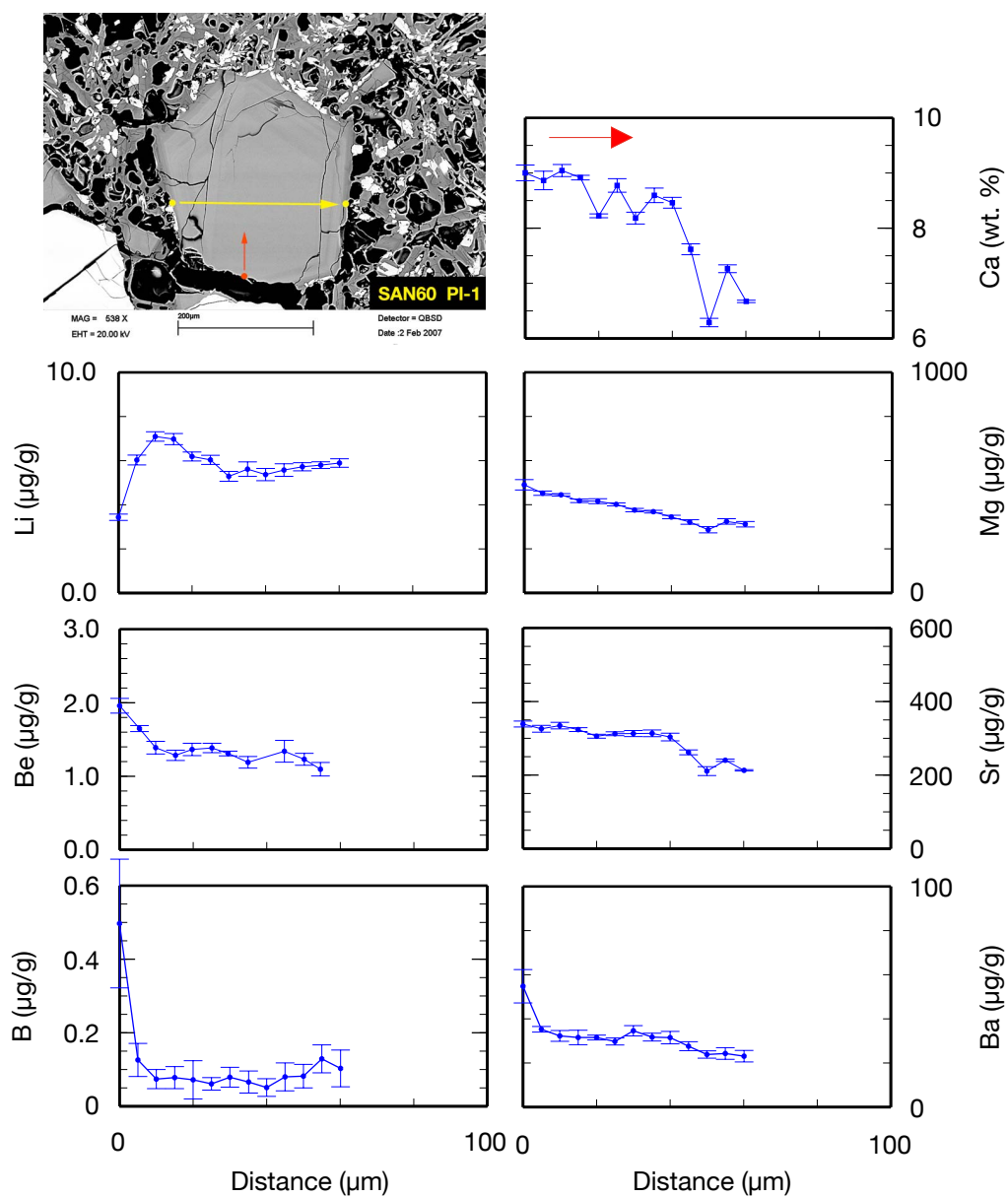**Fig. B.122.** SAN53-7: Pl-14. A short SIMS profile was analyzed to detect or exclude Li diffusion from broken rims into plagioclase.
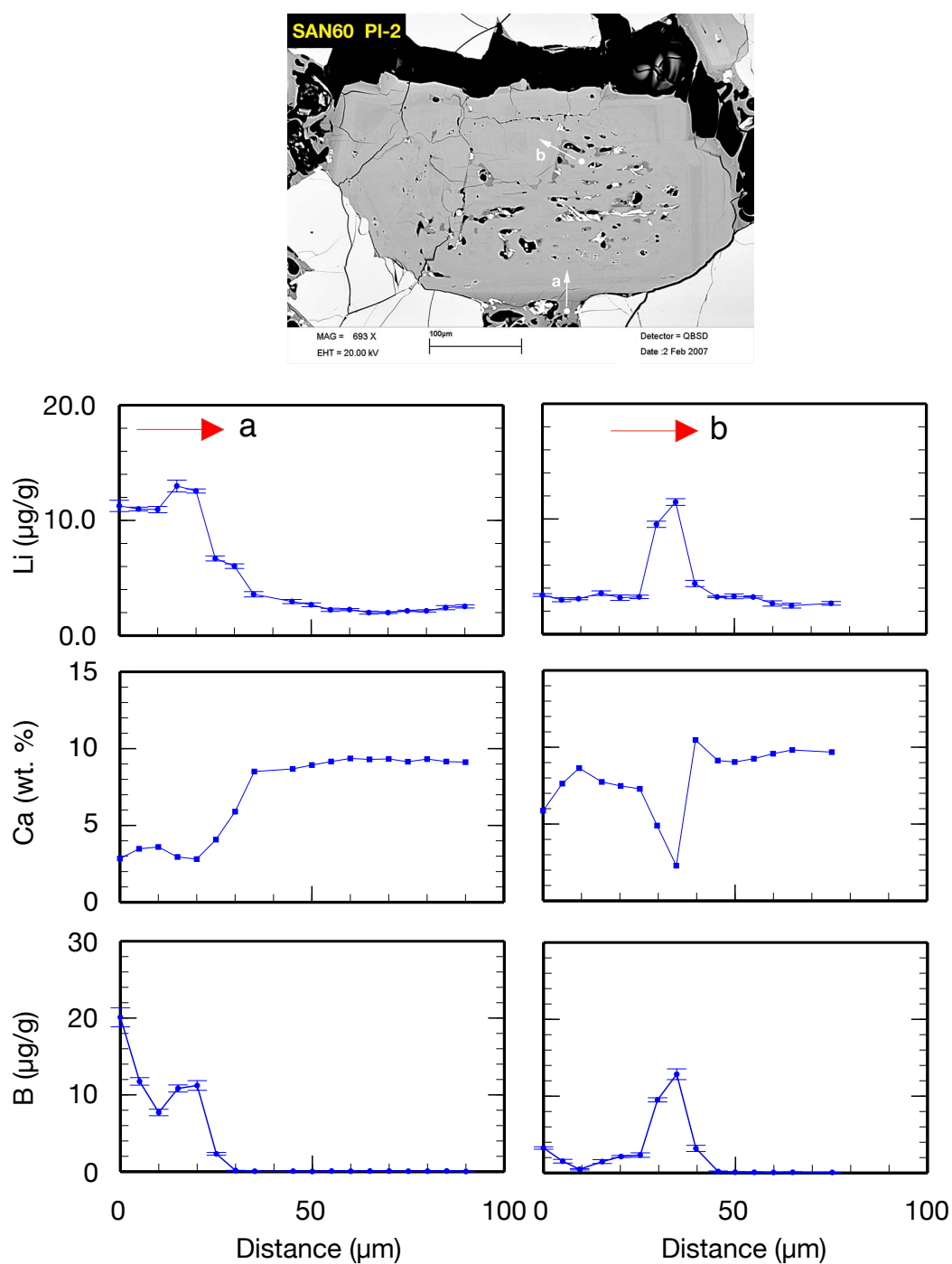
Fig. B.123. SAN56-1: Pl-12. EPMA and SIMS profiles. Formulas of EPMA analyses are calculated to 8 oxygens.

Fig. B.124. SAN56-1: Pl-13. EPMA and SIMS profiles. Formulas of EPMA analyses are calculated to 8 oxygens.

Fig. B.125. SAN56-1: Pl-20. EPMA and SIMS profiles. Formulas of EPMA analyses are calculated to 8 oxygens.

Fig. B.126. SAN56-1: Pl-22. A short SIMS profile was analyzed to detect or exclude diffusion of Li from glass selvages or inclusions into plagioclase.
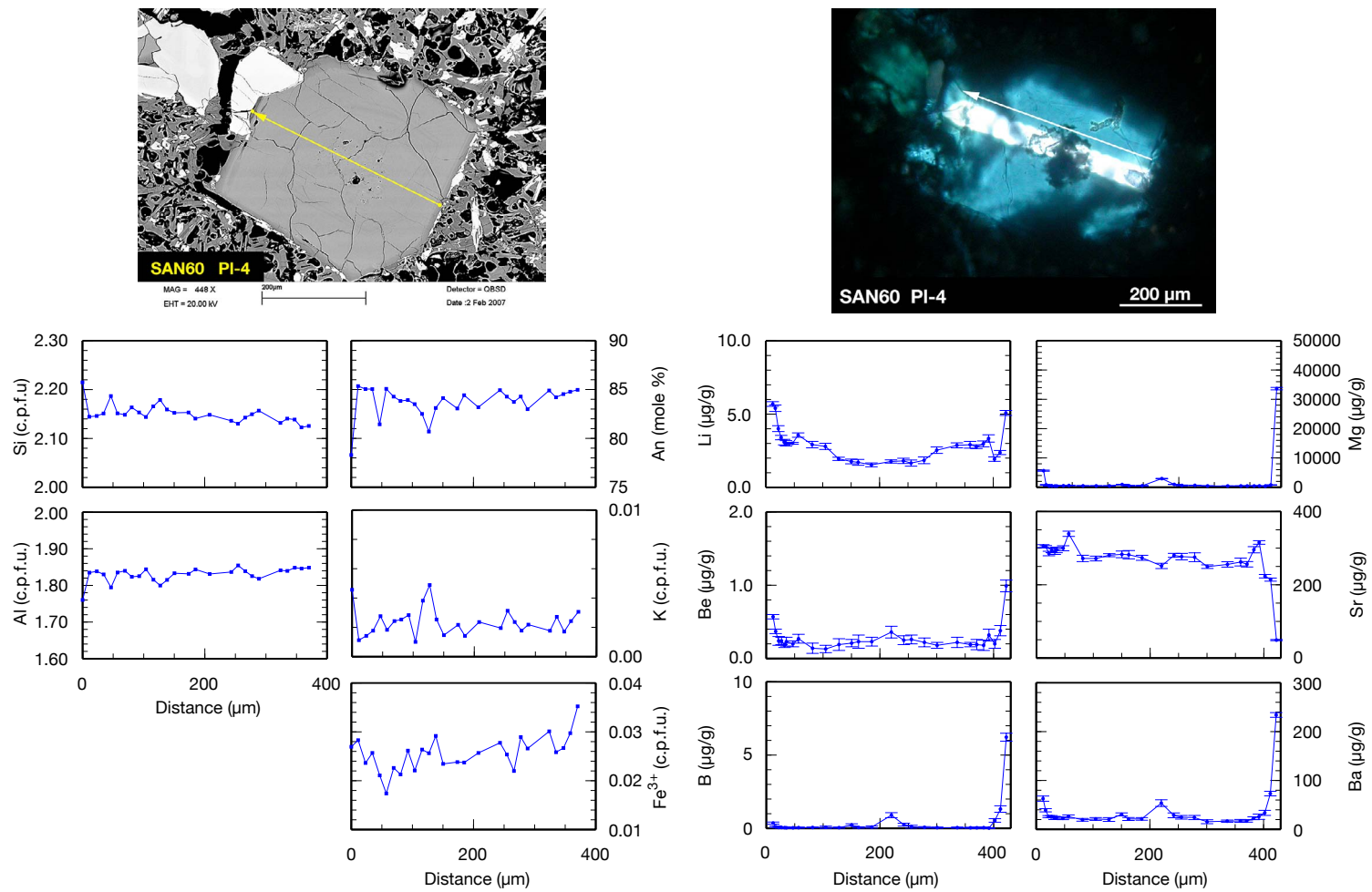
Fig. B.127. SAN60: Pl-1. A short SIMS profile was analyzed to detect or exclude Li diffusion from broken rims into plagioclase.

Fig. B.128. SAN60: Pl-2. A short SIMS profile was analyzed to detect or exclude diffusion of Li from glass selvages or inclusions into plagioclase.

Fig. B.129. SAN60: Pl-4. EPMA and SIMS profiles. Formulas of EPMA analyses are calculated to 8 oxygens.
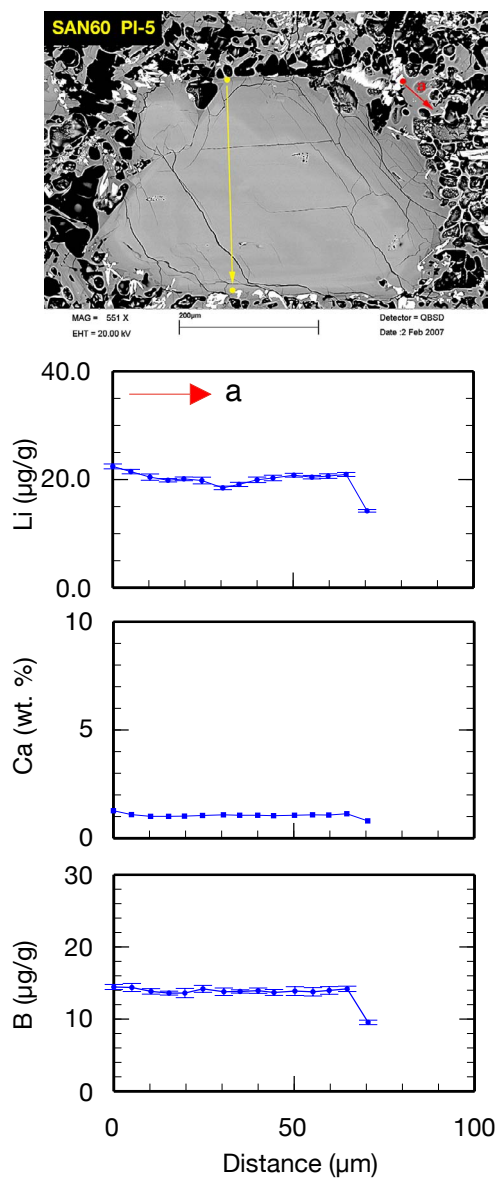
Fig. B.130. SAN60: Pl-5. A short SIMS profile was analyzed in matrix glass adjacent to plagioclase.
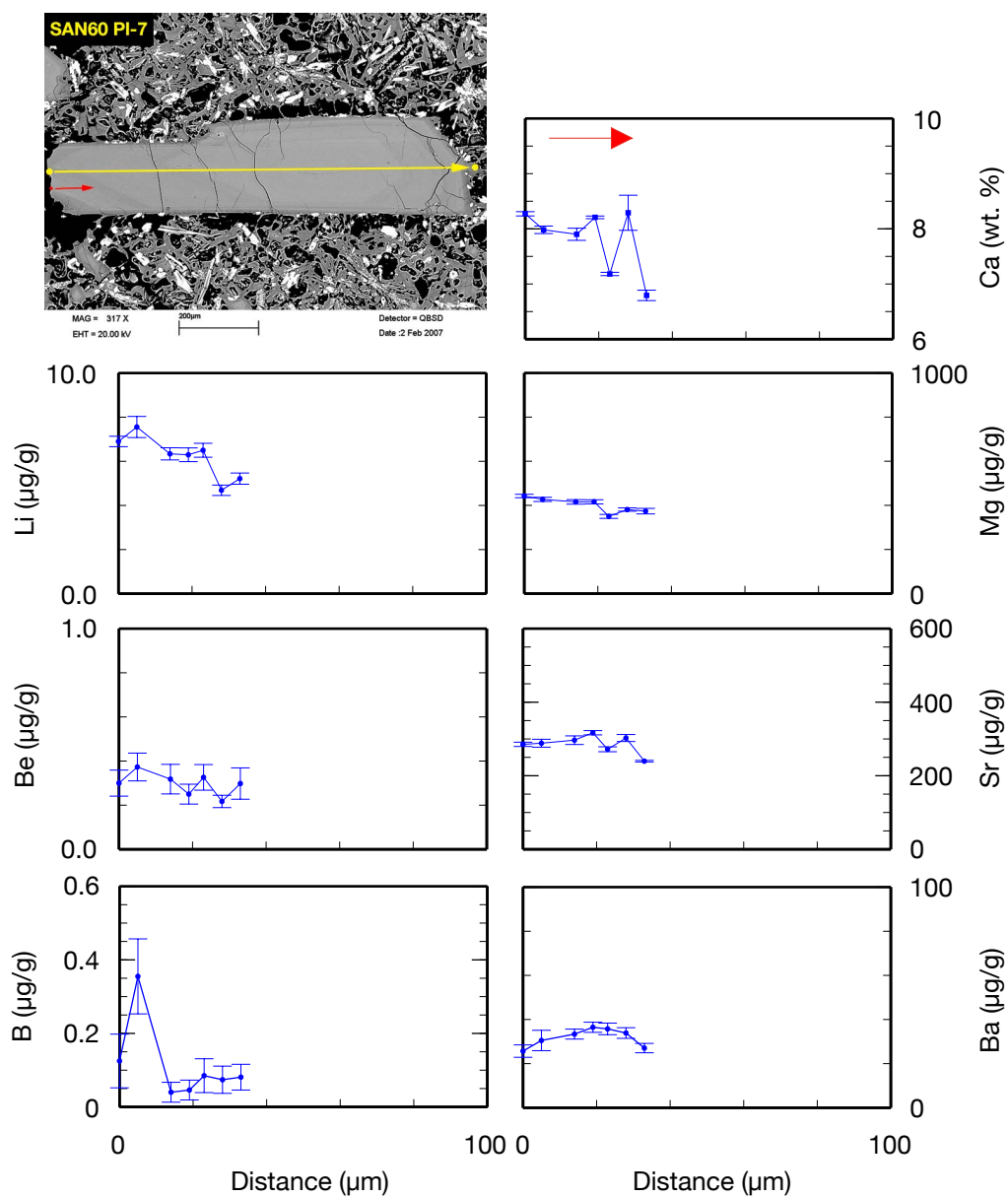
Fig. B.131. SAN60: Pl-7. A short SIMS profile was analyzed to detect or exclude Li diffusion from broken rims into plagioclase..
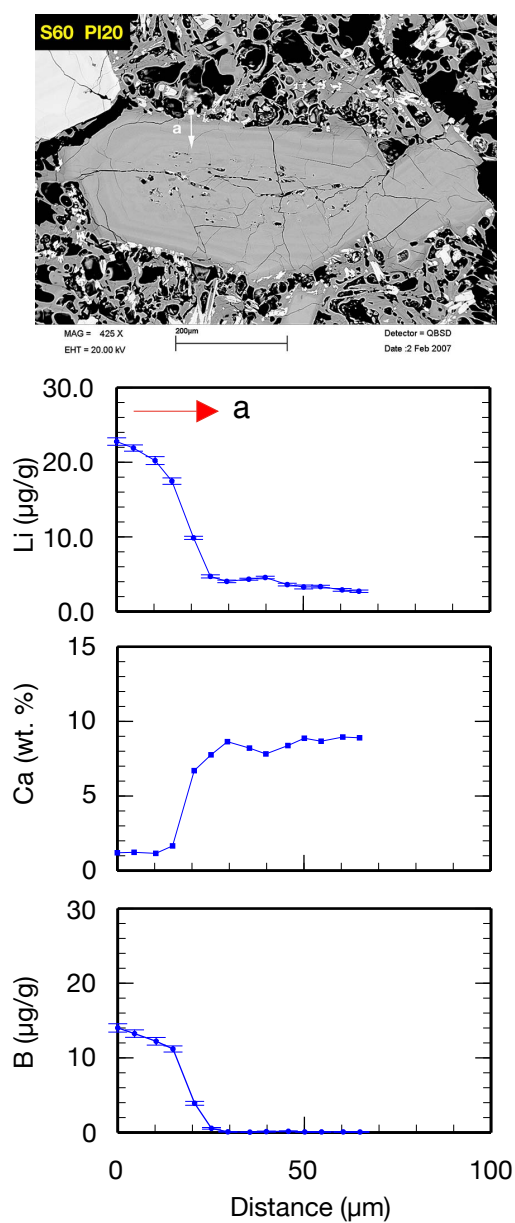
Fig. B.132. SAN60: Pl-20. A short SIMS profile was analyzed to detect or exclude diffusion of Li from glass selvages into plagioclase.
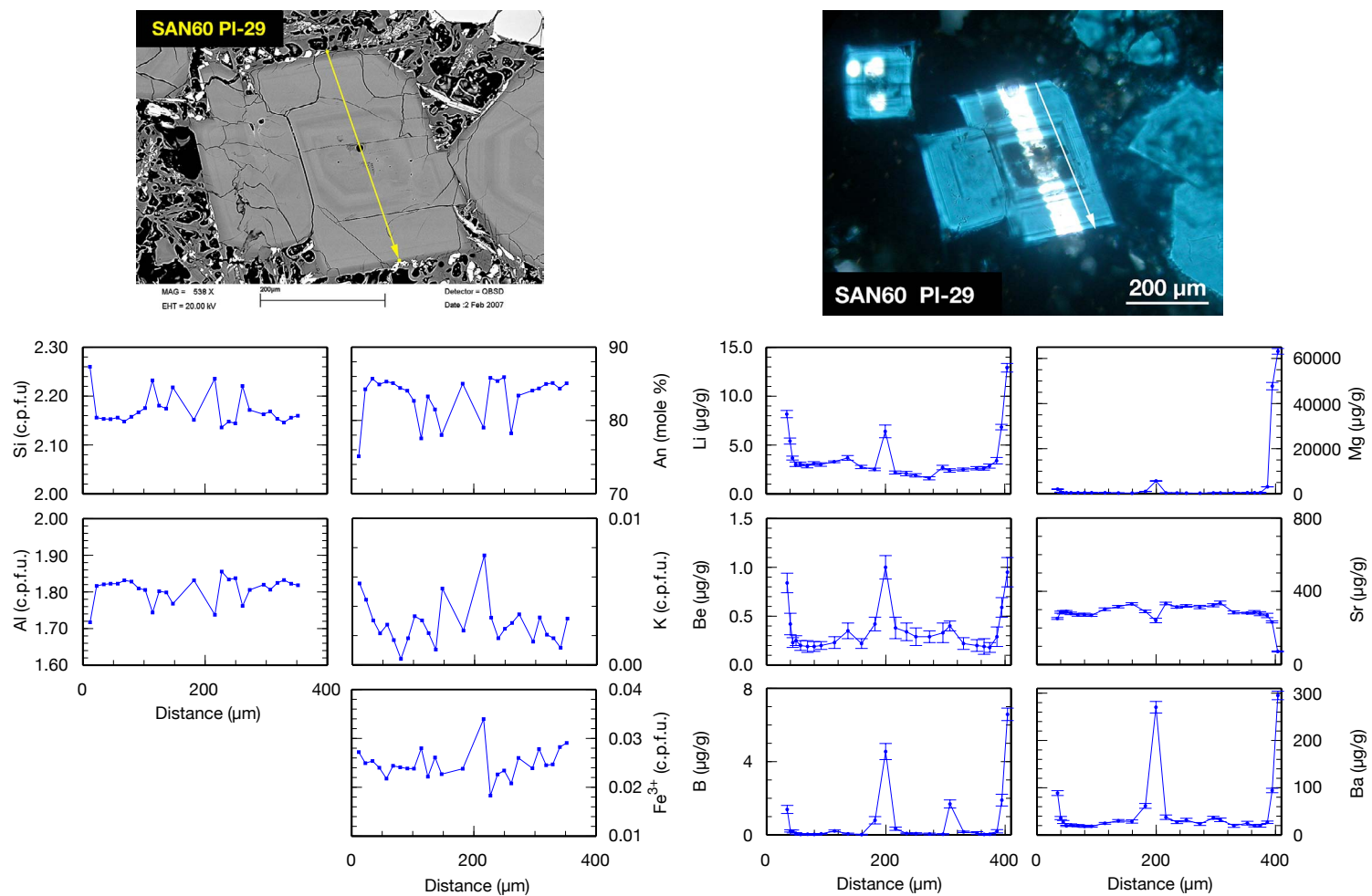
Fig. B.133. SAN60: Pl-29. EPMA and SIMS profiles. Formulas of EPMA analyses are calculated to 8 oxygens.

C. Danksagung

Ich danke Prof. Rainer Altherr dafür, dass er mir mit der Minoischen Eruption ein spannendes Thema für meine Doktorarbeit zur Verfügung gestellt hat. Ich danke ihm auch dafür, dass er mir alle Freiheiten für die Entwicklung eigener Ideen gelassen hat und ich meinen Dickkopf immer durchsetzen durfte.

Thomas Zack danke ich dafür, dass er sich bereit erklärt hat das Zweitgutachten zu übernehmen und hoffe, dass ihm das mysteriöse Verhalten von Lithium noch wohl bekannt ist.

Ich danke Thomas Ludwig für die angenehme und zuverlässige Betreuung an REM und SIMS und dafür, dass er immer für alle Fragen während der Entstehungsgeschichte dieser Arbeit offen war, auch wenn uns die Diskussionen um das Verhalten von Lithium manchmal in den Wahnsinn getrieben haben. Wenn es ein Problem gab, war er immer zur Stelle und hat mit viel konstruktiver Kritik zum Gelingen der Doktorarbeit beigetragen.

Peter Meyer danke ich für die freundliche Betreuung an der EMS, den vielen wertvollen Tipps beim Erstellen der Vorlagen für die Formelberechnung und dem Umgang mit den Daten, wenn eine Messung mal nicht so perfekt gelaufen ist. Und natürlich danke für die schöne Adventsmarktzeit.

Ilona Fin und Oliver Wienand sei für die sorgfältige Vorbereitung meiner Proben gedankt.

Michael Hanel danke ich dafür, dass er mir seine schönen Santorini-Fotos für die Arbeit zur Verfügung gestellt hat und er sich die Zeit genommen hat, meine Proben beim gemeinsamen Mikroskopieren ausführlich zu diskutieren.

Ich danke Iris Sonntag dafür, dass ich einen ihrer handgepickten Nisyros-Plagiklase für meine Arbeit entführen durfte.

Ansonsten danke ich allen Leidensgenossen, die sich mit mir ein Zimmer geteilt haben oder in den Nachbarzimmern mit Diplom- und Doktorarbeiten kämpften.

Ich danke vor allem aber meinem Freund Thomas, der mir in vielen Momenten zur Seite gestanden hat, auch wenn es vor allem mit der Gesundheit nicht immer gut lief. Mehr Unterstützung und Motivation hätte ich mir von ihm während dieser anstrengenden Zeit kaum wünschen können.

Meiner besten Freundin Maren danke ich für die vielen aufmunternden und lustigen Telefonate. Never go full retard!

Ich möchte mich auch bei meiner Familie bedanken, allen voran meiner Mut-

ter, die mich im Laufe meines Studiums nie im Stich ließ und bei meinem Bruder, dessen finanzielle Unterstützung mir vor allem während der Diplomarbeit geholfen hat das Studium überhaupt beenden zu können. Ohne diese Hilfe wäre eine Doktorarbeit letztendlich nicht möglich gewesen.

Den Freunden und Aktiven der NABU-Gruppe Heidelberg danke ich dafür, dass sie mich geduldig vertreten haben, wenn ich wegen der Doktorarbeit mal nicht zur Stelle war.

In diesem Sinne noch einmal ein dickes Dankeschön an alle - auch an diejenigen, die hier vielleicht vergessen wurden!

D. Eidesstattliche Erklärung

Hiermit erkläre ich, Sandra Panienka, geboren am 11.07.1978 in Marburg an der Lahn, an Eides statt, dass ich die vorliegende Dissertation selbst verfasst und mich dabei keiner anderen als der von mir ausdrücklich bezeichneten Quellen und Hilfen bedient habe.

Ich, Sandra Panienka, geboren am 11.07.1978 in Marburg an der Lahn, erkläre zudem an Eides statt, dass ich an keiner anderen Stelle ein Prüfungsverfahren beantragt habe, dass ich die Dissertation nicht in dieser oder anderer Form bereits anderweitig als Prüfungsarbeit verwendet habe und dass ich sie an keiner anderen Fakultät als Dissertation vorgelegt habe.

Heidelberg, den 21.11.2011